Universidade do Minho
I3Bs - Instituto de Investigação em Biomateriais,
Biodegradáveis e Biomiméticos

Carlos Ferreira Guimarães

Microfluidic Hydrogel Biofabrication for High-Throughput Screening, Modeling and Quantifying 3D Biological Phenomena

Janeiro de 2022

Microfluidic Hydrogel Biofabrication forHigh-Throughput Screening,
Modeling and Quantifying 3D Biological Phenomena
Carlos Ferreira Guimarães
UMinho | 2022

REPÚBLICA PORTUGUESA | CIÊNCIA, TECNOLOGIA E ENSINO SUPERIOR
FCT Fundação para a Ciência e a Tecnologia
UNIÃO EUROPEIA Fundo Social Europeu

Universidade do Minho

I3Bs - Instituto de Investigação em Biomateriais, Biodegradáveis e Biomiméticos

Carlos Ferreira Guimarães

Microfluidic Hydrogel Biofabrication for High-Throughput Screening, Modeling and Quantifying 3D Biological Phenomena

Tese de Doutoramento

Doutoramento em Engenharia de Tecidos, Medicina Regenerativa e Células Estaminais

Trabalho efetuado sob a orientação

Professor Doutor Rui Luís Gonçalves dos Reis

Janeiro de 2022

DIREITOS DE AUTOR E CONDIÇÕES DE UTILIZAÇÃO DO TRABALHO POR TERCEIROS

Este é um trabalho académico que pode ser utilizado por terceiros desde que respeitadas as regras e boas práticas internacionalmente aceites, no que concerne aos direitos de autor e direitos conexos.

Assim, o presente trabalho pode ser utilizado nos termos previstos na licença abaixo indicada.

Caso o utilizador necessite de permissão para poder fazer um uso do trabalho em condições não previstas no licenciamento indicado, deverá contactar o autor, através do RepositóriUM da Universidade do Minho.

Licença concedida aos utilizadores deste trabalho



Atribuição

CC BY

https://creativecommons.org/licenses/by/4.0/

ACKNOWLEDGMENTS

In 1675, Isaac Newton penned a letter to his fellow scientist Robert Hooke, in which he claimed that if he had seen any further, it was only so due to standing upon the shoulders of giants. If I am allowed the (very humble) comparison, this work was only possible due to all the giants that were part of my Ph.D. journey, and acknowledgements are in order, even if shortened by the 1-page thesis limit (sorry!).

To prof. Rui Reis, an acknowledgement in 3 parts (one for each B). First, for taking me as his Ph.D. student, when I had barely finished my master's, giving me a chance to pursue a science path in 3B's, and in my favorite city, Guimarães. Second, for believing and challenging me to go far beyond norm – it taught me that anything is possible if we work hard for it. Third, and probably most important, for giving me the freedom to explore my own ideas, no matter how crazy, and supporting me in their pursuit. The scientific freedom I was given is a rare privilege, which I will always treasure above everything else!

My journey in 3B's would also not work without the support of Alexandra Marques, and her team. Thank you for all the scientific input and advice, and sorry for all the long text reviews! I have thoroughly enjoyed discussing science and always learned a lot from it. To Luca Gasperini, my fellow microfluidics warrior, who taught me the tricks of the trade: Here's to all the long confocal sessions, and even longer conference nights! To my deskmate and partner in crime, Daniel "DPK"! And to the big 3B's family – you ALL impacted me in a way or another. To all the PhD students who came before and after - we are a fierce species! A shout out to the PhDynamics initiative, past and present members, stuff of legend.

To the BAMM Fam at Stanford! To prof. Utkan Demirci, for accepting me in his group in the craziest year of my life, amidst a full blown pandemic upon arrival at the USA. Thank you for the early support, and all the lessons in science, scholarly development, and grantsmanship. I have never learned so much in a single year! To Fernando, Rajib, Jie, and Ricky, which were my family far from home. I won't forget the city trips, crab fishing expeditions, camping madness, and all the impromptu meal parties!

To my dear old friends, who somehow stuck around for years and are fortunately too many to name here in person – those from Império dos Jabardos, Decanos de Abade, and H3 - thank you all so much!

To Sara, who has been by my side through a large chunk of this wild journey, while simulatenously dealing with her own Ph.D. – thank you for your care, support, help, and for being there for the ups and downs, even when we were forced to live so far apart! I will never forget it.

Finally, and foremost, to my family, who have supported me unconditionally since the beginning of times, and without whom I would be nothing at all. There just aren't enough pages in this whole thesis to thank them, but they know what I mean!

This work was funded by the Portuguese FCT, PhD Scholarship PD/BD/135253/2017 and Exceptional COVID Scholarship COVID/BD/152016/2021.

STATEMENT OF INTEGRITY

I hereby declare having conducted this academic work with integrity. I confirm that I have not used plagiarism or any form of undue use of information or falsification of results along the process leading to its elaboration.

I further declare that I have fully acknowledged the Code of Ethical Conduct of the University of Minho.

ABSTRACT

The functionality of living tissues depends entirely on their intricate 3D composition, architecture, and mechanics, which result from the complex interplay between cells and ECM. Correctly approaching these characteristics will be fundamental to engineer next-generation platforms for *in vitro* modeling of healthy and diseased tissues. Further, the capacity to miniaturize 3D microenvironments for faster **composition screening** and discovery will also be critical to benefit from the ever-growing toolbox of 3D hydrogels and tissue-like cues that can be integrated into engineered constructs. Within that arena, microfluidic biofabrication is a potent tool to miniaturize 3D cell-laden hydrogel constructs. Still, these are only relevant as models if important tissue characteristics such as **3D cell/ECM architectures** are integrated. Additionally, the complexity of 3D models is only helpful if some tools and methodologies enable efficient and **reliable quantification** of ongoing biological events into measurable data. This thesis presents advances in all these critical perspectives, aiming for microfluidics to fabricate improved 3D platforms that can model, screen, and quantify biological events with unprecedented efficiency. Initially, we demonstrate how the microfluidic manipulation of hydrogel precursors can be employed to create 3D gradients with space-varying **mechanics** and material **composition**. Allied to automated single-cell screening, we show how optimal hydrogel formulations can be detected with **high-throughput** to elicit biological responses ranging from cell adhesion to the triggering of stem cell differentiation. Then, we explore how 3D flow-focusing microfluidics can introduce a plethora of **3D architectures** within hydrogel microfibers, using a single-chip, down to sub-50μm diameters. We demonstrate how different architectures can be combined with various cells and materials to **model 3D** cancer invasion, vascular tissue networks, or function as all-in-one tissue engineering platforms. Finally, multi-compartment hydrogel fibers are interfaced with light-guiding in polysaccharide-based optical fibers. These fibers can detect 3D mechanical deformations, the presence of biotargets of interest, and transport live cells while simultaneously guiding light. The living optical fibers are then used to convert complex biological events into **directly quantifiable** optical signals, tracking the 3D growth of a cancer fiberoid and revealing inhibitory drug thresholds with unprecedented efficacy. Overall, this thesis demonstrates the wide adaptability and capabilities of microfluidic-driven hydrogel biofabrication, presenting high-throughput for miniaturizing, modeling, and direct conversion of complex biological events into quantifiable data, with high potential for the future of precision and data-driven medicine approaches.

Keywords: Bioengineering; Biomaterials; Cancer; Microfluidics; 3D Tissue Models

RESUMO

A funcionalidade dos tecidos biológicos é totalmente dependente das suas características 3D, nomeadamente **composição, arquitetura, e mecânica**, que resultam da complexa interação entre células e matriz extracelular. Recapitular estas características *in vitro* será fundamental para criar as próximas plataformas para modelar tecidos saudáveis e doentes. Para além disso, a capacidade de miniaturizar microambientes 3D para uma mais rápida **análise e descoberta da composição ideal** será crítico para beneficiar da ampla lista de hidrogéis 3D e as suas modificações, em engenharia de tecidos. Nessa perspetiva, a biofabricação por microfluídica é uma ferramenta poderosa para miniaturizar estruturas de hidrogéis, mas estas só serão relevantes como modelos se capazes de integrar as importantes características dos tecidos, como a referida **arquitectura 3D em termos de células e matrizes**. Para além disso, a complexidade destes modelos 3D é útil apenas se existirem metodologias capazes de **quantificar os eventos biológicos** que lá ocorrem. Esta tese apresenta avanços em todas estas perspetivas críticas, usando microfluídica para a fabricação de plataformas 3D capazes de modelar, analisar, e quantificar eventos biológicos com alta eficácia. Inicialmente, demonstramos como a manipulação microfluídica de precursores de hidrogéis pode ser usada para gerar gradientes 3D com transições na sua **composição** e **propriedades mecânicas**. Combinado com a análise de respostas de células individuais automatizada, mostramos como formulações ideais de hidrogéis podem ser detetadas com **alto rendimento**, para induzir respostas biológicas desde a adesão celular até à estimulação da diferenciação de células estaminais. Depois, exploramos a microfluídica de foco 3D para introduzir **arquiteturas** e compartimentos no interior de microfibras de hidrogéis, usando um único chip, até diâmetros totais inferiores a 50μm. Demonstramos também como estas arquiteturas podem ser combinadas com células e biomateriais para **modelar** a invasão 3D de cancro, redes vasculares, bem como criar estruturas multifuncionais de engenharia de tecidos. Finalmente, estabelecemos uma interface entre fibras de hidrogéis com diferentes compartimentos e o transporte de luz, em fibras óticas à base de polissacáridos. Estas fibras conseguem detetar deformações 3D, a presença de biomoléculas de interesse, bem como transportar células vivas, enquanto guiam luz. As fibras óticas vivas são depois usadas para converter eventos biológicos complexos em sinais óticos **diretamente quantificáveis**, acompanhando o crescimento 3D de células tumorais e identificando patamares inibitórios de fármacos com alta eficiência. Os resultados desta tese demonstram a ampla aplicabilidade da biofabricação de hidrogéis guiada por microfluídica, bem como a sua capacidade para miniaturizar, modelar, e converter eventos biológicos em dados quantificáveis, com alto potencial para o futuro da medicina de precisão.

Palavras chave: Bioengenharia; Biomateriais; Cancro; Microfluídica; Modelos de Tecidos 3D

TABLE OF CONTENTS

ACKNOWLEDGMENTS ..... *iii*

STATEMENT OF INTEGRITY ..... *iv*

ABSTRACT ..... *v*

TABLE OF CONTENTS ..... *vii*

LIST OF ABBREVIATIONS ..... *xi*

LIST OF EQUATIONS ..... *xiv*

LIST OF FIGURES ..... *xv*

LIST OF SUPPLEMENTARY FIGURES ..... *xviii*

LIST OF TABLES ..... *xxi*

LIST OF SUPPLEMENTARY TABLES ..... *xxii*

SHORT CURRICULUM VITAE ..... *xxiii*

SECTION 1 ..... *29*

INTRODUCTION *29*

Chapter I *30*

General Introduction **31**

I.1. THE CHARACTERISTICS OF LIVING TISSUES AND IMPLICATIONS FOR THEIR ENGINEERING 32

I.2. NATURAL BIOMATERIALS, CELL-DRIVING CUES, AND COMBINATORIAL BIOFABRICATION 33

I.3. MICROFLUIDIC HYDROGEL BIOFABRICATION 33

I.4. PHOTONICS TO EXPAND BIOMEDICAL CAPABILITIES OF HYDROGELS BEYOND TISSUE ENGINEERING SCAFFOLDS 34

Chapter II *36*

The Stiffness of Living Tissues and its Implications for Tissue Engineering **37**

II.1. INTRODUCTION 38

II.2. THE CONCEPT OF STIFFNESS 39

II.3. TISSUE MECHANICS AT INCREASING SCALES 47

II.4. THE STIFFNESS RANGE OF LIVING TISSUES 58

II.5. ABNORMAL TISSUE STATES 65

II.6. ENGINEERING STIFFNESS INTO TISSUES 69

II.7. FUTURE PERSPECTIVES 75
II.8. CONCLUSIONS 76
II.9. REFERENCES 77
II.10. SUPPLEMENTARY MATERIAL: 89
II.11. SUPPLEMENTARY REFERENCE LIST 95

Chapter III 101

Pushing the Natural Frontier: Progress on the Integration of Biomaterial Cues towards Combinatorial Biofabrication and Tissue Engineering. 102

III.1. INTRODUCTION 103
III.2. NATURAL MATERIALS IN TE 104
III.3. INTEGRATING BIOMATERIAL CUES FOR CONTROLLED CELL BEHAVIOR 109
III.4. SOLVING THE PUZZLE – NATURAL BIOMATERIAL LIBRARIES AND HT SCREENING PLATFORMS 134
III.5. CONCLUDING REMARKS AND FUTURE PERSPECTIVES 140
III.6. REFERENCES 142

Chapter IV 152

Microfluidic-Driven Biofabrication and the Engineering of Cancer-Like Environments 153

IV.1. INTRODUCTION 154
IV.2. MICROFLUIDICS – A VERSATILE TOOL FOR 3D HYDROGEL PROCESSING 155
IV.3. MICROFLUIDIC REAL-TIME CONTROL OF 3D CONSTRUCT COMPOSITION 160
IV.4. MICROFLUIDIC FLOW-BASED GENERATION OF 3D AND CANCER-LIKE ARCHITECTURES 166
IV.5. MICROFLUIDIC-ENABLED BIOPRINTING 172
IV.6. CONCLUSIONS 176
IV.7. REFERENCES: 178

Chapter V 182

Engineering Hydrogel-Based Biomedical Photonics: Design, Fabrication and Applications 183

V.1. INTRODUCTION 184
V.2. HYDROGEL-BASED PHOTONICS 187
V.3. TECHNIQUES FOR FABRICATING PHOTONIC HYDROGEL CONSTRUCTS 195
V.4. PHOTONIC APPLICATIONS OF HYDROGEL STRUCTURES 199
V.5. ACTIVE OPTICS AT THE CELL/HYDROGEL INTERFACE 208
V.6. MULTI-RESPONSIVE HYDROGELS IN LIGHT-BASED APPLICATIONS 211
V.7. LIGHT-DRIVEN HYDROGEL ROBOTS 214
V.8. HYDROGELS IN PHOTOMEDICINE 216
V.9. HYDROGEL-LIGHT INTERACTIONS FOR ORGAN-ON-CHIP APPLICATIONS 219

V.10. CONCLUSIONS AND OUTLOOK 221
V.11. REFERENCES 224

SECTION 2 235

EXPERIMENTAL DESIGN 235

Chapter VI 236

Materials and Methods 237

VI.1. CHOICE OF HYDROGEL MATERIALS 238
VI.2. PREPARATION OF NATURAL HYDROGEL PRECURSORS 239
VI.3. HYDROGEL CROSSLINKING METHODS 240
VI.4. HYDROGEL CHARACTERIZATION 241
VI.5. MICROFLUIDIC-DRIVEN WET SPINNING 241
VI.6. CELL SOURCES AND GLOBAL CULTURE METHODS 243
VI.7. CELL VIABILITY TESTS 245
VI.8. IMMUNOCYTOCHEMISTRY METHODS 246
VI.9. GLOBAL STATISTICAL ANALYSIS 247
VI.10. REFERENCES 247

SECTION 3 249

EXPERIMENTAL STUDIES 249

Chapter VII 250

High-Throughput Fabrication of Cell-Laden 3D Biomaterial Gradients 251

VII.1. INTRODUCTION 252
VII.2. MATERIALS AND METHODS 253
VII.3. RESULTS AND DISCUSSION 258
VII.4. CONCLUSIONS 266
VII.5. REFERENCES 269
VII.6. SUPPLEMENTARY MATERIAL 271

Chapter VIII 286

3D Flow-Focusing Microfluidic Biofabrication: One-chip-fits-all Hydrogel Fiber Architectures 287

VIII.1. INTRODUCTION 288
VIII.2. MATERIALS AND METHODS 289
VIII.3. RESULTS AND DISCUSSION 293
VIII.4. CONCLUSIONS 306

VIII.5. REFERENCES 307
VIII.6. SUPPLEMENTARY MATERIAL: 310

Chapter IX 321

Engineering Polysaccharide-Based Hydrogel Photonic Constrcuts: From Multi-Scale Detection to the Biofabrication of Living Optical Fibers 322

IX.1. INTRODUCTION 323
IX.2. MATERIALS AND METHODS 324
IX.3. RESULTS AND DISCUSSION 335
IX.4. CONCLUSIONS 352
IX.5. REFERENCES 353
IX.6. SUPPLEMENTARY MATERIAL 356

SECTION 4 379

Concluding Remarks 379

Chapter X 380

Conclusions and Outlook 381

LIST OF ABBREVIATIONS

A

AFM – Atomic Force Microscopy

ALP – Alkaline Phosphatase

(Calcein) AM – Acetoxymethyl

ANOVA – Analysis of Variance

AP-Antibody – Alkaline Phosphatase Conjugated Antibody

ASC – Adipose Stem Cells

ASTM – American Society for Testing and Materials

ATB - Antibiotic

B

BCA - Bicinchoninic Acid

BM – Basement Membrane

BMMSC – Bone Marrow Mesenchymal Stem Cells

BMP – Bone Morphogenic Protein

BSA – Bovine Serum Albumin

C

CMAC - 7-amino-4-chloromethylcoumarin

CMRA - chloromethylfluorescein diacetate

CNS – Central Nervous System

COVID-19 – Coronavirus Disease 2019

CPC – Cardiac Progenitor Cell

CS – Chondroitin Sulfate

D

DAPI - 4′,6-diamidino-2-phenylindole

DFs – Dermal Fibroblasts

DMA – Dynamic Mechanical Analysis

DMEM - Dulbecco's Modified Eagle Medium

DS – Degree of Substitution

DTT - Dithithreitiol

E

E – Young's Modulus

E' – Storage Modulus (Tensile)

E'' – Loss Modulus (Tensile)

ECM – Extracellular Matrix

EDTA - Ethylenediaminetetraacetic Acid

EGM – Endothelial Growth Medium

EMEM – Essential Modified Eagle Medium

ESC – Embryonic Stem Cell

F

FBS – Fetal Bovine Serum

FDA – Food and Drug Administration

FF – Flow-Focusing

FGF – Fibroblast Growth Factor

FITC - Fluorescein isothiocyanate

FUCRW - FU-Cre-CRW Cloning Vector

G

G' – Storage Modulus (Shear)

G'' – Loss Modulus (Shear)

GAG – Glycosaminoglycan

GelMA – Gelatin Methacryloyl

GG – Gellan Gum

H

HA – Hyaluronic Acid

HAV - Histidyl Alanyl Valine

HCL – Hydrochloric Acid

hDMEC – Human Dermal Microvascular Endothelial Cell

hDF – Human Dermal Fibroblast

HIF – Hypoxia-Inducible Factor

HLB – Hydrophilic, Lipophilic Balance

HT – High-Throughput

HUVEC – Human Umbilical Vein Endothelial Cell

I

IBMX - 3-isobutyl-1-methylxanthine

L

LAMP - Loop-Mediated Isothermal Amplification

M

MEM – Modified Eagle Medium

MGF – Mechano Growth Factor

MIMO – Multi-Input Multi-Output

MMP – Matrix Metalloproteinase

MSC – Mesenchymal Stem Cell

N

NA – Not Applicable

NC - Non-Chondro

NGF – Neural Growth Factor

NIR – Near Infrared Light near infrared light

NP - Nanoparticle

P

P2VP - Poly(2-vinylpyridine)

PAAM - Polyacrylamide

PBS – Phosphate Buffer Saline

PBSA – Phosphate Buffer Saline with Bovine Serum Albumin

PDGF – Platelet-Derived Growth Factor

PDGI - Poly-dodecyl Glyceryl Itaconate

PDMS – Poly-Dimethyl Syloxane

PDT - Photodynamic Therapy

PEG – Poly-Ethylene Glycol

PEGDA – Poly-Ethylene Glycol Diacrylate

pHEMA - Poly(2-hydroxyethyl methacrylate)

PI – Propidium Iodide

PLGA -Poly(lactic-co-glycolic acid)

PML – Perfectly Matched Layer

PMMA - Polymethyl Pethacrylate

PPAR - Peroxisome Proliferator-Activated Receptor

PTFE - Polytetrafluoroethylene

R

RFP – Red Fluorescence Protein

RGD – Arginine-Glycine-Aspartic Acid

RI – Refractive Index

RIPA - Radioimmunoprecipitation Assay Buffer

RITC - Rhodamine Isothiocyanate

ROS – Radical Oxygen Species

RT – Room Temperature

S

SARS-CoV-2 Severe Acute Respiratory Syndrome Coronavirus-2

SCF - Stem Cell Factor

SDS - Sodium Dodecyl Sulfate

SEM – Scanning Electron Microscopy

SF – Silk Fibroin

SGR – Solid Glass Rheology

SZP – Superficial Zone Protein

T

TBS – Tris Buffered Saline

TE – Tissue Engineering

TERM – Tissue Engineering and Regenerative Medicine

TGF – Transforming Growth Factor

TIR – Total Internal Reflection

U

USD – United States Dollar

UV - Ultraviolet

V

VEGF – Vascular Endothelial Growth Factor

Y

YAP – Yes-Associated Protein

YIGSR - Tyrosine – Isoleucine – Glycine – Serine – Arginine

LIST OF EQUATIONS

$$E \equiv \frac{\sigma(\varepsilon)}{\varepsilon} = \frac{F/A}{\Delta L/L_0} = \frac{FL_0}{A\,\Delta L}$$ (Equation II-1) 41

$k = EAL0$ (Equation II-2) 41

$E = 2G(1 + v)$ (Equation II-3) 42

$Vcol = Final\ Volume\ V * Final\ Collagen\ (C)\ (mgml) Stock\ Collagen\ mgml$ (Equation VI-1) 240

$VH2O = V - Vcol - Volume\ of\ 10x\ PBS - Volume\ of\ H2O$ (Equation VI-2) 240

$Viability(\%) = Calcein\ Positive\ Cells - Double\ Positive\ CellsTotal\ Cells$ (Equation VI-3) 246

$I \sim I01 - SF$ (Equation IX-1) 339

$I(\mu W) \sim 4.51 - 8.2FN$ (Equation IX-2) 339

$IB\lambda = Ibulb\lambda \times HFiber\lambda$ (Equation IX-3) 341

$IAuNP\lambda = Ibulb\lambda \times HFiber\lambda \times TAuNP\lambda$ (Equation IX-4) 341

LIST OF FIGURES

Figure II-1: Main mechanical deformations and representative curves. 40

Figure II-2: The stiffness of living tissues spans a full Pa–GPa range..... 59

Figure II-3: Tissue mechanics are altered in disease states.. 68

Figure II-4: Engineering of life-like tissue mechanics.. 70

Figure III-1: New Paradigms in Material Susceptibility. 108

Figure III-2: The Cell-Biomaterial Compass.. 110

Figure III-3: Growth factors as powerful cues to boost the activity of natural materials. 118

Figure III-4: A Timeline of Cellular Taxis. 122

Figure III-5: The stiffness of natural biomaterials has a profound impact on the behavior of different cells. 125

Figure III-6: The topography of natural materials and surfaces affects cell morphology and organization in 2D and 3D..... 129

Figure III-7: Advances towards natural material libraries and HT platforms. 137

Figure IV-1: Airflow-assisted generation of microfluidic droplets with controlled inner 3D architectures. 158

Figure IV-2: The combination of microfluidic droplet generation and continuous flow fiber fabrication enables for the creation of cell-bead-laden alginate fibers, which can transport highly cellular, packed spheroid-like structures within a single support fiber. 160

Figure IV-3: High-throughput fabrication of 3D hydrogel fiber gradients with single (a) and multi-material (b) configurations for automated single-cell screening. 162

Figure IV-4: Microfluidic-driven generation of hydrogel droplets and microgel annealing for creating 3D gradients suitable for cell culture and high-throughput screening. 163

Figure IV-5: Chaotic generation of hydrogel fiber architectures with hydrogel compartmentalization and 3D cell/hydrogel alignment. 168

Figure IV-6: 3D Flow-focusing hydrogel biofabrication of multi-architecture hydrogel microfibers (A) and ribbon-like engineering of melanoma-on-a-fiber models (B)..... 169

Figure IV-7: Biofabrication of living optical fibers based on multi-layered polysaccharide hydrogel fibers (A), and the conversion of 3D cancer fiberoid growth to directly quantifiable optical data for drug inhibitory threshold discovery (B). 171

Figure IV-8: 3D Printing of heterogeneous bioinks via the combination of microfluidic biofabricated microgels within a uniform bioink blend for the integration of 3D cell-laden hydrogel depots within bioprinted constructs. 173

Figure IV-9: Microfluidic-enabled bioprinting for the assembly of complex 3D constructs with gradients in layer composition, and their application to density-varying breast cancer and complex vascular networks biofabrication. 175

Figure V-1: Overview of Hydrogel Optics. Schematic of the main events behind light going through biological tissues, solid-state silica, and hydrogels. 189

Figure V-2: Fabrication techniques for obtaining hydrogel structures with relevant photonic properties. 198

Figure V-3: Thin Hydrogel Films. 202

Figure V-4: Optical Hydrogel Fibers. 205

Figure V-5: Structured Hydrogels. 208

Figure V-6: Active Cell/Hydrogel interfaces.. 209

Figure V-7: Multi-Responsive Hydrogel Photonics. 212

Figure V-8: Light-Induced Hydrogel Motion. 215

Figure V-9: New Paradigms in Hydrogel Photomedicine. 218

Figure V-10: Light-hydrogel interactions for on-chip applications. 220

Figure VI-1: Microfluidic Chip-Based Wet-Spinning Setup 242

Figure VI-2: Pump-Driven Wet-Spinning Setups. 243

Figure VII-1: Low-Throughput Hydrogels and Uniform Microfibers. 260

Figure VII-2: Gellan Gum Gradients. 261

Figure VII-3: hASC differentiation triggering in GG Gradients. 262

Figure VII-4: Inert/Adhesive Gellan Gum-Gelatin Gradients. 264

Figure VII-5: hASC Responses in GG-GelMa Gradients. 265

Figure VIII-1: Flow Focusing Hydrogel Microfiber Architectures. 294

Figure VIII-2: Flow focusing Endothelial cell-laden Core-Shell Fibers. 298

Figure VIII-3: Flow focusing Ribbon Cancer/BM/Stroma Fibers.. 301

Figure VIII-4: Multi-Chemistry Biofabrication. 304

Figure IX-1: Fabrication of Purely Ionic Hydrogel Optical Fibers and their Light-Guiding Characterization. 337

Figure IX-2: Exploring ionic soft hydrogel versatility and fusion splicing for responsiveness to macro-scale force and shape.. 340

Figure IX-3: Engineering a plasmonic core modified hydrogel fiber for molecular-level SARS-CoV-2 detection. 343

Figure IX-4: Continuous single-step printing of living hydrogel optical fibers. 347

Figure IX-5: Living cancer optical fibers for the digitalization and quantification of 3D cancer growth and drug susceptibility. 351

LIST OF SUPPLEMENTARY FIGURES

Supplementary Fig. VII-1: Gellan Gum Rheology. 271

Supplementary Fig. VII-2: Gellan Gum Hydrogel Oscillation.. 272

Supplementary Fig. VII-3: Encapsulated hASC Viability. 273

Supplementary Fig. VII-4: Sox9 Western Blot. 274

Supplementary Fig. VII-5: Gradient Fabrication Setup. 275

Supplementary Fig. VII-6: hASC Viability Assessment. 276

Supplementary Fig. VII-7: Image Analysis Pipeline Example. 277

Supplementary Fig. VII-8: GG/GelMA Viscosity Tests.. 278

Supplementary Fig. VII-9: GG/GelMA Gradients Quantification. 278

Supplementary Fig. VII-10: GG/GelMA hASC Live/Dead Assay. 279

Supplementary Fig. VII-11: Gradients hASC Morphology. 280

Supplementary Fig. VII-12: Gradients hASC Paxillin.. 281

Supplementary Fig. VII-13: Gradients hASC Ki-67. 282

Supplementary Fig. VII-14: Gradients hASC YAP. 283

Supplementary Fig. VII-15: Western Blot of Paxillin. 284

Supplementary Fig. VII-16: Western Blot of YAP. 285

Supplementary Figure VIII-1: Detailed dimensions of the 3D Flow Focusing Chip used in this work. .. 310

Supplementary Figure VIII-2: Outcomes of solution's viscosity differences in the fiber architecture. ... 311

Supplementary Figure VIII-3: Shape variety and fidelity. 312

Supplementary Figure VIII-4: By applying pressure according to a time-changing function (e.g. sinusoidal), it is possible to change the dimension of the compartments along the fiber 312

Supplementary Figure VIII-5: Comparison between fibers formed using GG solutions at different concentrations 313

Supplementary Figure VIII-6: Rheological Characterization of core/shell fiber materials. 313

Supplementary Figure VIII-7: Core-Shell Endothelial cell-laden Fibers. 314

Supplementary Figure VIII-8: Brightfield (a) and Fluorescent (b) images of cancer/BM/stroma fibers 315

Supplementary Figure VIII-9: Representative Live/Dead fluorescent images of melanoma/stroma cells as used for the quantification presented in the main text. 316

Supplementary Figure VIII-10: Size and distribution manipulation of oil-core hydrogel-shell fibers. 317

Supplementary Figure VIII-11: Dexamethasone Quantification Data.. 318

Supplementary Figure VIII-12: Representative fluorescent images of BMSCs within the GG/GelMA fibers. 319

Supplementary Figure VIII-13: General Diagram of Chip Configurations 319

Supplementary Figure IX-1: Tunable Core Size Diameter. 356

Supplementary Figure IX-2: Comparison of fibers as fabricated, swollen and dried fibers (a), ... 359

Supplementary Figure IX-3: Photograph of the setup used for Power Meter quantification of light output power. 360

Supplementary Figure IX-4: a | Rationale behind the ion changes for fabricating neodymium-doped alginate hydrogel fibers 361

Supplementary Figure IX-5: a| Photograph of a fused hydrogel fiber undergoing tensile deformation. 362

Supplementary Figure IX-6: Quantification of the double-output system intensities with one fixed arm and a second one gradually moving away with increasing angle in relation to the common input branch (as schematized on the top). 363

Supplementary Figure IX-7: a | SEM image of an axial cut of the hydrogel fiber 364

Supplementary Figure IX-8: a | Experimental curves obtained by normalizing AuNP-fiber spectra to empty fiber spectra, representing the gold transmission or, reversely, absorbance (blue). 366

Supplementary Figure IX-9: a | Transmission curves obtained with gradual adition of glycerol solutions of increasing concentration. Curves represent the normalization between AuNP fibers and empty fibers (to derive the resonance-induced effect in transmission. 367

Supplementary Figure IX-10: Dot-blot validation of the Antigen/Antibody affinity 368

Supplementary Figure IX-11: a | Optical fiber output curves with stepwise addition of SARS-CoV-2 antigen solutions with a total of 10ng protein. 369

Supplementary Figure IX-12: 700nm intensity variation over time (each measurement represents the addition of ~10ng of protein solution).. 369

Supplementary Figure IX-13: Dot-blot validation of the antigen-virus interaction. 370

Supplementary Figure IX-14: Schematic representation of the reverse-immuno protocol used to stain and amplify the signal derived from SARS-CoV-2 bound to gold NPs within the fiber 371

Supplementary Figure IX-15: a | Rationale behind the dynamic swelling behavior of fibers, where a controlled swelling takes place during PBS incubation facilitating molecule permeation, and recovery after washing in the presence of calcium. 372

Supplementary Figure IX-16: a | Photograph of PCR tubes after LAMP RNA detection, evidencing the positive change in color in the fibers containing anti-SARS-CoV antibody after SARS-CoV-2 incubation. 373

Supplementary Figure IX-17: a| Tri-coaxial nozzle configuration and detailed dimensions. 374

Supplementary Figure IX-18: a | Comparison between the optical fiber spectrum of cells stained with calcein versus unstained, with zoomed in region around the specific 495nm wavelength of metabolized Calcein AM..... 375

Supplementary Figure IX-19: DU145 individual channel fluorescent tests (representative images) on the top, followed by microscopic image analysis and quantification of RFP and Calcein intensities on different culture conditions (bottom)..... 376

Supplementary Figure IX-20: Additional Cell lines tested in optical fiber fingerprinting analysis.. 377

Supplementary Figure IX-21: Individual channel fluorescent images of representative 22RV1 (top) and LNCaP-RFP-Trop2-OV (bottom) optical fibers after culture in the presence of drugs and control conditions. 378

LIST OF TABLES

Table II-1: Commonly used techniques for the mechanical characterization of living tissues. 43

Table II-2: Mechanical moduli of extracellular matrix components. 48

Table II-3: Mechanical moduli of distinct cell types. 51

Table II-4: Mechanical moduli of human tissues. 60

Table III-1: Natural polymers commonly used in the field of TE. 106

Table III-2. Most commonly used bioactive molecules for TE applications of natural biomaterials 120

Table III-3: Studies on the outcomes of different cell densities in TE constructs. 133

Table V-1: Commonly Used Polymers in Hydrogel-based Photonics. 193

Table VI-1: List of cells, culture medium and densities used. 244

LIST OF SUPPLEMENTARY TABLES

Supplementary Table II-1: The Stiffness of Living Tissues 89

Supplementary Table VIII-1: Pressure Working Ranges for the fabrication of reported shapes. 320

Supplementary Table IX-1: Preliminary core-clad and core-clad-shield tests with varying polymer concentrations and visually detectable light guiding distances. 357

Supplementary Table IX-2: Preliminary gradient-index tests with varying polymer concentrations and visually detectable light guiding distances. 358

SHORT *CURRICULUM VITAE*

Carlos F. Guimarães obtained his Master's in Bioengineering, jointly awarded by the Faculty of Engineering of the University of Porto and the Abel Salazar Biomedical Sciences Institute, University of Porto, in 2017. That same year, he was awarded a national merit scholarship award for graduating in the top 50 best-graded students at the University of Porto. During his master's, Carlos performed research on high-throughput biomaterial surfaces and stem cell interactions for six months at the biomedical engineering department, University of Groningen (NL), under Dr. Patrick Van Rijn's supervision, being awarded an Erasmus+ scholarship. He conducted his master's thesis on fibroblast-macrophage interactions within the colorectal cancer microenvironment in the Institute for Research and Innovation in Health (I3S), Porto, under the supervision of Dr. Sérgia Velho and Dr. Maria José Oliveira. Since 2017, Carlos has been conducting his Ph.D. in 3B's Research Group, University of Minho, under the supervision of Prof. Rui L. Reis, supported by an FCT Ph.D. grant in the Tissue Engineering, Regenerative Medicine and Stem Cells doctoral program. During his Ph.D., Carlos worked for over a year as a visiting Ph.D. student at Stanford University Canary Center for Early Cancer Detection (USA), under the supervision of prof. Utkan Demirci. Carlos has participated in different international projects, such as the ERC Advanced Grant ComplexiTE awarded to prof. Rui L. Reis, and twinning projects such as Gene2Skin led by Dr. Alexandra P. Marques. He served as representative in the University of Minho Doctoral College, is the current Ph.D. student representative of the I3B's institute, and a founding member of the PhDynamics initiative in the 3B's research group since 2018.

At 28, his track record of innovation and research excellence includes three ongoing patent applications, 11 published papers (6 as first author), in top peer-reviewed scientific journals, such as Nature Reviews Materials and Advanced Materials, 3 other papers undergoing review (2 as first author), 1 book chapter (first author), 7 first-author oral presentations in international conferences (2 of them invited), and several poster presentations. His work has been cited nearly 500 times in the past 4 years and recognized by multiple awards, including the National Portuguese Science Foundation (FCT) Ph.D. Fellowship, the Luso American Foundation for Development (FLAD) R&D@PhD Fellowship, two prestigious seed grants from Stanford University, best scientific ideas and art competitions, journal front covers, and other honorable mentions. Carlos was also invited as a reviewer to the 6th IEEE Portuguese Bioengineering Committee and participated as co-chair in the TERMIS EU 2019 Conference.

LIST OF PUBLICATIONS

The work performed during the PhD period resulted in the publications listed below.

Papers in international scientific journals with peer-review (as first-author):

1. Guimarães, C. F., Gasperini, L., Marques A. P., Reis, R. L. (2020) The Stiffness of Living Tissues and Implications for Tissue Engineering. *Nature Reviews Materials (IF=66)*. **Web of Science Highly Cited Paper, Web of Science Hot Paper.**
2. Guimarães, C.F., Gasperini, L., Ribeiro, R. S., Carvalho, A. F., Marques, A. P., Reis, R. L. (2020) High-throughput fabrication of cell-laden 3D Biomaterial Gradients. *Materials Horizons* (IF=13).
3. Guimarães, C.F., Ahmed, R., Marques, A.P., Reis, R. L., Demirci, U. (2021) Engineering Hydrogel-based Biomedical Photonics: Design, Fabrication and Applications. *Advanced Materials* (IF=31).
4. Guimarães, C.F.[1], Soto, F.[1], Reis, R.L., Franco, W., Rizvi, I. Demirci, U. (2021) Emerging biofabrication approaces for gastrointestinal organoids towards patient specific cancer models. *Cancer Letters* (IF=9). ([1]Co-First Authorship)
5. Guimarães, C. F., Gasperini, L., Marques A. P., Reis, R. L. (2021) 3D Flow Focusing Microfluidic Biofabrication: One-chip-fits-all hydrogel fiber architectures. *Applied Materials Today (IF=10)*.
6. Guimarães, C. F., Ahmed, R., Mataji-Kojouri, A., Soto, F., Wang, J., Liu, S., Stoyanova, T., Marques, A.P., Reis, R.L., Demirci, U. (2021) Engineering Polysaccharide-Based Hydrogel Photonics: From Multi-Scale Detection to the Biofabrication of Living Optical Fibers. *Advanced Materials* (IF=31). **Journal Front Cover.**
7. Guimarães, C.F., Marques, A.P., Reis, R.L., (2022) Pushing the Natural Frontier: Progress on the Integration of Biomaterial Cues for Combinatorial Biofabrication and Tissue Engineering. *Advanced Materials* (Revising).
8. Guimarães, C.F., Soto, F., Wang, J., Akin, D., Reis, R.L., Demirci, U., (2022) Engineered living bioassemblies for healthcare and functional material applications. *Current Opinion in Biotechnology* (Under Review).

Papers in international scientific journals with peer-review (as co-author):

9. Soto, F., Ozen, M. O., Guimarães, C. F., Wang, J., Hokanson, K., Ahmed, R., Reis, R. L., Paulmurugan, R., Demirci, U. (2021) Wearable Collector for Noninvasive Sampling of SARS-CoV-2 from Exhaled Breath for Rapid Detection. *ACS Applied Materials & Interfaces (IF=9).*

10. Gimondi, S., Guimarães, C.F., Vieira, S.F., Gonçalves, V.M.F., Tiritan, M.E., Reis, R.L., Ferreira, H. and Neves, N.M., 2021. Microfluidic mixing system for precise PLGA-PEG nanoparticles size control. *Nanomedicine: Nanotechnology, Biology and Medicine* (IF=6.5)

Patents:

1. Guimarães, C. F., Gasperini, L., Marques, A. P., & Reis, R. L., Multicompartement hydrogel fibre their preparation and uses thereof, WO2021165905A1 (2021)
2. Guimarães, C. F., Ahmed, R., Reis, R.L., & Demirci, U., Hydrogel Optical Fibers and Their Application and Use*, Patent Filled*.

Book Chapter

1. Guimarães, C.F., Gasperini, L. Reis, R.L, Microfluidic-Driven Biofabrication and the Engineering of Cancer-like Microenvironments, in Microfluidics and Biosensors in Cancer Research, Springer Nature, 2022.

Conference Oral Presentations (first-author and invited)

1. Guimarães, C.F., Gasperini, L., Ahmed, R., Marques, A.P., Demirci, U., Reis, R.L. "Hydrogel Bioarchitectures for Modeling and Digitalizing 3D Cancer Dynamics toward the Discovery of Functional Drug Thresholds", Final FoReCaST Conference, Porto, Portugal, October 2021

2. Guimarães, C.F., Gasperini, L., Marques, A.P., Reis, R. L., "Microfluidic-Driven Hydrogel Biofabrication for Engineering Living Microtissue Architectures", 31st European Conference on Biomaterials, Porto, Portugal, September 2021

3. *Invited talk* on "How to Publish High-Impact Review Articles", Nanophotonics & Biosensors Bangladesh Chapter, October 2020 (Virtual).

4. *Invited Talk* on "Microfluidics as a tool for high-throughput biomaterial screening and complex biofabrication", January 2020, Iberian Nanotechnology Institute (INL), Braga, Portugal.

5. Guimarães, C.F., Gasperini, L., Ribeiro, R.S., Pinto, A.C., Carvalho, A.F., Marques, A.P., Reis, R.L., Microfluidic fabrication of 3D biomaterial libraries for high-throughput screening stem cell responses, TERMIS EU 2019, Rhodes, Greece, May 2019. Indexed in eCM Conferences (open access)
6. Guimarães, C.F., Gasperini, L., Ribeiro, R.F., Carvalho, A.F., Bishi, D.K., Marques, A.P., Reis, R.L. "From low to high-throughput: Development of a 3D Gellan Gum gradient to screen the effect of hydrogel mechanics on ASC commitment", Chem2Nature Summer School 2018, Porto, Portugal.
7. Guimarães, C.F., Gasperini, L., Ribeiro, R.S., Carvalho, A.F., Marques, A.P., Reis, R.L., "From low- to high-throughput: Microfluidic fabrication of novel 3D biomaterial libraries for screening cell responses" 29th European Conference on Biomaterials, Maastricht, Netherlands, 2018.

Posters (First Author):

1. Guimarães, C. F., Gasperini, L., Ribeiro, R. S., Carvalho, A. F., Marques, A. P., Reis, R. L. (2018) Microfluidic fabrication of 3D biomaterial libraries towards high-throughput quantitative stem cell responses screening. Chem2Nature Final Conference, Guimarães, Portugal.
2. Guimarães, C.F., Gasperini, L., Marques, A.P., Reis, R.L. 3D Microfluidic Gradients: A Powerful High-Throughput Screening Platform for Detecting Best-Fit Biomaterial Formulations towards Cellular Stimulation (2019). 2nd FoReCaST workshop on Nanotechnology in Cancer Detection and Treatment: from the Lab to the Clinic, Porto, Portugal
3. Guimarães, C.F., Gasperini, L., Marques, A.P., Reis, R.L., 3D Microfluidic Gradients: A Powerful High-Throughput Screening Platform for Detecting Best-Fit Biomaterial Formulations towards Cellular Stimulation (2019) First Achilles Conference on Molecular and biological mechanisms of tendon homeostasis and repair, Porto, Portugal
4. Guimarães, C.F., Gasperini, L., Marques, A.P., Reis, R.L. Microfluidic Fabrication of Cell-Laden 3D Biomaterial Gradients (2019) TERM STEM 2019, Braga, Portugal

Awards:

1. Awarded with a 4-year FCT PhD Scholarship (PD/BD/135253/2017)
2. Awarded the "Best Tissue Engineering Idea" prize, Gene2Skin winter school, November 2017, Porto, Portugal.

3. Awarded with a Luso-American Foundation for Development (FLAD) scholarship for supporting a 1-year (12.000EUR) research period in Stanford University (USA) (2020).
4. Honorable Mention, Alfredo da Silva Awards for Scientific Investigation in Technological Innovation, Project Ultra-facile Biofabrication of Tubular Hydrogels to catapult vascularization in tissue engineering, Top 2 Projects, 2021, Portugal.
5. Awarded with an exceptional 4 months FCT COVID Grant (COVID/BD/152016/2021)

Funded Grants (as main researcher):

1. "Swab-Couplable Hydrogel Optical Fibers for COVID19 in situ diagnostics", Stanford RISE COVID-19 Crisis Response Seed Grant Program (2020) – $45k direct, 1 year.
2. "Swab-Couplable Hydrogel Optical Fibers for *in situ* diagnostics of SARS-CoV-2 and other respiratory viruses", Stanford PHIND Individual Seed Grant (2020) – $40k direct, 1 year.

Peer Reviewing, Chairing:

1. Invited as Reviewer of the 6th IEEE Portuguese Bioengineering Comittee, 22-23 February 2019, Lisbon, Portugal.
2. Co-chair for the Discovery Centre Symposium at the TERMIS EU 2019 Conference, Rhodes, Greece.
3. Peer Review of Microchimica Acta Publications (Publons-indexed).
4. Peer Review of International Journal of Nanomedicine (Publons-indexed)

"*If you're going to try, go all the way. Otherwise, don't even start. There is no other feeling like that. You will be alone with the gods, and the nights will flame with fire. Do it. Do it. Do it. All the way. You will ride life straight to perfect laughter. It's the only good fight there is.*"

Charles Bukowski, in *Factotum*.

SECTION 1

INTRODUCTION

Chapter I

GENERAL INTRODUCTION

Overview

This brief chapter presents a general overview of the introductory chapters, which explore distinct topics that introduce the different experimental realms this thesis explores. Herein we will discuss the relevance of the particular review works and how these connect in the overall thesis concept.

I.1. THE CHARACTERISTICS OF LIVING TISSUES AND IMPLICATIONS FOR THEIR ENGINEERING

While the earliest research on manipulating cells for approaching the creation of living tissues focused primarily on biochemical cues, the past decades have been marked by the ever-growing evidence that physical characteristics, such as shape and mechanics, represent equally essential cues. To understand how to engineer 3D microenvironments that can recapitulate essential characteristics of living tissues to approach their proper functionality, one must understand how shapes and mechanics come together and contribute to their functionality. Chapter II reviews these different themes by providing a perspective into living tissues from a materials engineering perspective – After all, nature has engineered living tissues using cells and biological matrixes. A tissue engineer attempts to control material features to recapitulate cell responses similarly.

With a particular focus on mechanical properties, chapter II presents a global and introductory perspective into tissue stiffness, how it can be assessed, and the challenges and difficulties in understanding and comparing features from different tissues. Therein, essential characteristics that are sometimes overlooked, such as spatial scale, time scale, and tissue anisotropy, are discussed. Then, we present an evolving perspective on how the complex architecture and mechanics of living tissues arise, from single cells to whole tissues and organs, benchmarking developmental knowledge towards lessons for tissue engineering.

Additionally, chapter II explores the differences and essential characteristics of altered tissue states, *i.e.,* diseased tissues, such as those found in cancer. Indeed, for properly engineering diseased tissues, different considerations may have to be made to ensure the recapitulation of diseased tissue characteristics for truly modeling relevant disease outcomes.

Finally, chapter II discusses what techniques and approaches are or may be used to engineer live-tissue-like physical characteristics, exploring which avenues of tissue engineering may lead to advances in the recapitulation of such features within fabricated constructs. These characteristics are then important pillars of all experimental works. Chapter VII focuses on 3D hydrogel microfiber composition and mechanics for stimulating different cell responses, and chapter VIII explores the creation of 3D architectures within the engineered hydrogel fibers.

I.2. NATURAL BIOMATERIALS, CELL-DRIVING CUES, AND COMBINATORIAL BIOFABRICATION

After understanding the intricacies of living tissues and the type of characteristics that must be approached when attempting their engineering, it is critical to understand which kinds of tools can be used to control the fate of cells. From a tissue engineering perspective, those tools are the biomaterials, the cues these can integrate, and the cells themselves. With that in mind, chapter III overviews the recent progress on using natural biomaterials, and the integration of physical and biochemical cues towards combinatorial biofabrication and tissue engineering.

Beginning with an overview of the different classes of natural biomaterials, their advantages, and disadvantages *versus* synthetic ones, chapter III critically analyzes biomaterial-induced cell responses, ranging from simple adhesion to more complex stem cell differentiation. Therein, the presence of bioactive ligands in soluble and bound configurations are discussed, as well as the roles of biomaterial shape, mechanical characteristics, susceptibility to remodeling, and the often-overlooked impact of cell-cell interactions and cellular density in tissue engineering.

Throughout this discussion, chapter III highlights reports of synergistic and antagonistic combinations across different biomaterial stimuli both *in vitro* and *in vivo*, evidencing the need for high-throughput approaches. These approaches may quickly identify these combinatorial possibilities and lead to advances in the future of complex tissue engineering. The development of these types of platforms is then addressed experimentally in chapter E1.

I.3. MICROFLUIDIC HYDROGEL BIOFABRICATION

Once a straightforward biomaterial toolbox is established, it is essential to understand how these materials can be processed to create constructs that can integrate characteristics that go far beyond a uniform scaffold. Indeed, to be able to engineer and model microenvironments that can approach those present in living tissues, it is important to screen several conditions in a faster manner and miniaturizing constructs to save precious biomaterials and cells during optimization. With that in mind, chapter IV explores the advantages of microfluidics to manipulate hydrogels and process them for creating living constructs at small dimensions.

Beginning with an overview of the advantages of microfluidics and their role in biomaterial processing, chapter IV discusses how the capacity to control different materials in real-time, allowing or preventing their mixing within very small flow channels, can be leveraged to create complex tissue-like characteristics such as space-varying mechanics. Furthermore, spatial variation, namely 3D biomaterial gradients, is explored not only from a tissue-like perspective but also as high-throughput screening libraries. Combining multiple conditions in a single sample presents meaningful opportunities for advancing biomaterial discovery and optimization. These opportunities are then the ground for the experimental research reported in chapter VII.

Then, as referred before, not only 3D composition but also shapes and inner construct architectures are critical for adequately approaching living tissue environments. For that, chapter IV discusses some of the latest advances in using microfluidics and the control of flows alone to generate 3D microfiber architectures. These structures can model varied living environments, namely those present in invading cancer tissues, and their importance in understanding the efficiency of therapeutics way beyond classical cancer-only studies. These advances are then experimentally reported in chapter VIII.

I.4. PHOTONICS TO EXPAND BIOMEDICAL CAPABILITIES OF HYDROGELS BEYOND TISSUE ENGINEERING SCAFFOLDS

In all the effort to create more faithful 3D models that can integrate more living tissues' characteristics in health and disease, a critical parameter is sometimes forgotten: the need to extract relevant and quantifiable data from the model. 2D models have been and still are widely used because the scientific community has created hundreds of different methodologies to analyze cellular responses within plane surfaces. However, moving to 3D models, the ability to do this decreases considerably. Even if some engineered models can represent critical biological processes, the capacity to convert those into quantifiable, comparable data can be a daunting challenge.

Therefore, chapter V discusses hydrogel materials from a less classical perspective, not only as tissue scaffolds but also as optical materials. Indeed, optical interactions and photonics are the fastest and most sensitive approaches to analyze and quantify biologically relevant processes, and the integration of such technologies within engineered constructs may be game-changing. By overviewing

the differences and similarities between hydrogels and typical optical materials such as silica, the chapter outlines the opportunities for hydrogels to integrate the realm of photonics.

We then discuss what type of hydrogel processing and fabrication tools developed over the years in biofabrication and tissue engineering can be leveraged to create photonic-relevant constructs, such as thin films or hydrogel optical fibers. Then, chapter V explores current and possible biomedical applications of those structures, ranging from sensors, robots, actuators, or organ-on-a-chip technologies.

The chapter exposes the significant number of untapped potentials for integrating photonic events such as light guiding with living entities in hydrogel constructs to enable the quantification of biological responses within 3D environments. This challenge is experimentally addressed in chapter IX.

Chapter II

THE STIFFNESS OF LIVING TISSUES AND ITS IMPLICATIONS FOR TISSUE ENGINEERING

THE STIFFNESS OF LIVING TISSUES AND ITS IMPLICATIONS FOR TISSUE ENGINEERING

Abstract

The past 20 years have witnessed ever- growing evidence that the mechanical properties of biological tissues, from nanoscale to macroscale dimensions, are fundamental for cellular behavior and consequent tissue functionality. This knowledge, combined with previously known biochemical cues, has greatly advanced the field of biomaterial development, tissue engineering and regenerative medicine. It is now established that approaches to engineer biological tissues must integrate and approximate the mechanics, both static and dynamic, of native tissues. Nevertheless, the literature on the mechanical properties of biological tissues differs greatly in methodology, and the available data are widely dispersed. This Review gathers together the most important data on the stiffness of living tissues and discusses the intricacies of tissue stiffness from a materials perspective, highlighting the main challenges associated with engineering lifelike tissues and proposing a unified view of this as yet unreported topic. Emerging advances that might pave the way for the next decade's take on bioengineered tissue stiffness are also presented, and differences and similarities between tissues in health and disease are discussed, along with various techniques for characterizing tissue stiffness at various dimensions from individual cells to organs.

This chapter is reproduced from the following publication:

Guimarães, C. F., Gasperini, L., Marques, A. P., & Reis, R. L. (2020). The stiffness of living tissues and its implications for tissue engineering. *Nature Reviews Materials*, *5*(5), 351-370.

II.1. INTRODUCTION

Materials engineering involves the design or tuning of the structure of a material to produce a set of desired properties[1]. Living tissues are essentially materials engineered by nature itself to have a specific structure that affects cell properties and drives all consequent biological events. Tissue engineering tries to replicate this feat by designing the structure of a material to recapitulate a predetermined cell response.

When tissue engineering arose, more than 25 years ago, stiffness was already a term mentioned in the literature[2]. In the beginning, the premise was simple: a tissue substitute must be biomechanically able to fulfill the functions of the tissue it replaces and, as such, should have similar mechanics to the native tissue. Hard scaffolds began to be employed to engineer bone-like structures and hydrogels for soft tissue structures, which were combined with specific biochemical cocktails that could direct the behavior of cells on these structures, which simply served the purpose of support. However, this paradigm shifted with the understanding that the stiffness of surfaces, independently of their shape, could be detected and responded to by cells[3].

The ripples of this discovery are still reverberating throughout diverse fields of research, but it truly revolutionized tissue engineering as the supremacy of biochemical cues in driving cellular behavior began to be questioned. Currently, when considering the stiffness of engineered constructs comprising cells on a three-dimensional (3D) support, one must think not only of its biomechanical integration with host tissue but also of cell mechanostimulation.

From adhesion to differentiation, the most relevant cellular events from early embryogenesis onwards[4] are all, in some way, affected by tissue stiffness. As such, any modern tissue-engineering strategy must consider the stiffness of the native biological tissue, as well as the implications of this stiffness for the behavior of resident cells. These factors require not only bulk material analysis but also an understanding of the microscale and nanoscale domains within which the native extracellular matrix (ECM) components function *in vivo*. Moreover, cells themselves have a characteristic stiffness, which is a consequence not only of their interaction with the surrounding microenvironment but also of their biological and/or genetic status. For example, cancer cells frequently have altered (either increased or decreased) stiffness[5]. If tissue stiffness was initially considered a simple concept, it is now undeniably worthy of thorough and integrative study.

The Review brings together these topics using an approach that aims to be as interdisciplinary as the field of tissue engineering itself. After a brief overview of what stiffness is and how the mechanical properties of living tissues are measured, we consider each component in turn, starting with the smallest — ECM molecules and single cells — and continuing up to bulk living tissues and organs, which are compared and discussed from a biomaterials perspective. Finally, we outline the main avenues to follow when attempting to engineer life-like tissues, emphasizing the most recent advances in time-changing mechanics and identifying the main challenges for the future — the questions that must be answered to enable tissue stiffness to be fully decoded and manipulated.

II.2. THE CONCEPT OF STIFFNESS

The mechanical properties of a material — most notably its stiffness — relate to loads and deformations; that is, the forces exerted on the material and the resulting changes in its shape. To fully understand the stiffness of living tissues, one has first to explore these underlying concepts. The stiffness of a structure derives from the following two premises: first, that when a structure is exposed to a certain load, it will deform; and second, that the ratio between this load and the consequent deformation yields the stiffness of the structure, meaning how much load is necessary to achieve a certain deformation[6]. Although there is no absolute definition of what constitutes a 'stiff' or 'soft' material, rubber and foodstuffs are generally considered soft materials, wood and plastics are of intermediate stiffness, and steel is among the stiffest commonly encountered materials. Clearly, the load necessary to deform a stiff material, such as steel, will be far higher than that required to similarly deform a softer material such as wood or rubber.

The stiffness of materials commonly used in manufacturing is far higher than that of human tissues or organs, including the stiffness of materials employed specifically because of their deformability, such as the plastics used in ketchup bottles. The vast majority of industrial plastics (such as polypropylene, nylon or polyethylene) have elastic moduli in the range of 0.2–5.0 GPa, higher than that of all biological tissues except bone. By contrast, the stiffness of some foodstuffs is comparable to that of tissues: the elastic moduli of pannacotta are in the 100 Pa–1 kPa range[7,8], gummy bears and bananas are between 50 kPa and 100 kPa, an apple is about 1Mpa and a carrot is around 7 Mpa[9,10]. Similarly, from a biological perspective, fat is clearly far softer than muscle tissue, which itself is far softer than bone. Naturally, the stiffness of a tissue can be quantified and precisely analyzed but,

despite the term being widely mentioned in the biomedical field, analyses of tissue stiffness are sometimes insufficiently detailed.

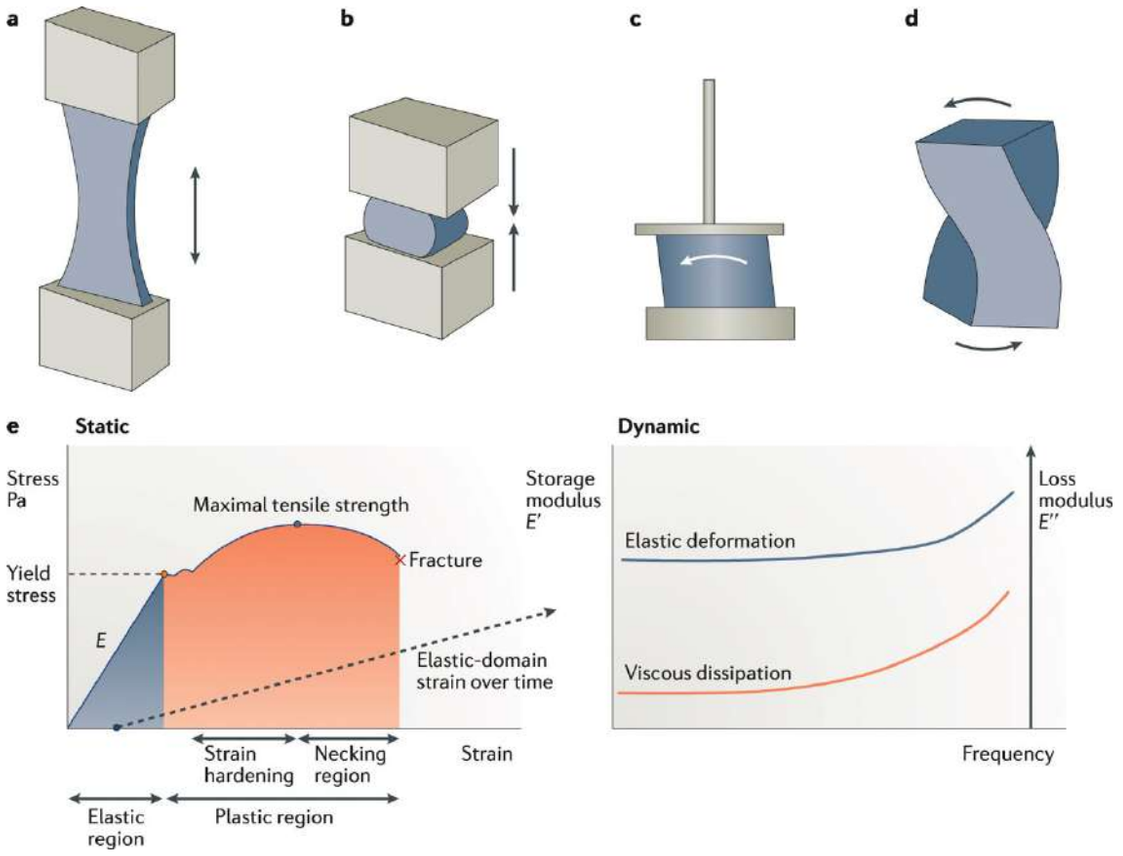


Figure II-1: Main mechanical deformations and representative curves. The main types of mechanical analysis include a | tensile, b | compressive, c | shear and d | torsion deformations. e | Typically, static deformations (such as tensile or strain deformations) yield a complex curve within which distinct regions can be identified, each of which has important mechanical correlates. Young's modulus (E) is calculated as the slope of the stress versus strain curve in the linear (elastic) region. With higher levels of strain, the material enters the plastic domain of the curve, where deformations are no longer reversible and the material deforms permanently until fracture occurs. Alternatively, a dynamic analysis can be performed, in which a strain within the linear (viscoelastic) region is applied repeatedly over time, in cycles often with changes in frequency or temperature, to yield storage (E′) and loss (E″) moduli . The storage modulus is related to elastic deformation of the material whereas the loss modulus represents the energy dissipated by internal structural rearrangements.

Stiffness is a general structural property that depends not only on the material itself but also on its amount and distribution (shape). For example, the hollow nature of bones confers an increased stiffness-to-weight ratio. During compression or extension (stretching) of a material, the whole cross-

sectional area of the material equally sustains the stress, whereas during bending or torsion the material furthest away from the midpoint or centre line sustains most of the stress. For this reason, structural construction elements often have T-shaped or L-shaped cross-sectional shapes, which maximize their stiffness while minimizing the weight and amount of material used. Moduli and stiffness are intimately related concepts and therefore frequently used as synonyms. However, stiffness is a property of a structure, whereas moduli describe the properties of the material composing that structure. As such, various moduli relating to the intrinsic elastic properties of materials[6] are reflected in the stiffness of the final structure. These moduli are derived from mathematical conversions of load versus deformation relationships obtained from standardized tests on samples of a standardized size and shape (**Box 1**).

For example, Young's modulus (E) can be calculated by subjecting a material to uniaxial stress resulting from compression or extension and measuring elastic (that is, reversible) deformation (strain) in the linear region of the stress–strain curve:

$$E \equiv \frac{\sigma(\varepsilon)}{\varepsilon} = \frac{F/A}{\Delta L/L_0} = \frac{FL_0}{A\,\Delta L} \qquad \text{(Equation II-1)}$$

where σ is uniaxial stress (force per unit surface); ε is strain; F is the force exerted on an object (uniaxial stress); A is the cross-sectional area perpendicular to the applied force; ΔL is the amount by which the length of the object changes (ΔL has a positive value for a stretched material and a negative value for a compressed material); and L_0 is the original length of the object. Thus, the axial stiffness (k) of a longitudinal structure such as a beam can be calculated as:

$$k = \frac{EA}{L_0} \qquad \text{(Equation II-2)}$$

It is worth noting that the above equations assume a linear relationship between strain and stress (that is, Hooke's law). In real-life scenarios this assumption might not hold for all levels of strain, particularly for polymers. The proportional limit represents the maximum stress at which stress and strain are proportional, and varies for different materials. Below this limit, the chemical bonds between atoms in the material stretch when under load but will recover completely when the load is released. Above this limit, the bonds will break and slip past each other, leading to non-proportionality. Therefore, the elastic modulus is typically measured at low strain values (0.2%)[11,12].

Young's modulus is one of the most common measures of intrinsic material stiffness. Because it is independent of structure, Young's modulus is widely used to characterize the stiffness of both

manufactured materials and tissues (**Fig. II-1 a,b**). However, in addition to uniaxial stress, biological tissues might also be subjected to deformations resulting from shear forces (**Fig. II-1c**). The shear modulus (G) is calculated similarly to Young's modulus in that stress (force per unit area) is divided by strain. However, whereas for Young's modulus stress and strain are both normal to the cross-sectional area, for the shear modulus they are parallel and associated with an angular change. In isotropic materials, E and G are related to each other through Poisson's ratio (ν), given by the following equation:

$$E = 2G(1 + \upsilon) \qquad \text{(Equation II-3)}$$

For many common materials, Poisson's ratio is similar to that of incompressible rubber (ν = 0.5); thus, E is frequently approximated to ~$3G$. Together, the shear and elastic moduli represent the properties of materials under two different types of load, which might suffice to give a general idea of the rigidity of various biological tissues. However, different loads can be simultaneously applied to the same tissue: for example, cartilaginous tissues are routinely subjected to both compressive and shear deformations[13]. Furthermore, such complex loads can cause materials to deform in multiple ways, such as torsion and bending (**Fig. II-1d**). In the case of bending, one side of the sample is subjected to compressive stress and the opposite side to tensile stress. The mineralized constituent of bone, for example, as for other brittle materials, is highly resistant to compressive stress but not so much to tensile forces; consequently, bending can result in fracture. As such, it is important to consider different types of stress even in the same tissue. The most relevant types of stress in tissue engineering are those that are similar to physiological loads.

Furthermore, it is important to outline that some of these mechanical relationships do not apply directly to most biological tissues. Equation II-3, for example, applies only to isotropic materials but is frequently erroneously used for anisotropic materials (those whose mechanical characteristics differ according to the direction of measurement). Similarly, biological tissues have very complex, anisotropic structures (in which many types of matter are present and unevenly distributed) that differ greatly from the typically isotropic, continuum structures used in manufacturing (in which few types of matter are present and are continuously distributed in the containing space). As such, even though it is useful to discuss the relationships that exist between mechanical concepts at this simple level, these will, in practice, be affected by length scale, anisotropy, spatial variations, nonlinear behavior and other characteristics of biological tissues, discussed further in this article.

Viscoelasticity is another important point to discuss, as the natural response of all solid materials to stress is not purely elastic but also has a viscous component, which is also the case with

living tissues. When elastic and viscous components are both prominent in defining the mechanical behavior of a material, the material is generally referred to as viscoelastic. This type of material can only be fully characterized by time-dependent tests, which apply strain and measuring the required force as a function of time (stress relaxation) or apply stress and measuring strain as induced changes in shape (creep), or through dynamic mechanical analysis (DMA)[14]. In DMA, loads are applied and released cyclically, often at varying frequencies or temperatures, which facilitates measurement of the viscoelastic response of a material during faster deformations than those derived by creep and stress relaxation tests.

The viscoelastic response of a material is used to derive the dynamic or complex modulus, which is usually represented by storage and loss moduli. For uniaxial forces, the storage modulus (E') represents the elastic, instantaneous and reversible response of the material: deformation or stretching of chemical bonds while under load stores energy that is released by unloading. The loss modulus (E'') represents the viscous time-dependent response of the material and is related to irreversible rearrangements and remodeling of their internal structure, such as the slippage of polymer chains past each other. Similarly, for deformations resulting from shear forces, the shear storage (G') and shear loss (G'') moduli[15] are frequently evaluated by rheology and oscillatory experiments (**Table II 1**). As biological tissues generally have viscoelastic responses, these tests are extremely relevant in the biomechanical field.

Table II-1: Commonly used techniques for the mechanical characterization of living tissues.

Technique	Concept	Moduli	Sample	Dimension	Standard test methods*	Refs.
Tensile deformation	Classic stress–strain analysis. Uniaxial stress is applied to stretch the material and a relationship is established with the resulting strain	E (elastic)	Mostly ex vivo tissue	Macroscale	D412, D638, D882, D1623, D1708, D3039, D3039M	214
Compressive deformation	Classic stress–strain analysis. Uniaxial stress is applied to compress the material and a relationship is established with the resulting strain; the compressor is as the same size or larger than the sample	E (elastic)	Ex vivo tissue	Macroscale	D695, D1621	215

Dynamic mechanical analysis	Cycles of tensile and compressive deformations	E', E'' (viscoelastic)	Ex vivo tissue	Macroscale	D5024,D5026	216
Shear rheometry	Application of small-amplitude oscillatory shear stress and quantification of the resulting strain	G', G'' (shear, viscoelastic)	Ex vivo tissue	Macroscale	D5279	217,218
Pipette or micropipette aspiration	Establishment of the relationship between the pressure of aspiration and aspirated volume of the sample	E (elastic)	Ex vivo tissue	(Microscale), macroscale	NA	219,220
Indentation	Indentation of the tissue with a probe of defined geometry, and calculation of the relationship between indentation depth and probe load (the probe must be smaller than the sample)	E (elastic)	Mostly ex vivo tissue	Nanoscale to macroscale	E2546-15	106,221
Atomic force microscopy	Atomic-level indentation (nanoindentation) or shear rheology (atomic force microscopy-based rheology)	E (indentation), G', G'' (shear)	Dry or wet ex vivo tissue	Microscale, nanoscale	NA	5,142,222
Magnetic resonance elastography	Magnetic resonance visualization of tissue deformation resulting from the introduction of shear waves into the tissue derived from external vibrations	G', G'' (shear, viscoelastic)	In vivo tissue	Macroscale (millimetric)	NA	223,224
Ultrasonic shear wave elastography	Ultrasonic pulses produce shear waves through the tissue; the velocity of these waves is measured and used to derive the tissue's Young's modulus	E (elastic)	In vivo tissue	Macroscale (millimetric)	NA	225

*Additional test methods are suggested by American Society for Testing and Materials (ASTM) F2150-13 where applicable; sample preparation and conditioning guidelines are provided by ASTM F1634 and F163.

II.2.1. Time scale

Some materials exhibit different responses when deformed at different speeds. For example, the toy Silly Putty is made of a silicone blend that exhibits a strong elastic response at high rates of deformation and a strong viscous or liquid-like response at low rates of deformation[16]. Mechanical tests

need to take into consideration the potential for time dependency. A frequency sweep, for example, is commonly performed in dynamic tests to evaluate the response of the sample to different speeds of deformation. During these tests, the storage modulus typically increases with rising deformation frequency; that is, the elastic response of these materials increases with the speed of deformation. Thus, deformation speed can play a crucial part in defining the response of a material under load[17,18]. Particularly slow speeds of deformation can approximate a static system. Some mechanical tests can be performed either under such quasi-static or dynamic conditions[19].

Three important consequences can be derived from these considerations: first, that under quasi-static conditions, the time-dependent behavior (viscoelasticity) of materials is simplified because the behavior of the material corresponds to its 'associated' elasticity[20,21]; second, that quasi-static testing cannot provide information about the viscous and/or elastic responses that take place under dynamic loads — namely, those resembling physiological deformations; and third, that substantial differences can be expected to occur at distinct load time scales, and as such, direct comparisons between scales are inadvisable (**Box 1**).

BOX 1 Standards in mechanical testing:

Standardized protocols must be followed in mechanical analyses if the data so obtained are to be interpreted with a good level of confidence and comparable between different investigational studies. Accordingly, in the past decade, there has been a great effort to introduce standardized methods for the analysis of tissue-engineered products, such as the American Society for Testing and Materials (ASTM) standards developed by committee F04 and related subcommittees, which aim to improve the safety, quality and consistency of these products. Although these standards were not specifically developed for the purpose of performing mechanical tests on human tissues, they can provide guidance for appropriate testing. For example, ASTM F561–19 covers recommendations for the handling and analysis of postmortem tissue and living tissue samples surgically removed from human and animal subjects, whereas ASTM F2150–13 provides guidance on the selection of appropriate test methods for analyzing the bulk physical, chemical, mechanical and surface properties of such samples. ASTM D638–14, a standard for testing polymeric materials under uniaxial extension, states that it might not be meaningful to compare the results of tests made over widely different loads or time scales. Although biological systems differ substantially from the plastics referred to in ASTM D638–14, when taking a

cautious approach we might reasonably extend these concepts to human tissues. Overall, however, the tissue-engineering literature seems to be reluctant to adopt similar standards, or even to attempt to follow existing standards. In most published reports, mechanical tests are either not performed according to any consensus standard, or if they are, the standard followed is rarely referenced.

II.2.2. Spatial scale

Differences between the macroscopic properties and bulk properties of a material, and the effects of surface microscale or nanoscale features should also be considered. Surfaces can behave very differently to bulk material: according to the Nobel laureate Wolfgang Pauli, "God made the bulk; surfaces were invented by the devil."[22]. Atoms on the surface of a solid are in an anisotropic environment because they can interact with other atoms on the surface, in the bulk below, and in liquid or gaseous phases. The macroscopic definition of Young's modulus as an intrinsic material property that is independent of size sometimes fails at nanoscale or microscale dimensions, where the moduli of materials might not only differ but also can become size-dependent[23]. As such, assessments of the mechanical properties of biological materials should examine the bulk tissue as well as its constituents at nanoscale or microscale dimensions because not only are the moduli themselves likely to be different at different scales but also because at these smaller dimensions cells sense the material and individually respond to its mechanical characteristics[24]. These intricacies, together with the wide range of available investigative techniques, make the mechanical characterization of biological tissues highly complex, and suggest that standardization could lead to improvement (**Table II-1, Box 1**).

Considerable research effort has focused on ways to homogenize the microscale properties of a material and thereby to derive those ruling at the macroscale. Approaches such as computational homogenization are based, in brief, on defining a representative volume element of smaller (usually microscale) dimensions than the complete structure, which can then be used to model its governing macroscale behavior[25,26]. Within the context of tissue mechanical properties, such an approach involves first defining the microscale components that govern the mechanical properties of the tissue, such as the elastin and collagen fibers of the arterial wall. Second, the properties of these components can be assessed by a technique that probes their mechanics at the same scale, such as atomic force microscopy (AFM) indentation. Finally, the characteristics of the small-scale elements can be used to mathematically model their macroscale mechanics, which in this example are those of the whole

arterial wall[27]. Similarly, complex scaffolds used in tissue engineering can also be designed by modeling the individual components of their architecture, which are then combined to find best-fit shapes that closely approach the mechanical properties of biological tissues[28].

In the next few sections we critically explore the properties of different tissues in terms of their static and dynamic mechanics, beginning with the microscale and nanoscale domains of biological structures and continuing in size order up to the macroscale level.

II.3. TISSUE MECHANICS AT INCREASING SCALES

To understand the mechanical complexity of an organ or a complete functional tissue, one must first consider its smallest constituents. A biological tissue is fundamentally composed of ECM and cells, which coexist in a delicate synergy: the ECM is deposited by cells, which strongly interact with it. Beyond the fact that ECM structures themselves have inherent mechanical properties, they are also involved in cellular signaling (derived from both biochemical cues and mechanotransduction events), which has consequences for the mechanical properties of cells[29,30]. ECM mechanics and cell mechanics are intimately intertwined and together contribute to overall tissue behavior. As such, one must not only consider the individual properties of ECM and cells but also understand the development of functional biological tissues. Multicellular structures require analyses of the locations where cell–cell connections are established and how these cellular structures bind to the ECM they produce and thereby create the basal mechanical framework of biological tissues. Here, we use a sequential approach, starting with an analysis of ECM and cells and gradually integrating their mechanical behavior, informed by remarkable insights from developmental biology studies.

II.3.1. Extracellular matrix components

The type, concentration and organization of ECM components (which are all fabricated by cells) deeply affect the mechanical properties of both healthy and diseased tissues (discussed further in the ‘Abnormal tissue states’ section). The literature on mechanical properties of individual ECM components is scarce, and most reported analyses were done on bulk tissue samples or on structures (such as hydrogels) engineered from ECM components[31]. Nonetheless, several well-known ECM

components occur in many different tissues and are critical for homeostasis, healing and regeneration, namely proteins (such as collagen, elastin, fibronectin, laminin, tenascin, vitronectin) and glycosaminoglycans (GAGs)[32]. Each of these components has distinct functions and, naturally, different mechanical properties (**Table II-2**).

Table II-2: Mechanical moduli of extracellular matrix components.

Component	Technique	*E* values	Refs.
Collagen molecule	X-ray diffraction	3–9 GPa	33
Collagen fibril	AFM indentation or tensile deformation	2–7 GPa (tensile), 5.0–11.5 GPa (indentation)	34
Collagen fiber	Micro-bending	100–360 MPa	226
Fibronectin fiber	Microelectromechanical systems tensile deformation	Up to 3.5 MPa (strain-dependent)	50
Fibrin fiber	AFM tensile deformation or micro-bending	1–28 MPa	227,228
Elastin fiber	Tensile deformation	1.1–1.2 MPa	229,230

AFM, atomic force microscopy; *E*, uniaxial elastic Young's modulus.

II.3.1.1. Collagen.

Collagen is the most abundant ECM component and is consequently the one that has been most thoroughly explored in terms of its mechanics. From single molecules to fibrils, collagen structures have elastic moduli in the GPa range[33,34]. The final contribution of these structures to the bulk mechanics of living tissues depends mainly on collagen abundance and organization. Collagen exists in 28 currently known types, which act not only as structural proteins but also have other functions such as cellular adhesion that are similarly important for overall ECM assembly and its consequent tissue mechanics

(reviewed elsewhere)[35,36]. Collagen structures and specific domains within the molecule can also be mineralized, leading to the formation of truly stiff ECMs such as those present in bone[37].

Interestingly, some tissues are soft at low strains owing to a random collagen fiber orientation. Upon stretching, the collagen molecules align and become an extremely stiff network, which shifts the Young's modulus of the tissue towards that of the collagen fibers themselves[38–40]. Thus, tensile deformation leads to a J-shaped stress–strain curve in which deformation can initially be obtained by relatively low stress, whereas much higher stress is needed to reach higher deformations. For example, it doesn't take much force to pinch and pull a few millimeters of skin, but further deformation requires a much higher (and more painful) force. Once the force is released, skin returns to its original shape.Thus, biological tissues have the capacity to limit the deformation resulting from high levels of strain owing to reorganization of their structural fibers (mainly collagen), which gradually increases tissue stiffness and prevents damage from excessive strain. As such, it is important to characterize the moduli of tissues at both high and low strain levels. An attempt to engineer a life-like tissue based on its low-strain stiffness would probably fail to fulfil its function of preventing high-strain damage. Conversely, a tissue engineered to reflect only the high-strain modulus would be too stiff to have the compliant mechanics required for limb movement. Thus, biological tissues with a J-shaped stress–strain curve should be substituted for by materials with similar J-shaped curves[41].

II.3.1.2. Elastin.

Elastin, so named for its elasticity-enhancing capabilities, is another ECM component that is intimately related to collagen in terms of its contribution to tissue mechanics. Both collagen and elastin form fibrous networks that are intimately interwoven but remain structurally independent from each other. Elastin is frequently present in organs such as skin, lungs, and bladder but its most important function relates to blood vessels, namely arteries, where specific combinations of collagen and elastin determine the mechanical properties of the arterial wall and consequently regulation of both blood pressure and blood flow[42]. Importantly, elastin shows a notably high linear elastic extension. Thus, the addition of elastin reduces the elastic modulus of a tissue, and as such leads to a more compliant (easier to deform) structure. This effect is accounted for by the two orders of magnitude difference between the elastic moduli of collagen and elastin fibers (**Table II-2**).

The main function of hydrated elastin is to elastically stretch and contract, thereby acting as the driving force of elastic tissue recoil upon release of the force that caused the deformation[43,44]. The interplay of elastin and collagen leads to J-shaped stress–strain curves that show a high initial linear elastic extension, owing to the alignment of elastin's disordered structure (entropic), with linear behavior at increased deformations owing to the molecular stretching of collagen fibers (enthalpic). In practical terms, increasing the elastin:collagen ratio leads to a decrease in overall tissue stiffness and an increase in its deformability and recoil, which can be employed in the development of elastic tissue-engineering scaffolds[45]. By contrast, a decreased elastin:collagen ratio has the opposite effects, as observed in several arterial conditions[46].

II.3.1.3. Other ECM molecules.

GAGs are also highly represented across distinct tissues, but their mechanics are poorly understood. In part, this lack of investigation could be due to their apparently minor contribution to the tensile-like moduli of tissues compared with that of ECM components such as collagen[47]. Nevertheless, GAGs are fundamental for water retention, shock absorption, lubrication and tissue viscoelasticity, properties that make them extremely important for the biomechanics of tissues such as cartilage, specifically its bulk compressive stiffness[48].

In fact, the mechanical contribution of GAGs in articular cartilage is highly dynamic. Aggrecan, one of the main cartilage GAGs, can have distinct mechanical contributions depending on the loading conditions. Upon quasi-static loading, both electrostatic and steric interactions are responsible for the mechanical function of GAGs in cartilage, whereas under dynamic load (such as during running), solid–fluid interactions (that is, between GAGs and the interstitial fluid within cartilage) become the main contributor. These interactions, also known as poroelasticity, lead to cartilage interstitial fluid pressurization and self-stiffening of cartilage with increasing loading frequencies[49].

Fibronectin, another common component of the ECM in various tissues, also has an interesting role in tissue mechanics. Softer than most fibrillar ECM structures, fibronectin can be stretched by cell-generated tension and is able to extend more than eightfold before 50% of the fibers will experience rupture[50]. Furthermore, fibronectin fiber stiffening leads to an increase in E of up to 3.5 MPa **(Table II-2)**, a process accompanied by a force-dependent exposure of cryptic binding sites, which leads to

changes in cell behavior[50]. This evidence indicates a highly dynamic synergy between cell and fibronectin mechanics, which has also been shown to contribute prominently to the mechanical driving of tissue development[51].Collagen, fibronectin and many other ECM components interact directly with cells, which not only synthesize but also remodel and adhere to them. The interaction is mutual: cells both create and influence the ECM components that drive tissue mechanics, which in turn regulate the behavior of cells. Thus, it is easy to understand how small defects in ECM molecules might lead to devastating diseases such as osteogenesis imperfecta (brittle bone disease)[52], junctional[53] and dystrophic[54] epidermolysis bullosa (severe blistering of the skin), as well as Ehlers–Danlos syndrome collagenopathies (widespread connective tissue fragility, including life-threatening vascular instability)[55,56].

II.3.2. Cellular mechanics

The mechanical properties of cells (as well as their shape[57]) are closely intertwined with their behavior. Only a few hours after fertilization, the mechanical properties of the oocyte already dictate its viability potential[4]. In 2007, the publication of a pivotal review entitled "The cell as a material"[58] for the first time considered cells as a material in their own right with characteristic mechanical properties that could be investigated using distinct techniques, one of the most important of which was AFM indentation. Overall, cells are soft entities; most have bulk elastic moduli in the 0.1–10.0 kPa range, which hardly varies with cell type (**Table II-3**). However, some variability-generating details require further discussion.

Table II-3: Mechanical moduli of distinct cell types.

Cell type	Technique	Moduli	Moduli values (condition)	Refs.
Differentiating MSCs	Micropipette aspiration	*E*	0.89 kPa (osteogenic), 0.22 kPa (adipogenic)	78
MSCs	AFM indentation	*E*	2.5 kPa (spherical[a]), 3.2 kPa (spread[b])	100
Osteoblasts	AFM indentation	*E*	2.6 kPa (spherical[a]), 6.5 kPa (spread[b])	100

Pancreatic cells	AFM indentation	*E*	0.54 kPa (healthy cell), 0.54 kPa (carcinoma)	5
Cervical epithelial cells	AFM indentation	*E*	2.05 kPa (healthy cell), 2.80 kPa (carcinoma)	160
Fibroblasts	AFM indentation	*E*	0.5–30.0 kPa (cell body)	71,231
Pleural effusion cells	AFM indentation	*E*	0.38 kPa (metastatic cell), 2.53 kPa (healthy cell)	161
Lung cells	AFM rheology	*G'*	0.5 kPa (alveolar cell), 0.7 kPa (bronchial cell)	232
Embryonic stem cells	Magnetic twisting cytometry	*G*	0.55 kPa (naive), Up to 2 kPa (differentiated)	80
Adipose stem cells	AFM indentation	*E*	0.6–1.6 kPa	77
Smooth muscle cells	AFM indentation	*E*	5.9–7.7 kPa	233
Cardiomyocytes	AFM indentation	*E*	41 kPa	98
Keratinocytes	AFM indentation	*E*	120–340 kPa	234
Kidney proximal tubule cells	AFM indentation	*E*	0.35 kPa	235
Hepatocytes	AFM indentation	*E*	0.75-1 kPa	236
Thyroid cells	AFM indentation	*E*	1.2 kPa (healthy cell), 1.3 kPa (cancer)	73
Eye lens cells	AFM indentation	*E*	4.83 kPa (nuclear cells), 0.22 kPa (cortical cells)	237

[a] Spherical cells have a round morphology owing to a short culture duration. [b] Upon continued culture, cells lose their initial spherical morphology and exhibit spread over the surface. AFM, atomic force microscopy; *E,* uniaxial elastic Young's modulus; *G,* shear modulus; *G',* shear storage modulus (dynamic); MSC, mesenchymal stem cell.

Firstly, cells (like tissues) are heterogeneous. Despite the softness of whole cells, certain cellular constituents, namely cytoskeleton fibers, have elastic moduli in the GPa range[59]. The contribution of these fibers to the mechanics of cells varies with the type of load applied. Intermediate filaments, actin filaments and microtubules (in order of increasing stiffness) respond differently to distinct types of deformation. Microtubules and actin filaments show substantial resistance to

compressive forces, whereas intermediate filaments are best able to endure tensional loads[60]. Furthermore, some cytoskeleton fibers (such as microtubules and actin filaments) have a polarized molecular structure that enables them to act as molecular motors, which leads to a further level of mechanical complexity. Actin filaments, which dictate cell shape and consequently direct events ranging from motility to growth and differentiation, are frequently complexed with myosin to form a contractile structure termed actomyosin (also known as stress fibers)[61]. In the majority of animal cells, cell mechanics are dictated by a mesh of actomyosin known as the cortex, a mechanically rigid and highly plastic structure immediately below the cell membrane[62]. Within this actomyosin mesh, myosin is able to pull on actin fibers, which generates considerable tension, or pre-stress[61]. This actomyosin-generated tension in the cell cortex is responsible for cell shape and integrity in a fashion that parallels architectural tensegrity structures.[63] Moreover, this tension propagates through cell–cell and cell–ECM junctions and as such is fundamental to the architecture and function of living tissues[64]. Actomyosin-generated tension is typically increased in the intracellular stress fibers that act as an essential link between the cytoskeleton and focal adhesions, which connect cells to the ECM. This role explains why regions of the cell near focal adhesions are stiffer than the surrounding areas[61]. For all these reasons, when assessing cell mechanics by AFM indentation, the moduli derived will be highly dependent on the exact membrane zone indented[65], a clear source of variability.

Furthermore, it is important to understand that cytoskeleton fibers are not the only cell component to have an effect on cell stiffness or shape. Interactions of cytoskeletal fibers with the intracellular and extracellular environment are also involved. For example, cellular activity can take advantage of cytoplasmic changes and osmotic forces. Early theories hypothesized that local cell membrane protrusions (also termed blebs) were initiated by severing of cytoskeletal fibers, which was thought to locally reduce the elastic modulus and thereby lead to an increased cell volume owing to osmotic effects. The consequent rise in hydrostatic pressure was suggested to force the membrane into a protrusion, which would eventually be stabilized by actin diffusing into it and then polymerizing[66]. In 2005, however, a more likely mechanism was suggested: that local actomyosin contraction at the cortex compresses nearby cytoplasm, which increases local hydrostatic pressure and leads to the formation of blebs even when cell membrane protrusion is opposed by membrane tension and osmotic pressure[67].

Together, these complex phenomena indicate how an appreciation of the mechanical heterogeneity of cellular components can facilitate understanding of the mechanical properties of whole cells. It is useful to picture a cell as composed of a membrane encapsulating a very complex elastic network comprising the cytoskeleton and organelles within a fluid (cytosol), collectively termed the cytoplasm[67]. Unlike most engineered gels, the cytoplasm is continuously out of equilibrium owing to the active role of molecular motors such as myosin. These motors expend energy and the resulting fiber polymerization and network contraction enable intricate mechanical events to take place at the cellular cortex. Accordingly, the cortex is characterized as an active gel[68]. Overall, it is important to understand that living cells integrate a set of mechanical properties that are among the most unique and complex found in nature, and which can currently be explained only by resorting to several different theories (**Box 2**). This heterogeneity will undoubtedly need to be considered when trying to assess the bulk stiffness of single cells[69].

Secondly, when addressing the mechanical properties of cells in adhesive scenarios, it is important to understand that, as a consequence of adhesion and spreading, cells might become extremely thin[70]. As such, AFM indentation depths have to be taken into consideration to avoid 'bottom effects' (in which measured stiffness values are too high owing to an influence of the surface beneath the cells rather than the mechanics of cells themselves)[71]. Several methods of correcting for bottom effects can be applied in multilayer cell mechanics[72]. This effect might partially explain why some reported mechanical properties of cell monolayers grown on tissue culture polystyrene (TCP) might not recapitulate *in vivo* ones. Simultaneously, the surface to which the cells adhere also affects cytoskeletal tension and consequent bulk mechanics, and these factors should be preferentially analyzed on surfaces that are mechanically as native-like as possible. For example, the elastic modulus of thyroid cells is over twofold higher when cultured on TCP rather than on a softer, thyroid-like surface[73]. Nevertheless, even when the moduli mismatch of cells grown on a native-like surface is not as large as that of cells cultured on TCP, bottom effects might still have a considerable effect on measurements of relevant moduli, indicating the need for adequate correction[74].

Cell spreading and surface stiffness are not the only sources of variability. In fact, when cells are constrained in a fixed area, the shape they assume can have a greater effect on their mechanics than the surface stiffness itself, which is especially important to consider when cells are cultured on

surfaces with non-flat topographies (such as grooves or micropillars)[75,76]. This knowledge might also prove important in future initiatives to standardize the measurement of cell mechanics and thereby obtain more uniform, comparable results. The health status of cells can also give rise to large differences in stiffness (discussed in the 'Abnormal tissue states' section).

Altogether, the mechanical properties of cells reflect interesting biological events of relevance to tissue engineering. For example, with regard to cell differentiation, adult stem cells from different niches were shown to have distinct elastic moduli depending on their commitment: osteogenic stem cells were stiffer than adipogenic stem cells[77,78]. Similarly, the differentiation of embryonic stem cells (ESCs) is intimately connected to changes in stiffness[79,80]. Although the mechanical properties of cells themselves cannot yet be artificially engineered or directly manipulated, the mechanical properties of their surroundings and consequent cell mechanics can be[81,82]. Nevertheless, understanding the mechanics of bulk tissues requires not only an overview of single-cell and ECM structural mechanics but also an understanding of how single-cell mechanics integrate to generate the mechanics of multicellular structures, and of how single-cell and multicellular mechanics combine with ECM mechanics to generate overall tissue mechanics.

BOX 2 Towards a unified description of cellular mechanics.

The past three decades have seen substantial efforts to define the ruling principle behind cellular mechanics and its consequential effects on mechanotransduction responses and all consequent cellular events (including cell membrane protrusion, adhesion, migration and mitosis). The cellular tensegrity model proposed that the cytoskeleton is a tensioned or prestressed network responsible for maintaining cellular stability, in the same way that tensegrity architecture enables buildings and bridges to stay unchanged and robust for countless years[277]. Subsequently, other researchers hypothesized that cells behaved as a soft glassy material; that is, having time-scale free and frequency scale free rheological behavior that obeys a weak power-law[278]. This notion became known as the soft glassy rheology (SGR) model, which was later complemented by evidence that at extreme time-scales or frequencies, cellular behavior deviated from a single power law and showed time-scale dependency[279]. Nevertheless, among its fundamental characteristics, the SGR model implies that cells (in common with other soft glasses) are metastable structures that are naturally out of equilibrium. Although this

characteristic is in agreement with the recent description of cortical cell networks as out-of-balance, active gels[68], some difference exists between the SGR model and a stable, equilibrated tensegrity model. Until now, both models are still employed to describe the distinct phenomena governing cell function: both models suggest that actomyosin pre-stress is the link between cytoskeletal stabilization and power-law modulation of cell behavior[280]. Nevertheless, a general unification of these models is yet to be established.

II.3.3. Cell-cell and cell-ECM interactions

Many cell types are able to self-assemble into multicellular monolayers resembling the epithelial sheets formed during early development. Where cells contact each other, they form cell–cell adhesions through the binding and assembling of specific proteins, such as cadherins and catenins[83]. Interestingly, the resulting epithelial sheet still behaves actively in mechanical terms, just as single cells do, being able to sustain extreme strain under constant tension[84]. As the number of constituent cells increases, the active tension of the resulting monolayer also increases in a linear fashion[85]. In this scenario, where the predominant interactions are between cells rather than with the minimal ECM, stresses can propagate over long ranges[86]. In fact, monolayers of up to thousands of cells were shown to undergo stress relaxation very similarly to single cells, in that the cell–cell junctions serve as stable connections enabling these monolayers to behave in mechanical terms as single cells ruled by actomyosin dynamics[87]. Briefly, the application of sufficient stress leads to the rearrangement of intracellular actomyosin, which in turn promotes extension of the monolayer, thereby dissipating stress and resulting in a new mechanical steady state[87]. However, once a stiff ECM is present, stress no longer propagates across the monolayer in the same way[86].

As cells begin to aggregate and organize into multilayered 3D structures, such as organs and tissues, the number of cell–cell interactions increases substantially[88]. Interesting research on the mechanics underlying early development has shown that the viscoelastic (stress relaxation) behavior of cells still occurs in embryonic tissue and that the overall stiffness of this tissue is also close to that of single cells (below 1kPa)[89]. Nevertheless, the elastic modulus of embryonic tissues shows considerable

variation and is also responsible for driving morphogenesis[89]. At this stage, tissue responses are guided not only by quick-dissipating cellular stresses but also by supracellular, persistent ones[90].

The initial phases of tissue formation occur in extremely dynamic, active and soft environments, where three essential entities govern mechanical outcomes: volumetric growth (mainly driven by cellular proliferation), active forces and the material properties of local tissues[91]. The precursors of cartilage, bone, and other stiff and soft tissues are all present within this soft structure, some of which must progressively stiffen by up to seven orders of magnitude to reach the 20 GPa of cortical bone[92]. This requirement leads to two important principles: first that, fundamentally, tissue development always proceeds in the direction of increasing stiffness. Soft environments are always present before stiffer ones arise — even after a bone fracture, the regeneration of bone is preceded by the accumulation of considerably softer materials: haematoma, granulation tissue and fracture callus (in order of increasing stiffness), within which ECM fibers accumulate and eventually mineralize to form stiff bone[93,94]. In order to understand how early embryonic structures stiffen and eventually develop the mechanical characteristics of mature tissues, we must further consider the interplay of ECM and cellular mechanics.

The early embryonic ECM acts mostly as a basement membrane for embryonic epithelia. Nevertheless, the mechanical effects of cell–ECM interactions can first be observed here. Epithelial cells, as part of their normal activity, secrete and deposit ECM fibrils, which form the basement membrane to which the cells adhere, thereby gradually increasing its stiffness[95]. The stiffness of this early extracellular structure then begins to overtake that of the attached cells, increasing from 20 kPa at early embryonic stages up to 800 kPa at later time points. Additionally, the ECM fibrils have a preferential orientation that leads to heterogeneous directional stiffness[95], which represents the earliest appearance of ECM-related tissue anisotropy. In the embryonic stages of nematode development, the apical ECM was shown to be essential for cell anchoring and transmission of actin-derived stresses, through the formation of an actin–ECM composite with distinct mechanical properties[96]. It is this very early ECM configuration that causes the shift in mechanics from single cell-like to tissue-like, although the embryonic tissue still goes through considerable further dynamic changes related to cell migration and morphogenesis[97].

As the development of these embryonic structures continues, so does the deposition and accumulation of ECM, thereby generating ever more complex structures. Eventually, this process leads to the formation of stiffer tissues. The mechanics of some of these stiffer tissues are mostly dependent on the ECM, whereas the stiffness of softer, highly cellular tissues is closer to that of their constituent cells. Cardiomyocytes have elastic moduli close to those reported for cardiac tissue[98] because the mechanics of muscle tissue are principally dependent on those of its contractile, actomyosin-rich cells[99]. By contrast, both mesenchymal stem cells (MSCs, also known as bone marrow stromal cells) and the osteoblasts they differentiate into during osteogenesis are quite soft in comparison to bone[78,100] because bone mechanics are mostly governed by the abundant, highly mineralized ECM. Naturally, in highly cellular tissues at late stages of development, the heterogeneity and mechanics of the constituent cell types play an important part in the final stiffness of the tissue[101]. Behind this heterogeneity are differences in cell types and their respective structures, spanning from the cell membrane[102] to the previously discussed intricacies of intracellular architecture.

Benchmarking of tissue engineering approaches against knowledge obtained from developmental biology has already proved important in the recapitulation of adequate stimuli prompting the *in vitro* generation of desired cell phenotypes[103]. Even though much remains to be learned within this field, understanding of how the mechanics of different biological components are integrated into a tissue is already possible on a basic level, and is expected to facilitate similar analyses of fully developed biological structures.

II.4. THE STIFFNESS RANGE OF LIVING TISSUES

Not surprisingly, a system as complex as a human organism comprises tissues that span a remarkable spectrum of stiffness; elastic moduli range from the 11 Pa of intestinal mucus[104] to the 20 GPa of cortical bone[92]. Between these extremes, almost all orders of magnitude are represented by a distinct tissue (**Fig. II-2**).

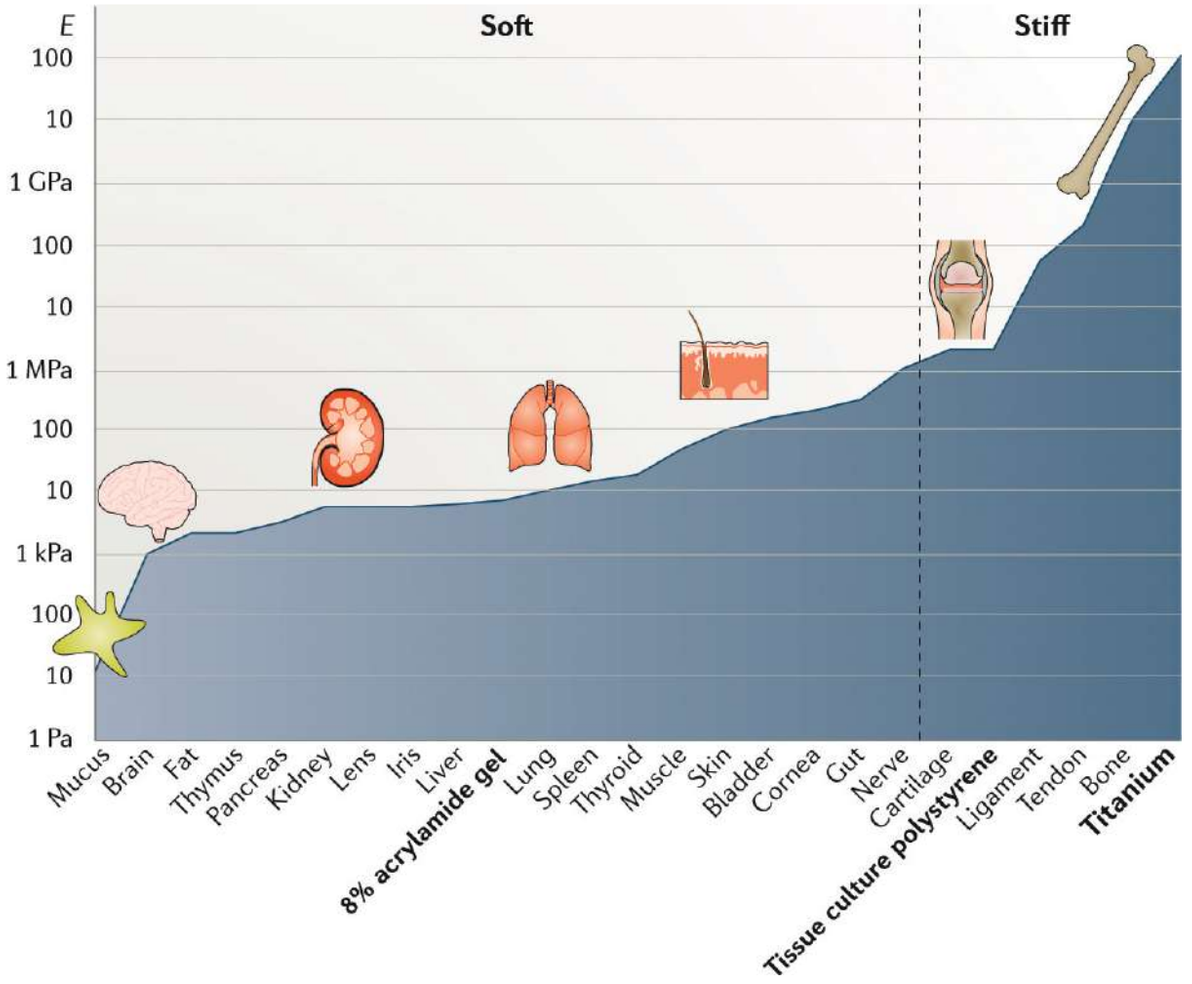


Figure II-2: The stiffness of living tissues spans a full Pa–GPa range. The literature-reported elastic moduli (E) of tdifferent tissues are reported in the left (logarithmic) scale. Tissues are organized by increasing crescent moduli. Central nervous system (CNS) tissues, as well as most abdominal organs and skin have moduli within the sub-MPa level and as such are generally characterized as soft tissues (in biological terms). Cartilage, ligament, tendon and bone are the stiffest tissues of the human body. For comparison purposes, the moduli of some common tissue engineering materials are included in the graph: 8% acrylamide gel274, tissue culture polystyrene275 and titanium (used for dental and bone implants) 276. Tissue culture polystyrene, the standard cell-culture substrate, is clearly stiffer than almost all biological tissues, an important source of error in mechanical analyses derived from in vitro studies. The reported moduli are derived from studies across different animal models and types of deformation, although we have prioritized studies using human tissues and physiological-like deformations (mostly at macroscale dimensions).

Neural tissues are amongst the softest of the human body[105], which should be expected considering their anatomical protection and how easily they can be damaged. These are followed by most abdominal organs (such as the pancreas, spleen and liver) and muscles, and finally by supportive structures such as cartilage, tendons, ligaments and eventually bone. From the analysis of the compiled

information (**Table II-4, Supplementary Table II-1**), some important points are worth discussing further.

Table II-4: Mechanical moduli of human tissues.

Tissue	Dimension	Moduli	Moduli value (condition)	Refs.
Nervous system				
Brain	Macroscale	*G*	1–3 kPa	170,238,239
Spinal cord	Macroscale	*E*	1.23 MPa (tensile)	110
Nerve	Macroscale	*E*	5 MPa	240
Connective tissue				
Bone	Nanoscale	*E*	1.28–1.97 GPa	128
Bone	Macroscale	*E*	10.4–20.7 GPa	92
Cartilage	Macroscale	*G*	5.7–6.2 MPa	241
Adipose tissue	Macroscale	*E*	1.6–5.5 kPa	131,139,242
Ligament	Macroscale	*E*	25–93 MPa	243–245
Muscle tissue				
Cardiac muscle	Macroscale	*E*	8 kPa	246
Cardiac muscle	Macroscale	*G*	5–50 kPa	171,247
Skeletal muscle	Macroscale	*E, G*	5–170 kPa	248–251
Endothelial or epithelial tissues				
Skin	Macroscale	*E*	60–850 kPa (35 kPa dermis, 2 kPa hypodermis)	111,117,120, 252
Skin	Nanoscale	*E*	4.5 MPa (epidermis), 0.1 MPa (dermis)	141
Lung	Macroscale	*G*	0.84–1.50 kPa	253,254

Lung	Nanoscale	*E*	1.96 kPa	255
Other organs				
Kidney	Macroscale	*G*	4 kPa (cortex), 5 kPa (medulla), 8 kPa (sinus)	256,257
Spleen	Macroscale	*G*	15–20 kPa	144–147
Liver	Macroscale	*E*	4.0–6.5 kPa	258–260
Liver	Macroscale	*G*	2 kPa	261,262
Thymus[a]	Macroscale	*E*	2.11 kPa	131
Thyroid	Macroscale	*E*	9–50 kPa	169,263–265
Thyroid	Macroscale	*G*	1.3–1.9 kPa	266
Pancreas	Macroscale	*E*	2.9 kPa	267
Pancreas	Macroscale	*G*	1.1–2.1 kPa	223,268,269
Bladder	Macroscale	*G*	50 kPa (empty) up to100 kPa (full)	270
Cornea	Macroscale	*E*	0.2 MPa	271
Cornea	Nanoscale	*E*	7.5–109.8 kPa[b]	272
Lens	Nanoscale	*E*	0.4 MPa (capsule)	273
Lens	Macroscale	*E*	2.3–3.3 MPa (capsule)	122,123
Lens	Macroscale	*G*	0.2–10.3 kPa	124

[a]Decellularized. [b]Distinct layers of the cornea have different moduli, as detailed in Supplementary Table II-1. *E*, elastic modulus; *G*, shear modulus.

II.4.1. Dimension scale and direction

Differences between tissue mechanics measured at nanoscale, microscale or macroscale dimensions are extremely relevant to tissue engineering and therefore dimension should always be

considered (**Table II-4, Supplementary Table II-1**). Such differences of scale are mostly a consequence of the heterogeneity of biological tissues, as other authors have already reported[106]. In general terms, if a tissue is deformed in a tensile manner or the whole tissue is compressed, the behavior of the bulk material contributes to the overall measured mechanical moduli. By contrast, if a tissue is indented, only the region where the indentation takes place (and eventually its nearby surroundings) will contribute to the measured moduli. The smaller the indenting tool (for example, microscale versus nanoscale), the less likely it is that the measured moduli will be representative of the whole tissue[106]. For example, the response to compression of a whole bone sample integrates both trabecular and cortical bone mechanics, whereas microindentation of the same sample is likely to reflect deformation of only one of these two types of bone[107] and nanoindentation will target only a single cell (such as an osteoblast) or ECM component (such as a collagen fiber)[108].

Similarly, microindentation studies of spinal cord reported values within the 0.5–1.5 kPa range[109], whereas tensile deformation studies reported values three orders of magnitude higher (1.23 MPa)[110]. However, microindentation involves not only a difference of scale when compared with tensile deformation, but also a difference in the direction of the applied force; microindentation is usually transverse to the tissue, whereas tensile deformation is mostly longitudinal. In fact, other corroborative evidence is provided in reports showing that dermis macroindentation results in elastic moduli of ~35 kPa[111] whereas tensile deformation results in elastic moduli in the 50–150 kPa range[112]. Even when, as in this case, analyses were conducted at the same scale (which might be expected to lead to a fairly small discrepancy), substantial differences can result from altered directionality. These factors explain why certain techniques are not appropriate for direct comparison. Even if the same type of modulus is derived, the dimension at which it is measured as well as its direction must always be considered.

The mechanics of engineered tissues at all dimensions are fundamental for their function: the bulk mechanics are important to ensure *in vivo* stability whereas microscale and/or nanoscale properties are essential for regulating cellular behavior[113].

II.4.2. Tissue anisotropy or composite material?

Composite materials are made of distinct components, each with different properties, that when combined form a material with properties that are different from those of the individual constituents. These materials are used in high-end applications owing to their optimal performance and as such, natural evolution might have followed a similar path[114]. In fact, many biological tissues easily fit within the above definition of composite materials[115]. Some even seem to be composite materials made of other composites, tendon being an obvious example[116]. A tendon is a hierarchical structure made of various types of collagen fibers bundled together in subfascicles, which in turn are bundled into fascicles of increasing hierarchy to form the tendon itself. This organization resembles that of synthetic composite materials consisting of fibers with specific unidirectional mechanical properties bundled together by a resin, which results in a highly anisotropic material. Similarly, tendons are capable of sustaining a high level of stress through tensile deformation of the collagen fibers and fascicles. The resulting tissue anisotropy is the reason why some mechanical relationships (such as equation II-3) do not hold true and should not be employed in the analysis of biological tissue mechanics, and also explains the differences in elastic moduli derived by mechanical tests employing different directions of deformation.

Parallels could also be drawn between laminated composite materials and organs such as the skin, which is composed of three layers of distinct but interacting tissue (epidermis, dermis and hypodermis). The skin has bulk elastic moduli of up to several hundred kPa[117] whereas the fiber-reinforced dermis[118] has elastic moduli of around 35–150 kPa and the hypodermis has elastic moduli of around 2 kPa, similar to adipose tissue[111,112,119,120]. The lens of the eye comprises a stiff capsule with elastic moduli of 2–3 MPa and a very soft core (0.8–11.8 kPa)[121–124]. In the lung, the pleura are also considerably stiffer than the parenchyma[125] (**Supplementary Table II-1**). In such tissues, the mechanics of individual components might be more relevant for their engineering than the bulk tissue properties. Finally, some organs also present variable mechanics along their length; for example, the elastic moduli of gut tissue range from 789 kPa at the ileum to 323 kPa at the descending colon[126].

II.4.3. Tissue condition

Tissue condition can also have important mechanical consequences. Bone mechanical properties can differ depending on collection site, processing method and storage[127]as well as host-related factors such as age and health status[128]. Several reports have also considered the mechanical properties of decellularized tissues, which not only lack the cellular component but are frequently stiffer than native tissue as a result of the treatments needed to remove cells. This increased tissue stiffness has been reported for decellularized lung[129], pancreas[130] and fat[131]. Furthermore, even with cellular tissues, increased preservation duration can also lead to stiffening, as shown with liver[132].

II.4.4. The applied deformation

Native-like deformations are generally the most useful to derive mechanical properties relevant to tissue engineering. For example, the mechanics of bone and cartilage might seem fairly straightforward to analyze. However, bone can be considered a composite material consisting of mineral, organic and water phases. A compressive test under static load would be useful to characterize the contribution of the mineral component (which mainly has an elastic response) to bone mechanics, but only dynamic analysis would be able to integrate the viscous contribution of the collagen-rich organic phase, which confers damping and shock-absorption properties on bone. Similarly, testing of dry bone will not assess the contribution of hydration[133]. Articular cartilage, moreover, must support the interfaces between bones at the joints and allow the relative movement of limbs. Therefore, cartilage is natively subjected to repetitive, cyclic stress involving compressive as well as shear forces, which is why engineering of this tissue presents such a therapeutic challenge[134]. As such, emphasis should be given to DMA and tests such as shear rheology. In fact, cartilage can have higher moduli under dynamic testing than under static deformation[135–137] as a consequence of the previously discussed electrostatic and solid–fluid interactions. Furthermore, the long-term responses of complete tissues to applied stress or deformation (such as creep and strain relaxation) are thought to be crucial for their physiological behavior. As an example, blood vessels dilate in response to increased blood flow[138]. Nevertheless, these responses are frequently not considered in studies of tissue mechanics.

II.4.5. Nonlinear behavior

Several biological tissues do not have a linear stress–strain relationship, and this nonlinearity can hinder comparisons of different studies on the mechanics of living tissues. Examples of nonlinearity show up in early epithelial monolayers[86,87] and can also be seen in adipose tissue, skin and even in tendons, which all deform easily at low levels of strain but become much stiffer as strain increases[38,139]. In tendons, as the tissue stretches, collagen fibrils and cells become more aligned, resulting in an extremely stiff structure that can easily reach elastic moduli of 100–200 MPa[140]. This particular mechanical response of tendons is also responsible for their negative Poisson's ratio[34]. Therefore, when studying tissues with nonlinear stress–strain relationships, emphasis should be given to strain levels and low strain deformations should not be compared to high strain ones.

II.4.6. Gaps in the literature

Many examples exist of tissues that have been far less thoroughly explored with regard to their mechanical properties. Peripheral nerves, ligaments, gut tissue and spleen have been analyzed in depth at bulk, macroscale dimensions, but lack further study at nanoscale or microscale levels. In other tissues, little to no exploration of mechanics has been done. For example, the mechanical properties of the thymus have only been reported for decellularized tissue[131]. Other tissues, such as skin, require further exploration at smaller scales to clarify some discrepancies; the mechanical stiffness of epidermis is higher than that of dermis in some[141] but not all[142] nanoindentation studies. Further analysis is necessary to fully understand and to engineer the multilayered mechanics of skin and skin-like constructs.

II.5. ABNORMAL TISSUE STATES

Scientists have identified several different causes of altered tissue stiffness, including cancer, advanced age, diabetes mellitus, cardiovascular disease and fibrosis[143]. Nevertheless, some changes in bulk mechanics are not truly caused by changes in the tissues themselves but rather are attributable to changes in blood pressure and their circulatory consequences. For example, spleen stiffness can

increase from 15–20 kPa in healthy individuals[144–147] to 50 kPa in patients with liver fibrosis[148] — an abnormal spleen state that is not a consequence of having abnormal spleen tissue. In the next sections, we discuss the main causes of abnormal tissue mechanics: fibrosis and cancer (**Fig. II-3**). Of note, most ECM changes in individuals with cancer are fibrotic responses to the neoplastic event[149].

II.5.1. Fibrosis

Fibrosis can be briefly described as the aberrant deposition and accumulation of connective-tissue-like ECM in a tissue or organ resulting from an imbalance between its production and degradation. This imbalance leads to the formation of a disorganized and excessively crosslinked fibrous network, along with the release of inflammatory signals, myofibroblast differentiation and other cellular and/or molecular events[150,151] resulting in a tissue with increased overall stiffness. Although these adverse effects of fibrosis and/or scarring can be disregarded in small wounds, large cutaneous scars and widespread fibrosis in tissues or organs such as the lung[152], kidney[153] and liver[154] are serious life-threatening conditions. Interestingly, increased liver stiffness is itself a major diagnostic criterion for liver disease[155]; a fibrotic liver is stiffer than a healthy one at both macroscopic[156,157] and microscopic levels[158].

II.5.2. Cancer

Unhealthy cells, including cancer cells, frequently have altered mechanical properties, although the direction of these alterations shows no consistent trend. Some authors report that cancerous cells are stiffer than their healthy counterparts[159,160], whereas others show the opposite[5,161]. Clearly, each type of tissue and disease can lead to distinct cell mechanical outcomes[162,163]. In fact, many of the signaling pathways that are frequently altered in cancer cells converge on changes in the expression of cytoskeleton-associated proteins, namely those responsible for actin fiber polymerization and myosin contraction[164,165]. These processes are fundamental for the mechanical properties of cells and can even have a direct effect on the ECM mechanics of tumors. Thus, since cancer cell signaling is highly

heterogeneous and varies not only with the type of cancer but also within the same disease type, it is natural that this heterogeneity might equally transpose to the resulting cancer cell stiffness.

Cancer has been characterized as "a wound that does not heal"[166]. As such, much of the characteristics of a non-healing, fibrotic wound are shared by neoplastic lesions. In both injury and neoplasia, abnormal cell proliferation leads to a desmoplastic response (that is, dense overgrowth of basement-membrane-like connective tissue with low cellularity and either a translucent, cartilage-like appearance or a hardened texture with disorganized blood vessel infiltration). ECM deposition and tissue stiffening similarly occur in the tumor microenvironment[149], where these processes are further amplified by the ability of cancer cells to drive stromal cells towards a profibrotic phenotype[167]. In cancer, moreover, the abnormal cell proliferation also generates increased solid stress, caused not by a change in the stiffness of the tissue itself but instead by the increased pressure resulting from tumor growth in a constrained physical volume (mass effects), which compresses nearby healthy tissue[149]. Together with the increased solid stress, the previously discussed increase in cancer cell tension derived from actin and myosin-related signaling might also increase the stiffness of nearby ECM via tensing or realignment of ECM fibers[168].The combination of increased cell stiffness and solid stress can drastically increase the stiffness of some malignant lesions: the elastic moduli of healthy thyroid tissue (9.0–11.4 kPa) can increase by a full order of magnitude to 44–110 kPa in patients with papillary adenocarcinoma[169].

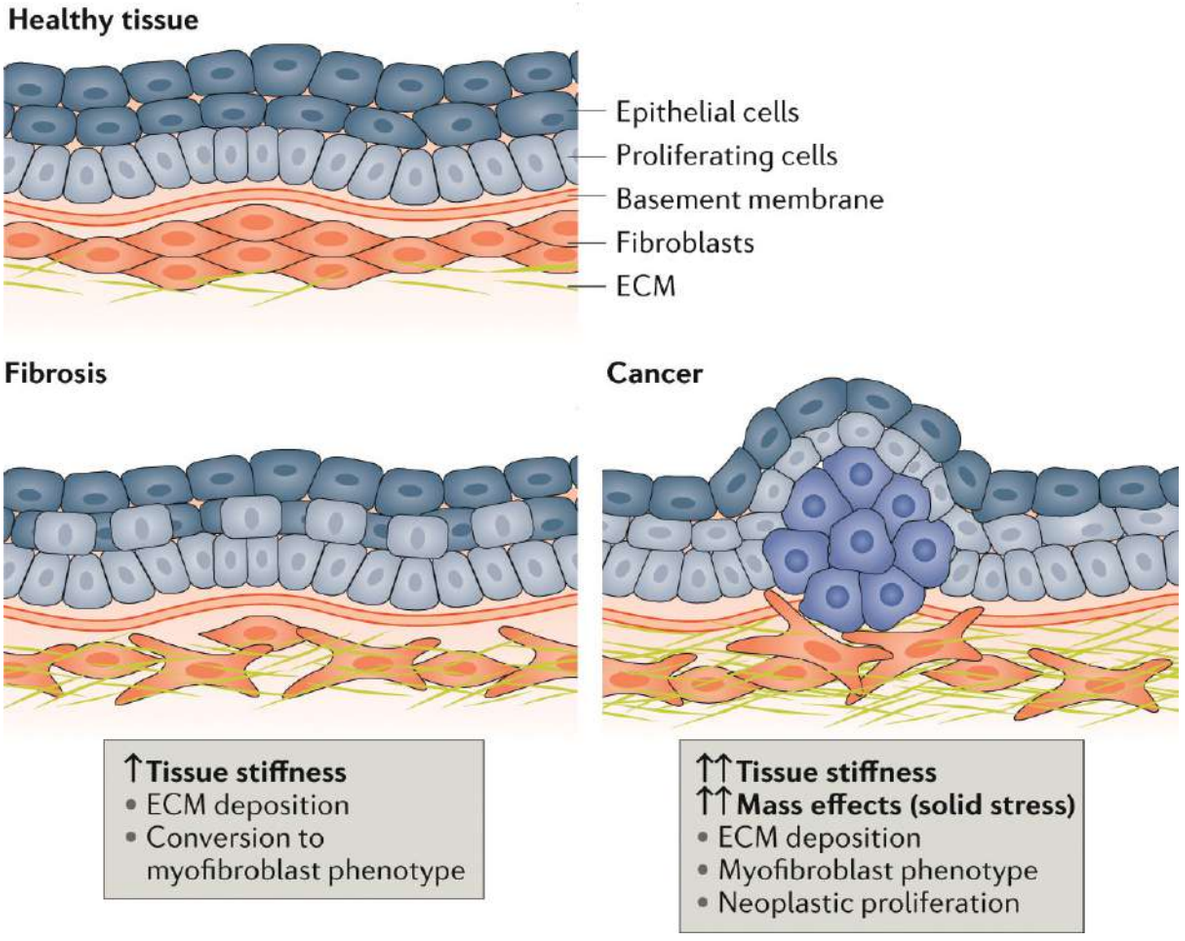


Figure II-3: Tissue mechanics are altered in disease states. Fibrosis and cancer are the two main disease states in which the mechanical properties of tissues are prominently affected. In both conditions, the desmoplastic deposition and crosslinking of extracellular matrix (ECM) fibers, together with fibroblast proliferation and differentiation into myofibroblasts, lead to increased tissue stiffness. These changes are a response to prolonged healing, tissue damage (fibrosis) or neoplastic lesions (cancer). Moreover, in tumors, aberrant cell proliferation compresses the surrounding healthy tissue compartments, leading to mass effects (such as nerve and blood vessel compression) and an increase in solid stress, which further stiffens the local tissue. Additionally, in cancer, malignant cells can further subvert stromal entities in the tumor microenvironment towards a profibrotic phenotype167, resulting in increased local fibrosis.

II.5.3. Chronic diseases

Last but not least, the mechanical properties of tissues might also be affected in other potentially life-threatening chronic diseases unrelated to fibrotic responses or neoplastic alterations. For example,

amyloid deposition diseases such as Alzheimer disease[170] and cardiac muscle hypertrophy both increase tissue stiffness[171], whereas osteoporosis reduces bone strength and stiffness[172].

Altogether, we believe that pathological changes in tissue stiffness can always be traced to altered amounts or functions of its two fundamental constituents: cells (number and/or phenotype) and ECM (deposition and/or degradation). Knowledge of abnormal tissue states and the mechanical changes that take place in disease are important not only for diagnostic purposes but also for tissue engineering and recapitulation of such diseases in *in vitro* models. These approaches are expected to generate novel therapeutic targets that enable restoration of healthy tissue mechanics and mechanotransduction responses[150].

II.6. ENGINEERING STIFFNESS INTO TISSUES

Once the mechanics of a complete native tissue are understood, the question that remains is how can one engineer such mechanics when attempting to construct a life-like tissue? This question led tissue engineers to search for novel materials, natural and synthetic, alone or blended together and processed through physically, chemically and biochemically distinct approaches in the attempt to recapitulate the properties of living tissues. Several main approaches to engineering the mechanical properties of living tissues and ways to trigger desired mechanotransduction responses by cells can be identified in the literature (**Fig. II-4**).

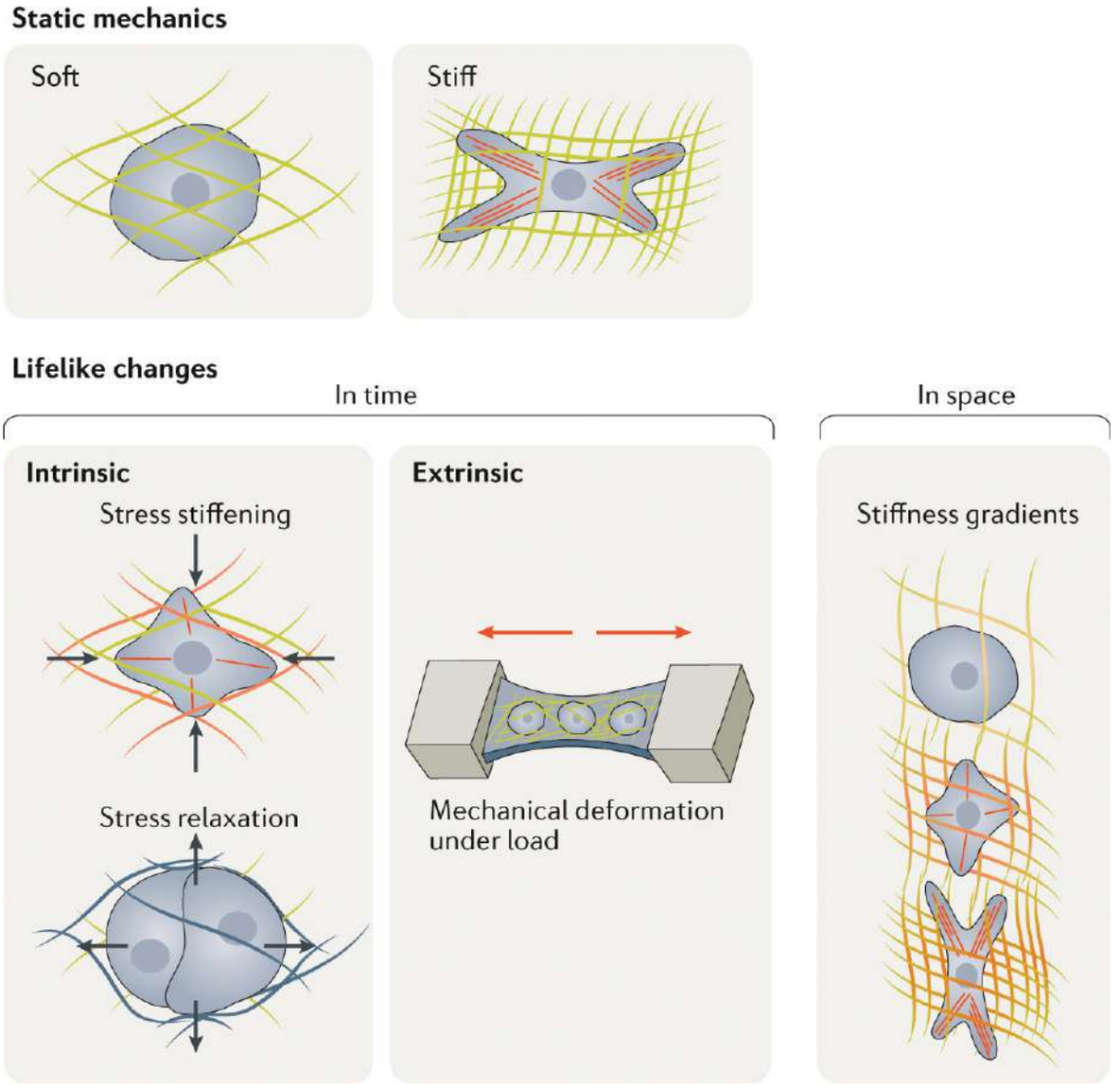


Figure II-4: Engineering of life-like tissue mechanics. The ultimate goal of considering stiffness in tissue engineering strategies is the recapitulation of the qualities of living tissue. Static mechanical properties are initially considered by trying to mimic the stiffness and/or softness of the native structure. However, the dynamic nature of biological tissues leads to a need for the incorporation of changes in mechanics (either in space or time). Time-varying mechanics can be obtained by exploiting materials with stress stiffening or stress relaxation responses (whereby the material either stiffens or relaxes in response to a continued duration or increased level of stress, respectively). Alternatively, mechanical deformation can be applied directly to constructs to mimic these properties when the material itself lacks such dynamicity. Space-changing mechanics are found in tissue interfaces such as those found in regions where cartilage is gradually becoming bone. The characteristics of these gradually changing structures can be mimicked by gradients of structure, composition and mechanical properties.

The stiffness of structures (in its simplest form, their elastic or shear moduli) is the oldest target within the field. If in the beginning the mechanical properties of a bulk material were only seen as a

requirement for scaffold integration and integrity[2], emerging discoveries and the rise of mechanobiology[113] have placed mechanical properties at the same level as long-known biochemical cues. Changing the elastic moduli of the cellular environment, either approaching or moving away from those of native tissues, can lead to tremendous differences in cellular responses from simple adhesion[173,174] and morphology[175–177] to the more complex differentiation[178–180]. In fact, this variation can be of such magnitude that high-throughput technologies are now being applied to derive the best-fit conditions in terms of surface stiffness for distinct cell types[174,181], and approaches to do the same in 3D environments are both needed and expected.

Nevertheless, the scientific community has started to shift its attention to more complex stiffness scenarios involving dynamic and active tissue mechanics (reviewed elsewhere in the epithelial context[182]). Two seminal works brought to light the possibility of achieving and tuning life-like, time-changing forces in 3D environments by exploring the properties of biomimetic material that have profound effects on cellular behavior, possibly greater than the influence of static stiffness[81,94]. Stress stiffening and stress relaxation represent the capability of specific materials to stiffen or relax with stress state or time, respectively. Initially reported on two-dimensional (2D) surfaces[183,184], these properties were soon translated to 3D environments and have proved to be very important.

II.6.1. Stress stiffening

Stress stiffening is a natural property observed in many biological structures, such as gels of the cytoskeletal proteins actin and vimentin. Other ECM molecules, such as collagen and fibrin, also exhibit substantial increases in stiffness beyond a critical stress value[185,186]. This behavior is fundamental for the proper function of many biological structures and its translation to synthetic materials eluded scientists for quite some time. Once engineering of stress stiffening became possible, controlled changes in the onset of stiffening alone (within the same final modulus) were shown to be single-handedly capable of redirecting the commitment of MSCs from adipogenic to osteogenic lineages[81]. A report published in 2019 showed that this kind of stress stiffening could be tuned to encompass a 50-fold increase, similar to the forces exerted by myosin molecular motors: a remarkably life-like scenario[187].

II.6.2. Stress relaxation

Stress relaxation represents the capability of a material to relax at a specific time point after the induction of stress, which dissipates energy through a viscoelastic response as opposed to a purely elastic one (for example slippage versus stretching of chemical bonds in a covalently crosslinked hydrogel)[183]. Viscoelasticity is also present in many biological tissues consisting of a fibrous network (such as collagen) within a non-fibrillary ECM[188]. Such viscoelastic behavior is fundamental for the normal functioning of tissues that are naturally subjected to dynamic loads, including the lung, cartilage and tendons. However, even stiff tissues such as bone exhibit appreciable stress relaxation during active regeneration[94]. Moreover, stress relaxation of engineered tissues is, like stress stiffening, capable of affecting stem cell differentiation[94]. Remarkably, in non-adhesive environments, stress relaxation alone was enough to completely shift the behavior of chondrocytes from round and static to life-like cartilage-forming entities[189]. This phenotype change was due to the ability of the engineered material to relax faster than a sample that lacked stress relaxation but had similar initial stiffness, which enabled the cells to become less confined, expand, proliferate, and behave as they would in their native environment.

However, all these studies involved hydrogel structures with low moduli of a few kPa. Despite being far from the stiffness of cartilage or bone, these hydrogel environments strongly promoted osteogenic and chrondrogenic commitment[81,189]. As previously mentioned, the natural evolution of tissues during development progresses from soft to stiff environments (for instance, bone and cartilage both develop from soft precursor structures), and so it is only logical that soft environments would promote tissue development. An engineered structure as soft as adipose tissue, which never matures into a stiffer tissue, can never mechanically replace missing mature cartilage or bone. Nonetheless, the evidence obtained in both living tissues and engineered structures clearly indicates that a certain degree of dynamicity resulting from either stress relaxation or stress stiffening (both of which approximate the natural stimuli that cells receive) is of primal importance for recapitulating appropriate cellular behavior.

II.6.3. Mechanical stimulation

Not all materials are capable of dynamic features and specific applications might require the use of static structures. As such, tissue engineers have been attempting to approximate in vitro the dynamic fluctuations in force and shape that happen in vivo by actively stimulating cell–material constructs with controlled mechanical deformations. This approach has in fact been exploited for quite some time[190] but is increasingly explored in tissue engineering for the maturation of constructs. Most of the time, the stimulus is an attempt to recapitulate stresses that the native tissue endure in vivo, such as compression and shear forces in cartilage differentiation[191] or tensile deformations in skin and hair regeneration[192]. In other circumstances, not-so-native forces can also prove effective, such as stretching in cartilage formation[193] or even nanovibrations of MSCs in osteogenesis[194].

II.6.4. Time-dependent changes

One further option to achieve time-dependent changes is to use cells as the actuators. In fact, this quite lively field of study represents a new paradigm in modern tissue engineering. Traditional tissue engineering approaches have aimed to direct cell behavior by actively stimulating specific cellular receptors and pathways using bioactive molecules, ligands and scaffolds. Although these methods have shown promising outcomes, we now appreciate that providing cells with a material environment that they can remodel, both biochemically and mechanically, might be equally or even more important. Such materials could be defined as biolabile rather than bioactive, meaning that they are prone to change and remodeling. Similarly, such environments enable cells to bind to, degrade, or plastically open up gaps to move through it[195], to physically contract and mechanically change its shape[196], or to expand, remodel and deposit their own proteins on it[197]. The results of these 2018–2019 studies[195–197]show that tissue engineering might benefit not only from highly specific cell stimulation cues but also from the cells "mastering their own fates through the matrix"[198], in vitro. Eventually, both types of stimuli might be employed, as happens in vivo where local entities remodel and regenerate tissues but also respond to systemic cues.

In fact, in vivo degradability and remodeling further highlight time-dependent changes as an important dimension of engineered tissue mechanics. The development of materials that degrade in

close conjunction with the formation of new tissue is the holy grail of tissue engineering — the desired outcome being total regeneration of native tissue and the complete removal of synthetic material or the appropriate remodeling of a natural scaffold. This degradability implies that the mechanical properties of the engineered tissue substitute will vary over time. Although it is outside the scope of this Review to discuss the complex concept of degradability after implantation, it is important to consider that different degradation mechanisms of the tissue substitute could lead to different changes in its mechanical properties through time. Degradation of polymeric substitutes, for example, might occur on the surface and/or in the bulk, with or without a change in molecular weight[199], which raises the prospect of time-varying changes in their mechanical properties after implantation[200] combined with the previously discussed matrix deposition and remodeling by cells both from the construct itself and resident in its vicinity. These changes, even if desirable and necessary for true construct integration, make post-implantation outcomes extremely complex. As such, advanced translational strategies might benefit from applying predictive methods such as machine learning[201] to understand and improve post-implantation outcomes.

II.6.5. Interface tissues

Additionally, the mechanical changes natively occurring in biological tissues often also have a spatial element, which can be challenging to recapitulate. However, some tissue structures naturally bridge two distinct environments with different mechanics (typically one soft and one stiff material). Such tissues are often found *in vivo* in locations where transitional tissues are formed, such as in cartilage-to-bone, meniscus-to-bone, tendon or ligament-to-bone and muscle-to-tendon interfaces[202].

Attempts to engineer similar structures have mainly focused on combining two mechanically distinct compartments (which might also have other distinct characteristics) into a single structure mimicking either a bone and tendon interface[203,204] or a cartilage and bone interface[205], while hoping that the interface region is stable enough (and large enough) to house intermediate cell phenotypes and behaviors. However, interface tissues *in vivo* typically demonstrate a gradient in which changes are gradual rather than binary. Similar gradients have been produced for osteochondral tissue engineering[206], an interesting yet challenging approach to the creation of life-like interfaces. Nevertheless, materials with 3D gradients in mechanical characteristics are still scarcely reported in the

literature, and it will be interesting to see what the future holds with regard to this approach to interface tissue fabrication, as scientists begin to develop the toolbox for soft-to-hard tissue bioengineering[207].

II.7. FUTURE PERSPECTIVES

Scientists are beginning to develop and employ advanced biofabrication technologies to mimic the natural properties of biological tissues across different scales. Examples can be seen in the fields of additive manufacturing, where the precise control and recapitulation of complex biological shapes[208] is being combined with advanced bioinks for 3D printing[209]. Meanwhile, metamaterial research is also delivering very exotic shapes with complex mechanical functionality to distinct structures[210,211] and it will be exciting to see how these properties might be combined with biological systems. Simultaneously, a clear trend is evident towards the engineering of materials with time-varying mechanics, which have been achieved either through material-intrinsic stress relaxation and/or stress stiffening or through external mechanical stimulation. Thus, modern approaches to mechanical tissue engineering, which focus on maximizing cell stimulation, seem to be drifting away from the classic paradigm of biomechanical tissue replacement.

Although these are very interesting approaches, they come with one overall caveat: extremely soft environments (up to few kPa) have been shown to promote the best cellular responses even when used for generation of a stiff tissue. How then can these soft engineered structures reach the elastic moduli of their living counterparts? Can we integrate time-dependent changes in mechanics into stiffer structures and still obtain the desired cellular responses? Will cellular proliferation, ECM deposition and overall tissue maturation lead to appropriate construct stiffening or can we push the capacity for stress-stiffening of currently available materials to even higher orders of magnitude?The answers to these essential questions will inform how to efficiently combine the biological advantages of soft environments with the mechanical resilience of stiff structures. Furthermore, an important need remains for further manipulating very uniform materials to approach natively non-uniform structures, such as the interfacial gradients, anisotropic environments and overall multiscale biological complexity discussed in this Review. In this regard, interesting advances have been reported in nanocomposite hydrogels[212]and combinations of hydrogel printing with electrospinning[213] that enable the introduction of shape and directionality into engineered constructs. Finally, the effects of post-implantation events, particularly

remodeling and degradability, on construct mechanics represents an additional level of complexity that is as yet far from being decoded and properly integrated within tissue engineering strategies.

II.8. CONCLUSIONS

We have seen that biological tissues have very distinctive mechanics due to their structural complexity and heterogeneity, which only increase with evaluations of the properties of their individual constituents (both ECM and cells). Regarding bulk tissue mechanics, a substantial amount of literature is derived from different animal models and distinct techniques. However, high levels of disparity persist when some values are derived and wrongful comparisons are made by not considering the dimension and/or type of deformation studied (in terms of its magnitude, directionality and dynamicity). Furthermore, some bulk tissues have only been analyzed at a single dimension (macroscale, microscale or nanoscale). As a consequence, these disparities raise questions that demand further research.

At microscale and nanoscale dimensions, the mechanics of several ECM structures remain unexplored, despite their well-known biochemical roles. Future research into these structures might be important to improve our understanding of how they contribute to bulk tissue mechanics and also for improving homogenization; that is, the prediction of bulk material properties informed by knowledge of their microscale components' mechanical behavior, as discussed in the 'Spatial scale' section. Additionally, cellular mechanics reveal themselves to be extremely complex, even in the cell types for which a good picture is already established. At this level, two main challenges seem to remain: first, the unification of tensegrity and soft glassy rheology models (**Box 2**), both of which might be linked by the pre-stress role of the cytoskeleton, and second, translation of the knowledge derived from cells in monolayer cultures to those within 3D environments, where further complexity is likely to arise. Closing these and other gaps in knowledge will illuminate the interplay of force and shape in biological tissues and will underlie the roadmap for engineering life-like structures in health and disease states.

It seems clear that there will never be a true standard for the mechanical analysis of biological tissue and that variability in the results of such analyses will always be high. Nevertheless, we believe that by properly integrating the results derived from different analysis methods towards material-translatable conclusions, the mechanical intricacies of living tissues can be well understood. Similarly, the tools to recapitulate each individual tissue might soon be at our disposal. Understanding how to exploit synergies between soft and stiff materials to maximize cell stimulation while also approaching

the mechanics of the mature biological tissue could be the final frontier for engineering truly life-like tissues.

II.9. REFERENCES

1. Callister, W. D. . J. & Rethwisch, D. G. *Materials Science and Engineering: An Introduction 8th Edition*. *Wiley* (2007). doi:10.1016/0025-5416(87)90343-0
2. Langer, R. & Vacanti, J. P. Tissue Engineering. *Science (80-.).* **260**, 920–926 (1993).
3. Discher, D. E., Janmey, P. & Wang, Y. Tissue Cells Feel and Respond to the Stiffness of Their Substrate *Science (80-.).* **310**, 1139–1143 (2005).

Seminal work reporting for the first time that mechanics alone affect the behavior of cells.

4. Yanez, L. Z., Han, J., Behr, B. B., Pera, R. A. R. & Camarillo, D. B. Human oocyte developmental potential is predicted by mechanical properties within hours after fertilization. *Nat. Commun.* **7**, 1–12 (2016).
5. Cross, S. E., Jin, Y. S., Rao, J. & Gimzewski, J. K. Nanomechanical analysis of cells from cancer patients. *Nat. Nanotechnol.* **2**, 780–783 (2007).
6. Baumgart, F. & Cordey, J. Stiffness - An unknown world of mechanical science? *Injury* **32**, 14–23 (2001).
7. Pang, Z., Deeth, H., Sopade, P., Sharma, R. & Bansal, N. Rheology, texture and microstructure of gelatin gels with and without milk proteins. *Food Hydrocoll.* **35**, 484–493 (2014).
8. Koga, Y., Koga, T., Kinekawa, Y. & Kitabatake, N. Properties of a Thermostable Emulsion Prepared from Process Whey Protein and Olive Oil; Use as a cream-substitute and Its Practical Application to Panna-Cotta. *J. Cook. Sci. Japan* **34**, 154–163 (2001).
9. Williams, S. H., Wright, B. W., Truong, V. den, Daubert, C. R. & Vinyard, C. J. Mechanical properties of foods used in experimental studies of primate masticatory function. *Am. J. Primatol.* **67**, 329–346 (2005).
10. Perry, J. M. G., Bastian, M. L., St Clair, E. & Hartstone-Rose, A. Maximum ingested food size in captive anthropoids. *Am. J. Phys. Anthropol.* **158**, 92–104 (2015).
11. Callister, W. D. & Rethwisch, D. G. *Materials science and engineering : an introduction*.
12. Davis, J. R. (Joseph R. . *Tensile testing*. (ASM International, 2004).
13. Wong, B. L., Bae, W. C., Gratz, K. R. & Sah, R. L. Shear deformation kinematics during cartilage articulation: effect of lubrication, degeneration, and stress relaxation. *Mol. Cell. Biomech.* **5**, 197–206 (2008).
14. Pothan, L. A., Oommen, Z. & Thomas, S. Dynamic mechanical analysis of banana fiber reinforced polyester composites. *Compos. Sci. Technol.* **63**, 283–293 (2003).
15. Meyers, M. A. & Chawla, K. K. *Mechanical Behavior of Materials*. *Mechanical Behavior of Materials* (2009).
16. Cross, R. Elastic and viscous properties of Silly Putty. *Am. J. Phys.* **80**, 870–875 (2012).
17. Omari, E. A., Varghese, T., Kliewer, M. A., Harter, J. & Hartenbach, E. M. Dynamic and quasi-static mechanical testing for characterization of the viscoelastic properties of human uterine tissue. *J. Biomech.* **48**, 1730–6 (2015).
18. Karunaratne, A., Li, S. & Bull, A. M. J. Nano-scale mechanisms explain the stiffening and strengthening of ligament tissue with increasing strain rate. *Sci. Rep.* **8**, 3707 (2018).
19. Wang, L. & Liu, X. Characterization of viscoelastic materials by quasi-static and dynamic indentation. *Meas. Sci. Technol.* **25**, 064017 (2014).
20. Schapery, R. A. Two Simple Approximate Methods of Laplace Transform Inversion for Viscoelastic Stress Analysis. (1961).
21. Schapery, R. A. Stress Analysis of Viscoelastic Composite Materials. *J. Compos. Mater.* **1**, 228–267 (1967).

22. Yofe, A. D. Physics at surfaces. *Contemp. Phys.* **29**, 411–414 (1988).

23. Abazari, A. M., Safavi, S. M., Rezazadeh, G. & Villanueva, L. G. Modeling the size effects on the mechanical properties of micro/nano structures. *Sensors (Switzerland)* **15**, 28543–28562 (2015).

24. McNamara, L. E. *et al.* The role of microtopography in cellular mechanotransduction. *Biomaterials* **33**, 2835–2847 (2012).

25. Peric, D., de Souza Neto, E. A., Feijóo, R. A., Partovi, M. & Carneiro Molina, A. J. On micro-to-macro transitions for multi-scale analysis of non-linear heterogeneous materials: unified variational basis and finite element implementation. *Int. J. Numer. Methods Eng.* **00**, 149–170 (2011).

26. Geers, M. G. D., Kouznetsova, V. G. & Brekelmans, W. A. M. Multi-scale computational homogenization: Trends and challenges. *J. Comput. Appl. Math.* **234**, 2175–2182 (2010).

27. Speirs, D. C. D., de Souza Neto, E. A. & Perić, D. An approach to the mechanical constitutive modeling of arterial tissue based on homogenization and optimization. *J. Biomech.* **41**, 2673–2680 (2008).

28. Hollister, S. J. & Lin, C. Y. Computational design of tissue engineering scaffolds. *Comput. Methods Appl. Mech. Eng.* **196**, 2991–2998 (2007).

29. Kim, S. H., Turnbull, J. & Guimond, S. Extracellular matrix and cell signalling: The dynamic cooperation of integrin, proteoglycan and growth factor receptor. *J. Endocrinol.* **209**, 139–151 (2011).

30. Miller, C. J. & Davidson, L. A. The interplay between cell signalling and mechanics in developmental processes. *Nat. Rev. Genet.* **14**, 733–744 (2013).

31. Alcaraz, J. *et al.* Laminin and biomimetic extracellular elasticity enhance functional differentiation in mammary epithelia. *EMBO J.* **27**, 2829–2838 (2008).

32. Keane, T. J., Horejs, C. M. & Stevens, M. M. Scarring vs. functional healing: Matrix-based strategies to regulate tissue repair. *Adv. Drug Deliv. Rev.* **129**, 407–419 (2018).

33. Sasaki, N. & Odajima, S. Stress-strain curve and Young's modulus of a collagen molecule as determined by the X-ray diffraction technique. *J. Biomech.* **29**, 655–658 (1996).

34. Wenger, M. P. E., Bozec, L., Horton, M. A. & Mesquidaz, P. Mechanical properties of collagen fibrils. *Biophys. J.* **93**, 1255–1263 (2007).

35. Bornstein, P. & Sage, H. Structurally Distinct Collagen Types. *Annu. Rev. Biochem.* **49**, 957–1003 (1980).

36. Shoulders, M. D. & Raines, R. T. Collagen Structure and Stability. *Annu. Rev. Biochem.* **78**, 929–958 (2009).

37. Zhang, W., Huang, Z. L., Liao, S. S. & Cui, F. Z. Nucleation sites of calcium phosphate crystals during collagen mineralization. *J. Am. Ceram. Soc.* **86**, 1052–1054 (2003).

38. Herchenhan, A. *et al.* Tenocyte contraction induces crimp formation in tendon-like tissue. *Biomech. Model. Mechanobiol.* **11**, 449–459 (2012).

39. Hornsby, J. *et al.* Quantitative multiphoton microscopy of murine urinary bladder morphology during in situ uniaxial loading. *Acta Biomater.* **64**, 59–66 (2017).

40. Wiesinger, H. P., Rieder, F., Kösters, A., Müller, E. & Seynnes, O. R. Are Sport-Specific Profiles of Tendon Stiffness and Cross-Sectional Area Determined by Structural or Functional Integrity? *PLoS One* **11**, 4–6 (2016).

41. Ma, Y., Feng, X., Rogers, J. A., Huang, Y. & Zhang, Y. Design and application of 'J-shaped' stress-strain behavior in stretchable electronics: A review. *Lab Chip* **17**, 1689–1704 (2017).

42. Wagenseil, J. E. & Mecham, R. P. Elastin in large artery stiffness and hypertension. *J. Cardiovasc. Transl. Res.* **5**, 264–273 (2012).

43. Muiznieks, L. D., Weiss, A. S. & Keeley, F. W. Structural disorder and dynamics of elastin. *Biochem. Cell Biol.* **88**, 239–250 (2010).

44. Muiznieks, L. D. & Keeley, F. W. Molecular assembly and mechanical properties of the extracellular matrix: A fibrous protein perspective. *Biochim. Biophys. Acta - Mol. Basis Dis.* **1832**, 866–875 (2013).

45. Ryan, A. J. & O'Brien, F. J. Insoluble elastin reduces collagen scaffold stiffness, improves viscoelastic properties, and induces a contractile phenotype in smooth muscle cells. *Biomaterials* **73**, 296–307 (2015).

46. Tsamis, A., Krawiec, J. T. & Vorp, D. A. Elastin and collagen fiber microstructure of the human aorta in ageing and disease: A review. *J. R. Soc. Interface* **10**, (2013).

47. Ahmadzadeh, H., Connizzo, B. K., Freedman, B. R., Soslowsky, L. J. & Shenoy, V. B. Determining the contribution of glycosaminoglycans to tendon mechanical properties with a modified shear-lag model. *J. Biomech.* **46**, 2497–2503 (2013).

48. Quinn, T. M., Dierickx, P. & Grodzinsky, A. J. Glycosaminoglycan network geometry may contribute to anisotropic hydraulic permeability in cartilage under compression. *J. Biomech.* **34**, 1483–1490 (2001).

49. Tavakoli Nia, H. *et al.* Aggrecan nanoscale solid-fluid interactions are a primary determinant of cartilage dynamic mechanical properties. *ACS Nano* **9**, 2614–2625 (2015).

50. Klotzsch, E. *et al.* Fibronectin forms the most extensible biological fibers displaying switchable force-exposed cryptic binding sites. *Proc. Natl. Acad. Sci.* **106**, 18267–18272 (2009).

51. Dray, N. *et al.* Cell-fibronectin interactions propel vertebrate trunk elongation via tissue mechanics. *Curr. Biol.* **23**, 1335–1341 (2013).

52. Gautieri, A., Uzel, S., Vesentini, S., Redaelli, A. & Buehler, M. J. Molecular and mesoscale mechanisms of osteogenesis imperfecta disease in collagen fibrils. *Biophys. J.* **97**, 857–865 (2009).

53. Mavilio, F. *et al.* Correction of junctional epidermolysis bullosa by transplantation of genetically modified epidermal stem cells. *Nat. Med.* **12**, 1397–1402 (2006).

54. Wagner, J. E. *et al.* Bone Marrow Transplantation for Recessive Dystrophic Epidermolysis Bullosa. *N. Engl. J. Med.* **363**, 629–639 (2010).

55. Germain, D. P. Clinical and genetic features of vascular Ehlers-Danlos syndrome. *Ann. Vasc. Surg.* **16**, 391–397 (2002).

56. De Paepe, A. & Malfait, F. The Ehlers-Danlos syndrome, a disorder with many faces. *Clin. Genet.* **82**, 1–11 (2012).

57. Von Erlach, T. C. *et al.* Cell-geometry-dependent changes in plasma membrane order direct stem cell signalling and fate. *Nat. Mater.* **17**, 237–242 (2018).

58. Kasza, K. E. *et al.* The cell as a material. *Curr. Opin. Cell Biol.* **19**, 101–107 (2007).

The first outline of cells as a material.

59. Suresh, S. Biomechanics and biophysics of cancer cells. *Acta Mater.* **55**, 3989–4014 (2007).

60. Fletcher, D. A. & Mullins, R. D. Cell mechanics and the cytoskeleton. *Nature* **463**, 485–492 (2010).

61. Kumar, S. *et al.* Viscoelastic retraction of single living stress fibers and its impact on cell shape, cytoskeletal organization, and extracellular matrix mechanics. *Biophys. J.* **90**, 3762–3773 (2006).

62. Salbreux, G., Charras, G. & Paluch, E. Actin cortex mechanics and cellular morphogenesis. *Trends Cell Biol.* **22**, 536–545 (2012).

Interesting perspective on the cell cortex dynamics.

63. Ingber, D. E. Tensegrity-based mechanosensing from macro to micro. *Prog. Biophys. Mol. Biol.* **97**, 163–179 (2008).

Complete view on tensegrity in cell mechanics and its parallel to architecture.

64. Ingber, D. E. From mechanobiology to developmentally inspired engineering. *Philos. Trans. R. Soc. B Biol. Sci.* **373**, 1–7 (2018).

65. Mandriota, N. *et al.* Cellular nanoscale stiffness patterns governed by intracellular forces. *Nat. Mater.* **18**, 1071-1077 (2019)

Evidence of how much influence intracellular forces and states have on the local cellular stiffness.

66. Condeelis, J. Life at the Leading Edge: The Formation of Cell Protrusions. *Annu. Rev. Cell Dev. Biol.* **9**, 411–444 (1993).

67. Charras, G. T., Yarrow, J. C., Horton, M. A., Mahadevan, L. & Mitchison, T. J. Non-equilibration of hydrostatic

pressure in blebbing cells. *Nature* **435**, 365–369 (2005).

68. Prost, J., Jülicher, F. & Joanny, J. F. Active gel physics. *Nat. Phys.* **11**, 111–117 (2015).

Complete description of the physics of active gels.

69. Guo, M. *et al.* Cell volume change through water efflux impacts cell stiffness and stem cell fate. *Proc. Natl. Acad. Sci.* **114**, E8618–E8627 (2017).

70. Lekka, M. & Laidler, P. Applicability of AFM in cancer detection. *Nat. Nanotechnol.* **4**, 72–72 (2009).

71. Gavara, N. & Chadwick, R. S. Determination of the elastic moduli of thin samples and adherent cells using conical atomic force microscope tips. *Nat. Nanotechnol.* **7**, 733–736 (2012).

72. Dimitriadis, E. K., Horkay, F., Maresca, J., Kachar, B. & Chadwick, R. S. Determination of elastic moduli of thin layers of soft material using the atomic force microscope. *Biophys. J.* **82**, 2798–2810 (2002).

73. Rianna, C. & Radmacher, M. Comparison of viscoelastic properties of cancer and normal thyroid cells on different stiffness substrates. *Eur. Biophys. J.* **46**, 309–324 (2017).

74. Kaushik, G., Fuhrmann, A., Cammarato, A. & Engler, A. J. In situ mechanical analysis of myofibrillar perturbation and aging on soft, bilayered Drosophila myocardium. *Biophys. J.* **101**, 2629–2637 (2011).

75. Tan, J. L. *et al.* Cells Lying on a bed of microneedles: An approach to isolate mechanical force. *Proc. Natl. Acad. Sci.* **2002**, 1–6 (2003).

76. Tee, S. Y., Fu, J., Chen, C. S. & Janmey, P. A. Cell shape and substrate rigidity both regulate cell stiffness. *Biophys. J.* **100**, L25–L27 (2011).

77. Gonzalez-Cruz, R. D., Fonseca, V. C. & Darling, E. M. Cellular mechanical properties reflect the differentiation potential of adipose-derived mesenchymal stem cells. *Proc. Natl. Acad. Sci.* (2012). doi:10.1073/pnas.1120349109

78. Yu, H. *et al.* Mechanical behavior of human mesenchymal stem cells during adipogenic and osteogenic differentiation. *Biochem. Biophys. Res. Commun.* **393**, 150–155 (2010).

79. Norcross, S., Horsley, V., Mertz, A. F., Rosowski, K. A. & Dufresne, E. R. Edges of human embryonic stem cell colonies display distinct mechanical properties and differentiation potential. *Sci. Rep.* **5**, 1–12 (2015).

80. Poh, Y.-C. *et al.* Material properties of the cell dictate stress-induced spreading and differentiation in embryonic stem cells. *Nat. Mater.* **9**, 82–88 (2009).

81. Das, R. K., Gocheva, V., Hammink, R., Zouani, O. F. & Rowan, A. E. Stress-stiffening-mediated stem-cell commitment switch in soft responsive hydrogels. *Nat. Mater.* **15**, 318–325 (2015).

82. Leong, K. W., Yim, E. K. F., Kulangara, K., Darling, E. M. & Guilak, F. Nanotopography-induced changes in focal adhesions, cytoskeletal organization, and mechanical properties of human mesenchymal stem cells. *Biomaterials* **31**, 1299–1306 (2009).

83. Conte, V. *et al.* Control of cell–cell forces and collective cell dynamics by the intercellular adhesome. *Nat. Cell Biol.* **17**, 409–420 (2015).

84. Latorre, E. *et al.* Active superelasticity in three-dimensional epithelia of controlled shape. *Nature* **563**, 203–208 (2018).

85. Vincent, R. *et al.* Active Tensile Modulus of an Epithelial Monolayer. *Phys. Rev. Lett.* **115**, 1–5 (2015).

86. Charras, G. & Yap, A. S. Tensile Forces and Mechanotransduction at Cell–Cell Junctions. *Curr. Biol.* **28**, R445–R457 (2018).

87. Khalilgharibi, N. *et al.* Stress relaxation in epithelial monolayers is controlled by the actomyosin cortex. *Nat. Phys.* (2019). doi:10.1038/s41567-019-0516-6

88. Gonzalez-Rodriguez, D., Guevorkian, K., Douezan, S. & Brochard-Wyart, F. Soft matter models of developing tissues and tumors. *Science (80-.).* **338**, 910–917 (2012).

89. Serwane, F. *et al.* In vivo quantification of spatially varying mechanical properties in developing tissues. *Nat. Methods* **14**, 181–186 (2017).

90. Mongera, A. *et al.* A fluid-to-solid jamming transition underlies vertebrate body axis elongation. *Nature* **561**, 401–

405 (2018).

91. Stooke-Vaughan, G. A. & Campàs, O. Physical control of tissue morphogenesis across scales. *Curr. Opin. Genet. Dev.* **51**, 111–119 (2018).

92. Rho, J. Y., Ashman, R. B. & Turner, C. H. Young's modulus of trabecular and cortical bone material: Ultrasonic and microtensile measurements. *J. Biomech.* **26**, 111–119 (1993).

93. McDonald, S. J. *et al.* Early fracture callus displays smooth muscle-like viscoelastic properties ex vivo: Implications for fracture healing. *J. Orthop. Res.* **27**, 1508–1513 (2009).

94. Chaudhuri, O. *et al.* Hydrogels with tunable stress relaxation regulate stem cell fate and activity. *Nat. Mater.* **15**, 326–334 (2015).

Seminal work on the effect of controlled 3D stress relaxation in the behavior of stem cells.

95. Chlasta, J. *et al.* Variations in basement membrane mechanics are linked to epithelial morphogenesis. *Development* **144**, 4350–4362 (2017).

96. Vuong-Brender, T. T. K., Suman, S. K. & Labouesse, M. The apical ECM preserves embryonic integrity and distributes mechanical stress during morphogenesis. *Development* **144**, 4336–4349 (2017).

97. Nerurkar, N. L., Lee, C. H., Mahadevan, L. & Tabin, C. J. Molecular control of macroscopic forces drives formation of the vertebrate hindgut. *Nature* **565**, 480–484 (2019).

98. Benech, J. C. *et al.* Diabetes increases stiffness of live cardiomyocytes measured by atomic force microscopy nanoindentation. *Am. J. Physiol. Physiol.* **307**, C910–C919 (2014).

99. Somlyo, A. P. *et al.* Ultrastructure, function and composition of smooth muscle. *Ann. Biomed. Eng.* (1983). doi:10.1007/BF02364087

100. Darling, E. M., Topel, M., Zauscher, S., Vail, T. P. & Guilak, F. Viscoelastic properties of human mesenchymally-derived stem cells and primary osteoblasts, chondrocytes, and adipocytes. *J. Biomech.* **41**, 454–464 (2008).

101. Li, X., Das, A. & Bi, D. Mechanical Heterogeneity in Tissues Promotes Rigidity and Controls Cellular Invasion. *Phys. Rev. Lett.* **123**, 058101 (2019).

102. Roduit, C. *et al.* Elastic membrane heterogeneity of living cells revealed by stiff nanoscale membrane domains. *Biophys. J.* **94**, 1521–1532 (2008).

103. Marturano, J. E. *et al.* Embryonically inspired scaffolds regulate tenogenically differentiating cells. *J. Biomech.* **49**, 3281–3288 (2016).

104. Sotres, J., Jankovskaja, S., Wannerberger, K. & Arnebrant, T. Ex-Vivo Force Spectroscopy of Intestinal Mucosa Reveals the Mechanical Properties of Mucus Blankets. *Sci. Rep.* **7**, 1–14 (2017).

105. Tyler, W. J. The mechanobiology of brain function. *Nat. Rev. Neurosci.* **13**, 867–878 (2012).

106. McKee, C. T., Last, J. A., Russell, P. & Murphy, C. J. Indentation Versus Tensile Measurements of Young's Modulus for Soft Biological Tissues. *Tissue Eng. Part B Rev.* **17**, 155–164 (2011).

107. Does, M. D. *et al.* Insights into reference point indentation involving human cortical bone: Sensitivity to tissue anisotropy and mechanical behavior. *J. Mech. Behav. Biomed. Mater.* **37**, 174–185 (2014).

108. Haase, K. & Pelling, A. Investigating cell mechanics with atomic force microscopy. *J. R. Soc. Interface* 1–7 (2016). doi:10.1098/rsif

109. Saxena, T., Gilbert, J., Stelzner, D. & Hasenwinkel, J. Mechanical Characterization of the Injured Spinal Cord after Lateral Spinal Hemisection Injury in the Rat. *J. Neurotrauma* **29**, 1747–1757 (2012).

110. Oakland, R. J., Hall, R. M., Wilcox, R. K. & Barton, D. C. The biomechanical response of spinal cord tissue to uniaxial loading. *Proc. Inst. Mech. Eng. Part H J. Eng. Med.* **220**, 489–492 (2006).

111. Pailler-Mattei, C., Bec, S. & Zahouani, H. In vivo measurements of the elastic mechanical properties of human skin by indentation tests. *Med. Eng. Phys.* **30**, 599–606 (2008).

112. Pissarenko, A. *et al.* Tensile behavior and structural characterization of pig dermis. *Acta Biomater.* **86**, 77–95 (2019).

113. Iskratsch, T., Wolfenson, H. & Sheetz, M. P. Appreciating force and shape — the rise of mechanotransduction in cell

biology. *Nat. Rev. Mol. Cell Biol.* **15**, 825–833 (2014).

114. Guo, K. & Buehler, M. J. Nature's Way: Hierarchical Strengthening through Weakness. *Matter* **1**, 302–303 (2019).

115. Ramakrishna, S., Mayer, J., Wintermantel, E. & Leong, K. W. Biomedical applications of polymer-composite materials: a review. *Compos. Sci. Technol.* **61**, 1189–1224 (2001).

116. Zhang, G. *et al.* Development of tendon structure and function: regulation of collagen fibrillogenesis. *J. Musculoskelet. Neuronal Interact.* **5**, 5–21 (2005).

117. Agache, P. G., Monneur, C., Leveque, J. L. & De Rigal, J. Mechanical properties and Young's modulus of human skin in vivo. *Arch. Dermatol. Res.* **269**, 221–232 (1980).

118. Menon, G. K. New insights into skin structure: scratching the surface. *Adv. Drug Deliv. Rev.* **54**, S3–S17 (2002).

119. Skulborstad, A. J., Swartz, S. M. & Goulbourne, N. C. Biaxial mechanical characterization of bat wing skin. *Bioinspiration and Biomimetics* **10**, 36004 (2015).

120. Hamasaki, T., Yamaguchi, T. & Iwamoto, M. Estimating the influence of age-related changes in skin stiffness on tactile perception for static stimulations. *J. Biomech. Sci. Eng.* **13**, 1–12 (2018).

121. Cui, J., Lee, C. H., Delbos, A., McManus, J. J. & Crosby, A. J. Cavitation rheology of the eye lens. *Soft Matter* **7**, 7827–7831 (2011).

122. Krag, S. & Andreassen, T. T. Mechanical Properties of the Human Posterior Lens Capsule. *Investig. Opthalmology Vis. Sci.* **44**, 691 (2003).

123. Danielsen, C. C. Tensile mechanical and creep properties of Descemet's membrane and lens capsule. *Exp. Eye Res.* **79**, 343–350 (2004).

124. Besner, S., Scarcelli, G., Pineda, R. & Yun, S. H. In vivo brillouin analysis of the aging crystalline lens. *Investig. Ophthalmol. Vis. Sci.* **57**, 5093–5100 (2016).

125. Tenorio, L. E. M., Devine, K. J., Lee, J., Kowalewski, T. M. & Barocas, V. H. Biomechanics of human parietal pleura in uniaxial extension. *J. Mech. Behav. Biomed. Mater.* **75**, 330–335 (2017).

126. Davis, N. F. *et al.* Urinary Bladder vs Gastrointestinal Tissue: A Comparative Study of Their Biomechanical Properties for Urinary Tract Reconstruction. *Urology* **113**, 235–240 (2018).

127. Faingold, A. *et al.* The effect of hydration on mechanical anisotropy, topography and fibril organization of the osteonal lamellae. *J. Biomech.* **47**, 367–372 (2014).

128. Milovanovic, P. *et al.* Age-related deterioration in trabecular bone mechanical properties at material level: Nanoindentation study of the femoral neck in women by using AFM. *Exp. Gerontol.* **47**, 154–159 (2012).

129. Melo, E. *et al.* Effects of the decellularization method on the local stiffness of acellular lungs. *Tissue Eng. Part C. Methods* **20**, 412–22 (2014).

130. Peloso, A. *et al.* The human pancreas as a source of protolerogenic extracellular matrix scaffold for a new-generation bioartificial endocrine pancreas. *Ann. Surg.* **264**, 169–179 (2016).

131. Omidi, E. *et al.* Characterization and assessment of hyperelastic and elastic properties of decellularized human adipose tissues. *J. Biomech.* **47**, 3657–3663 (2014).

132. Ocal, S., Ozcan, U. M., Basdogan, I. & Basdogan, C. Effect of Preservation Period on the Viscoelastic Material Properties of Soft Tissues With Implications for Liver Transplantation. *J. Biomech. Eng.* **132**, 101007 (2010).

133. Yamashita, J., Furman, B. R., Rawls, H. R., Wang, X. & Agrawal, C. M. The use of dynamic mechanical analysis to assess the viscoelastic properties of human cortical bone. *J. Biomed. Mater. Res.* **58**, 47–53 (2001).

134. Buckwalter, J. A. & Mankin, H. J. Articular cartilage: degeneration and osteoarthritis, repair, regeneration, and transplantation. *Instructional course lectures* **47**, 487–504 (1998).

135. Zhu, W., Mow, V. C., Koob, T. J. & Eyre, D. R. Viscoelastic shear properties of articular cartilage and the effects of glycosidase treatments. *J. Orthop. Res.* **11**, 771–781 (1993).

136. Nickien, M., Thambyah, A. & Broom, N. D. How a decreased fibrillar interconnectivity influences stiffness and swelling properties during early cartilage degeneration. *J. Mech. Behav. Biomed. Mater.* **75**, 390–398 (2017).

137. Brommer, H. *et al.* Functional consequences of cartilage degeneration in the equine metacarpophalangeal joint:

quantitative assessment of cartilage stiffness. *Equine Vet. J.* **37**, 462–7 (2005).

138. Kamiya, A. & Togawa, T. Adaptive regulation of wall shear stress to flow change in the canine carotid artery. *Am. J. Physiol.* **239**, H14-21 (1980).

139. Alkhouli, N. *et al.* The mechanical properties of human adipose tissues and their relationships to the structure and composition of the extracellular matrix. *AJP Endocrinol. Metab.* **305**, E1427–E1435 (2013).

140. Wood, L. K. & Brooks, S. V. Ten weeks of treadmill running decreases stiffness and increases collagen turnover in tendons of old mice. *J. Orthop. Res.* **34**, 346–353 (2016).

141. Peñuela, L. *et al.* Atomic force microscopy for biomechanical and structural analysis of human dermis: A complementary tool for medical diagnosis and therapy monitoring. *Exp. Dermatol.* **27**, 150–155 (2018).

142. Crichton, M. L. *et al.* The viscoelastic, hyperelastic and scale dependent behavior of freshly excised individual skin layers. *Biomaterials* **32**, 4670–4681 (2011).

143. Lampi, M. C. & Reinhart-King, C. A. Targeting extracellular matrix stiffness to attenuate disease: From molecular mechanisms to clinical trials. *Sci. Transl. Med.* **10**, eaao0475 (2018).

144. Stefanescu, H. *et al.* Spleen stiffness measurement using fibroscan for the noninvasive assessment of esophageal varices in liver cirrhosis patients. *J. Gastroenterol. Hepatol.* **26**, 164–170 (2011).

145. Hu, X. *et al.* Indirect prediction of liver fibrosis by quantitative measurement of spleen stiffness using the fibroscan system. *J. Ultrasound Med.* **33**, 73–81 (2014).

146. Veiga, Z. S. T. *et al.* Transient elastography evaluation of hepatic and spleen stiffness in patients with hepatosplenic schistosomiasis. *Eur. J. Gastroenterol. Hepatol.* **29**, 730–735 (2017).

147. Pawluś, A. *et al.* Shear wave elastography of the spleen: evaluation of spleen stiffness in healthy volunteers. *Abdom. Radiol.* **41**, 2169–2174 (2016).

148. Chien, C. H. *et al.* Transient elastography for spleen stiffness measurement in patients with cirrhosis role in degree of thrombocytopenia. *J. Ultrasound Med.* **35**, 1849–1857 (2016).

149. Kalli, M. & Stylianopoulos, T. Defining the Role of Solid Stress and Matrix Stiffness in Cancer Cell Proliferation and Metastasis. *Front. Oncol.* **8**, (2018).

150. Mancini, M. L. & Sonis, S. T. Mechanisms of cellular fibrosis associated with cancer regimen-related toxicities. *Front. Pharmacol.* **5 MAR**, 1–9 (2014).

151. Coelho, N. M. & McCulloch, C. A. Contribution of collagen adhesion receptors to tissue fibrosis. *Cell Tissue Res.* **365**, 521–538 (2016).

152. Martinez, F. J. *et al.* Idiopathic pulmonary fibrosis Review. *Nat. Rev. Dis. Prim.* **3**, 17074 (2017).

153. Meng, X. M., Nikolic-Paterson, D. J. & Lan, H. Y. Inflammatory processes in renal fibrosis. *Nat. Rev. Nephrol.* **10**, 493–503 (2014).

154. Tsochatzis, E. A., Bosch, J. & Burroughs, A. K. Liver cirrhosis. *Lancet* **383**, 1749–1761 (2014).

155. Li, Q., Chen, L. & Zhou, Y. Diagnostic accuracy of liver stiffness measurement in chronic hepatitis B patients with normal or mildly elevated alanine transaminase levels. *Sci. Rep.* **8**, 1–7 (2018).

156. Ogawa, S. *et al.* Relationship between liver tissue stiffness and histopathological findings analyzed by shear wave elastography and compression testing in rats with non-alcoholic steatohepatitis. *J. Med. Ultrason.* **43**, 355–360 (2016).

157. Pang, J. X. Q. *et al.* Liver stiffness by transient elastography predicts liver-related complications and mortality in patients with chronic liver disease. *PLoS One* **9**, 1–9 (2014).

158. Desai, S. S. *et al.* Physiological ranges of matrix rigidity modulate primary mouse hepatocyte function in part through hepatocyte nuclear factor 4 alpha. *Hepatology* **64**, 261–275 (2016).

159. Li, Q. S., Lee, G. Y. H., Ong, C. N. & Lim, C. T. AFM indentation study of breast cancer cells. *Biochem. Biophys. Res. Commun.* **374**, 609–613 (2008).

160. Gaikwad, R. M., Woodworth, C. D., Sokolov, I., Subba-Rao, V. & Iyer, S. Atomic force microscopy detects differences in the surface brush of normal and cancerous cells. *Nat. Nanotechnol.* **4**, 389–393 (2009).

161. Wong, R. *et al.* AFM-based analysis of human metastatic cancer cells. *Nanotechnology* **19**, 384003 (2008).

162. Lekka, M. Discrimination Between Normal and Cancerous Cells Using AFM. *Bionanoscience* **6**, 65–80 (2016).

163. Maciaszek, J. L. & Lykotrafitis, G. Sickle cell trait human erythrocytes are significantly stiffer than normal. *J. Biomech.* **44**, 657–661 (2011).

164. Lin, H.-H. H.-K. *et al.* Mechanical phenotype of cancer cells: cell softening and loss of stiffness sensing. *Oncotarget* **6**, (2015).

165. Gilkes, D. M. *et al.* Hypoxia-inducible factors mediate coordinated RhoA-ROCK1 expression and signaling in breast cancer cells. *Proc. Natl. Acad. Sci.* **111**, E384–E393 (2014).

166. Dvorak, H. F. Tumors: wounds that do not heal. Similarities between tumor stroma generation and wound healing. *N. Engl. J. Med.* **315**, 1650–1659 (1986).

167. Dias Carvalho, P. *et al.* KRAS Oncogenic Signaling Extends beyond Cancer Cells to Orchestrate the Microenvironment. *Cancer Res.* 1–9 (2017). doi:10.1158/0008-5472.CAN-17-2084

168. Huang, S. & Ingber, D. E. Cell tension, matrix mechanics, and cancer development. *Cancer Cell* **8**, 175–176 (2005).

169. Lyshchik, A. *et al.* Elastic Moduli Of Thyroid Tissues Under Compression. *Ultrason. Imaging* **110**, 101–110 (2005).

170. Murphy, M. C. *et al.* Regional brain stiffness changes across the Alzheimer's disease spectrum. *NeuroImage Clin.* **10**, 283–290 (2016).

171. Chaturvedi, R. R. *et al.* Passive stiffness of myocardium from congenital heart disease and implications for diastole. *Circulation* **121**, 979–988 (2010).

172. Vardakastani, V. *et al.* Increased intra-cortical porosity reduces bone stiffness and strength in pediatric patients with osteogenesis imperfecta. *Bone* **69**, 61–67 (2014).

173. Ye, K. *et al.* Matrix Stiffness and Nanoscale Spatial Organization of Cell-Adhesive Ligands Direct Stem Cell Fate. *Nano Lett.* **15**, 4720–4729 (2015).

174. Zhou, Q. *et al.* Development of a Novel Orthogonal Double Gradient for High-Throughput Screening of Mesenchymal Stem Cells–Materials Interaction. *Adv. Mater. Interfaces* **5**, 4–11 (2018).

175. Garreta, E. *et al.* Fine tuning the extracellular environment accelerates the derivation of kidney organoids from human pluripotent stem cells. *Nat. Mater.* **18**, (2019).

176. Uynuk-Ool, T. *et al.* The geometrical shape of mesenchymal stromal cells measured by quantitative shape descriptors is determined by the stiffness of the biomaterial and by cyclic tensile forces. *J. Tissue Eng. Regen. Med.* (2017). doi:10.1002/term.2263

177. Branco da Cunha, C. *et al.* Influence of the stiffness of three-dimensional alginate/collagen-I interpenetrating networks on fibroblast biology. *Biomaterials* **35**, 8927–8936 (2014).

178. Xie, J. *et al.* Substrate elasticity regulates adipose-derived stromal cell differentiation towards osteogenesis and adipogenesis through β-catenin transduction. *Acta Biomater.* **79**, 83–95 (2018).

179. Lv, H. *et al.* Biomaterial stiffness determines stem cell fate. *Life Sci.* **178**, 42–48 (2017).

180. Sun, A. X. *et al.* Chondrogenesis of human bone marrow mesenchymal stem cells in 3-dimensional, photocrosslinked hydrogel constructs: Effect of cell seeding density and material stiffness. *Acta Biomater.* **58**, 302–311 (2016).

181. Hadden, W. J. *et al.* Stem cell migration and mechanotransduction on linear stiffness gradient hydrogels. *Proc. Natl. Acad. Sci.* **114**, 5647–5652 (2017).

182. Xi, W., Saw, T. B., Delacour, D., Lim, C. T. & Ladoux, B. Material approaches to active tissue mechanics. *Nat. Rev. Mater.* **4**, 23–44 (2019).

183. Chaudhuri, O. *et al.* Substrate stress relaxation regulates cell spreading. *Nat. Commun.* 1–7 (2015). doi:10.1038/ncomms7365

184. Guvendiren, M. & Burdick, J. A. Stiffening hydrogels to probe short- and long-term cellular responses to dynamic mechanics. *Nat. Commun.* **3**, 792–799 (2012).

185. Storm, C., Pastore, J. J., MacKintosh, F. C., Lubensky, T. C. & Janmey, P. A. Nonlinear elasticity in biological gels. *Nature* **435**, 191–194 (2005).

186. Kouwer, P. H. J. *et al.* Responsive biomimetic networks from polyisocyanopeptide hydrogels. *Nature* **493**, 651–655 (2013).

187. de Almeida, P. *et al.* Cytoskeletal stiffening in synthetic hydrogels. *Nat. Commun.* **10**, 2–9 (2019).

Seminal work where hydrogels with cytoskeletal-like stress stiffening are obtained.

188. Dhume, R. Y. & Barocas, V. H. Emergent structure-dependent relaxation spectra in viscoelastic fiber networks in extension. *Acta Biomater.* **87**, 245–255 (2019).

189. Lee, H. P., Gu, L., Mooney, D. J., Levenston, M. E. & Chaudhuri, O. Mechanical confinement regulates cartilage matrix formation by chondrocytes. *Nat. Mater.* **16**, 1243–1251 (2017).

190. Kim, B. S., Nikolovski, J., Bonadio, J. & Mooney, D. J. Cyclic mechanical strain regulates the development of engineered smooth muscle tissue. *Nat. Biotechnol.* **17**, 979–983 (1999).

191. Cochis, A. *et al.* Bioreactor mechanically guided 3D mesenchymal stem cell chondrogenesis using a biocompatible novel thermo-reversible methylcellulose-based hydrogel. *Sci. Rep.* **7**, 45018 (2017).

192. Chu, S.-Y. *et al.* Mechanical stretch induces hair regeneration through the alternative activation of macrophages. *Nat. Commun.* **10**, 1524 (2019).

193. Lee, J. K. *et al.* Tension stimulation drives tissue formation in scaffold-free systems. *Nat. Mater.* **16**, 864–873 (2017).

194. Tsimbouri, P. M. *et al.* Stimulation of 3D osteogenesis by mesenchymal stem cells using a nanovibrational bioreactor. *Nat. Biomed. Eng.* **1**, 758–770 (2017).

195. Wisdom, K. M. *et al.* Matrix mechanical plasticity regulates cancer cell migration through confining microenvironments. *Nat. Commun.* **9**, 4144 (2018).

196. Ionescu, A. M. *et al.* 4D Corneal Tissue Engineering: Achieving Time-Dependent Tissue Self-Curvature through Localized Control of Cell Actuators. *Adv. Funct. Mater.* **1807334**, 1807334 (2019).

197. Loebel, C., Mauck, R. L. & Burdick, J. A. Local nascent protein deposition and remodeling guide mesenchymal stromal cell mechanosensing and fate in three-dimensional hydrogels. *Nat. Mater.* ***18****, 883-891* (2019).

Three important works that serve as foundation for our definition of biolabile environments, showing the importance of allowing cells to 'master their fate'.

198. Qiao, E. L., Kumar, S. & Schaffer, D. V. Mastering their own fates through the matrix. *Nat. Mater.* **18**, 779–780 (2019).

199. Vert, M., Li, S. M., Spenlehauer, G. & Guerin, P. Bioresorbability and biocompatibility of aliphatic polyesters. *J. Mater. Sci. ...* **3**, 432–446 (1992).

200. Hutmacher, D. W. Scaffolds in tissue engineering bone and cartilage. *Biomaterials* **21**, 2529–2543 (2000).

201. Deringer, V. L., Caro, M. A. & Csányi, G. Machine Learning Interatomic Potentials as Emerging Tools for Materials Science. *Adv. Mater.* **1902765**, 1902765 (2019).

202. Ansari, S., Khorshidi, S. & Karkhaneh, A. Engineering of gradient osteochondral tissue: From nature to lab. *Acta Biomater.* **87**, 41–54 (2019).

203. Silva, E. D. *et al.* Multifunctional magnetic-responsive hydrogels to engineer tendon-to-bone interface. *Nanomedicine Nanotechnology, Biol. Med.* **14**, 2375–2385 (2018).

204. Calejo, I., Costa-Almeida, R., Reis, R. L. & Gomes, M. E. A Textile Platform Using Continuous Aligned and Textured Composite Microfibers to Engineer Tendon-to-Bone Interface Gradient Scaffolds. *Adv. Healthc. Mater.* **1900200**, 1900200 (2019).

205. Ribeiro, V. P. *et al.* Enzymatically Cross-Linked Silk Fibroin-Based Hierarchical Scaffolds for Osteochondral Regeneration. *ACS Appl. Mater. Interfaces* **11**, 3781–3799 (2019).

206. Canadas, R. F. *et al.* Biochemical Gradients to Generate 3D Heterotypic-Like Tissues with Isotropic and Anisotropic Architectures. *Adv. Funct. Mater.* **28**, 1–12 (2018).

207. Calejo, I., Costa-Almeida, R., Reis, R. L. & Gomes, M. E. A Physiology-Inspired Multifactorial Toolbox in Soft-to-Hard Musculoskeletal Interface Tissue Engineering. *Trends Biotechnol.* 1–15 (2019). doi:10.1016/j.tibtech.2019.06.003

208. Grigoryan, B. *et al.* Multivascular networks and functional intravascular topologies within biocompatible hydrogels. *Science (80-.).* **364**, 458–464 (2019).

209. Chimene, D., Lennox, K. K., Kaunas, R. R. & Gaharwar, A. K. Advanced Bioinks for 3D Printing: A Materials Science Perspective. *Ann. Biomed. Eng.* **44**, 2090–2102 (2016).

210. Bertoldi, K., Vitelli, V., Christensen, J. & Van Hecke, M. Flexible mechanical metamaterials. *Nat. Rev. Mater.* **2**, (2017).

211. Frenzel, T., Kadic, M. & Wegener, M. Three-dimensional mechanical metamaterials with a twist. *Science (80-.).* **358**, 1027–1032 (2017).

212. Zhao, Z., Fang, R., Rong, Q. & Liu, M. Bioinspired Nanocomposite Hydrogels with Highly Ordered Structures. *Adv. Mater.* **29**, 1–16 (2017).

213. Chen, T., Bakhshi, H., Liu, L., Ji, J. & Agarwal, S. Combining 3D Printing with Electrospinning for Rapid Response and Enhanced Designability of Hydrogel Actuators. *Adv. Funct. Mater.* **28**, 3–9 (2018).

214. Brown, A. L. *et al.* 22 Week assessment of bladder acellular matrix as a bladder augmentation material in a porcine model. *Biomaterials* **23**, 2179–2190 (2002).

215. Barak, M. M. & Black, M. A. A novel use of 3D printing model demonstrates the effects of deteriorated trabecular bone structure on bone stiffness and strength. *J. Mech. Behav. Biomed. Mater.* **78**, 455–464 (2018).

216. Ramadan, S., Paul, N. & Naguib, H. E. Standardized static and dynamic evaluation of myocardial tissue properties. *Biomed. Mater.* **12**, 025013 (2017).

217. Yoo, L., Gupta, V., Lee, C., Kavehpore, P. & Demer, J. L. Viscoelastic properties of bovine orbital connective tissue and fat : constitutive models. *Biomech. Model. Mechanobiol.* **10**, 901–914 (2012).

218. Schachar, R. A., Chan, R. W. & Fu, M. Viscoelastic properties of fresh human lenses under 40 years of age: implications for the aetiology of presbyopia. *Br. J. Ophthalmol.* **95**, 1010–1013 (2011).

219. Ozawa, H., Matsumoto, T., Ohashi, T., Sato, M. & Kokubun, S. Comparison of spinal cord gray matter and white matter softness: measurement by pipette aspiration method. *J. Neurosurg. Spine* **95**, 221–224 (2001).

220. Lee, L. M. & Liu, A. P. The Application of Micropipette Aspiration in Molecular Mechanics of Single Cells. *J. Nanotechnol. Eng. Med.* **5**, 040902 (2014).

221. Moshtagh, P. R., Pouran, B., Korthagen, N. M., Zadpoor, A. A. & Weinans, H. Guidelines for an optimized indentation protocol for measurement of cartilage stiffness: The effects of spatial variation and indentation parameters. *J. Biomech.* **49**, 3602–3607 (2016).

222. Uriarte, J. J. *et al.* Early impairment of lung mechanics in a murine model of marfan syndrome. *PLoS One* **11**, 1–19 (2016).

223. Shi, Y., Glaser, K. J., Venkatesh, S. K., Ben-Abraham, E. I. & Ehman, R. L. Feasibility of using 3D MR elastography to determine pancreatic stiffness in healthy volunteers. *J. Magn. Reson. Imaging* **41**, 369–375 (2015).

224. Murphy, M. C. *et al.* Measuring the characteristic topography of brain stiffness with magnetic resonance elastography. *PLoS One* **8**, 1–14 (2013).

225. Anvari, A., Dhyani, M., Stephen, A. E. & Samir, A. E. Reliability of shear-wave elastography estimates of the young modulus of tissue in follicular thyroid neoplasms. *Am. J. Roentgenol.* **206**, 609–616 (2016).

226. Dutov, P., Antipova, O., Varma, S., Orgel, J. P. R. O. & Schieber, J. D. Measurement of elastic modulus of collagen type i single fiber. *PLoS One* **11**, 1–13 (2016).

227. Li, W. *et al.* Fibrin Fiber Stiffness Is Strongly Affected by Fiber Diameter, but Not by Fibrinogen Glycation. *Biophys. J.* **110**, 1400–1410 (2016).

228. Collet, J.-P., Shuman, H., Ledger, R. E., Lee, S. & Weisel, J. W. The elasticity of an individual fibrin fiber in a clot. *Proc. Natl. Acad. Sci.* **102**, 9133–9137 (2005).

229. Aaron, B. B. & Gosline, J. M. Elastin as a random-network elastomer: A mechanical and optical analysis of single elastin fibers. *Biopolymers* **20**, 1247–1260 (1981).

230. Gosline, J. *et al.* Elastic proteins: Biological roles and mechanical properties. *Philos. Trans. R. Soc. B Biol. Sci.* **357**, 121–132 (2002).

231. Zahn, J. T. *et al.* Age-dependent changes in microscale stiffness and mechanoresponses of cells. *Small* **7**, 1480–1487 (2011).

232. Alcaraz, J. *et al.* Microrheology of human lung epithelial cells measured by atomic force microscopy. *Biophys. J.* **84**, 2071–2079 (2003).

233. Nakamura, K. *et al.* Altered nano/micro-order elasticity of pulmonary artery smooth muscle cells of patients with idiopathic pulmonary arterial hypertension. *Int. J. Cardiol.* **140**, 102–107 (2010).

234. Lulevich, V., Yang, H. ya, Isseroff, R. R. & Liu, G. yu. Single cell mechanics of keratinocyte cells. *Ultramicroscopy* **110**, 1435–1442 (2010).

235. Siamantouras, E., Hills, C. E., Squires, P. E. & Liu, K. K. Quantifying cellular mechanics and adhesion in renal tubular injury using single cell force spectroscopy. *Nanomedicine Nanotechnology, Biol. Med.* **12**, 1013–1021 (2016).

236. Sun, S., Song, Z., Cotler, S. J. & Cho, M. Biomechanics and functionality of hepatocytes in liver cirrhosis. *J. Biomech.* **47**, 2205–2210 (2014).

237. Hozic, A., Rico, F., Colom, A., Buzhynskyy, N. & Scheuring, S. Nanomechanical characterization of the stiffness of eye lens cells: a pilot study. *Invest. Ophthalmol. Vis. Sci.* **53**, 2151–2156 (2012).

238. Kolipaka, A. *et al.* Magnetic resonance elastography to estimate brain stiffness: Measurement reproducibility and its estimate in pseudotumor cerebri patients. *Clin. Imaging* **51**, 114–122 (2018).

239. Arani, A. *et al.* Measuring the effects of aging and sex on regional brain stiffness with MR elastography in healthy older adults. *Neuroimage* **111**, 59–64 (2015).

240. Ma, Z. *et al.* In vitro and in vivo mechanical properties of human ulnar and median nerves. *J. Biomed. Mater. Res. - Part A* **101 A**, 2718–2725 (2013).

241. Robinson, D. L. *et al.* Mechanical properties of normal and osteoarthritic human articular cartilage. *J. Mech. Behav. Biomed. Mater.* **61**, 96–109 (2016).

242. Comley, K. & Fleck, N. A. A micromechanical model for the Young's modulus of adipose tissue. *Int. J. Solids Struct.* **47**, 2982–2990 (2010).

243. Savelberg, H. H. C. M., Kooloos, J. G. M., Huiskes, R. & Kauer, J. M. G. Stiffness of the ligaments of the human wrist joint. *J. Biomech.* **25**, 369–376 (1992).

244. Przybylski, G. J., Carlin, G. J., Patel, P. R. & Woo, S. L. Y. Human anterior and posterior cervical longitudinal ligaments possess similar tensile properties. *J. Orthop. Res.* **14**, 1005–1008 (1996).

245. Pintar, F. A. Geometric and Mechanical Properties of Human Cervical. *J. Biomed. Eng.* **122**, 623–629 (2000).

246. Arani, A. *et al.* Cardiac MR elastography for quantitative assessment of elevated myocardial stiffness in cardiac amyloidosis. *J. Magn. Reson. Imaging* **46**, 1361–1367 (2017).

247. Domian, I. J., Yu, H. & Mittal, N. On Materials for Cardiac Tissue Engineering. *Adv. Healthc. Mater.* **6**, 1–3 (2017).

248. Eby, S. F. *et al.* Shear wave elastography of passive skeletal muscle stiffness: Influences of sex and age throughout adulthood. *Clin. Biomech.* **30**, 22–27 (2015).

249. Leong, H. T., Hug, F. & Fu, S. N. Increased Upper Trapezius Muscle Stiffness in Overhead Athletes with Rotator Cuff Tendinopathy. *PLoS One* **11**, e0155187 (2016).

250. Brandenburg, J. E. *et al.* Feasibility and reliability of quantifying passive muscle stiffness in young children by using shear wave ultrasound elastography. *J. Ultrasound Med.* **34**, 663–670 (2015).

251. Souron, R. *et al.* Sex differences in active tibialis anterior stiffness evaluated using supersonic shear imaging. *J. Biomech.* **49**, 3534–3537 (2016).

252. Wang, L., Yan, F., Yang, Y., Xiang, X. & Qiu, L. Quantitative Assessment of Skin Stiffness in Localized Scleroderma Using Ultrasound Shear-Wave Elastography. *Ultrasound Med. Biol.* **43**, 1339–1347 (2017).

253. Marinelli, J. P. *et al.* Quantitative assessment of lung stiffness in patients with interstitial lung disease using MR

elastography. *J. Magn. Reson. Imaging* **46**, 365–374 (2017).

254. Mariappan, Y. K. *et al.* Estimation of the absolute shear stiffness of human lung parenchyma using 1h spin echo, echo planar MR elastography. *J. Magn. Reson. Imaging* **40**, 1230–1237 (2014).

255. Booth, A. J. *et al.* Acellular normal and fibrotic human lung matrices as a culture system for in vitro investigation. *Am. J. Respir. Crit. Care Med.* **186**, 866–876 (2012).

256. Bensamoun, S. F., Robert, L., Leclerc, G. E., Debernard, L. & Charleux, F. Stiffness imaging of the kidney and adjacent abdominal tissues measured simultaneously using magnetic resonance elastography. *Clin. Imaging* **35**, 284–287 (2011).

257. Samir, A. E. *et al.* Shear wave elastography in chronic kidney disease: A pilot experience in native kidneys. *BMC Nephrol.* **16**, 1–9 (2015).

258. Ling, W. *et al.* Effects of vascularity and differentiation of hepatocellular carcinoma on tumor and liver stiffness: In vivo and in vitro studies. *Ultrasound Med. Biol.* **40**, 739–746 (2014).

259. Cha, S. W. *et al.* Nondiseased liver stiffness measured by shearwave elastography a pilot study. *J. Ultrasound Med.* **33**, 53–60 (2014).

260. Leal-Egaña, A. *et al.* Tuning liver stiffness against tumors: An in vitro study using entrapped cells in tumor-like microcapsules. *J. Mech. Behav. Biomed. Mater.* **9**, 113–121 (2012).

261. Lee, D. H., Lee, J. M., Han, J. K. & Choi, B. I. MR elastography of healthy liver parenchyma: Normal value and reliability of the liver stiffness value measurement. *J. Magn. Reson. Imaging* **38**, 1215–1223 (2013).

262. Venkatesh, S. K., Wang, G., Teo, L. L. S. & Ang, B. W. L. Magnetic resonance elastography of liver in healthy asians: Normal liver stiffness quantification and reproducibility assessment. *J. Magn. Reson. Imaging* **39**, 1–8 (2014).

263. Gangadhar, K., Hippe, D. S., Thiel, J. & Dighe, M. Impact of Image Orientation on Measurements of Thyroid Nodule Stiffness Using Shear Wave Elastography. *J. Ultrasound Med.* **35**, 1661–1667 (2016).

264. Brezak, R., Hippe, D., Thiel, J. & Dighe, M. K. Variability in stiffness assessment in a thyroid nodule using shear wave imaging. *Ultrasound Q.* **31**, 243–249 (2015).

265. Lam, A. C. L., Pang, S. W. A., Ahuja, A. T. & Bhatia, K. S. S. The influence of precompression on elasticity of thyroid nodules estimated by ultrasound shear wave elastography. *Eur. Radiol.* **26**, 2845–2852 (2016).

266. Bahn, M. M. *et al.* Development and application of magnetic resonance elastography of the normal and pathological thyroid gland in vivo. *J. Magn. Reson. Imaging* **30**, 1151–1154 (2009).

267. Pozzi, R. *et al.* Point shear-wave elastography in chronic pancreatitis: A promising tool for staging disease severity. *Pancreatology* **17**, 905–910 (2017).

268. An, H., Shi, Y., Guo, Q. & Liu, Y. Test–retest reliability of 3D EPI MR elastography of the pancreas. *Clin. Radiol.* **71**, 1068.e7-1068.e12 (2016).

269. Kolipaka, A. *et al.* Magnetic resonance elastography of the pancreas: Measurement reproducibility and relationship with age. *Magn. Reson. Imaging* **42**, 1–7 (2017).

270. Nenadic, I. *et al.* Noninvasive evaluation of bladder wall mechanical properties as a function of filling volume: Potential application in bladder compliance assessment. *PLoS One* **11**, 1–14 (2016).

271. Matalia, J. *et al.* Correlation of Corneal Biomechanical Stiffness with Refractive Error and Ocular Biometry in a Pediatric Population. *Cornea* **36**, 1221–1226 (2017).

272. Last, J. A., Thomasy, S. M., Croasdale, C. R., Russell, P. & Murphy, C. J. Compliance profile of the human cornea as measured by atomic force microscopy. *Micron* **43**, 1293–1298 (2012).

273. Jardeleza, M. S. R., Daly, M. K., Kaufman, J. D., Klapperich, C. & Legutko, P. A. Effect of trypan blue staining on the elastic modulus of anterior lens capsules of diabetic and nondiabetic patients. *J. Cataract Refract. Surg.* **35**, 318–323 (2009).

274. Yip, A. K. *et al.* Anisotropic traction stresses and focal adhesion polarization mediates topography-induced cell elongation. *Biomaterials* **181**, 103–112 (2018).

275. Saruwatari, L. *et al.* Osteoblasts generate harder, stiffer, and more delamination-resistant mineralized tissue on titanium than on polystyrene, associated with distinct tissue micro- and ultrastructure. *J. Bone Miner. Res.* **20**,

2002–2016 (2005).

276. Kalyan Phani, M., Kumar, A., Arnold, W. & Samwer, K. Elastic stiffness and damping measurements in titanium alloys using atomic force acoustic microscopy. *J. Alloys Compd.* **676**, 397–406 (2016).

277. Ingber, D. E. Cellular tensegrity: defining new rules of biological design that govern the cytoskeleton. *J. Cell Sci.* **104**, 613–627 (1993).

278. Fabry, B. *et al.* Scaling the microrheology of living cells. *Phys. Rev. Lett.* **87**, 1–4 (2001).

279. Stamenović, D. *et al.* Rheological behavior of living cells is timescale-dependent. *Biophys. J.* **93**, 39–41 (2007).

280. Ingber, D. E., Wang, N. & Stamenović, D. Tensegrity, cellular biophysics, and the mechanics of living systems. *Reports Prog. Phys.* **77**, (2014).

II.10. SUPPLEMENTARY MATERIAL:

Supplementary Table II-1: The Stiffness of Living Tissues

Tissue	Technique	Moduli (type)	Moduli (value)	Refs.
Nervous tissue				
Brain (mouse)	Atomic force microscopy indentation	Elastic (E)	0.4–3.0 kPa	1,2
Brain (cow)	Nanoindentation	Elastic (E)	0.59–2.36 kPa	3
Brain (pig)	Tensile deformation	Elastic (E)	3.1 kPa (up to 6.5 kPa)	4
Brain (human)	Magnetic resonance elastography	Shear (G)	1–3 kPa	5–7
Spinal cord (rat)	Microindentation	Elastic (E)	0.50–6.63 kPa	8,9
Spinal cord (rabbit)	Pipette aspiration	Elastic (E)	3–4 kPa	10
Spinal cord (human)	Tensile deformation	Elastic (E)	1.23 MPa	11
Sciatic nerve (mouse)	Tensile deformation	Elastic (E)	7 MPa	12
Sciatic nerve (rat)	Tensile deformation	Elastic (E)	0.5–4.0 MPa	13
Sciatic nerve (rabbit)	Tensile deformation	Elastic (E)	2 MPa[a]	14
Ulnar nerve (human)	Tensile deformation	Elastic (E)	5 MPa[a]	15
Connective tissue				
Tibial trabecular bone (human)	Ultrasound elastography	Elastic (E)	14.8 GPa	16
Tibial trabecular bone (human)	Tensile Deformation	Elastic (E)	10.4 GPa	16
Tibial cortical bone (human)	Ultrasound elastography	Elastic (E)	20.7 GPa	16

Tibial cortical bone (human)	Tensile Deformation	Elastic (E)	18.6 GPa	16
Metacarpal bone (horse)	Nanoindentation	Elastic (E)	12.4–12.8 GPa wet; 17.6–20.8 GPa dry	17
Femoral neck bone (human)	Atomic force microscopy indentation	Elastic (E)	1.28–1.97 GPa	18
Articular cartilage (human)	Compression	Elastic (E)	431.7–447.1 MPa	19
Articular cartilage (human)	Compression	Shear (G)	5.7–6.2 MPa	19
Articular cartilage (pig)	Compression	Elastic (E)	1 MPa	20
Articular cartilage (cow)	Rheology	Shear (G)	1.51 MPa	21
Articular cartilage (cow)	Tensile deformation	Elastic (E)	1.06 MPa	22
Articular cartilage (sheep)	Tensile deformation	Elastic (E)	5.0–12.9 MPa	23
Articular cartilage (goat)	Rheology	Shear storage (G′)	0.9 MPa	24
Articular cartilage (rat)	Microindentation	Elastic (E)	2.6–4.2 MPa	25
Articular cartilage (cow)	Atomic force microscopy, rheology	Elastic (E*)	0.15–2.5 MPa	26
Adipose tissue (human)	Compression	Elastic (E)	3.1 kPa pericardial; 5.5 kPa thymic; 3.5 kPa abdominal	27
Adipose tissue (human)	Tensile Deformation	Elastic (E)	1.6–2.9 kPa	28
Adipose tissue (human)	Compression	Elastic Storage (E')	2 kPa	29
Patellar tendon (human)	Shear wave elastography	Elastic (E)	200 kPa	30
Supraspinatus tendon (mouse)	Macroindentation	Elastic (E)	20–40 kPa	31
Supraspinatus tendon (mouse)	Atomic force microscopy rheology	Elastic (E)	4–20 kPa	31
Plantaris tendon (mouse)	Tensile deformation	Elastic (E)	100–200 MPa	32
Ocular tendon (cow)	Atomic force microscopy nanoindentation	Elastic (E)	60 MPa	33
Ligaments (human)	Tensile deformation	Elastic (E)	25–93 MPa	34–36
Annular ligament	Atomic force microscopy indentation	Elastic (E)	1.1–1.2 MPa	37
Muscle				
Smooth muscle —	Tensile Deformation	Elastic (E)	30–100 kPa	38

blood vessels				
Smooth muscle — aortic rings (rat)	Tensile Deformation	Elastic (E)	10–23 kPa	39
Cardiac muscle (rat, cow)	Tensile Deformation	Elastic (E)	30–145 kPa	40
Cardiac muscle (human)	Tensile Deformation	Elastic (E)	5–50 kPa	41,42
Cardiac muscle (cow, sheep)	Shear wave elastography	Elastic (E)	10–90 kPa	43
Cardiac muscle (human)	Magnetic resonance elastography	Shear (G)	8 kPa	44
Cardiac muscle (rat)	Magnetic resonance elastography	Shear (G)	2–4 kPa	45
Cardiac muscle (pig)	Tensile Deformation	Elastic (E)	110 kPa	46
Cardiac muscle (pig)	Magnetic resonance elastography	Shear (G)	3 kPa	46
Cardiac muscle (mouse)	Atomic force microscopy nanoindentation	Elastic (E)	21–39 kPa	47
Skeletal muscle (rat)	Tensile Deformation	Elastic (E)	20 kPa single fibers; 200 kPa bundles	48
Skeletal muscle (mouse)	Tensile Deformation	Elastic (E)	15–150 kPa	49,50
Skeletal muscle (human)	Shear wave elastography	Shear (G)	5–170 kPa	51–54
Skeletal muscle (pig)	Shear wave elastography	Shear (G)	Up to 150 kPa	55
Skeletal muscle (pig)	Tensile Deformation	Elastic (E)	Up to 800 kPa	55
Skeletal muscle (mouse)	Atomic force microscopy nanoindentation	Elastic (E)	3–8 kPa	56
Endothelial and epithelial tissues				
Skin (human)	Torsional deformation	Elastic (E)	420–850 kPa	57
Skin (human)	Shear wave elastography	Elastic (E)	60–130 kPa	58,59
Skin (bat wing)	Tensile Deformation (biaxial)	Elastic (E)	131 kPa	60
Skin dermis (pig)	Tensile Deformation	Elastic (E)	50–150 kPa	61
Skin (human)	Indentation	Elastic (E)	35 kPa dermis; 2kPa hypodermis	62
Skin (mouse)	Atomic force microscopy nanoindentation	Elastic (E)	7.3–13.5 MPa dermis; 0.49–1.51 MPa epidermis	63
Skin (human)	Atomic force microscopy nanoindentation	Elastic (E)	4.5 MPa epidermis; 0.1 MPa dermis	64

Lung (human)	Magnetic resonance elastography	Shear (G)	0.84–1.50 kPa	65,66
Decellularized lung (rat)	Atomic force microscopy nanoindentation	Elastic (E)	15–60 kPa	67
Decellularized lung (mouse)	Atomic force microscopy indentation	Elastic (E)	20–100 kPa	68
Decellularized lung (mouse)	Rheology	Shear storage (G′)	10 kPa	68
Lung (rat)	Atomic force microscopy nanoindentation	Elastic (E)	1.5 kPa	69
Lung (human)	Atomic force microscopy nanoindentation	Elastic (E)	1.96 kPa	70
Intestine (rat)	Tensile Deformation	Elastic (E)	350 kPa	71
Small intestine (guinea pig)	Tensile Deformation	Elastic (E)	430–441 kPa	72
Large intestine (goat)	Compression	Elastic (E)	600 kPa[a]	73
Intestine (pig)	Tensile Deformation	Elastic (E)	300–700 kPa	74
Viscera				
Kidney (human)	Magnetic resonance elastography	Shear (G)	4 kPa cortex; 5 kPa medulla; 8 kPa sinus	75,76
Kidney (sheep)	Nanoindentation	Elastic (E)	1–13 kPa	77
Kidney glomeruli (rat)	Atomic force microscopy indentation	Elastic (E)	2.5–4.0 kPa	78
Kidney glomeruli (rat)	Capillary aspiration	Shear (G)	1 kPa	78
Spleen (human)	Shear wave elastography	Shear (G)	15–20 kPa	79–82
Spleen (pig)	Macroindentation	Elastic (E)	110 kPa	83
Liver (human)	Shear wave elastography	Elastic (E)	4.0–6.5 kPa	84–86
Liver (human)	Magnetic resonance elastography	Shear (G)	2 kPa	87,88
Liver (rat)	Shear wave elastography	Elastic (E)	6.5 kPa	89
Liver (rat)	Compression	Elastic (E)	3.5 kPa	89
Liver (mouse)	Atomic force microscopy nanoindentation	Elastic (E)	0.15–6.00 kPa	90
Decellularized thymus	Macroindentation	Elastic (E)	2.11 kPa	27

Thyroid (nodule)	Shear wave elastography	Elastic (E)	19–50 kPa	91,92
Thyroid	Shear wave elastography	Elastic (E)	10.3 kPa	93
Thyroid	Magnetic resonance elastography	Shear (G)	1.3–1.9 kPa	94
Thyroid	Compression	Elastic (E)	9–11 kPa	95
Pancreas (human)	Magnetic resonance elastography	Shear (G)	1.1–2.1 kPa	96–98
Pancreas (human)	Shear wave elastography	Elastic (E)	2.9 kPa	99
Pancreas (mouse)	Compression	Elastic (E)	3.1 kPa	100
Pancreatic islet (mouse)	Atomic force microscopy nanoindentation	Elastic (E)	1 kPa	101
Bladder (pig)	Tensile Deformation	Elastic (E)	200–320 kPa	74,102
Bladder body (human)	Ultrasound vibrometry	Shear (G)	50 kPa (empty)–100 kPa (full)	103
Bladder neck	Shear wave elastography	Elastic (E)	22 kPa	104
Eye				
Cornea (pig)	Tensile Deformation	Elastic (E)	0.23–2.89 MPa	105,106
Cornea (pig)	Shear wave elastography	Elastic (E)	0.19 MPa	107
Cornea (human)	Compression	Elastic (E)	0.2 MPa	108
Cornea basement membrane (human)	Atomic force microscopy nanoindentation	Elastic (E)	7.5kPa	109
Cornea Bowman's layer (human)	Atomic force microscopy nanoindentation	Elastic (E)	109.8kPa	109
Cornea anterior stroma (human)	Atomic force microscopy nanoindentation	Elastic (E)	33.1 kPa	109
Cornea Descemet membrane (human)	Atomic force microscopy nanoindentation	Elastic (E)	50 kPa	109
Cornea (rat)	Nanoindentation	Elastic (E)	2.75–3.33 MPa	110
Lens capsule (human)	Tensile Deformation	Elastic (E)	2.3–3.3 MPa	111,112
Lens capsule (human)	AFM nanoindentation	Elastic (E)	0.4 MPa	113
Lens (cow)	Microindentation	Elastic (E)	25.6 kPa	114

Lens (human)	Rheology	Shear (G)	0.2–10.3 kPa	115
Lens (cow)	Cavitation rheology	Elastic (E)	0.8 kPa nucleus; 11.8 kPa cortex	116
Iris dilator (cow)	Tensile Deformation	Elastic (E)	27 kPa	117
Iris (pig)	Tensile Deformation, indentation	Elastic (E)	4–6 kPa	118,119
Iris (pig)	Microindentation	Elastic (E)	4.86 kPa	120

[a] Derived from the curves (that is, values were not directly reported by the authors).

II.11. SUPPLEMENTARY REFERENCE LIST

1. Holtzmann, K. *et al.* Brain tissue stiffness is a sensitive marker for acidosis. *J. Neurosci. Methods* **271,** 50–54 (2016).
2. Jorba, I. *et al.* Ageing and chronic intermittent hypoxia mimicking sleep apnea do not modify local brain tissue stiffness in healthy mice. *J. Mech. Behav. Biomed. Mater.* **71,** 106–113 (2017).
3. Weickenmeier, J. *et al.* Brain stiffness increases with myelin content. *Acta Biomater.* **42,** 265–272 (2016).
4. Rashid, B., Destrade, M. & Gilchrist, M. D. Mechanical characterization of brain tissue in Tensile Deformation at dynamic strain rates. *J. Mech. Behav. Biomed. Mater.* **33,** 1–31 (2012).
5. Murphy, M. C. *et al.* Regional brain stiffness changes across the Alzheimer's disease spectrum. *NeuroImage Clin.* **10,** 283–290 (2016).
6. Kolipaka, A. *et al.* Magnetic resonance elastography to estimate brain stiffness: measurement reproducibility and its estimate in pseudotumor cerebri patients. *Clin. Imaging* **51,** 114–122 (2018).
7. Arani, A. *et al.* Measuring the effects of aging and sex on regional brain stiffness with MR elastography in healthy older adults. *Neuroimage* **111,** 59–64 (2015).
8. Saxena, T., Gilbert, J., Stelzner, D. & Hasenwinkel, J. Mechanical Characterization of the Injured Spinal Cord after Lateral Spinal Hemisection Injury in the Rat. *J. Neurotrauma* **29,** 1747–1757 (2012).
9. Saxena, T., Gilbert, J. L. & Hasenwinkel, J. M. A versatile mesoindentation system to evaluate the micromechanical properties of soft, hydrated substrates on a cellular scale. *J. Biomed. Mater. Res. - Part A* **90,** 1206–1217 (2009).
10. Ozawa, H., Matsumoto, T., Ohashi, T., Sato, M. & Kokubun, S. Comparison of spinal cord gray matter and white matter softness: measurement by pipette aspiration method. *J. Neurosurg. Spine* **95,** 221–224 (2001).
11. Oakland, R. J., Hall, R. M., Wilcox, R. K. & Barton, D. C. The biomechanical response of spinal cord tissue to uniaxial loading. *Proc. Inst. Mech. Eng. Part H J. Eng. Med.* **220,** 489–492 (2006).
12. Beel, J. A., Groswald, D. E. & Luttges, M. W. Alterations in the mechanical properties of peripheral nerve following crush injury. *J. Biomech.* **17,** 185–193 (1984).
13. Borschel, G. H., Kia, K. F., Kuzon, W. M. & Dennis, R. G. Mechanical properties of acellular peripheral nerve. *J. Surg. Res.* **114,** 133–139 (2003).
14. Mekaj, A. Y. *et al.* Biomechanical properties of the sciatic nerve following repair: Effects of topical application of hyaluronic acid or tacrolimus. *Int. J. Clin. Exp. Med.* **8,** 20218–20226 (2015).
15. Ma, Z. *et al.* In vitro and in vivo mechanical properties of human ulnar and median nerves. *J. Biomed. Mater. Res. - Part A* **101 A,** 2718–2725 (2013).
16. Rho, J. Y., Ashman, R. B. & Turner, C. H. Young's modulus of trabecular and cortical bone material: Ultrasonic and microtensile measurements. *J. Biomech.* **26,** 111–119 (1993).
17. Faingold, A. *et al.* The effect of hydration on mechanical anisotropy, topography and fibril organization of the osteonal lamellae. *J. Biomech.* **47,** 367–372 (2014).
18. Milovanovic, P. *et al.* Age-related deterioration in trabecular bone mechanical properties at material level: Nanoindentation study of the femoral neck in women by using AFM. *Exp. Gerontol.* **47,** 154–159 (2012).
19. Robinson, D. L. *et al.* Mechanical properties of normal and osteoarthritic human articular cartilage. *J. Mech. Behav. Biomed. Mater.* **61,** 96–109 (2016).
20. Means, A. K., Shrode, C. S., Whitney, L. V., Ehrhardt, D. A. & Grunlan, M. A. Double Network Hydrogels that Mimic the Modulus, Strength, and Lubricity of Cartilage. *Biomacromolecules* **20,** acs.biomac.9b00237 (2019).
21. Zhu, W., Mow, V. C., Koob, T. J. & Eyre, D. R. Viscoelastic shear properties of articular cartilage and the effects of glycosidase treatments. *J. Orthop. Res.* **11,** 771–781 (1993).
22. Nickien, M., Thambyah, A. & Broom, N. D. How a decreased fibrillar interconnectivity influences stiffness and

swelling properties during early cartilage degeneration. *J. Mech. Behav. Biomed. Mater.* **75,** 390–398 (2017).

23. Brown, W. E., DuRaine, G. D., Hu, J. C. & Athanasiou, K. A. Structure-function Relationships of Fetal Ovine Articular Cartilage. *Acta Biomater.* **87,** 235–244 (2019).

24. Bhat, S., Lidgren, L. & Kumar, A. In Vitro Neo-Cartilage Formation on a Three-Dimensional Composite Polymeric Cryogel Matrix. *Macromol. Biosci.* **13,** 827–837 (2013).

25. Moshtagh, P. R., Pouran, B., Korthagen, N. M., Zadpoor, A. A. & Weinans, H. Guidelines for an optimized indentation protocol for measurement of cartilage stiffness: The effects of spatial variation and indentation parameters. *J. Biomech.* **49,** 3602–3607 (2016).

26. Nia, H. T. *et al.* High-Bandwidth AFM-based rheology reveals that cartilage is most sensitive to high loading rates at early stages of impairment. *Biophys. J.* **104,** 1529–1537 (2013).

27. Omidi, E. *et al.* Characterization and assessment of hyperelastic and elastic properties of decellularized human adipose tissues. *J. Biomech.* **47,** 3657–3663 (2014).

28. Alkhouli, N. *et al.* The mechanical properties of human adipose tissues and their relationships to the structure and composition of the extracellular matrix. *AJP Endocrinol. Metab.* **305,** E1427–E1435 (2013).

29. Comley, K. & Fleck, N. A. A micromechanical model for the Young's modulus of adipose tissue. *Int. J. Solids Struct.* **47,** 2982–2990 (2010).

30. Peltz, C. D. *et al.* ShearWave elastography: Repeatability for measurement of tendon stiffness. *Skeletal Radiol.* **42,** 1151–1156 (2013).

31. Connizzo, B. K. & Grodzinsky, A. J. Multiscale Poroviscoelastic Compressive Properties of Mouse Supraspinatus Tendons Are Altered in Young and Aged Mice. *J. Biomech. Eng.* **140,** 051002 (2018).

32. Wood, L. K. & Brooks, S. V. Ten weeks of treadmill running decreases stiffness and increases collagen turnover in tendons of old mice. *J. Orthop. Res.* **34,** 346–353 (2016).

33. Yoo, L., Reed, J., Shin, A. & Demer, J. L. Atomic force microscopy determination of Young's modulus of bovine extra-ocular tendon fiber bundles. *J. Biomech.* **47,** 1899–1903 (2014).

34. Savelberg, H. H. C. M., Kooloos, J. G. M., Huiskes, R. & Kauer, J. M. G. Stiffness of the ligaments of the human wrist joint. *J. Biomech.* **25,** 369–376 (1992).

35. Przybylski, G. J., Carlin, G. J., Patel, P. R. & Woo, S. L. Y. Human anterior and posterior cervical longitudinal ligaments possess similar tensile properties. *J. Orthop. Res.* **14,** 1005–1008 (1996).

36. Pintar, F. A. Geometric and Mechanical Properties of Human Cervical. *J. Biomed. Eng.* **122,** 623–629 (2000).

37. Kwacz, M., Rymuza, Z., Michałowski, M. & Wysocki, J. Elastic Properties of the Annular Ligament of the Human Stapes—AFM Measurement. *JARO - J. Assoc. Res. Otolaryngol.* **16,** 433–446 (2015).

38. Steucke, K. E., Tracy, P. V., Hald, E. S., Hall, J. L. & Alford, P. W. Vascular smooth muscle cell functional contractility depends on extracellular mechanical properties. *J. Biomech.* **48,** 3044–3051 (2015).

39. Sehgel, N. L. *et al.* Augmented vascular smooth muscle cell stiffness and adhesion when hyperTensile Deformation is superimposed on aging. *HyperTensile Deformation* **65,** 370–377 (2015).

40. Wu, Y., Cazorla, O., Labeit, D., Labeit, S. & Granzier, H. Changes in titin and collagen underlie diastolic stiffness diversity of cardiac muscle. *J. Mol. Cell. Cardiol.* **32,** 2151–2161 (2000).

41. Domian, I. J., Yu, H. & Mittal, N. On Materials for Cardiac Tissue Engineering. *Adv. Healthc. Mater.* **6,** 1–3 (2017).

42. Chaturvedi, R. R. *et al.* Passive stiffness of myocardium from congenital heart disease and implications for diastole. *Circulation* **121,** 979–988 (2010).

43. Pernot, M. *et al.* Mapping myocardial elasticity changes after RF-ablation using supersonic shear imaging. *Comput. Cardiol.* 793–796 (2009).

44. Arani, A. *et al.* Cardiac MR elastography for quantitative assessment of elevated myocardial stiffness in cardiac amyloidosis. *J. Magn. Reson. Imaging* **46,** 1361–1367 (2017).

45. Liu, Y., Royston, T. J., Klatt, D. & Lewandowski, E. D. Cardiac MR elastography of the mouse: Initial results. *Magn. Reson. Med.* **76,** 1879–1886 (2016).

46. Arunachalam, S. P. *et al.* Regional assessment of in vivo myocardial stiffness using 3D magnetic resonance elastography in a porcine model of myocardial infarction. *Magn. Reson. Med.* **79,** 361–369 (2018).

47. Jacot, J. G., Martin, J. C. & Hunt, D. L. Mechanobiology of cardiomyocyte development. *J. Biomech.* **43,** 93–98 (2010).

48. Sato, E. J. *et al.* Skeletal muscle fibrosis and stiffness increase after rotator cuff tendon injury and neuromuscular compromise in a rat model. *J. Orthop. Res.* **32,** 1111–1116 (2014).

49. Chapman, M. A. *et al.* Disruption of both nesprin 1 and desmin results in nuclear anchorage defects and fibrosis in skeletal muscle. *Hum. Mol. Genet.* **23,** 5879–5892 (2014).

50. Wood, L. K. *et al.* Intrinsic stiffness of extracellular matrix increases with age in skeletal muscles of mice. *J. Appl. Physiol.* **117,** 363–369 (2014).

51. Eby, S. F. *et al.* Shear wave elastography of passive skeletal muscle stiffness: Influences of sex and age throughout adulthood. *Clin. Biomech.* **30,** 22–27 (2015).

52. Leong, H. T., Hug, F. & Fu, S. N. Increased Upper Trapezius Muscle Stiffness in Overhead Athletes with Rotator Cuff Tendinopathy. *PLoS One* **11,** e0155187 (2016).

53. Brandenburg, J. E. *et al.* Feasibility and reliability of quantifying passive muscle stiffness in young children by using shear wave ultrasound elastography. *J. Ultrasound Med.* **34,** 663–670 (2015).

54. Souron, R. *et al.* Sex differences in active tibialis anterior stiffness evaluated using supersonic shear imaging. *J. Biomech.* **49,** 3534–3537 (2016).

55. Eby, S. F. *et al.* Validation of shear wave elastography in skeletal muscle. *J. Biomech.* **46,** 2381–2387 (2013).

56. Lacraz, G. *et al.* Increased stiffness in aged skeletal muscle impairs muscle progenitor cell proliferative activity. *PLoS One* **10,** 1–13 (2015).

57. Agache, P. G., Monneur, C., Leveque, J. L. & De Rigal, J. Mechanical properties and Young's modulus of human skin in vivo. *Arch. Dermatol. Res.* **269,** 221–232 (1980).

58. Hamasaki, T., Yamaguchi, T. & Iwamoto, M. Estimating the influence of age-related changes in skin stiffness on tactile perception for static stimulations. *J. Biomech. Sci. Eng.* **13,** 1–12 (2018).

59. Wang, L., Yan, F., Yang, Y., Xiang, X. & Qiu, L. Quantitative Assessment of Skin Stiffness in Localized Scleroderma Using Ultrasound Shear-Wave Elastography. *Ultrasound Med. Biol.* **43,** 1339–1347 (2017).

60. Skulborstad, A. J., Swartz, S. M. & Goulbourne, N. C. Biaxial mechanical characterization of bat wing skin. *Bioinspiration and Biomimetics* **10,** 36004 (2015).

61. Pissarenko, A. *et al.* Tensile behavior and structural characterization of pig dermis. *Acta Biomater.* **86,** 77–95 (2019).

62. Pailler-Mattei, C., Bec, S. & Zahouani, H. In vivo measurements of the elastic mechanical properties of human skin by indentation tests. *Med. Eng. Phys.* **30,** 599–606 (2008).

63. Crichton, M. L. *et al.* The viscoelastic, hyperelastic and scale dependent behavior of freshly excised individual skin layers. *Biomaterials* **32,** 4670–4681 (2011).

64. Peñuela, L. *et al.* Atomic force microscopy for biomechanical and structural analysis of human dermis: A complementary tool for medical diagnosis and therapy monitoring. *Exp. Dermatol.* **27,** 150–155 (2018).

65. Marinelli, J. P. *et al.* Quantitative assessment of lung stiffness in patients with interstitial lung disease using MR elastography. *J. Magn. Reson. Imaging* **46,** 365–374 (2017).

66. Mariappan, Y. K. *et al.* Estimation of the absolute shear stiffness of human lung parenchyma using 1h spin echo, echo planar MR elastography. *J. Magn. Reson. Imaging* **40,** 1230–1237 (2014).

67. Melo, E. *et al.* Effects of the decellularization method on the local stiffness of acellular lungs. *Tissue Eng. Part C. Methods* **20,** 412–22 (2014).

68. Uriarte, J. J. *et al.* Early impairment of lung mechanics in a murine model of marfan syndrome. *PLoS One* **11,** 1–19 (2016).

69. Lartey, F. M. *et al.* Dynamic CT imaging of volumetric changes in pulmonary nodules correlates with physical

measurements of stiffness. *Radiother. Oncol.* **122,** 313–318 (2017).

70. Booth, A. J. *et al.* Acellular normal and fibrotic human lung matrices as a culture system for in vitro investigation. *Am. J. Respir. Crit. Care Med.* **186,** 866–876 (2012).

71. Radhakrishnan, R. S. *et al.* Resuscitation-induced intestinal edema decreases the stiffness and residual stress of the intestine. *Shock* **24,** 165–170 (2005).

72. Storkholm, J. H. *et al.* Biomechanical remodeling of the chronically obstructed guinea pig small intestine. *Dig. Dis. Sci.* **52,** 336–346 (2007).

73. Higa, M. *et al.* Passive mechanical properties of large intestine under in vivo and in vitro compression. *Med. Eng. Phys.* **29,** 840–844 (2007).

74. Davis, N. F. *et al.* Urinary Bladder vs Gastrointestinal Tissue: A Comparative Study of Their Biomechanical Properties for Urinary Tract Reconstruction. *Urology* **113,** 235–240 (2018).

75. Bensamoun, S. F., Robert, L., Leclerc, G. E., Debernard, L. & Charleux, F. Stiffness imaging of the kidney and adjacent abdominal tissues measured simultaneously using magnetic resonance elastography. *Clin. Imaging* **35,** 284–287 (2011).

76. Samir, A. E. *et al.* Shear wave elastography in chronic kidney disease: A pilot experience in native kidneys. *BMC Nephrol.* **16,** 1–9 (2015).

77. Srinivasan, S., Krouskop, T. & Ophir, J. A quantitative comparison of modulus images obtained using nanoindentation with strain elastograms. *Ultrasound Med. Biol.* **30,** 899–918 (2004).

78. Wyss, H. M. H. *et al.* Biophysical properties of normal and diseased renal glomeruli. *Am. J. cell Physiol.* **300,** 397–405 (2011).

79. Stefanescu, H. *et al.* Spleen stiffness measurement using fibroscan for the noninvasive assessment of esophageal varices in liver cirrhosis patients. *J. Gastroenterol. Hepatol.* **26,** 164–170 (2011).

80. Hu, X. *et al.* Indirect prediction of liver fibrosis by quantitative measurement of spleen stiffness using the fibroscan system. *J. Ultrasound Med.* **33,** 73–81 (2014).

81. Veiga, Z. S. T. *et al.* Transient elastography evaluation of hepatic and spleen stiffness in patients with hepatosplenic schistosomiasis. *Eur. J. Gastroenterol. Hepatol.* **29,** 730–735 (2017).

82. Pawluś, A. *et al.* Shear wave elastography of the spleen: evaluation of spleen stiffness in healthy volunteers. *Abdom. Radiol.* **41,** 2169–2174 (2016).

83. Carter, F. J., Frank, T. G., Davies, P. J., McLean, D. & Cuschieri, A. Measurements and modeling of the compliance of human and porcine organs. *Med. Image Anal.* **5,** 231–236 (2001).

84. Ling, W. *et al.* Effects of vascularity and differentiation of hepatocellular carcinoma on tumor and liver stiffness: In vivo and in vitro studies. *Ultrasound Med. Biol.* **40,** 739–746 (2014).

85. Cha, S. W. *et al.* Nondiseased liver stiffness measured by shearwave elastography a pilot study. *J. Ultrasound Med.* **33,** 53–60 (2014).

86. Leal-Egaña, A. *et al.* Tuning liver stiffness against tumors: An in vitro study using entrapped cells in tumor-like microcapsules. *J. Mech. Behav. Biomed. Mater.* **9,** 113–121 (2012).

87. Lee, D. H., Lee, J. M., Han, J. K. & Choi, B. I. MR elastography of healthy liver parenchyma: Normal value and reliability of the liver stiffness value measurement. *J. Magn. Reson. Imaging* **38,** 1215–1223 (2013).

88. Venkatesh, S. K., Wang, G., Teo, L. L. S. & Ang, B. W. L. Magnetic resonance elastography of liver in healthy asians: Normal liver stiffness quantification and reproducibility assessment. *J. Magn. Reson. Imaging* **39,** 1–8 (2014).

89. Ogawa, S. *et al.* Relationship between liver tissue stiffness and histopathological findings analyzed by shear wave elastography and compression testing in rats with non-alcoholic steatohepatitis. *J. Med. Ultrason.* **43,** 355–360 (2016).

90. Desai, S. S. *et al.* Physiological ranges of matrix rigidity modulate primary mouse hepatocyte function in part through hepatocyte nuclear factor 4 alpha. *Hepatology* **64,** 261–275 (2016).

91. Gangadhar, K., Hippe, D. S., Thiel, J. & Dighe, M. Impact of Image Orientation on Measurements of Thyroid Nodule Stiffness Using Shear Wave Elastography. *J. Ultrasound Med.* **35,** 1661–1667 (2016).

92. Brezak, R., Hippe, D., Thiel, J. & Dighe, M. K. Variability in stiffness assessment in a thyroid nodule using shear wave imaging. *Ultrasound Q.* **31,** 243–249 (2015).

93. Lam, A. C. L., Pang, S. W. A., Ahuja, A. T. & Bhatia, K. S. S. The influence of precompression on elasticity of thyroid nodules estimated by ultrasound shear wave elastography. *Eur. Radiol.* **26,** 2845–2852 (2016).

94. Bahn, M. M. *et al.* Development and application of magnetic resonance elastography of the normal and pathological thyroid gland in vivo. *J. Magn. Reson. Imaging* **30,** 1151–1154 (2009).

95. Lyshchik, A. *et al.* Elastic Moduli Of Thyroid Tissues Under Compression. *Ultrason. Imaging* **110,** 101–110 (2005).

96. Shi, Y., Glaser, K. J., Venkatesh, S. K., Ben-Abraham, E. I. & Ehman, R. L. Feasibility of using 3D MR elastography to determine pancreatic stiffness in healthy volunteers. *J. Magn. Reson. Imaging* **41,** 369–375 (2015).

97. An, H., Shi, Y., Guo, Q. & Liu, Y. Test–retest reliability of 3D EPI MR elastography of the pancreas. *Clin. Radiol.* **71,** 1068.e7-1068.e12 (2016).

98. Kolipaka, A. *et al.* Magnetic resonance elastography of the pancreas: Measurement reproducibility and relationship with age. *Magn. Reson. Imaging* **42,** 1–7 (2017).

99. Pozzi, R. *et al.* Point shear-wave elastography in chronic pancreatitis: A promising tool for staging disease severity. *Pancreatology* **17,** 905–910 (2017).

100. Naujok, O., Bandou, Y., Shikama, Y., Funaki, M. & Lenzen, S. Effect of substrate rigidity in tissue culture on the function of insulin-secreting INS-1E cells. *J. Tissue Eng. Regen. Med.* **11,** 58–65 (2017).

101. Nagy, N. *et al.* Hyaluronan content governs tissue stiffness in pancreatic islet inflammation. *J. Biol. Chem.* **293,** 567–578 (2018).

102. Farhat, W. A. *et al.* Porcine bladder acellular matrix (ACM): protein expression, mechanical properties. *Biomed. Mater.* **3,** 25015 (2008).

103. Nenadic, I. *et al.* Noninvasive evaluation of bladder wall mechanical properties as a function of filling volume: Potential application in bladder compliance assessment. *PLoS One* **11,** 1–14 (2016).

104. Sheyn, D. *et al.* Trans-abdominal ultrasound shear wave elastographyfor quantitative assessment of female bladder neck elasticity. *Int. Urogynecol. J.* **28,** 763–768 (2017).

105. Wang, T. *et al.* Photochemical activation increases the porcine corneal stiffness and resistance to collagenase digestion. *Exp. Eye Res.* **123,** 97–104 (2014).

106. Wang, L., Tian, L., Huang, Y., Huang, Y. & Zheng, Y. Assessment of Corneal Biomechanical Properties with Inflation Test Using Optical Coherence Tomography. *Ann. Biomed. Eng.* **46,** 247–256 (2018).

107. Tanter, M., Touboul, D., Gennisson, J. L., Bercoff, J. & Fink, M. High-resolution quantitative imaging of cornea elasticity using supersonic shear imaging. *IEEE Trans. Med. Imaging* **28,** 1881–1893 (2009).

108. Matalia, J. *et al.* Correlation of Corneal Biomechanical Stiffness with Refractive Error and Ocular Biometry in a Pediatric Population. *Cornea* **36,** 1221–1226 (2017).

109. Last, J. A., Thomasy, S. M., Croasdale, C. R., Russell, P. & Murphy, C. J. Compliance profile of the human cornea as measured by atomic force microscopy. *Micron* **43,** 1293–1298 (2012).

110. Wu, K. S. *et al.* Micro-scale stiffness change of cornea tissues suffered from elevated intraocular pressure investigated by nanoindentation. *Soft Mater.* **11,** 244–253 (2013).

111. Krag, S. & Andreassen, T. T. Mechanical Properties of the Human Posterior Lens Capsule. *Investig. Opthalmology Vis. Sci.* **44,** 691 (2003).

112. Danielsen, C. C. Tensile mechanical and creep properties of Descemet's membrane and lens capsule. *Exp. Eye Res.* **79,** 343–350 (2004).

113. Jardeleza, M. S. R., Daly, M. K., Kaufman, J. D., Klapperich, C. & Legutko, P. A. Effect of trypan blue staining on the elastic modulus of anterior lens capsules of diabetic and nondiabetic patients. *J. Cataract Refract. Surg.* **35,** 318–323 (2009).

114. Yoo, L. *et al.* Characterization of ocular tissues using microindentation and Hertzian viscoelastic models. *Investig. Ophthalmol. Vis. Sci.* **52,** 3475–3482 (2011).

115. Besner, S., Scarcelli, G., Pineda, R. & Yun, S. H. In vivo brillouin analysis of the aging crystalline lens. *Investig. Ophthalmol. Vis. Sci.* **57,** 5093–5100 (2016).

116. Cui, J., Lee, C. H., Delbos, A., McManus, J. J. & Crosby, A. J. Cavitation rheology of the eye lens. *Soft Matter* **7,** 7827–7831 (2011).

117. Heys, J. & Barocas, V. H. Mechanical characterization of the bovine iris. *J. Biomech.* **32,** 999–1003 (1999).

118. Whitcomb, J. E., Barnett, V. A., Olsen, T. W. & Barocas, V. H. Ex vivo porcine iris stiffening due to drug stimulation. *Exp. Eye Res.* **89,** 456–461 (2009).

119. Whitcomb, J. E., Amini, R., Simha, N. K. & Barocas, V. H. Anterior-posterior asymmetry in iris mechanics measured by indentation. *Exp. Eye Res.* **93,** 475–481 (2011).

120. Yoo, L. *et al.* Characterization of ocular tissues using microindentation and Hertzian viscoelastic models. *Investig. Ophthalmol. Vis. Sci.* **52,** 3475–3482 (2011).

Chapter III

PUSHING THE NATURAL FRONTIER: PROGRESS ON THE INTEGRATION OF BIOMATERIAL CUES FOR COMBINATORIAL BIOFABRICATION AND TISSUE ENGINEERING

PUSHING THE NATURAL FRONTIER: PROGRESS ON THE INTEGRATION OF BIOMATERIAL CUES TOWARDS COMBINATORIAL BIOFABRICATION AND TISSUE ENGINEERING.

Abstract

The engineering of fully functional, biological-like tissues requires biomaterials to direct cellular events to a near-native, 3-Dimensional niche extent. Natural biomaterials are generally seen as a safe option for cell support, but their biocompatibility and biodegradability can be just as limited as their bioactive/biomimetic performance. Furthermore, integrating different biomaterial cues and their final impact on cellular behavior is a complex equation where the outcome might be very different from the sum of individual parts. This review critically analyses recent progress on biomaterial-induced cellular responses, from simple adhesion to more complex stem cell differentiation, looking at the ever-growing possibilities of natural materials modification. Starting with a discussion on native material formulation and the inclusion of cell-instructive cues, we delve into the roles of shape and mechanical stimuli, the susceptibility to cellular remodeling, and the often-overlooked impact of cellular density and cell-cell interactions within constructs. Along the way, synergistic and antagonistic combinations reported *in vitro* and *in vivo* are singled out, identifying needs and current lessons on the development of natural biomaterial libraries to solve the cell-material puzzle efficiently. This review brings together knowledge from different fields envisioning next-generation, combinatorial biomaterial development towards complex tissue engineering.

This chapter is reproduced from the following publication:

Guimarães, C. F., Marques, A. P., & Reis, R. L., Pushing the Natural Frontier: Progress on the Integration of Biomaterial Cues towards Combinatorial Biofabrication and Tissue Engineering, *Advanced Materials* (Revising).

III.1. INTRODUCTION

There have been undeniable advances in the field of tissue engineering (TE). Some tissue-engineered organs such as the bladder [1], urethra [2], and vagina [3] have reached the clinical stage and shown able to integrate the organism and maintain physiological function for many years after implantation. Even though these are examples of success, they represent mostly non-vital organs generally simpler in terms of morphology and cellular complexity. On the other hand, vital organs like the kidney, heart, liver, or lungs top the list of transplant requirements worldwide [4]. Yet, there are no TE equivalents of these organs so far, resulting from their complex cellular function and architecture, which are extremely hard to engineer, leading to a continuous effort to better organ recovery and transplantation [5].

Biomaterials have been faithful companions of cells in TE strategies, physically supporting them and allowing the maintenance of their phenotype in distinct environments. In fact, with the recent advances in the field of 3D printing, biomaterial-based 3D structures can now be manipulated to approach the architecture of complex tissues and organs, such as vascular beds and cardiac components [6,7]. However, shape and architecture alone cannot assure the ultimate TE challenge: recapitulation of physiological cellular and tissue function. As such, there is one additional burden for biomaterials to carry – the control of cellular behavior. These requirements force upon biomaterials the need to be intelligent and dynamic, supporting and efficiently directing the behavior of cells towards specific outcomes.

Natural-origin materials have been continuously derived from different animal and plant components, gathering attention as biomaterials due to their original role in biological environments [8]. However, their bioactivity and biodegradability can be just as limited as that of synthetic components. Thus, this review explores some of the leading natural materials that have been used in TE approaches, looking at their typical applications, degradability properties, and ability to interact with and be modified by the action of cells – a biomimetic, Extracellular Matrix (ECM)-like behavior. Furthermore, we explore the progress on the use of adhesive sequences and growth factors and their combinatorial applications with emerging synergistic results and novel biological outcomes. Likewise, as force and shape establish themselves as fair opponents to classical biochemical cues [9,10], we review the recent progress in

manipulating stiffness and topography within 3D natural materials and how they can further boost cellular responses.

When engineering tissues, one must also recognize that cells can play a significant role in the outcome, not just by responding to the material itself but by representing a direct parameter of influence. This impact can be due to complex cell-cell signaling within materials and the effect of cells in the construct's mechanics. Since cell density within biomaterial constructs is usually underrated and understudied, we delved into this parameter, embracing it as a cue on its own and establishing a roadmap for approaching cell density when engineering live-like tissues.

This review differentiates itself from previous documents by providing an integrative view of the different types of cell-controlling cues and identifying their combinatorial potential by exposing previously unreported synergies or antagonistic interactions between different biomaterial's properties.

By integrating all these different biomaterial-cell and cell-cell cues into a single analysis, we were able to identify that the most critical future challenges relate to the need for studying different materials, formulations, cells, and combinations thereof in a time-efficient and comprehensive fashion. Therefore, we conclude our review by discussing the development of libraries of natural materials and high-throughput (HT) screening platforms. Finally, we analyze recent advances in the fabrication or progress that might allow future development of these highly efficient screening platforms, which now begin transitioning to 3D environments and including biomaterials that are not just synthetic.

III.2. NATURAL MATERIALS IN TE

A continuous search has marked the past decades for the most appropriate natural materials to approach the physiological function of different tissues. **Table III-1** summarizes some of the leading natural polymers their typical uses in the TE field, where they have been proven to be biocompatible to some extent. Most of these materials were selected for their mechanics and ability to form specific structures such as hydrogels (e.g., Alginate [11]), fibers (e.g., silk fibroin (SF) [12]), or more classic scaffolds (e.g., Chitosan [13], Collagen [14]) both separately or in combinations (**table III-1**). In TE, these materials are used together with cells as a way of approaching live biological tissues. As so, assuring the lowest cytotoxicity possible and the support of cell viability is of first importance. As far as these parameters go, natural materials have performed well in varied situations. However, cytocompatibility is a necessary but insufficient property for the TE of complex cellular environments and organs. When attempting to

replace tissues, it is required to ensure that the engineered construct can fulfill specific functional requirements. Thus, biomaterials must allow not only viable cell maintenance but also their organization and phenotypic profile. This profile includes particular tissue characteristics such as more static architecture (e.g., cell/ECM orientation), or more dynamic responses as contractility, barrier function, neural impulse guidance, among others - depending on the tissue being targeted [15].

One other important property is the ability of the biomaterial to degrade within a typical biological environment without releasing toxic byproducts or becoming exaggeratedly unstable in terms of mechanics, compromising its function [16,17]. Furthermore, the degradation should happen at a rate similar to that of neotissue formation [18] – synchronous biodegradation - assuring that patients need only one surgery to implant TE constructs that will, in time, degrade, as what is currently standard with bioresorbable sutures [19].

Even though some natural-derived materials present biodegradability, it is not always the case (**table III-1**). Alginate, one of the most frequently used polysaccharides for hydrogel development, is not degradable in the organism when unmodified [20]: an excellent example that the most used is not necessarily the adequate solution for all applications. In such cases, degradability must be engineered into the materials. For instance, researchers approached this by introducing Poly(lactic-co-glycolic acid) (PLGA) microspheres containing alginate lyase within alginate hydrogels to achieve tunable degradation [21]. Even though the construct was no longer natural but a natural/synthetic blend, it was possible to tune its degradability. This tunable degradation rate is essential even when materials are naturally biodegradable, as the synchronism between material degradation and neotissue formation is still a significant hurdle [17]. This challenge is especially relevant when entrapped bioactive molecules are released *via* material degradation [22]. Natural biomaterials can be selected and modified according to the desired degradation rate, which can vary significantly. For example, esterified hyaluronic acid hydrogels can degrade as fast as one week and as slow as five months, depending on the degree of esterification [19]. Similarly, a 2% (w/v) injectable chitosan hydrogel with 98% acetylation only degrades about 50% after two months *in vitro,* whereas at 1% (w/v) and with 83% acetylation, it degrades over 80% in the same period [23]. Hence, different strategies can be employed to manipulate the chemistry of the same material and thus tune its degradation rate.

Table III-1: Natural polymers commonly used in the field of TE.

Material	Origin	Bioactive	Biodegradable	Common 3D Structures	Common TE Applications	Refs.
ECM Proteins						
Collagen	Tissue	Yes	Yes	Scaffolds, Coatings, Blends	Varied	14,24,25
Fibronectin	Tissue	Yes	Yes	Patterning, Surface Coatings	Bone	26,27
Fibrin	Tissue	Yes	Yes	Scaffolds, Gels, Glues	Cardiovascular, Neuronal	28–31
Laminin	Tissue	Yes	Yes	Scaffolds, Gels (as a conjugate)	Neuronal	31–33
Elastin	Tissue	Yes	Yes	Scaffolds, Conjugates	Vascular, Skin	13,34–36
Other Proteins						
Gelatin	Collagen/ECM	Yes	Yes	Scaffolds, Hydrogels	Bone, Cartilage	20,37,38
Silk Fibroin (SF)	Silk	No	Yes	Fibers, Scaffolds	Cartilage, Bone	12,39–41
ECM Glycosaminoglycans (GAGs)						
Hyaluronic Acid (HA)	ECM	Yes	Yes	Hydrogels, Scaffolds (conjugates)	Cartilage, Bone	22,31,42–44
Chondroitin Sulfate (CS)	ECM	Yes	Yes	Scaffolds, Hydrogels	Cartilage	45–47
Aggrecan	ECM	Yes	Yes	Hydrogels (conjugates)	Cartilage	48,49
Other Polysaccharides						
Chitosan	Crustaceans	No	Yes	Scaffolds, Hydrogels, Sponges	Varied	50–54
Starch	Plants	No	Yes	Scaffolds (conjugated)	Bone	55–57
Alginate	Algae	No	No	Hydrogels	Varied	11,20,58
Agarose	Algae	No	No	Hydrogels	Cartilage	49,59–61
Carrageenan	Algae	No	Yes	Hydrogels	Cartilage, Bone	62–64
Gellan Gum (GG)	Bacteria	No	No	Hydrogels	Cartilage, Bone, Skin	65–69

III.2.1. Bioinert, Bioactive, and Biolabile Materials

The notion that all-natural polymers have a biological activity must be dismissed. While most protein-based materials have some degree of interaction with other proteins and cells, many polysaccharides used in the field of TE are just as inert as other synthetic materials, having limited to non-existent cell interaction (**table III-1**).

Many ECM-derived proteins possess bioactive sequences that are naturally capable of specific cellular interaction and elicit very well-defined cellular responses. Collagen, laminin, and fibronectin are good examples of ECM-derived adhesive proteins. These have RGD (arginine-glycine-aspartate) sequences in their amino acid composition, which bind to cell-surface integrins, playing an essential role in assembling focal adhesions and the consequent cytoskeletal rearrangement [70]. This potent property has been exploited in several applications, from the use of adhesive proteins to the grafting of specific RGD motifs on otherwise inert surfaces to promote cell adhesion [71,72], as discussed in section 3.1.

Another branch of natural biomaterials is Glycosaminoglycans (GAGs) -polysaccharides and proteoglycans that are also part of the ECM in different tissues. Most GAGs are also imbued with some level of biological activity through cellular interaction. Hyaluronic acid (HA) and chondroitin sulfate (CS) are two widely used GAGs in the TE field [31,45,73,74]. CS has been identified as capable of direct cell interaction [75–77]. This interaction is not yet fully understood in the way that the proper cellular receptor and pathways triggered upon cellular contact are yet to be clearly described. On the other hand, HA specifically interacts with cells being the known ligand of the cell receptor CD44. This receptor is expressed by different cell types, namely by mesenchymal stem cells (MSCs) from different origins [78].

Nonetheless, not all natural materials possess such specific bioactivity. As previously mentioned, most polysaccharide-derived matrices are bio-inert (**table III-1**). While these materials can still encapsulate, support, and protect viable cells [61], the inability to promote cell adhesion, proliferation, or even their natural migration might restrict the development of the dynamic strategies that lead to functional engineered tissues [79]. Inert but safe polysaccharides have so been modified to increase their

bioactivity and biomimetic performance. In some cases, simple modifications can be pursued for some enhancement of mechanical flexibility and to manipulate the activity of materials within biological environments. Gellan gum, which is not biodegradable and mostly biologically inert, is frequently used to develop hydrogels for different applications (table III-1). Methacrylation and acylation have been used to tune both the mechanical properties and the activity of gellan gum gels in biological media, with different behavior regarding, e.g., mineral deposition [68,80].

Additionally, giving cells a 3D material environment that is not specifically bioactive but instead modifiable by cells themselves has gained momentum as a just - if not more - vital characteristic to attain optimal biological performance. *In vivo,* cells are the ones who synthesize, remodel, and degrade their 3D environment, and as such, it makes sense that allowing them to do the same in TE engineering strategies can lead to optimal outcomes. Such a type of material/environment was described as *Biolabile* [10] rather than *Bioactive*, by being prone to a) cell degradation through the action of, e.g., Matrix Metallo-Proteinases (MMPs) [81,82]; b) plastic enough for cells to widen gaps and protrude through [83]; c) viscoelastic in such way that cells can expand with less restriction [84]; or d) allowing for the synthesis and deposition of cell-derived nascent proteins that alter the material itself and reflect on the cellular responses (**Fig. III-1**) [85].

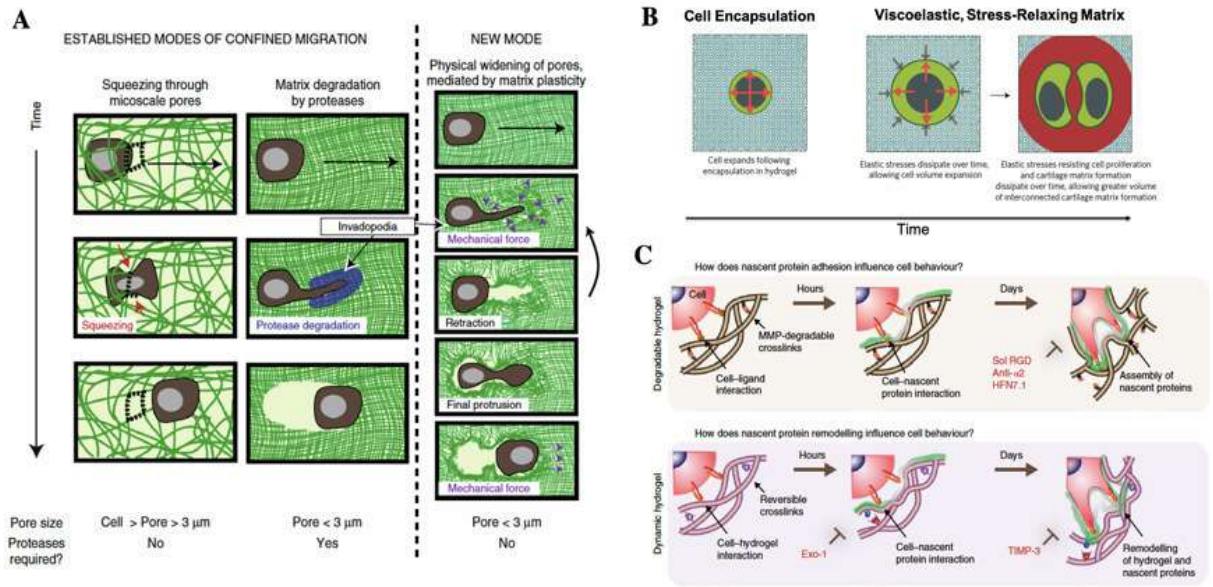


Figure III-1: New Paradigms in Material Susceptibility. Recent works demonstrate how important it might be to allow cells themselves to manipulate their surroundings instead of attempting to trigger specific pathways through classic bioactive ligands. Matrix elasticity might allow cells to move around by physically widening pores in addition to

squeezing through or degrading their surroundings through MMP activity (A). Copyright from [83]. Even within non-adhesive environments, the viscoelastic, stress-relaxing mechanics of cellular surroundings can significantly impact cell volume expansion, facilitating proliferation, ECM deposition, and generation of biological-like structures (B). Adapted from [84]. Similarly, cells themselves can deposit their proteins (nascent) onto hydrogels, degradable or dynamic, not only modifying their surroundings but simultaneously interacting with it through cell-derived proteins (C), with demonstrated impact in the final biological outcome. Adapted from [85].

Overall, a natural though biologically inert material should not be seen with a negative connotation. There is always the need for structural materials in TE strategies that can support cells and bioactive cues, with no material-derived biological effect, not to interfere with designed responses. Also, as referred to and reviewed in the following sections, primarily all natural materials have been modified to elicit tunable biological responses or support within biologically active surroundings such as cell differentiation media. Inert materials are a white canvas, on which specific outcomes can be designed step by step, in a controlled fashion, by the engineer or cells themselves.

III.3. INTEGRATING BIOMATERIAL CUES FOR CONTROLLED CELL BEHAVIOR

So far, adequate cell-material interaction has been pursued through engineering biomaterials by either mimicking the natural tissue's microenvironments or generating novel combinations of signals to guide cellular behavior, exploiting unknown synergies, and developing combinatorial strategies from them. The provided cues comprise biological signals, such as cell adhesive sequences and other ligands for cell surface receptors, and environment-sensitive features that render materials susceptible, e.g., to the action of cell-derived enzymes. Additionally, surrounding material stiffness and topography represent the mechanical cues that cells convert into specific activities – mechanotransduction – determining the overall biological response. Finally, cell-cell interactions, intimately related to the density of cells within a TE construct, have a prominent role in cellular outcomes. Altogether, we propose these six fundamental cues in the cell-biomaterial compass (**Figure III-2**), representing their potential for guiding the behavior of cells within materials. Some of these cues have been extensively explored in TE, while others still require deeper investigation. However, all have proven or developed potential in diverse

solutions regarding distinct biological events in tissues, from bone to brain, and cells, from cell adhesion to differentiation. The most recent advances in this context are explored below.

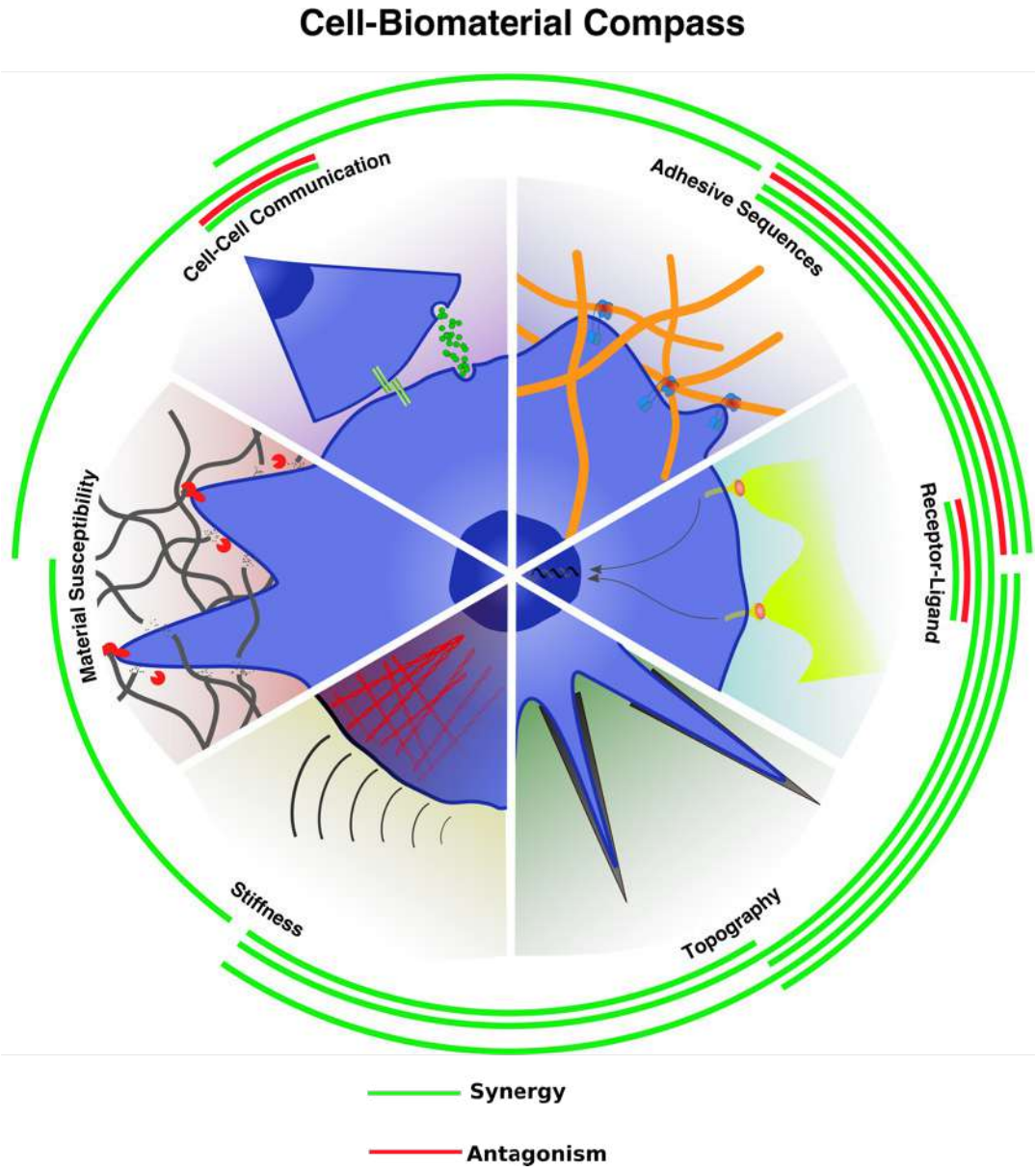


Figure III-2: The Cell-Biomaterial Compass. Schematic representation of the 6-fundamental biomaterial-cell cues within TE constructs. Moving clockwise, cell adhesive sequences can interact with cell-surface integrins promoting cell adhesion and consequent events. Other receptor-ligand interactions can also be exploited by presenting bioactive molecules to the cell surface to stimulate different and specific cell responses. Regarding the mechanotransduction of physical cues, cells can feel and react to the surrounding topography and stiffness, changing their morphology and cytoskeletal organization with a profound impact on different cellular events. Additionally, cells themselves can alter the structure and shape of the surrounding environment when placed in materials that are susceptible to the action of cell-derived enzymes such as MMPs (which can be secreted or membrane-bound) or material-displacing cell forces. Finally, the interaction between cells (cell-cell interaction) by direct contact or paracrine signals within materials can

also significantly alter the biological outcomes of the engineered constructs. The outer colored lines connect cues that have been reported to have some synergistic (green) or antagonistic (red) interaction upon combination.

III.3.1. Ligand-Receptor Interactions

The natural cellular niche can instruct cellular activities partially through the stimulation of specific cell-surface receptors. Generally speaking, there are two classes of stimuli: physical and soluble [86]. Physical cues comprise mainly the action of protein and peptide sequences that bind to specific cellular receptors. Among those, adhesive proteins, being insoluble fibers that comprise the bulk of the ECM, have been widely used for tissue engineering promoting processes such as cell adhesion, spreading, and alignment. On the other hand, soluble cues are mostly growth factors that can be entrapped within the ECM with a higher or lower degree of freedom. Both of these classes of signals and how they are presented to cells have been explored throughout different TE approaches.

III.3.1.1. Cell Adhesive Ligands

Cell adhesive ligands, mainly represented by peptides with the earliest RGD sequence, are proven powerful cues to manipulate cell-material interactions by enforcing adhesion to otherwise inert materials [87]. RGD-containing proteins have evolved and been replaced by smaller, protein-derived peptide sequences that allow for the maintenance of function while reducing immune rejection in biological systems. These smaller sequences also have the advantage of selecting and guaranteeing more specific responses since one total protein possesses a plethora of interactive sites in addition to the cell adhesive sequence [88]. Ideally, the proper motif promotes cellular adhesion while leading to no other outcome. For example, Yeo *et al.* identified a bioactive core in laminin's $\alpha 2$ chain that promoted cell adhesion as actively as the whole protein, despite possessing no secondary or tertiary structures.

Furthermore, they've shown that this peptide core could promote bone formation without detectable antigenic activity [32]. RGD sequences are still presently manipulated to confer some bioactivity to otherwise inert materials and promote an interaction that reflects (through adhesion) on more complex cell responses. For example, adipose-derived stem cells were shown to respond to RGD-modified alginate hydrogels (naturally non-adhesive) forming focal adhesions, which resulted in the

downstream enhancement of adipogenic differentiation [89]. Furthermore, even though RGDs are arguably the most common adhesive motifs, other protein sequences can also target cell adhesion, improving biological outcomes. The Tyr-Ile-Gly-Ser-Arg (YIGSR) is one such sequence that has also been known for several decades [90,91]. Naturally, adhesive proteins have complex structures which can interact with cells and adhesive integrins in different ways. Peptide screening technologies can aid in uncovering novel adhesive sequences that can be used to replace more traditional RGD or YIGSR and tune or provide specificity in the adhering cell. For example, in a 2012 study, researchers identified 11 adhesive sequences in the N-terminal of laminin, a known adhesive protein. Of those, five were capable of inducing PC12 neurite outgrowth [92]. Similarly, other examples of adhesive molecules and sequences are critical to different cell types, such as adhesive immunoglobulin-derived sequences and their interaction with immune cells [93] and tumor-derived adhesive proteins that can induce inappropriate angiogenic responses [94]. Together, these results demonstrate how different adhesive sequences can be employed and adjusted to the cell type and desired responses.

The type and the number of adhesive motives can have a varying impact on cellular behavior. For example, in retinal TE, RGD-modified alginate was shown to improve embryonic stem cell (ESC)- and induced pluripotent stem cell (iPSC)-derived embryoid bodies depicting optic vesicles and pigmented retinal epithelium. This response was further strengthened by a positive effect on the expression of genes from the retinal pool [95]. Furthermore, these alginate hydrogels performed better than naturally active, HA-based hydrogels and, curiously, 0.5% RGD-alginate hydrogels led to a more significant outcome than 1% RGD-alginate. This difference reveals that adhesive ligands can be beneficial. Still, the response to these motifs might not be linear, i.e., increasing the number of adhesive sequences does not necessarily translate into a better cellular response. This non-linear effect was also observed on HA/Pectin-RGD hydrogels, respectively combined at 3:7, 5:5, and 7:3 ratios to evaluate their impact on chondrocytes [96]. In this case, 5:5 hydrogels outperformed both blends at 3:7 and 7:3 ratios. These results highlight that it is crucial to use the appropriate adhesive motifs and tune their levels for an adequate response. It also highlights the need for HT methods for screening cellular responses to full spectra of ligand type and concentration to pinpoint the best-fit conditions for the desired cell response.

The use of adhesive ligands can still be attributed to another layer of complexity by including spatiotemporal control of their exposure to cells. Lee *et al.* specially engineered RGD-modified hydrogels: through the protection of RGD motifs by light-sensitive molecules, the authors could control the time at which the biomaterials would expose these sequences in mice [97]. The caged RGD sequences were exposed after transdermal UV stimulation, leading to increased inflammatory cell adhesion. They decreased inflammation that resulted in a thinner fibrous capsule and promotion of host blood vessels ingrowth. Furthermore, these responses were confined to a perimeter of 500μm around the irradiated area of the biomaterial and absent elsewhere. This spatiotemporal control of RGD exposure might allow better control of cellular behavior than indiscriminate RGD presentation and a localized and sequential regulation of cell adhesion, e.g., across different phases of the wound healing process. Finally, the lessons learned from structural studies of this RGD tripeptide have allowed the scientific community to synthetically approach the same structure without using the exact biological sequence. Rossi *et al.* tested the response of cells to foam with 4-(aminobutyl)guanidine moieties, recognized by the same receptors that sense RGD sequences. Different cell lines showed improved adhesion and viability on this material *in vitro* and a good integration upon *in vivo* implantation, with host vessels infiltrating the engineered constructs [98]. The use of adhesive sequences might be necessary for the future and allow the modification of inert biomaterials with more stable and less immunogenic moieties. Overall, these sequences are still employed to improve the adhesiveness and cellular interaction of otherwise inert materials. Still, the paradigm appears to be shifting from indiscriminate to tuned, spatiotemporally controlled adhesive sequence exposure, in parallel to the natural dynamics of living tissues.

III.3.1.2. Growth Factor-based Approaches

Growth factors represent the soluble component of cellular ligands, being cues that are too recognized by specific cell receptors promoting well-defined responses. However, these are not insoluble fibers but small molecules that might be entrapped or freely moving within the ECM. Several growth factors have been explored for tissue engineering and regenerative applications, depending on the desired cellular outcome, eliciting various responses ranging from chemotaxis (migration) to morphogenesis, apoptosis, metabolic modulation, and combinations thereof [99,100]. While it is not the scope of this review to evaluate all possible growth factors employed in the field, we discuss the most

important considerations. Below, we will focus on growth factors that have well-proven effects and are still currently used for advancing tissue engineering research.

Bone Morphogenic Proteins (BMPs) are one of the most well-established growth factors, widely used in the field of bone regeneration and engineered, being inclusively FDA-approved and used in some clinical areas [101]. BMPs are essentially utilized due to their osteoinductive action, i.e., the promotion of bone-like cell differentiation and bone tissue formation and maturation. Metallic implants, for example, have long benefited from BMP integration for increasing their bioactivity [102–104]. Porous titanium scaffolds filled with fibrin gels carrying BMP-2 implanted in segmental bone defects promoted complete regeneration within eight weeks, significantly improving empty and unmodified fibrin-containing titanium scaffolds [102]. Moving away from metallic implants, which have several application restraints due to non-degradability, BMPs have performed well also in combination with natural-derived matrixes. A work using collagen scaffolds showed that the integration of BMP2-presenting heparan sulfate led to the full bridging of femoral bone defects, increasing of bone formation to near 10-fold that of collagen alone (**Figure III-3, I**) [105]. These positive results combine natural, adhesive, and degradable materials and BMPs. The further use of self-assembling peptide amphiphiles fibers capable of displaying sulfated polysaccharides that can present heparin-binding cytokines to cells - in this case, BMPs - led to bridging bone defects with BMP levels which are an entire order of magnitude below those required to heal bone *in vivo* [105].

Similarly, adhesive peptide sequences grafted with BMP2 synergistically promoted the regeneration of bone defects *in vivo* in a study performed using inert, synthetic hydrogel templates [106]. However, a study investigating the combinatorial effects between the adhesive protein fibronectin and different BMPS showed that fibronectin could antagonize the effects of BMP7, despite synergizing with both BMP2 and BMP6, to different extents [107]. These results show that the simultaneous presence of natural polymers, adhesive sequences, and BMPs may have varied outcomes depending on the binding affinity between different molecules, altering the way adhering cells sense the presented growth factors. Furthermore, these combinatorial responses reinforce the need for adequately screening different combinations of commonly used molecules in terms of cellular responses. Furthermore, the effect of BMPs depends on cellular recognition and internalization, which are dependent on surface properties,

such as roughness [108] and stiffness [109]. While the uptake of growth factors in solution is mainly done by the dorsal side of cells (the side which does not adhere to any surface), factors bound and presented in surfaces interact with the ventral side of cells (the adhering side). The recognition and internalization of material-bound growth factors are significantly affected by the shape of the cells, the area they are covering on the surface, and the magnitude of cell-surface interactions, which are all dependent on shape and mechanics [10,108,109]. Therefore, this type of growth factor presentation enables a degree of modulation absent in soluble strategies. Therein, the uptake is primarily independent of the physical environment except potentially by diffusion coefficients in 3D matrixes such as hydrogels [110,111].

All these layers of complexity within the current knowledge on BMPs in bone TE leave plenty of room to find the perfect BMP/biomaterial combination for different applications. This case is further strengthened because whole BMPs have also been replaced by smaller peptides derived from the entire sequence. These were shown to maintain their bioactive effect, which will eventually be essential to circumvent the costs of producing recombinant human (rh)-BMPs on a large, clinical scale [112,113].

Vascular Endothelial Growth Factors (VEGFs) are also a class of bioactive, soluble molecules that have been widely explored in TE. VEGFs are natural regulators of physiological angiogenesis, through which new blood vessels are generated from pre-existing ones [114]. One of the significant pitfalls of TE and the integration of cell-biomaterial constructs in biological tissues is the lack of proper oxygenation and supply of nutrients, making vascularization one of the most critical issues in the field, as extensively reviewed elsewhere [115–117]. Hence, scientists have been using VEGFs to increase the angiogenic potential of biomaterials. Jia *et al.* created a fusion protein comprising VEGF and a collagen-binding domain generating a collagen scaffold to replace damaged urethral sections [118]. When implanted into the urethra of dogs, VEGF constructs significantly out-performed simple collagen scaffolds – achieving native-like urethral function, with indistinguishable urethral epithelial cells integrating VEGF-modified constructs (**Figure III-3, II**). Additionally, VEGF-collagen also led to blood vessel densities like those of the original tissue, significantly improving compared to unmodified collagen. The only difference between the engineered construct and the native tissue was a significantly lower density of smooth muscle tissue. This problem could probably be overcome by introducing platelet-derived growth factor (PDGF), which promotes smooth muscle cell recruitment, leading to blood vessel maturation [119,120]. Be

that as it may, even naturally biolabile materials, such as collagen, can still see their performance enhanced through additional modifications.

Similarly, Yin *et al.* conjugated VEGF to alginate for the encapsulation of pancreatic islets [121]. In this work, researchers reported a 14-fold increase in the formation of blood vessels upon subcutaneous implantation of the hydrogels, which were able to protect the pancreatic islets and allow *in vivo* maintenance of proper glucose levels for 50 days post-transplantation. This simple modification represented a drastic improvement compared to the 15 days of islet maintenance by unmodified alginate hydrogels.

In the field of bone TE, Quade *et al.* modified collagen scaffolds with a central depot of VEGF, showing gradients of VEGF concentration as a tunable approach to manipulate endothelial cell migration, envisioning future bone vascular development [122]. In addition, modifications with VEGF have recently been used to improve the vascular response to biomaterials in several other applications such as ischemic recovery [123], testicular [124], and adipose [125] TE, as well as spinal cord repair [126].

Furthermore, VEGF has been shown to behave synergistically when combined with several other growth factors - not only with the previously referred PDGF but also stromal cell-derived factor (SDF) [123], fibroblast growth factor (FGF) [127], angiopoietin [128] and BMPs [104,129,130]. This synergistic behavior was also reported in the fusion of VEGFs to adhesive molecules such as fibronectin domains [131], RGD sequences, and other integrin-targeting peptides [132].

Despite being fundamental to the development of most vascularized tissues, it is imperative to refer that the angiogenic response and vasculature development is not always desired in the field of TE. Specific tissues, such as cartilage or cornea, have naturally low levels of vascularization, which are essential to maintain physiological function. Therefore, strategies are also devised to sequestrate VEGF from cellular interaction to limit angiogenesis reversely. This sequestration has been approached through, e.g., the integration of VEGF blocker dendrons within hydrogels [133] or using VEGF-binding peptides in microspheres [134]. Naturally, these strategies target mostly soluble VEGF, promoting its binding to engineered moieties, not to present it to cells but to strongly inhibit cellular interaction through targeted sequestering. Future works focusing on VEGF sequestration for angiogenic inhibition

may also explore recent advances in molecular imprinting on polymeric particles and other biomaterial constructs [135,136].

Overall, the potential of VEGFs is undeniable. Still, now, the question is not whether to use them but how to tune the level of vascular development avoiding pathological responses, and find the proper material/growth factor combinations for the development and maintenance of vascularization (or absence of such) in different engineered tissues.

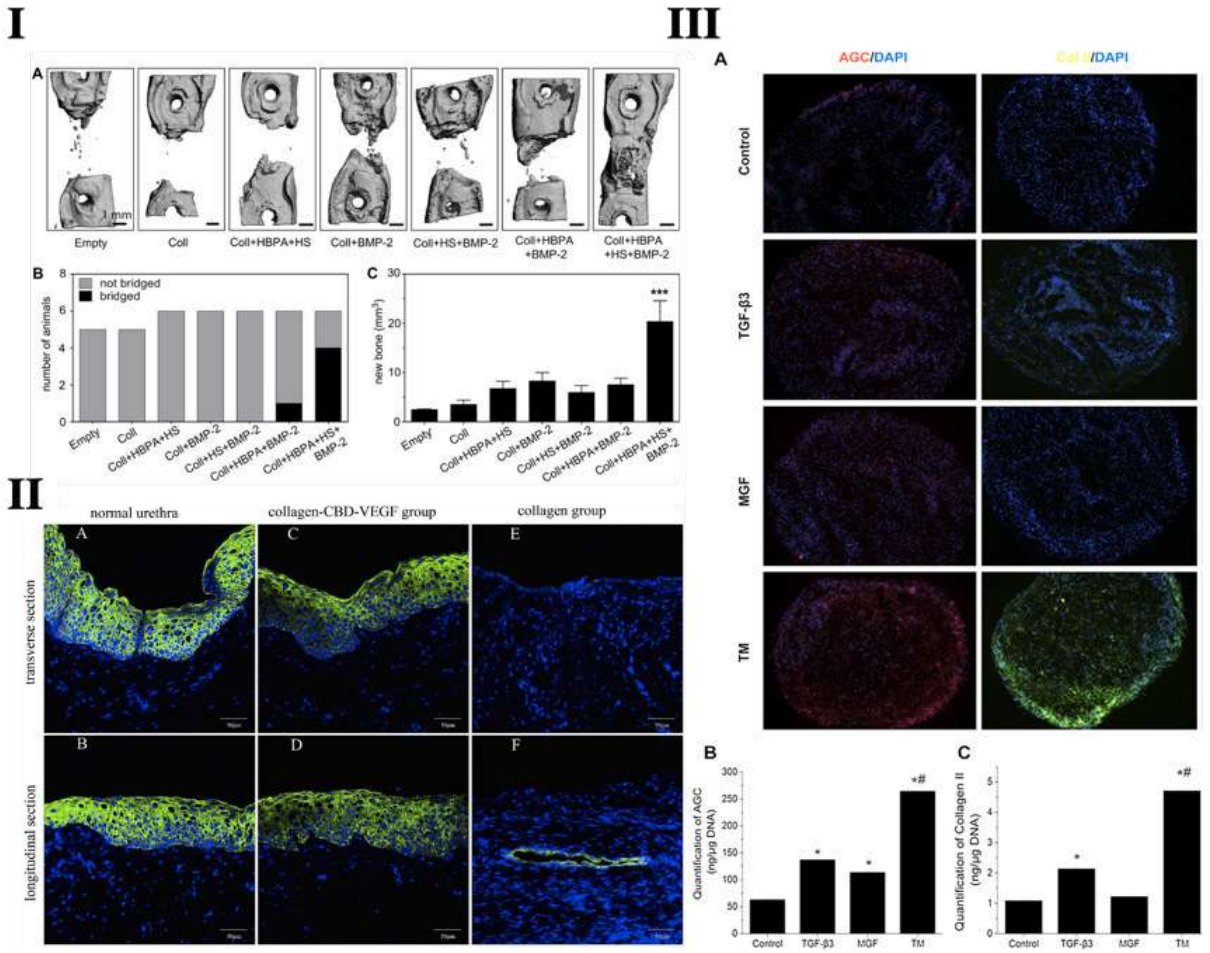


Figure III-3: Growth factors as powerful cues to boost the activity of natural materials. I- BMPs enhance bone regeneration - In segmental femur defects, loading collagen scaffolds with BMP-presenting, self-assembled nanofibers synergistically strengthen the regeneration of bone tissue when compared to collagen alone scaffolds and soluble BMP. Adapted from [105]. II- The use of collagen-bound VEGF on engineered urethral structures (C, D) in vivo leads to an almost indistinguishable neotissue when compared to native urethras (A, B), as opposed to unmodified collagen (E, F). Adapted from [118]. III – TGF-beta and MGF synergize on promoting chondrogenic differentiation of hMSCs in silk fibroin scaffolds. While alone, chondrogenic differentiation of hMSCs by these factors is limited but, upon combination (TM), there is a synergistic boost on the synthesis of aggrecan (B) and collagen II (C). Adapted from [137].

Other growth factors have also been combined with biomaterials in varied TE applications, even if to a lower extent than previously discussed. One example is the use of members of the transforming growth factor beta (TGF-β) family in the field of cartilage TE [138]. TGF-β factors, in their many isoforms, and similarly to other active molecules, can lead to different cellular outcomes depending on being immobilized in a scaffold or soluble in the medium [139]. *In vitro*, cellulose/gelatin hydrogels have been engineered to bind TGF-β-2 by mimicking the heparan sulfate affinity to that molecule and encapsulated

MSCs and chondrocytes were shown to synthesize and deposit significantly higher amounts of collagen II and aggrecan, two patent ECM components of cartilage [140]. A similar effect was reported with silk fibroin (SF) scaffolds entrapping TGF-β-3 within the beta-sheet protein regions, synergizing with the mechano growth factor (MGF) (**Figure III-3**, II), significantly improving hyaline cartilage regeneration by promoting stem cell recruitment [137]. Choi *et al.* have also tested the effect of TGF-β-1 bound via molecular affinity to chitosan scaffolds, showing that MSCs and chondrocytes increased their GAG deposition and formed neocartilage *in vivo* in the presence of this growth factor [141].

Neural Growth Factors (NGF) have also been integrated with biomaterials, especially for nervous TE strategies, primarily included in microspheres, alone for controlled brain delivery [142] or within tissue engineering scaffolds containing the NGF-releasing hydrogel spheres such as reported for Silk Fibroin ones [143] applied to spinal cord regeneration. Even though these approaches focus on the release of soluble NGF, researchers have also devised strategies for directly functionalizing scaffolds with NGF, such as conduits envisaging peripheral nerve regeneration [144], which may enhance biological function due to NGF immobilization and ECM-like presentation.

FGF has also been applied in different TE approaches, together with other growth factors such as VEGFs [127] and BMPs [145], but also alone within hydrogels and sponges to stimulate chondrocytes [146] and MSC chondrogenesis [147]. It has also been used to functionalize collagen scaffolds, synergizing with the naturally biolabile collagen to promote the proliferation of smooth-muscle cells and downstream vascularization responses [148].

Overall, several approaches are needed to increase the cellular interaction of naturally inert biomaterials by taking advantage of the particular receptor-ligand interaction (**Table III-2**). By doing so, several cellular responses can be elicited from simple adhesion events to complex stem cell differentiation.

Table III-2. Most commonly used bioactive molecules for TE applications of natural biomaterials

Ligand	Outcome	Main TE Application	References
Adhesive Sequences			
XRGDX	Cell Adhesion	Varied	89,95–97
Growth Factors			
BMPs	Osteoinduction	Bone	101–103,105,113
VEGFs	Angiogenesis	Varied (vascularization)	118,119,121,124
PDGF	Vascular Maturation	Vascularization	119,120
TGF-β	Varied	Cartilage	137,139–141
NGF	Neuronal Development	Nervous System	142–144
FGF	Varied	Bone, Cartilage	127,145,146,148
Minerals			
Hydroxyapatite	Osteoinduction	Bone	149–151

As briefly pointed out in the above sections, certain notions are fundamental to understand and apply for future growth-factor cell interaction and optimal combinatorial construct development. The most important are non-linear growth factor effectiveness, synergistic combinations, and soluble *versus* bound growth factor presentation.

The topic of non-linearity relates to the fact that biological responses may vary unexpectedly with different concentrations/doses of growth factors. While certain responses increase with increasing growth factor amounts, there are several cases where a maximum reaction happens at a specific dosage, decreasing below and above that threshold. This non-linearity has been reported with BMPs, where different responses such as bone formation [106] or tendon healing [152] were maximal at intermediate BMP concentrations, decreasing at both high and low levels. Similarly, the response of outgrowth endothelial cells and circulating angiogenic cells to VEGF exhibited similar non-linear trends, further amplified by synergy in the presence of other growth factors [121,123]. Together, these and similar results emphasize the need to properly screen complete and continuous ranges of growth factors and combinations of such for each relevant cell type. Even if experimental approaches are usually limited to a discrete range of three to four possibilities, future discovery and optimization approaches may be significantly enhanced by continuous high-throughput methods, as described in the later sections of this review.

One other important notion that must be highlighted is that matrix- or biomaterial-bound growth factors may have a completely different effect on the cells when compared to soluble molecules simply added to the mix. This difference was previously discussed in terms of growth factor binding and surface-dependent uptake, and biological response, but one further example can be seen in the case of cardiac progenitor cell transplantation. Among the different solutions to treat heart failure, cardiac progenitor cells (CPC) can be transplanted to the heart to regenerate the tissue but die shortly after injection if implanted alone. These cells can be encapsulated in hydrogels but still fail to integrate the native tissue even when combined with soluble growth factors [82]. However, when encapsulated in the hydrogel with bound growth factors that can present them as a natural ECM, CPCs functionally integrate the native tissue with the formation of anastomoses [82]. These critical results show that the way growth factors are presented impacts their biological activity. Enhanced functionality can be increased retention, binding in proximity to adhesive protrusions and closer cell-surface interactions in ventral *versus* dorsal surfaces, or possibly to more physical characteristics such as stress propagation or mechanosensing synergies [10,108,109]. Therefore, it is fundamental to consider how the growth factor's functionality can be amplified by changing the way molecules are presented to cells. In order words, *what to present* must always be considered together with *how to present it*. Advanced tissue engineering approaches must always integrate this complex balance, where non-linearity, synergistic/antagonistic combinations, and spatial molecule presentation will be fundamental for functional tissue engineering and successful implant integration.

III.3.2. Force, Shape, and Cellular Mechanotransduction

The idea that cells can sense the mechanical properties of their surroundings and translate them into cellular events is not new [152]. However, it was an elusive concept until recent times when the tools to interpret these events arose. From there, the number of scientists working in this field and the number of mechanotransduction-related publications significantly increased [153]. It is now established that force and shape are just essential cues for cells as any other [9,10]. The mechanisms behind cellular migration, or *taxis*, are still continuously updated to integrate a growing number of newly reported mechano-driven cellular motility events. The long-known biochemical chemotaxis [154] and haptotaxis [155]

have seen their supremacy questioned by durotaxis [156], rheotaxis [157], topotaxis [158], curvotaxis [159] and, more recently, viscotaxis [160] (**Figure III-4**). As we continue to discover how surface shape and stiffness can direct cellular movement, understanding how it translates to 3D environments will prove fundamental for integrating such parameters in TE approaches.

Simultaneously, the understanding of mechanobiology-related pathologies and the development of therapeutics that target these complications have also been expanding [161]. Scientists are also unveiling the complete 3D structure and function of the ion channels that act as receptors for mechanical cues [162], results that prove the complexity of mechanical signaling and its significant physiological relevance.

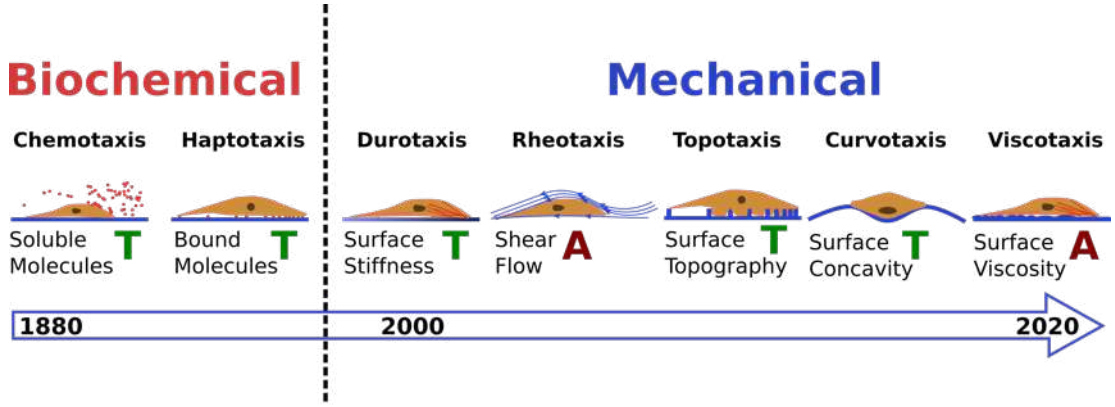


Figure III-4: A Timeline of Cellular Taxis. The supremacy of biochemical cues as drivers of cellular motility has been continuously questioned by growing reports of mechano-induced cell migration. Chemotaxis and haptotaxis are established modes of cellular migration towards soluble and bound biochemical cues, respectively. However, after the late 1990s/early 2000s and for the past 20 years, novel mechanisms of cell migration based on stiffness (durotaxis), fluid stresses (rheotaxis), topography (topotaxis), curvature (curvotaxis), and viscosity (viscotaxis) have been proposed, revealing the increasing impact of force and shape in cell motility. In the figure, T indicates cases where the motility is mainly towards the referred stimuli, whereas A indicates movement against the represented cue.

Naturally, cells from different tissues are subjected to various mechanical stresses just as they are subjected to other biochemical signals [10,163]. In TE, the idea that the first might regulate cell fate similar to the latter was tested. Some interesting results on the effects of mechanical stimuli in cells have emerged in the field of cartilage TE, where the application of mechanical deformation was shown to promote major shifts in chondrocyte metabolic profiles, protein expression, and matrix deposition [164–166]. MSCs were also demonstrated to differentiate through the application of cyclical shear stress [167],

proving that stem cell differentiation can be achieved by taking advantage of mechanotransduction responses alone. Finally, the stiffness of cell-derived matrixes has been recently shown to significantly impact human pluripotent stem cells [168]. It is, however, necessary to state that even though cells respond to changes in the bulk mechanics of materials, they only do so due to changes in the range of cell-sensing mechanisms. Therefore, it is important to look at the way cells respond to mechanical and topographical cues at the cell-biomaterial interface.

III.3.2.1. Biomaterial Stiffness

Within natural niches, cells from different tissues are in contact with varying degrees of stiffness. If neural cells are usually within incredibly soft environments, bone cells reside in much stiffer ones [10]. Different physiological cell responses arise from their ability to sense and translate their surrounding stiffness, as reviewed elsewhere [169,170]. Furthermore, it has been shown that cells sense their immediate surroundings, but they can also respond to changes in stiffness that happen beyond the scaffolds they are seeded in [171]. Altogether, this makes biomaterial stiffness a powerful cue to control and direct the behavior of cells. As such, there have been several advances in preventing the stiffness of scaffolds from achieving desired outcomes in several TE fields such as pancreatic [172], neural [173,174], bone [175], liver [176], and cardiovascular [177,178], as well as in the fields of cancer [179,180] and wound-healing [181,182]. Alginate hydrogels have been manipulated to yield constructs with varying degrees of stiffness by tuning polymer concentration, ionic concentration, crosslinking type, among others [181,183–185], leading to differences in simple cell responses such as cellular viability [183] or more complex cell differentiation. Guneta *et al.* reported that lower-stiffness alginate promoted adipose-derived stem/stromal cells (ASC) adipogenesis while stiffer gels favored their osteogenic commitment [184]. Branco da Cunha *et al.* had previously shown that including collagen within alginate networks allowed tuning the stiffness of the structures [181], with a drastic effect on fibroblast morphology (**Figure III-5**, I). Silk Fibroin (SF) scaffolds have also been recently manipulated in terms of stiffness. Floren *et al.* controlled the initial SF solution concentration to obtain hydrogels with different stiffness while maintaining other structural parameters [178]. In this work,

the differentiation of MSCs into smooth muscle-like cells was favored on 33kPa, which outperformed others within the 6-64kPa spectrum. This non-linear effect of stiffness has been reported in other works [175,186], and once again reinforces the need for proper multi-condition screening. Still, within stiffness-tunable SF scaffolds, it has been demonstrated that even slight differences in mechanical moduli can significantly affect the myogenic differentiation of human MSCs [186] (**Figure III-5, II**). Moving to other natural biomaterials, Murphy *et al.* showed how fibrin gel stiffness had a noticeable impact on the secretion of different growth factors by MSCs, especially those identified as relevant for wound healing applications [187]. While VEGF secretion was favored in stiffer gels, prostaglandin was secreted to a greater extent by cells within softer environments **(Figure III-5, III**). This soft/stiff duality has also been reported in the development of neuronal networks on laminin-polylysine patterns [173]. Softer surfaces enhanced the speed of neuronal network formation, but alternatively, neural cells' synaptic behavior was significantly favored on stiff substrates (**Figure III-5, IV**). This dual, almost inverted effects of stiffness on cell responses that might be needed sequentially within the same application is a consequence of the fact that living tissues are not static. Despite looking like an unsolvable problem, this might be overcome in the future with intelligent biomaterials where stiffness can be controlled not only spatially but also temporally [188]. Time-changing mechanical properties and mechanical dynamicity such as stress stiffening and stress relaxation might be the key to recapitulating the soft-to-stiff evolution in tissue development and regeneration [10].

At last, it is essential to stress that conclusions regarding the effect of biomaterial stiffness can only be drawn when stiffness changes are obtained without other relevant cell-affecting parameter modifications, which are not always observed. For example, Elango *et al.* tested collagen, collagen-HA, and collagen-chitosan scaffolds in mechanical properties and their effects on the alkaline phosphatase activity of osteoblasts [189]. Since collagen-chitosan scaffolds were stiffer than collagen-HA ones, while the latter outperformed the first in alkaline phosphatase (ALP) activity, one could wonder that softer environments would favor this osteogenic response. However, HA is a naturally bioactive molecule while chitosan is not (table III-1), and the differences in ligand-receptor interaction may very well overcome or confound the differences in stiffness. Recently, Wagner and colleagues tackled the manipulation of stiffness independently from other relevant properties in 3D by designing a colloidal crystal system that allowed studying cellular migration between two regions where mechanical differences were decoupled

from porosity and adhesive moieties [190]. By doing so, the authors were able to derive the actual effect of stiffness on fibroblast migration, showing the preference of these cells to move towards stiffer regions (durotaxis) and on the development of neurites by neural cells, which was reversely favored by softer 3D environments.

Altogether, these works confirm that stiffness has a powerful effect on cells, changing their behavior like that of more traditionally recognized biochemical signals, with emerging potential and synergies for the manipulation of cell behavior.

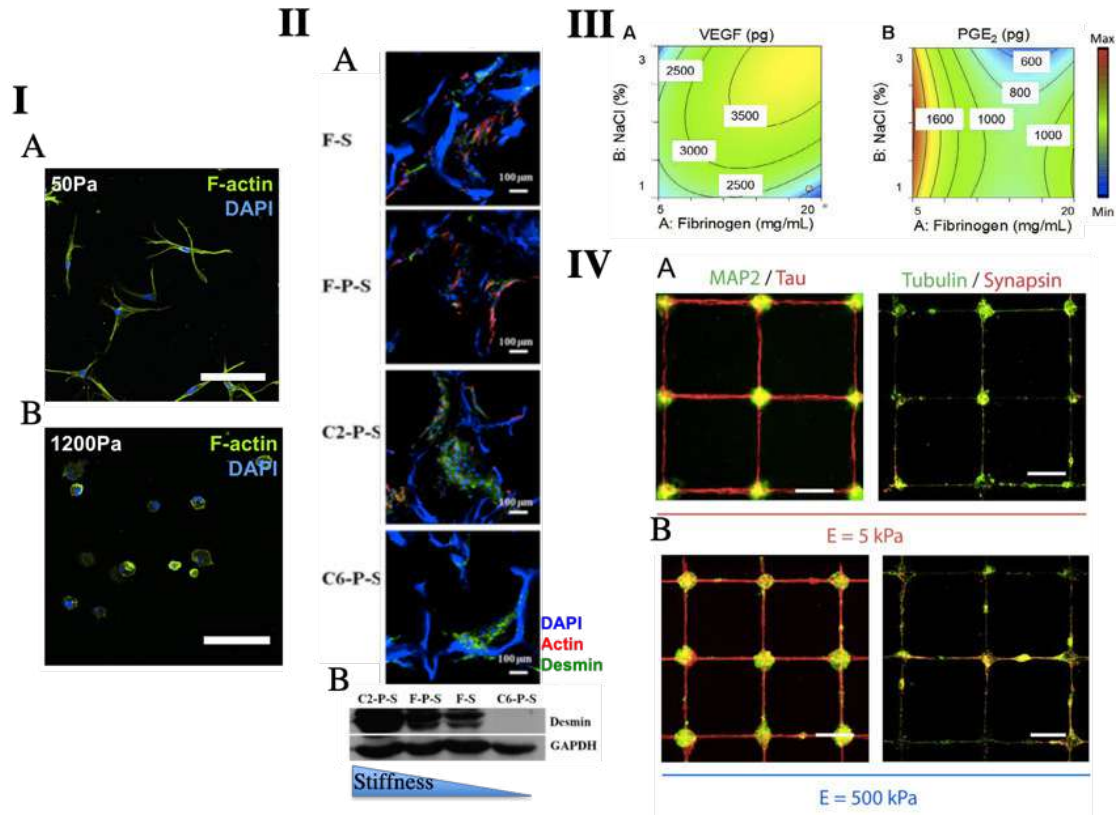


Figure III-5: The stiffness of natural biomaterials has a profound impact on the behavior of different cells. I – Simple cell responses, such as cell morphology, can be dramatically affected by stiffness. Within soft collagen/alginate networks, fibroblasts present extended membrane protrusions (A), whereas, on stiffer surroundings, these cells are confined to a circular shape (B). Adapted from [181]. II – Differentiation of MSCs into muscle-like cells changes in SF materials with different stiffness. Increases in stiffness lead to increased Desmin expression, visible in the immunocytochemistry images (A) and western blot quantification (B). Adapted from [186]. III- MSC growth factors secretion changes within materials of different stiffness. While VEGF secretion is favored in stiffer fibrin hydrogels (A), prostaglandin (PGE2) is secreted at higher levels in softer environments (B, C). Lines limit areas of similar stiffness values. Adapted from [187]. IV- The stiffness of biomaterial surfaces impacts neural development. Within laminin

patterns, softer surfaces promote the faster formation of neuron cell bodies (A), but the development of synapsis requires stiffer conditions to be established (B). Adapted from [173].

III.3.2.2. Biomaterial Topography

At the cell-biomaterial interface, shape, just as force, can profoundly impact the final biological outcome [9]. The cellular effects that arise from different topographies at the surface of biomaterials have been explored within several fields and identified as capable of solely directing cell fate [191,192]. However, most of the recent and overall research into biomaterial topography is done with synthetic biomaterials. This choice is most likely because creating defined topographical features at the micro or nanoscale depends on tightly regulated procedures and environments (*e.g.,* clean-room facilities). Further, the inherent variability of natural materials also complicates the reproducibility required for fabricating such intricate surface shape features.

Nevertheless, there are some recent works related to topography on naturally derived structures. For example, Lawrence *et al.* tested the effect of the topography of silk films in the context of corneal TE [193], showing that films with lined topographies significantly outperformed flat or ring-feature films, leading to an increase in corneal cell attachment and focal adhesion development. The presence of microgroove topography on SF films was shown to promote a similar level of adhesion as flat films of adhesive ECM molecules, such as collagen and fibronectin [194]. Also, within SF materials, the alignment of electrospun meshes was shown to significantly increase the myogenic differentiation of myoblasts compared to surfaces comprising randomly oriented fibers [195]. Similarly, Yao *et al.* compared the effects of random versus aligned fibrillar fibrin surfaces with low elastic modulus. The authors reported that the alignment of fibers was powerful enough to significantly promote the neural differentiation of human umbilical cord MSCs, increase neurite outgrowth, and lead to the formation of aligned neural cables *in vivo* (**Figure III-6**, I) [196]. Other authors have also analyzed the effects of the topography (nano-roughness and orientation) of films made of chitosan [197] and chitosan/poly(octanediol citrate) [198]. Both works report differences in cell proliferation and metabolic activity derived from differences in topography. Collagen and collagen/chondroitin sulfate scaffolds were also developed with a specific

topography of uniaxially aligned pores [199], impacting cell morphology and orientation. These works highlight how the control of biomaterial surface shapes can be leveraged to guide the shape and orientation of cellular layers. These features may be essential to recapitulate anisotropic tissue's structure and consequent biomechanics. However, these studies focus primarily on 2D surfaces and, while providing necessary fundamental knowledge, are still distanced from applied tissue engineering and 3D functional constructs.

Indeed, one other reason why topography is not so explored with natural materials is that a significant part of these materials is used to create hydrogels within which cells are encapsulated (**table III-1**), and topography within a 3D hydrogel can be an elusive concept. Despite working primarily with matrigel, which is a mixture of ECM proteins and not a biomaterial *per se*, Kim *et al.* devised an exciting concept in which protein-coated magnetic nanoparticles were entrapped within those hydrogels [200]. Applying a controlled magnetic field oriented these particles iso or anisotropically during gelation, creating different shapes within the 3D environment, which significantly impacted the morphology of fibroblasts and length of neural cell dendrites (**Figure III-6,** II). Even though this work uses the natural composition of biological ECM's, it paves the way for introducing topographical cues within hydrogel constructs for TE. This strategy was already approached in natural materials through the inclusion of magnetic nanoparticles within collagen gels to remotely orient them into strings and induce fiber alignment, significantly impacting the behavior of neural cells [201]. More recently, a similar approach was used to introduce 3D anisotropy within gelatin hydrogels with a clear impact on cellular orientation [202]. Moving from nano- to micro-features, recent work from Rose *et al.* introduced and magnetically oriented RGD-functionalized microgels in both synthetic (Polyethylene Glycol, PEG) and natural (Fibrin) hydrogels [203]. The combination of 3D topographies, hydrogel anisotropy, and adhesive cues influenced 3D fibroblast adhesion and orientation and consequently the synthesis of cell-derived ECM (**Figure III-6**, III). Within this system, neural cells could also interact with the 3D-oriented RGD-microgels and develop oriented neurites. Samandari and colleagues have recently demonstrated that chaotic mixing and printing of compartmentalized Alginate/Gelatin Methacryloyl (GelMA) hydrogel fibers could integrate 3D topographical cues by the orientation of the different hydrogel filaments, controlling muscle cell alignment and promoting myotube formation [204]. These works prove that the introduction of

topographical features in 3-dimensional hydrogel can go beyond traditional 2D outcomes, significantly improving the cell-biomaterial interaction in more physiologically relevant environments.

One other exciting effect that relates to topographical cues is the vibrational stimulation of cells. Tsimbouri *et al.* created a bioreactor capable of transmitting nano-sized vibrations of high frequency (1000 Hz) to MSCs within soft, non-osteogenic collagen hydrogels [205]. When the vibration amplitude was within the exact dimension of previously reported osteoinductive topographies (20nm), this motion could single-handedly direct MSCs towards the osteogenic phenotype, capable of forming mineralized tissue. Together with the previously discussed reactor capable of compression/shear-induced osteogenesis [167], these works represent a transition towards dynamic rather than static mechanostimulation - with obvious potential.

Finally, it is worth mentioning that different synergies have been identified between biomaterial topography, stiffness, and the presentation of bioactive molecules. Some interesting examples of such combinatorial cues and biological outcomes can be seen in neural tissue engineering and neuron-biomaterial interactions. A work on nanopatterned laminin surfaces showed that the combination of patterns that could guide neural development and laminin coating and stiff substrates maximized neurite outgrowth, which was hindered when the same molecules and patterns were presented on a soft surface [173]. However, a separate study with neural cells cultured in electrospun fibrin meshes showed that soft and aligned fibers maximized neurite outgrowth with this particular material and scaffold architecture [196]. These two works show how topography, stiffness and molecular components can synergize towards very distinct cellular responses and how different combinations between these properties may have to be adjusted as structures move from purely 2D surfaces to 3D environments. Studies with other cell types, namely those focusing on osteogenic responses, have shown that calcium phosphate surfaces presenting high stiffness and nano-sized topography enhanced MSCs' osteogenic commitment compared to micron-sized features on the same surface[206]. This response also evidences that the dimensional aspect of topography is also important to consider. Small topographies sensed by single cells in multiple regions can lead to more powerful responses such as the induction of cell differentiation. Differentiated cells, such as osteoblasts, were also shown to interact differently with stiff calcium phosphate surfaces of varying topography sizes. A non-linear response could also be observed.

Cells interacted significantly more with shaped than flat surfaces, but increasing feature sizes on the 3-5 micrometer range led to a gradual reduction of binding strength [207].

Overall, the development of methods for creating topographies in natural materials is undergoing significant growth. Most importantly, scientists start to devise ways to introduce topographies within 3D constructs such as cell-laden hydrogels. The manipulation of shape in 3D environments is a much more relevant and biomimetic approach when compared to traditional 2D topographies and should continue to give rise to more impactful outcomes.

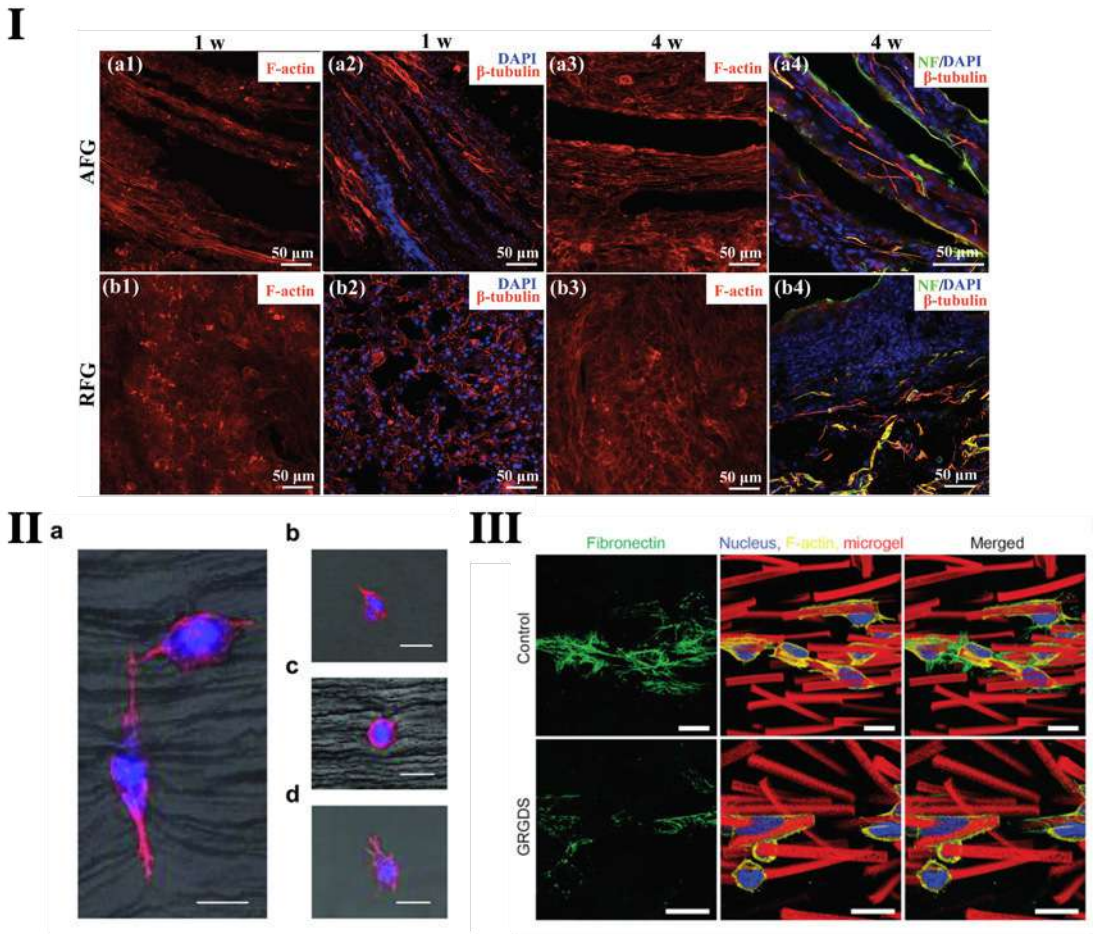


Figure III-6: The topography of natural materials and surfaces affects cell morphology and organization in 2D and 3D. I – Topographical alignment is fundamental for native-like neural stem cell organization. When cultured in aligned fibrillar fibrin hydrogels (AFG), human umbilical cord MSCs differentiated in the neural lineage, leading to organized neural cables (a1-a4). When this topographical alignment is not present, i.e., in randomly oriented structures (RFG), the differentiation markers are visible, but the required organization is absent (b1-b4). Reproduced from [196]. II – 3D features can be introduced in hydrogels and guide cell morphology. In matrigel hydrogels with aligned magnetic particles, fibroblasts respond to the anisotropic 3D features and align (a) with

increased protrusion numbers and size, something that does not occur in isotropic gels (b) or with myosin inhibition (blebbistatin) (c,d). Adapted from [200]. III- Microgels can also be aligned within hydrogels to create shape in 3D environments. Cell adhesion, morphology, and ECM (fibronectin) synthesis are affected by the anisotropic alignment of RGD-functionalized microgels within fibrin hydrogels (anisogel). Adapted from [203].

III.3.3. Cell-Cell Interactions and the Underestimated Cue of Cellular Density

After looking into the effects that different biologically active material-presented molecules and mechanical properties of natural materials have on the behavior of cells, there is one last level of cues that affect cellular responses – their own interaction. Cells communicate with each other either through the secretion of soluble factors or direct contact. In biomaterials and TE, cell-cell interaction is mainly related to the density of cells, i.e., how many and how close cells are within constructs. Recently, Singh *et al.* showed that embryonic stem cell (ESC) differentiation towards vascular progenitors was significantly affected by cell seeding density even though it was not affected by varying VEGF concentrations [208]. Similarly, Wiesner *et al.* reported that cell density profoundly impacted the adipogenic differentiation of ASCs [209]. Even though these two works focus only on cell biology and not on biomaterials, they prove that cell density can have a real effect on complex and relevant cellular responses for TE applications. In this field, most authors use fixed numbers of cells to study their response to biomaterial properties. However, cell density is essential for the biomaterial-induced cell response as any other parameter [210], if not more. For example, it was proven that changes in cellular density were capable of overriding the effects of 2D substrate stiffness in MSC morphology and proliferation [211]. Additionally, the adequate cell density on TE constructs might even disagree with the number of cells in native tissues – cartilage, for example, is naturally low on cells. Still, several works have reported that higher cell densities within engineered constructs lead to better chondrogenic outcomes. Cigan *et al.* used agarose gels to comprehensively analyze the effect of human chondrocytes at different initial densities (from 15 to 90 $x10^6$ cells/mL). Globally, the authors reported that, when seeded at higher density, cells synthesize more ECM molecules such as GAGs and collagen. Curiously, GAG's quantity increased continuously up to the higher cell densities, but collagen appeared to peak at the intermediate concentration, decreasing at the highest ones. The researchers also showed that

constructs with higher cell densities ended up with higher mechanical properties. This improvement is an interesting outcome since the increase in cell density and overall cell-occupied volume could be expected to diminish the construct's stiffness, but the increase in ECM deposition appears to compensate for that, resulting into more robust constructs. [212]. Even though the authors did not normalize all these responses against the number of cells, it is possible to observe, for example, that at 28 days of culture, double cell seeding densities from 33-40M cells/mL to 70-90M cells/mL leads to not doubling but almost tripling GAG amounts, and a similar quantity of collagen. This comparison suggests that the increase in ECM deposition may not be only a consequence of higher cell numbers but also from each cell's individual synthetic activity. Similarly, alike collagen levels lead to the conclusion that as the number of cell doubles, the production of collagen per cell halves (assuming the initial cell proportions are maintained overtime), demonstrating the complex dynamics between ECM type, and synthesis and/or degradation (remodeling), as a function of cellular density.

This work supports older reports showing beneficial effects of high cell densities on cartilage TE using different materials. In Silk Fibroin scaffolds, chondrocytes were also shown to produce an increasing amount of GAGs/cell and decreasing amounts of Collagen/cell when cell density ranged between 25 and 100M cells/mL, with improved mechanical properties on denser constructs [213]. In collagen sponges, chondrocytes have been shown to enhance GAG synthesis/cell when densities of 4M cells/mL and 1.5Mcells/mL were compared. Curiously, this work showed an increase also in collagen synthesis. However, the authors used cell densities a magnitude below the ones previously discussed, at which collagen synthesis/cell is likely still in the linearly increasing range [214].

Furthermore, important consequences of high seeding densities have also been observed in other TE strategies. Looking at MSCs, researchers used RGD-alginate hydrogels to study the effect of density in the osteogenic differentiation of these cells. The results showed that increasing cell densities from 2 to 15M cells/mL led to enhanced cell-cell contacts, formation of cellular clusters, and improved osteogenic marker expression and matrix deposition[215]. In a study focusing on ASCs proliferation and adipogenesis, researchers have also reported that varying cell densities on chondroitin sulfate surfaces led to distinct proliferation dynamics and metabolic activity over time. The authors also show that the percentage of perlipin-expressing cells increased when cultured at 0.5M cells/mL *versus* 0.25M cells/mL [216].

Conversely, in other applications, lower cell densities have proven to be more valuable for obtaining improved cellular responses. These results were reported some time ago in cardiac TE. Lower cardiomyocyte densities within fibrin gels led to increased construct active force (desired in a cardiac approach), even though it decreased at the lowest densities of 1M cells/mL (non-linear). In this work, the authors postulate that the decrease in active force happens since higher cell densities negatively affect implanted cells' viability, inferred from decreased levels of smooth-muscle-actin together with a reduction in collagen deposition [217]. The fact that cell density can have such different outcomes in distinct TE strategies could be related to cell-cell interactions and cell-induced changes in construct mechanical properties, which can be due to two main processes. The first is the previously discussed impact cell density may have in ECM deposition/degradation. In this case, the alteration of the surrounding environment by adding newly synthesized ECM can enhance the construct mechanical properties.

In contrast, increased construct degradation will likely lead to diminished mechanical robustness. The second relates to direct cell-material mechanical deformation. For example, adherent cells such as fibroblasts can exert forces on their surroundings, applying strains that may contract the surrounding ECM. In this context, it was shown that higher cell densities could lead to an increase in construct net strain within scaffolds but simultaneously lower buckling force per cell [218]. In some cases, such as cartilage TE, the overall strain promoted by higher cell densities can benefit the increased mechanical resilience of the construct through tensegrity stabilization [10]. Reversely, with, *e.g.*, cardiac TE, the forces per cell may be more significant than the bulk mechanics, and lower densities may provide a better framework for adequate tissue development.

Furthermore, it is essential to note that there are considerable differences between different works and authors on the definition of high and low cell densities. Indeed, what is high in one context can be low in the other, therefore using these terms across studies can lead to flawed comparison. **Table III-3** compiles observations in some of the main reviewed works on cell density effects in TE, including the range of densities under testing and the adequate conditions within that studied range.

Table III-3: Studies on the outcomes of different cell densities in TE constructs.

Cell Type	Biomaterial	Cell Density Range	Optimal	Cellular Outcome	Ref.
Chondrocytes	Agarose	15-90E6 cells/mL	90E6 (+)	GAG synthesis/density, Mechanics	212
ASCs	Chond.Sulfate	2.5-5E5 /construct	5E5 (+)	Adipogenic Differentiation (% cells)	216
Chondrocytes	SF	25-100E6 /mL	100E6 (+)	GAG content/cell, Mechanics	213
Chondrocytes	Collagen	1.5-4E6 /construct	4E6 (+)	GAG content/cell, Collagen Synthesis/cell	214
MSCs	Alginate	2-15E6 /mL	15E6 (+)	Osteogenic Differentiation	215
Cardiomyocytes	Fibrin	1-20E6 /construct	5E6 (-)	Active contraction (viability effect)	217
MSCs	(decel. vein)	3-10E6 /mL	3E6 (-)	Proliferation, tensile strength (viability and construct degradation effect)	219

Additionally, similarly to what we reported in previous sections, cell density can also present a synergistic effect with other cues, namely growth factors. For example, in a study with chondrocyte layers, researchers showed that cellular density gave compelling synergistic interactions with the addition of soluble TGF-ß1. Looking at the production of superficial zone protein (SZP, an important cartilage lubricator), the authors show that the SZP production per cell doubles when TGF-ß1 is added to low cell density cell layers. However, SZP production experiences a 40-50 times increase when high-density layers are treated with the same molecule [220]. The authors hypothesize that higher cell densities are critical for adequate self-assembly of the chondrocyte sheets and optimal cell-ligand interactions, boosting lubrication responses. This work shows that the complex consequences of increasing cellular density and cell-cell interactions within tissue-engineered constructs can significantly impact the development and maturation of constructs when multiple cues are integrated and synergistic responses arise.

Overall, the literature focusing on studying the effects of cell number and cell-cell interactions and the consequent outcome in biological responses seems to expose this cue as the least investigated in the topics herein discuss. Most of the conducted TE works that consider the effects of cellular density and cell-cell communication do so by testing two or three different cellular densities as a way to find an adequate condition, but sometimes lack the required normalization to total DNA or cell number. Even though those results serve as a framework for those particular studies, it leaves a gap in understanding how this cue can be leveraged to improve the development and ultimately the biofunctionality of

engineered tissues. There is a clear need for methods and platforms to control and study the outcomes derived from different cellular densities more comprehensively. Namely, it is crucial to precisely assess the interaction between cells within the construct, their consequences in mechanical properties *via* ECM deposition/degradation or direct construct deformation, and the relative expression of biological markers of interest. Future investigation in these topics will enlighten how cell density can be manipulated as a cue on its own, with synergistic outcomes that can potently improve tissue maturation.

III.4. SOLVING THE PUZZLE – NATURAL BIOMATERIAL LIBRARIES AND HT SCREENING PLATFORMS

From the use of different naturally derived materials, alone or in combination with others, with or without modifications - including the addition of adhesive molecules or growth factors - to the tuning of mechanical properties such as stiffness or the shape of the biomaterial-cell interface, as well as the fitting of specific cell densities, the possibilities for developing new TE constructs are ever-growing. For each cell type and application, endless parameters can be combined to approach the physical, chemical, and biological dimensions of live tissues with more or less optimal results. All of this is further amplified when considering that several of these parameters can have synergistic or antagonistic interactions - at different levels - as discussed across the previous sections (**Figure III-2**). Moreover, the responses of cells to different parameters rarely follow a linear, predictable trend. Putting all these hypotheses to test using traditional, single experiments becomes highly complex. Vegas *et al.* developed a remarkable library of 774 variants of one single material – alginate –to identify three analogs that could substantially reduce foreign body reactions *in vivo* [221]. This work is a perfect example of the effort necessary to study a complete material library more traditionally. Considering the number of materials, modifications, and cells that can be combined and the 774 variations that one single material may have, the number of samples and tests required quickly grow out of hand, becoming a practical impossibility. Therefore, it is fundamental to develop biomaterial libraries and platforms that allow high-throughput (HT) screening of cellular responses to a wide range of conditions and combinations simultaneously and in a time-efficient fashion.

III.4.1. Biomaterial Arrays

Biomaterial arrays or (more frequently) microarrays are the most obvious example of HT platforms, which consist primarily of the concentration of up to thousands of small spots of different biomaterials within a small surface [222]. These spots are built to have variations in parameters such as surface chemistry, topography, or even to be composed of 3D droplet-like microtissues with different cell-laden materials, usually based on synthetic polymers as reviewed elsewhere [223]. On the other hand, arrays based on natural biomaterials are still struggling to catch up with their synthetic counterparts, mainly because the micromanipulation of natural polymers is not as trivial. Nevertheless, there are some recent works of natural material arrays where the study of the interaction of cells with ECM components is done in an HT fashion. Dolatshahi-Pirouz *et al.* developed arrays where cell-laden gels resulting from the combination of gelatin with different single and combined ECM proteins (such as fibronectin, osteocalcin, osteopontin, and laminin) were printed as 96 different 3D combinations [224]. They also compared other cell media (inductive and non-inductive) to identify the most suitable conditions for the osteogenic differentiation of MSCs using simultaneous analysis (**Figure III-7**, I). Something similar was done by Floren *et al.,* but in this case, the ECM microenvironments were printed on surfaces with different stiffness resulting in soft versus stiff arrays [225] (**Figure III-7, II**). Guermani *et al.* showed that arrays of MSCs-laden gelatin/HA gels could be created. Additionally, these gels could be printed with different shapes. Both the composition and the shape had some effect on the ALP expression of cells [226].

Additionally, arrays in which cell-ligand interaction (other than ECM-associated molecules) can be studied were proposed by Caliari *et al..* Arrays of collagen scaffolds were prepared using a gradation technique to obtain different levels of PDGF and BMP2 and identify the most promising conditions for MSC differentiation [227]. Chen *et al.* also approached the effects of hydroxyapatite within gelatin by printing microgels with different Gelatin/HAp ratios [228]. More recently, researchers developed arrays based on PEG and alginate, where unique 3D environments integrated varying biochemical and physical characteristics, namely adhesive ligand presentation, stiffness, and degradability. The authors also showed how the array could be assembled into a dynamic culture platform where soluble cues could be tested in separate array regions and dynamic mechanical deformation could be applied to the discrete

microenvironments [229]. *In vitro* and *in vivo* studies corroborated that the highest-ranking culture conditions from the HT screening system led to improved cartilage repair, validating the use of such a comprehensive screening platform for the fast discovery of optimal tissue engineering biochemical and physical cue combination.

Overall, the array approach allows the separate analysis of discrete conditions comprising virtually any combination with the caveat of usually requiring micro-mixing or microprinting, which is complex and expensive. At the same time, mixing and printing materials is not always a straightforward approach. These need to be modified to become printable or enable automated deposition [230]. Since these modifications are likely to affect the biological performance of the material to some extent, fabricating arrays for this type of screening might not always be a possibility. As such, different strategies, such as gradients, have been devised.

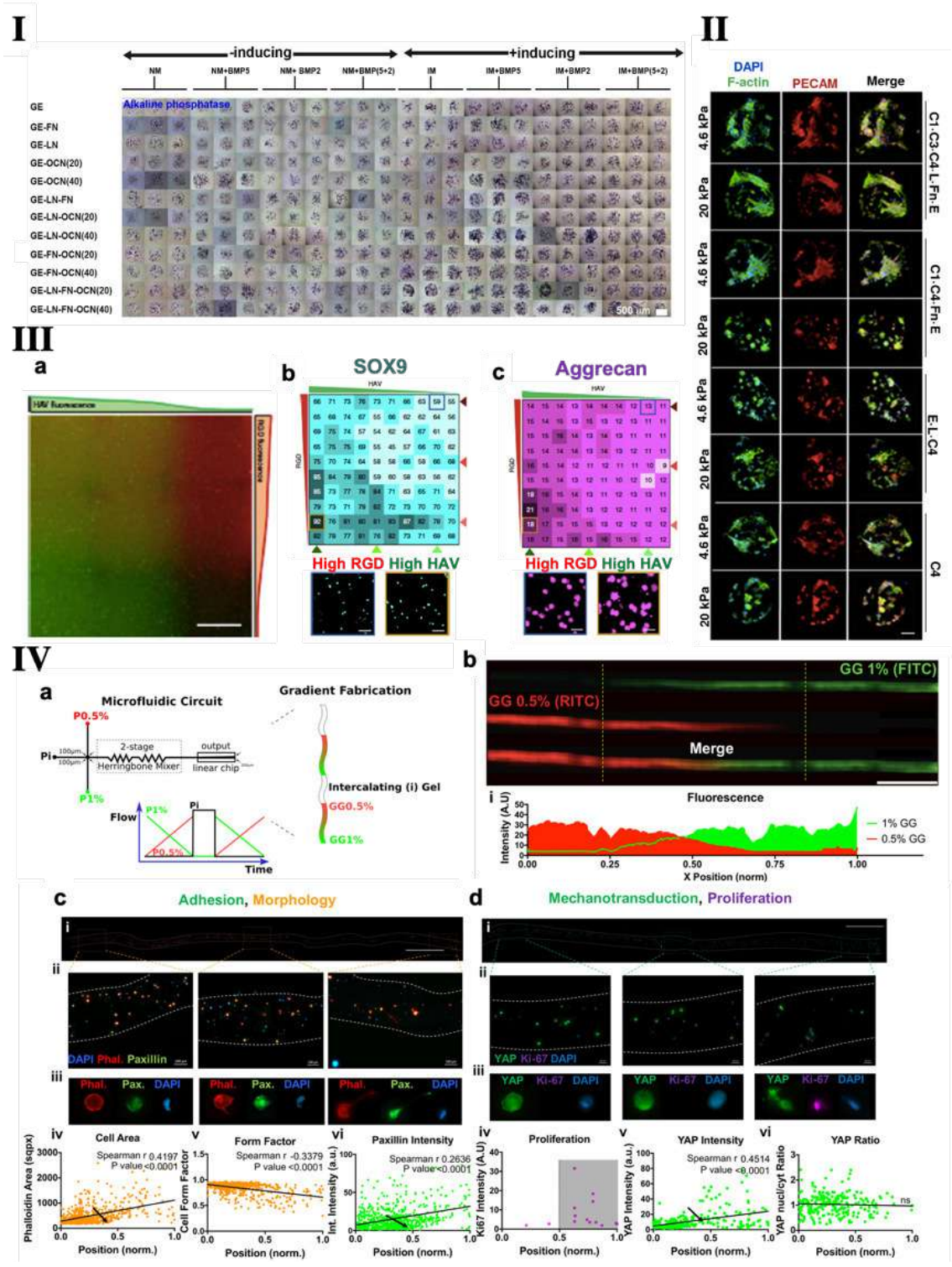


Figure III-7: Advances towards natural material libraries and HT platforms. I. Gelatin has been used to create 3D droplets with different ECM molecules and encapsulated MSCs. Upon imaging the whole array stained for ALP, it is possible to identify the most suitable conditions (traced back to the ECM molecule combination) for osteogenic differentiation. This analysis can also be further amplified by introducing soluble signals (as BMPs) and inductive or non-inductive medium. Adapted from [231]. II – Similarly, ECM arrays can be deposited in surfaces of

different stiffness, allowing screening of the combinatorial effects of surface stiffness and ECM signals. Adapted from [225]. III – Gradients have also been approached with natural materials. In this case, Hyaluronic Acid Hydrogel was engineered to contain an orthogonal gradient of peptide sequences (RGD x HAV) (a) to derive the responses of encapsulated cells in 100 simultaneous possible combinations of both peptide levels, evaluating the chondrogenic differentiation of mesenchymal stem cells by screening Sox9 expression (b) and aggrecan synthesis (c), pinpointing the best combinations for cartilage formation. Adapted from [232]. IV – Microfluidic-driven biofabrication and hydrogel precursor manipulation can enable sequential, high-throughput fabrication of 3D gradient libraries. Encapsulated cells can therein be cultured, and automated single-cell image analysis employed for screening and identifying best-fit conditions for diverse responses, from adhesion to differentiation. Adapted from [233].

III.4.2. Gradients within materials

Gradients represent a more straightforward and usually easier-to-fabricate alternative to HT screening. Simply put, gradients are a continuous spectrum of different conditions gradually changing across space. Unlike arrays, gradients can be obtained through a plethora of approaches, increasing as their applications widen in the high-throughput screening context. Poly-dimethylsiloxane (PDMS) is a paradigmatic material in this scenario, as it has been extensively manipulated to give rise to different surface gradients with chemical or physical variations (linear and orthogonal) such as surface wettability [234], topography [235,236], and stiffness [234]. Similar studies can also be found using different materials such as polycaprolactone [237] or acrylamide [238]. However, most of these gradients are not only made of synthetic materials but are also primarily two-dimensional platforms, which are relevant as representations of biomaterial and implant surfaces but deviate from the typical 3D environments cells inhabit. In TE, more important than understanding how to manipulate the 2D surface of biomaterials is the ability to create functional biological-like 3D architectures. As such, the translation of gradient-like platforms to 3D allows the derivation of more significant conclusions.

Some researchers have been developing natural 3D gradients, not as HT platforms but to approach biological gradients such as those in the osteochondral interface. Collagen scaffolds with gradations in alignment, structure, and mineral content have been developed to approach the bone-to-cartilage transition [239,240]. Guo *et al.* also created gradients of a biosilica within SF hydrogels [241] – achieving soft-to-stiff transition and proposing that, within this gradient, MSCs could differentiate into

osteoblast-like cells. Even though these works focus on the gradient as a direct TE application, some lessons can be extrapolated towards HT 3D screening. Expanding the ranges of properties integrated in the gradient can enable a more comprehensive assessment of a considerably higher number of conditions instead of focusing on approaching the biological transition. Also, within the field of tumor microenvironment engineering, Pedron *et al.* created gradients of cell number, stiffness, and hyaluronic acid concentration within gelatin gels, identifying different conditions that influence glioma cells VEGF and MMP expression [242]. The same group also developed gradients of stem cell factor (SCF) to analyze the response of hematopoietic stem cells to different levels of this molecule within 3D gelatin hydrogels [243]. Santo *et al.* created a 3D gradient of platelet lysate within gellan gum fibers, a platform with the potential to explore the cell-ligand interactions across a range of conditions [232]. All these studies approach 3D gradients for HT screening cell responses to different cues (mechanical, ligand, and cell-cell). However, throughout these examples, the analysis is limited to 3 or 4 conditions within the gradient, which is quite common across the literature and highlights another critical issue: HT libraries are only so when coupled with HT analysis. An excellent example where something similar has been achieved is the nanotopochip technology reported by de Boer *et al.* – a synthetic biomaterial library on a chip comprising a vast array of topographies (thousands) coupled with HT and automated analysis of cell responses [244–246]. In the field of gradient-like platforms, recent work from Vega *et al.* reported the study of 100 distinct peptide ligand combinations by creating 3D orthogonal hydrogel gradients based on hyaluronic acid [247]. Using norbornene photochemistry, the authors could bind gradual amounts of RGD and HAV (histidyl-alanyl-valine) peptides in an orthogonal fashion, quickly pinpointing the best-fit combinations for MSC chondrogenic differentiation out of 100 distinct scenarios (**Figure III-7**, III). Despite being a complete 3D gradient approach to high throughput, this technique relies on UV light for gradient generation, which has some inherent cytocompatibility caveats. Distinctly, the use of ionic hydrogel crosslinking and microfluidic precursor mixing was very recently employed to sequentially fabricate individual, cell-laden 3D gradients based on gellan gum and the highly versatile microfluidic spinning biofabrication techniques [233248]. The researchers showed how these gradients could be combined with automated single-cell image analysis to quickly discover and optimize different biomaterial blends towards distinct adipose-derived stem cells-material interactions and commitment (**Figure III-7**, IV). They further demonstrate how this versatile technique can be employed for obtaining

3D gradients by entirely changing materials (gellan gum-to-GelMA), crosslinking type (ionic-to-light), and physical performance (adhesion-to-differentiation) [233].

The scientific community is now laying down the necessary foundations for developing HT platforms for screening biomaterial-cell interactions, especially within the field of naturally derived materials. Further advances and widespread HT testing through these platforms will likely prove fundamental for discovering and optimizing next-generation biomaterials for TE purposes with unprecedented efficiency and precision.

III.5. CONCLUDING REMARKS AND FUTURE PERSPECTIVES

Natural materials have been widely used to create cell-supporting structures within the field of TE. Their use was initially triggered by the fact that they were derived from natural tissues and organisms. In addition, these materials were biocompatible in diverse applications and biodegradable. However, these properties are absent in some naturally derived materials and insufficient when the progression towards complex TE calls for the proper regulation of cellular behavior. Nowadays, biomaterials are no longer static, inert entities but dynamic systems that can influence and direct cell behavior.

To approach the function of native ECM, materials have been altered to become adhesive and sensible to the action of cell-derived enzymes and forces so that cells themselves can manipulate their surroundings. Furthermore, biological ligands such as growth factors, traditionally employed in soluble cocktails, have been gradually grafted in material meshes to achieve ECM-like presentation, with more potent biological outcomes and synergistic interactions than the traditional mixology of solutions.

In addition to the presentation of molecules, mechanotransduction of biomaterial stiffness and topography has also revealed itself as a powerful cue for manipulating cells *via* tuning material shape and mechanical characteristics. At the same time, there are increasingly more attempts to bridge the knowledge in force and shape to 3-dimensional environments, namely exploring more challenging aspects such as the introduction of aligned features (3D topographies) within hydrogels.

Finally, we identified cell-cell interactions within engineered constructs as the sixth cue that, despite not deriving from the material itself, can still have powerful consequences on the outcomes of the whole construct. This parameter revealed itself to be still underexplored in this context but impactful at several levels of biological and mechanical results.

Within these six cardinal points of the biomaterial-cell interaction compass (**Figure III-2**), there is increasing evidence that different combinations of cues can synergize or antagonize and give rise to unique and distinct cellular outcomes. This complex puzzle is continuously growing in pieces. As a result, there is an increasing need for platforms that allow efficient and combinatorial screening of different materials, modifications, cell types, and consequent interactions. Natural-based biomaterial arrays have been created to study the effects of stiffness, degradability, and ECM-derived proteins on cells. However, array creation to devise biomaterial libraries can be impaired because most array-fabrication techniques require material printability, which is complex, expensive, and may not be possible with every type of material, requiring confounding modifications. As an alternative, gradients are proving themselves capable of integrating different materials and combinations through spatial variation along with one single sample. The earliest gradient screening platforms were mainly based on synthetic materials and 2-dimensional. Nevertheless, the scientific community is breaking ground towards creating 3D gradients, and novel approaches start translating these advances to the field of natural materials, namely those on microfluidic-driven biofabrication and high-throughput cell-laden structure fabrication.

In the future, we expect further development and widespread utilization of natural biomaterial libraries to explore different material formulations, combinations of growth factors, mechanical cues, and cellular densities, highlighting yet-poorly known synergistic and antagonistic interactions. Simultaneously, platforms such as these will most certainly include more complex 3D environments and types of cell-driving cues. Developments within the field will undoubtedly give rise to a more significant body of knowledge and catapult the field of biomaterial development and combinatorial TE by allowing scientists to control and define the behavior of cells through the multi-cue integration towards native-like tissue functionality more precisely. The increasing amount of information that can also be extracted from high-throughput screening platforms and the correlation between material characteristics, biophysical and biochemical stimuli, and consequent cellular events will also generate unprecedented amounts of data. In the coming future, one can expect artificial intelligence tools to be employed to kick-start the next generation of biomaterial discovery and development. In this context, data mining and machine learning tools will be critical for decoding this very complex puzzle of combinatorial tissue engineering [249,250]. As the field of tissue engineering enters its mature years, and the technologies at hand allow for screening, discovery, and optimization of biomaterial characteristics

with unprecedented efficiency, the informed engineering of natural materials is likely to break the final barriers between fabricated constructs and functional living tissues.

III.6. REFERENCES

1. Atala, A., Bauer, S. B., Soker, S., Yoo, J. J. & Retik, A. B. Tissue-engineered autologous bladders for patients needing cystoplasty. *Lancet* **367**, 1241–1246 (2006).
2. Raya-Rivera, A. *et al.* Tissue-engineered autologous urethras for patients who need reconstruction: An observational study. *Lancet* **377**, 1175–1182 (2011).
3. Raya-Rivera, A. M. *et al.* Tissue-engineered autologous vaginal organs in patients: A pilot cohort study. *Lancet* **384**, 329–336 (2014).
4. Organ Donation Statistics. (2019). Available at: https://www.organdonor.gov/statistics-stories/statistics.html. (Accessed: 4th December 2019)
5. Hozain, A. E. *et al.* Xenogeneic cross-circulation for extracorporeal recovery of injured human lungs. *Nat. Med.* **26**, 1102–1113 (2020).
6. Mandrycky, C., Wang, Z., Kim, K. & Kim, D. H. 3D bioprinting for engineering complex tissues. *Biotechnol. Adv.* **34**, 422–434 (2016).
7. Lee, A. *et al.* 3D bioprinting of collagen to rebuild components of the human heart. *Science (80-.).* **365**, 482–487 (2019).
8. Mano, J. F. *et al.* Natural origin biodegradable systems in tissue engineering and regenerative medicine: present status and some moving trends. *J. R. Soc. Interface* **4**, 999–1030 (2007).
9. Iskratsch, T., Wolfenson, H. & Sheetz, M. P. Appreciating force and shape — the rise of mechanotransduction in cell biology. *Nat. Rev. Mol. Cell Biol.* **15**, 825–833 (2014).
10. Guimarães, C. F., Gasperini, L., Marques, A. P. & Reis, R. L. The stiffness of living tissues and its implications for tissue engineering. *Nat. Rev. Mater.* **5**, 351–370 (2020).
11. Lee, C. S. D. *et al.* Integration of layered chondrocyte-seeded alginate hydrogel scaffolds. *Biomaterials* **28**, 2987–2993 (2007).
12. Zhang, F. *et al.* Regeneration of high-quality silk fibroin fiber by wet spinning from CaCl2-formic acid solvent. *Acta Biomater.* **12**, 139–145 (2015).
13. Kuo, Y. C., Ku, H. F. & Rajesh, R. Chitosan/γ-poly(glutamic acid) scaffolds with surface-modified albumin, elastin and poly-L-lysine for cartilage tissue engineering. *Mater. Sci. Eng. C* **78**, 265–277 (2017).
14. Levingstone, T. J. *et al.* Multi-layered collagen-based scaffolds for osteochondral defect repair in rabbits. *Acta Biomater.* **32**, 149–160 (2016).
15. Xi, W., Saw, T. B., Delacour, D., Lim, C. T. & Ladoux, B. Material approaches to active tissue mechanics. *Nat. Rev. Mater.* **4**, 23–44 (2019).
16. Nair, L. S. & Laurencin, C. T. Biodegradable polymers as biomaterials. *Prog. Polym. Sci.* **32**, 762–798 (2007).
17. Li, C. *et al.* Design of biodegradable, implantable devices towards clinical translation. *Nat. Rev. Mater.* (2019). doi:10.1038/s41578-019-0150-z
18. Freed, L. E. *et al.* Biodegradable Polymer Scaffolds for Tissue Engineering. *Nat. Biotechnol.* **12**, 689–693 (1994).
19. Ulery, B. D., Nair, L. S. & Laurencin, C. T. Biomedical applications of biodegradable polymers. *J. Polym. Sci. Part B Polym. Phys.* **49**, 832–864 (2011).
20. Balakrishnan, B., Joshi, N., Jayakrishnan, A. & Banerjee, R. Self-crosslinked oxidized alginate/gelatin hydrogel as injectable, adhesive biomimetic scaffolds for cartilage regeneration. *Acta Biomater.* **10**, 3650–3663 (2014).
21. Ashton, R. S., Banerjee, A., Punyani, S., Schaffer, D. V. & Kane, R. S. Scaffolds based on degradable alginate hydrogels and poly(lactide-co-glycolide) microspheres for stem cell culture. *Biomaterials* **28**, 5518–5525 (2007).
22. Holloway, J. L., Ma, H., Rai, R. & Burdick, J. A. Modulating hydrogel crosslink density and degradation to control bone morphogenetic protein delivery and in vivo bone formation. *J. Control. Release* **191**, 63–70 (2014).
23. Ganji, F., Abdekhodaie, M. J. & Ramazani, A. Gelation time and degradation rate of chitosan-based injectable hydrogel. *J. Sol-Gel Sci. Technol.* **42**, 47–53 (2007).
24. Ma, Z., Gao, C., Gong, Y. & Shen, J. Cartilage tissue engineering PLLA scaffold with surface immobilized collagen and basic fibroblast growth factor. *Biomaterials* **26**, 1253–1259 (2005).
25. Pawelec, K. M., Best, S. M. & Cameron, R. E. Collagen: a network for regenerative medicine. *J. Mater. Chem. B* **4**, 6484–6496 (2016).

26. Ma, J. *et al.* Multiphoton Fabrication of Fibronectin-Functionalized Protein Micropatterns: Stiffness-Induced Maturation of Cell-Matrix Adhesions in Human Mesenchymal Stem Cells. *ACS Appl. Mater. Interfaces* **9**, 29469–29480 (2017).
27. Won, J. E. *et al.* Fibronectin immobilization on to robotic-dispensed nanobioactive glass/polycaprolactone scaffolds for bone tissue engineering. *Biotechnol. Lett.* **37**, 935–942 (2015).
28. Bensaïd, W. *et al.* A biodegradable fibrin scaffold for mesenchymal stem cell transplantation. *Biomaterials* **24**, 2497–2502 (2003).
29. Christman, K. L., Fok, H. H., Sievers, R. E., Fang, Q. & Lee, R. J. Fibrin Glue Alone and Skeletal Myoblasts in a Fibrin Scaffold Preserve Cardiac Function after Myocardial Infarction. *Tissue Eng.* **10**, 403–409 (2004).
30. Gardin, C. *et al.* Hyaluronan and fibrin biomaterial as scaffolds for neuronal differentiation of adult stem cells derived from adipose tissue and skin. *Int. J. Mol. Sci.* **12**, 6749–6764 (2011).
31. Arulmoli, J. *et al.* Combination scaffolds of salmon fibrin, hyaluronic acid, and laminin for human neural stem cell and vascular tissue engineering. *Acta Biomater.* **43**, 122–138 (2016).
32. Yeo, I. S. *et al.* Identification of a bioactive core sequence from human laminin and its applicability to tissue engineering. *Biomaterials* **73**, 96–109 (2015).
33. Santiago, L. Y., Nowak, R. W., Rubin, J. P. & Marra, K. G. Peptide-surface modification of poly(caprolactone) with laminin-derived sequences for adipose-derived stem cell applications. *Biomaterials* **27**, 2962–2969 (2006).
34. Tejeda-Montes, E. *et al.* Mineralization and bone regeneration using a bioactive elastin-like recombinamer membrane. *Biomaterials* **35**, 8339–8347 (2014).
35. Rnjak-Kovacina, J. *et al.* Tailoring the porosity and pore size of electrospun synthetic human elastin scaffolds for dermal tissue engineering. *Biomaterials* **32**, 6729–6736 (2011).
36. Han, J. *et al.* Co-electrospun blends of PLGA, gelatin, and elastin as potential nonthrombogenic scaffolds for vascular tissue engineering. *Biomacromolecules* **12**, 399–408 (2011).
37. Mouser, V. H. M. *et al.* Yield stress determines bioprintability of hydrogels based on gelatin-methacryloyl and gellan gum for cartilage bioprinting. *Biofabrication* **8**, 035003 (2016).
38. Dhandayuthapani, B., Krishnan, U. M. & Sethuraman, S. Fabrication and characterization of chitosan-gelatin blend nanofibers for skin tissue engineering. *J. Biomed. Mater. Res. - Part B Appl. Biomater.* **94**, 264–272 (2010).
39. Kasoju, N. & Bora, U. Silk fibroin in tissue engineering. *Adv. Healthc. Mater.* **1**, 393–412 (2012).
40. Nilebäck, L. *et al.* Silk-silk interactions between silkworm fibroin and recombinant spider silk fusion proteins enable construction of bioactive materials. *ACS Appl. Mater. Interfaces* acsami.7b10874 (2017). doi:10.1021/acsami.7b10874
41. Yan, L. P. *et al.* Macro/microporous silk fibroin scaffolds with potential for articular cartilage and meniscus tissue engineering applications. *Acta Biomater.* **8**, 289–301 (2012).
42. Ishida, O., Tanaka, Y., Morimoto, I., Takigawa, M. & Eto, S. Chondrocytes are regulated by cellular adhesion through CD44 and hyaluronic acid pathway. *J. Bone Miner. Res.* **12**, 1657–63 (1997).
43. Fan, J. & Yang, J. Preparation and characterization of a chitosan/galactosylated hyaluronic acid/heparin scaffold for hepatic tissue engineering. *J. Biomater. Sci. Polym. Ed.* **28**, 569–581 (2017).
44. Dahlmann, J. *et al.* Fully defined in situ cross-linkable alginate and hyaluronic acid hydrogels for myocardial tissue engineering. *Biomaterials* **34**, 940–951 (2013).
45. Recha-Sancho, L. & Semino, C. E. Chondroitin sulfate- and decorin-based self-Assembling scaffolds for cartilage tissue engineering. *PLoS One* **11**, 1–24 (2016).
46. Wang, D.-A. *et al.* Multifunctional chondroitin sulphate for cartilage tissue–biomaterial integration. *Nat. Mater.* **6**, 385–392 (2007).
47. Wiltsey, C. *et al.* Characterization of injectable hydrogels based on poly(N-isopropylacrylamide)-g-chondroitin sulfate with adhesive properties for nucleus pulposus tissue engineering. *J. Mater. Sci. Mater. Med.* **24**, 837–847 (2013).
48. Ingavle, G. C., Frei, A. W., Gehrke, S. H. & Detamore, M. S. Incorporation of aggrecan in interpenetrating network hydrogels to improve cellular performance for cartilage tissue engineering. *Tissue Eng. Part A* **19**, 1349–59 (2013).
49. Ingavle, G. C., Gehrke, S. H. & Detamore, M. S. The bioactivity of agarose-PEGDA interpenetrating network hydrogels with covalently immobilized RGD peptides and physically entrapped aggrecan. *Biomaterials* **35**, 3558–3570 (2014).
50. Liu, H. Y. *et al.* Chitosan-assisted differentiation of porcine adipose tissue-derived stem cells into glucose-responsive insulin-secreting clusters. *PLoS One* **12**, 1–15 (2017).
51. Muxika, A., Etxabide, A., Uranga, J., Guerrero, P. & de la Caba, K. Chitosan as a bioactive polymer: Processing, properties and applications. *Int. J. Biol. Macromol.* (2017). doi:10.1016/j.ijbiomac.2017.07.087
52. Xu, Y., Yuan, S., Han, J., Lin, H. & Zhang, X. Design and fabrication of a chitosan hydrogel with gradient structures via a step-by-step cross-linking process. *Carbohydr. Polym.* **176**, 195–202 (2017).
53. Gonçalves, R. M., Pereira, A. C. L., Pereira, I. O., Oliveira, M. J. & Barbosa, M. A. Macrophage response to

chitosan/poly-(γ-glutamic acid) nanoparticles carrying an anti-inflammatory drug. *J. Mater. Sci. Mater. Med.* **26**, 1–12 (2015).

54. Oliveira, J. M. *et al.* Novel hydroxyapatite/chitosan bilayered scaffold for osteochondral tissue-engineering applications: Scaffold design and its performance when seeded with goat bone marrow stromal cells. *Biomaterials* **27**, 6123–6137 (2006).
55. Komur, B. *et al.* Starch/PCL composite nanofibers by co-axial electrospinning technique for biomedical applications. *Biomed. Eng. Online* **16**, 40 (2017).
56. Ghosh, S., Viana, J. C., Reis, R. L. & Mano, J. F. Bi-layered constructs based on poly(l-lactic acid) and starch for tissue engineering of osteochondral defects. *Mater. Sci. Eng. C* **28**, 80–86 (2008).
57. Rodrigues, A. I., Gomes, M. E., Leonor, I. B. & Reis, R. L. Bioactive starch-based scaffolds and human adipose stem cells are a good combination for bone tissue engineering. *Acta Biomater.* **8**, 3765–3776 (2012).
58. Malafaya, P. B., Silva, G. A. & Reis, R. L. Natural-origin polymers as carriers and scaffolds for biomolecules and cell delivery in tissue engineering applications. *Adv. Drug Deliv. Rev.* **59**, 207–233 (2007).
59. Balgude, A. P., Yu, X., Szymanski, A. & Bellamkonda, R. V. Agarose gel stiffness determines rate of DRG neurite extension in 3D cultures. *Biomaterials* **22**, 1077–1084 (2001).
60. DeKosky, B. J. *et al.* Hierarchically Designed Agarose and Poly(Ethylene Glycol) Interpenetrating Network Hydrogels for Cartilage Tissue Engineering. *Tissue Eng. Part C Methods* **16**, 1533–1542 (2010).
61. Gasperini, L., Mano, J. F. & Reis, R. L. Natural polymers for the microencapsulation of cells. *J. R. Soc. Interface* **11**, 20140817–20140817 (2014).
62. Pourjavadi, A., Barzegar, S. & Zeidabadi, F. Synthesis and properties of biodegradable hydrogels of κ-carrageenan grafted acrylic acid-co-2-acrylamido-2-methylpropanesulfonic acid as candidates for drug delivery systems. *React. Funct. Polym.* **67**, 644–654 (2007).
63. Santo, V. E. *et al.* Carrageenan-based hydrogels for the controlled delivery of PDGF-BB in bone tissue engineering applications. *Biomacromolecules* **10**, 1392–1401 (2009).
64. Popa, E. G., Caridade, S. G., Mano, J. F., Reis, R. L. & Gomes, M. E. Chondrogenic potential of injectableκ-carrageenan hydrogel with encapsulated adipose stem cells for cartilage tissue-engineering applications. *J. Tissue Eng. Regen. Med.* **9**, 550–563 (2015).
65. Pereira, D. R. *et al.* Development of Gellan Gum-Based Microparticles/Hydrogel Matrices for Application in the Intervertebral Disc Regeneration. *Tissue Eng. Part C Methods* **17**, 961–972 (2011).
66. Oliveira, J. T. *et al.* Gellan gum: A new biomaterial for cartilage tissue engineering applications. *J. Biomed. Mater. Res. - Part A* **93**, 852–863 (2010).
67. J. T. Oliveira, T. C. Santos, L. Martins, M.A. Silva, A.P.Marques, A. G. Castro, N. M. Neves, R. L. R. Performance of new gellan gum hydrogels combined with human articular chondrocytes for cartilage regeneration when subcutaneously implanted in nude mice. *J. Tissue Eng. Regen. Med.* **4**, 524–531 (2010).
68. Pereira, D. R. *et al.* Gellan Gum-Based Hydrogel Bilayered Scaffolds for Osteochondral Tissue Engineering. *Key Eng. Mater.* **587**, 255–260 (2013).
69. Cerqueira, M. T. *et al.* Gellan gum-hyaluronic acid spongy-like hydrogels and cells from adipose tissue synergize promoting neoskin vascularization. *ACS Appl. Mater. Interfaces* **6**, 19668–19679 (2014).
70. Ebara, M. *et al.* A novel approach to observing synergy effects of PHSRN on integrin-RGD binding using intelligent surfaces. *Adv. Mater.* **20**, 3034–3038 (2008).
71. Rammelt, S. *et al.* Coating of titanium implants with collagen, RGD peptide and chondroitin sulfate. *Biomaterials* **27**, 5561–5571 (2006).
72. Dawson, J. *et al.* Collagen scaffolds with or without the addition of RGD peptides support cardiomyogenesis after aggregation of mouse embryonic stem cells. *Vitr. Cell. Dev. Biol. - Anim.* **47**, 653–664 (2011).
73. Poldervaart, M. T. *et al.* 3D bioprinting of methacrylated hyaluronic acid (MeHA) hydrogel with intrinsic osteogenicity. *PLoS One* **12**, 1–15 (2017).
74. Mohan, N., Wilson, J., Joseph, D., Vaikkath, D. & Nair, P. D. Biomimetic fiber assembled gradient hydrogel to engineer glycosaminoglycan enriched and mineralized cartilage: An in vitro study. *J. Biomed. Mater. Res. - Part A* **103**, 3896–3906 (2015).
75. Schneiders, W. *et al.* Effect of chondroitin sulfate on osteogenetic differentiation of human mesenchymal stem cells. *Mater. Sci. Eng. C* **32**, 1926–1930 (2012).
76. Ni, Y. *et al.* Tough and elastic hydrogel of hyaluronic acid and chondroitin sulfate as potential cell scaffold materials. *Int. J. Biol. Macromol.* **74**, 367–375 (2015).
77. Ozaltin, K., Lehocký, M., Kuceková, Z., Humpolíček, P. & Sáha, P. A novel multistep method for chondroitin sulphate immobilization and its interaction with fibroblast cells. *Mater. Sci. Eng. C* **70**, 94–100 (2017).
78. Musina, R. A., Bekchanova, E. S. & Sukhikh, G. T. Comparison of mesenchymal stem cells obtained from different human tissues. *Bull. Exp. Biol. Med.* **139**, 504–509 (2005).
79. Furth, M. E., Atala, A. & Van Dyke, M. E. Smart biomaterials design for tissue engineering and regenerative

medicine. *Biomaterials* **28**, 5068–5073 (2007).
80. Khang, G. *et al.* Biological evaluation of intervertebral disc cells in different formulations of gellan gum-based hydrogels. *J. Tissue Eng. Regen. Med.* **9**, 265–275 (2015).
81. Fonseca, K. B., Bidarra, S. J., Oliveira, M. J., Granja, P. L. & Barrias, C. C. Molecularly designed alginate hydrogels susceptible to local proteolysis as three-dimensional cellular microenvironments. *Acta Biomater.* **7**, 1674–1682 (2011).
82. Jha, A. K. *et al.* Matrix metalloproteinase-13 mediated degradation of hyaluronic acid-based matrices orchestrates stem cell engraftment through vascular integration. *Biomaterials* **89**, 136–147 (2016).
83. Katrina M. Wisdom1, Desai, R., Rossen, N. S., Rafat, M., West, R. & Hodgson, L. Matrix mechanical plasticity regulates cancer cell migration through confining microenvironments. *Nat. Commun.* (2018). doi:10.1038/s41467-018-06641-z
84. Lee, H. P., Gu, L., Mooney, D. J., Levenston, M. E. & Chaudhuri, O. Mechanical confinement regulates cartilage matrix formation by chondrocytes. *Nat. Mater.* **16**, 1243–1251 (2017).
85. Loebel, C., Mauck, R. L. & Burdick, J. A. Local nascent protein deposition and remodeling guide mesenchymal stromal cell mechanosensing and fate in three-dimensional hydrogels. *Nat. Mater.* (2019). doi:10.1038/s41563-019-0307-6
86. Lutolf, M. P. & Hubbell, J. A. Synthetic biomaterials as instructive extracellular microenvironments for morphogenesis in tissue engineering. *Nat. Biotechnol.* **23**, 47–55 (2005).
87. Lin, H. B. *et al.* Endothelial cell adhesion on polyurethanes containing covalently attached RGD-peptides. *Biomaterials* **13**, 905–914 (1992).
88. Kikkawa, Y. *et al.* Identification of laminin α5 short arm peptides active for endothelial cell attachment and tube formation. *J. Pept. Sci.* **23**, 666–673 (2017).
89. Kang, S. *et al.* The Effect of Conjugating RGD into 3D Alginate Hydrogels on Adipogenic Differentiation of. *Macromol. Biosci.* 673–679 (2011). doi:10.1002/mabi.201000479
90. García, A. J. Interfaces to Control Cell-Biomaterial Adhesive Interactions. in *Polymers for Regenerative Medicine* (ed. Werner, C.) 171–190 (Springer Berlin Heidelberg, 2006). doi:10.1007/12_071
91. Saiki, I. *et al.* Antimetastatic effects of synthetic polypeptides containing repeated structures of the cell adhesive arg-gly-asp (RGD) and tyr-ile-gly-ser-arg (YIGSR) sequences. *Br. J. Cancer* **60**, 722–728 (1989).
92. Hozumi, K. *et al.* Identification of cell adhesive sequences in the N-terminal region of the laminin α2 chain. *J. Biol. Chem.* **287**, 25111–25122 (2012).
93. Dunehoo, A. L. *et al.* Cell adhesion molecules for targeted drug delivery. *J. Pharm. Sci.* **95**, 1856–1872 (2006).
94. Friedli, A. *et al.* The soluble form of the cancer-associated L1 cell adhesion molecule is a pro-angiogenic factor. *Int. J. Biochem. Cell Biol.* **41**, 1572–1580 (2009).
95. Hunt, N. C. *et al.* 3D culture of human pluripotent stem cells in RGD-alginate hydrogel improves retinal tissue development. *Acta Biomater.* **49**, 329–343 (2017).
96. Chen, F. *et al.* Self-crosslinking and injectable hyaluronic acid/RGD-functionalized pectin hydrogel for cartilage tissue engineering. *Carbohydr. Polym.* **166**, 31–44 (2017).
97. Lee, T. T. *et al.* Light-triggered in vivo activation of adhesive peptides regulates cell adhesion, inflammation and vascularization of biomaterials. *Nat. Mater.* **14**, 352–360 (2014).
98. Rossi, E. *et al.* Biomaterials Biologically and mechanically driven design of an RGD-mimetic macroporous foam for adipose tissue engineering applications. *Biomaterials* **104**, 65–77 (2016).
99. Mitchell, A. C., Briquez, P. S., Hubbell, J. A. & Cochran, J. R. Engineering growth factors for regenerative medicine applications. *Acta Biomater.* **30**, 1–12 (2016).
100. Chen, F. M., Zhang, M. & Wu, Z. F. Toward delivery of multiple growth factors in tissue engineering. *Biomaterials* **31**, 6279–6308 (2010).
101. Bessa, P. C., Casal, M. & Reis, R. L. Bone morphogenetic proteins in tissue engineering: The road from laboratory to clinic, part II (BMP delivery). *Journal of Tissue Engineering and Regenerative Medicine* **2**, 81–96 (2008).
102. Stok, J. Van Der *et al.* Full Regeneration of Segmental Bone Defects Using Porous Titanium Implants Loaded With Bmp-2 Containing Fibrin Gels. *Eur. Cells Mater.* **29**, 141–154 (2015).
103. Poth, N., Seiffart, V., Gross, G., Menzel, H. & Dempwolf, W. Biodegradable chitosan nanoparticle coatings on titanium for the delivery of BMP-2. *Biomolecules* **5**, 3–19 (2015).
104. Lv, J. *et al.* Enhanced angiogenesis and osteogenesis in critical bone defects by the controlled release of BMP-2 and VEGF: implantation of electron beam melting-fabricated porous Ti_6Al_4V scaffolds incorporating growth factor-doped fibrin glue. *Biomed. Mater.* **10**, 035013 (2015).
105. Lee, S. S. *et al.* Bone regeneration with low dose BMP-2 amplified by biomimetic supramolecular nanofibers within collagen scaffolds. *Biomaterials* **34**, 452–459 (2013).
106. Shekaran, A. *et al.* Bone regeneration using an alpha 2 beta 1 integrin-specific hydrogel as a BMP-2 delivery vehicle. *Biomaterials* **35**, 5453–5461 (2014).

107. Brigaud, I. *et al.* Synergistic effects of BMP-2, BMP-6 or BMP-7 with human plasma fibronectin onto hydroxyapatite coatings: A comparative study. *Acta Biomater.* **55**, 481–492 (2017).
108. Huang, B. *et al.* Nanostructured hydroxyapatite surfaces-mediated adsorption alters recognition of BMP receptor IA and bioactivity of bone morphogenetic protein-2. *Acta Biomater.* **27**, 275–285 (2015).
109. Gilde, F. *et al.* Stiffness-dependent cellular internalization of matrix-bound BMP-2 and its relation to Smad and non-Smad signaling. *Acta Biomater.* **46**, 55–67 (2016).
110. Dromel, P. C. *et al.* Controlling Growth Factor Diffusion by Modulating Water Content in Injectable Hydrogels. *Tissue Eng. Part A* (2021). doi:10.1089/ten.tea.2020.0313
111. Wang, P. *et al.* Controlled Growth Factor Release in 3D-Printed Hydrogels. *Adv. Healthc. Mater.* **9**, 1–9 (2020).
112. Pan, H., Zheng, Q., Guo, X., Wu, Y. & Wu, B. Polydopamine-assisted BMP-2-derived peptides immobilization on biomimetic copolymer scaffold for enhanced bone induction in vitro and in vivo. *Colloids Surfaces B Biointerfaces* **142**, 1–9 (2016).
113. Kim, Y., Renner, J. N. & Liu, J. C. Incorporating the BMP-2 peptide in genetically-engineered biomaterials accelerates osteogenic differentiation. *Biomater. Sci.* **2**, 1110 (2014).
114. Ferrara, N., Gerber, H.-P. & LeCouter, J. The biology of VEGF and its receptors. *Nat. Med.* **9**, 669–676 (2003).
115. Rouwkema, J. & Khademhosseini, A. Vascularization and Angiogenesis in Tissue Engineering: Beyond Creating Static Networks. *Trends Biotechnol.* **34**, 733–745 (2016).
116. Novosel, E. C., Kleinhans, C. & Kluger, P. J. Vascularization is the key challenge in tissue engineering. *Adv. Drug Deliv. Rev.* **63**, 300–311 (2011).
117. Auger, F. A., Gibot, L. & Lacroix, D. The Pivotal Role of Vascularization in Tissue Engineering. *Annu. Rev. Biomed. Eng.* **15**, 177–200 (2013).
118. Jia, W. *et al.* Urethral tissue regeneration using collagen scaffold modified with collagen binding VEGF in a beagle model. *Biomaterials* **69**, 45–55 (2015).
119. Zhang, H. *et al.* Dual-delivery of VEGF and PDGF by double-layered electrospun membranes for blood vessel regeneration. *Biomaterials* **34**, 2202–2212 (2013).
120. Richardson, T. P., Peters, M. C., Ennett-Shepard, A. B. & Mooney, D. J. Polymeric system for dual growth factor delivery. *Nat. Biotechnol.* **19**, 1029–1034 (2001).
121. Yin, N. *et al.* VEGF-conjugated alginate hydrogel prompt angiogenesis and improve pancreatic islet engraftment and function in type 1 diabetes. *Mater. Sci. Eng. C* **59**, 958–964 (2016).
122. Quade, M. *et al.* Central Growth Factor Loaded Depots in Bone Tissue Engineering Scaffolds for Enhanced Cell Attraction. *Tissue Eng. Part A* ten.tea.2016.0483 (2017). doi:10.1089/ten.tea.2016.0483
123. Anderson, E. M. *et al.* Local Delivery of VEGF and SDF Enhances Endothelial Progenitor Cell Recruitment and Resultant Recovery from Ischemia. *Tissue Eng. Part A* **21**, 1217–1227 (2015).
124. Poels, J. *et al.* Transplantation of testicular tissue in alginate hydrogel loaded with VEGF nanoparticles improves spermatogonial recovery. *J. Control. Release* **234**, 79–89 (2016).
125. Zhang, Q. *et al.* Engineering vascularized soft tissue flaps in an animal model using human adipose-derived stem cells and VEGF+PLGA/PEG microspheres on a collagen-chitosan scaffold with a flow-through vascular pedicle. *Biomaterials* **73**, 198–213 (2015).
126. Des Rieux, A. *et al.* Vascular endothelial growth factor-loaded injectable hydrogel enhances plasticity in the injured spinal cord. *J. Biomed. Mater. Res. - Part A* **102**, 2345–2355 (2014).
127. Yuan, X. *et al.* Hybrid Biomaterial with Conjugated Growth Factors and Mesenchymal Stem Cells for Ectopic Bone Formation. *Tissue Eng. Part A* **22**, 928–939 (2016).
128. Chiu, L. L. Y. & Radisic, M. Scaffolds with covalently immobilized VEGF and Angiopoietin-1 for vascularization of engineered tissues. *Biomaterials* **31**, 226–241 (2010).
129. Jia, J., Siheng, W., Fang, C., Chengchong, A. & Shiyi, C. The study on vascularisation and osteogenesis of BMP/VEGF co-modified tissue engineering bone in vivo. *RSC Adv.* **6**, 41800–41808 (2016).
130. Zhang, H. X. *et al.* In vitro and in vivo evaluation of calcium phosphate composite scaffolds containing BMP-VEGF loaded PLGA microspheres for the treatment of avascular necrosis of the femoral head. *Mater. Sci. Eng. C* **60**, 298–307 (2016).
131. Traub, S. *et al.* The promotion of endothelial cell attachment and spreading using FNIII10 fused to VEGF-A165. *Biomaterials* **34**, 5958–5968 (2013).
132. Garcia, J. R., Clark, A. Y. & Garcia, A. J. Integrin-specific hydrogels functionalized with VEGF for vascularization and bone regeneration of critical-size bone defects. *J. Biomed. Mater. Res. - Part A* **104**, 889–900 (2016).
133. Perugini, V. *et al.* Anti-angiogenic potential of VEGF blocker dendron loaded on to gellan gum hydrogels for tissue engineering applications. *J. Tissue Eng. Regen. Med.* (2017). doi:10.1002/term.2340
134. Belair, D. G. *et al.* Differential regulation of angiogenesis using degradable VEGF-binding microspheres. *Biomaterials* **93**, 27–37 (2016).
135. Teixeira, S. P. B. *et al.* Biomaterials for Sequestration of Growth Factors and Modulation of Cell Behavior. *Adv.*

Funct. Mater. **30**, 1–26 (2020).
136. Teixeira, S. P. B. *et al.* Epitope-Imprinted Nanoparticles as Transforming Growth Factor-β3 Sequestering Ligands to Modulate Stem Cell Fate. *Adv. Funct. Mater.* **31**, 1–10 (2021).
137. Luo, Z. *et al.* Mechano growth factor (MGF) and transforming growth factor (TGF)-β3 functionalized silk scaffolds enhance articular hyaline cartilage regeneration in rabbit model. *Biomaterials* **52**, 463–475 (2015).
138. Tang, Q. O. *et al.* TGF-β3: A potential biological therapy for enhancing chondrogenesis. *Expert Opin. Biol. Ther.* **9**, 689–701 (2009).
139. Diederichs, S., Baral, K., Tanner, M. & Richter, W. Interplay Between Local Versus Soluble Transforming Growth Factor-Beta and Fibrin Scaffolds: Role of Cells and Impact on Human Mesenchymal Stem Cell Chondrogenesis. *Tissue Eng. Part A* **18**, 1140–1150 (2012).
140. Arora, A., Mahajan, A. & Katti, D. S. TGF-β1 presenting enzymatically cross-linked injectable hydrogels for improved chondrogenesis. *Colloids Surfaces B Biointerfaces* **159**, 838–848 (2017).
141. Choi, B. *et al.* Visible-light-initiated hydrogels preserving cartilage extracellular signaling for inducing chondrogenesis of mesenchymal stem cells. *Acta Biomater.* **12**, 30–41 (2015).
142. Samal, J. *et al.* Fibrin-based microsphere reservoirs for delivery of neurotrophic factors to the brain. *Nanomedicine (Lond).* **10**, 765–83 (2015).
143. Jiao, G. *et al.* A bridging SF/Alg composite scaffold loaded NGF for spinal cord injury repair. *Mater. Sci. Eng. C* **76**, 81–87 (2017).
144. Dinis, T. M. *et al.* 3D multi-channel bi-functionalized silk electrospun conduits for peripheral nerve regeneration. *J. Mech. Behav. Biomed. Mater.* **41**, 43–55 (2015).
145. Lei, L. *et al.* Optimization of release pattern of FGF-2 and BMP-2 for osteogenic differentiation of low-population density hMSCs. *J. Biomed. Mater. Res. - Part A* **103**, 252–261 (2015).
146. Otani, Y. *et al.* Optimal Amount of Basic Fibroblast Growth Factor in Gelatin Sponges Incorporating β-Tricalcium Phosphate with Chondrocytes. *Tissue Eng. Part A* **21**, 627–636 (2015).
147. Buckley, C. T. & Kelly, D. J. Expansion in the presence of FGF-2 enhances the functional development of cartilaginous tissues engineered using infrapatellar fat pad derived MSCs. *J. Mech. Behav. Biomed. Mater.* **11**, 102–111 (2012).
148. Pang, Y. *et al.* Local delivery of a collagen-binding FGF-1 chimera to smooth muscle cells in collagen scaffolds for vascular tissue engineering. *Biomaterials* **31**, 878–885 (2010).
149. Jo, Y. Y. *et al.* Silk fibroin-alginate-hydroxyapatite composite particles in bone tissue engineering applications in vivo. *Int. J. Mol. Sci.* **18**, (2017).
150. Niu, B. *et al.* In vitro evaluation of electrospun silk fibroin/nano-hydroxyapatite/BMP-2 scaffolds for bone regeneration. *J. Biomater. Sci. Polym. Ed.* **28**, 257–270 (2017).
151. Anu Priya, B. *et al.* Nickel doped nanohydroxyapatite: vascular endothelial growth factor inducing biomaterial for bone tissue engineering. *RSC Adv.* **5**, 72515–72528 (2015).
152. Rice, M. J., Galun, R. & Finlayson, L. H. Mechanotransduction in insect neurones. *Nat New Biol* **241**, 286–288 (1973).
153. Wall, M. *et al.* Key Developments that Impacted the Field of Mechanobiology and Mechanotransduction. *J. Orthop. Res.* 20–22 (2017). doi:10.1002/jor.23707
154. Schiller, R. Bacterial chemotaxis: A survey. *Gen. Relativ. Gravit.* **7**, 127–133 (1976).
155. McCarthy, J. B., Palm, S. L. & Furcht, L. T. Migration by haptotaxis of a Schwann cell tumor line to the basement membrane glycoprotein laminin. *J. Cell Biol.* **97**, 772–777 (1983).
156. Lo, C. M., Wang, H. B., Dembo, M. & Wang, Y. L. Cell movement is guided by the rigidity of the substrate. *Biophys. J.* **79**, 144–152 (2000).
157. Polacheck, W. J., German, A. E., Mammoto, A., Ingber, D. E. & Kamm, R. D. Mechanotransduction of fluid stresses governs 3D cell migration. *Proc. Natl. Acad. Sci. U. S. A.* **111**, 2447–2452 (2014).
158. Park, J. S., Kim, D. H. & Levchenko, A. Topotaxis: A New Mechanism of Directed Cell Migration in Topographic ECM Gradients. *Biophys. J.* **114**, 1257–1263 (2018).
159. Pieuchot, L. *et al.* Curvotaxis directs cell migration through cell-scale curvature landscapes. *Nat. Commun.* **9**, (2018).
160. Shirke, P. U. *et al.* 'Viscotaxis' - Directed Migration of Mesenchymal Stem Cells in Response to Loss Modulus Gradient. *bioRxiv* 804492 (2019). doi:10.1101/804492
161. Lampi, M. C. & Reinhart-King, C. A. Targeting extracellular matrix stiffness to attenuate disease: From molecular mechanisms to clinical trials. *Sci. Transl. Med.* **10**, eaao0475 (2018).
162. Nung, Y. & Jan, L. Force-activated ion channels in close-up. *Nature* 469–470 (2018). doi:10.1038/d41586-018-01631-z
163. Jones, D. L. & Wagers, A. J. No place like home: anatomy and function of the stem cell niche. *Nat. Rev. Mol. Cell Biol.* **9**, 11–21 (2008).

164. Mccutchen, C. N., Zignego, D. L. & June, R. K. Metabolic Responses Induced by Compression of Chondrocytes in Variable- Stiffness Microenvironments. *J. Biomech.* 1–10 (2017). doi:10.1016/j.jbiomech.2017.08.032
165. Shioji, S. *et al.* Extracellular and intracellular mechanisms of mechanotransduction in three- Dimensionally embedded rat chondrocytes. *PLoS One* **9**, 1–13 (2014).
166. He, Z. *et al.* Strain-induced mechanotransduction through primary cilia, extracellular ATP, purinergic calcium signaling, and ERK1/2 transactivates CITED2 and downregulates MMP-1 and MMP-13 gene expression in chondrocytes. *Osteoarthr. Cartil.* **24**, 892–901 (2016).
167. Cochis, A. *et al.* Bioreactor mechanically guided 3D mesenchymal stem cell chondrogenesis using a biocompatible novel thermo-reversible methylcellulose-based hydrogel. *Sci. Rep.* **7**, 45018 (2017).
168. Kim, I. G. *et al.* Mechanotransduction of human pluripotent stem cells cultivated on tunable cell-derived extracellular matrix. *Biomaterials* **150**, 100–111 (2017).
169. Discher, D. E., Janmey, P. & Wang, Y. Tissue Cells Feel and Respond to the Stiffness of Their Substrate. *Science (80-.).* **310**, 1139–1143 (2005).
170. Lv, H. *et al.* Biomaterial stiffness determines stem cell fate. *Life Sci.* **178**, 42–48 (2017).
171. Könnig, D., Herrera, A., Duda, G. N. & Petersen, A. Mechanosensation across borders: Fibroblasts inside a macroporous scaffold sense and respond to the mechanical environment beyond the scaffold walls. *J. Tissue Eng. Regen. Med.* (2017). doi:10.1002/term.2410
172. Richardson, T., Barner, S., Candiello, J., Kumta, P. N. & Banerjee, I. Capsule stiffness regulates the efficiency of pancreatic differentiation of human embryonic stem cells. *Acta Biomater.* **35**, 153–165 (2016).
173. Lantoine, J. *et al.* Matrix stiffness modulates formation and activity of neuronal networks of controlled architectures. *Biomaterials* **89**, 14–24 (2016).
174. Jiang, X. *et al.* Polysaccharide nanofibers with variable compliance for directing cell fate. *J. Biomed. Mater. Res. - Part A* **103**, 959–968 (2015).
175. Chen, G., Dong, C., Yang, L. & Lv, Y. 3D Scaffolds with Different Stiffness but the Same Microstructure for Bone Tissue Engineering. *ACS Appl. Mater. Interfaces* **7**, 15790–15802 (2015).
176. Deegan, D. B., Zimmerman, C., Skardal, A., Atala, A. & Shupe, T. D. Stiffness of hyaluronic acid gels containing liver extracellular matrix supports human hepatocyte function and alters cell morphology. *J. Mech. Behav. Biomed. Mater.* **55**, 87–103 (2015).
177. Ryan, A. J. & O'Brien, F. J. Insoluble elastin reduces collagen scaffold stiffness, improves viscoelastic properties, and induces a contractile phenotype in smooth muscle cells. *Biomaterials* **73**, 296–307 (2015).
178. Floren, M. *et al.* Human mesenchymal stem cells cultured on silk hydrogels with variable stiffness and growth factor differentiate into mature smooth muscle cell phenotype. *Acta Biomater.* **31**, 156–166 (2016).
179. Zustiak, S. P. *et al.* Three-dimensional matrix stiffness and adhesive ligands affect cancer cell response to toxins. *Biotechnol. Bioeng.* **113**, 443–452 (2016).
180. Berger, A. J., Linsmeier, K. M., Kreeger, P. K. & Masters, K. S. Decoupling the effects of stiffness and fiber density on cellular behaviors via an interpenetrating network of gelatin-methacrylate and collagen. *Biomaterials* **141**, 125–135 (2017).
181. Branco da Cunha, C. *et al.* Influence of the stiffness of three-dimensional alginate/collagen-I interpenetrating networks on fibroblast biology. *Biomaterials* **35**, 8927–8936 (2014).
182. El-Mohri, H., Wu, Y., Mohanty, S. & Ghosh, G. Impact of matrix stiffness on fibroblast function. *Mater. Sci. Eng. C* **74**, 146–151 (2017).
183. Kühn, P. T. *et al.* Non-Covalently Stabilized Alginate Hydrogels as Functional Cell Scaffold Material. *Macromol. Biosci.* **16**, 1693–1702 (2016).
184. Guneta, V., Loh, Q. L. & Choong, C. Cell-secreted extracellular matrix formation and differentiation of adipose-derived stem cells in 3D alginate scaffolds with tunable properties. *J. Biomed. Mater. Res. - Part A* **104**, 1090–1101 (2016).
185. Cipitria, A. *et al.* In-situ tissue regeneration through SDF-1α driven cell recruitment and stiffness-mediated bone regeneration in a critical-sized segmental femoral defect. *Acta Biomater.* **60**, 50–63 (2017).
186. Xiao, L. *et al.* Fabrication of Silk Scaffolds with Nanomicroscaled Structures and Tunable Stiffness. *Biomacromolecules* **18**, 2073–2079 (2017).
187. Murphy, K. C., Whitehead, J., Zhou, D., Ho, S. S. & Leach, J. K. Engineering Fibrin Hydrogels to Promote the Wound Healing Potential of Mesenchymal Stem Cell Spheroids. *Acta Biomater.* (2017). doi:10.1016/j.actbio.2017.10.007
188. Burdick, J. A. & Murphy, W. L. Moving from static to dynamic complexity in hydrogel design. *Nat. Commun.* **3**, 1–8 (2012).
189. Elango, J. *et al.* Rheological, biocompatibility and osteogenesis assessment of fish collagen scaffold for bone tissue engineering. *Int. J. Biol. Macromol.* **91**, 51–59 (2016).
190. Wagner, K. *et al.* Colloidal crystals of compliant microgel beads to study cell migration and mechanosensitivity in

3D. *Soft Matter* 9776–9787 (2019). doi:10.1039/c9sm01226e

191. Krishna, L. *et al.* Nanostructured scaffold as a determinant of stem cell fate. *Stem Cell Res. Ther.* 1–12 (2016). doi:10.1186/s13287-016-0440-y
192. Long, J., Kim, H., Kim, D., Lee, J. B. & Kim, D.-H. A biomaterial approach to cell reprogramming and differentiation. *J. Mater. Chem. B* **5**, 2375–2389 (2017).
193. Lawrence, B. D., Pan, Z., Liu, A., Kaplan, D. L. & Rosenblatt, M. I. Human corneal limbal epithelial cell response to varying silk film geometric topography in vitro. *Acta Biomater.* **8**, 3732–3743 (2012).
194. Gosselin, E. A. *et al.* Multi-layered silk film co-culture system for human corneal epithelial and stromal stem cells. *J. Tissue Eng. Regen. Med.* 1–11 (2017). doi:10.1002/term.2499
195. Manchineella, S. *et al.* Pigmented Silk Nanofi brous Composite for Skeletal Muscle Tissue Engineering. *Adv. Healthc. Mater.* 1222–1232 (2016). doi:10.1002/adhm.201501066
196. Yao, S. *et al.* Co-effects of matrix low elasticity and aligned topography on stem cell neurogenic differentiation and rapid neurite outgrowth. *Nanoscale* **8**, 10252–10265 (2016).
197. Khaledian, M., Jiroudhashemi, F. & Biazar, E. Chitosan- and polypropylene-oriented surface modification using excimer laser and their biocompatibility study. *Artif. Cells, Nanomedicine, Biotechnol.* **1401**, (2016).
198. Zeimaran, E. *et al.* Development of poly (1, 8-octanediol citrate)/chitosan blend films for tissue engineering applications. *Carbohydr. Polym.* **175**, 618–627 (2017).
199. Osmond, M., Bernier, S. M., Pantcheva, M. B. & Krebs, M. D. Collagen and Collagen-Chondroitin Sulfate Scaffolds With Uniaxially Aligned Pores for the Biomimetic , Three Dimensional Culture of Trabecular Meshwork Cells. *Biotechnol. Bioeng.* **114**, 915–923 (2017).
200. Kim, J., Staunton, J. R. & Tanner, K. Independent Control of Topography for 3D Patterning of the ECM Microenvironment. *Adv. Mater.* **28**, 132–137 (2016).
201. Antman-Passig, M. & Shefi, O. Remote Magnetic Orientation of 3D Collagen Hydrogels for Directed Neuronal Regeneration. *Nano Lett.* **16**, 2567–2573 (2016).
202. Araújo-Custódio, S. *et al.* Injectable and Magnetic Responsive Hydrogels with Bioinspired Ordered Structures. *ACS Biomater. Sci. Eng.* **5**, 1392–1404 (2019).
203. Rose, J. C. *et al.* Biofunctionalized aligned microgels provide 3D cell guidance to mimic complex tissue matrices. *Biomaterials* (2018). doi:10.1016/j.biomaterials.2018.02.001
204. Samandari, M. *et al.* Controlling cellular organization in bioprinting through designed 3D microcompartmentalization. *Appl. Phys. Rev.* **8**, 21404 (2021).
205. Tsimbouri, P. M. *et al.* Stimulation of 3D osteogenesis by mesenchymal stem cells using a nanovibrational bioreactor. *Nat. Biomed. Eng.* **1**, 758–770 (2017).
206. Zhang, J. *et al.* Topography of calcium phosphate ceramics regulates primary cilia length and TGF receptor recruitment associated with osteogenesis. *Acta Biomater.* **57**, 487–497 (2017).
207. Yang, S. P., Yang, C. Y., Lee, T. M. & Lui, T. S. Effects of calcium-phosphate topography on osteoblast mechanobiology determined using a cytodetacher. *Mater. Sci. Eng. C* **32**, 254–262 (2012).
208. Singh, S. J., Turner, W., Glaser, D. E., McCloskey, K. E. & Filipp, F. V. Metabolic shift in density-dependent stem cell differentiation. *Cell Commun. Signal.* **15**, 44 (2017).
209. Wiesner, M., Berberich, O., Hoefner, C., Blunk, T. & Bauer-Kreisel, P. Gap junctional intercellular communication in adipose-derived stromal/stem cells is cell density-dependent and positively impacts adipogenic differentiation. *J. Cell. Physiol.* (2017). doi:10.1002/jcp.26178
210. Carrier PM, R. L. *et al.* Cardiac tissue engineering: Cell seeding, cultivation parameters,and tissue construct characterization. *Biotechnol Bioeng* **64**, 580–589 (1999).
211. Venugopal, B., Mogha, P., Dhawan, J. & Majumder, A. Cell density overrides the effect of substrate stiffness on human mesenchymal stem cells' morphology and proliferation. *Biomater. Sci.* **6**, 1109–1119 (2018).
212. Cigan, A. D. *et al.* High seeding density of human chondrocytes in agarose produces tissue-engineered cartilage approaching native mechanical and biochemical properties. *J. Biomech.* **49**, 1909–1917 (2016).
213. Talukdar, S., Nguyen, Q. T., Chen, A. C., Sah, R. L. & Kundu, S. C. Effect of initial cell seeding density on 3D-engineered silk fibroin scaffolds for articular cartilage tissue engineering. *Biomaterials* **32**, 8927–8937 (2011).
214. Francioli, S. E. *et al.* Effect of three-dimensional expansion and cell seeding density on the cartilage-forming capacity of human articular chondrocytes in type II collagen sponges. *J. Biomed. Mater. Res. - Part A* **95**, 924–931 (2010).
215. Maia, F. R., Lourenço, A. H., Granja, P. L., Gonçalves, R. M. & Barrias, C. C. Effect of cell density on mesenchymal stem cells aggregation in RGD-alginate 3D matrices under osteoinductive conditions. *Macromol. Biosci.* **14**, 759–771 (2014).
216. Brown, C. F. C. *et al.* Effect of decellularized adipose tissue particle size and cell density on adipose-derived stem cell proliferation and adipogenic differentiation in composite methacrylated chondroitin sulphate hydrogels. *Biomed. Mater.* **10**, 045010 (2015).
217. Birla, R. *et al.* Force characteristics of in vivo tissue-engineered myocardial constructs using varying cell seeding

densities. *Artif. Organs* **32**, 684–691 (2008).
218. Corin, K. A. & Gibson, L. J. Cell contraction forces in scaffolds with varying pore size and cell density. *Biomaterials* **31**, 4835–4845 (2010).
219. Issa, R. I., Engebretson, B., Rustom, L., McFetridge, P. S. & Sikavitsas, V. I. The Effect of Cell Seeding Density on the Cellular and Mechanical Properties of a Mechanostimulated Tissue-Engineered Tendon. *Tissue Eng. Part A* **17**, 1479–1487 (2011).
220. Iwasa, K. & Reddi, A. H. Optimization of Methods for Articular Cartilage Surface Tissue Engineering: Cell Density and Transforming Growth Factor Beta Are Critical for Self-Assembly and Lubricin Secretion. *Tissue Eng. Part C Methods* **23**, 389–395 (2017).
221. Vegas, A. J. *et al.* Combinatorial hydrogel library enables identification of materials that mitigate the foreign body response in primates. *Nat. Biotechnol.* **34**, 345–352 (2016).
222. Anderson, D. G., Putnam, D., Lavik, E. B., Mahmood, T. A. & Langer, R. Biomaterial microarrays: Rapid, microscale screening of polymer-cell interaction. *Biomaterials* **26**, 4892–4897 (2005).
223. Kim, H. D. *et al.* High throughput approaches for controlled stem cell differentiation. *Acta Biomater.* **34**, 21–29 (2016).
224. Beachley, V. Z. *et al.* Tissue matrix arrays for high-throughput screening and systems analysis of cell function. *Nat. Methods* **12**, 1197–1204 (2015).
225. Floren, M. & Tan, W. Three-dimensional, soft neotissue arrays as high throughput platforms for the interrogation of engineered tissue environments. *Biomaterials* **59**, 39–52 (2015).
226. Guermani, E. *et al.* Engineering complex tissue-like microgel arrays for evaluating stem cell differentiation. *Sci. Rep.* **6**, 30445 (2016).
227. Caliari, S. R. *et al.* Collagen scaffold arrays for combinatorial screening of biophysical and biochemical regulators of cell behavior. *Adv. Healthc. Mater.* **4**, 58–64 (2015).
228. Chen, X. *et al.* Fabrication of gelatin methacrylate / nanohydroxyapatite microgel arrays for periodontal tissue regeneration. *Int. J. Nanomedicine* 4707–4718 (2016). doi:10.2147/IJN.S111701
229. Lee, J. *et al.* Combinatorial screening of biochemical and physical signals for phenotypic regulation of stem cell-based cartilage tissue engineering. *Sci. Adv.* **6**, 1–14 (2020).
230. Kyle, S., Jessop, Z. M., Al-Sabah, A. & Whitaker, I. S. 'Printability'' of Candidate Biomaterials for Extrusion Based 3D Printing: State-of-the-Art'. *Adv. Healthc. Mater.* **6**, 1–16 (2017).
231. Dolatshahi-Pirouz, A. *et al.* A combinatorial cell-laden gel microarray for inducing osteogenic differentiation of human mesenchymal stem cells. *Sci. Rep.* **4**, 3896 (2014).
232. Santo, V. E. *et al.* Engineering Enriched Microenvironments with Gradients of Platelet Lysate in Hydrogel Fibers. *Biomacromolecules* **17**, 1985–1997 (2016).
233. Guimarães, C. F. *et al.* High-throughput fabrication of cell-laden 3D biomaterial gradients. *Mater. Horiz.* **7**, 2414–2421 (2020).
234. Kuhn, P. T. *et al.* Double Linear Gradient Biointerfaces for Determining Two- Parameter Dependent Stem Cell Behavior. *ChemNanoMat* 10.1002/cnma.201600028 (2016). doi:10.1016/S0740-5472(96)90021-5
235. Zhou, Q. *et al.* Directional nanotopographic gradients: a high-throughput screening platform for cell contact guidance. *Sci. Rep.* **5**, 16240 (2015).
236. Zhou, Q. *et al.* Screening Platform for Cell Contact Guidance Based on Inorganic Biomaterial Micro/nanotopographical Gradients. *ACS Appl. Mater. Interfaces* **9**, (2017).
237. Faia-Torres, A. B. *et al.* Osteogenic differentiation of human mesenchymal stem cells in the absence of osteogenic supplements: A surface-roughness gradient study. *Acta Biomater.* **28**, 64–75 (2015).
238. Sunyer, R. *et al.* Collective cell durotaxis emerges from long-range intercellular force transmission. *Science (80-.).* **353**, 1157–1161 (2016).
239. Mozdzen, L. C., Thorpe, S. D., Screen, H. R. C. & Harley, B. A. C. The Effect of Gradations in Mineral Content, Matrix Alignment, and Applied Strain on Human Mesenchymal Stem Cell Morphology within Collagen Biomaterials. *Adv. Healthc. Mater.* **5**, 1731–1739 (2016).
240. Manferdini, C. *et al.* Specific inductive potential of a novel nanocomposite biomimetic biomaterial for osteochondral tissue regeneration. *J. Tissue Eng. Regen. Med.* **10**, 374–391 (2016).
241. Guo, J. *et al.* Multiscale design and synthesis of biomimetic gradient protein/biosilica composites for interfacial tissue engineering. *Biomaterials* **145**, 44–55 (2017).
242. Pedron, S., Becka, E. & Harley, B. A. Spatially gradated hydrogel platform as a 3D engineered tumor microenvironment. *Adv. Mater.* **27**, 1567–1572 (2015).
243. Mahadik, B. P., Pedron Haba, S., Skertich, L. J. & Harley, B. A. C. The use of covalently immobilized stem cell factor to selectively affect hematopoietic stem cell activity within a gelatin hydrogel. *Biomaterials* **67**, 297–307 (2015).
244. Cornelissen, K. *et al.* An algorithm-based topographical biomaterials library to instruct cell fate. *Proc. Natl. Acad.*

Sci. **110**, 5731–5731 (2013).
245. Hulshof, F. F. B. *et al.* NanoTopoChip: High-throughput nanotopographical cell instruction. *Acta Biomater.* **62**, 188–198 (2017).
246. Vermeulen, S. *et al.* Expanding Biomaterial Surface Topographical Design Space through Natural Surface Reproduction. *Adv. Mater.* **2102084**, (2021).
247. Vega, S. L. *et al.* Combinatorial hydrogels with biochemical gradients for screening 3D cellular microenvironments. *Nat. Commun.* **9**, 614 (2018).
248. Guimarães, C. F., Gasperini, L., Marques, A. P. & Reis, R. L. 3D flow-focusing microfluidic biofabrication: One-chip-fits-all hydrogel fiber architectures. *Appl. Mater. Today* **23**, (2021).
249. de Boer, J. Shifting Gears in Biomaterials Discovery. *Matter* **2**, 1358–1360 (2020).
250. Hakimi, O., Krallinger, M. & Ginebra, M. P. Time to kick-start text mining for biomaterials. *Nat. Rev. Mater.* **5**, 553–556 (2020).

Chapter IV

MICROFLUIDIC-DRIVEN BIOFABRICATION AND THE ENGINEERING OF CANCER-LIKE ENVIRONMENTS

MICROFLUIDIC-DRIVEN BIOFABRICATION AND THE ENGINEERING OF CANCER-LIKE ENVIRONMENTS

Abstract

Despite considerable advances in cancer research and oncological treatments, the burden of the disease is still extremely high. While past research has been cancer cell-centered, it is now clear that to understand tumors, the models that serve as framework for research and therapeutic testing need to improve and integrate cancer microenvironment characteristics such as mechanics, architecture, and cell heterogeneity. Microfluidics is a powerful tool for biofabrication of cancer-relevant architectures given its capacity to manipulate cells and materials at very small dimensions and integrate varied living tissue's characteristics. This chapter outlines the current microfluidic toolbox for fabricating living constructs, starting by explaining the varied configurations of 3D soft constructs microfluidics enables when used to process hydrogels. Then, we analyze of the possibilities to control material flows and create space-varying characteristics such as gradients or advanced 3D micro-architectures. Envisioning the trend to approach the complexity of tumor microenvironments also at higher dimensions, we discuss microfluidic-enabled 3D bioprinting and recent advances in that arena. Finally, we summarize the future possibilities for microfluidic biofabrication to tackle important challenges in cancer 3D modeling, including tools for the fast quantification of biological events towards data-driven and precision medicine approaches.

This chapter is reproduced from the following publication:

Guimarães, C. F., Gasperini, L., & Reis, R. L., Microfluidic-Driven Biofabrication and the Engineering of Cancer-Like Microenvironments, in Microfluidics and Biosensors for Cancer Research, *Springer Nature* (Accepted).

IV.1. INTRODUCTION

The past couple of decades have been marked by remarkable advances in the engineering of living tissues. More than ever, it is nowadays established that the architecture of biological tissues, their physical and mechanical characteristics, are important modulators of cellular responses and contribute to the overall tissue and organ functionality - to a similar extent to that of biochemical cues [1]. This notion applies to healthy tissues, but also diseased ones, such as cancer, where changes in the architecture of the tissue, extracellular matrix composition and consequent mechanics play critical outcomes in cellular responses, from early proliferation to late metastasis [2]. Therefore, when attempting to approach and miniaturize living tissues for creating important research models, which are capable of recapitulating critical physiological responses, it is essential to reconstruct the tissue microenvironment and approach its 3D complexity to derive relevant responses, such as predicting the outcome of a certain drug in cancer cell invasion.

In biofabrication, a more recent area of the global tissue engineering field, there has been continuous development of technologies which allow for constructing complex cell/material structures with increasing level of detail and complexity. In the field of bioprinting, for example, the latest advances have enabled the creation of human-sized organ constructs such as the heart [3], or even other 3D structures in a matter of seconds [4]. Even though bioprinting presents an important advance to recreate tissues or even approach whole organs, it entails a resolution which is not yet fine enough to reproduce the intricacies of very fine biological environments, namely those of the cancer microenvironment [5–7]. Therein, differences at the single-cell level can be found, with a variety of cellular entities and extracellular matrix components, interacting in a very small niche, which gradually grows and evolves towards a more mature cancer tissue. As such, creating smaller structures that still encompass the 3D characteristics of cancer environments can take advantage of microfluidic technologies and their finer resolution capacities.

In microfluidic conditions, liquids such as hydrogel precursors flow in very small sized channels, where turbulence is extremely low and thus fluids tend to maintain their trajectory without typically mixing. This characteristic can be employed to translate multiple precursor flow 3D configurations into hydrogel shapes by taking advantage of crosslinking precursors upon extrusion, using a varied toolbox of hydrogel crosslinking techniques [8–12]. By manipulating materials and cells at very small scales, microfluidics enables for a whole set of possibilities for biofabrication. Unlike typical on-chip technologies that attempt at recreating the physiology of tissues and organs within plastic chips in

dynamic cultures, this chapter will mostly explore microfluidics as a direct biofabrication tool to create independent structures with advanced 3D complexity at very small scales.

Starting with an overview of how microfluidic flows can be combined with hydrogel technologies to create soft, 3D structures that can approach the mechanics of living tissues and integrate cells, within structures such as cell-laden fibers, droplets, and combinations of such. Then, we will discuss how the quick and easy manipulation of different flows can be used to create space-varying compositional characteristics within fabricated structures, such as gradient-like transitions that can approach those transitions typically found in healthy and diseased tissues, or be leveraged towards high-throughput, single-sample screening approaches. After, we will discuss how flows alone can be used to create complex 3D architectures within microfluidic-biofabricated structures, from hundreds of micrometers to near single-cell dimensions, approaching the organization of several living microenvironments, namely those of cancer in early invasive stages. We will then explore how additional complexity can be obtained by combining different technologies with microfluidic biofabrication, namely bioprinting for the gradual assembly living constructs with complex shapes due to microfluidic-enabled manufacturing.

By providing an overview of the current microfluidic biofabrication toolbox, this chapter exposes the opportunities and current needs within the field of cancer-like environment engineering. We outline a clear set of strategies that can be used to imbue purely 3D, soft, microfabricated constructs with material and cellular architectures that can approach important characteristics of living cancers. By allowing to do so in fast, standardized, and affordable ways, microfluidic biofabrication is likely to grow in the next few years and overcome other technologies when cellular-level resolution is required, such as the recreation of truly physiological cancer microenvironment models.

IV.2. MICROFLUIDICS – A VERSATILE TOOL FOR 3D HYDROGEL PROCESSING

Microfluidic techniques are designed to manipulate liquids of various viscosities, and different available techniques are best suited to process liquids of different nature. When the liquid is a hydrogel precursor, typically a water-based solution of specific polymers, some conditions induce its sol-gel transition or, in other terms, the crosslinking of the dissolved polymers and hardening of the liquid into a hydrogel [13]. These conditions depend on the gel forming solution and determine which is the most suitable microfluidic technique to process them into a 3D hydrogel. These gel forming polymers are

categorized, sometimes improperly, into two main families based on their sol-gel mechanism: those that form gels physically and those that form gels chemically.

The family of polymers that physically forms gels include those polymers that do so thanks to non-covalent (ionic and weak interactions) bonds between the polymeric chains. Alternatively, chemically cross-linked polymers form a gel by strong covalent bonds between the chains. Some physically cross-linked polymers are thermoresponsive polymers that rearrange due to temperature variation into insoluble structures. Gelatin and collagen belong to this family, and the former presents an upper critical solution temperature above which gelatin and water are miscible and the gel is formed by cooling a warm solution below the critical temperature, which is around 35 °C [14]. Collagen, regardless of being the precursor of gelatin, form gels in the opposite way and presents a low critical solution temperature close to physiological conditions, above which forms a gel. The formation of gels by temperature variation can be a relatively slow process, especially when strong cooling or heating is not allowed [15]. This limitation is particularly evident when cells are present in the solution because of their sensibility to drastic variation of temperature that affects their viability. For this reason, polymers as collagen and gelatin are well suited for droplet based microfluidic techniques that allow the necessary time for them to harden.

With this technique, the droplet is formed thanks to a microfluidic set up that comprises a junction of two or more channels containing different phases. The water-based droplet forming phase is forced into the hydrophobic continuous phase at the junction, then the shear stresses applied by the continuous phase breaks the stream of the water-based solution, forming a droplet. This process leads to high throughput formation of highly monodisperse and separate droplets of liquids in an immiscible phase[16]. The outlet channel can be connected to a tube of variable length and can be treated at different temperatures than the temperature of the starting solutions. The separation of the droplet is ensured by the presence of surfactants that avoid coalescence, thus allowing enough time for the gel droplet to form, and then be collected by various means such as centrifugation or filtration. A similar technique is typically used to produce droplets of photo crosslinked polymers.

Photocrosslinkable polymers are chemically crosslinkable polymers containing functional groups along the backbone that are sensible to radical chemical reactions that form covalent bonds among the polymeric chains. These polymers can be obtained by chemical modification of natural polymers, such as hylauronic acid [17] or can naturally have this characteristics, such as collagen using riboflavin as photoinitiator [18]. Here, the microfluidic set-up for the production of 3D hydrogels is similar to the one

used for the thermoresponsive polymers because also these photocrosslinking process tends to be relatively slow [19]. In fact, a light of high intensity that makes the formation of gel quicker is not optimal because it could also harm cells. The droplet forming solution contains a photoinitiator that forms a radical reactive species when exposed to light of a specific wavelength, so the outlet channel or tube where the droplet flow is exposed to light and the hardened droplets can be collected. Here, the material that makes the outlet should be transparent to the specific wavelenght that excites the photoinitiator into the radical (e.g fluorinated ethylen propylen for UV light). While droplets based techniques are optimal for thermoresponsive and photocrosslinkable polymers, they still require a careful selection of the materials used for the microfluidic system.

For the fabrication of hydrogel droplets, the system must be hydrophobic so that the oil can efficiently wet the channels of the microfluidic set-up to avoid contact between the droplets and the system. The materials that make the system should be compatible with the oil used, a suitable and well performing surfactant should be present, be compatible with the oil and should favor the formation of water droplets in oil. Considering two commonly used surfactants, for example, as Tween and Span, the former is characterized by a high HLB number (Hydrophilic, Lipophilic Balance, is an index of the solubilizing properties of emulsifiers) thus favoring the formation of oil in water droplets, oppositely the latter has a low HLB number and favors the formation of water droplets in oil [20,21].

Droplet techniques, due to their nature and in particular of being emulsion-based, are challenging when used to process ionically crosslinkable materials, which represent an important family of biopolymers that include alginate and gellan gum. These polymers contain carboxyl groups along their backbone that carry a net negative charge. In the presence of positive ions, they form insoluble complexes due to the complexation of those groups that are responsible for the solubility of the polymer in water. Emulsion-based microfluidic techniques are less straightforward to employ with these polymers due to the challenges in using dissolved ions in these systems. The positive ions derive from the dissolution of salts in water that should be placed in contact with the polymeric solution to obtain the gel. To do this, its possible to follow a more complex approach and fabricate two different droplets, one containing the polymer and the other containing the salts, that coalesce forming a gel before collection. Another approach is to use a hardening bath containing the dissolved salts. When the suspension of water droplets and oil reaches the bath, the droplets can separate from the oil due to differences in density so that they can reach the water solution containing the salts. During this process , the droplets must pass through the oil-hardening bath interface that acts as a barrier that can deform the droplets or can block them if the difference in density is limited. Overall droplets based techniques

are interesting approaches for the fabrication of 3D hydrogels that are highly monodispersed in size. The size can vary from submicron to some hundred microns based on the viscosity of the solution used, the size of the channels, the flow rates of the oil and the gel forming solution. Furthermore, given their round shape and sub needle size, the hydrogels can be easily handled with a pipette and can be injected if needed. Moreover, recent advances in microfluidic droplet fabrication are even opening new possibilities for increasing their 3D complexity, such as the creation of inner architectures using airflow (**Fig. IV-1**) [22].

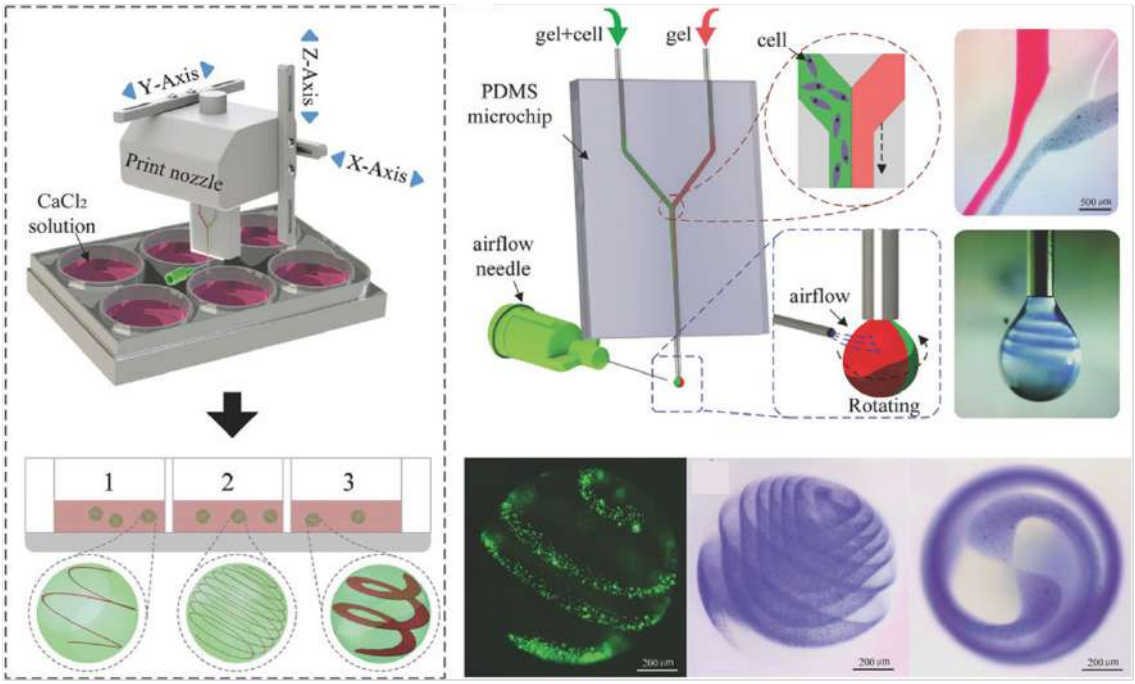


Figure IV-1: Airflow-assisted generation of microfluidic droplets with controlled inner 3D architectures. Reprinted with permission from [22].

Other than droplets, microfluidic techniques can be used to produce fibers and those techniques are generally referred to as continuous flow microfluidics. These techniques are wet spinning techniques, where a microfluidic chip is used to extrude a polymeric solution into the hardening bath. These techniques are simpler than droplet-based techniques if applied to those materials that rapidly crosslink in the presence of a hardening bath, and for this reason they are well suited to process ionically crosslinkable materials. Here, when the solution exits the chip, the surface in contact with the bath quickly crosslinks forming a fiber, that can then sink or float based or the density ratio between gel-forming solution and bath. The fiber can be collected easier than droplets because the oil is not present and post processing steps to remove it are not needed.

Oppositely to droplet techniques, continuous flow is challenging when used to process polymers that do not crosslink rapidly since the gel forming solution doesn't have enough time to form the gel and end up being dissolved into the bath. While droplet and continuous flow microfluidic are different, they share the same microfluidic concept related on how fluids behave in microchannels, that is, they flow in laminar conditions. In laminar conditions fluids have a tendency not to mix so that it's possible to design a microfluidic chip with two inlets that meet at a junction, thus obtaining two fluids flowing side by side in the outlet. Similarly, it is possible to design a junction so that one fluid flows on the inner portion of the outlet and one on the outer part forming a coaxial flow [23].

More complex designs that encompass more fluids are possible, for example, obtaining two fluids side by side enwrapped in the third liquid. One or more fluids, e.g the fluid generating the shell in the previous example, can be a polymeric solution that forms solid hydrogels in specific conditions. Those conditions can be triggered on-demand to solidify one or more of the streams to obtain outside the chip a micro-hydrogel with the same spatial distribution of the generating fluids. The outcome is a hydrogel fiber with different regions recognizable in its cross-section. The amount of space that these regions will occupy in the fiber is determined by the flow rate of the liquid they were made from. By changing the flow rate of the fluids, for example, one can obtain a coaxial fiber with a big core and a thin shell or a small core and a thick shell by inverting the initial flow rates. This size distribution can be obtained into a single fiber with a constant diameter using programmable flow pumps that linearly change the flow so that one side of the fiber can have a small core and the other side a bigger core with a thinner shell.

Finally, it is worth to mention that certain approaches aim at combining discrete droplet generation with continuous hydrogel fiber spinning. A recent work has shown that GelMa droplets generated by oil-water separation could be integrated in a continuous stream of alginate, originating an hydrogel fiber with highly packed cellular spheroids (**Fig. IV-2**). This approach represents a very interesting alternative to fabricating single cancer cell droplets or spheroids, as the hydrogel fiber serves as support for improving the manipulation of several droplets at once, making it easier for applying different culture treatments (e.g. anti-cancer drugs) as well as analyzing (e.g. fixing, staining, imaging).

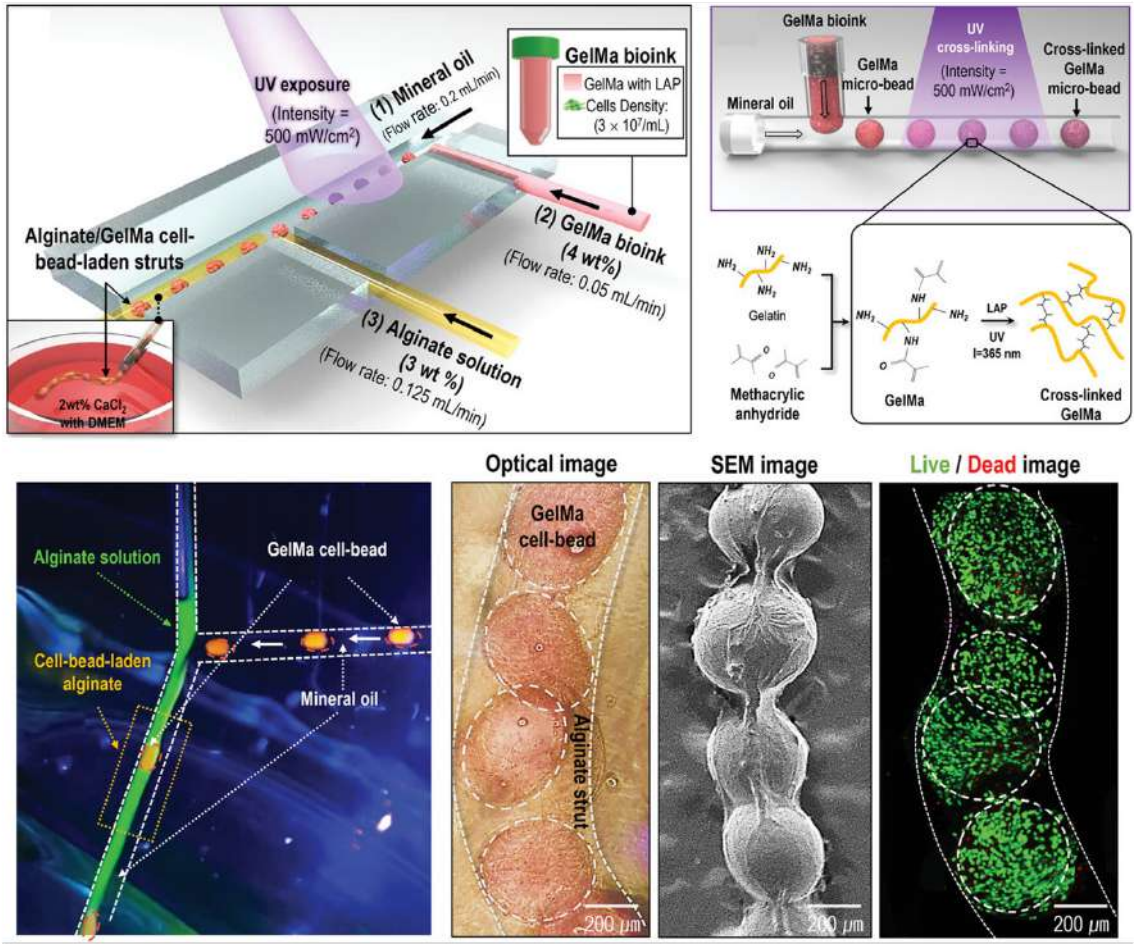


Figure IV-2: The combination of microfluidic droplet generation and continuous flow fiber fabrication enables for the creation of cell-bead-laden alginate fibers, which can transport highly cellular, packed spheroid-like structures within a single support fiber. Reprinted, with permission, from [24].

IV.3. MICROFLUIDIC REAL-TIME CONTROL OF 3D CONSTRUCT COMPOSITION

Using microfluidics-based techniques for processing hydrogel materials presents also unique opportunities to control the composition of constructs, namely, to obtain gradient-like distributions. Gradients are interesting architectures for tissue engineering and biofabrication for two main reasons. The first, is that biological tissues present natural gradients formed at interfaces such as tendon-bone or cartilage-bone interfaces [1], a characteristic which is very important when attempting to engineer, e.g., osteochondral tissues [25]. The second, is that gradients are able to integrate an array of conditions in a single sample, serving as very powerful platforms for high-throughput screening cell-material interactions [26]. In this regard, gradually changing material composition, cellular density, or ECM

molecule distribution are important characteristics of 3D niches that must be optimized for engineering cancer microenvironments, in which microfluidic biofabrication has enabled unique advances.

For some time, microfluidic mixer chips have been used to manipulate liquid hydrogel precursors and establish gradients ranging between two extreme conditions, coupled with different crosslinking strategies, such as photopolymerization of PEG hydrogels [27]. Moreover, the manipulation of hydrogel precursors for gradient formation can be simultaneously combined with cell encapsulation in such chips, creating not just surfaces for cell adhesion but gradient-like 3D environments where cell's responses can be studied, as a function of crosslinking density, polymer concentration or even cellular density, in order to optimize the engineering of the tumor microenvironments [28]. In that work, researchers have shown that this platform was able to successfully present glioma cells with varying tumor-microenvironment relevant characteristics, such as extracellular matrix density, mechanics, and glioma cell density, where *in situ* analysis could be performed at the molecular and genomic level, such as the expression of genes of interest (VEGF and HIF-1) or the secretion of MMPs. Even though these gradient-forming chips present interesting opportunities for library building and 3D biomaterial screening, the engineered environments are still confined to the chip and limited by its size and the possibilities for post-fabrication manipulation of the construct. Typically, these are also analyzed in a limited number (e.g., three or four) regions, which reduces the overall throughput of the technique. To overcome these limitations, researchers have developed techniques to fabricate 3D gradients using microfluidic biofabrication to derive individual out-of-chip constructs, which can be further manipulated and yield higher levels of throughput.

In such an approach, researchers have combined microfluidic-driven precursor mixing with wet-spinning to fabricate cell-laden 3D hydrogel fibers with compositional gradients, which were able to integrate a gradient of 3D hydrogel stiffness, used to screen stem cell differentiation triggering, but representing an equally important characteristic to assess for cancer microenvironment engineering [29] (**Fig. IV-3**). In this work, the team has also demonstrated that a similar approach could be combined with multiple crosslinking stimuli to fabricate multi-material, multi-crosslinking gradients, where further responses ranging from adhesion to proliferation and mechanotransduction could be studied. In previous work, 3D hydrogel fibers were also shown to be interesting platforms for quickly engineering 3D tumor-like environments, where different cancer cell : macrophage ratios in proximity could be adjusted for mimicking different cancer stages [30].

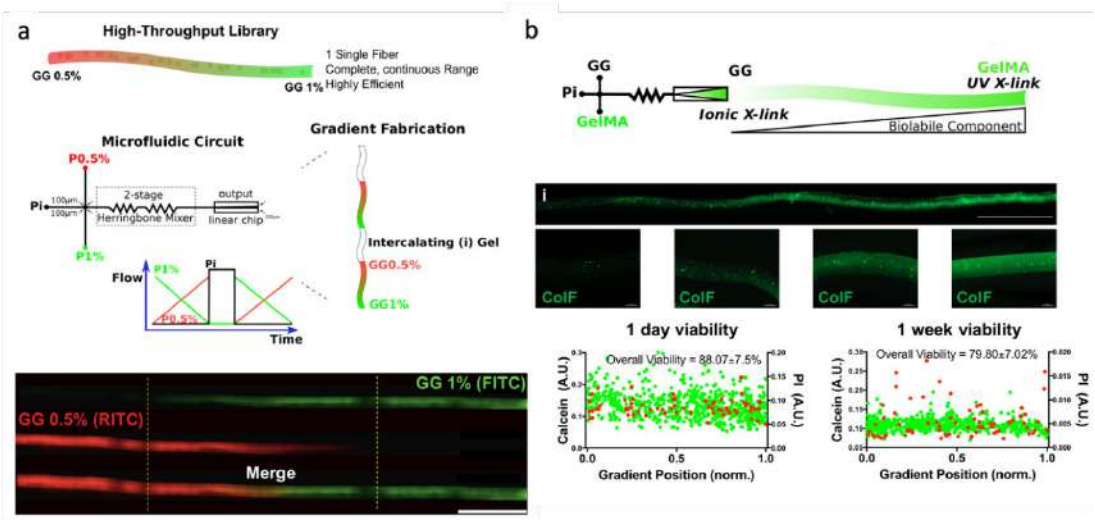


Figure IV-3: High-throughput fabrication of 3D hydrogel fiber gradients with single (a) and multi-material (b) configurations for automated single-cell screening. Adapted with permission from [29].

Droplet-like microgels have also been explored as an alternative to continuous fibers for gradient fabrication. A team has demonstrated that droplets could be fabricated from different precursors using microfluidic water/oil emulsions and UV-crosslinking, then aggregating the resulting microgels to create patterns or gradients. By annealing the microgels, the researchers showed that a continuous 3D microgel scaffold could be deposited with gradients in stiffness or biodegradability. Mesenchymal stem cells were then cultured to screen their adhesion and morphology with the varying 3D microenvironment characteristics [31] (**Figure IV-4**). This approach may be further combined with recently developed microgel jamming and printing technologies [32], where 3D gradients can be assembled in more complex shapes for approaching the architectures of tissues or, for example, different compartments relevant to approach the cellular heterogeneity of the cancer microenvironment.

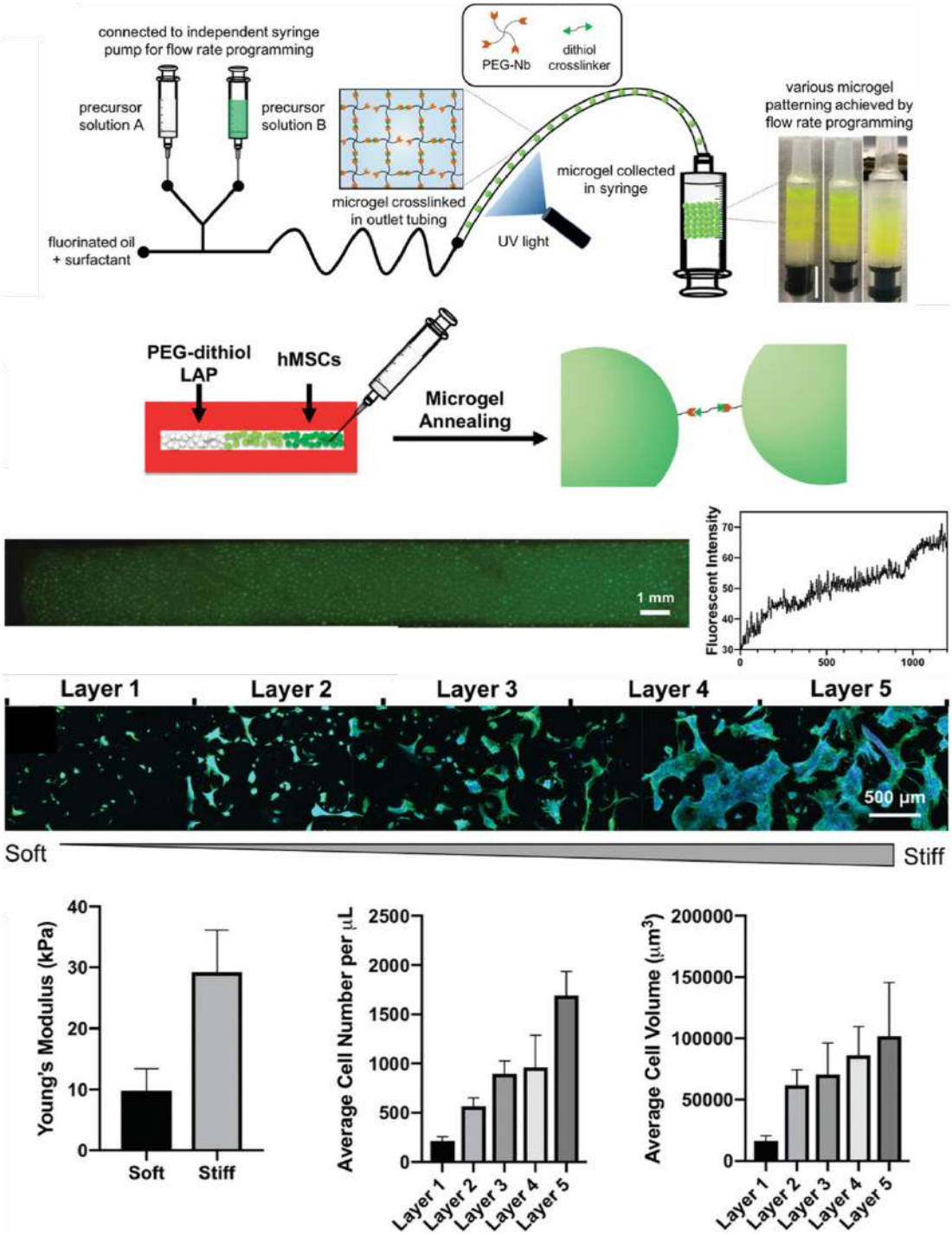


Figure IV-4: Microfluidic-driven generation of hydrogel droplets and microgel annealing for creating 3D gradients suitable for cell culture and high-throughput screening. Adapted with permission from [31].

The cancer heterogeneity is not only related with architecture and mechanics but also with the presence of distinct cell populations and sub-populations, where varying numbers of cells and ratios between e.g., cancer, stromal and immune cells come into play as in any other functional organ [33]. In that regard, microfluidic-driven platforms have also been applied, albeit to a lower extent, to cellular and

cell density gradient studies. By manipulating hydrogel precursors with suspension cells similarly to the previously discussed results, researchers have also demonstrated how intricate cellular niches, such as those of hematopoietic stem cells, can be studied in a high-throughput fashion, by creating cellular gradients ranging from pure hematopoietic progenitor cells to pure osteoblast populations [34]. More recently, 3D gradients of vascular density were also fabricated *via* microfluidic mixing to study the effect of angiocrine cues in stem cell behavior [35]. Similar approaches can be leveraged to cancer microenvironment engineering, where the cancer cell niche and cell-cell interactions can be studied and optimized quickly taking advantage of broad ranges of ratios between cancer cells, vasculature, stromal cells (e.g., cancer-associated fibroblasts), and immune cells (e.g., macrophages or T-cells).

Moreover, other type of cancer hallmarks can be approached in high-throughput fashion for screening drugs or modeling physiologically relevant responses, such as hypoxia. Typically, cancers are characterized by highly dense environments with deficient vasculature, where certain regions of the tumor tissue experience low oxygen levels (hypoxia), which in turn lead to altered metabolism, and trigger signaling cascades such as those promoting angiogenesis [36]. Indeed, hypoxic conditions can alter the response and resistance of cancer cells to drugs, and the absence of such physiologically relevant parameters in 3D cancer models may lead to wrongful conclusions when testing new therapeutic strategies. Microfluidic chips and platforms present interesting opportunities to tackle this scenario by allowing for the creation of gradients also in oxygen concentration [37]. Researchers have shown that oxygen levels ranging from 0% to 20% could be obtained in a single chip, where cancer spheroids could be cultured in gradually changing levels of oxygen, demonstrating how varying oxygen levels could alter the metabolic activity of cancer and immune cells, as well as differences in the success of the anti-cancer drugs Doxorubicin and Tirapazamine [38]. The team demonstrated that lower oxygen levels (hypoxia) led to increased resistance to both drugs, highlighting the need for approaching physiological conditions when miniaturizing cancers for drug testing.

Lastly, it is important to refer that microfluidic-biofabricated gradients are not only important as fundamental and applied research tools, but these may also be more closely interfaced with clinical settings for patient specific, personalized, and precision medicine approaches. A recent work has demonstrated how patient-derived tumor xenografts of glioblastoma could be integrated in gradients of brain-mimicking stiffness, showing how varying 3D mechanics affected cellular proliferation and, particularly, regions with increased stiffness led to increased resistance to the drug temozolomide [39]. Even though the work does not employ microfluidic techniques, it clearly demonstrates the importance of creating physiologically relevant platforms for assessing patient-derived cell responses to treatments,

namely going beyond traditional 2D plates with non-physiological stiffness. By further combining this knowledge with the high-throughput and speed of microfluidic-driven biofabrication, future platforms may enable a much faster and personalized approach to therapies, where patient cells can be quickly employed for *in vitro* therapeutical studies, also requiring lower amounts of cells and materials due to the unique microfluidic miniaturization capabilities.

IV.3.1. Discrete Generation of Individual Microfluidic Segments

Even though the previous section focuses on continuous microfluidic structures, it is also important to discus the possibility to create individualized segments within microfluidic-fabricated structures, which can be separated by inert gaps and function as an array of 3D environemtns.

Indeed, the fluid tendency to not mix withi microchips can be exploited to fabricate vertically segmented fibers using a microfluidic chip containing a junction. The junction can be a simple T or Y junction or can have a more advanced geometry able to connect more channels together. The junction is made in such way that the fluids coming from different inlet channels can join in one a common exit channel. By applying pressure on one or more channels, only the fluids from those channels will flow to the exit channel. By stopping the application of pressure on those channels the flow will stop. By pressurizing other channels new and different fluids will flow in the exit channel pushing forward the fluid already present in the exit channel. By repeating this process, the exit channel is filled by different fluids, such fluids do not mix (or with minimal mixing) so that different compartments along the path of the exit channel can be identified. After this, some or all the fluids composing the segments of interest are hardened so that the compartments can keep separated. The segments may not perfectly shaped cylinders due to the rheological nature of the generating fluids. Fluids that behave as Newtonian fluids develop a parabolic speed profile inside the channel and as such the segment generated by these fluids may have a parabolic profile at the bases [40]. Oppositely, a fluid following a non-newtonian power law model develops a different speed profile forming cylinders with a flatter base in the middle and a parabolic profile on the sides. The final product of this technique is a fiber composed of segments that can be composed of different materials.

This feature can be exploited to obtain single segments, making this technique an oil-less alternative approach to droplet microfluidic. The advantage of this technique is the absence of oil that simplifies the fabrication (see section 2) and that cylinders are formed rather than spherical objects. Spheres are the geometrical shape that include the highest amount of mass in the lowest amount of

surface and this is how water-based droplets minimize the surface in contact with the oil. Oppositely, cylinders present a higher surface to volume ratio which favors the diffusion of nutrients and metabolites when cells are encapsulated [41]. To obtain single segments there are two main approaches that can be followed: the use of a sacrificial gelling agent or the use of a non-gelling agent as one of the segments. In the first case, a fiber is formed and sacrificial gelling agent can be degraded and removed. One example is a fiber composed of gellan gum and alginate segments, where the alginate can be removed by enzymatically accelerated degradation using alginase or by using chelating agents that do not affect gellan gum [42,43]. Considering the second case, segments are formed directly by using any solution with a similar viscosity that the one of the segments of interest that does not form gels in the hardening bath, such as hyaluronic acid. When extruded, the non-gelling phase dissolves in the hardening bath while the gelling phase hardens forming cylindrical gels that can be collected for further use.

IV.4. MICROFLUIDIC FLOW-BASED GENERATION OF 3D AND CANCER-LIKE ARCHITECTURES

As initially outlined, the shapes and architectures present within living tissues is as important as their composition and plays an important role in the consequent mechanical properties and biological events. Characteristics such as ECM orientation, tissue anisotropy, and the presence of multiple compartments with different cellular and ECM composition are critical to approach and model living tissues [1]. In 2D surfaces, oriented topographies and their impact on cellular behavior have been explored for a long time [44–46], but their translation to 3D systems is not so straightforward. Typically, to introduce orientation and shape in 3D hydrogels, there is a need to use composite systems where nanoparticles [47] or microgels [48] are aligned using externally-driven methodologies such as magnetic fields, to create 3D orientation and introduce shape control in hydrogels. Alternatively, the process of hydrogel crosslinking can also be combined with the manipulation of ice crystal formation to induce a certain degree of control in pore dimension and orientation [49]. Even though the discussed technologies present high versatility and can be employed for introducing 3D shapes and topographies within constructs, these require multiple steps and component manipulation to implement and control structure within the fabricated hydrogels. However, recent studies have demonstrated that taking advantage of microfluidic flows alone, it is possible to create organization within hydrogel precursors

pre-crosslinking, which, if maintained upon crosslinking, can lead to varied and interesting architectures at very small dimensions.

One interesting approach is that of leveraging chaotic hydrogel flows with different precursors mixing and swirling together due to the presence of helical elements in microfluidic channels within a print head [50,51]. Researchers have demonstrated how this approach could combine continuous, high-throughput wet spinning with the orientation of separate compartments of different hydrogel precursors (between alginate and alginate-gelatin methacryloyl (GelMA) blends), resulting in 3D hydrogel microfibers with intrinsic 3D architectures, generated by flows alone and without the need for any additional entities (**Fig. IV-5**). The researchers demonstrated that chaotic flows enabled spinning fibers with incremental numbers of semi-parallel GelMA filaments within alginate ones, and these 3D hydrogel pockets were single-handedly capable of promoting muscle cell alignment and muscle-fiber-like maturation [51]. Previously, the team also applied a similar strategy of chaotic flows to create densely packed cellular structures, enabling *e.g.,* the creation of constructs where different degrees of intimacy between cancer cells and healthy cells could be obtained [52]. The combination of both concepts presents interesting opportunities for the high-throughput fabrication of fibers where multiple compartments can mimic the interaction between cancer cells and other microenvironment entities, approaching and miniaturizing important processes and providing very interesting platforms for therapy testing.

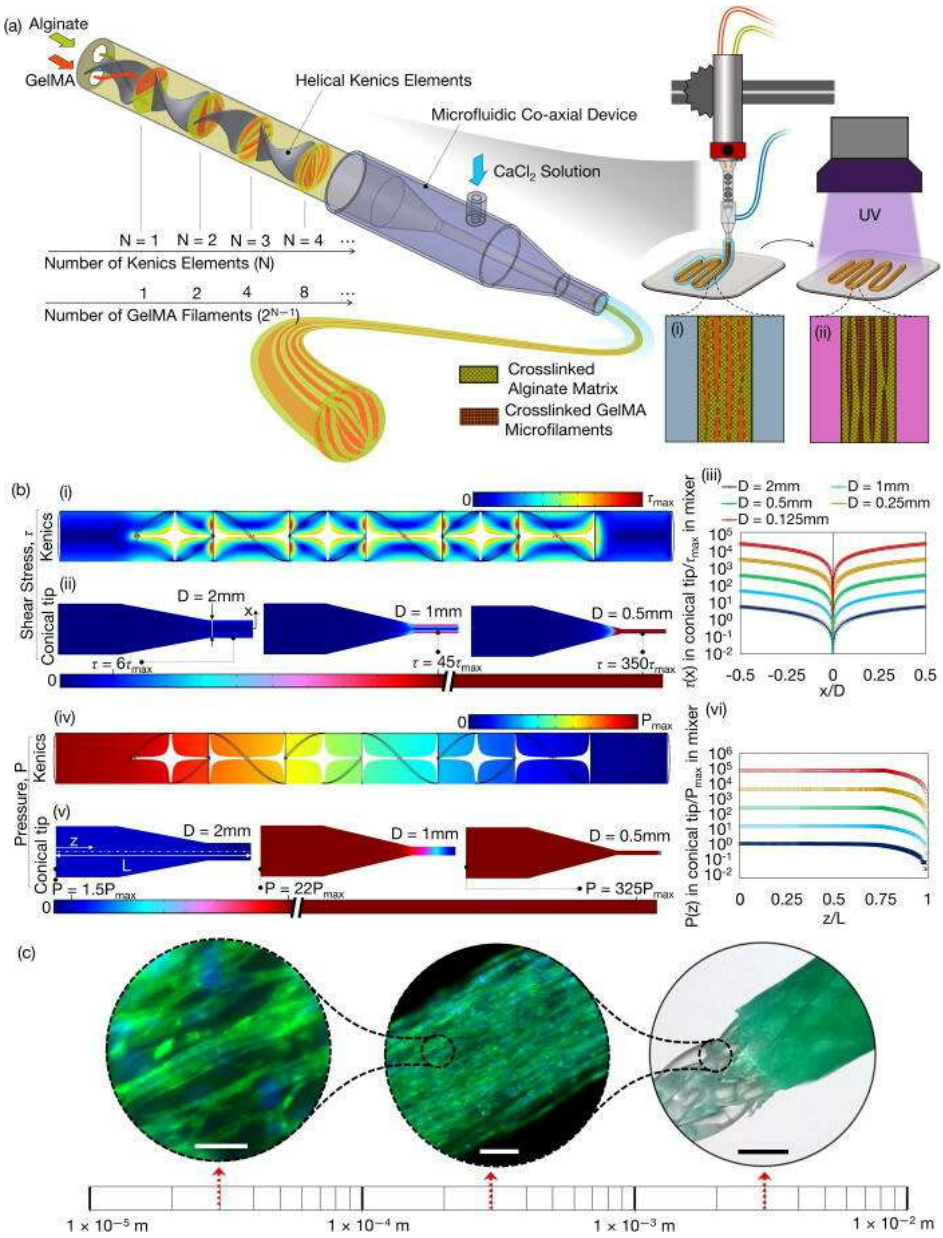


Figure IV-5: Chaotic generation of hydrogel fiber architectures with hydrogel compartmentalization and 3D cell/hydrogel alignment. Reprinted with permission from [53].

Indeed, the creation of hydrogel microfibers is a particularly powerful approach for cancer modeling. Using less chaotic, more organized 3D flow-focusing hydrogel biofabrication, it was also demonstrated how a single microfluidic setup could be employed together with the tuning of hydrogel precursor viscosity and the organization of flows within the chip, to create a plethora of multi-compartment hydrogel fibers with very small dimensions down to sub-50μm diameters [54] (**Fig. IV-6, A**). These unique microfibers were validated as suitable platforms to mimic and miniaturize important biological organizations, namely those present in cancer.

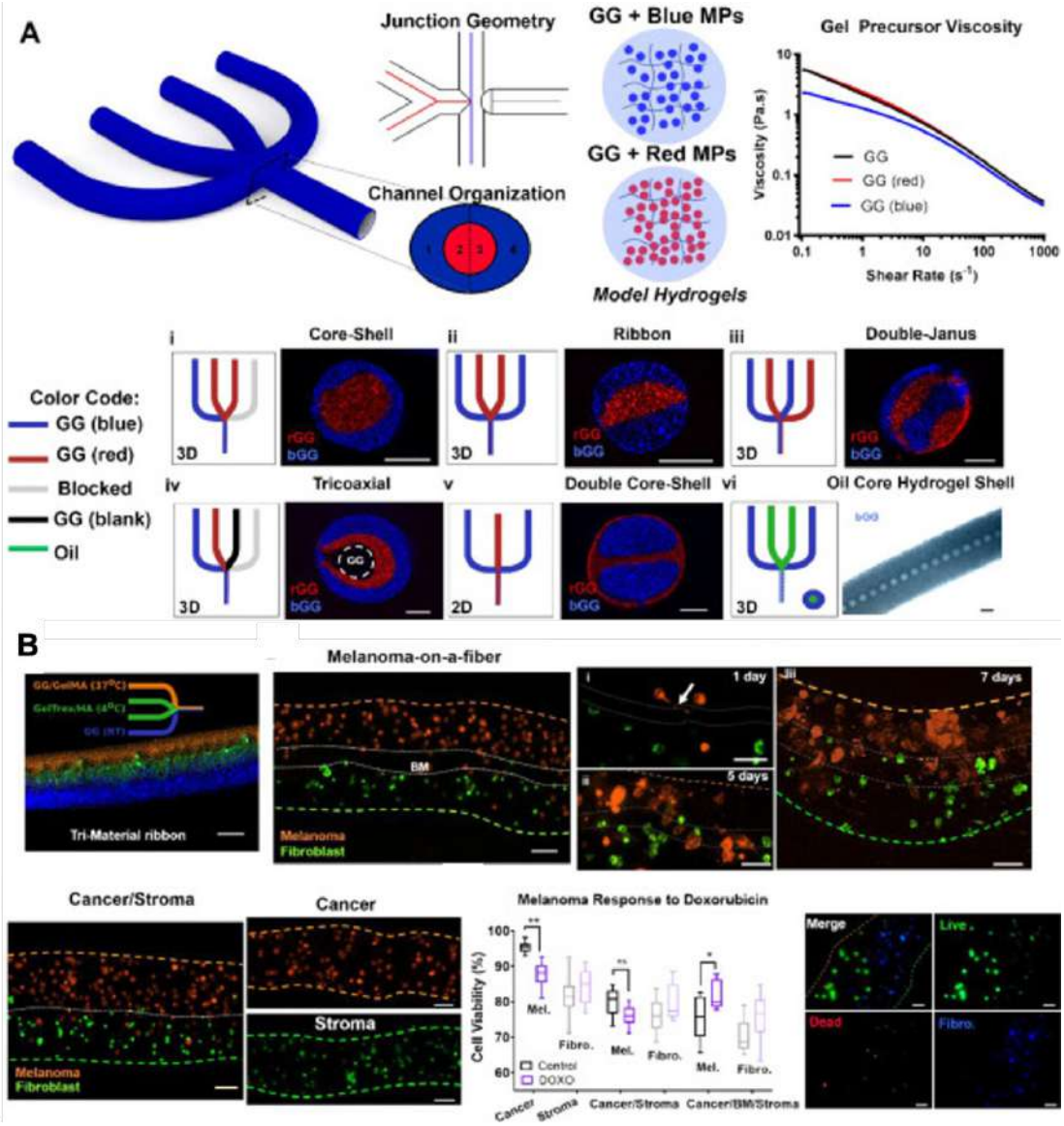


Figure IV-6: 3D Flow-focusing hydrogel biofabrication of multi-architecture hydrogel microfibers (A) and ribbon-like engineering of melanoma-on-a-fiber models (B). Adapted with permission from [54].

By exploring a specific shape, called ribbon-like, the team demonstrated that cancer/basement membrane/stroma compartments could be organized in a parallel manner, encapsulating melanoma cells in the cancer compartment, fibroblasts in the stromal one, and a thin basement membrane separating both, recreating the first steps of cancer cell invasion, potentially preceding metastasis (**Fig. IV-6, B**). The results demonstrated that the basement membrane invasion started as early as 1 day post fabrication, becoming more and more evident as the cancer cells overtook the construct invading towards the stroma. Furthermore, the team showed that the complexity of the 3D construct directly affected the outcome of cancer cell responses to doxorubicin, as their resistance to the drug increased

with higher model complexity. This results evidence how the recapitulation of tumor microenvironments in their multiple dimensions is important to obtain relevant responses in *in vivo* cancer models [54].

Moreover, it is also important to consider that modeling the 3D complexity of cancer microenvironments needs to be coupled with advances that enable the efficient analysis of ongoing biological processes, to derive clear and quantifiable data that can be used for next generation testing platforms and precision medicine approaches. In this regard, microfluidic biofabrication and microfiber compartment architectures may also present exciting opportunities by interfacing the engineering of 3D microtissues with advances in hydrogel optical fibers [55–58]. Very recent work has demonstrated that cytocompatible, polysaccharide-based hydrogel fibers could take advantage of co-centrical layers in order to clad a cell-laden fiber core with lower refractive index layers, to transport and maintain cancer cells while simultaneously enabling the guiding of light [59] (**Fig. IV-7, A**). In these living optical fibers, the team demonstrated that light-cell interactions could transport information regarding cellular events, such as metabolic activity, proliferation, and protein expression. By taking advantage of this process, the study demonstrated how the growth of cancer fiberoids (fiber-like organoids) could be tracked overtime *via* fast, non-destructive optical analysis, directly converting the complex process of cancer 3D proliferation to directly quantifiable optical data. This quantification was then leveraged to quickly screen and identify inhibitory thresholds of the anti-cancer drug cisplatin, easily pinpointing the concentration level at which the drug successfully inhibited 3D cancer growth (**Fig. IV-7, B**). The capacity to perform the digitalization of biological events presents exciting new avenues for the generation of biological data from cancer *in vitro* 3D models and paves the way for faster personalized medicine testing and precision, data-driven approaches.

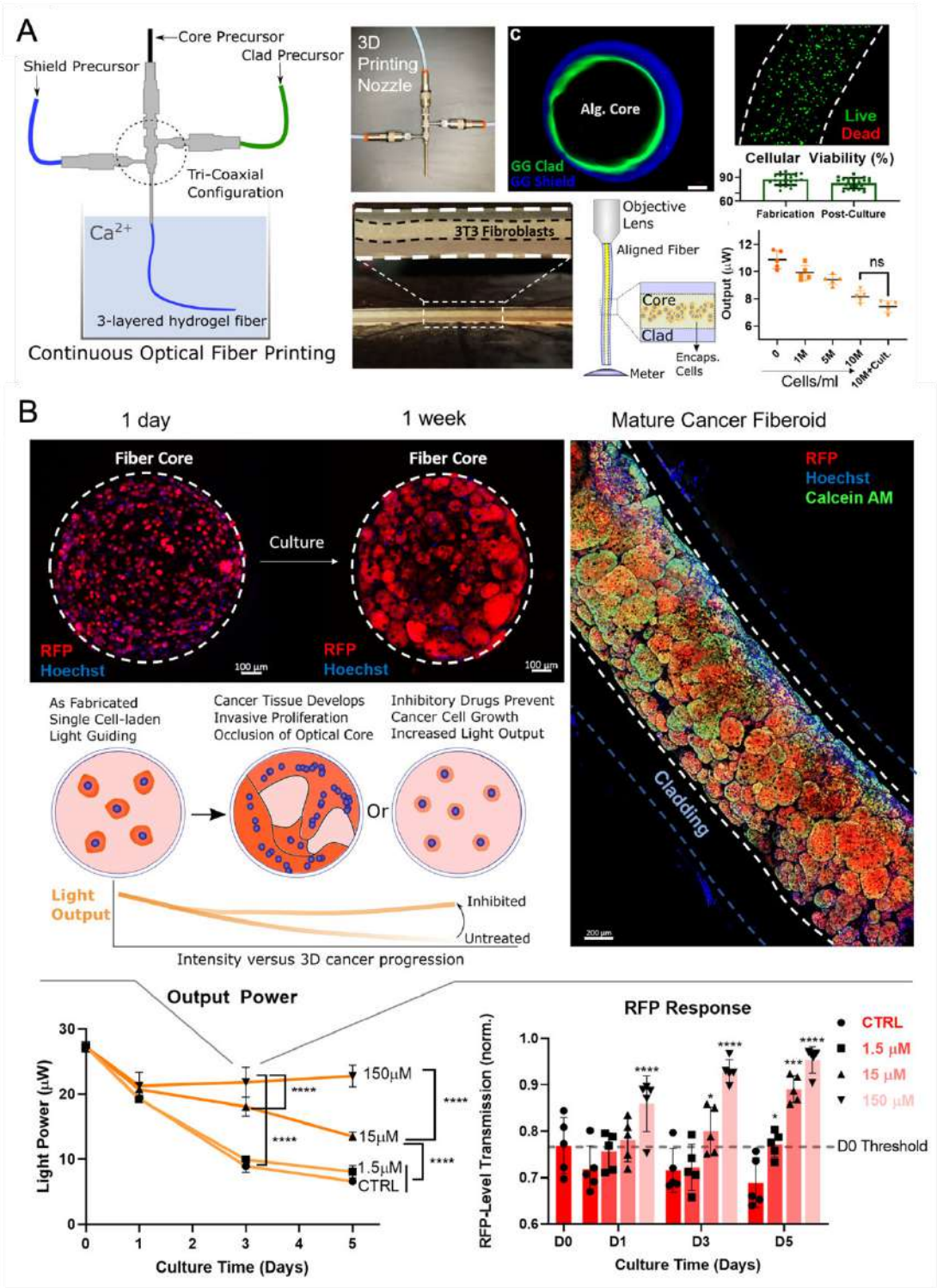


Figure IV-7: Biofabrication of living optical fibers based on multi-layered polysaccharide hydrogel fibers (A), and the conversion of 3D cancer fiberoid growth to directly quantifiable optical data for drug inhibitory threshold discovery (B). Adapted, with permission, from [59].

Overall, microfluidic biofabrication and, particularly, the continuous, high-throughput spinning of hydrogel fibers has presented very interesting technological advances, ranging from the creation

miniaturized microenvironments, with living tissue-like architectures, to the tackling of new challenges in the conversion of biological events into quantifiable data. Even though these hydrogel structures have evolved to integrate significant complexity within single fibers, the combination of microfluidic biofabrication with bottom-up, additive manufacturing approaches such as bioprinting, presents further possibilities for increasing dimensions and obtain further complex biological constructs and models, as discussed ahead.

IV.5. MICROFLUIDIC-ENABLED BIOPRINTING

So far, we have been discussing the possibilities for microfluidic-fabricated structures such as fibers or droplets to integrate a broad arrange of characteristics encompassing important materials, shapes, and cues within inner architectures that can mimic relevant biological environments. Even though these constructs can be seen as the final model, they can also serve as building blocks, which can further be assembled towards larger, more complex 3D structures. In particular, this process can be approached by leveraging 3D bioprinting principles to deposit and assemble microfluidic biofabricated building blocks [60,61].

An earlier example is that of using microfluidics to obtain two side-by-side, non-mixing flows, printing them as single fibers with two compartments, frequently named as Janus Fibers. This type of structures, unlike single-composition fibers, enable close contact between, *e.g.,* different cell populations [62]. For example, researchers 3D printed constructs with dual fibers containing fibroblasts and muscle cells, each in a different Janus-fiber compartment, assembling the construct and demonstrating improved *in vivo* integration when compared to a uniform hydrogel construct [63]. With the advances in microfluidic-driven bioprinter devices, the dual inlet chips evolved to more complex configurations, where multiple materials can be controlled as well as their crosslinking, employing independent channel pressures [64]. This type of approach has been explored to create 3D muscle tissue models that responded physiologically to a variety of biochemical stimuli [65]. Similarly, microfluidic bioprinting was used to create renal models, where core-shell configurations could be manufactured to approach renal tubules, with dimension and compartment size resolutions which are typically hard to approach with classical 3D printing nozzles [64]. These technological advances may further improve previously reported multi-material 3D printing approaches, where a single nozzle connected to a variety of hydrogel precursors can be controlled to alternate between deposited material on-demand, enabling *e.g.,* the creation of vascularized 3D models, which would be very interesting for approaching cancer

tissue vascularization modeling [66]. More recently, the integration of microfluidic-fabricated microgels within hydrogel inks has also been demonstrated as an interesting approach to obtain heterogeneous constructs with pockets of cell-laden hydrogels surrounded by an environment of a different bioink [67]. Even though the authors did not focus on cancer applications, this strategy can be very interesting to obtain micro-tumors surrounded by a distinct cellular environment in a byphasic composition that can be printed in an arbitrary shape (**Fig. IV-8**).

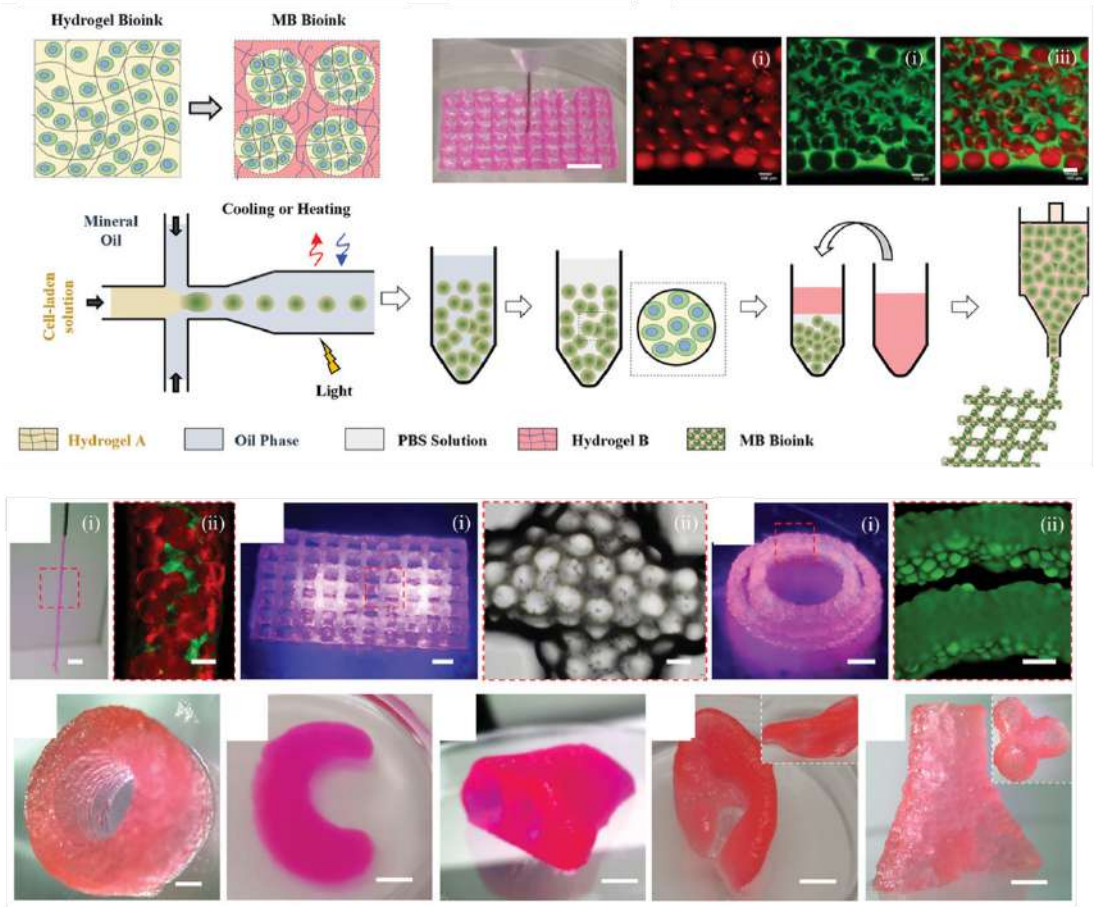


Figure IV-8: 3D Printing of heterogeneous bioinks via the combination of microfluidic biofabricated microgels within a uniform bioink blend for the integration of 3D cell-laden hydrogel depots within bioprinted constructs. Adapted, with permission, from [67].

Other than taking advantage of microfluidics to create complex, multi-compartment, but continuous fiber composition, the field of bioprinting has recently explored the capacities to obtain space-varying compositions. Microfluidics has been used to combine and mix different inputs, timing it with the 3D bioprinting deposition to obtain not only single fiber gradients but gradual composition changes in whole 3D printed constructs. By developing a custom print head where a coaxial extrusion nozzle received

material from a passive microfluidic mixer, which was connected to the inlets, researchers have shown how different bioinks could be deposited individually or together at the same time. By uniformly mixing inlet material before extrusion, the researchers were able to deposit layers with gradually changing composition toward approaching the osteochondral (bone-cartilage) transition [68]. In a more recent work, a similar concept was explored where a custom setup connected different material inlets to a chaotic mixer, and then to an outlet [69]. Researchers demonstrated how light-based crosslinking could then be used to crosslink multiple hydrogel layers that could contain intricate gradients of composition, in different shapes (**Fig. IV-9**). The team then used this process to fabricate 3D cancer cell density models, where the number of cancer cells decreased radially from the center, approaching the dense characteristic of highly hypoxic tumor centers. They also demonstrated the capacity to create complex vascular structures with gradually changing configuration and channel dimensions (**Fig. IV-9**). The combination of both types of models would be also extremely relevant to approach cancer vascularization and the hypoxic dynamics behind angiogenesis, blood vessel growth, and potential metastatic disease.

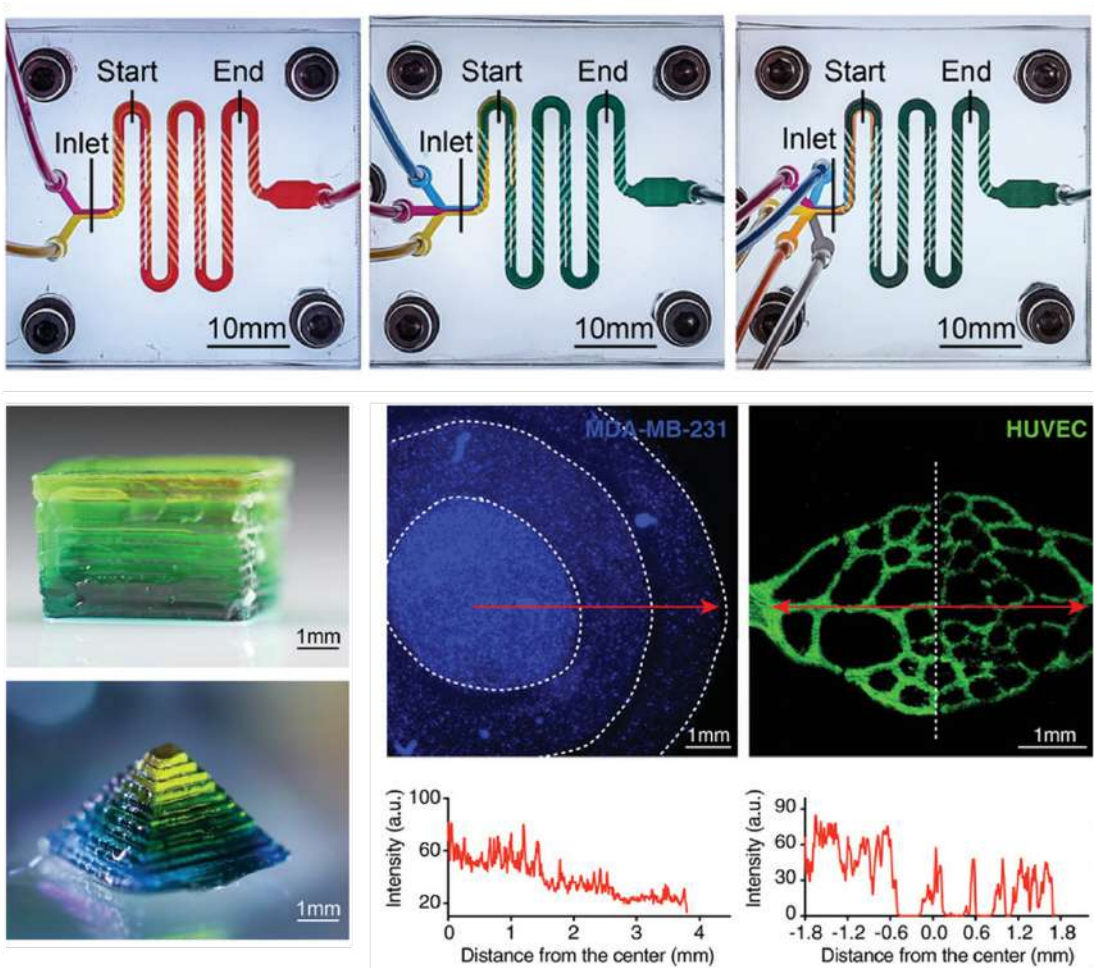


Figure IV-9: Microfluidic-enabled bioprinting for the assembly of complex 3D constructs with gradients in layer composition, and their application to density-varying breast cancer and complex vascular networks biofabrication. Adapted with permission from [69].

Another interesting combination at the interface of microfluidics, bioprinting, and biofabrication, is the creation of intricate 3D architectures within chips. This can be approached through different manners, namely by bioprinting structures directly inside microfluidic chips, such as vascular channels that can then be perfused in dynamic culture conditions, among other examples [70]. However, bioprinting directly within a microfluidic chip presents limitations, as either the printing resolution is not fine enough to create complex microfluidic architectures or, alternatively, the resulting chip presents very large dimensions and diverges from the main purposes of having a microfluidic setting. To overcome this, researchers have also developed maskless lithography, exploring the way materials flow within microfluidic conditions, and then "locking" them in a particular 3D configuration using light-based crosslinking [71]. Among other applications, this approach allowed for the creation of small tumor environments with a randomly distributed vascular-like network, all limited to an area of around 10mm^2,

which represents a very small size within which relevant 3D shapes could be miniaturized without the restraints of having to physically print them.

Overall, microfluidics has enabled very interesting advances in the field of 3D bioprinting by allowing the controlled deposition of different fiber shapes, as well as quickly altering between different inks in real printing time to create gradients and approach important transitions of living tissues both within health and disease contexts. It will be interesting to see how some of these advances come together soon, *e.g.,* how the combination of printed 3D cancer models may incorporate the advances in printing of blood vessel networks to recapitulate important events behind metastatic disease, which represents the highest disease burden scenario of most cancers. Similarly, the creation of more complex, multi-cellular constructs may provide important platforms to understand the complex cancer microenvironment crosstalk, as well as model the effect of next-generation, microenvironment-disruptive therapeutics.

IV.6. CONCLUSIONS

Microfluidic techniques present unique opportunities to miniaturize important characteristics of biological environments in fabricated structures, ranging from individual droplets to continuous fibers. The capacity to manipulate hydrogel precursors as liquids within low turbulence settings, allied with the broad toolbox that exists in hydrogel crosslinking on-demand, microfluidic biofabrication is primed to lead the field of biofabrication at the smallest of scales and highest level of 3D resolution. Indeed, microfluidic biofabrication has enabled important advances in the miniaturization of multi-compartment 3D constructs, as well as the particularly important space-varying composition creation, either from a high-throughput screening perspective or to simply recapitulate the complexity of living tissues.

In the specific case of cancer, the complexity of the diseased tissue and its similarity to an organ on its own, requires a paradigmatic shift in the way it is modelled *in vitro*, namely to integrate the multi-cellular dynamics of the microenvironment, as well as the ECM characteristics such as the typical fibrotic responses [72]. In this regard, microfluidic biofabrication has enabled important breakthroughs in the creation of complex multi-cellular, multi-material, and multi-compartment 3D architectures which can enable, e.g., closely monitoring cancer/stroma and basement membrane invasion dynamics. Indeed, the creation of 3D shapes within structures such as hydrogel fibers represents important

advances to model 3D cancer environments, but a further challenge remains: the way to translate ongoing biological events into quantifiable, comparable data.

Indeed, models are only useful if their complexity can be matched by means to extract data, where advances such as the integration of optical, electrical, thermal, and similar means of analyzing biological constructs such as 3D hydrogel fibers [59] or spheroids and organoids [73] will play an ever-growing role in future *in vitro* models. As the ways to analyze engineered constructs evolve, so does the amount of data which can be generated in brief amounts of time. This data will create unique opportunities for mining, analyzing, and creating large 3D biology model databases, where its interface with machine learning and other artificial intelligence algorithms may expand *in silico* modeling informed on 3D *in vitro* constructs. Simultaneously, those technologies can also be explored to drive the optimization of microfluidic biofabrication parameters, resulting in improved models, and so on and so forth in successive synergistic iterations [74,75].

Finally, the combination of microfluidic biofabrication with approaches that typically function at slightly different dimensions, such as 3D bioprinting, is also providing important advances where the powerful real-time material manipulation *via* microfluidics can be combined with 3D material deposition to create larger constructs. Thus, characteristics such as multi-compartment fibers and space-varying compositions can be translated to 3D printed constructs. This area can still evolve towards the unique combination of multiple structures, such as cancer hypoxic 3D environments and bioprinted vascular beds, leading to a significant step forward in the understanding of multi-entity events, such as those involved in metastatic disease [76]. Furthermore, it is still important to mention that microfluidic fabrication has also been employed for some time at smaller dimensions, namely for the fast fabrication of nanoparticles of different dimensions for drug delivery purposes [72,77,78]. Even if not so straightforward, it would be interesting to see advances where microfluidic nanosynthesis could be combined with biofabrication platforms to assess, for example, the interaction and distribution of nanoparticles in complex 3D cancer models as well as their therapeutic efficacy. These models are primed to partially replace *in vivo* animal studies while remaining closer to human physiology using human-derived cell sources.

After decades of cancer research and development of anti-cancer therapeutics, the societal burden of the disease is still among the highest, and several cancers are extremely hard to treat, especially those undergoing metastasis. Uncovering the intricate 3D complexity of the disease and the multi-entity interactions that contribute to the development and prognostics of cancer may likely hold the key for

next-generation therapeutics. In this context, the unique capacity of microfluidic biofabrication to miniaturize 3D biological environments in high-throughput fabrication and analysis setups is primed to open new avenues for cancer research by enabling unprecedentedly complex, easily adaptable models. Combining these models with tools for the direct quantification of biological events and data analysis is likely to unlock a whole new frontier in precision, data-driven cancer research and medicine.

IV.7. REFERENCES:

1. Guimarães, C. F., Gasperini, L., Marques, A. P. & Reis, R. L. The stiffness of living tissues and its implications for tissue engineering. *Nat. Rev. Mater.* **5**, 351–370 (2020).
2. Kalli, M. & Stylianopoulos, T. Defining the Role of Solid Stress and Matrix Stiffness in Cancer Cell Proliferation and Metastasis. *Front. Oncol.* **8**, (2018).
3. Mirdamadi, E., Tashman, J. W., Shiwarski, D. J., Palchesko, R. N. & Feinberg, A. W. FRESH 3D Bioprinting a Full-Size Model of the Human Heart. *ACS Biomater. Sci. Eng.* **6**, 6453–6459 (2020).
4. Bernal, P. N. *et al.* Volumetric Bioprinting of Complex Living-Tissue Constructs within Seconds. *Adv. Mater.* **31**, (2019).
5. Lee, J. M., Ng, W. L. & Yeong, W. Y. Resolution and shape in bioprinting: Strategizing towards complex tissue and organ printing. *Appl. Phys. Rev.* **6**, (2019).
6. Miri, A. K. *et al.* Effective bioprinting resolution in tissue model fabrication. *Lab Chip* **19**, 2019–2037 (2019).
7. Bakht, S. M. *et al.* 3D Bioprinting of Miniaturized Tissues Embedded in Self-Assembled Nanoparticle-Based Fibrillar Platforms. *Adv. Funct. Mater.* **31**, (2021).
8. Kato-Negishi, M., Onoe, H., Ito, A. & Takeuchi, S. Rod-Shaped Neural Units for Aligned 3D Neural Network Connection. *Adv. Healthc. Mater.* **6**, 1–7 (2017).
9. Grolman, J. M., Zhang, D., Smith, A. M., Moore, J. S. & Kilian, K. A. Rapid 3D Extrusion of Synthetic Tumor Microenvironments. *Adv. Mater.* **27**, 5512–5517 (2015).
10. Cheng, Y. *et al.* Bioinspired multicompartmental microfibers from microfluidics. *Adv. Mater.* **26**, 5184–5190 (2014).
11. Xu, P. *et al.* Bioinspired Microfibers with Embedded Perfusable Helical Channels. *Adv. Mater.* **29**, 1–7 (2017).
12. Cheng, Y. *et al.* Controlled Fabrication of Bioactive Microfibers for Creating Tissue Constructs Using Microfluidic Techniques. *ACS Appl. Mater. Interfaces* **8**, 1080–1086 (2016).
13. Gasperini, L., Mano, J. F. & Reis, R. L. Natural polymers for the microencapsulation of cells. *J. R. Soc. Interface* **11**, 20140817–20140817 (2014).
14. Young, S., Wong, M., Tabata, Y. & Mikos, A. G. Gelatin as a delivery vehicle for the controlled release of bioactive molecules. *J. Control. Release* **109**, 256–74 (2005).
15. Caliari, S. R. & Burdick, J. A. A practical guide to hydrogels for cell culture. *Nat. Methods* **13**, 405–414 (2016).
16. Ushikubo, F. Y., Birribilli, F. S., Oliveira, D. R. B. & Cunha, R. L. Y- and T-junction microfluidic devices: effect of fluids and interface properties and operating conditions. *Microfluid. Nanofluidics* 1–10 (2014). doi:10.1007/s10404-014-1348-4

17. Smeds, K. A. *et al.* Photocrosslinkable polysaccharides for in situ hydrogel formation. *J. Biomed. Mater. Res.* **54**, 115–121 (2001).

18. Heo, J. *et al.* Riboflavin-induced photo-crosslinking of collagen hydrogel and its application in meniscus tissue engineering. *Drug Deliv. Transl. Res.* **6**, 148–158 (2016).

19. Loessner, D. *et al.* Functionalization, preparation and use of cell-laden gelatin methacryloyl–based hydrogels as modular tissue culture platforms. *Nat. Protoc.* **11**, 727–746 (2016).

20. Jiao, J. & Burgess, D. J. Rheology and Stability of Water-in-Oil-in-Water Multiple Emulsions Containing Span 83 and Tween 80. *AAPS PharmSci* **5**, (2003).

21. Miller, R. Emulsifiers: Types and Uses. *Encycl. Food Heal.* 498–502 (2016). doi:10.1016/B978-0-12-384947-2.00249-X

22. Zhao, H. *et al.* Airflow-Assisted 3D Bioprinting of Human Heterogeneous Microspheroidal Organoids with Microfluidic Nozzle. *Small* **14**, 1–7 (2018).

23. Onoe, H. *et al.* Metre-long cell-laden microfibers exhibit tissue morphologies and functions. *Nat. Mater.* **12**, 584–590 (2013).

24. Kim, J. Y. *et al.* A Microfluidic Device to Fabricate One-Step Cell Bead-Laden Hydrogel Struts for Tissue Engineering. *Small* **2106487**, 1–17 (2021).

25. Canadas, R. F. *et al.* Biochemical Gradients to Generate 3D Heterotypic-Like Tissues with Isotropic and Anisotropic Architectures. *Adv. Funct. Mater.* **28**, (2018).

26. Yang, L. *et al.* High-Throughput Methods in the Discovery and Study of Biomaterials and Materiobiology. *Chem. Rev.* **121**, 4561–4677 (2021).

27. Burdick, J. a, Khademhosseini, A. & Langer, R. Fabrication of Gradient Hydrogels Using a Microfluidics/ Photopolymerization Process. *Langmuir* **20**, 8–11 (2004).

28. Pedron, S., Becka, E. & Harley, B. A. Spatially gradated hydrogel platform as a 3D engineered tumor microenvironment. *Adv. Mater.* **27**, 1567–1572 (2015).

29. Guimarães, C. F. *et al.* High-throughput fabrication of cell-laden 3D biomaterial gradients. *Mater. Horiz.* **7**, 2414–2421 (2020).

30. Grolman, J. M., Zhang, D., Smith, A. M., Moore, J. S. & Kilian, K. A. Rapid 3D Extrusion of Synthetic Tumor Microenvironments. *Adv. Mater.* **27**, 5512–5517 (2015).

31. Xin, S., Dai, J., Gregory, C. A., Han, A. & Alge, D. L. Creating Physicochemical Gradients in Modular Microporous Annealed Particle Hydrogels via a Microfluidic Method. *Adv. Funct. Mater.* **30**, (2020).

32. Highley, C. B., Song, K. H., Daly, A. C. & Burdick, J. A. Jammed Microgel Inks for 3D Printing Applications. *Adv. Sci.* **6**, (2019).

33. Kochetkova, M. & Samuel, M. S. Differentiation of the tumor microenvironment : are CAFs the Organizer ? *Trends Cell Biol.* 1–10 (2021). doi:10.1016/j.tcb.2021.11.008

34. Mahadik, B. P., Wheeler, T. D., Skertich, L. J., Kenis, P. J. A. & Harley, B. A. C. Microfluidic Generation of Gradient Hydrogels to Modulate Hematopoietic Stem Cell Culture Environment. *Adv. Healthc. Mater.* **3**, 449–458 (2014).

35. Ngo, M. T. *et al.* Hydrogels Containing Gradients in Vascular Density Reveal Dose-Dependent Role of Angiocrine Cues on Stem Cell Behavior. *Adv. Funct. Mater.* (2021). doi:10.1002/adfm.202101541

36. Liao, D. & Johnson, R. S. Hypoxia: A key regulator of angiogenesis in cancer. *Cancer and Metastasis Reviews* **26**, 281–290 (2007).

37. Wang, W., Li, L., Ding, M., Luo, G. & Liang, Q. A Microfluidic Hydrogel Chip with Orthogonal Dual Gradients of Matrix Stiffness and Oxygen for Cytotoxicity Test. *Biochip J.* **12**, 93–101 (2018).

38. Berger Fridman, I., Ugolini, G. S., Vandelinder, V., Cohen, S. & Konry, T. High throughput microfluidic

system with multiple oxygen levels for the study of hypoxia in tumor spheroids. *Biofabrication* **13**, (2021).

39. Zhu, D., Trinh, P., Li, J., Grant, G. A. & Yang, F. Gradient hydrogels for screening stiffness effects on patient-derived glioblastoma xenograft cellfates in 3D. *J. Biomed. Mater. Res. - Part A* **109**, 1027–1035 (2021).

40. Sutera, S. P. & Skalak, R. The History of Poiseuille's Law. *Annu. Rev. Fluid Mech.* **25**, 1–20 (1993).

41. Uludag, H., De Vos, P. & Tresco, P. a. Technology of mammalian cell encapsulation. *Adv. Drug Deliv. Rev.* **42**, 29–64 (2000).

42. Wong, T. Y., Preston, L. A. & Schiller, N. L. ALGINATE LYASE: review of major sources and enzyme characteristics, structure-function analysis, biological roles, and applications. *Annu. Rev. Microbiol.* **54**, 289–340 (2000).

43. Gasperini, L., Maniglio, D. & Migliaresi, C. Electro Hydro Dynamic (EHD) encapsulation of cells in alginate based hydrogels. in *International Journal of Artificial Organs* **34**, 685 (Wichtig Editore s. r. l., Via Friuli 72 Milan MI 20135 Italy, 2011).

44. Kuhn, P. T. *et al.* Double Linear Gradient Biointerfaces for Determining Two- Parameter Dependent Stem Cell Behavior. *ChemNanoMat* 10.1002/cnma.201600028 (2016). doi:10.1016/S0740-5472(96)90021-5

45. Zhou, Q. *et al.* Development of a Novel Orthogonal Double Gradient for High-Throughput Screening of Mesenchymal Stem Cells–Materials Interaction. *Adv. Mater. Interfaces* **5**, 4–11 (2018).

46. Zhou, Q. *et al.* Screening Platform for Cell Contact Guidance Based on Inorganic Biomaterial Micro/nanotopographical Gradients. *ACS Appl. Mater. Interfaces* **9**, (2017).

47. Araújo-Custódio, S. *et al.* Injectable and Magnetic Responsive Hydrogels with Bioinspired Ordered Structures. *ACS Biomater. Sci. Eng.* **5**, 1392–1404 (2019).

48. Rose, J. C. *et al.* Biofunctionalized aligned microgels provide 3D cell guidance to mimic complex tissue matrices. *Biomaterials* (2018). doi:10.1016/j.biomaterials.2018.02.001

49. Canadas, R. F. *et al.* Tunable anisotropic networks for 3-D oriented neural tissue models. *Biomaterials* **181**, 402–414 (2018).

50. Bolívar-Monsalve, E. J. *et al.* Continuous chaotic bioprinting of skeletal muscle-like constructs. *Bioprinting* **21**, (2021).

51. Samandari, M. *et al.* Controlling cellular organization in bioprinting through designed 3D microcompartmentalization. *Appl. Phys. Rev.* **8**, (2021).

52. Trujillo-De Santiago, G. *et al.* Chaotic printing: Using chaos to fabricate densely packed micro- and nanostructures at high resolution and speed. *Mater. Horizons* **5**, 813–822 (2018).

53. Samandari, M. *et al.* Controlling cellular organization in bioprinting through designed 3D microcompartmentalization. *Appl. Phys. Rev.* **8**, 21404 (2021).

54. Guimarães, C. F., Gasperini, L., Marques, A. P. & Reis, R. L. 3D flow-focusing microfluidic biofabrication: One-chip-fits-all hydrogel fiber architectures. *Appl. Mater. Today* **23**, (2021).

55. Guimarães, C. F., Ahmed, R., Marques, A. P., Reis, R. L. & Demirci, U. Engineering Hydrogel-Based Biomedical Photonics: Design, Fabrication and Applications. *Adv. Mater.* (2021). doi:10.1002/adma.202006582.

56. Elsherif, M., Hassan, M. U., Yetisen, A. K. & Butt, H. Hydrogel optical fibers for continuous glucose monitoring. *Biosens. Bioelectron.* **137**, 25–32 (2019).

57. Guo, J. *et al.* Highly Stretchable, Strain Sensing Hydrogel Optical Fibers. *Adv. Mater.* **28**, 10244–10249 (2016).

58. Yetisen, A. K. *et al.* Glucose-Sensitive Hydrogel Optical Fibers Functionalized with Phenylboronic Acid. *Adv. Mater.* **29**, (2017).

59. Guimarães, C. F. *et al.* Engineering Polysaccharide-Based Hydrogel Photonic Constructs: From Multiscale Detection to the Biofabrication of Living Optical Fibers. *Adv. Mater.* **n/a**, 2105361 (2021).

60. Ma, J., Wang, Y. & Liu, J. Bioprinting of 3D tissues/organs combined with microfluidics. *RSC Adv.* **8**, 21712–21727 (2018).

61. Richard, C., Richard, C., Neild, A., Cadarso, V. J. & Cadarso, V. J. The emerging role of microfluidics in multi-material 3D bioprinting. *Lab Chip* **20**, 2044–2056 (2020).

62. Colosi, C. *et al.* Microfluidic Bioprinting of Heterogeneous 3D Tissue Constructs Using Low-Viscosity Bioink. *Adv. Mater.* **28**, 677-684a (2016).

63. Costantini, M. *et al.* Microfluidic-enhanced 3D bioprinting of aligned myoblast-laden hydrogels leads to functionally organized myofibers in vitro and in vivo. *Biomaterials* **131**, 98–110 (2017).

64. Addario, G. *et al.* Microfluidic bioprinting towards a renal in vitro model. *Bioprinting* **20**, (2020).

65. Dickman, C. T. D. *et al.* Functional characterization of 3D contractile smooth muscle tissues generated using a unique microfluidic 3D bioprinting technology. *FASEB J.* **34**, 1652–1664 (2020).

66. Liu, W. *et al.* Rapid Continuous Multimaterial Extrusion Bioprinting. *Adv. Mater.* **29**, (2017).

67. Fang, Y. *et al.* 3D Printing of Cell-Laden Microgel-Based Biphasic Bioink with Heterogeneous Microenvironment for Biomedical Applications. *Adv. Funct. Mater.* 2109810 (2021). doi:10.1002/adfm.202109810

68. Idaszek, J. *et al.* 3D bioprinting of hydrogel constructs with cell and material gradients for the regeneration of full-thickness chondral defect using a microfluidic printing head. *Biofabrication* **11**, (2019).

69. Wang, M. *et al.* Digital Light Processing Based Bioprinting with Composable Gradients. *Adv. Mater.* (2021). doi:10.1002/adma.202107038

70. Sun, H., Jia, Y., Dong, H., Dong, D. & Zheng, J. Combining additive manufacturing with microfluidics: an emerging method for developing novel organs-on-chips. *Curr. Opin. Chem. Eng.* **28**, 1–9 (2020).

71. Miri, A. K. *et al.* Microfluidics-Enabled Multimaterial Maskless Stereolithographic Bioprinting. *Adv. Mater.* **30**, 1–9 (2018).

72. Chandler, C., Liu, T., Buckanovich, R. & Coffman, L. G. The double edge sword of fibrosis in cancer. *Transl. Res.* **209**, 55–67 (2019).

73. Park, Y. *et al.* Three-dimensional, multifunctional neural interfaces for cortical spheroids and engineered assembloids. *Sci. Adv.* **7**, (2021).

74. Galan, E. A. *et al.* Intelligent Microfluidics: The Convergence of Machine Learning and Microfluidics in Materials Science and Biomedicine. *Matter* **3**, 1893–1922 (2020).

75. Hakimi, O., Krallinger, M. & Ginebra, M. P. Time to kick-start text mining for biomaterials. *Nat. Rev. Mater.* **5**, 553–556 (2020).

76. Pape, J. *et al.* Cancer invasion regulates vascular complexity in a three-dimensional biomimetic model. *Eur. J. Cancer* **119**, 179–193 (2019).

77. Gimondi, S. *et al.* Microfluidic mixing system for precise PLGA-PEG nanoparticles size control. *Nanomedicine Nanotechnology, Biol. Med.* **40**, 102482 (2022).

78. Karnik, R. *et al.* Microfluidic platform for controlled synthesis of nanoparticles. *Nano Lett.* **8**, 2906 (2008).

Chapter V

ENGINEERING HYDROGEL-BASED BIOMEDICAL PHOTONICS: DESIGN, FABRICATION AND APPLICATIONS

ENGINEERING HYDROGEL-BASED BIOMEDICAL PHOTONICS: DESIGN, FABRICATION AND APPLICATIONS

Abstract

Light guiding and manipulation in photonics have become ubiquitous in events ranging from everyday communications to complex robotics and nanomedicine. The speed and sensitivity of light–matter interactions offer unprecedented advantages in biomedical optics, data transmission, photomedicine, and detection of multi-scale phenomena. Recently, hydrogels have emerged as a promising candidate for interfacing photonics and bioengineering by combining their light-guiding properties with live tissue compatibility in optical, chemical, physiological, and mechanical dimensions. Herein, the latest progress over hydrogel photonics and its applications in guidance and manipulation of light is reviewed. Physics of guiding light through hydrogels and living tissues, and existing technical challenges in translating these tools into biomedical settings are discussed. A comprehensive and thorough overview of materials, fabrication protocols, and design architectures used in hydrogel photonics is provided. Finally, recent examples of applying structures such as hydrogel optical fibers, living photonic constructs, and their use as light-driven hydrogel robots, photomedicine tools, and organ-on-a-chip models are described. By providing a critical and selective evaluation of the field's status, this work sets a foundation for the next generation of hydrogel photonic research.

This chapter is reproduced from the following publication:

Guimarães, C. F., Ahmed, R., Marques, A. P., Reis, R. L., & Demirci, U. (2021). Engineering Hydrogel-Based Biomedical Photonics: Design, Fabrication, and Applications. *Advanced Materials*, *33*(23), 2006582.

V.1. INTRODUCTION

Looking into their past and current applications, hydrogel materials are proven to be versatile tools in biomedicine [1–4]. Since the earliest reports on hydrogel fabrication and their initial applications, their use and applications have been growing considerably and continues to do so. They are opening new avenues of research and development in fields such as tissue engineering and regenerative medicine, not only as biomaterials [5–8] but also creating more advanced and recent applications such as hydrogel machines [9] and 3D organ-on-a-chip technologies [10,11]. Among the different fields where hydrogels have been used, one can find a more recent niche of applications in guiding and manipulating light. From the time Leonardo da Vinci first schematized the most primitive contact lenses in the 1500s, it would take until the 1960s for their soft versions to be fabricated using synthetic hydrogels, such as poly(2-hydroxyethylmethacrylate) (pHEMA). In fact, this was likely the first true biomedical use of hydrogels as we know them today [12]. From that point onwards, hydrogel research gained gradually increasing momentum and the complexity of these materials grew accordingly. The first studied hydrogels (1960s) were mainly employed as cross-linked meshes with interesting swelling and mechanical properties, which then gave birth to responsive hydrogels (1970s), whose swelling behavior can change as a response to environmental conditions, such as pH [13]. It did not take long for scientists to combine these highly hydrated meshes with sound nutrient diffusion as supportive environments for cells. The 1980s were particularly transformative in that regard, as Langer and Vacanti established the concept of tissue engineering [14] and Lim and Sun reported seminal work on cell encapsulation within hydrogel structures [15]. In the tissue engineering field, hydrogels were increasingly employed, wet, dried, or cryo-modified, to fabricate the most distinct structures: ranging from nanoscale [16,17] to macroscale dimensions [18,19], with increasing complexity, stimuli responsiveness, swelling, and degradation properties. With time, these types of hydrogels were translated both commercially and clinically, finding many applications as reviewed recently elsewhere [20,21]. Consequentially, the hydrogel market has also grown considerably and is predicted to reach a value of over 15 Billion USD by 2022 [21].

Overall, what makes hydrogels so unique is the fact that these are highly hydrophilic, viscoelastic self-supporting meshes, composed mostly of water like so many biological tissues [22] and also have

mechanical properties in the relevant ranges for living tissues [23]. These properties make hydrogels some of the most suitable candidates for supporting, transporting, and releasing cells and other biological entities such as growth factors and proteins [24–27].

Further, in parallel to hydrogels' direct biological uses, these materials revealed themselves as essential tools in other fields [28–30]. Of note, it did not take long for these highly hydrated, responsive meshes to populate the optical field with exciting applications. After the advent of laser light and the simultaneous emergence of the first hydrogel soft lenses (1960), the first 3D holograms were obtained using Gelatin [31,32]. This very early advance likely represents the first optical application of a natural hydrogel. Despite this report of natural hydrogel holograms dating 60 years ago, the combination of optics and hydrogels directly applied to the biomedical field is a recent development. Henceforth, this topic constitutes the scope of this review.

Initially, we review hydrogels' properties in biomedical photonics, specifically focusing on the behavior of light within biological interfaces and the requirements for hydrogels to serve as photonic entities, *i.e.*, to guide and manipulate light. Within that context, we establish a comparison between hydrogels and classic solid-state optical materials, focusing on integrating such structures within biological environments, evaluating their compatibility with living entities such as cells and tissues. From there, we review what techniques have been employed in the past to fabricate optically relevant hydrogel structures. From earlier film assembly techniques to more recent 3D fabrication approaches, we also comment on how advances in different fields such as tissue engineering and bioprinting can be translated or combined with optical hydrogel architectures. Then, we cover the up-to-date hydrogel optical structures and their respective biomedical applications. Starting with the earliest thin hydrogel-film-photonics, we gradually move to more advanced systems such as optical hydrogel fibers and bioinspired structural hydrogels. These different arrangements and designs have been explored for different purposes within the biomedical field. They have proven to be powerful tools in optical sensing, light guiding, and other optical applications, as reviewed in section 4.

Previous reviews have summarized advances in the biomedical applications of hydrogels from various perspectives [33–36], some of which have recently evaluated previous applications of hydrogel photonic constructs [37]. In this review, we cover some of these topics, provide an update on recent advances, and mostly focus this knowledge on how such photonic systems might evolve in the coming

years and integrate distinct fields in a cross disciplinary manner with parallel advances, informed by current trends. In that sense, we discuss possible avenues to increase such systems' functionality through multi-responsive constructs, where optical properties can be combined with electrical or magnetic responsiveness for increasing sensing capabilities and/or manipulation and structuring of hydrogel constructs. Additionally, we delve into the optical interface between engineered hydrogels and live cells, where photonics might be combined with both entities to create next-generation *in vitro* platforms. In these systems, we discuss how tissue emulation or disease reconstruction might be combined with real time, label free sensing or light actuation, namely, for inducing motion in hydrogels – the basal requirement for creating and controlling movement in micro-sized architectures (microrobots).

Additionally, it is crucial to consider that light might not be simply of interest for stimulating and sensing different phenomena but rather be delivered to specific locations within the body for therapeutic purposes. With that in mind, we look at the current landscape of hydrogel-based photomedicine, where exciting new progress on light-based multifactorial tumor therapies and tissue regeneration have come to light in the past few years. On a smaller scale, one might not only consider the full living organism as an essential target but also state of the art in recreation and micro-modeling of biological tissues and organs. Through that perspective, we explore the role of hydrogels and their interactions with light using organ-on-a-chip models, where optical signals might be employed towards the fabrication of complex 3D architectures on-chip. Simultaneously, we discuss the possibility of integrating photonic hydrogel sensing components within those micro-sized biological environments, where small and fast optical readouts might lead to advances with transformative potential.

Bringing together all these distinct topics, we outline the current state of the art for hydrogels in biomedical photonics critically and selectively. We discuss the current caveats of these novel applications of hydrogel structures and outline which new research avenues might arise soon, considering the ongoing technological advances. By connecting seemingly distinct fields through an optics-focused perspective, we set a roadmap for integrating advanced light-hydrogel materials, constructs, and designs in a broad array of novel biomedical platforms and applications.

V.2. HYDROGEL-BASED PHOTONICS

Photonics can be briefly described as the guidance and manipulation of light, regardless of its varying characteristics, mostly through specific structures that interact with light [38–40]. Naturally, light guidance cannot be achieved without particular settings, *e.g.*, transparency, as opaque materials will not allow photons to move through but rather block them. Therefore, several photonics applications use surfaces with distinct topographies, in which air is the medium of light-wave propagation. In most cases, light waves' interaction with surface structures such as edges leads to diffraction or plasmonic resonances and consequent changes in properties such as wavelength (colors in the visible range). This process is the basis for several surface-based nanophotonic systems, which have been reported in the past decade for biomedical applications such as sensing and diagnostics [41,42]. In that context, a specific readout marks the presence of a particular analyte of interest. As such, there is a need to guide light and ensure that an analyte's presence will lead to detectable changes in the incident light properties.

On the other hand, to simply guide light, there doesn't need to be a specific change in light properties but rather a way to contain and direct it across space with, *e.g.*, optical fibers. Therefore, the type of structure and its interactions with light will depend on the intended application. Their different properties have led to their use for various purposes in hydrogels, from structural photonics to more general fiber optic light-guiding. In the following sections, we discuss the behavior of light in the hydrogel and living tissue environments. We describe which parameters should be taken into account for balancing different optical events, such as transmission, loss, or scattering, to design hydrogels as complementary alternatives to the classical materials in the biomedical optics field.

V.2.1. Optical coupling losses at the material/tissue interface

Hydrogels, just as any other material, interact with light leading to multiple fates upon such contact. The light might either be transmitted or reflected, scatter after colliding with specific structures that will change its direction of propagation, leave the medium, or be contained within *via* the phenomenon of total internal reflection (TIR) (**Figure V-1**). Even though hydrogels and biological tissues share similar water-based environments, biological tissues' complexity goes far beyond simple polymeric meshes. As a very complex and multi-organized structure, biological tissues are lossy for light propagation: as waves interact with tissues, they suffer from absorption and multiple scattering [43],

which significantly reduce light intensity over traveled distance. It takes less than 1 mm of penetration in soft tissues for light intensity to reduce to 37% (1/e) [44]. Hence, the power required for light to reach as deep as human subcutaneous tissue might already have to be above the safety thresholds (4 W cm^{-2}), naturally depending also on wavelength and exposure [44]. For a millimeter of penetration depth, soft biological tissues have losses in the range of tens if not hundreds of dB cm^{-1}. For comparison, solid-state materials such as silica used in optical fibers can have optical losses as low as 0.2 dB Km^{-1} [45]. However, despite their favorable light-guiding properties, solid-state materials have a critical biomedical limitation, *i.e.*, they are far from compatible when interacting with biological tissues [46]. This challenge has led the scientific community to look for alternatives that could bring together biological compatibility with proper light guidance in biological tissues.

Other than light to travel through materials, one other relevant optical parameter is the refractive index, *i.e.*, how light slows down in a particular medium compared to vacuum [47]. As a baseline reference, the refractive index for water (n) is 1.33. While classical solid-state materials have a considerably higher refractive index (up to 1.55 for silica oxide-based materials), biological tissues, most of which have high portions of water [22], have n ranging from 1.38 to 1.42 [48]. This significant mismatch also makes classic solid-state materials problematic in an optical context: high refractive index differences lead to inherent coupling losses as light tends to reflect to its origin, as observed in optical fiber-air interfaces. When combined, both the low biological compatibility and refractive index mismatch make solid-state materials sub-optimal for integration with biological tissues. Even though solid-state optical materials can be found in the biomedical field in the form of optical fibers such as in endoscopes, they are mainly employed to look at inner cavities and surfaces [49,50]. So far, these materials have not been directly integrated into biological tissues for potential long-term, real-time monitoring applications. The search for a material that would combine optical guiding capabilities with biological compatibility (both without toxicity and optical mismatch) points to hydrogels as a potential candidate (**Figure V-1**).

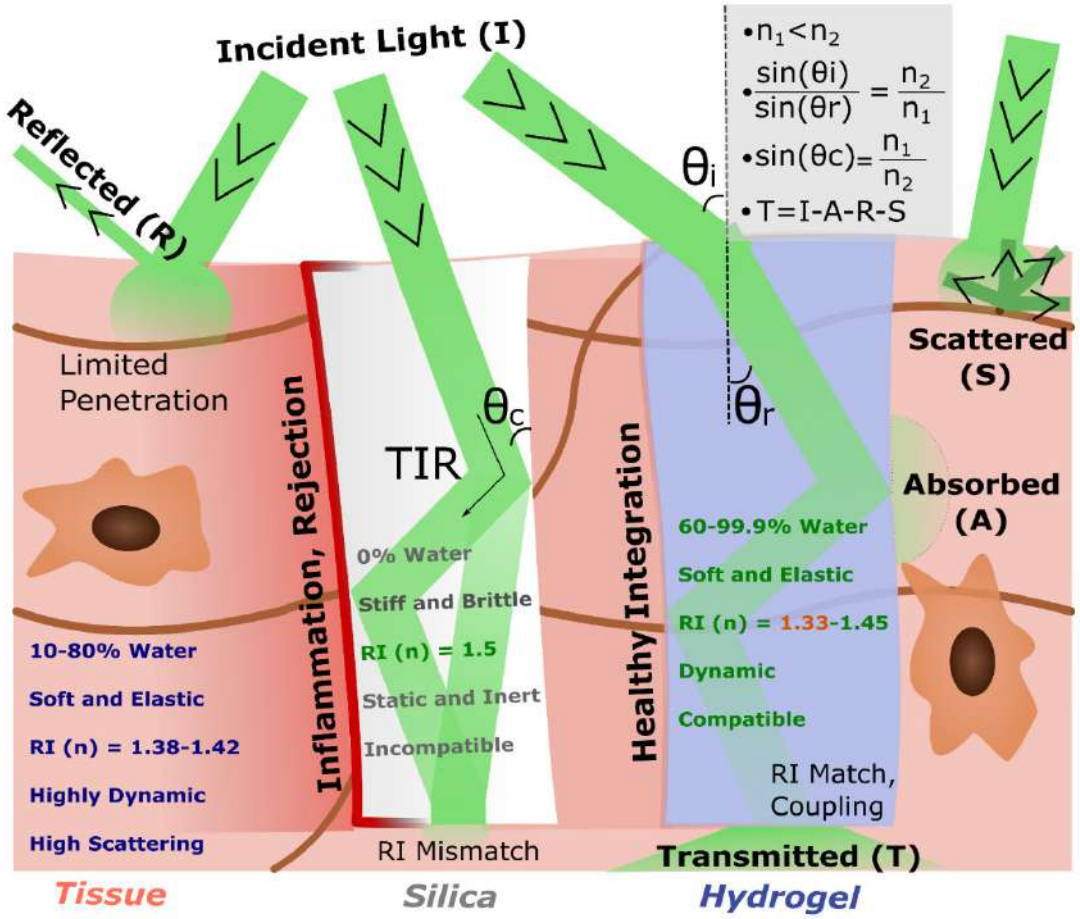


Figure V-1: Overview of Hydrogel Optics. Schematic of the main events behind light going through biological tissues, solid-state silica, and hydrogels. The denser media have inherently higher refractive indexes (n_2), leading to a slowing down of light going through and an angle of refraction (θ_r) inferior to that of incidence (θ_i). The refractive index difference allows for total internal reflection (TIR) when the incident angle is equal or below the critical angle (θ_c), containing light within the denser material. This process leads to coupling losses when there is a high refractive index difference (mismatch), as with silica *versus* living tissues. The light which is transmitted (T) results from the Incident light (I) minus the light that is reflected (R) and/or scattered (S). The general mathematical equations that connect these different concepts, namely Snell's Law, are represented on the right panel. An overview of the main properties that make hydrogels more like biological tissues than classical solid-state alternatives is also outlined.

V.2.2. Hydrogel requirements as photonic entities

Naturally, for hydrogels to perform well in optical settings, the requirement that these materials need to fulfill are different from those commonly looked after for applications in tissue engineering and regenerative medicine [4,51]. On the one hand, it is essential to maintain these materials' cytocompatibility

to the greatest extent possible to introduce them in biological environments. However, beyond biological compatibility, other characteristics might be needed depending on whether the goal is to guide light or rather to engineer a way to manipulate changes in the incident light. These changes are relevant when considering the need to obtain a responsive system (*e.g.*, sensing and diagnostics).

When pursuing sensing applications, a shift in a detectable response marks the target entity's presence to be detected. In optical terms, a change in light properties happens as a response to the target molecule/structure's presence to be detected. Throughout the literature, different approaches for engineering such responsive systems, several of which are connected with structural coloration, are described ahead. As previously referred to, light propagates as waves that interact with specific structures (*e.g.*, edges or slits), leading to diffraction (bending), refraction (changing direction), or plasmonics (resonance). Typically, edges, slits, and other geometric structures are not commonly present in hydrogels. In fact, hydrogels are naturally isotropic structures with no specific shape or orientation unless engineered to obtain anisotropic features such as mesh alignment or space-varying porosity [52,53]. As such, one of the main challenges for hydrogel photonics is engineering structures into the hydrogels, either in bulk or on the surface. Using distinct patterning and structuring techniques, hydrogels can have optical interactions that alter when the hydrogel contacts the target analyte. Frequently, hydrogels and analytes' interactions lead to a swelling/deswelling behavior that will change (expand/contract) the patterned structure, leading to a shift in the characteristics of incident light and therefore creating a readout signal [54,55].

In a distinct context, one’s goal might be to guide light and not necessarily have it change properties. In this case, the main challenge then becomes the length at which light guiding is effectively done with minimal loss. Earlier [44], simple rectangular hydrogel slabs were used to encapsulate cells and transmit light. Taking advantage of the material's transparency and the 1.35 refractive index of PEG 10wt% being higher than that of air (n close to 1), light traveled throughout the gel in a zig-zag fashion. This phenomenon, which we discussed in section 2, is due to total internal reflection (TIR) and is also present in standard optical fibers that are coated with a material (cladding) with a lower refractive index than that of the silica core [56]. However, biological tissues have a refractive index closer to those of hydrogels (**Figure V-1**), making light-guiding within tissues and across more extensive lengths a considerable challenge, which led to the development of hydrogel optical fibers - explored later in this review.

Overall, one can bring hydrogels' requirements for light guiding and manipulation down to two essential parameters. The first is transparency, which ensures that light can move through the material. The second is structure, which provides that either light can be guided throughout the material over significant lengths (*e.g.*, through layers with different refractive indices) or interact with light, giving rise to measurable changes as a response to the presence of target analytes. As such, when devising any optical hydrogel architecture, there are two essential points to reflect upon. (i) The choice of polymer, with all its accompanying characteristics in terms of transparency and refractive index, and (ii) the fabrication technique, which will be responsible for giving the material a specific structure. Both points are reviewed in the following sections.

V.2.3. Common polymers in optical hydrogels

The choice of polymers to fabricate hydrogel structures in the optical context needs to be informed by the hydrogel's distinct characteristics and requirements for specific applications, which can vary greatly (**Table V-1**).

When using hydrogels for optical applications, the material's interaction with light is likely the most critical parameter to consider, together with properties like transparency or particular refractive indices, as previously discussed. Nevertheless, the complexity of optical hydrogel systems in the biomedical field might require different characteristics, such as biological compatibility, which also need to be considered when deciding the material to use.

Overall, both natural and synthetic polymers have been used for different optical applications (Table V-1). Synthetic polymers are frequently used to fabricate hydrogels due to the ease of their modification and the ability to obtain tunable responses with a higher degree of reproducibility in terms of material consistency, mechanical properties, degradation rates, and optical transparency [57,58]. Acrylamide-based hydrogels are among the most commonly used for optical applications, being employed in the core of hydrogel optical fibers and thin hydrogel films that are discussed later in detail in Sections 3 and 4 [59,60]. These acrylamide-based structures can be functionalized with chemical moieties, *e.g.,* phenylboronic acid towards glucose sensing, or simply take advantage of swelling/de-swelling events for detecting changes in pH and other target analytes [61,62]. Interestingly, acrylamide/methacrylamide blends were proposed to overcome one significant limitation of hydrogels, *i.e.*, their high water content and consequent low refractive indices (close to water). Reducing hydrogels'

water content leads to an increase in the refractive index but brings significant cytocompatibility challenges. By manipulating the ratio of both acrylamide variants, researchers tuned these hydrogels to achieve a high, silica-like refractive index (n=1.53) in a structure still containing major water content (66%), remaining transparent and compatible with skin cells [63]. Overall, acrylamide has been reported as a versatile platform for optical hydrogel development, further capable of enduring considerable mechanical stretching, which can be employed for strain sensing [59]. Poly(ethylene glycol) (PEG) has been used as a versatile hydrogel in similar settings, namely within optical fiber cores [62,64–66]. PEG is modified for sensing applications such as glucose and metal detection, more frequently in its PEGDA (PEG diacrylate) form, which allows for UV crosslinking within molds [65]. In fact, crosslinking is also an important parameter, which depending on the experimental setting, might weigh heavily on the polymer choice [67,68]. While UV crosslinking is useful for obtaining fiber-like PEGDA structures [65] or complex structural colored gelatin methacryloyl (GelMA) hydrogels [69], thermal crosslinking might be easier to employ for fabricating gelatin layers and films [70,71]. Ionic crosslinking might be a quick and straightforward way to create alginate cladding layers in optical fibers, bringing the advantage of its high water content and low refractive index [59,64–66]. Alginate and gelatin are two examples of natural polymers used extensively in the optical context, starting with the early hydrogel optical experiments with gelatin [31,32]. Nevertheless, other natural polymers were shown to perform just as well in optical terms, combining transparency and light guiding capabilities with similar natural degradability and even biological compatibility [72,73]. Examples of such polymers are agarose [70,74], cellulose [75], silk fibroin [76] and chitosan [77]. All of these polymers have been classically used for tissue engineering and regenerative medicine applications [78,79]. The fact that they have also been validated within the optical context suggests that future innovation might bring together 3D cellular engineered structures with light guiding and manipulation, with interesting possibilities for *in vitro* tissue/disease modeling. Simultaneously, it can allow for the integration of real-time sensing and detection of relevant events such as pharmacological responses and overall drug testing, as discussed in the organ-on-chip section 9.

Globally, the choice of polymer for biomedical hydrogel photonics needs to integrate distinct properties depending on how closely the construct is designed to integrate into biological environments. For biomedical platforms used to screen analytes at the bench and not integrate into tissues, the choice

might be of synthetic polymers that can be widely modified without concerns for biological compatibility. In order to integrate optical constructs into biological tissues, other properties such as biocompatibility need to be considered. In this context, naturally derived polymers can potentially receive increased interest for applications where intricate cell-material interactions might be wanted.

Similarly, some naturally derived polymers can easily be degraded in the tissues, which is relevant for designing implantable constructs that degrade with time, avoiding removal surgery if no longer needed. Naturally, degradability is a very elaborate process involving changes in structure, mechanics, and optical properties. While it is not the scope of this review to delve into the complex changes of biodegradability in biomaterials, it is essential to highlight that the process of degradability is most likely to comprise optical performance of the biomedical constructs. As such, engineering degradable photonic devices depends on the stability required for the material to perform as desired, delaying any considerable degradation to the point where the construct is no longer needed, and removal surgery can therefore be avoided.

Nevertheless, the material alone is not always sufficient to create complex optical/biological architectures, fabrication steps are also essential to give shape and structure to the final construct, as discussed in the fabrication techniques section 3.

Table V-1: Commonly Used Polymers in Hydrogel-based Photonics.

Material	**Source**	**Type of Structure**	**Exploited Property**	**Application**	**Refs.**
Alginate	Natural (Seaweed)	Optical Fiber Shell (Cladding)	Low Refractive Index	Optical Fiber Sensing	59,64–66
Alginate	Natural (Seaweed)	Optical Bioinks	Adequate Printing Rheology, Particle Encapsulation	O_2 Imaging	80
Agarose	Natural (Algae)	Thin Films	Electrostatic Interaction with Carbon dots	Heavy-Metal Sensing	81
Agarose	Natural (Algae)	Linear Fibers, Cladding layers	Cytocompatibility	Waveguide	70,74
Acrylamide	Synthetic	No-Core Fiber	Analyte-induced Refractive index changes	Ph Sensing, Glucose sensing	61,62
Acrylamide	Synthetic	Optical Fiber Core	Mechanical Stretchability	Strain Sensing	59
Poly-Acrylamide	Synthetic	Thin Films	Easy Functionalization	Glucose Sensing	60
Acrylamide/Methacrylamide	Synthetic	Classic Hydrogel	High Refractive index, high water content	Ophthalmological	63
Polymethacrylic Acid (PMAA)	Synthetic	Thin Films	Ph Sensitivity	Ph Sensing	82

Poly(ethylene glycol) Diacrylate (PEGDA)	Synthetic	Optical Fiber Core	High refractive index	Glucose Sensing, Metal Sensing	62,64–66
Poly(2-vinyl pyridine) P2VP	Synthetic	Thin Films	pH Responsiveness, dynamic swelling	pH Sensing, molecule-induced changes	83,84
Poly(hydroxy-ethyl methacrylate) (PHEMA)	Synthetic	Thin Films	UV Crosslinking, Ion perfusion	Holographic pH Sensing	85
Chitosan	Natural (Chitin)	Hydrogel Photonic Crystals	No particular property	pH Sensing	86
Chitosan	Natural (Chitin)	Lbl films with Dextran	Charge Interactions with Dextran	Glucose Sensing	77
Gelatin	Natural (Collagen)	Uniform Layer Core	Thermal Crosslinking, Transparency	Waveguide	70
Gelatin	Natural (Collagen)	Thin Films	Thermal Crosslinking	Holographic Retroreflection	71
Gelatin/Alginate	Natural	Thin Films	Tunable pH Swelling	pH Sensing	55
Gelatin Methacryloyl (GelMA)	Natural Modified (Collagen)	Inverse Opal Scaffold	UV crosslinking on templated structures	Structural Colored Hydrogels	69,87
Cellulose	Natural (Plants)	Multi-core Fibers	Degradability	Waveguide	75
Silk Fibroin	Natural (Silk)	Core (film) – Clad (hydrogel) structures	Biological Compatibility, Transparency	Waveguide	76,88

Abbreviations: Lbl – Layer-by-layer

V.3. TECHNIQUES FOR FABRICATING PHOTONIC HYDROGEL CONSTRUCTS

Different fabrication strategies have been adopted to create photonic hydrogel structures (**Figure V-2**), with the earliest ones focusing on creating thin hydrogel films by deposition onto clean surfaces. Even though there might be slight variations in the specific protocols to develop these films depending on the processing requirements of the materials (*e.g.* temperature, type of crosslinking), two main fabrication routes are used to create hydrogel thin films (**Figure V-2, a**). The first and most straightforward one consists of depositing the hydrogel precursor onto a clean surface and then crosslink the precursor through various means, including chemical, thermal, or light-based (UV) stimuli. This type of approach has been used for fabricating synthetic films such as acrylamide ones [60] or natural gelatin-alginate films [55]. In this technique, there are essentially two critical steps for obtaining the thin film configuration. The first is the attachment of the hydrogel to the working surface [89] with the deposition of a thin layer, which is frequently done through spin coating techniques that use centrifugal forces to uniformly deposit materials on a surface, leading to hydrogel films ranging from tens to hundreds of micrometers in thickness [89]. The second widely used approach to fabricate hydrogel thin films is based on layer-by-layer assembly. This method uses sequential and alternated deposition of differently charged (positive *versus* negative) polymer solutions, which will gradually assemble on top of each other, growing towards a thin film [90]. The number of deposited bilayers will then dictate the thickness of this film. Each molecular bilayer is naturally very thin (nanometer-sized). As such, hundreds of bilayers are needed to reach thicknesses of hundreds of micrometers [91] as those obtained by spin-coating deposition. In both cases (single-step or layer-by-layer), hydrogel films can swell/de-swell depending on distinct stimuli. Swelling is frequently the main change leading to optical shifts, often exploited for different biomedical applications, as discussed in the thin film section. Further details on hydrogel thin film fabrication specifics, types of crosslinking, and surface manipulation have been reviewed elsewhere [92,93].

Hydrogel films have been demonstrated as powerful devices for photonics in the biomedical field in detection and sensing applications, and are usually employed at laboratory benchtop experiments and not directly integrated into biological tissues. In these films, physiologically relevant molecules and fluids can be tested for analyte detection [77] as within other types of surface-based assays such as lateral flow

chips [94,95], which are not required to integrate into biological tissues. For that purpose, different kinds of structures have been fabricated, where 3D complexity adds to the optical capabilities and biological compatibility of constructs. One such type of construct is hydrogel fibers (**Figure V-2, b**). Hydrogel fibers and microfibers are truly versatile structures in the fields of biofabrication and tissue engineering, being highly suitable to recapitulate biological-like tissue structures with meter-long lengths [96,97]. They have seen gradually increasing shape and architectural complexity [98–100]. In the optical context, fiber-like designs are also motivated by the paradigm-shifting invention of optical fibers, representing the fastest and more efficient solution for transporting information [45]. As previously discussed, optical fibers are built with non-biocompatible materials, namely solid-state silica. As such, hydrogels have been increasingly studied as candidates for fabricating biologically relevant optical fibers. The fabrication and complexity of these hydrogel architectures in the photonic field are still limited using relatively simple techniques. Mostly, hydrogel fibers for optical applications have been fabricated by injecting precursors into a transparent tube that facilitates light-based crosslinking of the material which is then extruded towards a fiber-shaped gel, frequently made of PEGDA [65,66] or Acrylamide [62]. This single-material fiber represents a core structure, which can then be coated by another material of low refractive index as a cladding structure for approaching Total Internal Reflection (TIR) and improved light propagation. Recently, alginate has been used for cladding optical fiber cores, mainly due to the ease of dipping the core material into the alginate solution and then crosslinking the alginate shell by dipping it into a divalent cationic solution such as $CaCl^{2+}$ [64,66]. This simple strategy appears to dominate recent advances in optical hydrogel fiber fabrication strategies and could still evolve by taking advantage of the progress happening in hydrogel fiber biofabrication [101–103]. The translation of these technologies, which allow multi-material and multi-compartment hydrogel fiber biofabrication towards the field of optical fibers, can lead to the creation of faster single-step methods for fabricating optical hydrogel fibers. Such methods bring not only higher fabrication efficiency. Further, they can also facilitate the encapsulation of micro and nanostructures in different compartments for, *e.g.*, multi-responsive characteristics or inclusion of living cells. Nevertheless, the simple core-clad optical hydrogel fibers so far fabricated are interesting complementary tools to solid state fibers, performing well in the biomedical field as we discuss in the optical hydrogel fiber section 4.

One other fabrication technique that has truly grown in biofabrication is 3D printing that enables integrating complex shapes, precise deposition of distinct materials and cells. Due to this precise

control on cell/material deposition, this technique facilitates the recapitulation of biological tissue complexity, topics discussed in other reviews [104,105]. However, while 3D bioprinting has already reached outer space [106], bridging those advances to the photonics field is still an emerging area of study. Nevertheless, the capabilities of 3D printing allow envisioning interesting applications for matching complex 3D shapes and tissue-like architectures with optically functional structures. 3D bioprinting employs different biomaterials as inks, which in the biomedical field are frequently hydrogel-based bioinks, named so due to their ability to support cells and maintain their viability while having favorable rheological properties. [107,108]. Even though the combination of hydrogel photonics and 3D printing has not yet been extensively explored, optical inks can also emerge soon, where hydrogels are structured or combined with optically-relevant entities such as particles for plasmonic resonance. 3D printing can then be employed to introduce these shapes and materials within complex environments. Printing optical inks could enable biofabrication of optical channels within a tissue-like construct that can guide light and report on different relevant events such as cellular proliferation and ECM remodeling (**Figure V-2, c**). Researchers recently created bioinks of alginate and cells, containing optical sensor particles which responded to oxygen levels by imageable fluorescent changes [80]. This work can be seen as one of the first examples of an optical bioink. Similar approaches can be further tuned to not only derive fluorescent signals but guide and manipulate light within 3D printed channels and shapes.

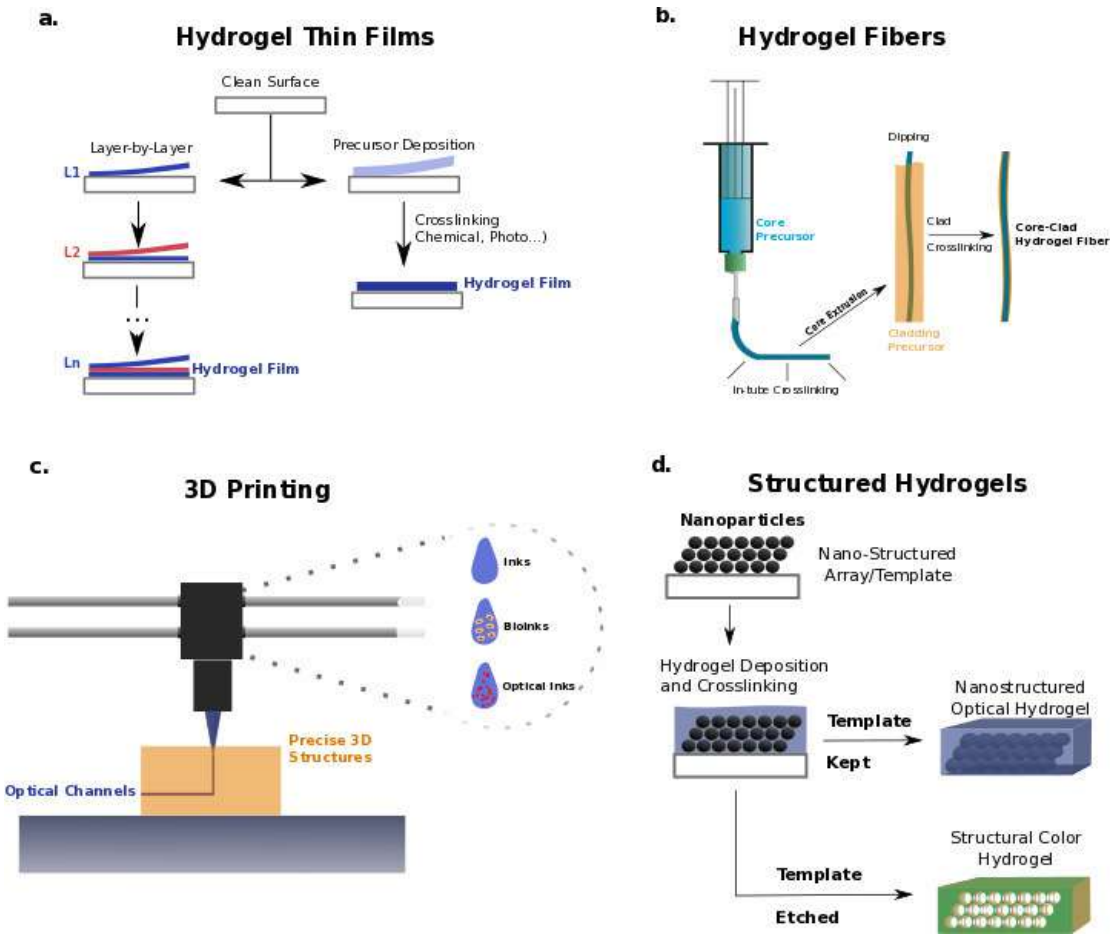


Figure V-2: Fabrication techniques for obtaining hydrogel structures with relevant photonic properties. a | Hydrogel thin films can be produced by deposition on a surface of either layer-by-layer molecular structures or single-step precursor deposition and crosslinking. b | Hydrogel fibers for optical applications are usually fabricated through UV crosslinking materials, structured in fiber-like shapes inside a tube, and then pushed out. These fibers can then be coated with a different hydrogel by, *e.g.,* ionic crosslinking, as frequently pursued core-clad architectures. c | 3D printing techniques allow precise deposition of other materials and be further explored in the optical context. These techniques facilitate the fabrication of complex 3D structures where inks and bioinks are combined with novel types of optical inks that can interact with light differently in, *e.g.*, optical channels within constructs. d | Structured hydrogels are frequently fabricated by depositing these materials within a nano-structured template, which can then be kept inside the hydrogel (*e.g.*, spaced particles) to add further optical interactions (*e.g.,* plasmonic resonance). Alternatively, these nanostructures can be etched out (by, *e.g.,* thermal or chemical processes), leaving only their shape in the hydrogel, as used to obtain hydrogels with structural colors (*i.e.*, the color given by the interaction of light with nanostructures and not by the presence of dyes)

Additionally, hydrogels for optical applications can depend on the introduction of 3D structuring, which allows for more complex light interactions such as structural colors. These interactions can be used for either sensing, holographic imaging, or biomechanical-optical transduction, as discussed in the

structured hydrogel section 4. Once again, the distinct techniques employed to fabricate structural hydrogels revolve around simple concepts that can be brought down to one essential step. Usually, structuring starts by depositing hydrogel precursors on a previously structured array, frequently with shapes on the nanometer size (**Figure V-2, d**). Once the hydrogel is crosslinked around this template, two distinct paths can be followed to fabricate different structures.

On one hand, this template might be kept within the hydrogel, creating an array within the 3D water mesh that can interact with light and even be arranged optically [109]. This type of structure is highly relevant for holographic-related applications. Even if not directly employed in biological environments, it could still be used for biomedical-data encoding and sensing applications [109,110]. On the other hand, once the hydrogel is crosslinked around the nanostructured template, the latter can be etched out, leaving only the hydrogel containing the negative shape of the structure that was once within. These structures, frequently named inverse opal scaffolds, obtain structural colors, in which the interaction of physical patterns with light will give rise to varying shades [69,87]. Changes in these colors can be employed for highly relevant biomedical sensing through real-time optical transduction of biological events, as discussed in the structured hydrogel applications section 4.

As we have outlined in section 3, different techniques with allow fabricating hydrogel-based structures with interesting optical properties. Some of these approaches still have room for development, such as 3D printing and more complex optical hydrogel fibers. The combination of distinct fabrication techniques such as 3D printing and optical fiber integration within constructs is not impossible. This approach might be explored to combine advanced *in vitro* tissue emulation with real-time sensing and reporting of relevant responses through light-based readouts. Overall, the fabrication method depends on the optical structure required by the target application, and such examples are discussed in the next section.

V.4. PHOTONIC APPLICATIONS OF HYDROGEL STRUCTURES

Applying hydrogels as optical and photonic entities in the biomedical field is related to the type, architecture and materials of the construct that is fabricated, as previously discussed. Next, we review the recent applications of hydrogels by focusing on the main types of optical constructs with validated

applications: Hydrogel Thin Films, Optical Fibers and Waveguides, and Bioinspired Nanostructured Hydrogels.

V.4.1. Thin hydrogel films

Thin hydrogel films are one of the earliest types of photonic constructs used in biomedical sensing applications—some of the first examples of such platforms date back to the early 2000s [111,112]. Hydrogel thin films rely mostly on polymer mesh swelling/deswelling changes, causing the film thickness/height to shift leading to changes in its interaction with light [54]. Functionalized hydrogels can have selective molecule binding and drive a shift in water content where they can be employed as a sensing platform. Most optical thin films have also been assembled with other structures, *e.g.*, nanoparticles, to integrate hydrogel film properties with plasmonic-like sensing or even holographic arrangements [71,85].

Some interesting approaches to engineer hydrogels where swelling alone can be used for thin film optical sensing showed that the combination with nanostructures might not be necessary to achieve detectable shifts in light behavior. Researchers used a layer-by-layer approach to obtain phenylboronic-acid-functionalized, acrylamide-based hydrogel films with sub-micrometer thickness, where the direct binding of glucose molecules could lead to hydrogel swelling. This swelling caused a shift in incident light wavelength and allowed analyte detection without further structuring [54]. One other study reported the engineering of block-copolymer lamellar hydrogel films, which could bind to distinct counterions and lead to varying degrees of hydration, changing the wavelength of interacting light and hydrogel film color accordingly [84]. Even though these films were not directly used for biomedical applications, they represent an exciting advance on pure swelling-based optical thin film applications. A more recent example is that where layer-by-layer assembly was used to form hydrogel films of dextran, chitosan, and glucose oxidase, creating a multi-step change in film characteristics resulting in the shift of light properties. Glucose oxidase converts glucose to gluconic acid, lowering the film's local pH, which, being pH-sensitive, swells, leading to a shift in optical properties that was be used for detection [77]. pH sensing has also been approached with hydrogels containing nanostructures, such as the inclusion of nanoparticles on a pH-sensitive P2VP hydrogel, in which pH-induced changes in swelling altered the distance between particles leading to a pH-dependent shift in wavelength [83] (**Figure V-3, a**). pHEMA hydrogels were also used for structured pH sensing, where researchers introduced nanoparticles in the

hydrogel through diffusing silver ions and then reducing these ions to nanoparticles. By then slightly tilting the film and backing it with a mirror, the authors obtained a holographic system where pH-induced changes in swelling led to changes in the wavelength of light resulting in distinct colors across a broad range of pH [85]. The strategy of taking advantage of holographic changes was also more recently bridged to natural, biocompatible gelatin films. Silver nanostructures could also be embedded in the films and lead to swelling-induced changes in detectable wavelength [71] (**Figure V-3, b**). The inclusion of nanostructures was combined with phenylboronic functionalization to obtain glucose-induced swelling in the hydrogel and subsequent optical shifts based on analyte concentration [60]. This responsiveness was further expanded to sense not only glucose but other sugars such as lactate and fructose, representing a versatile, adaptable system [60] (**Figure V-3, c**).

These hydrogel film platforms have also been engineered to sense other molecules such as alcohols and heavy metals [113,114]. Even though thin-film research has been around for some time, it is still possible to see significant advances in their use towards increasingly complex applications such as smart displays. Very recently, researchers showed how PEGDA/P2VP hydrogel films could be combined with hygroscopic ionic liquids to obtain variations in structural colors on a surface depending on the relative humidity [115]. This principle was then used to obtain a touchless display where a human finger could trigger a response from a distance [115] (**Figure V-3, d**).

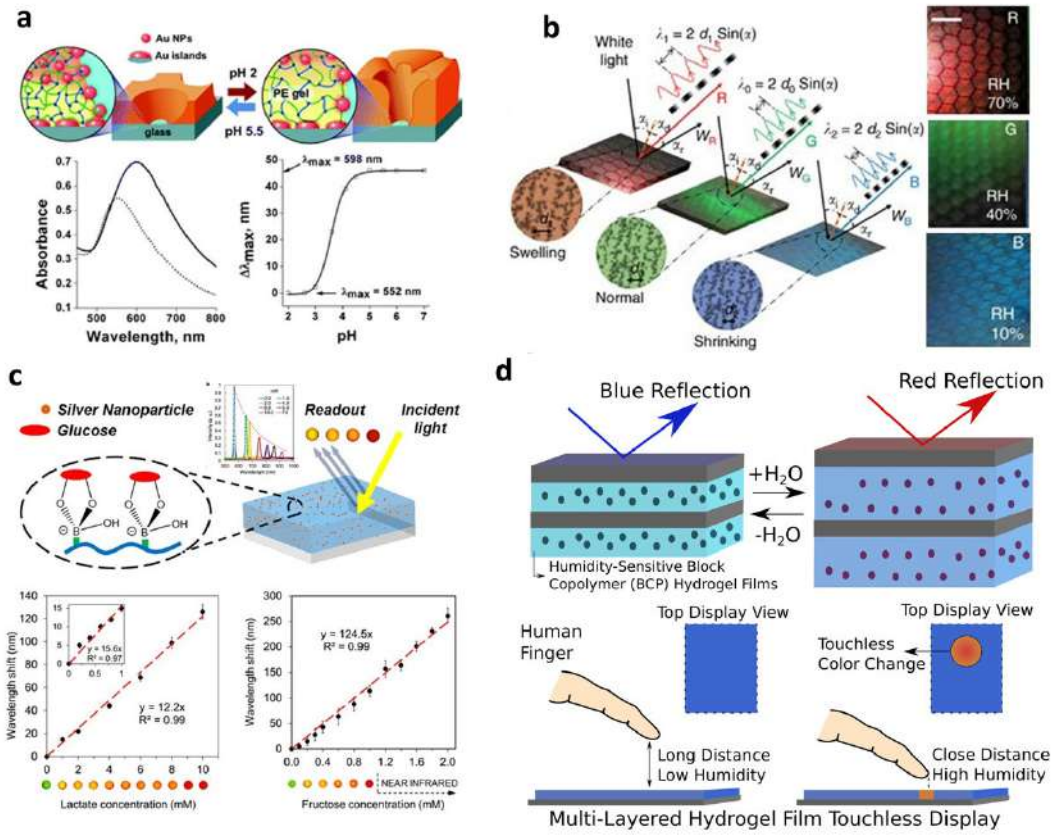


Figure V-3: Thin Hydrogel Films. a| Engineered hydrogel films incorporating silver particles for pH sensing. Adapted with permission [116]. Copyright 2008, Wiley. b| Gelatin-based holographic films with swelling-shrinking shifts in wavelength and color. Adapted under the terms of CC BY License [71]. Copyright 2016, the authors. c| Thin-Film holographic sensors with phenylboronic modifications for glucose and another analyte sensing. Reproduced with permission from reference [60]. Copyright 2014, American Chemical Society. d| Block co-polymer hydrogels with varying hydration levels respond to proximity to the human finger as touchless response platforms.

Overall, thin films have seen significant evolution in the past decade and are undoubtedly powerful platforms for sensing distinct analytes based on label-free, fast optical shifts. Nevertheless, despite some advances in including biologically compatible, natural, and degradable materials in these structures, their use in close contact with biological systems is still limited. This limitation is either due to toxic components or simply because these films are engineered as surfaces to be used in an air/film interface for sensing. The thin film sensors are not integrated into biological tissues. These sensors have potential to be integrated at the skin-air interface [117,118]. In addition to the thin films, other hydrogel architectures and constructs (*e.g.*, hydrogel fibers) have been used to take optical hydrogel engineering

closer to biological environments, *i.e.,* from cell-material constructs to living tissues. Such structures are discussed in the next section.

V.4.2. Optical hydrogel fibers and waveguides

It is essential to start this discussion by differentiating optical fibers from waveguides. Generally, optical waveguides include a broad range of structures capable of guiding light across space. Optical fibers can be included in that definition as a type of waveguide [119]. However, optical fibers represent a more sophisticated structure that improves light-guiding, such as fiber-like geometry when compared to the optical waveguides. Therefore, optical fibers typically perform better than more rudimentary waveguide structures. In the text, we will refer to optical fibers and waveguides independently, where we see waveguides as more general structures with an asymmetrical shape that can guide light but do not present a fiber-like shape.

Focusing on waveguide structures, a strategy was reported to obtain a core of gelatin within two agarose layers (cladding) to guide light through gelatin, as one of the earliest degradable waveguides reported [70]. This study presented a simple planar structure, *i.e.*, a core with a lower refractive index than the cladding leading to light being conducted across the space inside the core via total internal reflection (TIR). Others also resorted to agarose to create optical waveguide structures combined with live-cell encapsulation [74]. Further, synthetic PEG hydrogels were used to create planar hydrogel waveguides and encapsulated cells to screen cytotoxicity *in vitro* and *in vivo* [44]. Similar PEGDA waveguides were also used more recently to detect heavy metal ions [120]. Other natural materials have also been used to fabricate waveguides, such as silk fibroin, which not only brings exciting compatibility and cell interaction properties but can also be genetically engineered for optimized light-guiding [88]. Although all these waveguide studies represent significant advances in light guiding with demonstrated applicability to sense target analytes and screen cytotoxicity, these structures of planar or tubular shape have limited efficiency in guidance for light to travel. This limitation is due to increased loss *via* asymmetrical cladding as light moves through the planar architectures, making it such that these structures frequently are designed to be no more than 4 cm in length [44,120]. As a more efficient alternative, optical fibers have been fabricated to overcome this limitation, granting much more efficient light-guiding due to the fiber-like geometry where the tubular organization of different material layers

ensures that the core is fully covered with cladding material. Therein, a beam of light can be conducted in a confined space due to TIR, leading to low losses and amplifying the possibility of transporting light across more considerable lengths (**Figure V-4, a**).

Solid-state silica optical fibers have been around for a long time, but complex core-clad hydrogel optical fibers are more recent. In that work, researchers used two hydrogels to obtain a step-index optical fiber with a PEG core and an alginate shell, to guide light due to refractive index differences (around 1.45 for PEG and 1.33 for alginate) [65]. Here, authors showed that while core-only fibers enabled only tissue penetration depths of around 5 cm, the core-shell optical fiber provides a penetration depth of up to 15 cm depending on the wavelength. Shortly after, by replacing the PEG core with acrylamide, researchers obtained mechanically resilient optical fibers (**Figure V-4, b**), which were able to report on applied strain levels upon tensile deformation [59]. Both technologies were later combined when a PEGDA-Acrylamide core that were shelled with alginate and combined with phenylboronic acid functionalization for glucose sensing [66]. These fibers were shown to guide light through 3D hydrogel environments (**Figure V-4, c**) as well as in biological tissues (**Figure V-4, d**). The change in swelling due to glucose-phenylboronic acid interactions was then used to sense glucose levels *in vitro* (**Figure V-4, e**). Previously, researchers evaluated oxygen levels *in vivo* showing how these fibers could be directly implanted into biological tissues (**Figure V-4, f**) [65].

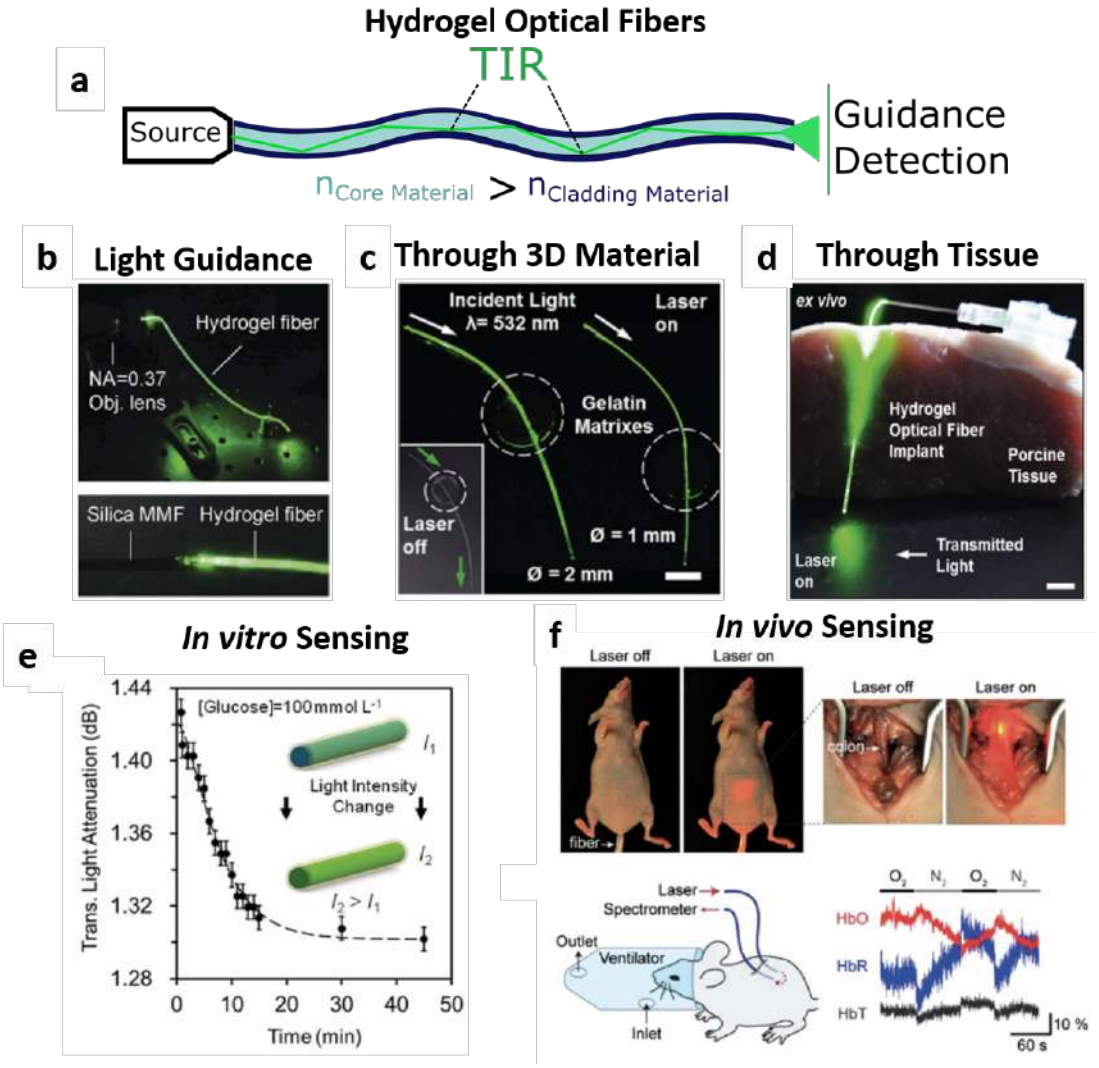


Figure V-4: Optical Hydrogel Fibers. a | Step-Index Optical Hydrogel Fiber Light Guiding due to refractive index differences b |Light Coupling and Guidance through an engineered hydrogel optical fiber. Adapted with permission from ref. [59]. Copyright 2016, Wiley c| Core-Clad light-guiding across 3D Gelatin matrixes and d| Porcine Tissue. Adapted under the terms of CC-BY license from ref. [66] Copyright 2017, the authors. e| In Vitro Hydrogel Optical Fiber for Glucose Sensing. Adapted under the terms of CC-BY license from ref.[66] Copyright 2017, the authors. f| In Vivo hydrogel optical fiber implementation and Oxygen Level Real-Time Detection. Reproduced with permission from ref. [65] Copyright 2015, Wiley.

Other labs have also focused on similar strategies, such as the use of quantum-dot-doped PEGDA core-alginate Shell fibers for metal sensing [121]. Researchers also created a smartphone-based approach to detect glucose levels, again using PEGDA fibers [62]. Acrylamide/PEGDA core, alginate clad fibers were

also adapted for laser photomedicine purposes. [122]. Recently, scientists combined similar PEG-based optical fiber structures with 3D printing to guide light into tissues, demonstrating its capability to trigger the exposure of RGD (arg-gly-asp) amino acidic motifs and control cellular adhesion [123]. Recently, agarose was used to create optical fibers in a slightly different manner in fabrication. By pouring agarose in a mold with rods, authors fabricated cylindrical fibers with a core surrounded by air-filled holes. The core was able to guide light and generate speckle fields due to being surrounded by these holes. Solutions could be perfused into these holes and lead to light behavior changes for potential sensing applications [124].

Overall, hydrogel optical fibers have demonstrated exemplary performance in guiding light in terms of distance and coupling with living tissues. This property adds to their advantages over solid-state fibers in terms of improved biological compatibility. Nevertheless, the materials explored so far for these structures and their fabrication methods are still limited. One can expect that future studies on this topic, will take advantage of different materials and crosslinking methods. These methods can lead to faster throughput in fiber fabrication, possibly taking advantage of current developments in core-shell microfluidics and bioprinting [98,100,125]. Adapting this knowledge to the optical context will potentiate core-cladding fabrication and light guiding properties with unprecedented efficiency while maintaining or further improving biological performance and compatibility using polymers capable of improved cell-material interactions.

V.4.3. Bioinspired structured hydrogels

Among the various pigments and colors found in nature, structural colors are amongst the most fascinating. Unlike dies or pigments, these are observable colors due to light interaction with sub-micron shapes present in structures as those found in plants, flowers, bird feathers, or insect shells [126–128]. Structural colors are the basis of chameleon's changing colors due to alterations in organized 3D lattices present on the skin (**Figure V-5, a**) [129]. In an approach to mimic nature, scientists have used similar strategies to generate and engineer structurally colored materials [130]. Also, in hydrogels, fabrication of reverse opal scaffolds - as discussed in the fabrication section (section 3) - has been pursued to obtain intricate shapes leading to structural coloration. In the earliest examples, the materials used lacked biological compatibility, hence limiting their biomedical applications. An excellent

example of this concept is the vast body of literature focusing on the use of poly-dodecyl glyceryl itaconate/polyacrylamide networks (PDGI/PAAM) [131–133], which have been successfully engineered for various color properties combined with their mechanical responsiveness. Even if these materials have potential use in devices for sensing and diagnostics outside of living tissues, they are not particularly compatible with biological entities. On the other hand, inverse opal scaffolds have been engineered with materials widely known to be cyto-compatible and were further employed as direct scaffolds for tissue engineering due to their intricate shapes that provide cues for cell adhesion and orientation [134]. These studies, however, neglect the photonic properties of the opal hydrogels.

Most of the studies on structured hydrogels where biological compatibility and optical properties are reported in the recent years. In this period, researchers used a nanostructured template to introduce colors in gelatin methacryloyl (GelMA) hydrogels, combined with enzymatic glutaraldehyde crosslinking to give them self-healing properties [69]. Here, authors demonstrated that these hydrogels could exhibit exuberant structural colors, be arranged in complex 3D architectures, and had no negative impact on cell viability (**Figure V-5, b**). Almost at the same time, it was reported that silk hydrogels could also be templated similarly, and could have remarkable light interactions, and be suitable for smart contact lenses that could potentially grant night vision [135]. Even though the authors did not evaluate biological compatibility of the constructs, silk fibroin is long known to be biocompatible and is widely used as a biomaterial for various applications [136]. Both studies are examples of the combination of biologically compatible materials and structural coloration. Later, a group of researchers took the nanostructured GelMA inverse opal scaffolds one step forward by engineering living structural color hydrogels [87]. By combining the structural-colored scaffolds with cardiomyocytes, authors obtained a construct where the mechanical forces induced by cardiac cell contraction could lead to changes in the hydrogel lattice (**Figure V-5, c**). Then, just like the color changes in chameleons' skin, this shape change led to color shifting in the engineered hydrogel - direct transduction of physiological response (cardiomyocyte contraction) to an optical signal (change in structural color) [87]. This work represents hydrogel photonics for fast, label-free detection of cellular events by a simple analysis of the material's interaction with light and subsequent changes in color wavelength. Exciting future studies might outline the potential of these rapidly detectable changes to elucidate the mechanics of single cells and multi-cellular structures, much of which yet remains to be investigated fully [23,137].

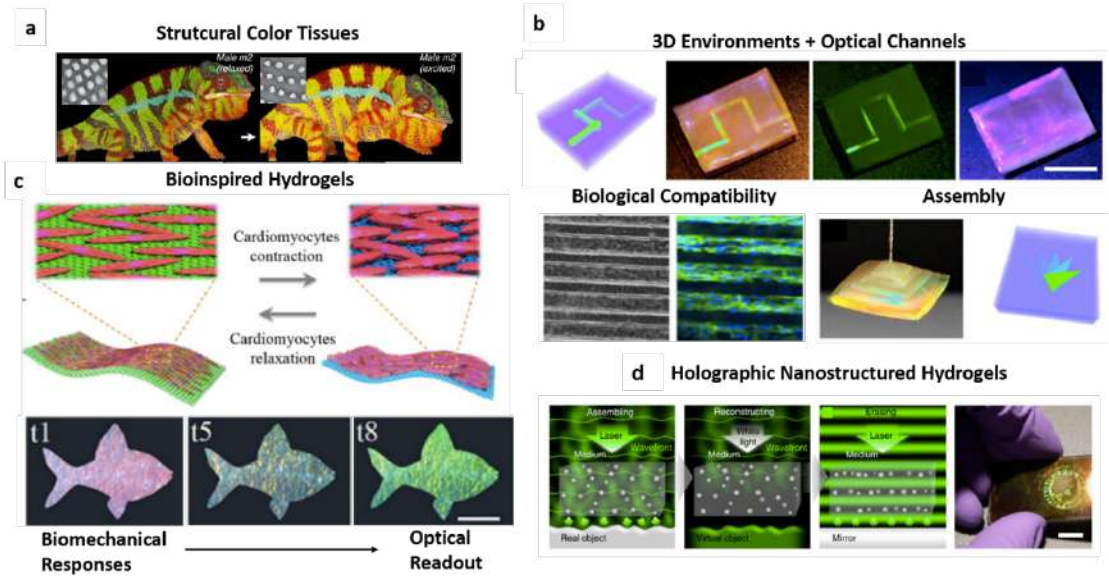


Figure V-5: Structured Hydrogels. a| Naturally inspired biomimetic structural tissues. Adapted under the terms of CC-BY license. [129] Copyright 2015, the authors. b| Structural color hydrogels as channels and assembled structures with cyto-compatible properties. Adapted, with permission, from references [69,87]. Copyright 2017, National Academy of Sciences and Copyright 2018, AAAS. c| Structural hydrogels use for biomechanical-optical transduction through cardiomyocyte-induced hydrogel contraction and color change. Adapted with permission from reference [87]. Copyright 2018, AAAS. d| Hydrogels with nanostructures as assembled by light and holographic image generation for data encoding. Adapted under the terms of CC-BY license from reference [109]. Copyright 2016, the authors.

Further, organized nanostructures not only serve as a template for structurally colored architectures but can also remain within hydrogel meshes and interact with light in such a way that their organization forms a holographic representation of a particular image (**Figure V-5, d**) [109]. These structures are sometimes also combined with hydrogel film technology and are discussed in section 4.1. The holographic hydrogels can potentially be used for coding relevant information and data can be used in the biomedical data context, ever-growing in complexity [138].

V.5. ACTIVE OPTICS AT THE CELL/HYDROGEL INTERFACE

As previously discussed, the various ways to engineer hydrogels and obtain optically relevant architectures for guiding and manipulating light in close contact with biological tissues have developed significantly over the past years. Nevertheless, the direct combination of hydrogels, cellular structures,

and light-guidance is still under development and can further lead to exciting new applications. Initial approaches from different labs on light-guiding hydrogels have shown that light guiding can be simultaneously associated with cell encapsulation, such as in agarose waveguides with encapsulated cancer cells [74] or light-guiding PEG hydrogels with HeLa cells [44]. These reports represent two of the earliest studies where there was a direct combination between light-guiding hydrogels and cellular components. Simultaneously, on the other side of the spectrum, researchers have assembled *E. Coli* to obtain cell-only waveguides [139] (**Figure V-6, a**). More recently, it was demonstrated that cells in suspension could also guide light by obtaining cyanobacteria waveguides (**Figure V-6, b**). The suspended cells were shown to trap light beams, guiding light with reduced diffraction [140]. These experiments demonstrate that, unlike studies where cells had no influence on the construct's light-guiding properties, they can take an active role by trapping and directing light.

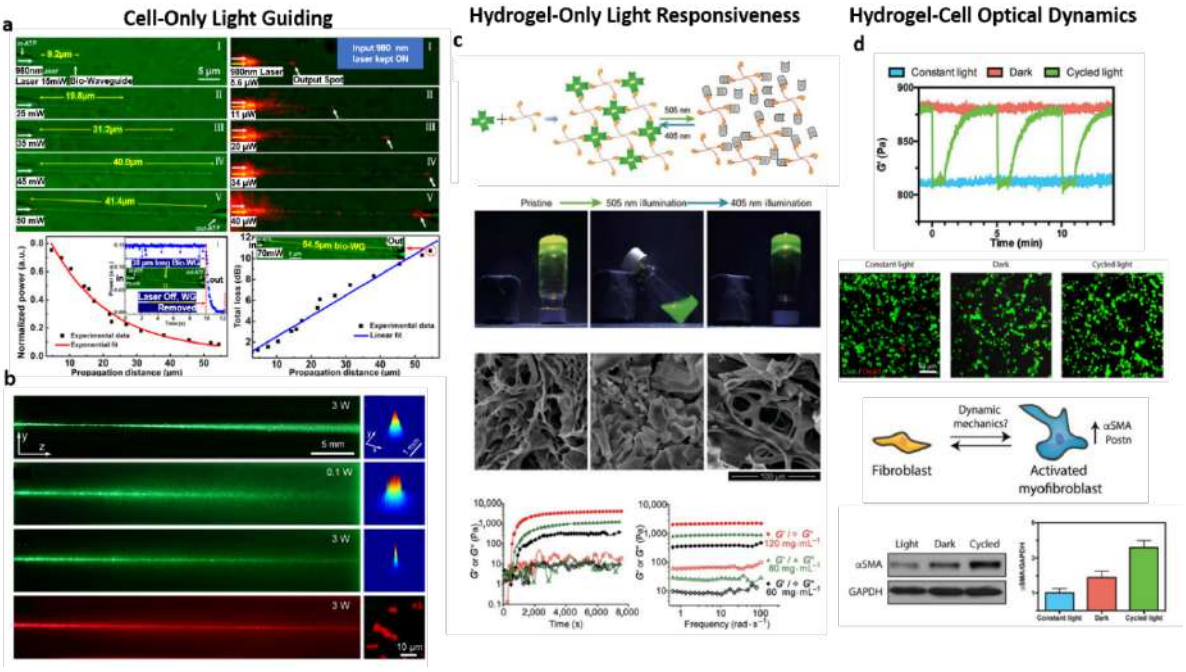


Figure V-6: Active Cell/Hydrogel interfaces. a| Cell-only optical waveguide structures made from E. *Coli*. Adapted with permission from ref. [139]. Copyright 2013, American Chemical Society. b| Cell-only waveguide of cyanobacteria in suspension. Adapted with permission from ref. [140]. Copyright 2017, American Physical Society. c| Hydrogel-only light-responsiveness can be engineered as demonstrated for polymeric gels, with light-induced gelling and mechanical switching. Adapted with permission from ref. [141]. Copyright 2018, Springer. d| Light effects in hydrogel and cells can be combined to translate optical signals into hydrogel mechanical dynamics and tune the

phenotype of fibroblasts as an example of a living, light-responsive construct. Adapted with permission from ref [142]. Copyright 2018, Wiley.

Moreover, similar to hydrogels being highly hydrated meshes, one can envision that cells can be used to guide light in hydrogels, as demonstrated in water and glycerol suspensions [140]. Additionally, these studies resorted mostly to the use of bacteria. It was also recently shown that eukaryotic cells and their intracellular constituents also have very particular interactions with light [143]. Light-cell interaction becomes even more interesting as we consider that cells are highly active structures. As such, they might not only be able to manipulate light passively but also simultaneously respond to it, as observed by the capability of polarized light to affect cellular cytoskeleton organization [144]. Very recent evidence further hints at the possibility of genetically manipulating the optical properties (refractive index) of living cells by taking advantage of reflectins (proteins), which are natively responsible for the structural coloration of cephalopods [145]. These results suggest that exciting discoveries and applications of cell-light interactions will likely become a reality in the near future.

Further, hydrogels themselves can also be engineered to respond to light actively, leading to changes in crosslinking and influencing encapsulated cells. An excellent example of this process happens with hydrogels based on the photoswitchable protein dronpa. Light-based crosslinking changes can dynamically control the hydrogel formation and mechanical properties (**Figure V-6, c**), influencing the migration of cells [141,146]. Another recent example of protein-based, light-responsive environments was reported, where light-induced hydrogel mechanical changes could function as a cyclic mechanical loading platform [142]. Therein, this mechanical responsiveness to light induced myofibroblast activation (**Figure V-6, d**) [142]. Overall, there are very distinct ways to approach the interface between light guidance, cells, and hydrogels, and engineering active responses from both entities to light. The transition from passive light manipulation to the dynamic interaction between light, cells, and materials can lead to more exciting developments such as live hydrogel photonic structures. These constructs might inform on changes within the biological environment, simultaneously responding to it from a mechanical point of view and subsequent cell mechanotransduction.

Moreover, engineered hydrogel systems can present additional degrees of complexity and functionality, especially if they are also engineered to respond to other types of stimuli that can be combined with light interactions, as explored next.

V.6. MULTI-RESPONSIVE HYDROGELS IN LIGHT-BASED APPLICATIONS

Hydrogels have been engineered to respond to a wide variety of stimuli, a topic which has been broadly discussed in the literature by others [147–150]. Here, we focus on the combination of hydrogel responsiveness with photonic applications. We previously discussed some responsive hydrogels and their swelling behavior in response to changes in, *e.g.*, pH or upon the presence of analytes such as glucose. However, there are other stimuli that hydrogels have been engineered to respond to such as electrical, thermal, and magnetic, which can be combined with their optical characteristics. These stimuli can be interesting complementary approaches for multi-responsive detection and also for the fabrication and assembly of optically-relevant hydrogel constructs. [151]

Regarding the combination of hydrogel photonics and magnetic responsiveness, there have been recent advances where magnetic-based manipulation of hydrogel structures was proven to be relevant for tuning optical properties. It was shown that by nanostructuring the hydrogels with magnetic particles, it was possible to arrange their orientation and lead to distinct shifts in the wavelength of the incident light, obtaining a photonic hydrogel structure which responded to alternating magnetic fields (**Figure V-7, a**) [152]. In this study, the previously discussed photonic hydrogel structures were combined with multi-responsiveness strategies. Similarly, it was shown that hydrogels can be patterned with magnetic regions, becoming inherently responsive to magnetic fields and simultaneously capable of changing the polarization plane of incident light [153]. In another study on polarization, coupled gelatin hydrogels with magnetically responsive bicelles were manipulated to polarize light *via* temperature changes. This work represents an engaging multi-responsive platform integrating distinct stimuli (magnetic, thermal, and optical) into a single construct [154]. Further, a multi-responsive platform that combined thermo-responsive hydrogels with gold nanorods and magnetic silica particles was reported to employ magnetic stimuli to control swelling/de-swelling states causing a detectable shift in the plasmonic light resonance [155]. Indeed, these studies present optically engineered hydrogels that might benefit from additional responsiveness, where distinct stimuli can then be recognized and translated

into an optical change. Additionally, magnetic manipulation of hydrogels has been used for assembling complex structures in the biofabrication field [156,157], which can also be applied for hydrogel optical structuring. This magnetic manipulation can potentially be used to assemble different parts with heterogenous properties, leading to platforms with multi-stimuli responsiveness actuated by optical, magnetic, thermal, or chemical stimuli.

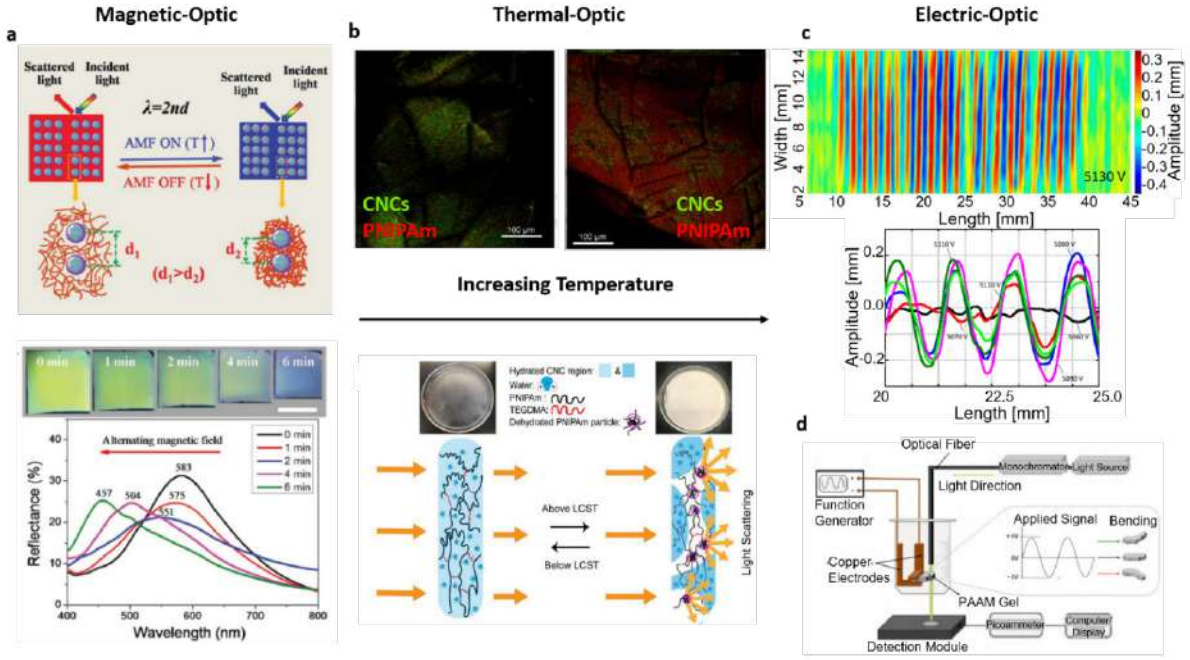


Figure V-7: Multi-Responsive Hydrogel Photonics. a| The conjugation of hydrogel magnetic responsiveness and optical structuring allows to modulate incident light wavelength by changing the structure via the changing magnetic field. Adapted with permission from ref. [152]. Copyright 2017, Wiley. b| Thermo-responsive PNIPAAm (Poly(N-isopropyl acrylamide) hydrogel films with cellulose nanocrystals can change their structure and shift their interaction with the light on temperatures above or below the critical value. Adapted with permission from ref. [158]. Copyright 2019, Elsevier. c| Electro-responsive hydrogels can change their shape and light interactions with varying voltage. Adapted under the terms of CC-BY license from ref. [159]. Copyright 2018, the authors. d| Electro-responsive hydrogels in devices capable of optical sensing electric field variations such as those in cardiac muscle contraction. Adapted with permission from ref. [160]. Copyright 2010, Elsevier.

Similarly, thermoresponsive hydrogels have been mostly used for temperature-induced gelation changes and consequent applications for drug and cell delivery [161,162]. However, temperature as a response-triggering stimulus has also been combined with photonic hydrogel engineering. For example,

thin-film structures described in this review can be combined with thermoresponsive hydrogels leading to films where temperature can also affect the photonic properties and lead to changes in interacting light characteristics [163,164]. This property might be further applied to distinct hydrogel structures, namely particle-based systems [165] and films with transparency/opacity transitions above or below certain temperature levels (**Figure V-7, b**). Further, the fact that temperature can also play a role in the performance of optical-fiber structures suggests it can also be explored for additional functionality, *e.g.*, in the proximity of tissues at body temperature levels [166].

Electrically responsive hydrogels have also gathered significant attention, namely as muscle tissue engineering platforms where electrical stimulation and conductivity are important [167,168]. Nevertheless, electro-responsive hydrogels brings another dimension to the range of stimuli that photonic hydrogel structures can respond to. Even though not widely explored yet, some interesting examples of this combination, such as temperature-responsive polymers with conductive particles, allowed researchers to obtain conducting hydrogel thin films [169]. Further, scientists combined hydrogel photonics and electric responsiveness towards applications in direct biomedical sensing [160]. This work reported electroactive polyacrylamide hydrogels that could respond to an electric field leading to a change in the light passing through the construct and facilitating the transduction of electrical signals for wireless optical detection (**Figure V-7, d**). More recently, researchers have also shown that hydrogel surface topography [159] and swelling states [170] could also lead to electrically-induced changes in the interaction with incident light (**Figure V-7, c**). This kind of electrical-induced changes can be coupled with well-established systems where surface topography is employed for highly sensitive and specific plasmonic sensing [171–173]. All these results show that the combination of electrically responsive hydrogels and photonics is relevant for approaches to analyze electrical changes such as those happening in muscle tissues. Alternatively, it can allow using electrical fields to manipulate light-hydrogel interactions within sensing devices and platforms. Simultaneously, progress is being made on incorporating graphene - known for extraordinary electrical and optical performance [174,175] – within hydrogels [176]. Exciting advances in electro-optical platforms will likely derive new application through these advances in the future.

V.7. LIGHT-DRIVEN HYDROGEL ROBOTS

Engineering hydrogels can translate optical signals not only into bulk mechanics or structural changes but also into motion, *i.e.*, hydrogel robots - particularly microrobots. Inducing controlled movement in small structures is very interesting for biomedical applications due to the possibility of moving and transporting biologically-relevant cargo to locations that are typically hard to reach within an organism [177]. Additionally, integration of cells with hydrogels and their manipulation towards motion can further lead to living robots [178,179]. Overall, these are very lively fields of research, and the topic of soft microrobots has been extensively reviewed throughout recent years [180–183]. As such, here, we focus our discussion on the recent advances in light-driven hydrogel robots.

As previously described, hydrogels can respond to multiple stimuli, sometimes even in a single structure. Naturally, these distinct responses have been exploited to create motion in hydrogel structures via, *e.g.*, pH responsiveness and magnetic stimuli [184,185]. However, it is possible to observe cases where light and hydrogel interaction is the main driving force for hydrogel motion and robotic function. Moreover, motion can be obtained with light alone, coupled with thermal responsiveness and light-triggered plasmonic heating. Indeed, a large volume of recent research has focused on combining thermo-responsive hydrogels with optically active structures, such as gold nanoparticles, for inducing light-triggered changes in the local hydrogel environment. The most common example of such systems employs PNIPAAm (Poly(N-isopropyl acrylamide) hydrogels, which encapsulate gold particles that lead to an increase in temperature upon exposure to visible light. This temperature increase causes the hydrogel to contract towards the light (positive phototaxis) (**Figure V-8, a**) [186]. Different variations of this strategy have been reported in the past year, such as gold nanopatterned-disks that wrinkle at the air-water interface when exposed to light [187], spiral-shaped structures which move through light-controlled spinning [188], and photo-responsive microcrawlers motioned by light-modulated friction [189]. Researchers have recently combined these advances with 3D printing technology to print PNIPAAm/Gold nanorod actuators with designer shape and improved resolution [190]. Similar hydrogels have also been previously integrated within microfluidic devices [191,192].

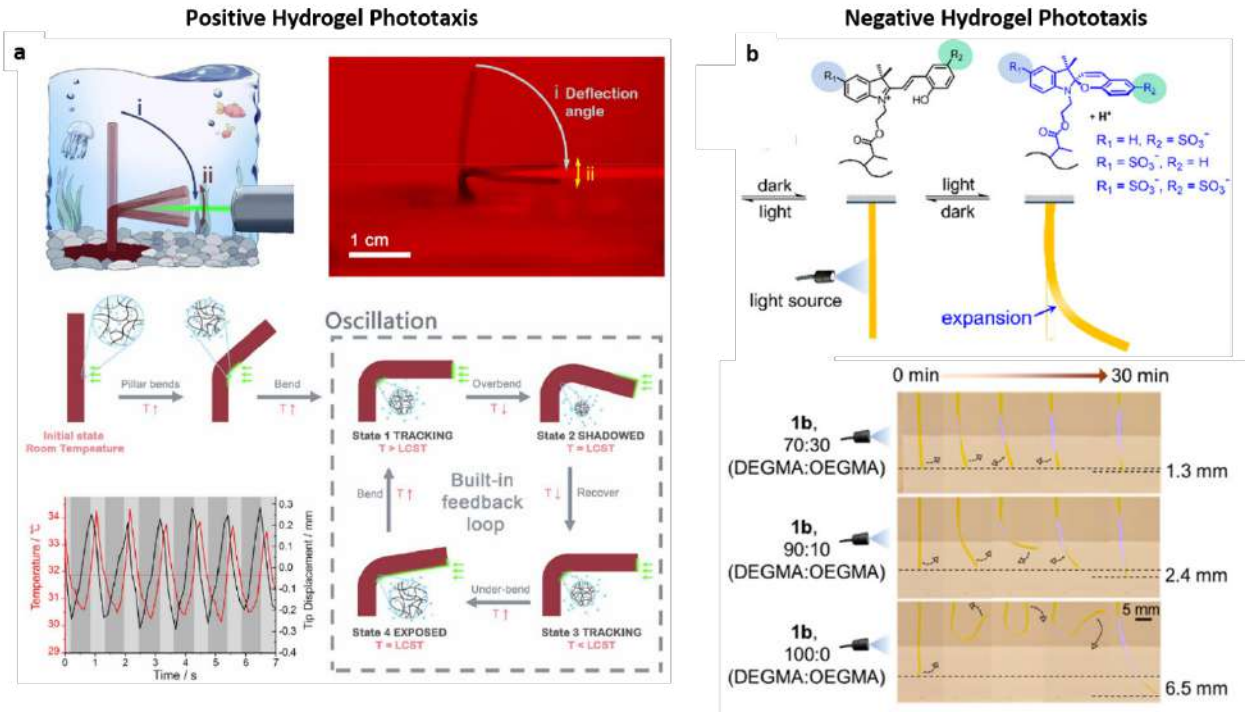


Figure V-8: Light-Induced Hydrogel Motion. a| Thermo-responsive PNIPAAm hydrogels containing plasmonic gold structures can respond to light by the local increase in temperature through gold-photon interactions, contracting the gel and leading to positive (towards light) phototaxis. Reproduced with permission from ref. [186]. Copyright 2019, AAAS. b| Distinctly, specific molecular switches can be integrated within hydrogels, directly responding to light and causing a local expansion of the hydrogel mesh, leading to motion against the light source (negative phototaxis). The integration of both behaviors can lead to 180° motion ranges capable of moving both towards and away from light. Adapted with permission from ref. [193]. Copyright 2020, American Chemical Society.

Overall, combination of PNIPAAm hydrogels and heat-generating gold plasmonic structures dominates the current landscape of light-driven hydrogel robots. However, there are also exciting advances in developing gels that can directly respond to light without plasmonic-based photothermal changes. This possibility was explored by using molecular switches that, unlike the previously discussed examples, can trigger a volumetric expansion in the hydrogels (instead of contraction) [193]. This difference in behavior leads to a relatively novel type of negative phototaxis, where motion happens away from and not towards light [193] (**Figure V-8, b**). On another exciting approach, scientists took inspiration from aquatic invertebrates to create liquid crystal gels (LCGs), which can molecularly respond to light and bend through photothermal changes that can be translated into crawling, walking, jumping, and swimming [194]. Even though these structures differ significantly from classical hydrogels, it

is interesting to see how the combination of specific molecular changes and their incorporation into hydrogel meshes can be employed. These approaches can soon replace the need to incorporate plasmonic structures or even bypass the need for thermal changes and obtain purely light-responsive hydrogel robots. Finally, it is also relevant to mention that light-responsive hydrogels might not necessarily be used to fabricate microrobots but rather serve as the 3D environments for motion. This phenomenon was demonstrated with light-controlled local hydrogel melting and consequent induction of traveling-wave motions in elastomer robots [195].

V.8. HYDROGELS IN PHOTOMEDICINE

Focusing on the biomedical use of hydrogels as light-interacting entities, we also discuss the field of photomedicine, where hydrogels are used as entities that can aid or potentiate light-driven therapeutics. These therapeutic strategies usually gravitate around photodynamic events, *i.e.*, events that can be modulated by light, such as Photodynamic Therapy (PDT), already established at the clinical level for cancer treatment [196,197]. Photodynamic strategies integrate a broad set of approaches that aim to destroy unwanted biological entities, such as bacteria or tumor cells. Recent advances in this field have taken advantage of hydrogels as structures that can carry other photo-responsive and photo-active structures, respond themselves to light, or combine both. The topic of photodynamic therapies was broadly reviewed elsewhere [198–201]. Here, we will explore how hydrogels have been engineered as a tool for optical modulation of therapeutically relevant strategies.

In the case of antibacterial- and antimicrobial-focused approaches, hydrogels are frequently used as a passive carrier for the transport and release of photosensitizers - molecules that can increase the sensitivity of specific bacterial strains to light (*e.g.,* methylene blue) [202–204]. These approaches can take advantage of hydrogels such as chitosan, with natural anti-bacterial properties [205]. However, more interesting for this review's scope are strategies wherein hydrogel interactions with light can be weaponized to kill unwanted microbes and promote healthy tissue healing. An excellent example of this duality is a study that combined thermoresponsive hydrogels with copper/silica nanoparticles. Upon interaction with near-infrared (NIR) light, these constructs experienced an increase in temperature (photothermal) combined with a release of radical oxygen species (ROS) (photodynamic) and of copper ions, which directly stimulated cell proliferation and angiogenesis (pro-regenerative) [206]. This work is an

example of a complete synergy between killing bacteria and promoting healthy cell responses. This process was controlled by NIR light and consequent volumetric changes on the hydrogel composites [206]. Photodynamic anti-bacterial therapies have also been approached by combining peptide self-assembly with photosensitizer molecules. In such strategies, the hydrogel structure itself is reinforced by the photosensitizer's presence, allowing the latter to be locally delivered for improving responses, *e.g.*, wound-healing outcomes [205]. As reviewed elsewhere, self-assembling biomolecular hydrogels have gained significant traction for phototherapy in recent years [207].

In anti-tumor strategies, a vast body of literature focuses on using various hydrogels to enhance light-driven therapeutics. Similar to anti-bacterial approaches, some of these strategies share standard features and employ hydrogels to efficiently deliver photosensitizers for improving light-induced killing of cancer cells [208–213]. Further, another recent avenue of studies focuses on killing cancer cells and stimulating anti-tumor immunogenic responses. In these approaches, hydrogels were used to transport structures of interest, such as drug-carrying nanosheets [214], or taking advantage of oxygen-generating events to revert intratumoral hypoxia [215]. Light-driven changes in gelation have also been recently studied to enhance therapeutic approaches. With that in mind, researchers engineered PEGDA-based solutions, which could be injected in the vicinity of solid tumors, and posteriorly form a gel upon light actuation. The authors were then able to fixate the whole structure in the desired region to deliver toxic radical oxygen species (ROS) and pro-immunogenic nanoparticles simultaneously [216], resulting in a complex network of tumor-suppressive events (**Figure V-9, a**). On another approach, researchers created a method where the light was delivered to the tumor site by integrating luminescent materials within calcium alginate hydrogels [217]. These hydrogels fixated in the desired region, persistently releasing light and leading to continuous ROS production and significant tumor size decreases [217].

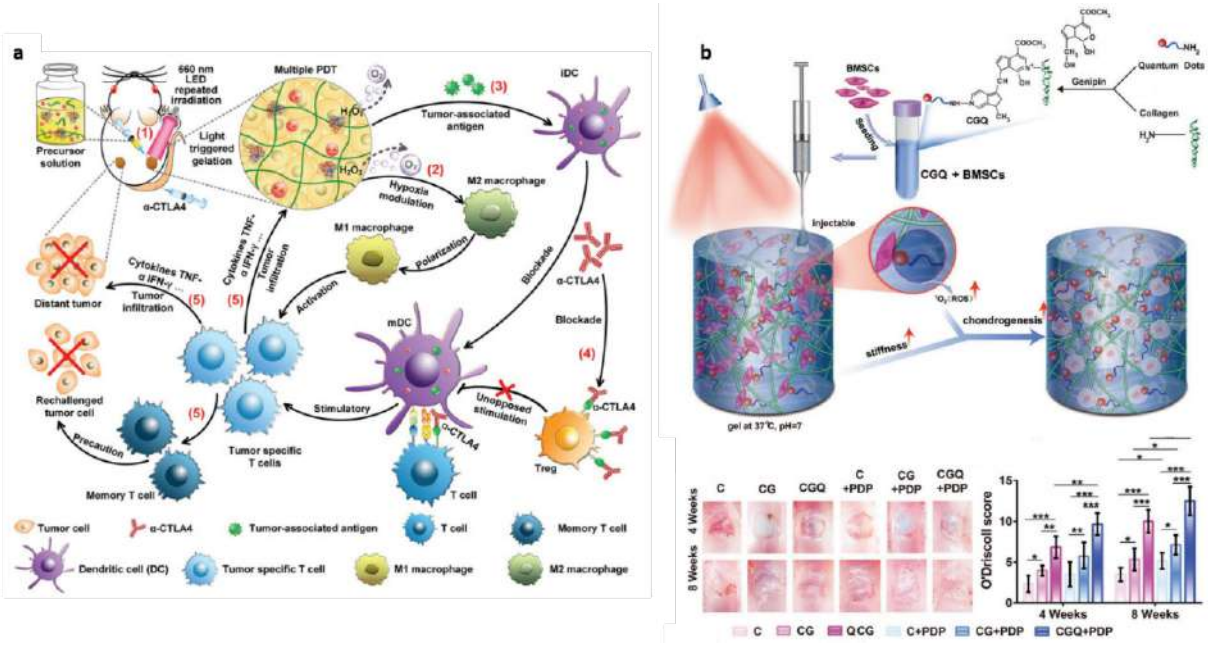


Figure V-9: New Paradigms in Hydrogel Photomedicine. a | Engineered PEGDA precursor solutions with pro-immunogenic entities can be locally immobilized through light-induced hydrogel crosslinking to modulate a wide variety of tumor-suppressing events. Reproduced with permission from ref. [216]. Copyright 2019, Wiley. b | Similar light-hydrogel interactions can be employed on collagen-based hydrogels to direct mechanical stiffening and ROS production towards cell proliferation, chondrogenic differentiation, and improve cartilage healing. Adapted under the terms of CC-BY license from ref. [218]. Copyright 2019, the authors.

Even though most of the discussed studies use hydrogel-light interactions to kill certain biological entities, there are other recent approaches where the goal is quite the opposite: to potentiate cell proliferation and differentiation towards achieving benign phenotypic conversion for tissue engineering and regeneration purposes. In two distinct studies, collagen hydrogels were engineered to change in mechanical properties upon a light trigger, causing an increase in hydrogel stiffness combined with moderate ROS release. ROS were shown not to be cytotoxic at that level but instead favored the chondrogenic commitment of mesenchymal stem cells [218,219], significantly improving cartilage healing (**Figure V-9, b**). These two recent studies demonstrate that light-responsive structures can synergize with the hydrogels for complex chemical changes, mechanics, and release of molecules. As shown by these advances, this process can have applications that go far beyond killing unwanted cells and instead be tuned so that cytotoxic effects turn into cyto-compatible and bioactive events. Future studies exploring these concepts will likely yield exciting phototherapy solutions where light stimuli and hydrogels can heal damaged tissues. This process might not only happen by removing unwanted

biological players but also by actively promoting phenotypic reversion or regeneration through cell proliferation and guided stem cell differentiation.

V.9. HYDROGEL-LIGHT INTERACTIONS FOR ORGAN-ON-CHIP APPLICATIONS

Recent advances in hydrogels and microfluidics enable recapitulating critical physiological events in miniaturized platforms. These platforms frequently referred to as organ-on-chip or even body-on-chip, are fascinating alternatives to simpler models such as 2D static cultures that lack important architectural and biological tissue dynamics. Organ-on-chip models present potential advantages over more complex animal models, as animals have fundamentally different physiological characteristics compared to human organs and tissues.

In this field, hydrogels have been used as important components to miniaturize cell culture compartments with 3-dimensional arrangements as complex and vascularized structures or bone marrow niches [220–222]. Within this field, hydrogel light interactions can be employed for two essential processes: The first is the fabrication of such intricate architectures and biologically relevant 3D niches. The second focuses on integrating the fast, label-free optical on-chip sensing to detect and track critical biological events.

Fabrication-wise, the most exciting advances in light-based hydrogel uses hydrogel precursors within microfluidic chips and takes advantage of light-based crosslinking to generate 3D structures with controlled shape and architecture. Using this approach, PEGDA and GelMA hydrogels were arranged through flow alone and led to intricate shapes without needing light-covering masks [223]. By shining light to crosslink hydrogel precursors in specific stages of flow, researchers were able to mimic 3D arrangements of distinct tissues such as tumor, muscle, and tendon-bone interfaces (**Figure V-10, a**). Indeed, the potential for light-based laser-writing might have further applications in the organ-on-chip context. Recently, optical manipulation of drug-containing particles combined with light-based hydrogel writing was employed to engineer tunable drug cocktails [224]. This strategy can be utilized to obtain on-chip drug depots with varying characteristics allowing the combination of 3D environment, cell culture, and drug testing, all with controllable shape and positioning. Further, light-based hydrogel crosslinking and manipulation have proven to be valuable tools for fabricating 3D gradients that combine ranges of chemical and mechanical properties for faster (high-throughput) screening of cellular responses to the

surrounding environment [225,226]. Such approaches to modulate the 3D microenvironment of cells can be further explored to recreate naturally space-varying niches such as hematopoietic stem cells within microfluidic devices [227]. Additionally, hydrogels might be manipulated by light to recreate environments within which cells can be integrated and serve as translucent 3D platforms wherein cells can be exposed to light to promote differentiation towards specific phenotypes. This idea was earlier utilized to obtain neural-muscular motor units on-a-chip [228].

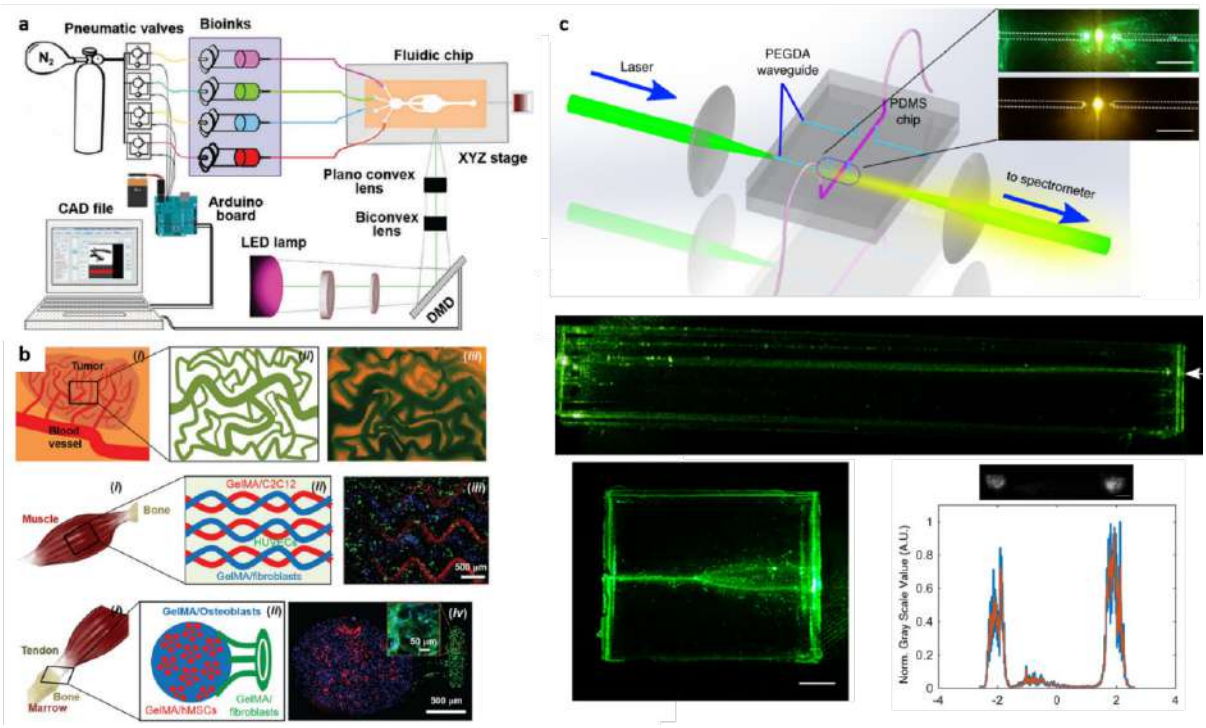


Figure V-10: Light-hydrogel interactions for on-chip applications. a| Manipulation of hydrogel precursors within microfluidic devices combined with light-based crosslinking to fabricate on-chip biologically relevant architectures such as b| Tumor, muscle, and tendon-bone interfaces. Adapted with permission from ref. [223]. Copyright 2018, Wiley. c| Integration of hydrogel waveguides within PDMS chips for light guiding and multi-output detection. Adapted under the terms of CC-BY license from ref. [229]. Copyright 2019, the authors.

Even though light-hydrogel interactions have led to exciting advances in microfabricating 3D environments for chip-based cell culture, hydrogel photonics might have a more significant role to play. Indeed, it can facilitate integration of fast, label-free optical sensing and detection within microfluidic chips of higher design complexity. At present, microfluidics and organ-on-chip techniques rely mostly on imaging, image processing, and analysis to derive quantitative data from biological assays [230,231]. Nevertheless, this process is likely to change once hydrogel photonic structures come into play to obtain

real-time readouts without needing for fixation, staining, or other sample-destructive procedures. Even if this possibility is still explored little, recent studies demonstrate its feasibility. Some of these studies are close to the field of optofluidics, where micro-optical events are combined with microfluidic structures. On such an approach, researchers introduced PEGDA microlenses on microfluidic chips, showing that these hydrogel structures could react to presence of salts, changing their shape and leading to a shifting of focal planes, which could be used to evaluate the concentrations of analytes of interest [232]. It was also demonstrated that PEGDA waveguides could be integrated into PDMS structures [229]. Therein, the authors showed that PEGDA waveguides were capable of guiding light through the 3D PDMS structures; function as beam splitters with multiple outputs, and possibly facilitate the measurement of relevant on-chip events (**Figure V-10, b**).

Overall, even if some of these recent approaches for responsive hydrogel structures are integrated within microfluidic chips and have been effectively used to obtain fast optical readouts, they are not yet integrated within organ-on-chip systems. Together, these earlier microfluidic studies pave the way for combining photonic structures with miniaturized 3D biological architectures. The possibility of having real-time sensing through optical hydrogel components in organ-on-chip applications is likely to emerge in the near future.

V.10. CONCLUSIONS AND OUTLOOK

Over the past decade, we have observed considerable advances in engineering of hydrogels towards photonic biomedical applications. These hydrogels emerge as complementary materials within the biomedical scope to the solid-state materials that are classically used for light guiding and manipulation applications. Hydrogels represent a safer, biocompatible, and adaptable platform technology for efficient optical interactions and contact with cells, tissues, and organs.

Overall, a wide range of polymers has been utilized for this purpose, both from synthetic and natural origins (Table V-1). On the one hand, synthetic polymers have a higher degree of purity and capability to be modified and tuned to enhance optical or biological performance. On the other hand, natural polymers are more variable and harder to modify, but were also presented as good candidates in photonic structures due to potential advantages related to degradability and biological compatibility. Nevertheless, both branches of polymers have been shown to have equally important roles in hydrogel photonics. As we keep moving forward, we will potentially see some of these polymers being replaced

by smarter engineered alternatives that can further push the optical performance of photonic systems, such as guiding characteristics. This advance can occur by modifying refractive indexes by decreasing water content to lower levels while maintaining cytocompatibility. Also, in a hydrogel-fabrication landscape that is still dominated by UV-based crosslinking, future studies will likely focus on distinct crosslinking methods. For example, visible-light crosslinking can lead to similar structures like those reported with UV but with higher biological safety, *e.g.*, for encapsulating cells within constructs [233,234]. Other types of crosslinking, such as ionic and supramolecular assembly, represent more recent alternatives that can become substantial players in hydrogel photonics.

In addition to the choice of material, the construct architecture dictates the capabilities of these materials to interact with light for guiding and manipulating its properties towards sensing. Here, we identified four main types of optical hydrogel structures and respective fabrication techniques (Figure V-2). Thin films are the earliest used constructs for hydrogel photonics, and these structures can be obtained mainly through either layer-by-layer or single-step deposition techniques. Thin hydrogel films have been engineered and adapted to various scenarios but commonly represent platforms used on surfaces interfacing air outside of biological environments. However, thin films are still extremely efficient in detecting biologically relevant targets such as glucose, changes in pH, or heavy metals. Despite being a part of the hydrogel photonic landscape for a long time, there are recent creative ways to use thin films and to combine distinct responsiveness for fabricating, *e.g.*, touchless screens. These recent breakthroughs will potentially have broad implications for the future of electronic devices and interactive surfaces and their multitude of applications.

Hydrogel optical fibers pose more complex 3D structures than these films and they can transport light across considerable lengths. They have been engineered to respond and shift light properties from their interaction with several analytes of interest. Interestingly, most hydrogel optical fibers have focused on similar materials and relatively simple fabrication approaches. On that note, we expect significant advances in hydrogel fiber-optics as complex hydrogel fiber biofabrication methods merge towards the optical field. This translation will likely improve optical fiber performance and increase complexity in both shape and stimuli responsiveness. Similarly, 3D printing of hydrogels has presented remarkable developments in tissue engineering and regenerative medicine in recent years. Few studies have explored the possibility of combining the precise material deposition and organization of 3D printing technologies with optically relevant shapes, where novel types of optical inks can introduce light-guiding channels and conduits within complex 3D printed constructs [69,80].

As an alternative at smaller dimensions, nanostructured hydrogels have been shown to recapitulate the structural coloring found in nature. Similarly, by engineering hydrogels, scientists created structurally colored arrangements that can be assembled into complex optical structures that can actively respond to deformation. These constructs have been explored for tracking forces such as those made by contractile cells in novel real-time mechano-optical transduction platforms and living robots. Further, structuring of hydrogels and their active optical arrangement have been applied for holographic imaging and recapitulating shapes and information, which can be useful for bio medically relevant data storage and encryption.

One other important point we outlined is the need for hydrogel photonics to be combined with living entities such as encapsulated cells. Even though cells are considered optically inert in multiple studies, there have been others where cells are considered as an integral part of the active optical entity, e.g., biological waveguides. Simultaneously, hydrogels might not only passively guide light but also respond to it, as in reversible cross-linking events. Combined, the possibility of having light not only guided but also actively shaping the hydrogel/cell interface will likely lead to exciting advances in hydrogel optics. When these optics are fully integrated with live constructs, light can direct materials and cells towards distinct mechanical states and cellular phenotypes. At the same time, optical readouts might facilitate real-time screening. These readouts can inform on complex cellular events such as proliferation, differentiation, and matrix deposition, or even assess drug efficacy in 3D engineered tissues.

Further, we explored the possibility of combining hydrogel photonics with multi-responsive hydrogel systems, taking advantage of the years of scientific research in the topic. Therein, we presented examples of hydrogel photonic responsiveness combined with magnetic, thermal, and electric stimuli. The combination of these distinct responses in a single structure is shown to be possible and will likely allow systems to respond to and inform on a plethora of stimuli. These can be further leveraged towards assembling and structuring of complex hydrogel constructs as sensors.

Moreover, combination of multiple responses in hydrogel structures has also enabled impressive light-driven locomotion capabilities. Hydrogel robots have emerged as capable tools with motion omnidirectionality and exciting possibilities in micro-robotics which might reach clinical applications soon. Overcoming the challenge of combining both negative and positive hydrogel phototaxis within the same structure is likely the next step to obtain more comprehensive motion ranges of these soft, biocompatible structures.

We also discussed how the combination and engineering of multi-responsive hydrogel systems led to recent advances in photomedicine. In this scope, light actuation as a therapeutic trigger has been shown to modulate complex tumor microenvironmental events. Further, light-based therapies can go far beyond simple cancer cell death. These complex photosystems with aggressive anti-cancer effects might be tuned down and converted into healthy stem-cell friendly tools. Also, the possibility of actively promoting tissue regeneration with these systems is opening up an entirely new avenue of investigations.

As a final topic, we explored the field of organ-on-a-chip technologies, which have yielded complex biological models in recent years, with proven applications in drug testing and optimization. Hydrogels, commonly used as 3D environments within these systems, can be leveraged for designing intricate shapes and architectures on-chip via hydrogel precursor flow and controlled light-based crosslinking. Moreover, the integration of photonic hydrogel structures within on-chip models can potentially reveal a game-changing addition to the field by enabling rapid, label-free detection of on-chip events in real-time. This advance is likely to add entirely a new time-dependent dimension to the collected information, bringing the science ever closer to modeling the actual physiological microenvironment as a complementary alternative to animal models.

Globally, under the light of all recent advances and the broadening scope of emerging ideas and applications, the field of hydrogel photonics has a promising long path forward as an emerging field with broad applications that span from biosensing to tissue models. Additionally, the close relationship between the materials and the fabrication techniques, accelerated by advances in these fields across interdisciplinary areas, will likely bring along exciting new engineered photonic structures and innovative applications. Optical platforms are likely to remain - as light itself - the fastest and most efficient solutions for biomedical detection, sensing, and screening. Transposing these platforms towards living environments is becoming a reality through engineering hydrogels as photonic materials cutting across multiple disciplines. As we observe the advances in this promising field currently, hydrogels are continuing to emerge as biologically compatible alternatives or complementary tools for the creation of next generation of living tissue photonics, spanning broad applications from scientific experiments on the benchtop to serving the needs of patients at the clinic or at the point of care in the future.

V.11. REFERENCES

1. Zhang, Y. S. & Khademhosseini, A. Advances in engineering hydrogels. *Science* (2017).

doi:10.1126/science.aaf3627

2. Peppas, N. A., Hilt, J. Z., Khademhosseini, A. & Langer, R. Hydrogels in biology and medicine: From molecular principles to bionanotechnology. *Advanced Materials* (2006). doi:10.1002/adma.200501612
3. Yue, K. *et al.* Synthesis, properties, and biomedical applications of gelatin methacryloyl (GelMA) hydrogels. *Biomaterials* (2015). doi:10.1016/j.biomaterials.2015.08.045
4. Slaughter, B. V., Khurshid, S. S., Fisher, O. Z., Khademhosseini, A. & Peppas, N. A. Hydrogels in regenerative medicine. *Adv. Mater.* **21**, 3307–3329 (2009).
5. Wang, Y. Programmable hydrogels. *Biomaterials* **178**, 663–680 (2018).
6. Kamata, H., Li, X., Chung, U. Il & Sakai, T. Design of Hydrogels for Biomedical Applications. *Adv. Healthc. Mater.* **4**, 2360–2374 (2015).
7. Seliktar, D. Designing cell-compatible hydrogels for biomedical applications. *Science (80-.).* **336**, 1124–1128 (2012).
8. Geckil, H., Xu, F., Zhang, X., Moon, S. & Demirci, U. Engineering hydrogels as extracellular matrix mimics. *Nanomedicine* **5**, 469–484 (2010).
9. Liu, X., Liu, J., Lin, S. & Zhao, X. Hydrogel machines. *Mater. Today* **36**, 102–124 (2020).
10. Liu, H. *et al.* Advances in Hydrogels in Organoids and Organs-on-a-Chip. *Adv. Mater.* **31**, 1–28 (2019).
11. Verhulsel, M. *et al.* A review of microfabrication and hydrogel engineering for micro-organs on chips. *Biomaterials* **35**, 1816–1832 (2014).
12. Kirschner, C. M. & Anseth, K. S. Hydrogels in healthcare: From static to dynamic material microenvironments. *Acta Mater.* **61**, 931–944 (2013).
13. Rizwan, M. *et al.* pH sensitive hydrogels in drug delivery: Brief history, properties, swelling, and release mechanism, material selection and applications. *Polymers (Basel).* **9**, (2017).
14. Langer, R. & Vacanti, J. P. Tissue Engineering. *Science (80-.).* **260**, 920–926 (1993).
15. Lim, F. & Sun, A. M. Microencapsulated islets as bioartificial endocrine pancreas. *Science (80-.).* (1980). doi:10.1126/science.6776628
16. Raemdonck, K., Demeester, J. & De Smedt, S. Advanced nanogel engineering for drug delivery. *Soft Matter* **5**, 707–715 (2009).
17. Nochi, T. *et al.* Nanogel antigenic protein-delivery system for adjuvant-free intranasal vaccines. *Nat. Mater.* **9**, 572–578 (2010).
18. Zhao, C., Yuan, G., Jia, D. & Han, C. C. Macrogel induced by microgel: Bridging and depletion mechanisms. *Soft Matter* **8**, 7036–7043 (2012).
19. Lyon, L. A., Meng, Z., Singh, N., Sorrell, C. D. & John, A. S. Thermoresponsive microgel-based materials. *Chem. Soc. Rev.* **38**, 865–874 (2009).
20. Eggermont, L. J., Rogers, Z. J., Colombani, T., Memic, A. & Bencherif, S. A. Injectable Cryogels for Biomedical Applications. *Trends Biotechnol.* **38**, 418–431 (2020).
21. Cascone, S. & Lamberti, G. Hydrogel-based commercial products for biomedical applications: A review. *Int. J. Pharm.* **573**, 118803 (2020).
22. Naghii, M. R. The significance of water in sport and weight control. *Nutr. Health* **14**, 127–132 (2000).
23. Guimarães, C. F., Gasperini, L., Marques, A. P. & Reis, R. L. The stiffness of living tissues and its implications for tissue engineering. *Nat. Rev. Mater.* **5**, 351–370 (2020).
24. Hoffman, A. S. Hydrogels for biomedical applications. *Adv. Drug Deliv. Rev.* **64**, 18–23 (2012).
25. Nicodemus, G. D. & Bryant, S. J. Cell encapsulation in biodegradable hydrogels for tissue engineering applications. *Tissue Eng. - Part B Rev.* **14**, 149–165 (2008).
26. Tan, W. H. & Takeuchi, S. Monodisperse alginate hydrogel microbeads for cell encapsulation. *Adv. Mater.* **19**, 2696–2701 (2007).

27. Vermonden, T., Censi, R. & Hennink, W. E. Hydrogels for protein delivery. *Chem. Rev.* **112**, 2853–2888 (2012).

28. Eddington, D. T. & Beebe, D. J. Flow control with hydrogels. *Adv. Drug Deliv. Rev.* **56**, 199–210 (2004).

29. Karadağ, E., Saraydin, D., Çaldiran, Y. & Güven, O. Swelling studies of copolymeric acrylamide/crotonic acid hydrogels as carriers for agricultural uses. *Polym. Adv. Technol.* **11**, 59–68 (2000).

30. Hoffman, A. S. Conventional and environmentally-sensitive hydrogels for medical and industrial uses. A review paper. in *American Chemical Society, Polymer Preprints, Division of Polymer Chemistry* (1990). doi:10.1007/978-1-4684-5892-3_21

31. Leith, E. N. & Upatnieks, J. Reconstructed Wavefronts and Communication Theory*. *J. Opt. Soc. Am.* (1962). doi:10.1364/josa.52.001123

32. Denisyuk, Y. N. On the reflection of optical properties of an object in a wave field of light scattered by it. *Dokl. Akad. Nauk SSSR* **144**, 1275–1278 (1962).

33. Caló, E. & Khutoryanskiy, V. V. Biomedical applications of hydrogels: A review of patents and commercial products. *Eur. Polym. J.* **65**, 252–267 (2015).

34. Tavakoli, J. & Tang, Y. Hydrogel based sensors for biomedical applications: An updated review. *Polymers (Basel).* **9**, 1–25 (2017).

35. Singh, S. R. Advanced Hydrogels for Biomedical Applications. *Biomed. J. Sci. Tech. Res.* **5**, 4302–4306 (2018).

36. Choi, J. R., Yong, K. W., Choi, J. Y. & Cowie, A. C. Recent advances in photo-crosslinkable hydrogels for biomedical applications. *Biotechniques* **66**, 40–53 (2019).

37. Umar, M., Min, K. & Kim, S. Advances in hydrogel photonics and their applications. *APL Photonics* **4**, (2019).

38. Yan, R., Gargas, D. & Yang, P. Nanowire photonics. *Nat. Photonics* **3**, 569–576 (2009).

39. Lu, L., Joannopoulos, J. D. & Soljačić, M. Topological photonics. *Nat. Photonics* **8**, 821–829 (2014).

40. Yao, J. Microwave Photonics. *J. Light. Technol.* **27**, 314–335 (2009).

41. Li, Z. *et al.* Plasmonic-based platforms for diagnosis of infectious diseases at the point-of-care. *Biotechnol. Adv.* **37**, 107440 (2019).

42. Mejía-Salazar, J. R. & Oliveira, O. N. Plasmonic Biosensing. *Chem. Rev.* **118**, 10617–10625 (2018).

43. Kim, M. *et al.* Maximal energy transport through disordered media with the implementation of transmission eigenchannels. *Nat. Photonics* **6**, 581–585 (2012).

44. Choi, M. *et al.* Light-guiding hydrogels for cell-based sensing and optogenetic synthesis in vivo. *Nat. Photonics* **7**, 987–994 (2013).

45. Gambling, W. A. The rise and rise of optical fibers. *IEEE J. Sel. Top. Quantum Electron.* **6**, 1084–1093 (2000).

46. Nizamoglu, S., Gather, M. C. & Yun, S. H. All-biomaterial laser using vitamin and biopolymers. *Adv. Mater.* **25**, 5943–5947 (2013).

47. Born, M., Wolf, E. & Hecht, E. Principles of Optics: Electromagnetic Theory of Propagation, Interference and Diffraction of Light . *Phys. Today* (2000). doi:10.1063/1.1325200

48. Bolin, F. P., Preuss, L. E., Taylor, R. C. & Ference, R. J. Refractive index of some mammalian tissues using a fiber optic cladding method. *Appl. Opt.* (1989). doi:10.1364/ao.28.002297

49. Taffoni, F., Formica, D., Saccomandi, P., Di Pino, G. & Schena, E. Optical fiber-based MR-compatible sensors for medical applications: An overview. *Sensors (Switzerland)* **13**, 14105–14120 (2013).

50. Cibula, E., Donlagic, D. & Stropnik, C. Miniature Fiber Optic Pressure Sensor for Medical Applications. *Proc. IEEE Sensors* **1**, 711–714 (2002).

51. Khademhosseini, A. & Langer, R. Microengineered hydrogels for tissue engineering. *Biomaterials* **28**, 5087–5092 (2007).

52. Canadas, R. F. *et al.* Tunable anisotropic networks for 3-D oriented neural tissue models. *Biomaterials* **181**, 402–414 (2018).

53. Canadas, R. F. *et al.* Biochemical Gradients to Generate 3D Heterotypic-Like Tissues with Isotropic and Anisotropic

Architectures. *Adv. Funct. Mater.* **28**, (2018).

54. Zhang, X., Guan, Y. & Zhang, Y. Ultrathin hydrogel films for rapid optical biosensing. *Biomacromolecules* **13**, 92–97 (2012).

55. Tokarev, I., Tokareva, I., Gopishetty, V., Katz, E. & Minko, S. Specific biochemical-to-optical signal transduction by responsive thin hydrogel films loaded with noble metal nanoparticles. *Adv. Mater.* **22**, 1412–1416 (2010).

56. Knight, J. C., Birks, T. A., Russell, P. S. J. & Atkin, D. M. All-silica single-mode optical fiber with photonic crystal cladding. *Opt. Lett.* **22**, 484 (1997).

57. Cruz-Acuña, R. *et al.* Synthetic hydrogels for human intestinal organoid generation and colonic wound repair. *Nat. Cell Biol.* **19**, 1326–1335 (2017).

58. Cruz-Acuña, R. & García, A. J. Synthetic hydrogels mimicking basement membrane matrices to promote cell-matrix interactions. *Matrix Biol.* **57–58**, 324–333 (2017).

59. Guo, J. *et al.* Highly Stretchable, Strain Sensing Hydrogel Optical Fibers. *Adv. Mater.* **28**, 10244–10249 (2016).

60. Yetisen, A. K. *et al.* Reusable, robust, and accurate laser-generated photonic nanosensor. *Nano Lett.* **14**, 3587–3593 (2014).

61. Pathak, A. K. & Singh, V. K. A wide range and highly sensitive optical fiber pH sensor using polyacrylamide hydrogel. *Opt. Fiber Technol.* **39**, 43–48 (2017).

62. Elsherif, M., Hassan, M. U., Yetisen, A. K. & Butt, H. Hydrogel optical fibers for continuous glucose monitoring. *Biosens. Bioelectron.* **137**, 25–32 (2019).

63. Zhou, C. *et al.* High water content hydrogel with super high refractive index. *Macromol. Biosci.* **13**, 1485–1491 (2013).

64. Zhou, M., Guo, J. & Yang, C. Ratiometric fluorescence sensor for Fe3+ ions detection based on quantum dot-doped hydrogel optical fiber. *Sensors Actuators, B Chem.* **264**, 52–58 (2018).

65. Choi, M., Humar, M., Kim, S. & Yun, S. H. Step-Index Optical Fiber Made of Biocompatible Hydrogels. *Adv. Mater.* **27**, 4081–4086 (2015).

66. Yetisen, A. K. *et al.* Glucose-Sensitive Hydrogel Optical Fibers Functionalized with Phenylboronic Acid. *Adv. Mater.* **29**, (2017).

67. Hu, W., Wang, Z., Xiao, Y., Zhang, S. & Wang, J. Advances in crosslinking strategies of biomedical hydrogels. *Biomater. Sci.* **7**, 843–855 (2019).

68. Lu, L. *et al.* The Formation Mechanism of Hydrogels. *Current Stem Cell Research & Therapy* **13**, 490–496 (2018).

69. Fu, F. *et al.* Bio-inspired self-healing structural color hydrogel. *Proc. Natl. Acad. Sci. U. S. A.* **114**, 5900–5905 (2017).

70. Manocchi, A. K., Domachuk, P., Omenetto, F. G. & Yi, H. Facile fabrication of gelatin-based biopolymeric optical waveguides. *Biotechnol. Bioeng.* **103**, 725–732 (2009).

71. Ahmed, R., Yetisen, A. K., Yun, S. H. & Butt, H. Color-selective holographic retroreflector array for sensing applications. *Light Sci. Appl.* **6**, e16214-9 (2017).

72. Jeon, O., Bouhadir, K. H., Mansour, J. M. & Alsberg, E. Photocrosslinked alginate hydrogels with tunable biodegradation rates and mechanical properties. *Biomaterials* **30**, 2724–2734 (2009).

73. Bouhadir, K. H. *et al.* Degradation of partially oxidized alginate and its potential application for tissue engineering. *Biotechnol. Prog.* **17**, 945–950 (2001).

74. Jain, A., Yang, A. H. J. & Erickson, D. Gel-based optical waveguides with live cell encapsulation and integrated microfluidics. *Opt. Lett.* **37**, 1472 (2012).

75. Dupuis, A. *et al.* Prospective for biodegradable microstructured optical fibers. *Opt. Lett.* **32**, 109 (2007).

76. Applegate, M. B., Perotto, G., Kaplan, D. L. & Omenetto, F. G. Biocompatible silk step-index optical waveguides. *Biomed. Opt. Express* **6**, 4221 (2015).

77. Wang, X., Li, Q., Guan, Y. & Zhang, Y. Glucose oxidase-incorporated hydrogel thin film for fast optical glucose detecting under physiological conditions. *Mater. Today Chem.* **1–2**, 7–14 (2016).

78. Mano, J. F. *et al.* Natural origin biodegradable systems in tissue engineering and regenerative medicine: Present status and some moving trends. *J. R. Soc. Interface* **4**, 999–1030 (2007).

79. Gasperini, L., Mano, J. F. & Reis, R. L. Natural polymers for the microencapsulation of cells. *J. R. Soc. Interface* **11**, 20140817–20140817 (2014).

80. Trampe, E. *et al.* Functionalized Bioink with Optical Sensor Nanoparticles for O2 Imaging in 3D-Bioprinted Constructs. *Adv. Funct. Mater.* **28**, 1–11 (2018).

81. Gogoi, N., Barooah, M., Majumdar, G. & Chowdhury, D. Carbon dots rooted agarose hydrogel hybrid platform for optical detection and separation of heavy metal ions. *ACS Appl. Mater. Interfaces* **7**, 3058–3067 (2015).

82. Kozlovskaya, V. *et al.* Ultrathin layer-by-layer hydrogels with incorporated gold nanorods as pH-sensitive optical materials. *Chem. Mater.* **20**, 7474–7485 (2008).

83. Tokarev, I., Tokareva, I. & Minko, S. Gold-nanoparticle-enhanced plasmonic effects in a responsive polymer gel. *Adv. Mater.* **20**, 2730–2734 (2008).

84. Lim, H. S., Lee, J. H., Walish, J. J. & Thomas, E. L. Dynamic swelling of tunable full-color block copolymer photonic gels via counterion exchange. *ACS Nano* **6**, 8933–8939 (2012).

85. Yetisen, A. K. *et al.* Light-directed writing of chemically tunable narrow-band holographic sensors. *Adv. Opt. Mater.* **2**, 250–254 (2014).

86. Men, D. *et al.* Optical sensor based on hydrogel films with 2D colloidal arrays attached on both the surfaces: Anti-curling performance and enhanced optical diffraction intensity. *J. Mater. Chem. C* **3**, 3659–3665 (2015).

87. Fu, F., Shang, L., Chen, Z., Yu, Y. & Zhao, Y. Bioinspired living structural color hydrogels. *Sci. Robot.* **3**, eaar8580 (2018).

88. Qiao, X. *et al.* Synthetic Engineering of Spider Silk Fiber as Implantable Optical Waveguides for Low-Loss Light Guiding. *ACS Appl. Mater. Interfaces* **9**, 14665–14676 (2017).

89. Prucker, O., Brandstetter, T. & Rühe, J. Surface-attached hydrogel coatings via C,H-insertion crosslinking for biomedical and bioanalytical applications (Review). *Biointerphases* **13**, 010801 (2018).

90. Kozlovskaya, V., Kharlampieva, E., Erel, I. & Sukhishvili, S. A. Multilayer-derived, ultrathin, stimuli-responsive hydrogels. *Soft Matter* **5**, 4077–4087 (2009).

91. Wang, R., Zhang, M., Guan, Y., Chen, M. & Zhang, Y. A CO2-responsive hydrogel film for optical sensing of dissolved CO2. *Soft Matter* **15**, 6107–6115 (2019).

92. Mateescu, A., Wang, Y., Dostalek, J. & Jonas, U. Thin hydrogel films for optical biosensor applications. *Membranes (Basel).* **2**, 49–69 (2012).

93. Yetisen, A. K. *et al.* Photonic hydrogel sensors. *Biotechnol. Adv.* **34**, 250–271 (2016).

94. Jiang, N. *et al.* Lateral and Vertical Flow Assays for Point-of-Care Diagnostics. *Adv. Healthc. Mater.* **8**, 1–19 (2019).

95. Li, J. & Macdonald, J. Multiplexed lateral flow biosensors: Technological advances for radically improving point-of-care diagnoses. *Biosens. Bioelectron.* **83**, 177–192 (2016).

96. Onoe, H. *et al.* Metre-long cell-laden microfibers exhibit tissue morphologies and functions. *Nat. Mater.* **12**, 584–590 (2013).

97. Mirani, B. *et al.* Facile Method for Fabrication of Meter-Long Multifunctional Hydrogel Fibers with Controllable Biophysical and Biochemical Features. *ACS Appl. Mater. Interfaces* **12**, 9080–9089 (2020).

98. Pi, Q. *et al.* Digitally Tunable Microfluidic Bioprinting of Multilayered Cannular Tissues. *Adv. Mater.* **1706913**, 1706913 (2018).

99. Cheng, Y. *et al.* Bioinspired multicompartmental microfibers from microfluidics. *Adv. Mater.* **26**, 5184–5190 (2014).

100. Shao, L. *et al.* Fiber-Based Mini Tissue with Morphology-Controllable GelMA Microfibers. *Small* **14**, 1–8 (2018).

101. Davoodi, E. *et al.* Extrusion and Microfluidic-Based Bioprinting to Fabricate Biomimetic Tissues and Organs. *Adv. Mater. Technol.* (2020). doi:10.1002/admt.201901044

102. Dai, X. *et al.* Coaxial 3D bioprinting of self-assembled multicellular heterogeneous tumor fibers. *Sci. Rep.* **7**, 1–12

(2017).

103. Attalla, R., Puersten, E., Jain, N. & Selvaganapathy, P. R. 3D bioprinting of heterogeneous bi- and tri-layered hollow channels within gel scaffolds using scalable multi-axial microfluidic extrusion nozzle. *Biofabrication* **11**, 15012 (2018).

104. Arslan-Yildiz, A. *et al.* Towards artificial tissue models: Past, present, and future of 3D bioprinting. *Biofabrication* **8**, 0 (2016).

105. Mota, C., Camarero-Espinosa, S., Baker, M. B., Wieringa, P. & Moroni, L. Bioprinting: From Tissue and Organ Development to in Vitro Models . *Chem. Rev.* (2020). doi:10.1021/acs.chemrev.9b00789

106. Parfenov, V. A. *et al.* Magnetic levitational bioassembly of 3D tissue construct in space. *Sci. Adv.* **6**, eaba4174 (2020).

107. Skardal, A. *et al.* A hydrogel bioink toolkit for mimicking native tissue biochemical and mechanical properties in bioprinted tissue constructs. *Acta Biomater.* **25**, 24–34 (2015).

108. Chimene, D., Kaunas, R. & Gaharwar, A. K. Hydrogel Bioink Reinforcement for Additive Manufacturing: A Focused Review of Emerging Strategies. *Adv. Mater.* **32**, 1–22 (2020).

109. Montelongo, Y., Yetisen, A. K., Butt, H. & Yun, S. H. Reconfigurable optical assembly of nanostructures. *Nat. Commun.* **7**, (2016).

110. Ahmed, R., Yetisen, A. K., Yun, S. H. & Butt, H. Color-selective holographic retroreflector array for sensing applications. *Light Sci. Appl.* **6**, e16214-9 (2017).

111. Lee, Y.-J. & Braun, P. V. Tunable Inverse Opal Hydrogel pH Sensors. *Adv. Mater.* **15**, 563–566 (2003).

112. Suri, J. T., Cordes, D. B., Cappuccio, F. E., Wessling, R. A. & Singaram, B. Continuous Glucose Sensing with a Fluorescent Thin-Film Hydrogel. *Angew. Chemie - Int. Ed.* **42**, 5857–5859 (2003).

113. Yetisen, A. K. The Prospects for Holographic Sensors. in *Holographic Sensors* (Springer, 2015). doi:10.1007/978-3-319-13584-7_7

114. Yetisen, A. K. Fundamentals of Holographic Sensing. in *Holographic Sensors* (Springer, 2015). doi:10.1007/978-3-319-13584-7_2

115. Kang, H. S. *et al.* 3D touchless multiorder reflection structural color sensing display. *Sci. Adv.* **6**, (2020).

116. Tokarev, I. & Minko, S. Stimuli-responsive hydrogel thin films. *Soft Matter* **5**, 511–524 (2009).

117. Lei, Z., Wang, Q. & Wu, P. A multifunctional skin-like sensor based on a 3D printed thermo-responsive hydrogel. *Mater. Horizons* **4**, 694–700 (2017).

118. Lei, Z., Wang, Q., Sun, S., Zhu, W. & Wu, P. A Bioinspired Mineral Hydrogel as a Self-Healable, Mechanically Adaptable Ionic Skin for Highly Sensitive Pressure Sensing. *Adv. Mater.* **29**, 1–6 (2017).

119. Maurer, R. D. Strength of fiber optical waveguides. *Appl. Phys. Lett.* **27**, 220–221 (1975).

120. Guo, J., Zhou, M. & Yang, C. Fluorescent hydrogel waveguide for on-site detection of heavy metal ions. *Sci. Rep.* **7**, 1–8 (2017).

121. Zhou, M., Guo, J. & Yang, C. Ratiometric fluorescence sensor for Fe3+ ions detection based on quantum dot-doped hydrogel optical fiber. *Sensors Actuators, B Chem.* **264**, 52–58 (2018).

122. Jiang, N. *et al.* Functionalized Flexible Soft Polymer Optical Fibers for Laser Photomedicine. *Adv. Opt. Mater.* **6**, 1–10 (2018).

123. Feng, J. *et al.* Printed Degradable Optical Waveguides for Guiding Light into Tissue. *Adv. Funct. Mater.* **2004327**, 1–14 (2020).

124. Fujiwara, E., Cabral, T. D., Sato, M., Oku, H. & Cordeiro, C. M. B. Agarose-based structured optical fiber. *Sci. Rep.* **10**, 1–8 (2020).

125. Xu, P. *et al.* Bioinspired Microfibers with Embedded Perfusable Helical Channels. *Adv. Mater.* **29**, 1–7 (2017).

126. Parker, A. R. 515 Million Years of Structural Color. *J. Opt. A Pure Appl. Opt.* **2**, (2000).

127. Burg, S. L. & Parnell, A. J. Self-assembling structural color in nature. *J. Phys. Condens. Matter* **30**, (2018).

128. Guidetti, G., Sun, H., Marelli, B. & Omenetto, F. G. Photonic paper : Multiscale assembly of reflective cellulose sheets in Lunaria annua. *Sci. Adv.* **6**, (2020).

129. Teyssier, J., Saenko, S. V., Van Der Marel, D. & Milinkovitch, M. C. Photonic crystals cause active color change in chameleons. *Nat. Commun.* **6**, 1–7 (2015).

130. Kim, H. *et al.* Structural color printing using a magnetically tunable and lithographically fixable photonic crystal. *Nat. Photonics* **3**, 534–540 (2009).

131. Haque, M. A., Kurokawa, T., Kamita, G., Yue, Y. & Gong, J. P. Rapid and reversible tuning of structural color of a hydrogel over the entire visible spectrum by mechanical stimulation. *Chem. Mater.* **23**, 5200–5207 (2011).

132. Haque, M. A., Kamita, G., Kurokawa, T., Tsujii, K. & Gong, J. P. Unidirectional alignment of lamellar bilayer in hydrogel: One-dimensional swelling, anisotropic modulus, and stress/strain tunable structural color. *Adv. Mater.* **22**, 5110–5114 (2010).

133. Yue, Y. *et al.* Mechano-actuated ultrafast full-color switching in layered photonic hydrogels. *Nat. Commun.* **5**, (2014).

134. Zhang, Y. S., Zhu, C. & Xia, Y. Inverse Opal Scaffolds and Their Biomedical Applications. *Adv. Mater.* **29**, 1–25 (2017).

135. Min, K., Kim, S. & Kim, S. Deformable and conformal silk hydrogel inverse opal. *Proc. Natl. Acad. Sci. U. S. A.* **114**, 6185–6190 (2017).

136. Zhang, W. *et al.* Silk Fibroin Biomaterial Shows Safe and Effective Wound Healing in Animal Models and a Randomized Controlled Clinical Trial. *Adv. Healthc. Mater.* **6**, 1–16 (2017).

137. Latorre, E. *et al.* Active superelasticity in three-dimensional epithelia of controlled shape. *Nature* **563**, 203–208 (2018).

138. Vivian, J. *et al.* Toil enables reproducible, open source, big biomedical data analyses. *Nat. Biotechnol.* **35**, 314–316 (2017).

139. Xin, H., Li, Y., Liu, X. & Li, B. Escherichia coli -based biophotonic waveguides. *Nano Lett.* **13**, 3408–3413 (2013).

140. Bezryadina, A. *et al.* Nonlinear Self-Action of Light through Biological Suspensions. *Phys. Rev. Lett.* **119**, 1–6 (2017).

141. Wu, X. *et al.* Reversible hydrogels with tunable mechanical properties for optically controlling cell migration. *Nano Res.* **11**, 5556–5565 (2018).

142. Liu, L. *et al.* Cyclic Stiffness Modulation of Cell-Laden Protein–Polymer Hydrogels in Response to User-Specified Stimuli Including Light. *Adv. Biosyst.* **2**, 1–9 (2018).

143. Humar, M. & Yun, S. H. Whispering-gallery-mode emission from biological luminescent protein microcavity assemblies. *Optica* **4**, 222 (2017).

144. Constant, C., Bergano, A., Sugaya, K. & Dogariu, A. Guiding cellular activity with polarized light. *J. Biophotonics* **11**, 1–9 (2018).

145. Ogawa, J. *et al.* Genetic manipulation of the optical refractive index in living cells. *bioRxiv* 2020.07.09.196436 (2020). doi:10.1101/2020.07.09.196436

146. Lyu, S. *et al.* Optically controlled reversible protein hydrogels based on photoswitchable fluorescent protein Dronpa. *Chem. Commun.* **53**, 13375–13378 (2017).

147. Koetting, M. C., Peters, J. T., Steichen, S. D. & Peppas, N. A. Stimulus-responsive hydrogels: Theory, modern advances, and applications. *Mater. Sci. Eng. R Reports* **93**, 1–49 (2015).

148. Sharifzadeh, G. & Hosseinkhani, H. Biomolecule-Responsive Hydrogels in Medicine. *Adv. Healthc. Mater.* **6**, 1–35 (2017).

149. Hoque, J., Sangaj, N. & Varghese, S. Stimuli-Responsive Supramolecular Hydrogels and Their Applications in Regenerative Medicine. *Macromol. Biosci.* **19**, 1–16 (2019).

150. Zhao, X. *et al.* Active scaffolds for on-demand drug and cell delivery. *Proc. Natl. Acad. Sci. U. S. A.* **108**, 67–72 (2011).

151. Soto, F., Wang, J., Deshmukh, S. & Demirci, U. Reversible Design of Dynamic Assemblies at Small Scales. *Adv. Intell. Syst.* (2020).

152. Wang, W. *et al.* Magnetochromic Photonic Hydrogel for an Alternating Magnetic Field-Responsive Color Display. *Adv. Opt. Mater.* **6**, 1–9 (2018).

153. Gui, Q. *et al.* Inherently magnetic hydrogel for data storage based on the magneto-optical Kerr effect. *Soft Matter* **15**, 393–398 (2019).

154. Isabettini, S. *et al.* Development of Smart Optical Gels with Highly Magnetically Responsive Bicelles. *ACS Appl. Mater. Interfaces* **10**, 8926–8936 (2018).

155. Rittikulsittichai, S. *et al.* Multi-responsive hybrid particles: Thermo-, pH-, photo-, and magneto-responsive magnetic hydrogel cores with gold nanorod optical triggers. *Nanoscale* **8**, 11851–11861 (2016).

156. Zhao, L. B. *et al.* Generation of Janus alginate hydrogel particles with magnetic anisotropy for cell encapsulation. *Lab Chip* **9**, 2981–2986 (2009).

157. Tasoglu, S. *et al.* Guided and magnetic self-assembly of tunable magnetoceptive gels. *Nat. Commun.* **5**, (2014).

158. Sun, X. *et al.* Unique thermo-responsivity and tunable optical performance of poly(N-isopropylacrylamide)-cellulose nanocrystal hydrogel films. *Carbohydr. Polym.* **208**, 495–503 (2019).

159. Tang, C., Li, B., Zou, C., Liu, L. & Chen, H. Voltage-induced wrinkle performance in a hydrogel by dielectric elastomer actuation. *Polymers (Basel).* **10**, (2018).

160. Fernandes, M. S. *et al.* Hydrogel-based photonic sensor for a biopotential wearable recording system. *Biosens. Bioelectron.* **26**, 80–86 (2010).

161. Klouda, L. & Mikos, A. G. Thermoresponsive hydrogels in biomedical applications. *Eur. J. Pharm. Biopharm.* **68**, 34–45 (2008).

162. Taylor, M., Tomlins, P. & Sahota, T. Thermoresponsive Gels. *Gels* **3**, 4 (2017).

163. Seo, S.-W., Enemuo, A. N. & Azmand, H. R. Fast Thermoresponsive Optical Membrane Using Hydrogels Embedded in Macroporous Silicon. *IEEE Sensors Lett.* (2018). doi:10.1109/lsens.2018.2832006

164. Junk, M. J. N., Ilke, A., Menges, B. & Jonas, U. Analysis of optical gradient profiles during temperature- and salt-dependent swelling of thin responsive hydrogel films. *Langmuir* **26**, 12253–12259 (2010).

165. Zadražil, A. & Štěpánek, F. Investigation of thermo-responsive optical properties of a composite hydrogel. *Colloids Surfaces A Physicochem. Eng. Asp.* **372**, 115–119 (2010).

166. Zhao, Y., Lei, M., Liu, S. X. & Zhao, Q. Smart hydrogel-based optical fiber SPR sensor for pH measurements. *Sensors Actuators, B Chem.* **261**, 226–232 (2018).

167. Ramón-Azcón, J. *et al.* Dielectrophoretically aligned carbon nanotubes to control electrical and mechanical properties of hydrogels to fabricate contractile muscle myofibers. *Adv. Mater.* **25**, 4028–4034 (2013).

168. Ahadian, S. *et al.* Hybrid hydrogels containing vertically aligned carbon nanotubes with anisotropic electrical conductivity for muscle myofiber fabrication. *Sci. Rep.* **4**, 1–11 (2014).

169. Janovák, L. & Dékány, I. Optical properties and electric conductivity of gold nanoparticle-containing, hydrogel-based thin layer composite films obtained by photopolymerization. *Appl. Surf. Sci.* **256**, 2809–2817 (2010).

170. Lee, S. N., Baek, Y. Bin & Shin, D. M. Band gap control using electric field of photonic gel cells fabricated with block copolymer and hydrogel. *J. Nanosci. Nanotechnol.* **14**, 6053–6055 (2014).

171. Ahmed, R. *et al.* Tunable Fano-Resonant Metasurfaces on a Disposable Plastic-Template for Multimodal and Multiplex Biosensing. *Adv. Mater.* **1907160**, 1–11 (2020).

172. Hamon, C., Novikov, S., Scarabelli, L., Basabe-Desmonts, L. & Liz-Marzán, L. M. Hierarchical self-assembly of gold nanoparticles into patterned plasmonic nanostructures. *ACS Nano* **8**, 10694–10703 (2014).

173. Guay, J. M. *et al.* Laser-induced plasmonic colors on metals. *Nat. Commun.* **8**, (2017).

174. Kim, J. *et al.* Electrical control of optical plasmon resonance with graphene. *Nano Lett.* **12**, 5598–5602 (2012).

175. Jo, G. *et al.* The application of graphene as electrodes in electrical and optical devices. *Nanotechnology* **23**, (2012).

176. Song, H. S., Kwon, O. S., Kim, J. H., Conde, J. & Artzi, N. 3D hydrogel scaffold doped with 2D graphene materials for biosensors and bioelectronics. *Biosens. Bioelectron.* **89**, 187–200 (2017).

177. Sitti, M. *et al.* Biomedical Applications of Untethered Mobile Milli/Microrobots. *Proc. IEEE. Inst. Electr. Electron. Eng.* **103**, 205–224 (2015).

178. Ren, T., Chen, P., Gu, L., Ogut, M. G. & Demirci, U. Soft Ring-Shaped Cellu-Robots with Simultaneous Locomotion in Batches. *Adv. Mater.* **32**, 1–8 (2020).

179. Wang, J. *et al.* Engineering the Interaction Dynamics between Nano- Topographical Immunocyte-Templated Micromotors across Scales from Ions to Cells. *Small* 20055185 (2020). doi:10.1002/smll.202005185

180. Palagi, S., Singh, D. P. & Fischer, P. Light-Controlled Micromotors and Soft Microrobots. *Adv. Opt. Mater.* **7**, 1–18 (2019).

181. Zeng, H., Wasylczyk, P., Wiersma, D. S. & Priimagi, A. Light Robots: Bridging the Gap between Microrobotics and Photomechanics in Soft Materials. *Adv. Mater.* **30**, 1–9 (2018).

182. Nocentini, S., Parmeggiani, C., Martella, D. & Wiersma, D. S. Optically Driven Soft Micro Robotics. *Adv. Opt. Mater.* **6**, 1–17 (2018).

183. Soto, F., Wang, J., Ahmed, R. & Demirci, U. Medical micro/nanorobots in precision medicine. *Adv. Sci.* (2020).

184. Li, J. *et al.* Development of a magnetic microrobot for carrying and delivering targeted cells. *Sci. Robot.* **3**, 1–12 (2018).

185. Li, H., Go, G., Ko, S. Y., Park, J.-O. & Park, S. Magnetic actuated {pH}-responsive hydrogel-based soft micro-robot for targeted drug delivery. *Smart Mater. Struct.* **25**, 27001 (2016).

186. Zhao, Y. *et al.* Soft phototactic swimmer based on self-sustained hydrogel oscillator. *Sci. Robot.* **4**, 1–11 (2019).

187. Kim, H. *et al.* Light-Driven Shape Morphing, Assembly, and Motion of Nanocomposite Gel Surfers. *Adv. Mater.* **31**, (2019).

188. Zhang, H., Koens, L., Lauga, E., Mourran, A. & Möller, M. A Light-Driven Microgel Rotor. *Small* **15**, (2019).

189. Rehor, I. *et al.* Photoresponsive Hydrogel Microcrawlers Exploit Friction Hysteresis to Crawl by Reciprocal Actuation. *Soft Robot.* **00**, 1–9 (2020).

190. Nishiguchi, A. *et al.* 4D Printing of a Light-Driven Soft Actuator with Programmed Printing Density. *ACS Appl. Mater. Interfaces* **12**, 12176–12185 (2020).

191. Gurkan, U. A. *et al.* Smart interface materials integrated with microfluidics for on-demand local capture and release of cells. *Adv. Healthc. Mater.* **1**, 661–668 (2012).

192. Gurkan, U. A. *et al.* Controlled viable release of selectively captured label-free cells in microchannels. *Lab Chip* **11**, 3979–3989 (2011).

193. Li, C., Iscen, A., Palmer, L. C., Schatz, G. C. & Stupp, S. I. Light-Driven Expansion of Spiropyran Hydrogels. *J. Am. Chem. Soc.* **142**, 8447–8453 (2020).

194. Shahsavan, H. *et al.* Bioinspired underwater locomotion of light-driven liquid crystal gels. *Proc. Natl. Acad. Sci. U. S. A.* **117**, 5125–5133 (2020).

195. Palagi, S. *et al.* Locomotion of light-driven soft microrobots through a hydrogel via local melting. *Int. Conf. Manip. Autom. Robot. Small Scales, MARSS 2017 - Proc.* 1–5 (2017). doi:10.1109/MARSS.2017.8001916

196. Dolmans, D., Fukumura, D. & Jain, R. Photodynamic Therapy for Cancer. *Nat. Rev. Cancer* **3**, 375–380 (2003).

197. Agostinis, P. *et al.* Photodynamic therapy of cancer: An update. *CA. Cancer J. Clin.* **61**, 250–281 (2011).

198. Solban, N., Rizvi, I. & Hasan, T. Targeted photodynamic therapy. *Lasers Surg. Med.* **38**, 522–531 (2006).

199. Celli, J. P. *et al.* Imaging and photodynamic therapy: Mechanisms, monitoring, and optimization. *Chem. Rev.* **110**, 2795–2838 (2010).

200. Mallidi, S. *et al.* Beyond the barriers of light penetration: Strategies, perspectives and possibilities for photodynamic therapy. *Theranostics* **6**, 2458–2487 (2016).

201. Spring, B. Q., Rizvi, I., Xu, N. & Hasan, T. The role of photodynamic therapy in overcoming cancer drug resistance.

Photochem. Photobiol. Sci. **14**, 1476–1491 (2015).

202. Leung, B. *et al.* Development of thermosensitive hydrogel containing methylene blue for topical antimicrobial photodynamic therapy. *J. Photochem. Photobiol. B Biol.* **203**, 111776 (2020).

203. González-Delgado, J. A. *et al.* Hydrogels containing porphyrin-loaded nanoparticles for topical photodynamic applications. *Int. J. Pharm.* **510**, 221–231 (2016).

204. Mao, C. *et al.* Photo-Inspired Antibacterial Activity and Wound Healing Acceleration by Hydrogel Embedded with Ag/Ag@AgCl/ZnO Nanostructures. *ACS Nano* **11**, 9010–9021 (2017).

205. Zhang, Y. *et al.* An injectable dipeptide-fullerene supramolecular hydrogel for photodynamic antibacterial therapy. *J. Mater. Chem. B* **6**, 7335–7342 (2018).

206. Li, M. *et al.* Noninvasive rapid bacteria-killing and acceleration of wound healing through photothermal/photodynamic/copper ion synergistic action of a hybrid hydrogel. *Biomater. Sci.* **6**, 2110–2121 (2018).

207. Xing, R., Liu, Y., Zou, Q. & Yan, X. Self-assembled injectable biomolecular hydrogels towards phototherapy. *Nanoscale* **11**, 22182–22195 (2019).

208. Liu, C. *et al.* A near infrared-modulated thermosensitive hydrogel for stabilization of indocyanine green and combinatorial anticancer phototherapy. *Biomater. Sci.* **7**, 1705–1715 (2019).

209. Xu, X. *et al.* Near-infrared light-triggered degradable hyaluronic acid hydrogel for on-demand drug release and combined chemo-photodynamic therapy. *Carbohydr. Polym.* **229**, 115394 (2020).

210. Luo, L. *et al.* Thermosensitive nanocomposite gel for intra-tumoral two-photon photodynamic therapy. *J. Control. Release* **298**, 99–109 (2019).

211. Xing, R. *et al.* An Injectable Self-Assembling Collagen-Gold Hybrid Hydrogel for Combinatorial Antitumor Photothermal/Photodynamic Therapy. *Adv. Mater.* **28**, 3669–3676 (2016).

212. Meesaragandla, B., Sarkar, D. & Mahalingam, V. Methylene Blue-Loaded Upconverting Hydrogel Nanocomposite: Potential Material for Near-Infrared Light-Triggered Photodynamic Therapy Application. *ACS Omega* **4**, 3169–3177 (2019).

213. Chang, G. *et al.* Effective photodynamic therapy of polymer hydrogel on tumor cells prepared using methylene blue sensitized mesoporous titania nanocrystal. *Mater. Sci. Eng. C* **99**, 1392–1398 (2019).

214. Jin, R. *et al.* Antitumor immunity triggered by photothermal therapy and photodynamic therapy of a 2D MoS2 nanosheet-incorporated injectable polypeptide-engineered hydrogel combinated with chemotherapy for 4T1 breast tumor therapy. *Nanotechnology* **31**, (2020).

215. Zhou, T. J., Xing, L., Fan, Y. T., Cui, P. F. & Jiang, H. L. Inhibition of breast cancer proliferation and metastasis by strengthening host immunity with a prolonged oxygen-generating phototherapy hydrogel. *J. Control. Release* **309**, 82–93 (2019).

216. Meng, Z. *et al.* Light-Triggered In Situ Gelation to Enable Robust Photodynamic-Immunotherapy by Repeated Stimulations. *Adv. Mater.* **31**, 1–12 (2019).

217. Sun, S. K. *et al.* Turning solid into gel for high-efficient persistent luminescence-sensitized photodynamic therapy. *Biomaterials* **218**, 119328 (2019).

218. Zheng, L. *et al.* Intensified Stiffness and Photodynamic Provocation in a Collagen-Based Composite Hydrogel Drive Chondrogenesis. *Adv. Sci.* **6**, (2019).

219. Lu, Z. *et al.* An injectable collagen-genipin-carbon dot hydrogel combined with photodynamic therapy to enhance chondrogenesis. *Biomaterials* **218**, 119190 (2019).

220. Chou, D. B. *et al.* On-chip recapitulation of clinical bone marrow toxicities and patient-specific pathophysiology. *Nat. Biomed. Eng.* **4**, 394–406 (2020).

221. Herland, A. *et al.* Quantitative prediction of human pharmacokinetic responses to drugs via fluidically coupled vascularized organ chips. *Nat. Biomed. Eng.* **4**, 421–436 (2020).

222. Novak, R. *et al.* Robotic fluidic coupling and interrogation of multiple vascularized organ chips. *Nat. Biomed. Eng.* **4**, 407–420 (2020).

223. Miri, A. K. *et al.* Microfluidics-Enabled Multimaterial Maskless Stereolithographic Bioprinting. *Adv. Mater.* **30**, 1–9 (2018).

224. Chen, Y. S. *et al.* Generating digital drug cocktails: Via optical manipulation of drug-containing particles and photo-patterning of hydrogels. *Lab Chip* **19**, 1764–1771 (2019).

225. Guimarães, C. F. *et al.* High-throughput fabrication of cell-laden 3D biomaterial gradients. *Mater. Horiz.* **7**, 2414–2421 (2020).

226. Vega, S. L. *et al.* Combinatorial hydrogels with biochemical gradients for screening 3D cellular microenvironments. *Nat. Commun.* **9**, 614 (2018).

227. Mahadik, B. P., Wheeler, T. D., Skertich, L. J., Kenis, P. J. A. & Harley, B. A. C. Microfluidic Generation of Gradient Hydrogels to Modulate Hematopoietic Stem Cell Culture Environment. *Adv. Healthc. Mater.* **3**, 449–458 (2014).

228. Uzel, S. G. M. *et al.* Microfluidic device for the formation of optically excitable, three-dimensional, compartmentalized motor units. *Sci. Adv.* **2**, (2016).

229. Torres-Mapa, M. L. *et al.* Fabrication of a monolithic lab-on-a-chip platform with integrated hydrogel waveguides for chemical sensing. *Sensors (Switzerland)* **19**, (2019).

230. Wu, J., Zheng, G. & Lee, L. M. Optical imaging techniques in microfluidics and their applications. *Lab Chip* **12**, 3566–3575 (2012).

231. Mencattini, A. *et al.* From petri dishes to organ on chip platform: The increasing importance of machine learning and image analysis. *Front. Pharmacol.* **10**, 1–4 (2019).

232. Lv, C. *et al.* Integrated optofluidic-microfluidic twin channels: Toward diverse application of lab-on-a-chip systems. *Sci. Rep.* **6**, 1–9 (2016).

233. Wang, Z. *et al.* A simple and high-resolution stereolithography-based 3D bioprinting system using visible light crosslinkable bioinks. *Biofabrication* **7**, (2015).

234. Nele, V., Wojciechowski, J. P., Armstrong, J. P. K. & Stevens, M. M. Tailoring Gelation Mechanisms for Advanced Hydrogel Applications. *Adv. Funct. Mater.* **2002759**, 1–22 (2020).

SECTION 2

EXPERIMENTAL DESIGN

Chapter VI

MATERIALS & METHODS

MATERIALS AND METHODS

Overview

This chapter explains and describes the global experimental procedures used in the thesis. We overview the overall methodologies that were transversal to the different experimental chapters, from biofabrication approaches to material and biological characterization techniques. Each chapter of Section E: **Chapter VII-IX** contains experimental sections devoted to specific methodologies only used for that chapter's work.

VI.1. CHOICE OF HYDROGEL MATERIALS

The microfluidic manipulation of hydrogel precursors is a process that occurs at very small dimensions and narrow temporal windows, as typically small volumes flow in small channel dimensions for short periods of time (Chapter IV). Thus, to be able to manipulate hydrogel precursors towards the fabrication of fiber-like constructs and their continuous spinning into hydrogels, the crosslinking of such structures out-of-chip must be an equally fast process. In other words, to translate microfluidic flow organizations into crosslinked hydrogel architectures, the crosslinking must happen almost immediately as the solutions exit the microfluidic chip, otherwise these will change in dimension, or diffuse and rearrange into a different structure.

From the different types of hydrogel crosslinking agents, few are as fast as ionic-based crosslinking, where polymer chains are stabilized by the presence of ions in solution. This process is very characteristic in certain natural-derived polysaccharides, such as Gellan Gum and Alginate, classically crosslinked in the presence of Calcium ions (Ca^{2+}). Allied to their characteristic inert interaction with cells, these materials provide a great structural framework for fabricating hydrogel constructs where cell encapsulation can be done with high levels of viability and provide controllable level of mechanical restriction and consequent biological responses. Furthermore, other types of biological responses can be engineered regardless of the presence of these structural materials, namely by blending different type of molecules which can together make the 3D environment for cell encapsulation more bioactive or biolabile.

Once the fast crosslinking and stabilization of microfluidic-spun hydrogel structures is assured by the presence of an ionic component, materials which are typically harder to crosslink or take larger time to form stable hydrogels can be blended into the precursor mix. Upon crosslinking, the resulting blend is quickly stabilized by the ionic component and can then be processed for promoting the crosslinking of the more bioactive components. In this thesis, the main component employed to enhance cell-material interactions was Gelatin Methacryloyl (GelMA), a denaturated version of collagen which can crosslink in the presence of molecules that connect the methacryl groups, such as the commonly used Irgacure, when exposed to UV-light. The advantages of GelMA *versus* the native collagen are that GelMa does not present any type of charge and does not need to be neutralized with ionic buffers. As such, it enables broader possibilities for blending with ionic polysaccharides such as gellan gum, which would interact with collagen solutions and prevent their flow due to premature crosslinking and consequent channel clogging.

However, for certain applications, using more native matrixes such as pure collagen or even basement-membrane extracts (e.g Geltrex, Matrigel), may be important. In that regard, multi-shaped architectures were also leveraged to enable the integration of materials which present limitations when mixing with ionic polysaccharides. By leveraging separate compartments, it is possible to create fibers which are quickly stabilized by the ionic-crosslinking components, *e.g.,* in the outer compartments, and yet contain a thermal crosslinking material such as GelTrex in the inner compartment. The brief interactions the materials experience within the chip is not enough to promote significant crosslinking as would occur when blending them, thus enabling their stable flow until out-of-chip crosslinking. These types of ECM-derived components can then be crosslinked by incubating the ionically stabilized structures at 37°C or kept directly for cell culture. This approach is further detailed in Chapter VIII.

The next sections provide additional detail on the preparation of the different hydrogel precursor solutions, as well as the crosslinking methods and types of characterization.

VI.2. PREPARATION OF NATURAL HYDROGEL PRECURSORS

All reagents were obtained and used in their commercially available forms. Two ionic polysaccharides were used, Gellan Gum and Alginate. Gellan Gum (Sigma-Aldrich, Germany) hydrogels were prepared by dissolution in water at 90°C until no visible powder was present and a clear solution was obtained. Alginate (Sigma-Aldrich Germany) hydrogels were prepared by dissolving the powder in Phosphate Buffer Saline (PBS) by stirring overnight at room temperature. For obtaining sterile polymeric precursors for cell encapsulation, Alginate and Gellan Gum solutions were dissolved at a low concentration (0.5wt%), filtered through 0.22µm membranes, and freeze-dried (SP Scientific, USA) until a dry sterile material was obtained. The sterile material was then weighted to the desired volume and concentration and dissolved as follows: Gellan Gum powder was dissolved in 50% of the final volume of water at 90°C for around 15-20 minutes. Another 50% of the final volume of 0.5M sucrose (Sigma-Aldrich, Germany) solution was then added, yielding a final solution of gellan gum in 0.25M sucrose for osmotic pressure balancing, as previously described [1]. Differently, sterile Alginate solutions were obtained by dissolving at the desired concentration in PBS, by stirring overnight at room temperature.

Gelatin Methacryloyl (GelMA Bloom300) (Sigma-Aldrich, Germany) hydrogel precursor solutions were prepared by dissolving the freeze-dried reagent in a solution of 0.25M sucrose and in water

containing 0.3% 2-Hydroxy-4′-(2-hydroxyethoxy)-2-methylpropiophenone (Sigma-Aldrich, Germany), and kept at 37°C until use.

Rat Tail Collagen I (Gibco, USA) hydrogel precursors solutions were obtained by neutralization according to manufacturer's instructions. To prepare a given volume (V) at a certain concentration (C), the volume of collagen (Vcol) to use was calculated according to Equation VI-1.

$$Vcol = \frac{Final\ Volume\ (V) * Final\ Collagen\ (C)\ (\frac{mg}{ml})}{Stock\ Collagen\ (\frac{mg}{ml})}$$ (Equation VI-1)

A sterile tube was then prepared with the following components, in the respective volumes:

1. 10x PBS (Sigma-Aldrich, Germany): 0.1*Final Volume (V)
2. NaOH (Sigma-Aldrich, Germany) 1N: 0.023*Volume of Collagen (Vcol)
3. Cold Sterile MQ Water, to fill the remaining total volume according to the equation:

$$VH2O = V - Vcol - Volume\ of\ 10x\ PBS - Volume\ of\ H2O$$ (Equation VI-2)

The resulting mix was placed on ice and after pre-chilling, the collagen solution was added, uniformly blended, and kept on ice until use.

GelTrex Hydrogel Precursors (Thermo Fisher, USA) were used directly as provided, following an overnight thaw at 4°C, except for ready-to-use GelTrex which was used directly from the 4°C stored solution.

VI.3. HYDROGEL CROSSLINKING METHODS

Given the nature of the different hydrogel precursors, different types of crosslinking agents were employed for inducing the sol-gel solution of the solutions into stable crosslinked hydrogels. Gellan Gum- and Alginate-based hydrogels were formed by ionic crosslinking. Collagen and GelTrex hydrogels were crosslinked by thermal stimuli. GelMA hydrogels were crosslinked by UV light.

For ionic crosslinking, the hydrogels were globally exposed to a solution of 0.1M calcium chloride (Sigma-Aldrich, Germany). After crosslinking, these were transferred out of the solution to, *e.g.,* cell culture medium in the case of cell encapsulation studies.

For UV crosslinking, hydrogel precursors were exposed to UV light (320-500nm) (Omnicure series 2000) for 50 seconds at 0.6mW/cm2 at a distance of 8 cm from the lamp. GG/GelMA blends

were fabricated by mixing both solutions and combining both crosslinking (first ionic for a quick stabilization of the structure and then UV for crosslinking the GelMA component).

For thermal crosslinking, hydrogel precursors such as Collagen and GelTrex as well as their blends, were placed at 37°C, typically in cell culture incubator conditions, for crosslinking over at least 45 minutes.

VI.4. HYDROGEL CHARACTERIZATION

The characterization of precursor solutions and crosslinked hydrogels was globally carried out using a Rheometer (Malvern Kinexus Pro+, UK). The dynamic mechanical characterization was used due to the improved capacity to evaluate the viscous component of the hydrogels versus *e.g.*, linear tensile/compression tests.

For studying precursor viscosities, a cone plate geometry (40 mm/ 4°) was used to record the shear viscosity along a range of 0.1–10 0 0s −1 of Shear Rate, typically using around 2mL of solution for analysis.

For the derivation of storage and loss moduli, crosslinked hydrogel disks (8mm diameter, 3mm height) were loaded into the rheometer, and the geometry was moved into contact with the hydrogel, until a very small resistance (0.05N) was detected, point at which loading was complete. The hydrogels were then subjected to a strain amplitude sweep (from 0.01 to 10% strain amplitude), at a fixed 1Hz shear rate, in order to find the linear viscoelastic region. A fixed strain within that region was then selected to perform a frequency sweep (from 0.1 to 10 Hz) and then derive the storage (G') and loss (G'') shear moduli profile of the hydrogels. For quantifying and comparing different moduli throughout the thesis, the G' and G'' values recorded at 1Hz were selected.

Stress relaxation tests were performed by applying fixed 10% shear strain and following the change in shear stress (G(t)) over time, normalized against the initial shear stress, G (0).

VI.5. MICROFLUIDIC-DRIVEN WET SPINNING

Hydrogel precursors were spun into hydrogel fibers following a global wet-spinning protocol with conserved characteristics. Some variations between the distinct experimental chapters are outlined below.

In Chapters VII and VIII, a custom microfluidic system was employed for microfluidic wet-spinning [2]. An OB1 pressure controller and flow sensors (Elvesys, France) were used to regulate the flow of different hydrogel's precursor solutions, by directly applying pressure to individual Eppendorf's containing the distinct materials, connected to the chips by 30 cm of polytetrafluoroethylene microfluidic tubing (0.5x1.6mm). Hydrogel fibers were formed upon ionic crosslinking by directing the hydrogel precursors' flow towards a 0.1M $CaCl_2$ bath (**Fig. VI-1**).

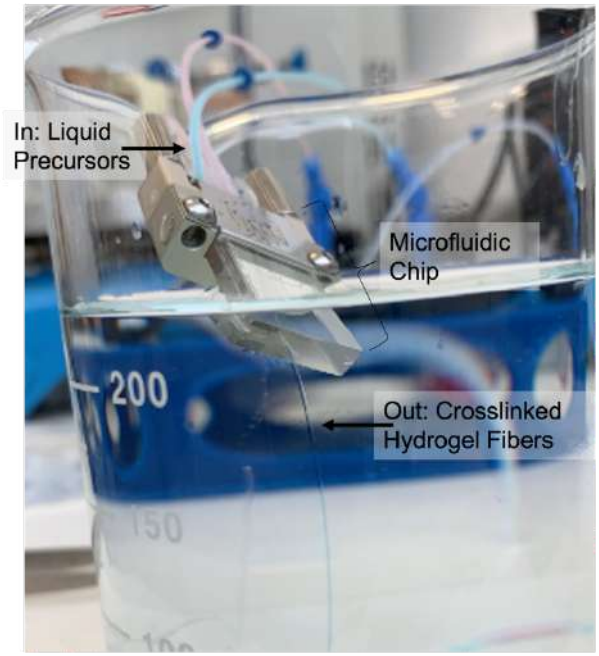


Figure VI-1: Microfluidic Chip-Based Wet-Spinning Setup

This setup was maintained through chapter VII and VIII, with variations in the chips employed for manipulating the hydrogel precursors before spinning. In chapter VII, the flows were forced through a custom-designed T-junction chip with two herringbone mixing stages (Translume, USA) to enable precursor mixing before spinning. The resulting blend was then directed into a linear microfluidic chip (Dolomite, UK) and wet-spun in the 0.1M $CaCl_2$ solution to crosslink the GG. In chapter VIII, a single 3D hydrodynamic flow-focusing chip (Dolomite, UK) was used to fabricate varying fiber's architectures, tuning material characteristics and the organization of precursors in the different chip channels. Further details regarding each experimental approach can be found in the respective methodology parts of the chapters.

In Chapter IX, a distinct setup was used to spin hydrogel fibers of slightly larger dimensions. For controlling precursor flows, the pressure controller was replaced by syringe pumps (Fusion 200, Chemyx). For single-layer fiber spinning, the solutions were inserted into syringes, connected to the

pumps, and then directed through a microfluidic tube of varying dimeter into a crosslinking solution (**Fig. VI-2, a, b**), resulting in fibers with slightly larger diameters than the tube inner size, as some hydrogel expansion happens upon extrusion into the crosslinking bath. For multi-layer fiber spinning, a custom-designed 3D printing coaxial nozzle (Ramé-Hart, USA) was used (**Fig. VI-2, c, d**). The nozzle was connected to the syringes via standard luer locks and immersed in the crosslinking solution for wet spinning.

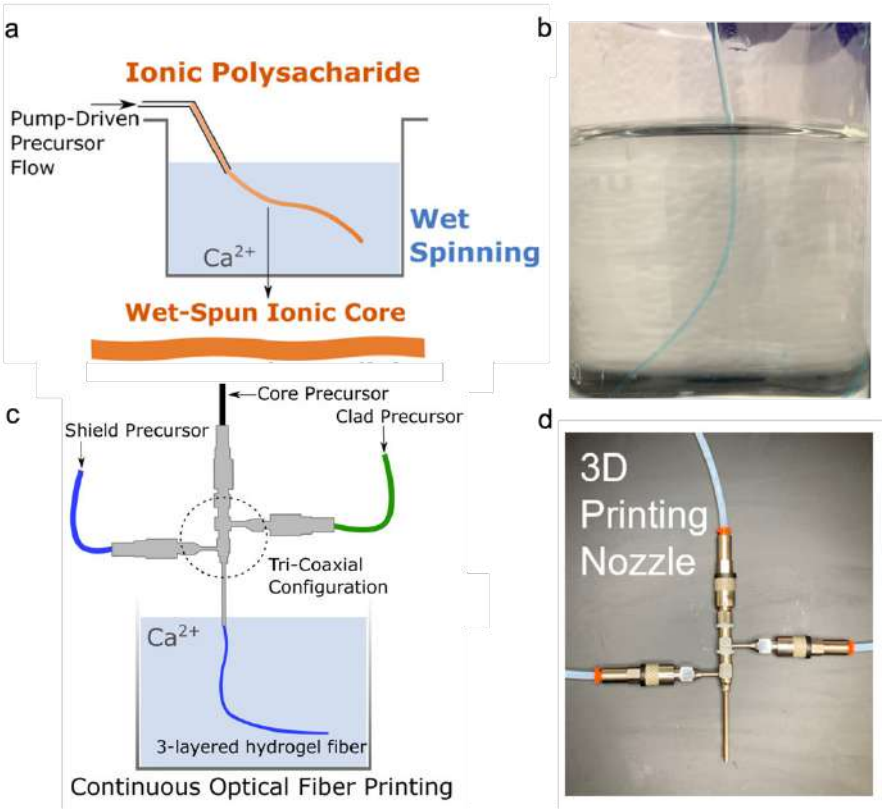


Figure VI-2: Pump-Driven Wet-Spinning Setups – a | Schematic representation of wet-spinning of single layer fibers and photograph of tube immersion setup (b). c | Schematic representaiton of multi-layer fiber wet-spinning *via* tricoaxial nozzle and photograph of the multi-inlet configuration (d).

Further detail regarding specific variations in the flows used, material organization within the channels, and fiber collection process are detailed in the respective experimental chapter IX.

VI.6. CELL SOURCES AND GLOBAL CULTURE METHODS

Throughout the different experimental chapters of this thesis, different types of cells were used, both from established cell lines as well as commercial and in-house isolated primary human

adipose-derived stromal/stem cells. The global list of cells used, the densities used, as well as the media employed for their culture can be found in **Table VI-1**.

Table VI-1: List of cells, culture medium and densities used.

Cell Name	Type	Medium	Densities	Chapters
Adipose-Derived Stromal/Stem Cells (hASCs)	Primary	Alpha-MEM (Gibco, USA)	1-3M/mL	E1
Human Umbilical Vein Endothelial Cells (HUVECs)	Primary (ATCC, USA)	EndoGro (Merck, Germany) /EGM (Lonza, USA)	3M/mL	E2
Human Dermal Microvascular Endothelial Cells	Primary	EndoGro (Merck, Germany) /EGM (Lonza, USA)	3M/mL	E2
Bone Marrow Mesenchymal Stem Cells (BMMSCs)	Primary (ATCC, USA)	Alpha-MEM (Gibco, USA)	1M/mL	E2
Human Dermal Fibroblasts (hDFs)	Primary	Alpha-MEM (Gibco, USA)	1.5M/mL	E2
SK-MEL 28 Melanoma	Cell Line (ATCC, USA)	E-MEM (Quality Biological, USA)	1.5M/mL	E2
3T3 Fibroblasts	Cell Line, ATCC (USA)	DMEM (Gibco, USA)	1-10M/mL	E3
LNCaP Prostate Cancer	Cell Line, ATCC (USA)	RPMI (Gibco, USA)	10M/mL	E3
22Rv1 Prostate Cancer	Cell Line, ATCC (USA)	RPMI (Gibco, USA)	10M/mL	E3
DU145 Prostate Cancer	Cell Line, ATCC (USA)	RPMI (Gibco, USA)	10M/mL	E3

Regarding the hASCs, these were isolated as previously described [3]. Cells were obtained from lipoaspiration surgeries of healthy individuals, after consent and under a collaboration agreement between Hospital da Prelada (Porto) and 3B's Research Group, approved by the respective ethical committees. The adipose tissue samples were subjected to enzymatic digestion, by immersion in a solution of 0.05% collagenase type II (Sigma-Aldrich) while under agitation for 45 min at 37 °C. Afterwards, the samples were centrifuged, and red cells were lysed. The cellular population was then collected and hASCs were selected by plastic adherence. Cultured ASCs are characterized as $CD73^{+}/CD90^{+}/CD105^{+}/CD44^{+}/CD45^{-}/CD31^{-}$ cells [3,4]. hASCs were expanded and cultured in alpha-MEM (Gibco, USA) with 10% FBS (Gibco, USA) and 1% antibiotic, antimycotic (Gibco, USA), up to a maximum passage 4 in the case of differentiation studies.

Regarding hDMECs and hDFs, these were harvested from skin samples obtained from the same surgeries and protocols. Skin samples were cut into small fragments and incubated overnight in dispase (BD Biosciences, USA) at 4° C. The epidermis was peeled off from the specimens and digested with 0.05% Trypsin–EDTA (Invitrogen, USA) at 37 C. Upon dissociating the epidermis, the dermis was further digested in 0.1% collagenase type I (Sigma, USA) for 3 h at 37 C, under agitation. The digested tissue was passed through a 100 μm cell strainer, and the hDFs obtained were cultured in a-MEM medium (Invitrogen, USA) supplemented with 10% fetal bovine serum (FBS) (Invitrogen, USA) and 1% antibiotic/antimycotic. hDMECs were obtained by filtering and centrifuging the discarded dispase solution, after dermis dissociation. hDMECs were cultured in flasks coated with 0.7% gelatin (Sigma, USA), with endothelial growth medium (EGM2, Lonza, USA).

VI.7. CELL VIABILITY TESTS

Common to all experimental chapters, cell viability tests were performed to evaluate the effect of fabrication protocols, culture conditions, or exposure to drugs. For all viability tests, a live/dead staining and image analysis protocol was employed:

Cell-laden hydrogels and microfabricated fibers were processed for viability analysis at varied timepoints by incubating them in the respective media of culture containing Calcein AM 1:1000 (Thermofisher, USA) and Propidium Iodide 1ug/ml (Thermofisher, USA) for 30 minutes at 37°C, 5% CO_2. At the end of the incubation, samples were washed twice with PBS before imaging to remove excess propidium iodide.

Samples were then imaged using an Axio Observer Inverted Microscope (Zeiss). Low-magnification (5x) was used together with Z-stacking for image acquisition. Z-stacks images of the fibers and hydrogels were processed to obtain maximum projection extended depth of focus. This allowed for a good balance between fast imaging and translation of responses from 3D to 2D, maximizing throughput and overcoming 3D computational limitations [5].

Images taken for cell screening were then analyzed with the CellProfiler software a [6]. A custom pipeline was then employed to calculate the percentage of viable cells, according to the following equation:

$$Viability(\%) = \frac{Calcein\ Positive\ Cells - Double\ Positive\ Cells}{Total\ Cells}$$ (Equation VI-3)

Double positive cells are those that show both a detectable Calcein AM and PI signalling. Even though these are, in principle, metabolically active, the internalization of propidium iodide evidences lack of membrane integrity and as such these were considered as dead cells for viability calculation.

Throughout the thesis, the only exception to this method is present in chapter IX, where viability tests were conducted using Ethidium Homodimer 1:1000 (Invitrogen, USA) instead of propidium iodide to perform wash-free viability assessments. The rest of the protocol was maintained without change.

VI.8. IMMUNOCYTOCHEMISTRY METHODS

For immunocytochemistry processing, samples were fixed in formalin 10% (Thermo Fisher, USA) for 10-15 mins at room temperature (RT) (45 minutes for larger hydrogels), washed with PBS and incubated with 0.2% Triton X-100 (Thermo Fisher) in PBS for 12 minutes (15 minutes for larger hydrogels) to enhance cell membrane permeability. After washing, non-specific interactions were blocked by incubation with 3% BSA (Sigma-Aldrich) in PBS for 30 minutes (45 minutes for larger hydrogels).

After blocking, samples were incubated with the primary antibody diluted in 1% BSA for 2 hours at RT, washed with PBS and incubated with the secondary antibody for 1 hour at RT. Longer incubation times of primary antibody overnight at 4°C, and secondary antibody 2 hours at room temperature were used for larger hydrogels. Cell cytoskeleton and nuclei were stained with Phalloidin-TRITC (Sigma-Aldrich, Germany) 2ug/mL and DAPI (Biotium, USA) 4ug/mL simultaneously added with the secondary

antibody. At the end, samples were washed with PBS and imaged or kept in PBS at 4°C, in the dark until that.

Primary antibodies (Anti-Human) used and their respective dilutions: Rabbit Anti-SOX9 1:500 (Merck, Germany), Rabbit Anti-PPAR-gamma 1:100 (Abcam, USA), Rabbit Anti-Ki67 1:250 (Abcam, USA), Mouse Anti-YAP 1:50 (Santa Cruz, USA), Rabbit Anti-Paxillin 1:250 (Abcam, USA), Mouse Anti-Runx2 1:300 (Merck, Germany), Mouse anti-CD31 1:50 (DAKO, USA).

Secondary Antibodies used and their dilutions: Alexa 594 donkey-anti-mouse 1:500 (Molecular Probes, USA), Alexa 488 donkey anti-rabbit 1:500 (Molecular Probes, USA), Alexa 488 donkey-anti-mouse 1:500 (Invitrogen, USA).

Variations in the imaging approach to stained samples as well as image analysis and quantification are further detailed in the different experimental chapters.

VI.9. GLOBAL STATISTICAL ANALYSIS

The statistical analysis performed in this thesis varies depending on the type of datasets and the type of tests needed to analyze them, and such variations are outlined in each experimental description.

In global terms, statistical Analysis was performed through the Prism Software (Graphpad). The different sets of samples were initially tested for Gaussian distribution (Normality). In case of a positive result, samples were analyzed by Ordinary 1-way ANOVA followed by Dunnett's Multiple Comparison Test. In the case of negative normality result, Kruskal-Wallis test followed by Dunn's Multiple Comparison Test was used instead.

In the case of correlation tests, upon positive Gaussian distribution, Pearson correlation tests were performed. Upon negative Gaussian distribution, nonparametric Spearman correlation values were computed instead. For single-cell quantification tests, only data sets with a minimum of 100 cell events were considered for analysis. In all cases, differences/correlations were considered statistically significant when $p<0.05$.

VI.10. REFERENCES

1. Carvalho, A. F., Gasperini, L., Ribeiro, R. S., Marques, A. P. & Reis, R. l. Control of osmotic pressure to improve cell viability in cell-laden tissue engineering constructs. *J. Tissue Eng. Regen. Med.* **12**, e1063–e1067 (2018).

2. Gasperini, L., Marques, A. P. & Reis, R. L. Fibers with segments, their preparation and applications thereof. *WO2018078562A1* **2018**, (2018).

3. Cerqueira, M. T. *et al.* Human adipose stem cells cell sheet constructs impact epidermal morphogenesis in full-thickness excisional wounds. *Biomacromolecules* **14**, 3997–4008 (2013).

4. Baer, P. C. Adipose-derived mesenchymal stromal/stem cells: An update on their phenotype in vivo and in vitro. *World J. Stem Cells* **6**, 256 (2014).

5. Booij, T. H., Price, L. S. & Danen, E. H. J. 3D Cell-Based Assays for Drug Screens: Challenges in Imaging, Image Analysis, and High-Content Analysis. *SLAS Discov.* **24**, 615–627 (2019).

6. Kamentsky, L. *et al.* Improved structure, function and compatibility for cellprofiler: Modular high-throughput image analysis software. *Bioinformatics* **27**, 1179–1180 (2011).

SECTION 3

EXPERIMENTAL STUDIES

Chapter VII

HIGH-THROUGHPUT FABRICATION OF CELL-LADEN 3D BIOMATERIAL GRADIENTS

HIGH-THROUGHPUT FABRICATION OF CELL-LADEN 3D BIOMATERIAL GRADIENTS

Abstract

High-throughput strategies for optimizing biomaterials to direct cellular behavior are a fundamental need for propelling tissue engineering and regenerative medicine. In 2D, biomaterial gradients have proven to be powerful platforms for simultaneously screening several surface conditions. However, their translation to 3D is yet limited to (1) exploiting light-based crosslinking and (2) nonsequential, single-gradient production. We built a microfluidic platform that allows distinct hydrogel precursors, as fluids, to be gradually mixed and crosslinked into 3D gradient fibers. Herein, we report how this system can be used for the sequential fabrication of independent cell-laden libraries with gradients of polymer concentration, non-adhesive/adhesive materials and both ionic and light crosslinking mechanisms. Automated image analysis of hundreds of single-cell events as a function of position yielded trends and pinpointed best-fit conditions based on cell shape, adhesion, proliferation and triggering of stromal/stem cell differentiation. We deliver a simple, versatile, and complete approach towards fully high-throughput 3D gradient fabrication for cell/material screening and optimization.

This chapter is reproduced from the following publication:

Guimarães, C. F., Gasperini, L., Ribeiro, R. S., Carvalho, A. F., Marques, A. P., & Reis, R. L. (2020). High-throughput fabrication of cell-laden 3D biomaterial gradients. *Materials Horizons*, *7*(9), 2414-2421.

VII.1. INTRODUCTION

The use of biomaterials for tissue engineering and regenerative medicine (TERM) is highly dependent on finding adequate formulations to support and direct cellular behavior [1]. The low efficiency of the traditional, single-sample screening approach fails in a time where a vast number of available biomaterials can potentially be used for a specific application. This leads to a fundamental need for faster and reliable high-throughput (HT) screening technologies. True HT platforms, however, require that all stages have equally high efficiency, namely the fabrication of the libraries, the automated analysis, and the processing of the output data [2]. Across the literature, one can find two major types of HT platforms: (micro)arrays and gradients.

On the one hand, arrays or (more frequently) microarrays are the most obvious example of HT platforms, which consist mostly on the concentration of up to thousands of small spots of different biomaterials within a small surface [3]. These spots have variations in surface parameters such as chemistry and topography or, instead, distinct 3D droplet-like micro structures with different cell-laden materials [4].

Gradients, on the other hand, are a type of HT library where full ranges of the conditions of interest are integrated within a single sample, which changes gradually with space. Like arrays, gradients have been used for screening cellular responses to distinct biomaterial properties, such as surface stiffness [5] and topography [6] . In 3D hydrogels, gradients have also been fabricated to integrate ranges of different physical and biochemical cues [7–9]. Most of these are, however, manufactured using controlled light exposure and light-crosslinking materials [7–10], a limitation that prevents the study of e.g. ionic crosslinking materials.

Additionally, for gradients to live up to the HT challenge and be fair opponents of high-throughput arrays, we believe these should be capable of not only performing as well in terms of production and automatization but go a step further by exploiting continuity of analysis instead of discrete array-like screening. For this to happen, we believe gradients should adhere to four main premises, which are yet to be conjugated in a single approach: 1) Automatable and sequential production – gradient fabrication should be easily reproducible, preferably sequentially as time-consuming strategies compromise throughput; 2) Continuous analysis of cell responses as a whole and not limited to 3 or 4 gradient regions – this compresses the information present within the gradient and moves closer to a low-throughput strategy with discrete samples; 3) Connection between cellular response and material composition - suggesting that gradients should be kept intact throughout all screening stages so that

cell responses can be associated to a gradient position, which can be associated to a specific formulation by knowing how the gradient is built, e.g., linearly changing compositions. This is the reason why microscopy and similar imaging approaches are the current best-in-slot techniques for gradient HT screening [5,6,9–11]. Finally, 4) cellular responses within the gradients must recapitulate those that take place in uniform, macro constructs: the ones which will eventually be used for TERM.

Herein, we report the generation of a HT platform for the screening of cell-biomaterial interactions that addresses all those needs. We started by exploring the potential of microfluidics for fabricating hydrogel libraries based only on ionic crosslinking materials, which form hydrogels under fast-yet-mild conditions and have seen continuously increasing value for TERM [12]. For this purpose we used Gellan Gum (GG), a common hydrogel that crosslinks in the presence of any cation such as Na+ and Ca^{2+} [13].

VII.2. MATERIALS AND METHODS

VII.2.1. Hydrogel Fabrication and Characterization

Gellan Gum (GG) (Gelzan, Sigma-Aldrich) solutions were prepared by dissolution of the powder in water at 90°C. After dissolving, it was mixed 50:50 with a 0.5M Sucrose solution, yielding a 0.25M sucrose final solution [14]. Gellan Gum was crosslinked by the addition of Calcium Chloride ($CaCl_2$) 0.1M solution. Gelatin Methacryloyl 80% DS (Sigma-Aldrich) solution was prepared in 0.25M Sucrose in water containing 0.3% 2-Hydroxy-4′-(2-hydroxyethoxy)-2-methylpropiophenone (Irgacure, Sigma-Aldrich). UV crosslinking was induced under UV light (320-500nm) (Omnicure series 2000) for 50 seconds at 0.6mW/cm^2 at a distance of 8 cm from the lamp. GG/GelMA Blends were fabricated by mixing both solutions and combining both crosslinking (first ionic for a quick stabilization of the structure and then UV for crosslinking the GelMA component). GelMA and GG up to 0.5% were sterilized by filtration. The 0.5% solution was filtered, freeze dried under sterile conditions, and the obtained powder was used to prepare the 1% GG solution.

The characterization of precursor solutions and hydrogels was performed on a Rheometer (Malvern Kinexus Pro+). For the derivation of storage and loss moduli, hydrogels were first subjected to a strain amplitude sweep in order to find the linear elastic region, which was then used for a frequency sweep and moduli derivation. Stress relaxation tests were performed by applying a 10% shear strain and following the change in shear stress (G(t)) over time, normalized against the initial G(0).

VII.2.2. Adipose stromal Cell Isolation and Encapsulation

Human adipose-derived stromal/stem cells (hASCs) were isolated as previously described [15]. Briefly, cells were obtained from lipoaspiration surgeries of healthy individuals, after consent and under a collaboration agreement between Hospital da Prelada (Porto) and 3B's Research Group, approved by the respective ethical committees. The adipose tissue samples were subjected to enzymatic digestion (0.05% collagenase type II (Sigma-Aldrich) under agitation for 45 min at 37 °C), and after centrifugation and red cell lysis, hASCs were selected by plastic adherence. Cultured ASCs are characterized as $CD73^{+}/CD90^{+}/CD105^{+}/CD44^{+}/CD45^{-}/CD31^{-}$ cells [15,16].

hASCs were expanded and cultured in alpha-MEM (Gibco) with 10% FBS (Gibco) and 1% antibiotic, antimycotic (Gibco) up to passage 4. Suspensions of 1M cells /ml and 3M cells /ml were used in the fabrication of GG fibers and gradients, and in the uniform GG/GelMA fibers, respectively. Prior to encapsulation, hASCs were detached with TrypLE Express (Gibco), washed, counted to reach proper numbers according to the desired concentration, and were then resuspended directly in the hydrogel precursor solutions before gelation. For the differentiation studies, the cell-laden fibers were cultured as indicated in the StemPro Chondrogenesis Differentiation Kit Medium (Gibco) for triggering of chondrogenic differentiation, and in alpha-MEM supplemented with 10% FBS, 1% ATB, 34 μM of D-pantothenate (Sigma-Aldrich) and 66 μM of biotin (Sigma-Aldrich), 200 nM of insulin (Sigma-Aldrich), 1 μM of dexamethasone (Sigma-Aldrich), 250 μM of 3-isobutyl-1-methylxanthine (IBMX) (Sigma-Aldrich), and 5 μM of troglitazone (Sigma-Aldrich) for the adipogenic differentiation. Throughout the work, hASCs from 4 different donors were used at random.

VII.2.3. Microfluidic Setup and Gradient Fabrication

A custom microfluidic system was employed to obtain the different gradients [17]. An OB1 pressure controller and flow sensors (Elvesys) were used to regulate the flow of different hydrogel's precursor solutions. Gradient fabrication started with a first endpoint material flow, which was linearly reduced according to a ramp-like function, while the second endpoint material gradually increased in the reverse manner (**Fig. VII-1, B**). The flows were forced through a custom-built T-junction chip with two herringbone mixing stages (Translume) to ensure the disruption of purely laminar flow and lead to precursor mixing and therefore uniform blending of the two endpoint materials.The flowing blend was then directed into a linear microfluidic chip (Dolomite) and wet-spun into a 0.1M $CaCl_2$ (Sigma-Aldrich)

solution to crosslink the GG. In the case of GG/GelMA gradients, UV light was further applied to the gradient fiber for 10 seconds upon collection. In all experiments, both endpoint materials were stained with soluble microfluidic dyes (Elvesys) in order to track the gradient formation in real-time. A third, transparent material (0.5% Gellan Gum) was used to separate the different gradients, visibly showing the ending of one and beginning of another. This allowed a clear visualization of the gradient start and end thus facilitating gradient collection. A looping algorithm was employed in the controller software in order to fabricate a gradient, push the intercalating solution, create a new gradient, and so forth, sequentially producing as many gradients as loop turns inputted. Each cell-laden gradient was collected and placed in 6-well cell culture plates (Sigma, TPP) under the conditions of culture described above.

VII.2.4. Gradient Tracking

To track the composition of the gradients and to validate their gradually changing components, three methods were used throughout this work:

The first one, previously described, consisted on the dissolution of soluble microfluidic dyes (Elvesys) of different colors which allowed tracking the gradient formation in real time (Supplementary Video).

Since these dyes diffuse, a more robust method was needed to confirm the gradient formation and material transition. For this purpose, we blended the endpoint materials (GG 1% and GG 0.5%) with either green FITC-GG (Yielding the GG 1% (FITC) nomenclature of the main text) or red RITC-Hyaluronate (1.5MDa, Lifecore) (Yielding the GG 0.5% (RITC) nomenclature), at 1:100 volume ratio. The fluorescent GG crosslinks together with the normal GG and the Hyaluronate, having high molecular weight, remains trapped in the crosslinking GG, allowing the observation of the gradient long after fabrication without the concern of diffusion. To observe the gradient distribution, the full gradients with fluorescent trackers were imaged and the contribution of each fluorescent tracker was measured along X-axis using ImageJ.

An additional method was employed to observe the gradient formation, in the GG-GelMA gradients. Being composed of highly different molecules, the gradient was fabricated as previously reported without any dye and later stained with the ColF probe (Immunochemistry Technologies) according to the manufacturer's instructions. The specificity of ColF to collagen and its denaturated forms [18] was then used to image and observe the presence of the gradient by targeting the Gelatin component.

VII.2.5. Cellular Viability and Immunocytochemistry

Cellular Viability was tracked by incubating cell-laden hydrogels and fibers with Calcein AM 1:1000 (Molecular Probes) and Propidium Iodide 1ug/ml (Molecular Probes) for 30 minutes, followed by 2 washes in PBS before imaging.

For immunocytochemistry, samples were fixed in formalin 10% for 10 mins at room temperature (RT), washed with PBS and incubated with 0.2% Triton X-100 (Thermo Fisher) in PBS for 12 minutes to enhance cell membrane permeability. After washing, non-specific interactions were blocked by incubation with 3% BSA (Sigma-Aldrich) in PBS for 30 minutes. Afterwards, samples were incubated with the primary antibody in 1% BSA for 2 hours at RT, washed with PBS and incubated with the secondary antibody for 1 hour at RT. Cell cytoskeleton and nuclei were also stained with Phalloidin-TRITC (Sigma-Aldrich) 2ug/mL and DAPI (Biotium) 4ug/mL simultaneously added with the secondary antibody. At the end, samples were washed with PBS and imaged or kept in PBS at 4°C, in the dark until that.

Primary antibodies used: Rabbit Anti-SOX9 1:500 (Merck), Rabbit Anti-PPAR-gamma 1:100 (Abcam), Rabbit Anti-Ki67 1:250 (Abcam), Mouse Anti-YAP 1:50 (Santa Cruz), Rabbit Anti-Paxillin 1:250 (Abcam).

Secondary Antibodies used: Alexa 594 donkey-anti-mouse 1:500 (Molecular Probes), Alexa 488 donkey anti-rabbit 1:500 (Molecular Probes).

VII.2.6. Microscopy and Image Analysis

Whole fiber and gradients were imaged using an Axio Observer Inverted Microscope (Zeiss), with an automated stage allowing for tile scan acquisition. Low-magnification was used together with Z-stacking for image acquisition. Z-stacks images of the fibers and gradients were processed to obtain maximum projection extended depth of focus. This allowed for a good balance between fast imaging (under 20 minutes per full gradient) and translation of responses from 3D to 2D, maximizing throughput and overcoming 3D computational limitations [19]. Additionally, higher resolution images of specific fiber details were acquired in higher magnification or in an Inverted Confocal Laser Scanning Microscope (Leica).

Images taken for cell screening were then analyzed with the CellProfiler software [20]. Generally, gradients were imaged as a whole whereas macro hydrogels were imaged at random positions on 3 sections per replicate. In all cases, a minimum of 100 cells was considered for quantification. Specific pipelines were used to process cell markers as objects (Supplementary Fig. VII-6) and from there derive count numbers, SOX9/Phalloidin and PPAR-γ/Phalloidin total pixel ratios (Mander's Co-localization Coefficient) and intensity of the distinct signals. The Marker/Phalloidin pixel ratios are in practice a direct normalization of the projected marker area to the projected cell area, reducing variability effects. Cell responses on gradients were tracked with object X position and plotted as a function of location along the gradient. Throughout the document, individual graphs of gradient responses represent a single replicate since the position of each cell is never the same between replicates.

Additionally, in order to identify trends within the gradients, cell responses were tested for positive or negative correlations, as described in the statistical section.

VII.2.7. Western Blot

For protein extraction, cell-laden hydrogels were collected from culture and washed thoroughly with cold PBS. Afterwards, hydrogels were transferred to an Eppendorf containing radio-immunoprecipitation assay (RIPA) buffer supplemented with 1:200 protease inhibitor (Sigma-Aldrich). Using a pestle, hydrogels were macerated until a slurry mixture was obtained. Samples were then centrifuged at 13000 rpm, 4°C for 15 minutes. The supernatant (protein extract) was collected and stored at -80°C until quantification.

Protein Quantification was performed using the Pierce BCA kit (Thermo Fisher), according to manufacturer's instructions. 10ug of protein were mixed with gel loading buffer composed of tris-HCL (ph8.8) (Sigma-Aldrich), 0.05% Bromophenol Blue (Sigma-Aldrich), 6% SDS (NZYtech), 30% Glycerol (Honeywell), 10% EDTA NaOH (6mM) (Lonza) and Dithithreitiol (DTT) (Sigma-Aldrich), heated for 60°C 10 minutes, 90°C 5 minutes for denaturation, and then loaded into 10% SDS Polyacrylamide gels (Sigma-Aldrich), together with a molecular weight marker (Thermo Fisher). After electrophoresis, bands were then transferred to a nitrocellulose membrane (GE Healthcare) and incubated with Ponceau Solution (Sigma-Aldrich). After washing excess ponceau, the blots were blocked in 5% Skim Milk in Tris-Buffered Saline (TBS) for 1h. After blocking, membranes were incubated with the primary antibody prepared in 5% Skim Milk in TBS overnight at 4°C. After thorough washing, the bound antibody was detected by incubation with an alkaline phosphatase-linked secondary antibody (Sigma-Aldrich) diluted

in 5% skim milk TBS for 1h at RT. After washing, bands were observed using an AP conjugate Substrate kit (Biorad), followed by scanning on an EPSON V600 Scanner. Band intensities were quantified through the FIJI (ImageJ) software.

Primary antibodies used: Rabbit Anti-SOX9 1:500 (Merck), Rabbit Anti-Paxillin 1:3000 (Abcam), Mouse Anti-YAP 1:100 (Santa Cruz), Rabbit Anti-Tubulin (Abcam) (loading Control) 1:500.

Secondary antibodies used: Goat-Anti-Rabbit AP-Conjugated 1:3000 (Sigma-Aldrich), Horse-Anti-Mouse AP-Conjugated 1:3000 (Vector Laboratories).

VII.2.8. Statistical Analysis

Statistical Analysis was performed through the Prism Software (Graphpad, v6). Generally, the sets of samples were initially tested for Gaussian distribution. In case of a positive result, samples were analyzed by Ordinary 1-way ANOVA followed by Dunnett's Multiple Comparison Testtest. In the case of negative normality result, Kruskal-Wallis test followed by Dunn's Multiple Comparison Test was used instead. In the case of gradient responses, upon negative Gaussian distribution, nonparametric Spearman correlation values were computed. For all gradients, only data sets with more than 100 cell events were considered for analysis. In all cases, differences/correlations were considered statistically significant when $p<0.05$

VII.3. RESULTS AND DISCUSSION

Hypothesizing that the concentration of GG and consequent hydrogel mechanics could impact the triggering of cell differentiation, we started our study on low-throughput macro-hydrogels with increasing gelling polymer concentration (**Fig. VII-1, a**) together with corresponding continuous microfluidic-generated 3D fibers (**Fig. VII-1, e**), which served as a framework for the validation of our high-throughput strategy. We established a concentration range of 0.5-1 w/vol% GG hydrogels, which led to a storage moduli interval of 5-20 kPa (**Fig. VII-1, b, i,** Supplementary Fig. VII-2), close to those of several living tissues [21]. We then studied the effects of varying the concentration of GG in the behavior of human adipose-derived stromal/stem cells (hASCs), which we used as a model primary cell type widely used in TERM [22]. To discard any negative effect of the encapsulation of these cells, their viability was assessed confirming 70-80% live cells throughout the first week of analysis (Supplementary Fig. VII-3), in line with previous reports using the same material [14]. Within 3D environments, the mechanical

properties of the encapsulating material can significantly impact the shape of cells as well as their commitment even if only through mechanical confinement which might be even more significant in non-adhesive environments [23,24]. Cell size and triggering of differentiation were then defined as the parameters to screen the effect of the mechanical environment provided by the different GG hydrogels. Image analysis of Calcein AM signal as an indicator of cell size revealed a decrease in projected cell area with increasing GG concentration and hydrogel stiffness (**Fig. VII-1, b, ii**), hinting at a mechanical restriction on cell expansion. Throughout this work, we used maximum projection images for analysis to condensate 3D information in 2D objects and allow for both faster full-structure imaging and automated image analysis, as described in the supplementary methods section. Even if some detail might be lost, 2D projections are still routinely used for efficiently analyzing 3D structures in the HT scenario [25].

When cultured in chondrogenic differentiation medium, hASCs expressed the master-regulator of chondrogenesis, SOX9 [26] (**Fig. VII-1, c**). Image analysis was used to quantify the percentage of SOX9 positive cells (**Fig. VII-1, d, i**) and the SOX9/Phalloidin total pixel (area) ratios (**Fig. VII-1, d, ii**). This analysis revealed a significant increase of SOX9 expression (chondrogenic triggering) in the stiffer hydrogels by both metrics. To reduce acquisition-related variations, we opted by performing this analysis based on the signal area instead of intensity (**Fig. VII-1, d iii**). By performing a normalization of SOX9 area to Phalloidin area (total pixels), we compensated for visible variation in the 3D volume and respective 2D projected area of cells, which could have very different SOX9 areas but in the end similar when considering the total cell size. The image analysis approach was validated through western blot where protein levels reflected the same response and identified also Blend 3 (25:75 mixture of 0.5% and 1% GG, respectively) and 1% GG as the best conditions for triggering chondrogenic differentiation of hASCs (Supplementary Fig. VII-4).

Once we understood the behavior of cells on macro hydrogels and validated our analysis metrics, we moved towards the miniaturization of 3D environments by fabricating uniform hydrogel microfibers. Gellan Gum fibers were created by wet-spinning the hydrogel precursor into a crosslinking bath using a linear microfluidic channel, creating continuous, linear hydrogels with encapsulated hASCs (**Fig. VII-1, e**, **i-iii**). In order to validate the hydrogel microfibers as suitable analysis platforms, the trend of SOX9 responses of individual cells were imaged and analyzed (Supplementary Fig. **VII-7**), as done for the macro hydrogels. In this case, the response of each individual cell was plotted according to its X position, obtaining a distance/response profile along the fiber. Herein, no significant changes in SOX9 responses were observed along the uniform environments, although responses in 1% GG fibers were

comparably higher than those in 0.5% GG fibers (**Fig. VII1-e, iv, v**), which approaches what we observed in the previously discussed macro hydrogels.

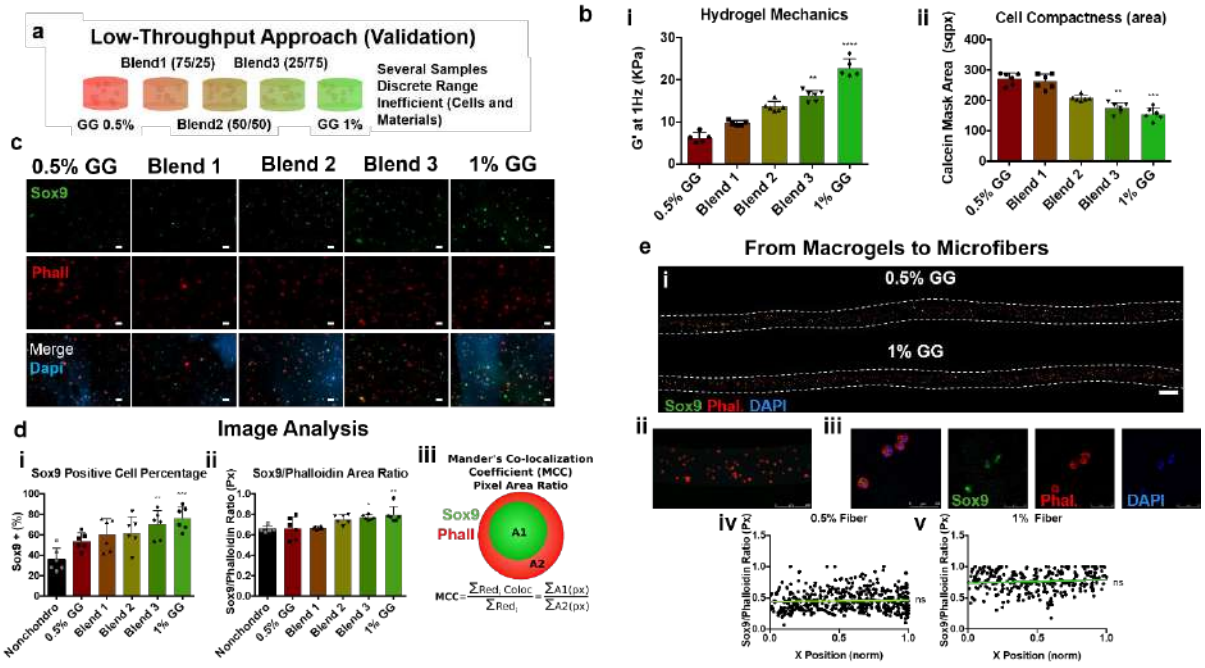


Figure VII-1: Low-Throughput Hydrogels and Uniform Microfibers. a | Rationale behind a low-throughput biomaterial testing strategy where single-sample testing takes place over a discrete range of specific conditions. b | On uniform Gellan Gum (GG) macro-hydrogels (8mm disks), the mechanical analysis revealed a 5-20 kPa range from gradually blending 0.5% and 1% solutions of the polymer (i). Image analysis after Calcein AM staining shortly after encapsulation revealed decreasing projected cell areas in the higher concentration hydrogels, hinting at increasing cell compactness (ii, Supplementary Fig. VII-3). Statistical values: ** p<0.01, *** p<0.001, compared to 0.5%GG. c | After 1 week in chondrogenic culture, significant changes could be observed in the expression of SOX9 by hASCs (Green, Scale bar 50µm). Cell nuclei were stained with DAPI (blue) and cytoskeleton actin with Rhodamine-labelled Phalloidin (Red). Slight blue background shades are visible due to a certain fluorescence of GG within the UV range. d | Using an image analysis pipeline, we could detect a significant increase in the percentage of SOX9+ cells (i) as well as in the SOX9/Phalloidin Pixel ratios (ii), which were obtained by taking advantage of Mander's Co-localization Coefficient and the particular signal co-localization that exists in encapsulated cells (iii). *Nonchondro*: no chondrogenic stimuli, NC. *Blend 1*: 75:25 Mixture of GG 0.5%:GG 1%; *Blend 2*: 50:50 Mixture of GG 0.5%:GG 1%; *Blend 3*: 25/75 Mixture of GG 0.5%:GG 1%. e | Cell-laden GG hydrogel microfibers of uniform composition (0.5% and 1%) were prepared by wet-spinning the material into a crosslinking bath (scale bar 500µm) via a linear microfluidic channel (i). Detailed confocal zoom-in into a specific gradient section (ii) and detail of single cells inside the hydrogel (iii) are imageable due to the low thickness and transparency of the fibers. hASCs-laden fibers were cultured and immunostained as described for the macro hydrogels. By performing image analysis, the behavior of cells was tracked according to their X position along the fibers, revealing no significant trend within these uniform structures (iv, v).

To move towards the fabrication of equivalent 3D gradient libraries **(Fig. VII-2, a**), we connected the distinct material components to an herringbone mixing stage [27] prior to the output linear chip (Supplementary Fig. VII-5) and gradually combined the flows of the 2 end-point materials (0.5% and 1% GG) (**Fig. VII-2, b**), resulting in a balanced gradation in composition, where the whole range of GG concentration was combined into a single sample (**Fig. VII-2, c, i**). Therein, no presence of Janus-like separation between the two endpoint components was present, evidencing a successful disruption of purely laminar flows and consequent mixing of the precursors. As such, we obtained a gradient which was composed of purely ionic-crosslinking components, formed by gradual mixing and spinning, representing the first library of its kind. Once the gradient was successfully fabricated, we tested if cells could be manipulated and mixed together with the materials and observed no negative impact on their viability (**Fig. VII-2c, ii,** Supplementary Fig. VII-6).

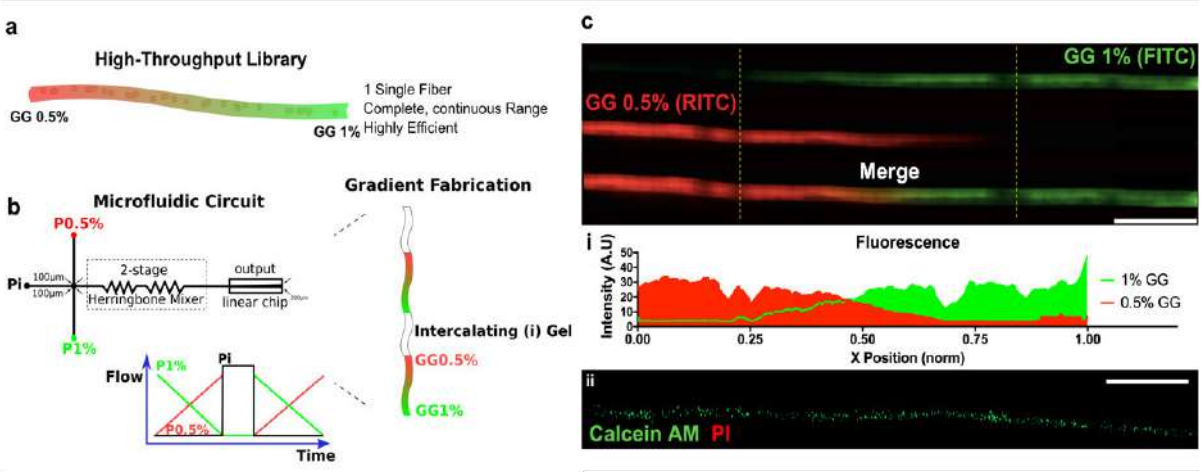


Figure VII-2: Gellan Gum Gradients. a | Rationale of a gradient fiber as a high-throughput library, where a full range of conditions is integrated into a single sample as opposed to several discrete ones. b | To fabricate gradients, a microfluidic circuit was used to manipulate 2 endpoint materials through pressure regulation (P0.5%, P1%), gradually increasing/decreasing the first/latter flows, forcing the total flow through an herringbone mixer chip in order to ensure mixing of the hydrogel precursors [27]. By intercalating gradients with an empty material (i), we were able to sequentially fabricate individual libraries. c | The gradient technique generates a fiber with a gradual change in composition (scale bars 0.5mm), which was followed by tracking RITC (red) and FITC (green) colored GG (i). The encapsulation of cells and their microfluidic manipulation had no negative impact on hASC viability (live Calcein AM (Green) and dead Propidium Iodide (Red) cells) (ii).

It has been reported by other authors that softer environments favour adipogenic commitment [28,29] and stiffer ones promote higher levels of chondrogenic differentiation [30]. To verify if we could screen similar responses within GG hydrogels, we used our gradients to track the response of each

encapsulated cell after 1 week of culture in either chondrogenic or adipogenic differentiation media, to look for the 3D environment which would better synergize with those distinct culture conditions and potentiate the triggering of differentiation. Plotting the expression of the respective master differentiation markers [26,31] as a function of distance, it was possible to observe that the triggering of chondrogenic differentiation (SOX9 expression) (**Fig. VII-3, a)** trended in a different direction than that of adipogenic commitment (PPAR-γ expression) (**Fig. VII-3, b)**. Based both on the SOX9/Phalloidin and PPAR-γ/Phalloidin pixel ratios (**Fig. VII-3, a, VII-3, b ii**) as well as intensity (**Fig. VII-3, a, VII-3b iii**) of the signals, chondrogenic triggering increased significantly with GG concentration (**Fig. VII-3, a**) while adipogenic differentiation seemed to oppositely benefit slightly more from the softer environments (lower GG concentrations) (**Fig. VII-3, b**). The observed SOX9 expression reflected the ones observed in the low-throughput approach (**Fig. VII-1**) for the chondrogenic differentiation. In regards to the PPAR-γ responses, the observed trend, overall slight yet detectable, also supports previous results concerning the adipogenic differentiation in soft GG hydrogels [32].

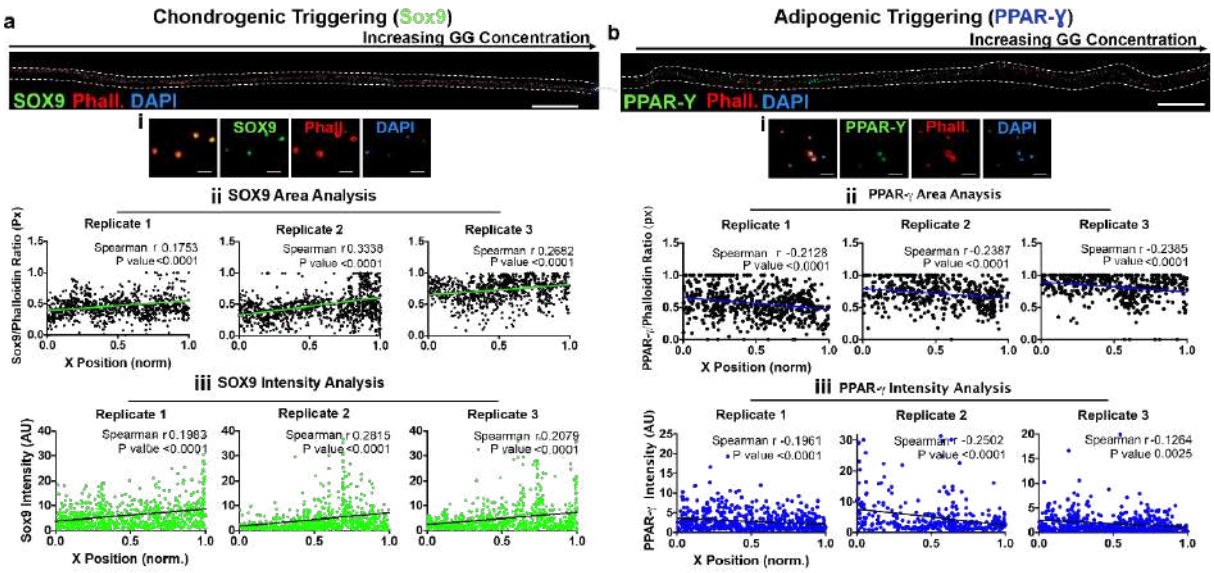


Figure VII-3: hASC differentiation triggering in GG Gradients. a| Within the gradients, hASC responses were tracked upon 1 week of culture in chondrogenic conditions (full gradient scale bar 0.2mm, single cells representative marker detail (i) scale bar 50μm). Hundreds of single-cell responses evidenced a significant increase in the SOX9 levels along all 3 gradient replicates (each graph containing data from a single replicate) both considering SOX9 area (ii) and intensity (iii), pinpointing stiffer environments as better triggers of chondrogenic differentiation. b | After 1 week under adipogenic stimuli, it was possible to see that, oppositely to chondrogenic differentiation, the adipogenic triggering as shown by the expression of PPAR-γ (full gradient scale bar 0.2mm, single cells representative marker detail (i) scale bar 50μm) decreased along all 3 gradient replicates (each graph containing data from a single replicate) both considering area (ii) and intensity (iii) of the staining, placing softer environments as slightly better fit for

adipogenic induction. Cell responses were evaluated after immunocytochemistry against SOX9 and PPAR-γ (green), cell nuclei counterstaining with DAPI (blue) and actin cytoskeleton with rhodamine-phalloidin (red). In all cases, r and p values correspond to the resulting Spearman correlation analysis.

Therefore, by single-sample screening, we were able to quickly detect trends and identify the most appropriate formulations to trigger two distinct commitment pathways, both mirroring the responses taking place at the molecular level on larger hydrogel structures.

Overall, the responses of cells encapsulated within non-adhesive environments such as pure GG are limited by the absence of direct cell-material interaction. Thus, in order to increase the complexity of our platform, going beyond extracellular mechanics and further screening cell adhesion-dependent responses - both properties that synergize in ECM-like environments [33] - we introduced an adhesive component, Gelatin Methacryloyl (GelMA), capable of direct cell-material interaction.

As we combined the mostly-bioinert GG with the much more biolabile GelMA [34] (**Fig. VII-4, a**) we could observe the formation of stable hydrogels with physiological-range [21] mechanics (**Fig. VII-4, b**). We then adapted our platform to operate at 37°C (Supplementary Fig. VII-8), allowing the production of gradients with a transition from GG to GelMA by gradually decreasing the first and increasing the latter (**Fig. VII-4, c**). This gradient, where a gradual increase in GelMA was confirmed by the specific ColF staining [18] (**Fig. VII-4, d, i,** Supplementary Fig. VII-9), represents two important advances. On one hand, it is a multi-material gradient integrating a full switch in composition rather than modifications of a same hydrogel as approached in previous works [7–9]. On the other hand, this change in materials is further combined with a shift in the crosslinking strategy, from the ionic-crosslinking GG to UV crosslinking GelMA, which also represents an important advance in gradient complexity. Nevertheless, regardless of the type of material or crosslinking used to produce the gradients, the proportion of viable cells was not visibly affected (**Fig. VII-4d ii, iii,** Supplementary Fig. VII-10).

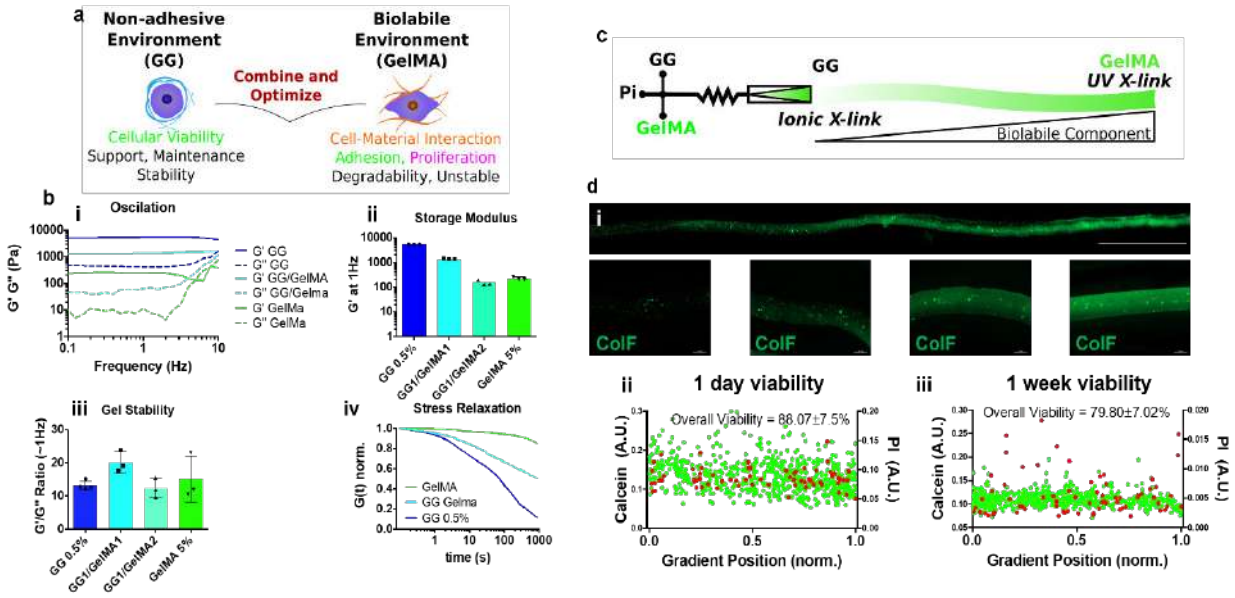


Figure VII-4: Inert/Adhesive Gellan Gum-Gelatin Gradients. a | GG and GelMA were considered as materials capable of supporting respectively non-adhesive and more biolabile environments for cells. b | Both materials were mixed and dually crosslinked forming hydrogels with physiological-range mechanics (i,ii) and stable structures (G'/G'' ratios above 10) (iii). Stress-relaxation analysis also revealed an intermediate GG/GelMA behavior between the stress-relaxing GG (ionic) and the non-relaxing GelMA (covalent) (iv). GG1/GelMA1 – 1:1 Blend of GG:GelMa, GG1/GelMA2 – 1:2 Blend of GG:GelMa. c | Schematics of the fabrication of the GG-GelMA gradients with our microfluidic system. d | Gradients were confirmed after staining the cell-laden structures with ColF (green, scale bar 0.5mm). Within the gradients, the proportion of viable (Calcein-positive cells in green dots, PI-positive cells in red dots) was maintained regardless of the local gradient composition and crosslinking both after 1 day (ii) and 1 week (iii) of culture.

In order to assess the applicability of these inert/adhesive gradients as platforms in which cell adhesion and consequent responses to different materials could be screened, we looked at cellular morphology and adhesion, as well as mechanotransduction and proliferation responses. Changes in cell morphology and adhesion upon 1 week of culture within the GG/GelMA gradients were assessed based on cell cytoskeleton-related parameters (cell shape and form factor) and on the overall expression of the adhesion protein Paxillin (**Fig. VII-5, a**). From the image analysis, a significant increase in cell area (**Fig. VII-5, a, iv**) and decrease in form factor (**Fig. VII-5, a, v**), evidence of larger, less round cells - hinting at increasing cell-material interaction - was detected for increasing GelMA amounts. Simultaneously, Paxillin intensity per cell increased along the gradient with the increasing GelMA amounts, evidencing a higher degree of cell adhesion (**Fig. VII-5, a, vi**). Curiously, we noticed not only a trend but also a specific region - within the gradients and among replicates - where both cell area and paxillin intensity trends appeared to shift from constant to successively increasing with GelMA amounts.

This happened at around half of the gradient position (arrows in **Fig. VII-5, a iv** and **vi,** Supplementary Fig. VII-11, VII-12), which corresponds to approximately 1:1 GG/GelMA ratio, as the gradient was built linearly (**Fig. 2b,** Supplementary Fig. VII-9).

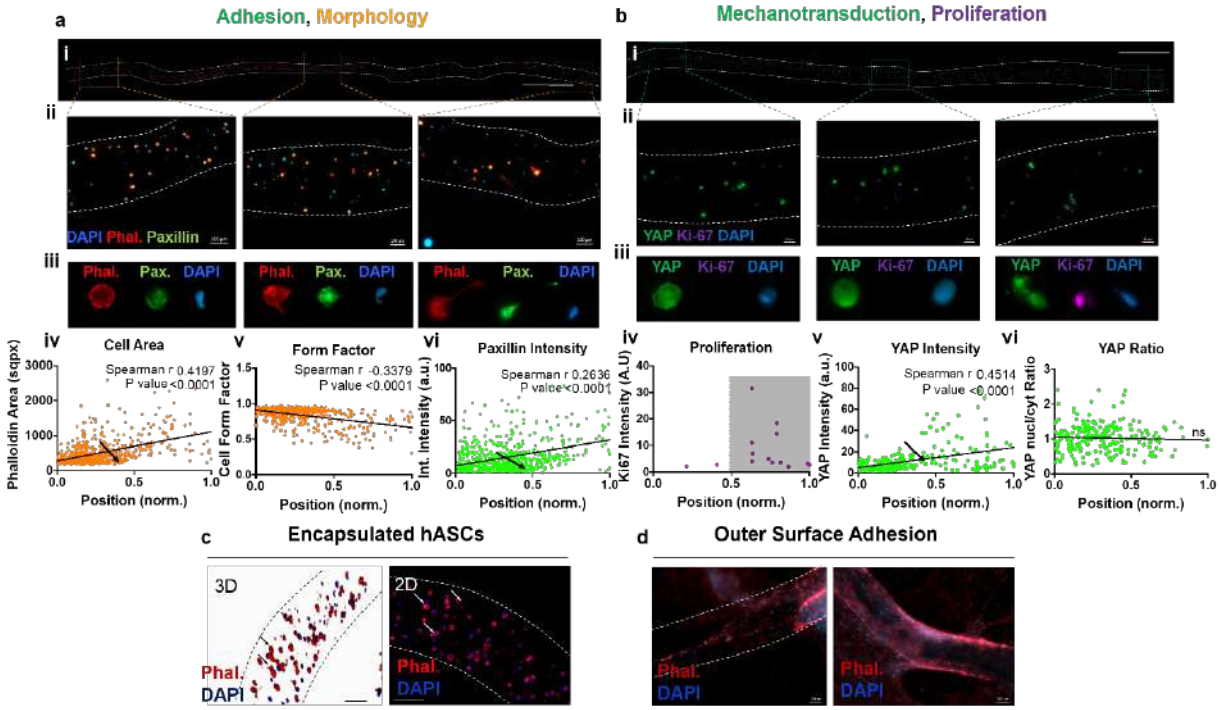


Figure VII-5: hASC Responses in GG-GelMa Gradients. a | hASC adhesion and morphology was tracked by Phalloidin (red) / Paxillin (green) / DAPI (blue) staining (i, scale bar 5000µm, ii, scale bar 100µm) upon 1 week of culture within GG-GelMA gradients. Single-cell representative images of 3 gradient regions (start, middle, end of the fiber) are also shown (iii). Representation of Cell Area (iv) and Form Factor (v) (phalloidin-based image analysis), and Paxillin intensity as a function of gradient distance (increasing GelMA-to-GG) (vi). Black arrows point to the half region of the gradient, where a shift in cell responses can be observed. b | Proliferation (Ki67, purple)- and mechanotransduction (YAP, green)-related markers' expression was also assessed (i, scale bar 5000µm, ii scale bar 50µm, iii representative single cells); Ki67+ cells (purple dots) were overall rare and mostly only detected after half of the gradient (1:1 GG:GelMA ratio) towards increasing GelMA amounts (iv). YAP intensities significantly increased along the gradient (v), also evidencing a slight shift around the 0.5 position (normalized) (black arrow). No significant differences were detected in the nuclear/cytoplasmic YAP ratios (vi). All graphics are representative of the gradient replicates found in supplementary data. c | Uniform hASC-laden fibers fabricated with 1:1 GG/GelMA confirming the functionality of the selected blend shortly after fabrication (3days) by Phalloidin (Red) / DAPI (blue) staining. Cell-Material interactions demonstrated by cell protrusions (arrows) are visible in 3D and 2D projection (scale bars 100µm). d | hASCs in suspension were also able to adhere to these 1:1 GG/GelMA fibers, fully engulfing them after 1 week of culture with the structure still retaining its shape (scale bars 100µm).

We further looked at markers of cell proliferation and mechanotransduction by quantifying the expression of Ki-67 and YAP, respectively (**Fig. VII-5, b**). Overall, the recreated environments did not

seem to extensively favour the proliferative state of the cells upon 1 week of culture, as only a few cells were Ki-67 positive (**Fig. VII-5, b, iv**). Nevertheless, most of these were present in the second half of the gradient, i.e., after the 1:1 GG/GelMA threshold (**Fig. VII-5, b, iv,** Supplementary Fig. VII-13). Interestingly, YAP intensities significantly increased along the gradient, also with an apparent shift present in some gradients around the 0.5 position (normalized) of the fibers (**Fig. VII-5, b v,** Supplementary Fig. VII-14). Nevertheless, no significant changes in the nuclear/cytoplasmic YAP ratios were detected (**Fig. VII-5, b vi,** Supplementary Fig. VII-14). Even if the increasing cell-material interaction leads to higher YAP expression, there appear to be no detectable differences in its nuclear shuttling. This suggests no specific YAP-dependent differentiation pathways were changing [35] under the gradient culture conditions. In fact, it was previously shown that YAP-related mechanotransduction might not be so impactful in soft 3D environments as it is in 2D scenarios [36].

Overall, our approach allowed to screen the impact of changes in the 3D cell environment on distinct, relevant markers, trends which - as we also show - recapitulate what takes place molecularly in GG *versus* GelMA macro hydrogels (Supplementary Fig. VII-15, VII-16). Moreover, we could not only detect said trends but also pinpoint a specific setpoint where the change from inert-like encapsulation to active cell-biomaterial interaction appears to take place. To put this to test, we fabricated uniform fibers of the 1:1 GG/GelMA blend with encapsulated and suspended hASCs. Shortly after fabrication, cell-material interactions could be already detected both within the fiber (**Fig. VII-5, c)** and also on the outer surface (**Fig. VII-5, d**), showing an immediate and successful application of the HT screening method to identify the most suitable material (composition) to maximize a specific cellular response for a certain application. On the one hand, this cell-material interaction was never observed on GG hydrogels and, on the other hand, pure GelMA structures quickly degrade and as such are not stable [37,38], yet both cell interaction and fiber stability were present in the optimized blend.

VII.4. CONCLUSIONS

In summary, we have demonstrated how the microfluidic manipulation of hydrogel precursors can be used to fabricate 3D material gradients sequentially and with high efficiency, creating independent cell-laden libraries that can integrate different types of materials and crosslinking, obtaining both gradients purely with ionic crosslinking materials and also gradients with a switch from an ionic-crosslinking material (GG) to an UV-crosslinking one (GelMA). These gradients were in all cases fabricated as individual structures and further subjected to different culture stimuli. Cell's responses

were tracked continuously along the gradient length connecting their relative position to the corresponding 3D environment composition, knowing gradients were linearly fabricated. We also validated our results by establishing a low-throughput parallel with macro, uniform hydrogels and molecular validation of microscopy and image analysis data, proving the recapitulation of the responses observed within the microfiber gradients.

Gradients with a range of GG concentration showed that hASCs' responses in non-adhesive encapsulation scenarios could be affected by softer/stiffer environments which can be optimized to better trigger the master regulators of adipogenesis /chondrogenesis, respectively (**Fig. VII-6, a**).

Gradients with a full switch in the composing material from ionic-crosslinkable GG to UV-crosslinkable GelMA revealed not only trends but a setpoint of cell-material interaction at around 1:1 GG/GelMA ratio, an efficient optimization of the combination of the structural stability of GG with the cell interaction properties of GelMA (**Fig. VII-6, b**).

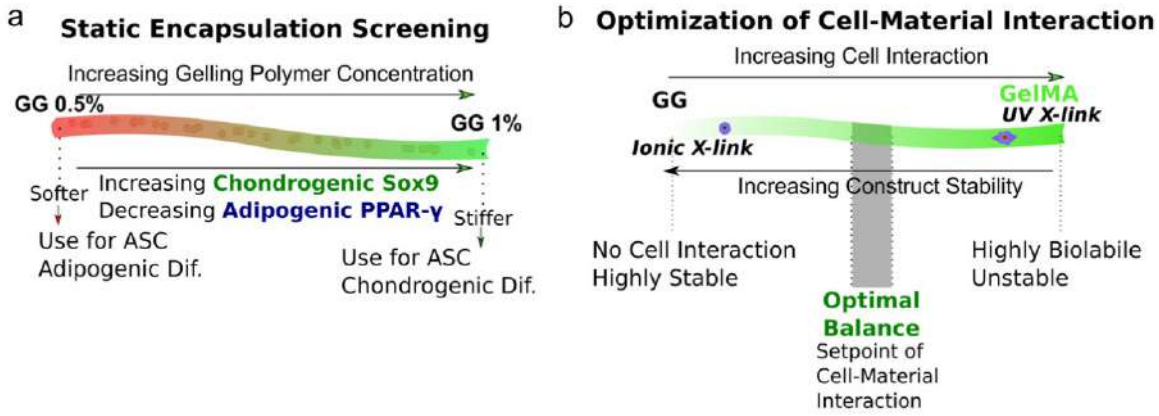


Figure VII-6: High-throughput Power of 3D Gradients: Our microfluidic approach can be used to fabricate gradient libraries of concentration of a single ionic crosslinking material (a) or to optimize the combination of distinct materials and crosslinking type to test different cell responses (b). Non-adhesive material-based fibres represent suitable platforms to assess the influence of the materials' mechanical properties over stromal/stem cells under pro-differentiation culture conditions as exemplified by the stiffer GG regions that provide a better triggering of chondrogenic differentiation whereas softer ones are more prone for triggering adipogenic commitment. Moreover, non-adhesive materials might benefit from blending with more biolabile and cell-adhesive ones such as the case of the blending of GG with GelMA (b). The gradient platforms fabricated with these distinct materials allowed not only screening cell adhesion-related responses but quickly detecting a setpoint and a specific formulation at which mechanical and biological performance were maximized, advantage of having a continuous approach where all in-between conditions are considered as opposed to discrete, low-throughput alternatives.

We believe the simplicity and generality of our approach might push cell-biomaterial screening to higher throughput and globally faster discoveries as well as optimization and personalization of TERM strategies. Within the same field, it might also prove to be a powerful tool for the biofabrication of interface tissues that naturally bridge distinct mechanical and cellular environments [39]. On a broader perspective, the possibility of creating hydrogel gradients without the need of light-dependent, covalent crosslinking might also bring answers to fundamental questions focusing on distinct cellular responses to gradually-changing conditions, e.g. durotaxis [40], by introducing ionic-crosslinkable and consequently stress-relaxing environments that more closely mimic living tissue environments [23].

There is nevertheless an important gap that remains open, which is the complete combination of 3D cell/material conditions with fully 3D imaging and analysis. Currently, imaging and computational limitations make this type of analysis a significant constraint in high-throughput by demanding complex, time-consuming operations [19]. We expect, however, that recent advances in faster 3D fluorescent imaging as well as efforts towards more efficient 3D data storage and processing will provide off-the-

shelf solutions and software soon. At that point, their integration with platforms as the one hereby communicated will likely break the final frontier of complete 3D HT cell/biomaterial screening.

VII.5. REFERENCES

1. Lutolf, M. P., Gilbert, P. M. & Blau, H. M. Designing materials to direct stem-cell fate. *Nature* **462**, 433–441 (2009).
2. Hulshof, F. F. B. *et al.* NanoTopoChip: High-throughput nanotopographical cell instruction. *Acta Biomater.* **62**, 188–198 (2017).
3. Anderson, D. G., Putnam, D., Lavik, E. B., Mahmood, T. A. & Langer, R. Biomaterial microarrays: Rapid, microscale screening of polymer-cell interaction. *Biomaterials* **26**, 4892–4897 (2005).
4. Kim, H. D. *et al.* High throughput approaches for controlled stem cell differentiation. *Acta Biomater.* **34**, 21–29 (2016).
5. Hadden, W. J. *et al.* Stem cell migration and mechanotransduction on linear stiffness gradient hydrogels. *Proc. Natl. Acad. Sci.* **114**, 5647–5652 (2017).
6. Zhou, Q. *et al.* Screening Platform for Cell Contact Guidance Based on Inorganic Biomaterial Micro/nanotopographical Gradients. *ACS Appl. Mater. Interfaces* **9**, (2017).
7. Jeon, O., Alt, D. S., Linderman, S. W. & Alsberg, E. Biochemical and physical signal gradients in hydrogels to control stem cell behavior. *Adv. Mater.* **25**, 6366–6372 (2013).
8. Chatterjee, K., F. Young, M. & G. Simon, C. Fabricating Gradient Hydrogel Scaffolds for 3D Cell Culture. *Comb. Chem. High Throughput Screen.* **14**, 227–236 (2011).
9. Vega, S. L. *et al.* Combinatorial hydrogels with biochemical gradients for screening 3D cellular microenvironments. *Nat. Commun.* **9**, 614 (2018).
10. Pedron, S., Becka, E. & Harley, B. A. Spatially gradated hydrogel platform as a 3D engineered tumor microenvironment. *Adv. Mater.* **27**, 1567–1572 (2015).
11. Major, L. G. *et al.* Volume adaptation controls stem cell mechanotransduction. *ACS Appl. Mater. Interfaces* 45520–45530 (2019). doi:10.1021/acsami.9b19770
12. Lee, A. *et al.* 3D bioprinting of collagen to rebuild components of the human heart. *Science (80-.).* **365**, 482–487 (2019).
13. Stevens, L. R., Gilmore, K. J., Wallace, G. G. & In het Panhuis, M. Tissue engineering with gellan gum. *Biomaterials Science* (2016). doi:10.1039/c6bm00322b
14. Carvalho, A. F., Gasperini, L., Ribeiro, R. S., Marques, A. P. & Reis, R. l. Control of osmotic pressure to improve cell viability in cell-laden tissue engineering constructs. *J. Tissue Eng. Regen. Med.* **12**, e1063–e1067 (2018).
15. Cerqueira, M. T. *et al.* Human adipose stem cells cell sheet constructs impact epidermal morphogenesis in full-thickness excisional wounds. *Biomacromolecules* **14**, 3997–4008 (2013).
16. Baer, P. C. Adipose-derived mesenchymal stromal/stem cells: An update on their phenotype in vivo and in vitro. *World J. Stem Cells* **6**, 256 (2014).
17. Gasperini, L., Marques, A. P. & Reis, R. L. Fibers with segments, their preparation and applications thereof. *WO2018078562A1* **2018**, (2018).
18. Biela, E. *et al.* Col-F, a fluorescent probe for ex vivo confocal imaging of collagen and elastin in animal tissues. *Cytom. Part A* **83 A**, 533–539 (2013).
19. Booij, T. H., Price, L. S. & Danen, E. H. J. 3D Cell-Based Assays for Drug Screens: Challenges in Imaging, Image Analysis, and High-Content Analysis. *SLAS Discov.* **24**, 615–627 (2019).
20. Kamentsky, L. *et al.* Improved structure, function and compatibility for cellprofiler: Modular high-throughput image

analysis software. *Bioinformatics* **27**, 1179–1180 (2011).

21. Guimarães, C. F., Gasperini, L., Marques, A. P. & Reis, R. L. The stiffness of living tissues and its implications for tissue engineering. *Nat. Rev. Mater.* **5**, 351–370 (2020).

22. Rada, T., Reis, R. L. & Gomes, M. E. Adipose tissue-derived stem cells and their application in bone and cartilage tissue engineering. *Tissue Eng. - Part B Rev.* **15**, 113–125 (2009).

23. Chaudhuri, O. *et al.* Hydrogels with tunable stress relaxation regulate stem cell fate and activity. *Nat. Mater.* **15**, 326–334 (2015).

24. Lee, H. P., Gu, L., Mooney, D. J., Levenston, M. E. & Chaudhuri, O. Mechanical confinement regulates cartilage matrix formation by chondrocytes. *Nat. Mater.* **16**, 1243–1251 (2017).

25. Samal, P., Maurer, P., Blitterswijk, C. Van, Truckenmüller, R. & Giselbrecht, S. A New Microengineered Platform for 4D Tracking of Single Cells in a Stem-Cell-Based In Vitro Morphogenesis Model. *Adv. Mater.* **1907966**, (2020).

26. Kawakami, Y., Rodriguez-León, J. & Belmonte, J. C. I. The role of TGFβs and Sox9 during limb chondrogenesis. *Curr. Opin. Cell Biol.* **18**, 723–729 (2006).

27. Kwak, T. J. *et al.* Convex grooves in staggered herringbone mixer improve mixing efficiency of laminar flow in microchannel. *PLoS One* **11**, 1–15 (2016).

28. Xie, J. *et al.* Substrate elasticity regulates adipose-derived stromal cell differentiation towards osteogenesis and adipogenesis through β-catenin transduction. *Acta Biomater.* **79**, 83–95 (2018).

29. Major, L. G. & Choi, Y. S. Developing a high-throughput platform to direct adipogenic and osteogenic differentiation in adipose-derived stem cells. *J. Tissue Eng. Regen. Med.* 1–8 (2018). doi:10.1002/term.2736

30. Teong, B. *et al.* The stiffness of a crosslinked hyaluronan hydrogel affects its chondro-induction activity on hADSCs. *J. Biomed. Mater. Res. - Part B Appl. Biomater.* **106**, 808–816 (2018).

31. Rosen, E. D. & MacDougald, O. A. Adipocyte differentiation from the inside out. *Nat. Rev. Mol. Cell Biol.* **7**, 885–896 (2006).

32. Lago, M. *et al.* Generation of Gellan Gum-Based Adipose-Like Microtissues. *Bioengineering* **5**, 52 (2018).

33. Hussey, G. S., Dziki, J. L. & Badylak, S. F. Extracellular matrix-based materials for regenerative medicine. *Nat. Rev. Mater.* **3**, 159–173 (2018).

34. Nichol, J. W. *et al.* Cell-laden microengineered gelatin methacrylate hydrogels. *Biomaterials* **31**, 5536–5544 (2010).

35. Dupont, S. *et al.* Role of YAP/TAZ in mechanotransduction. *Nature* **474**, 179–184 (2011).

36. Lee, H., Stowers, R. & Chaudhuri, O. Volume expansion and TRPV4 activation regulate stem cell fate in three-dimensional microenvironments. *Nat. Commun.* **10**, 529 (2019).

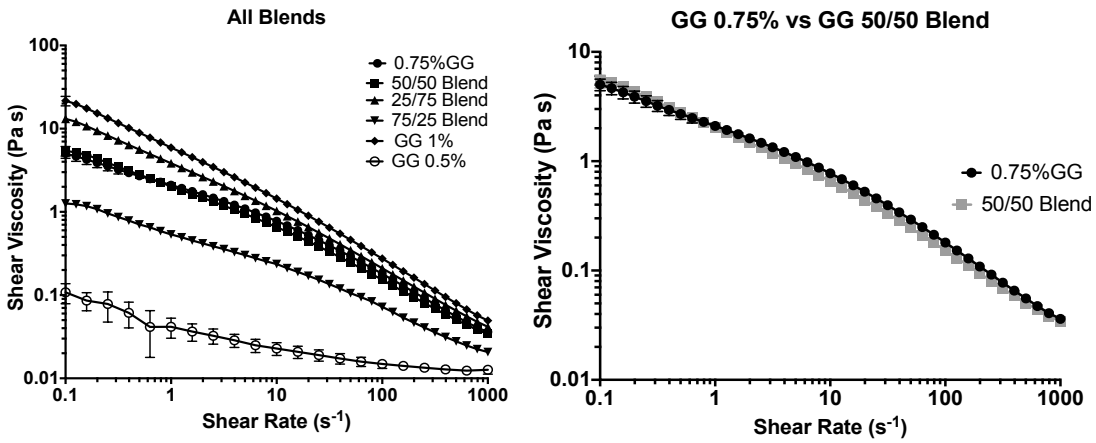
37. Zhu, M. *et al.* Gelatin methacryloyl and its hydrogels with an exceptional degree of controllability and batch-to-batch consistency. *Sci. Rep.* **9**, 1–13 (2019).

38. Fukunaka, Y., Iwanaga, K., Morimoto, K., Kakemi, M. & Tabata, Y. Controlled release of plasmid DNA from cationized gelatin hydrogels based on hydrogel degradation. *J. Control. Release* **80**, 333–343 (2002).

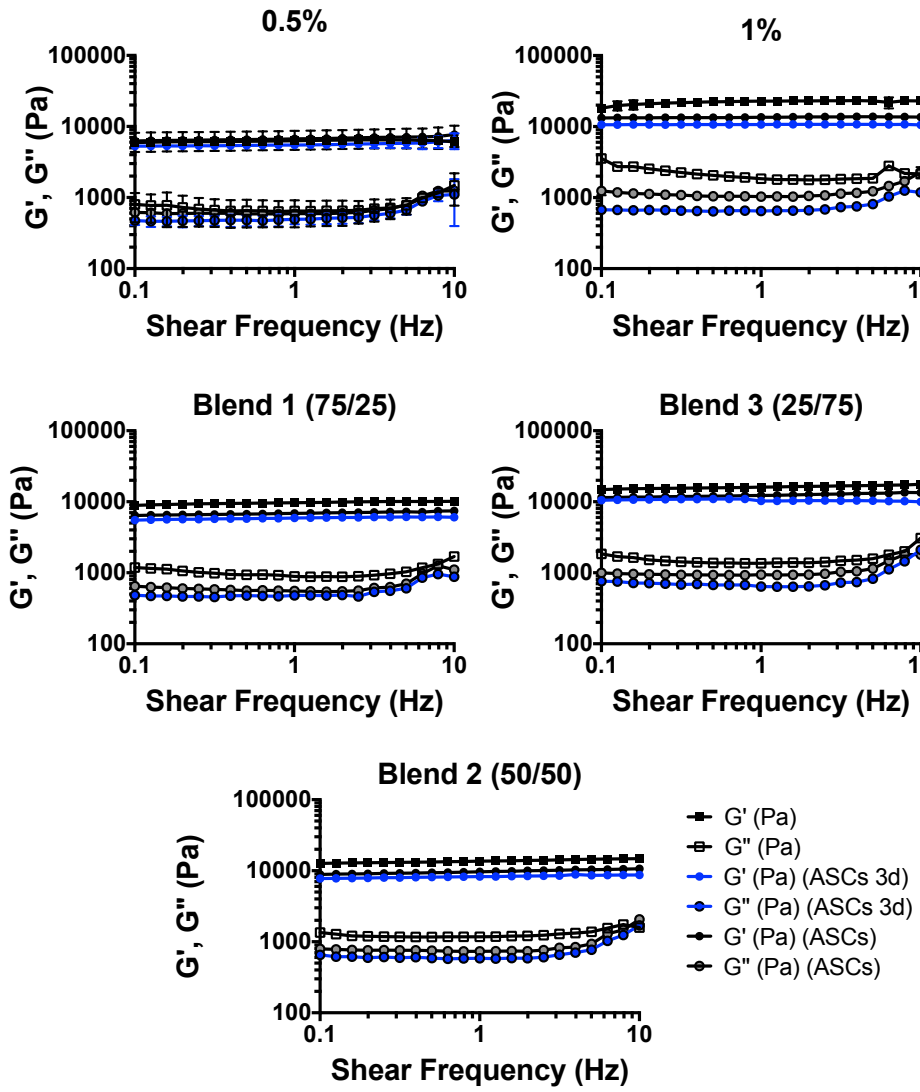
39. Ansari, S., Khorshidi, S. & Karkhaneh, A. Engineering of gradient osteochondral tissue: From nature to lab. *Acta Biomater.* **87**, 41–54 (2019).

40. Sunyer, R. *et al.* Collective cell durotaxis emerges from long-range intercellular force transmission. *Science (80-.).* **353**, 1157–1161 (2016).

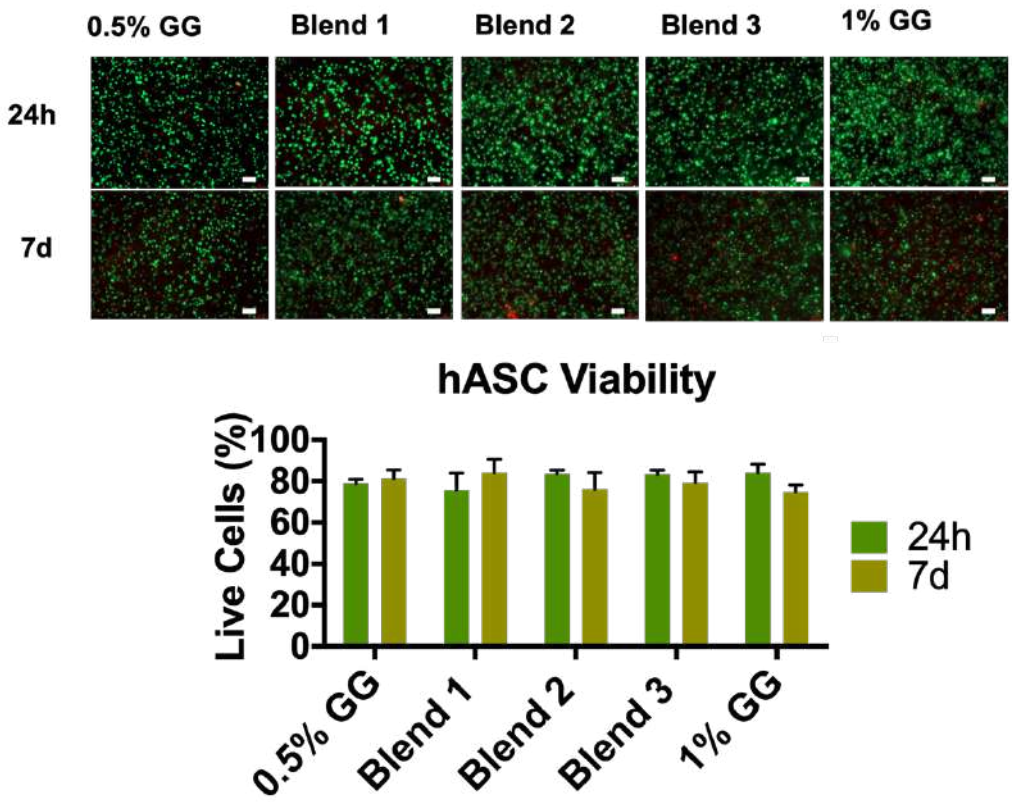
VII.6. SUPPLEMENTARY MATERIAL



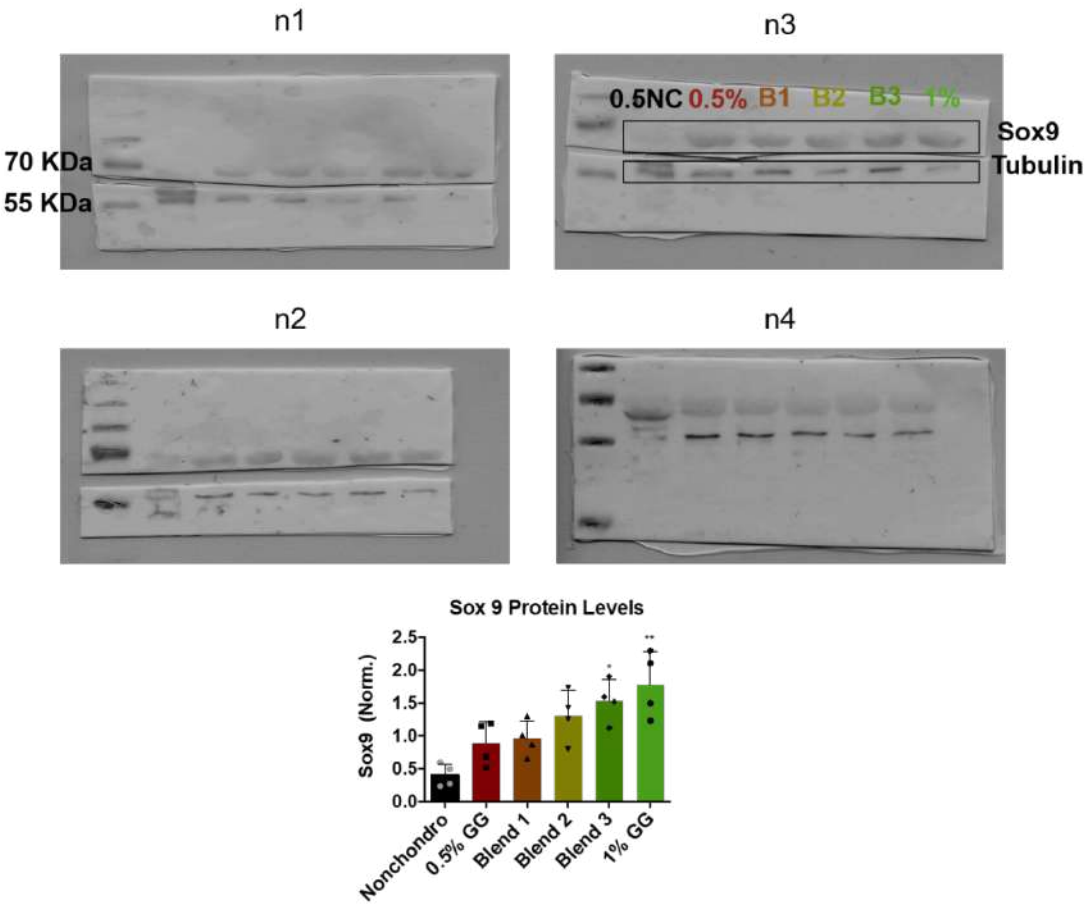
Supplementary Fig. VII-1: Gellan Gum Rheology. Analysis of the Shear viscosity of the different blends of Gellan Gum (a), showing the increase in viscosity with increasing polymer concentrations. The comparison of a 0.75% GG with a 50/50 blend of GG 0.5% and GG 1% (b) reveals that formulating the material at an intermediate concentration or obtaining it by mixing from different concentrations yields a similar mixture. The blending method was therefore followed once it mimics what happens in the microfluidic mixing, knowing it is the same as dissolving the polymer to the equivalent concentration. N=3.



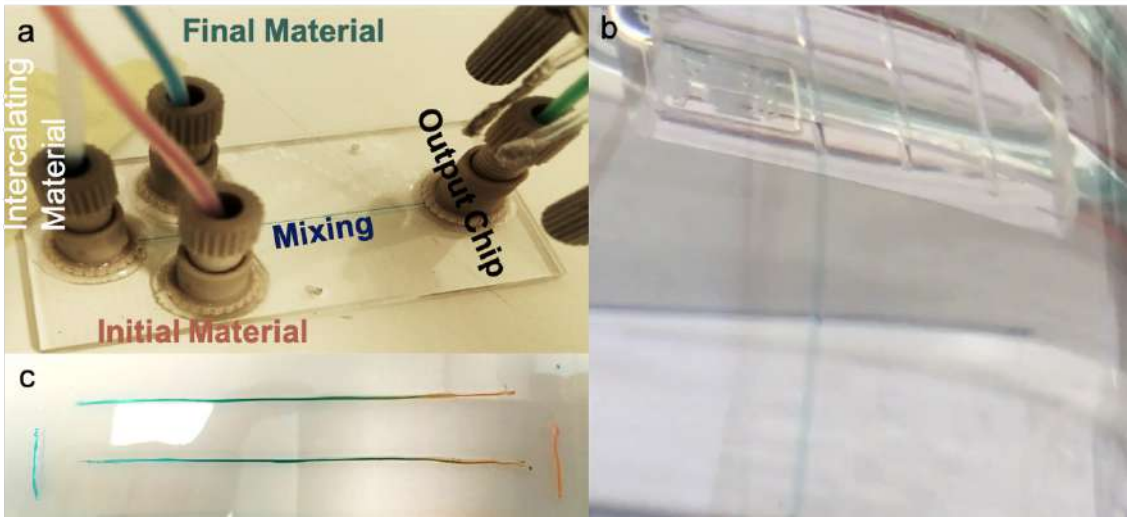
Supplementary Fig. VII-2: Gellan Gum Hydrogel Oscillation. All hydrogels were tested within their linear elastic region, performing a shear frequency sweep to derive the G' and G'' of the pure hydrogel, upon ASC encapsulation (ASCs) and after encapsulation and 3 days of culture (ASCs 3d). There is a slight decrease in mechanics on the stiffer gels upon ASC encapsulation, which is in most cases not further affected by short term cell culture. N=5.



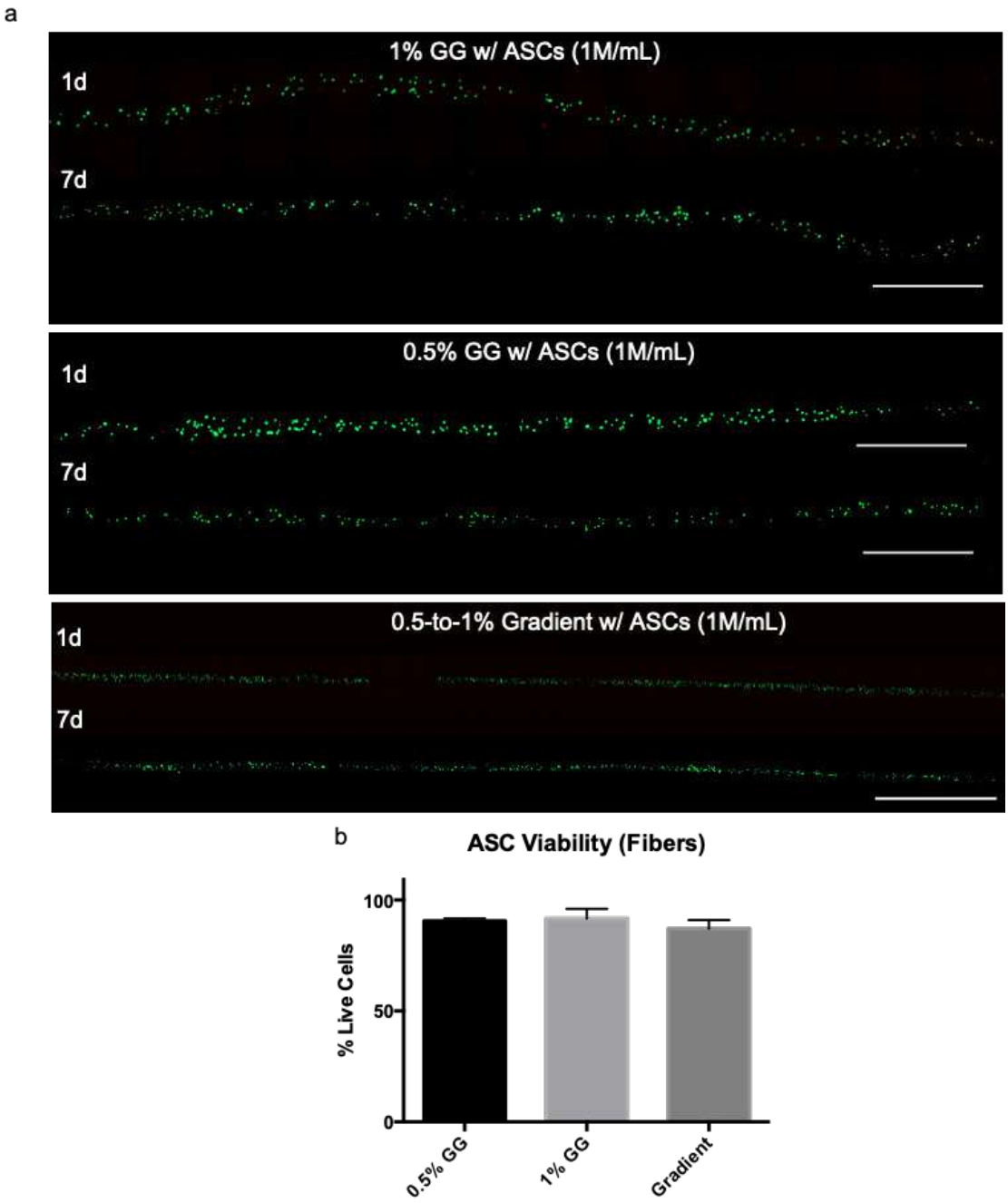
Supplementary Fig. VII-3: Encapsulated hASC Viability. Human adipose-derived stromal/stem cells (hASCs) viability (live Calcein AM (Green) and dead Propidium Iodide (Red) cells) remained high shortly after encapsulation and upon 1 week of culture (scale bar 100µm). Image analysis after Calcein AM staining shortly after encapsulation revealed decreasing projected cell areas in the higher concentration hydrogels as reported in the maintext.



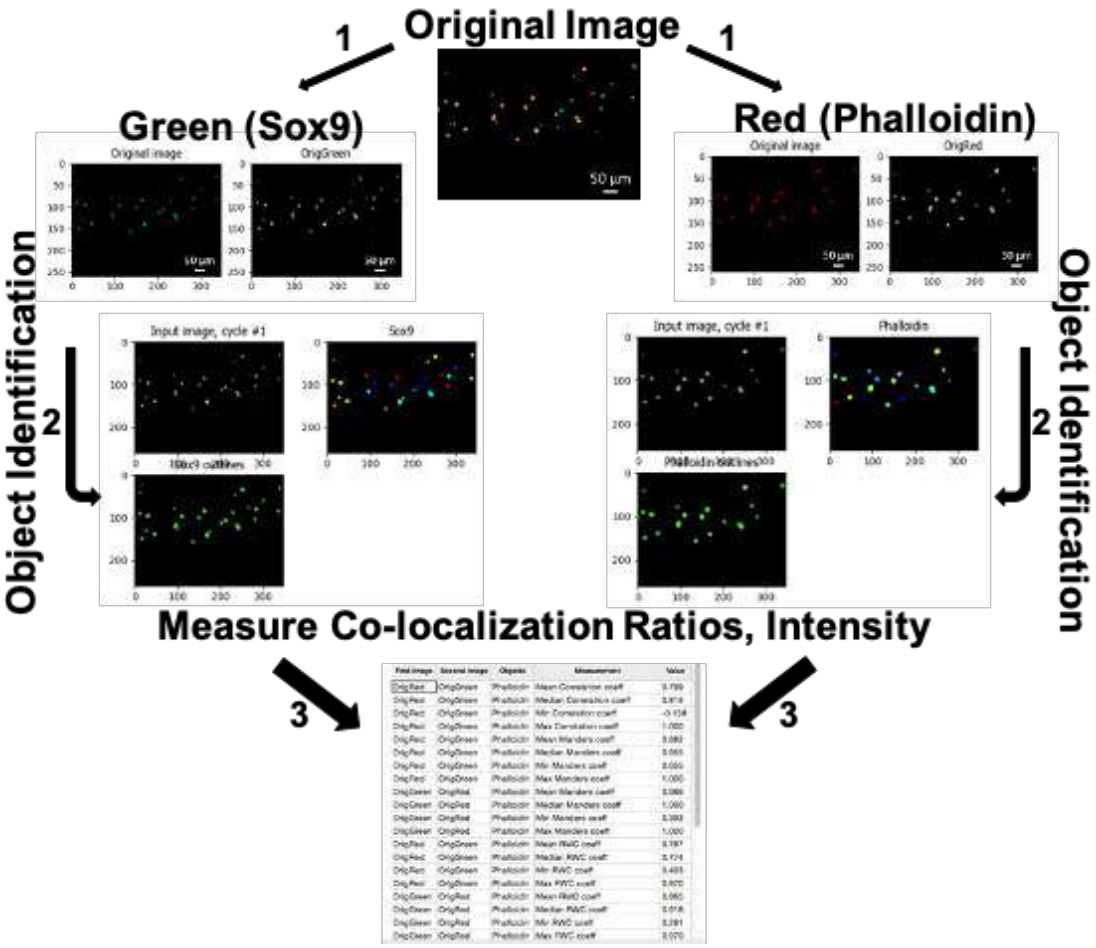
Supplementary Fig. VII-4: Sox9 Western Blot. Western blots for validation of Sox9 screening in the different hydrogels upon 1 week of chondrogenic culture. Different pictures represent replicated experiments. On the bottom, the semi-quantification of SOX9 protein was performed, confirming the image screening results. Statistical values: *p<0.05, ** p<0.01, *** p<0.001, compared to control (Nonchondro, meaning no chondrogenic stimuli. NC – Non-chondro, B1 – Blend 1, B2 – Blend 2, B3 – Blend 3. Blend compositions are detailed in the main text.



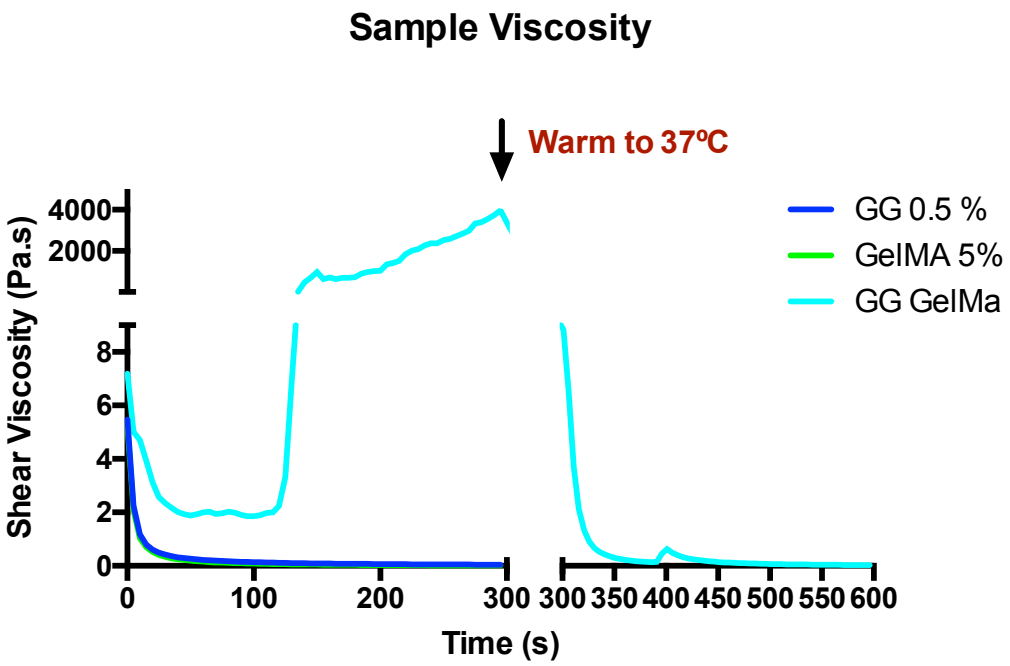
Supplementary Fig. VII-5: Gradient Fabrication Setup. The different endpoint materials (stained red and blue) are pushed to flow into a T-junction mixer chip (a), which disrupts the laminar flow allowing for an axially-uniform fiber instead of a Janus-like structure. This is in turn connected to a linear output chip that releases the solution into a crosslinking bath (b). The gradients are sequentially produced and collected; their composition tracked in real time by soluble food-dye staining – macroscopic view of 2 gradients immediately after production comparing to 2 single-material segments (c).



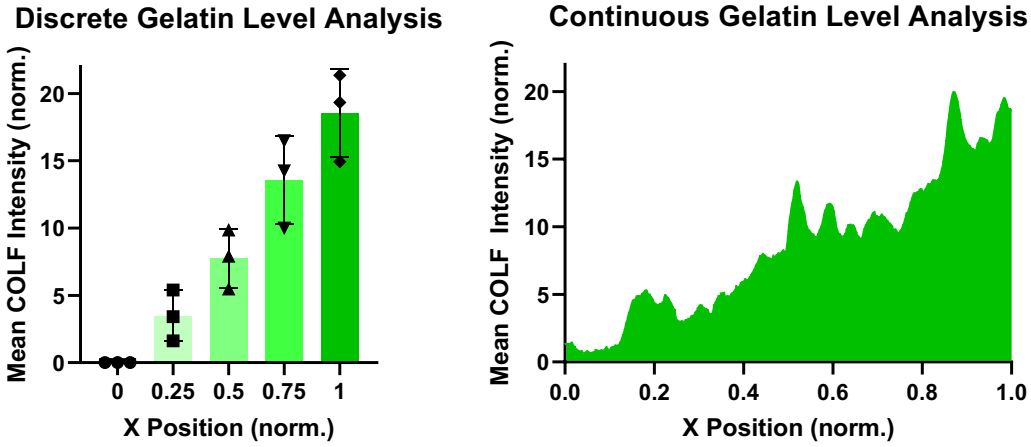
Supplementary Fig. VII-6: hASC Viability Assessment. hASC viability in uniform fibers and gradients is not impacted negatively by microfluidic manipulation, with most cells remaining viable (a, calcein AM signal in green, propidium iodide signal in red, scale bar 5mm). The percentage of viable cells is of 80% or higher in all cases (b), being similar to or higher than that of discrete hydrogels due to thinner structure and faster nutrient/waste diffusion from the fibers. N=3.



Supplementary Fig. VII-7: Image Analysis Pipeline Example. The original image is processed and separated according to the different channels (1). In this example, green is selected for Sox9 and Red for Phalloidin. Cell-profiler identifies the individual objects above a threshold of size for discarding debris/artifacts in both cases (2) and then superimposes the objects calculating co-localization values (3) as well as intensities for other approaches. Mander's Co-localization coefficient is selected yielding the ratio of Sox9 positive pixels within the Phalloidin area, on average (uniform gels) and per-object (gradients).

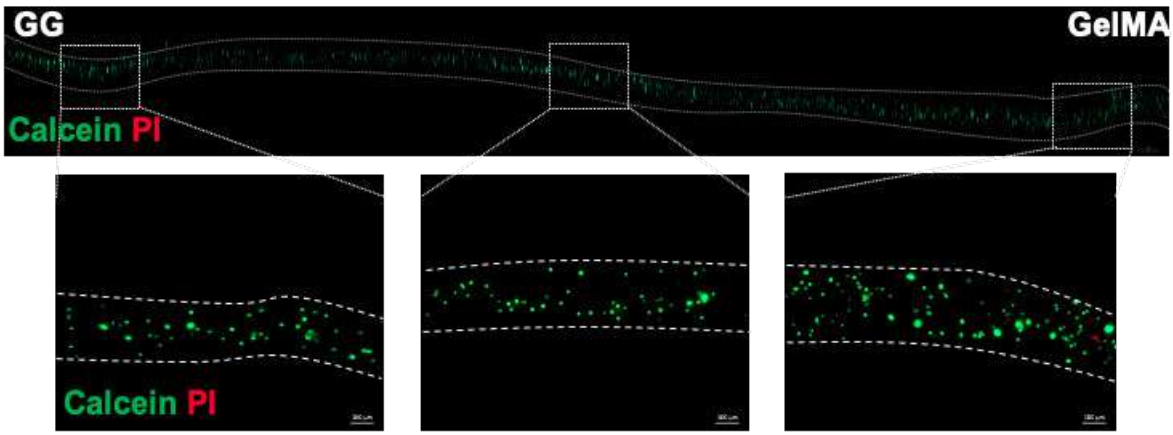


Supplementary Fig. VII-8: GG/GelMA Viscosity Tests. In order to test flow conditions for GG/GelMA gradient fabrications, the viscosity vs time of the distinct materials was assessed after mixing GelMA (37°C) and GG (25°) . At Room temperature, GG and GelMA do not see their viscosity increased for up to 5 minutes. However, when mixed, there is a fast increase in viscosity at around 120 seconds (2 minutes), suggesting thermal gelation (GelMA-induced and reversible). To prevent this from happening within the microfluidic channels, the temperature at which the materials were maintained during fabrication was kept at 37°C: When applied to the GG/GelMA mix, this temperature immediately reverses the viscosity to that of the other liquids.

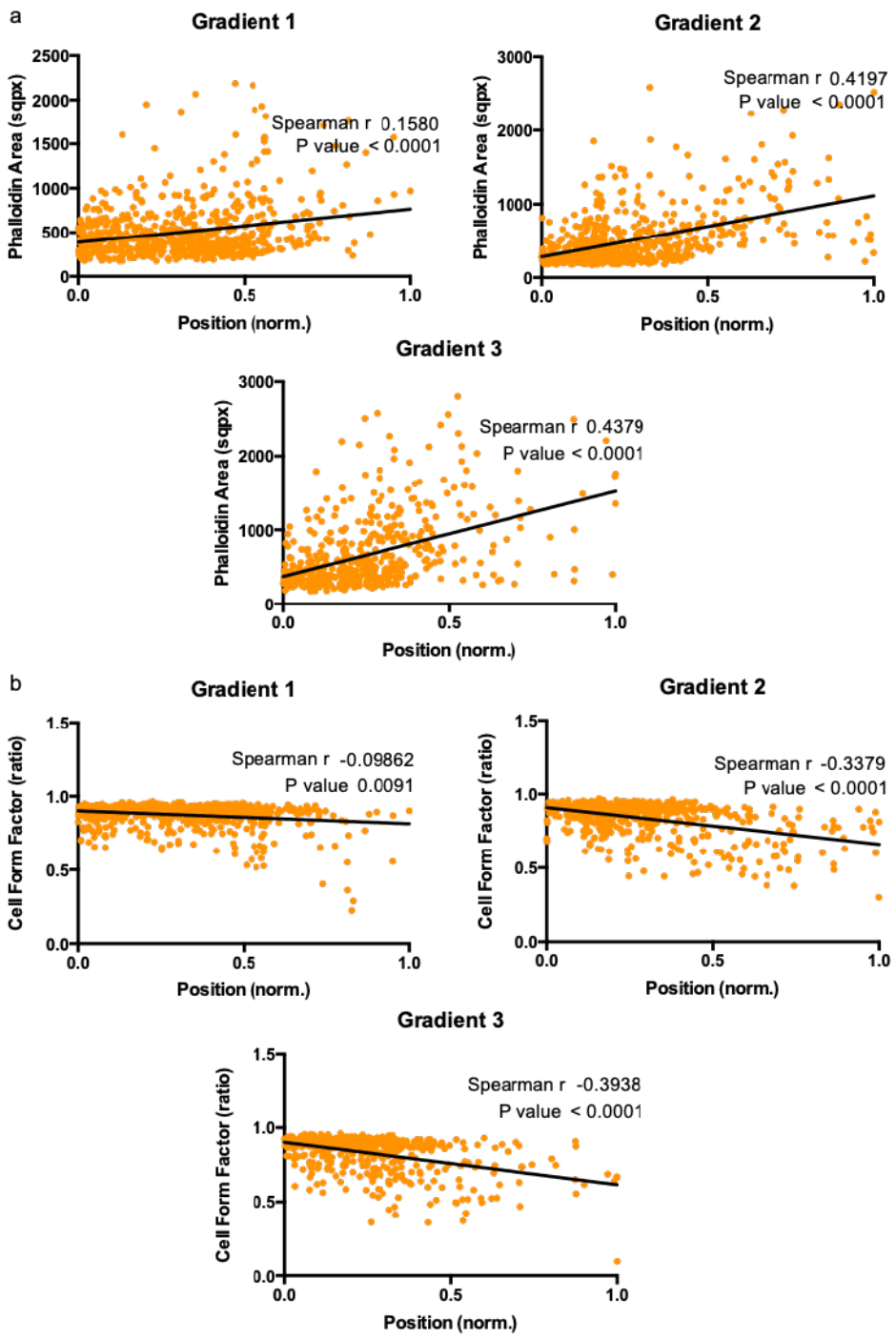


Supplementary Fig. VII-9: GG/GelMA Gradients Quantification. Quantitative analysis of the COLF signal (Gelatin staining) in 5 distinct positions of independent gradients (left) and continuous profile of the signal along the

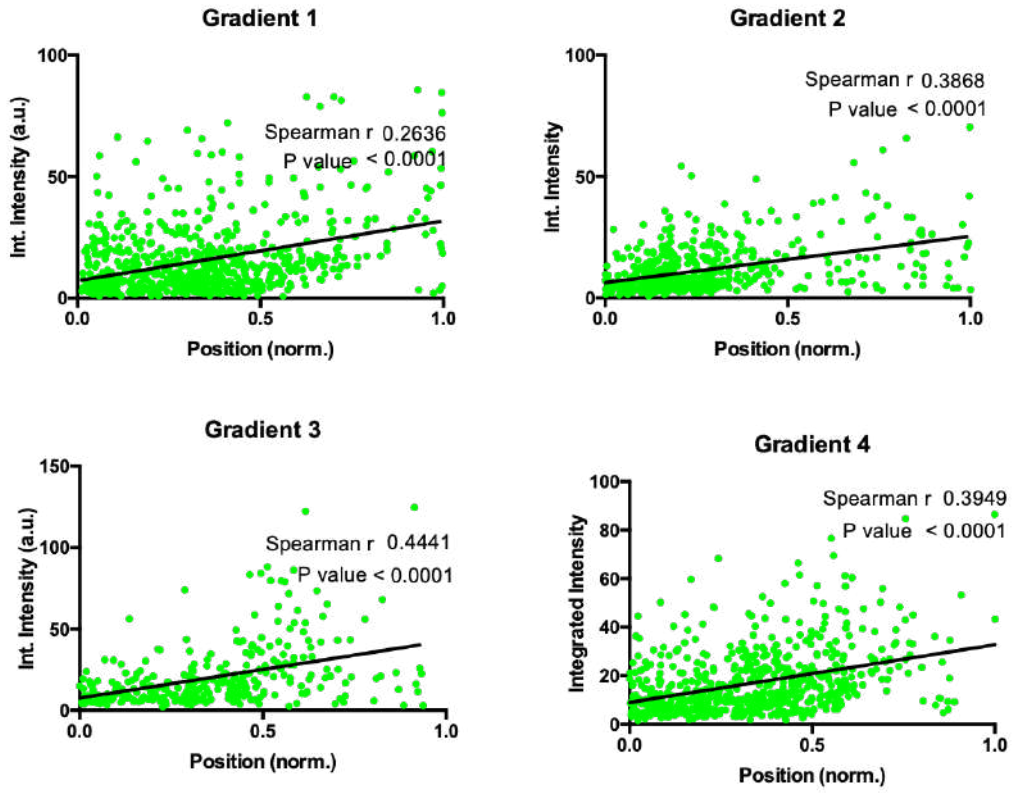
gradient (right). Both evidence a linear-like increase in the level of GelMA, agreeing with the programmed flows as well as the GG-based gradients.



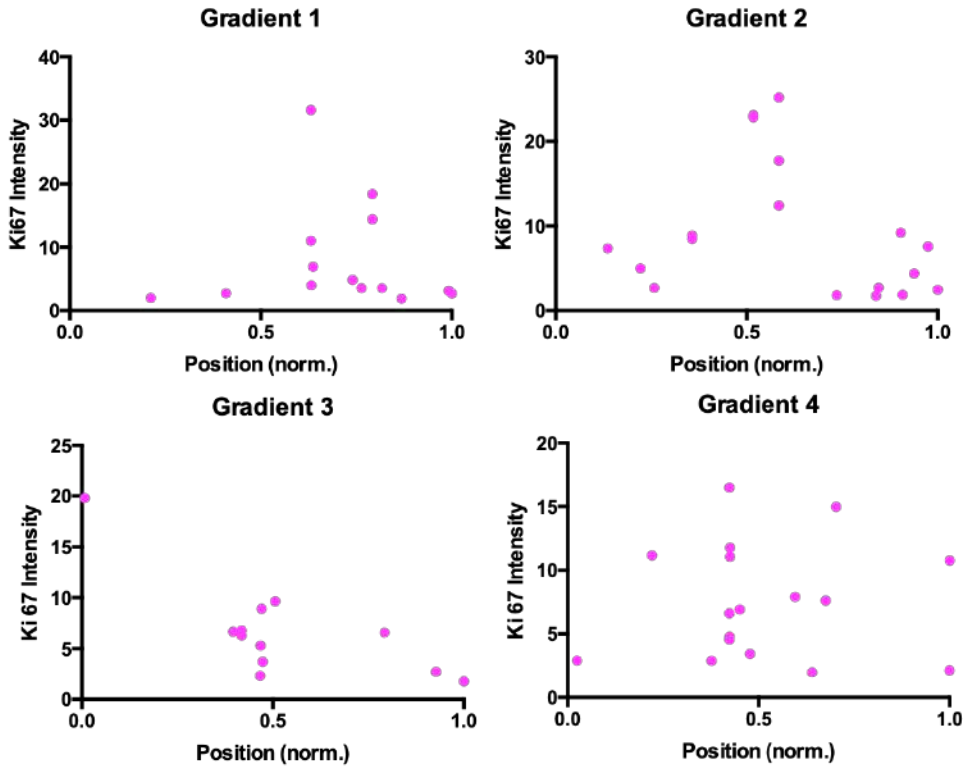
Supplementary Fig. VII-10: GG/GelMA hASC Live/Dead Assay. Viability test on the GG/GelMA gradient and some zoomed-in pictures of the beginning, middle and end. Detailed cell-by-cell plotting is present in the main text. In both cases, no significant changes are observed in the Calcein/PI proportions regardless of the material and crosslinking type.



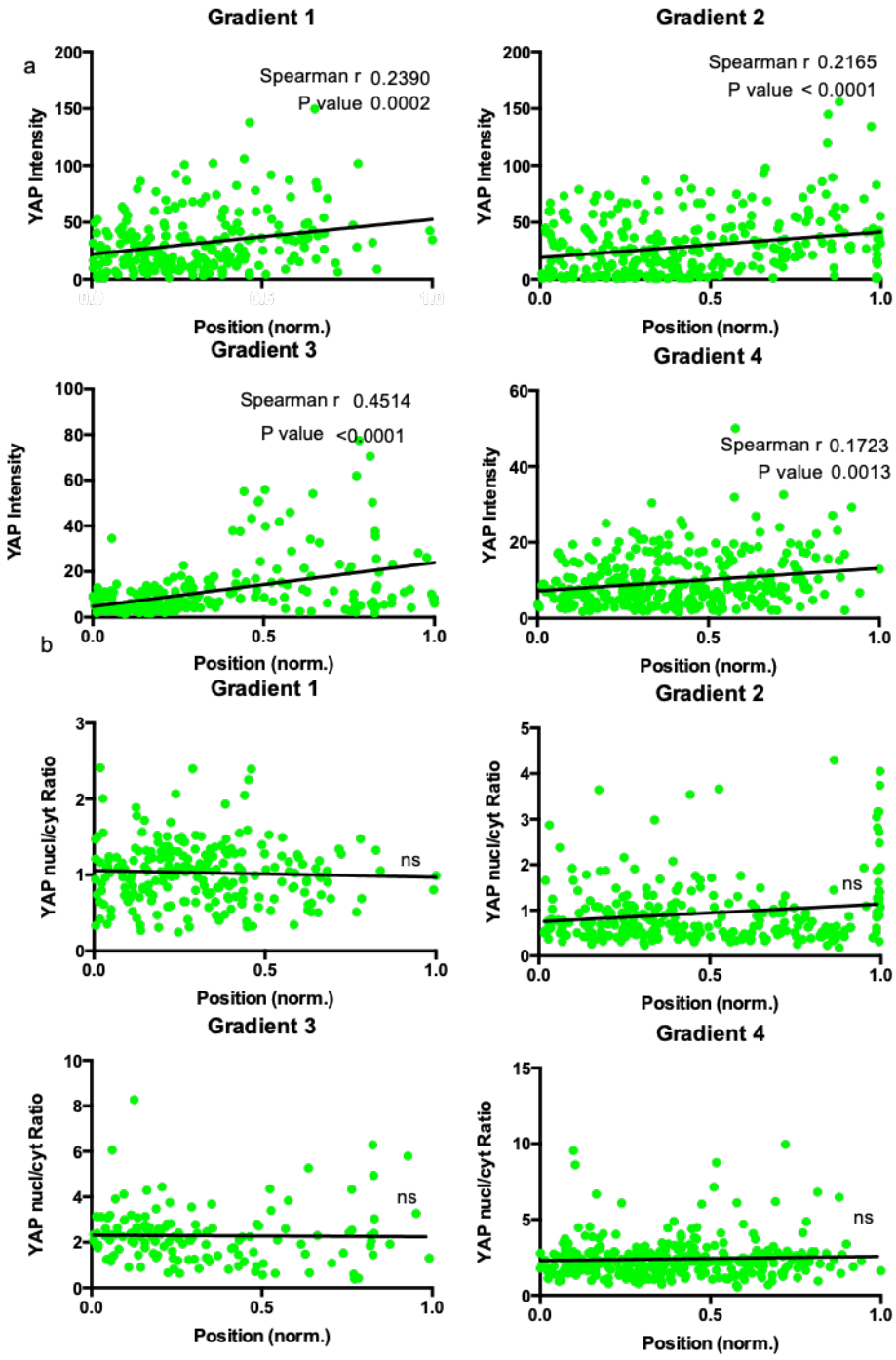
Supplementary Fig. VII-11: Gradients hASC Morphology. Analysis of cell morphology in the different gradient replicates. In all cases, significant increases in cell area (a) and decreases in form factor (b) can be observed, as well as a visible shift in area around the half position of the gradient (0.5, 1:1 GG/GelMA ratios).



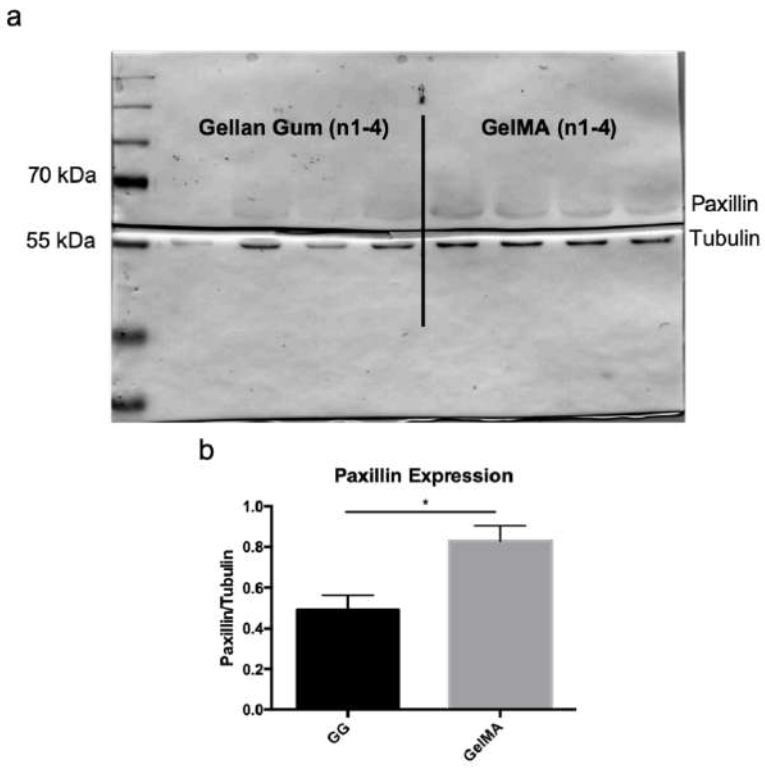
Supplementary Fig. VII-12: Gradients hASC Paxillin. Analysis of paxillin responses of cells on the different gradient replicates. In all cases, a significant increase in paxillin intensity is observed as function of gradient position, hinting at increased adhesion responses from cell-GelMA interactions, as well as a visible shift in area around the half position of the gradient (0.5, 1:1 GG/GelMA ratios).



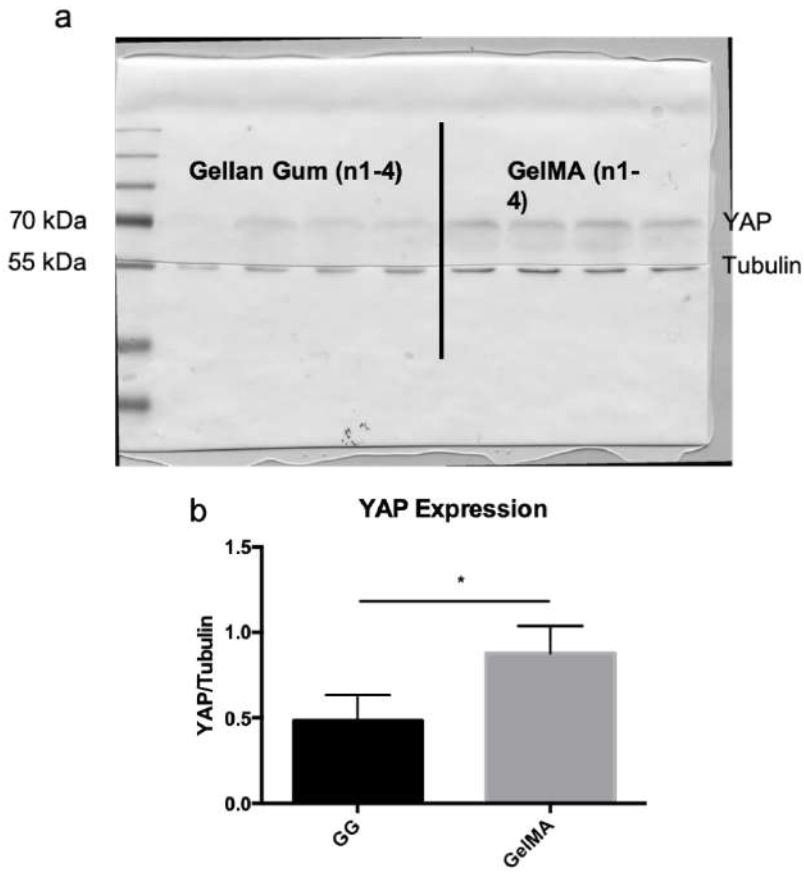
Supplementary Fig. VII-13: Gradients hASC Ki-67. Analysis of Ki-67 responses on the distinct gradient replicates. In all Cases, most Ki-67+ events appear only from half of the gradient onward, where the environment is prone to remodeling and degradation allowing cells to enter proliferation.



Supplementary Fig. VII-14: Gradients hASC YAP. Analysis of YAP responses. YAP intensities increase along the gradient replicates (a) but no change in the nuclear/cytoplasmic ratios was detected in any case (b).



Supplementary Fig. VII-15: Western Blot of Paxillin. Molecular validation of Paxillin responses on pure endpoint GG and GelMA macro hydrogels. 4 replicates of each condition were tested (a), evidencing a significant increase in paxillin expression at the molecular level (b) which validates the trends observed on the image analysis of gradients.



Supplementary Fig. VII-16: Western Blot of YAP. Molecular validation of YAP responses on pure endpoint GG and GelMA macro hydrogels. 4 replicates of each condition were tested (a), evidencing a significant increase in YAP expression at the molecular level (b) which validates the trend derived from the image analysis of the gradients.

Chapter VIII

3D Flow-Focusing Microfluidic Biofabrication: One-chip-fits-all Hydrogel Fiber Architectures

3D Flow-Focusing Microfluidic Biofabrication: One-chip-fits-all Hydrogel Fiber Architectures

Abstract

The microfluidic manipulation of hydrogels is a powerful tool to recapitulate functional biological architectures. A wide range of flow configurations and chip designs have been employed to create microfibers with increasingly complex shapes and compositions requiring individually engineered setups. Distinctly, we demonstrate how one single 3D hydrodynamic flow-focusing chip can be used to obtain a continuous flow of hydrogel precursors, which rearrange themselves based on viscosity and applied pressures. These can crosslink into fibers with a variety of new multi-compartment shapes down to yet-unreported minimal dimensions. To prove the potential of 3D flow-focusing for the biofabrication of complex, multi-compartment structures, we tuned material properties and flow conditions to obtain ribbon-like cancer/basement-membrane/stroma models; core-shell vascular-like structures and networks; and multi-chemistry fibers integrating stem cells, biomaterials, and pro-differentiation hydrophobic molecule depots. This innovative biofabrication method can be valuable for the recreation of a broad range of complex biological architectures and micro-modeling of distinct 3D environments.

This chapter is based on the following publications:

Guimarães, C. F., Gasperini, L., Marques, A. P., & Reis, R. L. (2021). 3D flow-focusing microfluidic biofabrication: One-chip-fits-all hydrogel fiber architectures. *Applied Materials Today*, *23*, 101013.

Guimarães, C. F., Gasperini, L., Marques, A. P., & Reis, R. L., Multicompartement hydrogel fibre their preparation and uses thereof, WO2021165905A1.

VIII.1. INTRODUCTION

The fabrication of cell-laden hydrogel microfiber structures represents an exciting approach to recapitulate biological tissues' architecture and functionality at the microscale [1]. Initial strategies for the fabrication of such structures were based mostly on spinning ionic-crosslinking hydrogel precursors, such as alginate, in a core-sheath setup, with the crosslinking solution, e.g., $CaCl_2$, being the sheath to the precursor hydrogel core [2,3]. Over the past decade, these approaches evolved towards more complex shapes to approach a variety of biological tissues [4,5]. Cylindrical hydrogel fibers [2] gradually branched into forms as varied as flat [6], core-shell [7–10], hollow[9], janus[11], helical[8,10], as well as combinations thereof such as hollow Janus [11] or helical core-shell [8] fibers. Most of these geometries are dictated by microfluidic chip designs or needle setups arranged to reproduce a specific shape [4]. Despite these advances, previous approaches present two significant caveats, 1) a clear need to devise a particular microfluidic setup to achieve each of these distinct structures and 2) a limited type of geometries obtained with a single setup.

As an alternative to existing systems, we investigated 3D microfluidic flow-focusing (FF) as an innovative approach for spinning hydrogel precursors into novel multi-material, multi-compartment hydrogel constructs. 3D FF consists of having distinct solutions flowing within separate microfluidic channels, which then meet at a junction or pore, generating a 3D-focused stream composed of all flowing solutions. After this junction, the organization of fluids is dictated by pressure and viscosity, and it is frequently employed for droplet generation with continuous/discontinuous phases [12–15]. Distinctly, we report for the first time how 3D FF can be used to obtain a threading flow regimen of hydrogel precursors to fabricate continuous hydrogel fibers with distinct materials, shapes, and compartments, by tuning the viscosity of solutions and manipulating the pressure applied to the inlets (and consequent flow).

We then employ this tool for the biofabrication of cell-laden hydrogel architectures that approach the dimensions, mechanics, and biological complexity of living tissues, from core-shell vascular-like structures and networks to novel cancer/basement membrane/stroma 3D disease models. We further explore the integration of hydrophobic drug depots in stem-cell-laden fibers, where the multi-chemistry composition allows for an all-in-one tissue engineering (TE) strategy that transports and controls the behavior of encapsulated cells. Achieving all of these structures using a single type of microfluidic chip highlights the high versatility and unprecedented application possibilities of 3D FF for the engineering and biofabrication of live-like fiber tissues and 3D models.

VIII.2. MATERIALS AND METHODS

VIII.2.1. General Flow Focusing Fabrication of Multi-Shape Fibers

Gellan Gum (Gelzan, Sigma) was used as the ionic gelling material for all the reported hydrogel fiber shapes. GG (Gellan Gum) was dissolved at 0.5 wt.% in water containing 0.25M sucrose as previously described [16]. GG was blended with red or blue, fluorescent microparticles (screenMag, Chemicell), 1:10 particle dilution for color tracking distinct compartments.

Fibers were fabricated using one single chip geometry (3D Flow Focusing, Dolomite) (Supplementary Figure VIII-1). The Double Core-Shell Shape was the only structure fabricated with a different chip (2D Flow Focusing, Dolomite). The chips were connected to a digitally controlled microfluidic pump system (OB1, Elveflow), which directly applied pressure to individual Eppendorf's containing the distinct materials, connected to the chip by 30 cm of polytetrafluoroethylene microfluidic tubing (0.5x1.6mm). The fibers were formed upon crosslinking (wet spinning) in a 0.1M $CaCl_2$ bath.

Slight variations on the setup led to the distinct fiber shapes. Flowing red-labelled GG in the 2 inside channels and blue-labelled GG in the 2 outer ones formed hydrogel fibers with a ribbon-like shape (3 compartments). Core-Shell fibers were produced by blocking the flow of one of the outer channels, allowing the inner flow to be surrounded by the outer one.

The oil-core hydrogel-shell was formed by flowing an apolar solution in the inner channels and GG in the outer ones. The tricoaxial shape was produced by flowing 2 distinct materials (GG and red-GG) in the inner channels in the core-shell configuration.

Double-Janus fibers were fabricated by alternating the materials flowing in the ribbon configuration, leading to the 4 distinct compartments (red-blue-red-blue or blue-red-blue-red).

The double core-shell shape was produced taking advantage of a Flow Focusing chip, without the 3D pore geometry, which allows the inner material to go around and surround the outer ones forming 2 compartments separated and covered by a third one.

VIII.2.2. Size and Composition Manipulation

The inlet pressures were tuned to manipulate the relative sizes of the core-shell and ribbon-shaped compartments, and these were directly responsible for larger/smaller compartments upon flowing with

higher/lower pressures. In order to reduce the global fiber diameter, these were pulled immediately after spinning in the $CaCl_2$ bath, with gradually increased speeds leading to gradually smaller diameters.

To prove that shapes could still be obtained by the combination of different materials, a blend of 1:1 GG 0.5%:GelMA5% was used as a shell solution. These fibers were collected upon spinning in the bath and further crosslinked under UV light (320-500nm) (Omnicure series 2000) for 50 seconds at 0.6mW/cm2. Fibers were also fused by crosslinking the shells when in close contact.

VIII.2.3. Core-Shell, Endothelial cell-laden Fibers

In order to increase GelMA viscosity above that of GG to create the core-shell fibers with a biolabile core, GelMA was dissolved in a solution of Hyaluronic Acid (Sodium Hyaluronate 1.5MDa, Lifecore) containing 0.25M sucrose and 0.3% Irgacure (Sigma). Differences in viscosity were studied using a Malvern Kinexus Pro+ Rheometer and a cone plate geometry (40mm/ 4°), where the shear viscosity was recorded along a range of 0.1-1000s^{-1} of Shear Rate. Oscillation tests were also performed to characterize the mechanical properties (Shear Modulus) of GG (shell) and GelMA/HA (core) hydrogels. Briefly, an amplitude sweep at 1Hz was performed to derive the linear viscoelastic region, within which a frequency sweep was then performed to derive the storage (G') and loss (G'') shear moduli of the hydrogels.

To produce vascular structures, human dermal microvascular endothelial cells (hDMECs) were suspended in the core solution of GelMA/HA prior to the fiber fabrication at a density of 3E6 cells/mL. Fibers were spun into the $CaCl_2$ solution and afterwards exposed to UV light (as previously reported) to crosslink the GelMA/HA core. To obtain fibers with a liquified core, the UV crosslinking step was skipped.

Post-fabrication endothelial cell viability was assessed by incubation with medium containing 1:1000 dilution of Calcein AM (Thermofisher) and 1μg/mL Propidium Iodide (Molecular Probes) for 30 mins at 37°C, 5% CO_2 and cells were then imaged under a fluorescent Axio Observer Inverted Microscope (Zeiss).

For CD31 immunocytochemistry, fibers were fixed in formalin 10% for 10 mins at room temperature (RT), washed with PBS and incubated with 0.2% Triton X-100 (Thermo Fisher) in PBS for 12 minutes to enhance cell membrane permeability. After washing, non-specific interactions were blocked by incubating with 3% BSA (Sigma) in PBS for 30 minutes. Afterward, samples were incubated

with the primary mouse CD31 antibody (DAKO, 1:50 dilution) in 1% BSA overnight at 4°C. These were then incubated with the secondary anti-mouse antibody (Alexa 488 donkey anti-mouse, Invitrogen, 1:500 dilution) for 1 hour at RT. At this stage, cell cytoskeleton and nuclei were also stained by adding Phalloidin-TRITC (Sigma) at 2ug/mL and DAPI (Biotium) at 4ug/mL. Afterwards, samples were taken to image in the fluorescent microscope.

To integrate vascular core-shell fibers in the 3D environments, human dermal fibroblasts (hDFs) were suspended at a density of 3E6/mL in a 2mg/mL solution of neutralized rat tail collagen type I (Gibco). Core-Shell endothelial cell-laden fibers were randomly placed within well plates and the fibroblast-containing collagen solution was added to these and crosslinked by incubating at 37°C. After 3 days of culture, samples were fixed and stained as previously described. To obtain 3D rendition of the environments, samples were imaged with a Z1 Light Sheet Microscope (Zeiss). Throughout this experiment, Fibroblasts were cultured in complete alpha-MEM medium (Gibco), hDMECs were cultured in EGM-2 Bullet medium (Lonza) and co-cultures were kept with 1:1 mix of both media.

VIII.2.4. Ribbon shaped, Cancer/BM/Stroma fibers

To obtain the BM structure within the 2 compartments, an overnight-thawed GelTrex Solution (Gibco) was mixed with the previously described Hyaluronic Acid 0.5% solution in order to yield a final GelTrex concentration of at least 9mg/mL according to the manufacturer's requirements for the formation of a gel. To observe GelTrex within the outer Gellan Gum compartments, the Blue and Red particles in the GG were used and GelTrex was mixed with a 1:100 dilution of a 1% GG-FITC solution. For obtaining the tri-material FF, a similar approach was followed, but instead of having GG 0.5% on both sides, one was replaced by GG/GelMA 1:1 blend. The distinct materials were kept at different temperatures during fabrication by maintaining the respective reservoir at RT (GG), 37°C (GelMA), and 4°C (GelTrex/HA) to ensure fluidity within the chip. Fibers were collected in the $CaCl_2$ bath, then the GelMA component was crosslinked by quick UV exposure (as previously described) and the GelTrex/HA was crosslinked by placing fibers in incubation at 37°C. Melanoma cells of the Sk-MEL-28 (ATCC) cell line were encapsulated in the GG/GelMa compartment, and fibroblasts (hDFs) were encapsulated in the GG compartment, both representing cancer and stroma, respectively, separated the GelTrex/HA. To track the different cell types, these were stained with CellBrite Green and Orange (Biotium) according to the manufacturer's instructions.

To fabricate the different modular fibers, we opened and/or blocked specific inlets, from flowing all (Cancer/BM/Stroma) to only the side channels (Cancer/Stroma, no BM) or individual ones (Stroma- and Cancer-alone). Fibers with tracked cells were observed under an Inverted Confocal Laser Scanning Microscope (Leica), throughout 1 week of culture.

For the drug tests, fibroblasts were stained prior to encapsulation using the CellTracker blue CMAC Dye (Molecular Probes) according to the manufacturer's instructions. These were then integrated into the fibers together with the cancer cells. 24h after fabrication, fibers were incubated with either culture medium (no treatment) or culture medium containing 1 μM of Doxorubicin (Carbosynth). 1 day after treatment, samples were incubated with Calcein AM/PI as previously described for viability assessment. Images of the fibers were acquired in the fluorescent microscope and a cell profiler [17] pipeline was used to derive the numbers of live and dead cells using the blue staining to distinguish fibroblasts from melanoma cells.

Throughout the experiment, fibroblasts were cultured in complete alpha-MEM medium, melanoma cells in EMEM medium (ATCC) and co-cultures with a 1:1 mix of both media.

VIII.2.5. Oil-Core Hydrogel-Shell Fibers

Fibers of GG/GelMA 1:1 encapsulating MSCs alone or including oil droplets were fabricated by wet spinning as previously described. After 1 day and 1 week of culture in alpha-MEM complete medium, the viability of cells was assessed through the previously detailed incubation with Calcein/PI, imaging and cell counting. The morphology of encapsulated cells was observed by fixing fibers and incubating with Phalloidin-TRITC (Sigma) 2 μg/mL and DAPI (Biotium) 4μg/mL for 1h at RT.

To visualize fibers with oil droplets containing dexamethasone, the labelled Dexamethasone-FITC (Molecular Probes) was dispersed in sesame oil by stirring at a concentration of 0.25mg/mL. When a uniform dispersion was obtained, fibers were fabricated and imaged under the fluorescent microscope.

To quantify the release of dexamethasone from the oil droplets, a Dexamethasone standard curve was obtained using solutions of pure Dexamethasone (Sigma) and its characteristic absorbance at 241nm. Using this information, dexamethasone was dispersed in mineral oil at a concentration of 20 mg/mL, estimated to yield a final concentration in 1 mL of PBS of 10^{-4}M (estimated, upon total release from the oil as detailed in Supplementary Fig. VII-11), high enough to be able to detect its gradual increase in concentration, measured through the 241nm absorbance on a microplate reader

(SYNERGY, Bio-tek instruments). The release was measured by keeping fibers in 6-well plates with 1mL of PBS, and removing 100μL of the well solution for measuring, replacing by 100μL of fresh PBS for up to 48h. Brightfield images of the oil droplets were also acquired to observe the presence/absence of dispersed dexamethasone.

To evaluate the effect of dexamethasone in oil within the 3D fibers, MSCs were encapsulated in 1:1 GG:GelMA fibers and cultured in standard medium, medium with 10^{-6}M of water-soluble dexamethasone (dexa in medium) or combined with oil droplets containing a dispersion of 0.5mg/mL Dexamethasone (estimated to release up to the same 10^{-6}M). After 72h in culture, fibers with the cells were fixed and immunostained against Runx2 (Mouse Anti-Runx2 (Millipore), 1:300 dilution) and later incubated with Alexa 488 donkey-anti-mouse secondary antibody (1:500 dilution, Invitrogen) as well as with Phalloidin-TRITC (Sigma) 2 μg/mL and DAPI (Biotium) 4μg/mL. These were then imaged in the fluorescent Axio Observer Inverted Microscope (Zeiss) to observe the expression of Runx2 and Cell Profiler was used to quantify the intensity of all Runx2+ cell events. Thousands of single cells were analyzed per condition. Details of the different conditions were also imaged using the Inverted Confocal Laser Scanning Microscope (Leica).

VIII.3. RESULTS AND DISCUSSION

VIII.3.1. Flow-Focusing yields a plethora of fiber compartment shapes

To fully assess the potential of 3D flow focusing, a custom-made microfluidic chip (**Fig. VIII-1, A,** Supplementary Fig. VIII-1) composed of four inlets and one outlet was used to flow hydrogel solutions into a Calcium Chloride ($CaCl_2$) crosslinking bath for forming hydrogel fibers upon extrusion (wet-spinning).

As model hydrogel, we used Gellan Gum (GG), an ionic-crosslinking material commonly used for tissue engineering [18], mixed with 1 μm fluorescent microparticles for tracking the final fiber shape. At room temperature, GG chains arrange into an intertwined helix conformation with the negatively charged carboxyl groups pointing outwards. Positive ions (such as Ca^{2+}) can electrically shield the carboxyl group leading to a tighter aggregation of the helices forming stable hydrogels [18,19]. The difference in viscosity between the two hydrogel/particle blends (**Fig. VIII-1, A**) was explored to understand the consequence of viscosity and flows in fiber shape and compartment organization.

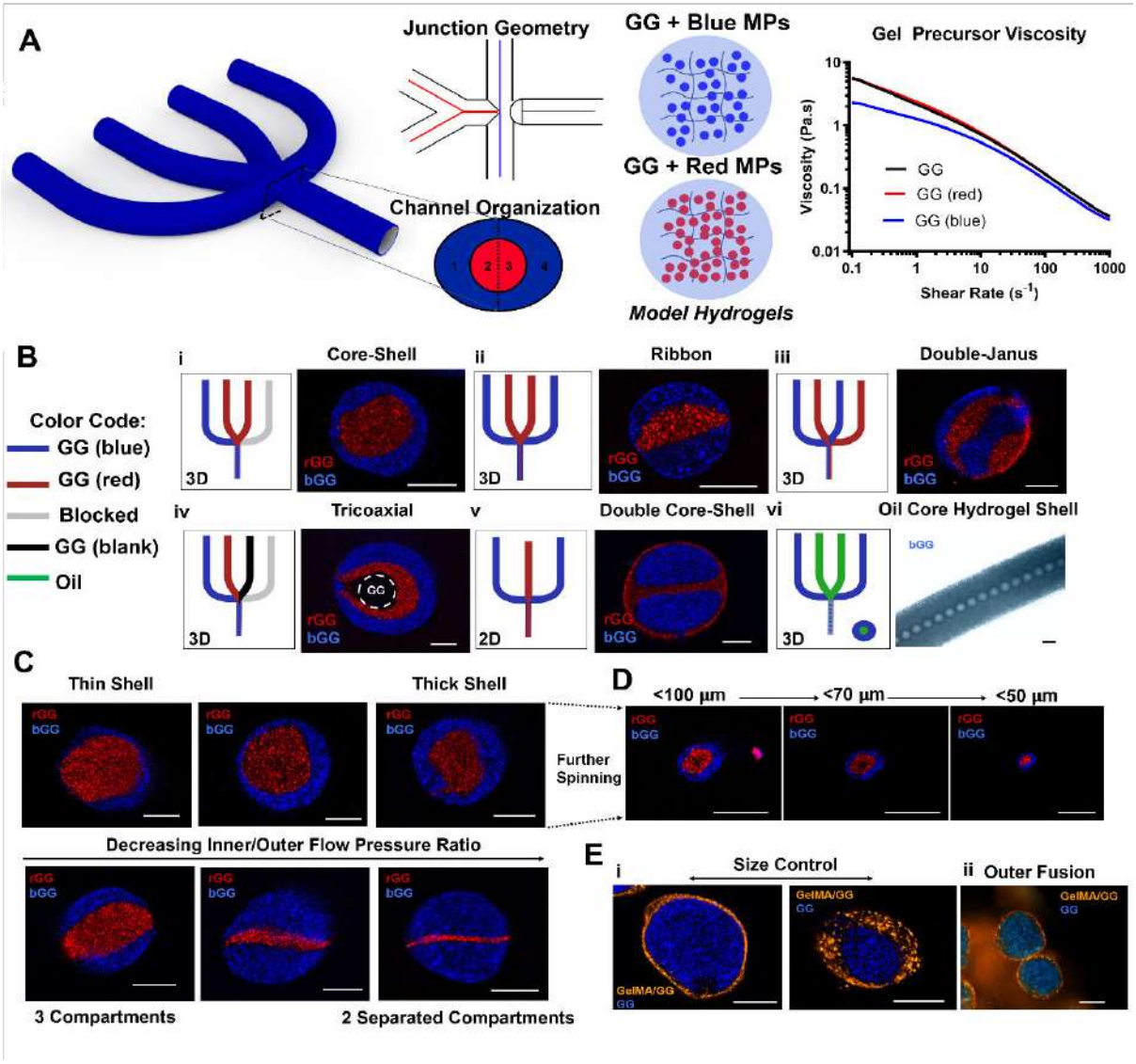


Figure VIII-1: Flow Focusing Hydrogel Microfiber Architectures. A | Schematic of 3D Flow-Focusing Chip Channel organization and junction configuration (left). Model Gellan Gum hydrogels encapsulating distinct microparticles and respective viscosity profiles (right). B | Representation of the channel configurations to employ for obtaining different hydrogel fiber shapes: Core-Shell (i), ribbon (ii), double-Janus (iii), tri-coaxial (iv), double Core-Shell (v), and Oil-Core-Hydrogel-Shell (vi). The colors represent the different solutions used, as sketched at the left of each microscope image. bGG - Gellan Gum with blue microparticles, rGG – Gellan Gum with red microparticles. C | Consequence of pressure ratios on the relative size of fiber compartments in the core-shell (top) and ribbon (bottom) shape examples. The Inner/Outer channels' pressure ratio is reduced from left to right, leading to a decrease in either core diameter or inner ribbon thickness. D | Fiber size reduction through the faster spinning of the multi-compartment fibers, which allows for maintenance of shape while significantly reducing the total diameter of fibers from 200 µm to less than 50 µm. E | Fiber shapes can also be maintained while incorporating distinct materials, as Gelatin Methacryloyl (GelMA) blended with GG (GelMA/GG, Orange), allowing for the manipulation of relative compartment

sizes (i). The ability of GelMA to crosslink through UV light also introduces the possibility of fusing the shell of two adjacent fibers as a bottom-up strategy (ii). All scale bars are 100μm.

By using three inlet channels of the chip and blocking the fourth, continuous fibers (**Video S1**) with the core-shell morphology (**Fig. VIII-1, B, i**) were obtained when the more viscous component was in the center channel and the less viscous one was flowing in the outer channel ($\frac{v_{inner}}{v_{outer}}$>1), as represented by the sketches in **Fig. VIII-1, B, i**. From here, we concluded that, when flowing similar solutions within this microfluidic configuration, there is a natural preference for the more viscous component (higher resistance to deformation) to maintain its initial position on the cross-section. In contrast, the less-viscous solution tends to squeeze around the more viscous counterpart surrounding it (**Supplementary Fig. VIII-2**). Similarly, a third material can be included in one of the center channels, yielding a tricoaxial-like shape (**Fig. VIII-1, B, iv**). Curiously, we observed that once the fourth channel was also filled with the less viscous solution, the formation of core-shell shape was no longer possible. The outer solution no longer surrounded the center one but instead pressed it, obtaining a flat, ribbon-like structure (**Fig. VIII-1, B, ii**). Similarly, the materials were alternated within the 4-channel setup, giving rise to 4 parallel compartments named double-Janus (**Fig VIII-1, B, iii**). Using similar solutions but further modulating the pressures within the different channel configurations yielded even more distinct and exotic shapes (Supplementary Fig. VIII-3, A).

To further assess continuous hydrogel FF's potential, we employed a simpler 2D FF chip where the 3D pore geometry is absent and channels meet in a T-like junction (Supplementary Fig. VIII-1). We obtained a shape that we named as double core-shell (**Fig. VIII-1B, v**). Notably, in this more straightforward configuration where the 3D pore is absent, the different viscosities' effects seem to become less relevant. The materials flow similarly, leading to the same shape even if inner/outer viscosities are reversed (**Supplementary Fig. VIII-3, B**).

Once we observed all the possibilities of flowing hydrogel precursors in these distinct configurations, we tested the introduction of an apolar solution to form confined droplets within the outer hydrogel materials. As a model, we used mineral oil and observed the formation of a core of oil droplets within the hydrogel fiber or, in other words, the oil core-hydrogel shell structure (**Fig. VIII-1, B, vi**). Researchers have recently also demonstrated the fabrication of bubble-filled hydrogel fibers by introducing air within alginate fibers using a co-axial flow system [20]. While very interesting as a fabrication approach with possibilities for the breakage of fibers into small structures, the air is not an efficient method for transporting biologically relevant components. Instead, by introducing oil droplets in

fibers, our approach facilitates the inclusion of hydrophobic features, adding a different chemical behavior to otherwise purely hydrophilic hydrogel structures.

VIII.3.2. Manipulation of Fiber Size and Composition

Once microfiber compartment shapes were explored, we investigated how varying the applied pressures could affect flow ratios and change the relative compartment dimensions and overall microfiber sizes. During the wet-spinning process, different factors contribute to the fiber shape, among which are the applied pressure and consequent flows, the dimension of the microfluidic chip output channel, and gravitational and buoyancy forces. Overall, the microfluidic channel size will dictate the global fiber diameter ranges, which can then be slightly manipulated by controlling precursor flow through inlet pressure regulation. In all cases, the formed fiber was collected at the bottom of the coagulating bath, indicating higher gravitational forces than buoyancy forces (**Supplementary Video 1**).

From here, we observed that changing the relative inner/outer pressures and consequently flows altered the distinct compartments' size. This change led to, e.g., thick/thin core/shell or considerable changes such as for the ribbon structure (from 3 individual compartments to 2 main compartments separated by a thin sheet of a third material) (**Fig VIII-1, C**). Furthermore, we were able to tune the flow conditions by applying pressure in a sinusoidal fashion (increasing or decreasing in time), showing that it is possible to obtain, e.g., a fiber with a constant diameter but a gradually increasing core-to-shell size ratio (Supplementary Fig. VIII-4).

Since the hydrogel precursors are spun into a crosslinking CaCl2 solution, it is possible to draw the fiber into the bath while crosslinking. By pulling the fiber at a higher speed than that at which it is spinning, a considerable size reduction can be achieved, leading to thinner multi-compartment hydrogel fibers. This process may influence the alignment of the hydrogel precursor's polymeric chains, which may affect the mechanical properties of the fibers. Still, drawn fibers maintain their shape even at smaller dimensions (**Fig. VIII-1, D**). With this approach, we fabricated full core-shell fibers with less than 50µm of the total diameter. This dimension represents the smallest hydrogel core-shell fiber so far fabricated, to the best of our knowledge. Most examples within the literature do not reach sizes below 200 µm [7,21]. Shao and colleagues report core-shell fibers with core dimensions approaching 75µm, but these have a shell of around 1mm [22]. Therefore, our approach can be highly relevant for biological applications as it is the first to approach the magnitude of single-cell size [23] and blood arterioles

diameter [24]. The fact these fibers are composed of soft hydrogel compartments is also relevant as these small blood vessels, and soft biological tissues have similar mechanical properties, frequently on the 5-20kPa stiffness range [18,25,26].

All the structures so far discussed were composed only of ionic-crosslinking GG, which is relevant for the biofabrication of different structures but limited as a single material option. As such, we investigated if other materials could be included without compromising fiber shape. We had observed that the concentration of GG and consequent viscosity could be changed and still lead to similar core-shell structures (Supplementary Fig. VIII-5) if the viscosity ratios were kept. With this in mind, we then blended gelatin methacryloyl (GelMA) 5% with GG 0.5% at a 1:1 ratio and still observed the formation of core-shell structures with a tunable compartment size (**Fig. VIII-1, E, i**). As the GG/GelMA blend is less viscous than the normal GG, the positive inner/outer viscosity ratio is not violated, and as described above, the requirement for core-shell shape holds. Furthermore, the possibility of GelMA to be crosslinked by UV light allowed us to imbue these fibers with two stages of crosslinking: the immediate GG ionic crosslinking upon spinning - which derives the core-shell shape - followed by the UV crosslinking of the GelMA shell component, allowing individual fibers to be fused, potentially interesting for bottom-up assembly (**Fig. VIII-1, E, ii**).

VIII.3.3. Endothelial Cell-laden Flow Focusing Core-Shell

To explore the fast fabrication of core-shell structures, we approached vascular-like fibers by encapsulating endothelial cells within a soft, biolabile [26] core supported by a more robust and more stable GG shell (**Fig. VIII-2, A**). Since a pure GG core would not be remodeled by endothelial cells, a different core material is required. Several works have shown that 3D environments of 5% GelMA can naturally promote endothelial cell proliferation and tubular-like arrangements [22,27], with an inherent FF caveat: GelMA 5% solutions have very low, water-like viscosity. Even if easily mixed with GG and used to form the fiber shell (**Fig. VIII-1, D**), placing GelMA within the core flow would violate the FF viscosity ratio (inner>outer) of the core-shell shape, voiding its fabrication.

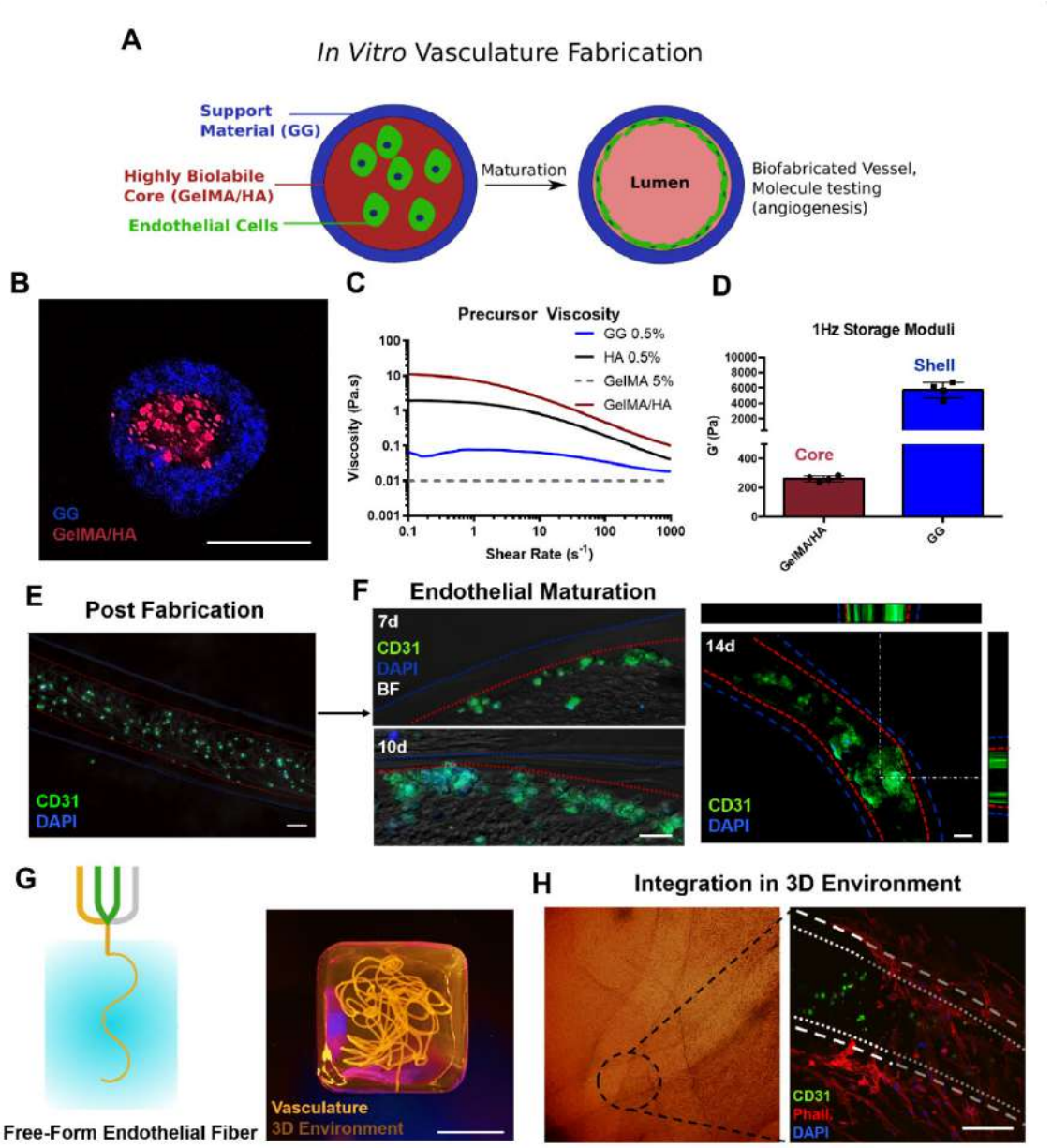


Figure VIII-2: Flow focusing Endothelial cell-laden Core-Shell Fibers. A | Rationale behind the core-shell structure in which the biolabile core allows endothelial cells' organization and maturation towards lumen-like tubularization. B | Core-Shell fibers with a non-ionic crosslinking, biolabile core (GelMA/HA, light red) within the GG shell (blue). Scale bar: 200μm. C | Viscosity profiles of the different materials involved. D | Bulk mechanical characterization of both core and shell hydrogels, evidencing the full order of magnitude of difference between core and shell material's shear moduli. E | Immunocytochemistry of CD31 positive human dermal microvascular endothelial cells (hDMECs, green) within the fibers' core, post-fabrication. Scale bar: 100μm. F | With culture time, endothelial cells are mostly present at the core/shell interface, gradually accumulating in that region. Upon 14 days of culture, certain fiber regions become more populated with endothelial cells surrounding a hollow core region, as shown on the right. Scale bars: 100μm. G | Rationale behind the manipulation of the free-form core-shell fibers and inclusion in a 3D hydrogel environment. Scale bar: 5mm H | Endothelial cell-laden core-shell networks within a

collagen matrix populated with human dermal fibroblasts upon three days of culture (left - brightfield image, right - fluorescence image). Fibroblasts (Rhodamine-phalloidin, red) populate the collagen mesh and gradually surround the endothelial cell-laden core-shell network. Scale bar: 200μm.

To overcome this, we blended GelMA5% in a solution of hyaluronic acid (HA) 0.5%, which allowed us to increase the viscosity of GelMA to overcome that of GG (**Fig. VIII-2, C**) and thus lead to the formation of GelMA/HA Core – GG Shell fibers (**Fig. VIII-2, B, D,** Supplementary Fig. VIII-6). Human dermal microvascular endothelial cells (hDMECs) were encapsulated within this core, remaining viable post-fabrication (**Fig. VIII-2, E,** Supplementary Fig. VIII-7). Upon cell culture, it was possible to observe the gradual migration of endothelial cells to the core/shell interface and some organization around an empty lumen, from 7 to 14 days (**Fig. VIII-2, F**). These structures were visible in some regions of the fibers on the later time points of 14 days, the frequently reported length of time to achieve such responses of endothelial tubularization [21]. However, further optimization might be required to obtain fully tubularized endothelial structures, which is the final need for a functional vascular network. We believe there is still a gap to close in finding optimal levels of cell density, material softness, and degradability to achieve continuously uniform tubularization. Researchers recently approached tubular-like channel perfusion by using cell densities one order of magnitude above the ones here tested, hinting at the importance of that parameter for efficient vascularization [28]. As a different example, the rolling of cellular layers was also recently shown to allow the fabrication of perfectly tubular endothelial structures [29]. However, these are small cellular cylinders that are still far from the vascular dimensions needed for tissue engineering applications.

In our case, these endothelial cell-laden core-shell fibers can be spun to considerable lengths and remain free in culture. We tested the integration of fibers within a 3D environment with different cell types to explore this advantage, mimicking a natural 3D vascular network (**Fig. VIII-2, G**). The core-shell endothelial cells-laden fibers were placed within a 3D collagen matrix with encapsulated fibroblasts, co-cultured for three days, forming a complex collagen-fibroblast 3D mesh surrounding the endothelial cell-laden core-shell network (**Fig. VIII-2, H**, Supplementary Video VIII-2). The potential for fabricating considerable lengths of these vascular-like fibers and their simple integration within 3D scenarios shows explicit value in such an approach, with further focus being needed for continuous and uniform endothelial tubularization. From there, it is also essential to consider that the material in the fiber lumen must degrade towards a hollow, perfusable structure. Using GelMA/HA blends, the precursor viscosity can be increased but still result in a soft, degradable core, which can then degrade with culture time and endothelial maturation [22]. A specific flow setup can then be engineered to connect

the vascular fibers to the flowing medium, which aids in removing degraded core material and its conversion to an empty, perfusable lumen.

VIII.3.4. Melanoma-on-a-ribbon shaped fiber

Once the ribbon-like fibers with two different compartments separated by a third material were observed, we explored the possibility of fabricating cancer models where one compartment could be used to encapsulate cancer cells and another to include stromal ones, separated by a basement membrane-like ribbon (**Fig. VIII-3, A**). To focus on cancer cells' behavior and potentially screen the effect of drugs within the model, we used an adhesive and degradable matrix for the cancer cell compartment and a more inert, non-biodegradable material for stromal cell encapsulation. Moreover, we hypothesized that the separating material could be one that would mimic the native Basement Membrane (BM), which naturally bridges epithelial from stromal tissue compartments and is considered the first barrier for cancer cells entering metastasis [30]. As the recapitulation of such a scenario would be of high value for modeling cancer cell invasion and *in vitro* testing of many sorts, we first demonstrated the use of a growth-factor reduced BM analog (GelTrex) and its placement between two GG compartments following an approach similar to the one used for core-shell structures (HA blending) but with the ribbon configuration (**Fig. VIII-3, B**). From here, we increased the complexity of these structures by fabricating tri-material fibers, using a GG/GelMA 1:1 blend as the cancer compartment material, GelTrex/HA as the basement membrane, and GG alone as the stromal environment. The simplicity of our setup and fast processing times (one second inside the chip) allowed us to successfully manipulate the different materials at distinct temperatures and obtain the desired structures, with the further possibility of changing compartment size, namely BM thickness (**Fig. VIII-3, C,** Supplementary Fig. VIII-8, A, B).

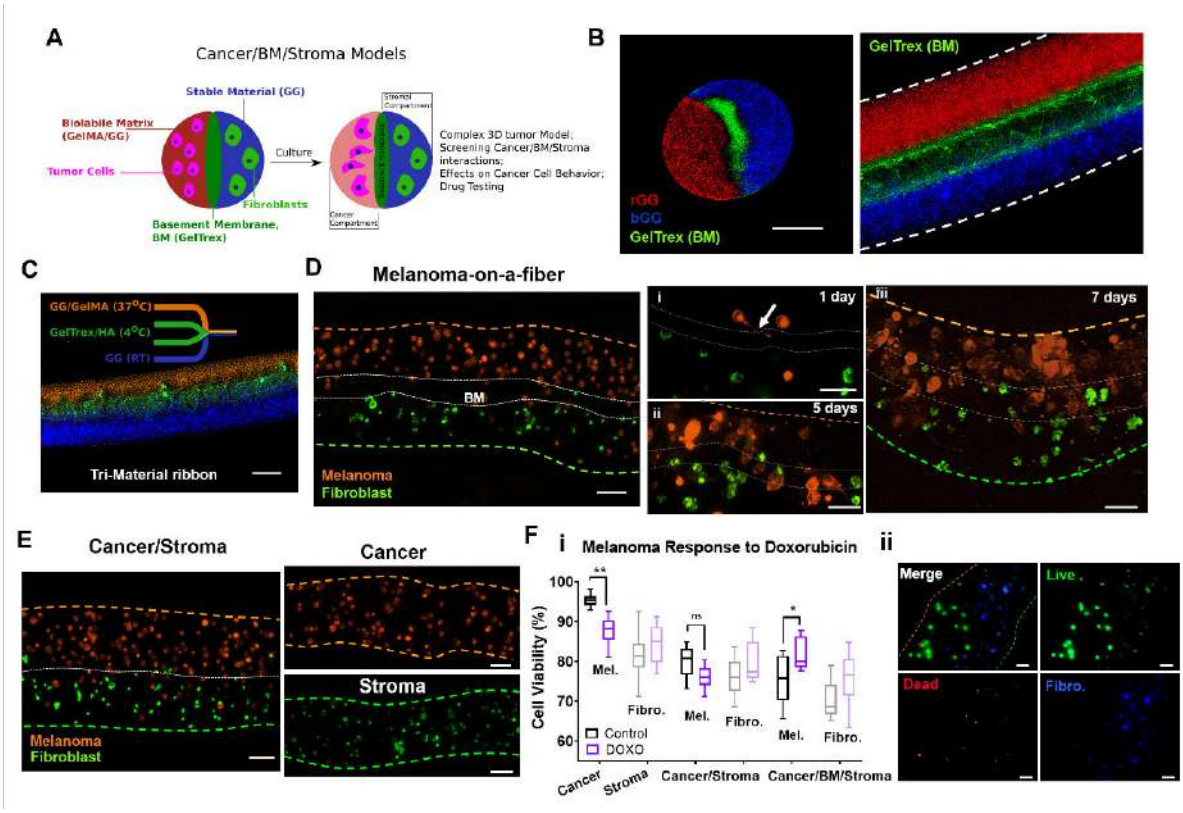


Figure VIII-3: Flow focusing Ribbon Cancer/BM/Stroma Fibers. A | Rationale behind the use of ribbon fibers for modeling cancer/BM/stroma *in vitro*. B | inclusion of a BM-like material (GelTrex/HA, Green) in between the outer GG compartments, axial (left, fiber cut cropped into an entirely black background), and longitudinal (right) views. Scale bars: 200μm. C | Fabrication of tri-material ribbon fibers, highlighting the material and the respective temperature used in each channel (drawing). Scale bars: 200μm. D | Melanoma-on-a-fiber model obtained by encapsulating SK-MEL-28 cells in the cancer compartment (orange) and human dermal fibroblasts (hDFs) in the stromal compartment (green). Scale bar: 100μm. After one day of culture, it was possible to observe melanoma cells protruding into the BM compartment (space between white-spotted lines) towards stromal cells (i, scale bar 50μm). This behavior was even more evident after five days (ii, scale bar 50μm) and seven days (iii), when cancer cells invaded the stroma interface. E | Modular deconstruction of fiber compartments by altering the materials/cells flowing towards simpler cancer/stroma fibers (left), stroma (bottom right), or cancer (top right). Scale bars: 100μm. F | Proof of concept test of melanoma cell response to doxorubicin. Cell viability analysis (Calcein AM/Propidium Iodide Live/Dead) was combined with a cell tracker to detect each type's percentage of viable cells (ii). Scale bar: 50μm. Image analysis results for the percentage of viable cancer cells (mel.) and fibroblasts (fibro.) in each model after 24h of treatment (i). ** $p<0.01$, * $p<0.05$, ns – not significant, as derived by 2-way ANOVA followed by Sidak's multiple comparison test. No statistical significance obtained when comparing control/treatment stroma conditions.

To recapitulate cancer/BM/stroma structures, we encapsulated melanoma cells (SK-Mel-28) within the cancer compartment and human dermal fibroblasts (hDFs) within the stromal compartment, obtaining a melanoma-on-a-fiber model (**Fig. VIII-3, D**). After one day of culture, it was possible to

observe melanoma cells emitting protrusions into the BM towards the stroma (**Fig. VIII-3, D, i**). This response was even more relevant upon 5 and 7 days of culture where invasive melanoma cells can be seen going through the BM compartment and reaching the stroma (**Fig. VIII-3, D, ii, iii**). The ability to change the materials that flow on-the-fly allowed Cancer/BM/Stroma fibers to simultaneously be tested with Cancer/Stroma (no BM), Stroma-only, or Cancer-only structures (**Fig. VIII-3, E**), to observe the effect of the different arrangements in the behavior of cancer cells. Even though cells are initially encapsulated within the same matrix for all cases, the number and type of fiber compartments and consequent overall cellular composition changes, and this 3D complexity affects cancer cells' response. The previously discussed cancer cell invasion was not so evident in the absence of BM and much less so when cancer cells were alone. Differences were even more apparent after seven days of culture (Supplementary Fig. VIII-8, C). These differences in cancer cells' outcome demonstrate how important it might be to approach the biological scenario not only from a biochemical point of view but also considering the distinct materials' architecture.

It has been widely shown that basement-membrane-like proteins can widely impact cancer cell invasion and migration [31]. Further pro-invasive outcomes derive from stromal fibroblasts in the vicinity of tumor cells [32–34]. Indeed, we could observe the most significant changes in cancer cell invasion when both BM and stromal cells were present. This behavior evidences both their synergistic effects and the need for adequately approaching this complexity when attempting to, e.g., test the influence of anti-cancer drugs *in vitro*.

As a proof of concept, we tested the effects of the anti-cancer drug doxorubicin on the viability of cancer and stromal cells within these fibers with distinct architectures. Doxorubicin is a long-known drug that promotes cancer cell death by interfering with DNA replication and proliferation pathways [35]. As we could observe cancer cells responding shortly after building the model, we looked to the viability of both cell types after 24h of culture. To do so, we combined a live/dead assay with fluorescent tracking of fibroblasts to quantify and derive the number of viable cells of each type after treatment (**Fig. VIII-3, F**). Curiously, after treatment with doxorubicin, different responses could be observed depending on the model's complexity. Stromal cells, encapsulated in a mostly inert matrix, did not suffer any significant change in viability. Cancer cells, on the other hand, responded to the drug. As one could expect, a significant decrease in cancer cell viability was seen on cancer-only fibers, but this response changed as the complexity of the 3D model increased. With the presence of fibroblasts, the decrease in cancer cell viability was no longer significant. Oppositely to cancer-only fibers, in the more complex model composed of stromal cells and a BM, the viability of melanoma cells treated with

doxorubicin was higher than those of non-treated cells (**Fig. VIII-3, F,** Supplementary Fig. VIII-9). As it seems, the presence of fibroblasts exerts a protective effect on the doxorubicin-induced cancer cell death, a response that has been previously observed in organotypic models of the disease [36]. Partly, this might be due to fibroblast-melanoma cell communication, which can stimulate cancer cells' pro-survival mechanisms to overcome the drug's effect [37,38].

Furthermore, additional mechanisms to overcome doxorubicin-induced cancer cell death appear to be at play once a BM-like matrix separates cancer and stroma. Even though this particular response type was not reported previously, it is well described that doxorubicin's effects are intimately related to cell motility and adhesion [39]. This drug's impact might be diminished when cancer cells can migrate through the extracellular matrix (ECM)-like gels versus standard culture conditions [40]. As such, we believe that the pro-survival stimulation by fibroblasts nullifies the negative effect of the doxorubicin treatment on cancer cells. When this is combined with a highly biolabile BM-like matrix, melanoma cells can further move and proliferate with ease and effectively recover from the doxorubicin challenge. Indeed, the effects we could observe warrant further investigation on this particular response.

Nevertheless, this test demonstrates that our novel melanoma-on-a-fiber platform can integrate several of the previously reported intricacies on cancer cell responses to doxorubicin due to the novel combination of 3D environments, multi-compartment, multi-material, and multi-cellular architectures. It also highlights how significant it might be to recapitulate the complexity of live tissues to derive the most relevant responses, as oversimplification can lead to different and eventually erroneous conclusions.

VIII.3.5. All-in-one Multi-Chemistry Tissue Engineering

As a more distinct structure, we explored the biological potential of the hydrogel fibers with an oil droplet core. The introduction of apolar solutions opens the possibility of transporting hydrophobic molecules within a highly hydrophilic hydrogel structure. The distinct polar/apolar compartments, therefore, represent a unique platform to transport cells in a 3D construct (polar hydrogel) together with pro-differentiation hydrophobic molecules within isolated depots (apolar droplets) (**Fig. VIII-4, A)**.

We initially verified that distinct pressure/flow ratios between the hydrogel sheath and the oil core allowed the fabrication of structures with oil droplets of different sizes and distribution, where hydrophobic dexamethasone could be dispersed (**Fig. VIII-4, B,** Supplementary Fig. VIII-10). Knowing these structures were possible, our priority was to confirm if cells could be encapsulated within these

fibers with oil droplets without any adverse impact on viability. Indeed, we demonstrated that the introduction of oil had no adverse effect on the viability of Bone Marrow Mesenchymal Stromal Cells (BMMSCs) for up to 7 days in culture (**Fig. VIII-4, C, D**) nor on the morphology of these cells (**Fig. VIII-4, G**), regardless of their proximity to the oil droplets. Overall, cells behaved similarly to those in hydrogel fibers without oil.

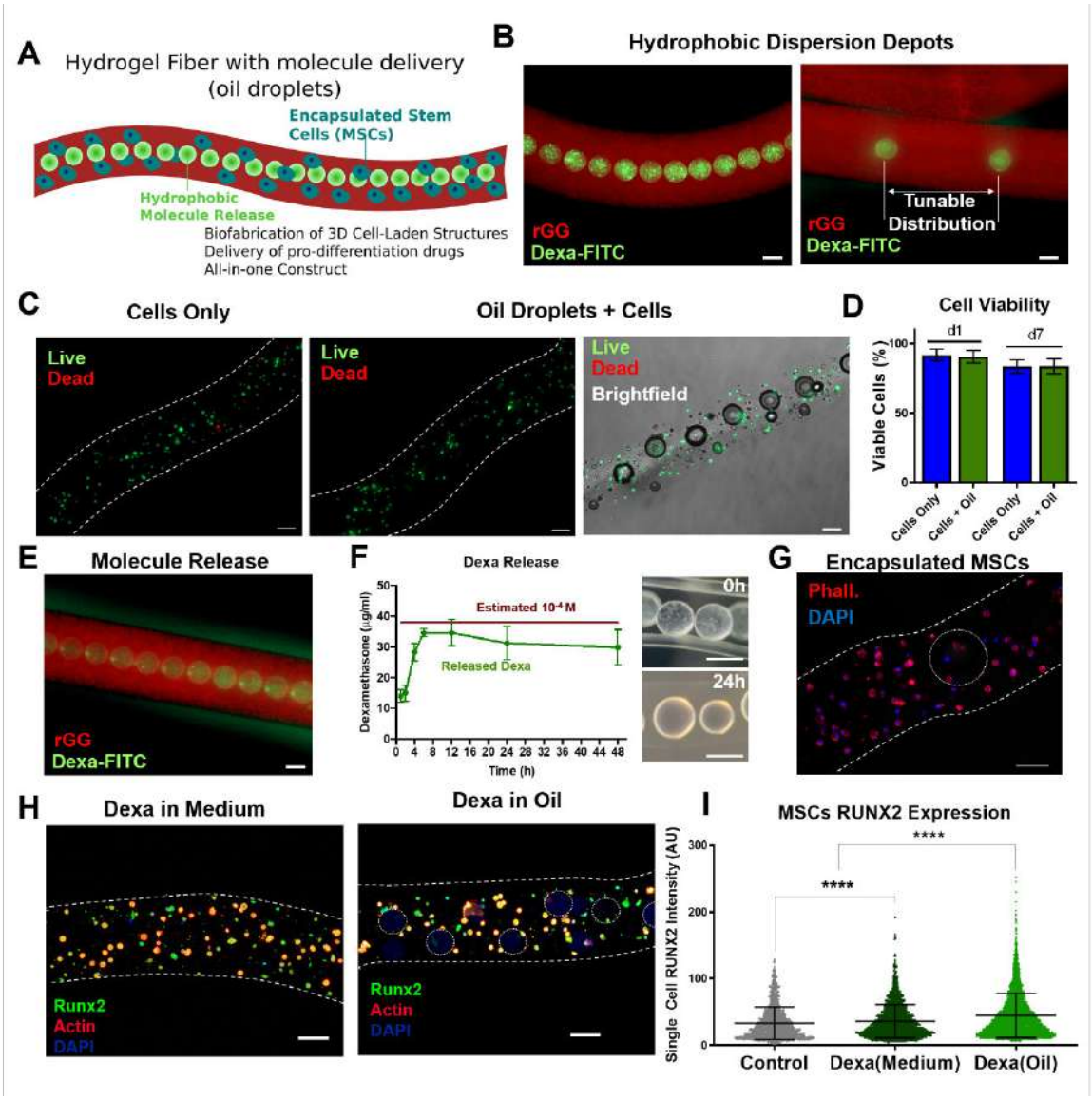


Figure VIII-4: Multi-Chemistry Biofabrication. A | Rationale behind the fabrication of hydrogel fibers of a biolabile GG/GelMA matrix (red) with oil droplets containing hydrophobic molecules (green) to stimulate encapsulated stem cells (blue). B | Fluorescent imaging of the fibers with sesame oil droplets containing Dexamethasone-FITC (Dexa-FITC). C | Assessment of BMMSC viability in the fibers with (cells + oil) and without (cells only) oil droplets. Scale bars: 100μm D| Similar viability upon live/dead quantification after one day and up to 1 week of culture. E | Release of Dexa-FITC from the fibers when these are kept in PBS (right). Scale bar: 100μm. F | Quantification of the Dexamethasone released from fibers incubated in PBS as measured (green curve) compared to the theoretical

estimation of concentration upon full release (red line represents the maximum estimated concentration). On the right, brightfield images of the oil droplets within the fibers after fabrication (0h) and upon 24h of incubation. Scale bar: 50μm. G | Encapsulated BMMSC morphology in the vicinity of an oil droplet. H | Representative immunocytochemistry images of hydrogel fibers (limited by dashed white lines) encapsulating BMSCs stained for Runx2 (Green), Actin (Red), and DNA (blue) after culture in the presence of Dexamethasone provided in the medium or released from the oil droplets (highlighted with white circles) Scale bars: 100μm. G | quantification of single-cell Runx2 signal intensity. Cells in the fibers are cultured in standard culture medium (control), the same supplemented with 10^{-6}M soluble dexamethasone (Dexa in Medium) or in the fibers with oil droplets containing dexamethasone (Dexa in Oil). **** $p<0.0001$ as derived from One-way ANOVA followed by Kruskal-Wallis multi-comparison test.

After this initial validation, we tested the hypothesis that the oil compartment could be used to transport hydrophobic molecules that could direct the differentiation of BMMSCs, replacing the use of soluble factors in the medium in an all-in-one approach (**Fig. VIII-4, A**). Dexamethasone is a synthetic corticosteroid used in stem cell differentiation protocols, frequently modified to become water-soluble and used in the cell culture medium. Alternatively, using the oil core, we could transport the unmodified molecule, observing its gradual release into the medium (**Fig. VIII-4, E**, **F**, Supplementary Fig. VIII-11). Dexamethasone was previously shown to directly impact BMMSC osteogenic differentiation by promoting Runx2 expression [41]. We compared the effect of transporting and releasing pure dexamethasone from the oil droplets in BMMSCs encapsulated in 3D GG:GelMA fibers with the impact of the drug present in the culture medium (**Fig. VIII-4, H**, Supplementary Fig. VIII-12). Based on the expression of Runx2, we demonstrate that the dexamethasone released from the oil could not just replace soluble dexamethasone but stimulate cells even more potently (**Fig. VIII-4, I**). This difference can be a consequence of two different events. First, by transporting the unmodified dexamethasone molecule, we might be looking at a different extent of cell-drug interaction than the water-soluble Dexamethasone counterpart, which is long-known to happen within organisms [42]. Second, having a gradual (within hours) release, instead of a single burst, more closely mimics the way corticosteroids are produced and see their concentrations fluctuate within the organism [43], which might also have an impact on the consequent cell responses.

Even though we have employed a simple dispersion in oil, there are more possibilities to explore in the future to tune dexamethasone release, such as binding it directly to the oil [44] or even transporting it within liposomes [45]. Using strategies such as this one may be relevant for distinct tissue engineering approaches where both stem cells and the hydrophobic molecules that drive their differentiation can be integrated within the same structure. As demonstrated, the transport of unmodified hydrophobic

molecules might potentially lead to improved differentiation outcomes. Simultaneously, these molecules are not added to the culture but transported within the same 3D construct, which might facilitate its application as an all-in-one tissue engineering approach.

VIII.4. CONCLUSIONS

We have employed a hydrodynamic 3D flow-focusing setup to fabricate hydrogel fibers with various multi-compartment shapes and organizations. Using a single chip, we show how manipulating pressure and tuning material's viscosity and different channel organizations can be employed to fabricate very different fibers, from hydrogels and hydrophobic core-shell to ribbon-like structures. We further explore how the pressure and consequent flow can manipulate the separate compartments' size and how these fibers can be drawn immediately after crosslinking, maintaining the same compartments' shapes and resulting in full diameters below 50 μm.

To prove the potential of our strategy for the biofabrication of diverse structures, we started by showing how flow-focusing can match existing systems and recapitulate structures such as the core-shell fibers. In these fibers, endothelial cells can be introduced and gradually organize overtime. Also, by forming free-floating fibers, our approach allowed us to easily incorporate these fibers within a 3D environment created by distinct materials and cell types, quickly obtaining a vascular-like network that can be cultured inside other engineered tissues.

High novelty is also presented by the fabrication of melanoma-on-a-fiber models using a triple ribbon shape to recreate Cancer/Basement Membrane/Stroma tissue organization. Within these fibers, cancer cells' invasive behavior can be recapitulated, and detailed responses to anti-cancer drugs can be analyzed instead of traditional models that are limited in representing the complexity of living tissues.

Finally, we show how hydrophobic fluids can be combined with the hydrogels by integrating a core of oil droplets within a hydrogel fiber encapsulating BMMSCs. By dispersing pure dexamethasone within the oil, we show that its release can promote the expression of Runx2 (osteogenic regulator and early marker) by the cells to a greater extent than that of soluble dexamethasone dissolved in the culture medium. This strategy represents an all-in-one tissue engineering and molecule delivering approach.

Overall, we demonstrate the potential of 3D FF to fabricate hydrogel structures with various shapes, compartments, materials, and cells. These, in turn, can be used to engineer biological-like

tissues for regeneration or for creating 3D models with high biological relevance for a wide variety of *in vitro* tests, such as vascularization responses or cancer drug testing. This broadly adaptable fabrication was possible by manipulating materials and flows with the same technique and setup, using a single microfluidic chip.

VIII.5. REFERENCES

1. Onoe, H. *et al.* Metre-long cell-laden microfibers exhibit tissue morphologies and functions. *Nat. Mater.* **12**, 584–590 (2013).
2. Kang, E. *et al.* Digitally tunable physicochemical coding of material composition and topography in continuous microfibers. *Nat. Mater.* **10**, 877–883 (2011).
3. Shin, S. J. *et al.* 'On the fly' continuous generation of alginate fibers using a microfluidic device. *Langmuir* **23**, 9104–9108 (2007).
4. Du, X., Li, Q., Wu, G. & Chen, S. Multifunctional Micro/Nanoscale Fibers Based on Microfluidic Spinning Technology. *Adv. Mater.* **1903733**, 1903733 (2019).
5. Jun, Y., Kang, E., Chae, S. & Lee, S. H. Microfluidic spinning of micro- and nano-scale fibers for tissue engineering. *Lab Chip* **14**, 2145–2160 (2014).
6. Leng, L., McAllister, A., Zhang, B., Radisic, M. & Günther, A. Mosaic hydrogels: One-step formation of multiscale soft materials. *Adv. Mater.* **24**, 3650–3658 (2012).
7. Kato-Negishi, M., Onoe, H., Ito, A. & Takeuchi, S. Rod-Shaped Neural Units for Aligned 3D Neural Network Connection. *Adv. Healthc. Mater.* **6**, 1–7 (2017).
8. Grolman, J. M., Zhang, D., Smith, A. M., Moore, J. S. & Kilian, K. A. Rapid 3D Extrusion of Synthetic Tumor Microenvironments. *Adv. Mater.* **27**, 5512–5517 (2015).
9. Cheng, Y. *et al.* Bioinspired multicompartmental microfibers from microfluidics. *Adv. Mater.* **26**, 5184–5190 (2014).
10. Xu, P. *et al.* Bioinspired Microfibers with Embedded Perfusable Helical Channels. *Adv. Mater.* **29**, 1–7 (2017).
11. Cheng, Y. *et al.* Controlled Fabrication of Bioactive Microfibers for Creating Tissue Constructs Using Microfluidic Techniques. *ACS Appl. Mater. Interfaces* **8**, 1080–1086 (2016).
12. Takeuchi, S., Garstecki, P., Weibel, D. B. & Whitesides, G. M. An axisymmetric flow-focusing microfluidic device. *Adv. Mater.* **17**, 1067–1072 (2005).
13. Chiu, Y. J. *et al.* Universally applicable three-dimensional hydrodynamic microfluidic flow focusing. *Lab Chip* **13**, 1803–1809 (2013).
14. Rhee, M. *et al.* Synthesis of size-tunable polymeric nanoparticles enabled by 3D hydrodynamic flow focusing in single-layer microchannels. *Adv. Mater.* **23**, 79–83 (2011).
15. Carneiro, J., Campos, J. B. L. M. & Miranda, J. M. High viscosity polymeric fluid droplet formation in a flow focusing microfluidic device – Experimental and numerical study. *Chem. Eng. Sci.* **195**, 442–454 (2019).
16. Carvalho, A. F., Gasperini, L., Ribeiro, R. S., Marques, A. P. & Reis, R. l. Control of osmotic pressure to improve cell viability in cell-laden tissue engineering constructs. *J. Tissue Eng. Regen. Med.* **12**, e1063–e1067 (2018).
17. Kamentsky, L. *et al.* Improved structure, function and compatibility for cellprofiler: Modular high-throughput image analysis software. *Bioinformatics* **27**, 1179–1180 (2011).
18. Guimarães, C. F. *et al.* High-throughput fabrication of cell-laden 3D biomaterial gradients. *Mater. Horiz.* **7**, 2414–2421 (2020).
19. Gasperini, L., Mano, J. F. & Reis, R. L. Natural polymers for the microencapsulation of cells. *J. R. Soc. Interface* **11**,

20140817–20140817 (2014).

20. Chaurasia, A. S. & Sajjadi, S. Transformable bubble-filled alginate microfibers via vertical microfluidics. *Lab Chip* **19**, 851–863 (2019).

21. Pi, Q. *et al.* Digitally Tunable Microfluidic Bioprinting of Multilayered Cannular Tissues. *Adv. Mater.* **1706913**, 1706913 (2018).

22. Shao, L. *et al.* Fiber-Based Mini Tissue with Morphology-Controllable GelMA Microfibers. *Small* **14**, 1–8 (2018).

23. Charras, G. T. & Horton, M. A. Single cell mechanotransduction and its modulation analyzed by atomic force microscope indentation. *Biophys. J.* **82**, 2970–2981 (2002).

24. Peppiatt, C. M., Howarth, C., Mobbs, P. & Attwell, D. Bidirectional control of CNS capillary diameter by pericytes. *Nature* **443**, 700–704 (2006).

25. Muller-Delp, J. *et al.* Effects of aging on vasoconstrictor and mechanical properties of rat skeletal muscle arterioles. *Am. J. Physiol. - Hear. Circ. Physiol.* **282**, 1843–1854 (2002).

26. Guimarães, C. F., Gasperini, L., Marques, A. P. & Reis, R. L. The stiffness of living tissues and its implications for tissue engineering. *Nat. Rev. Mater.* **5**, 351–370 (2020).

27. Nichol, J. W. *et al.* Cell-laden microengineered gelatin methacrylate hydrogels. *Biomaterials* **31**, 5536–5544 (2010).

28. Maharjan, S. *et al.* Article Symbiotic Photosynthetic Oxygenation within 3D-Bioprinted Vascularized Tissues Symbiotic Photosynthetic Oxygenation within 3D-Bioprinted Vascularized Tissues. *Matter* 1–24 (2020). doi:10.1016/j.matt.2020.10.022

29. Jin, Q. *et al.* Biomimetic human small muscular pulmonary arteries. *Sci. Adv.* **6**, (2020).

30. Sherwood, D. R. Cell invasion through basement membranes: an anchor of understanding. *Trends Cell Biol.* **16**, 250–256 (2006).

31. Benton, G., Kleinman, H. K., George, J. & Arnaoutova, I. Multiple uses of basement membrane-like matrix (BME/Matrigel) in vitro and in vivo with cancer cells. *Int. J. Cancer* **128**, 1751–1757 (2011).

32. Erdogan, B. *et al.* Cancer-associated fibroblasts promote directional cancer cell migration by aligning fibronectin. *J. Cell Biol.* **216**, 3799–3816 (2017).

33. Luga, V. *et al.* Exosomes mediate stromal mobilization of autocrine Wnt-PCP signaling in breast cancer cell migration. *Cell* **151**, 1542–1556 (2012).

34. Glentis, A. *et al.* Cancer-associated fibroblasts induce metalloprotease-independent cancer cell invasion of the basement membrane. *Nat. Commun.* **8**, 1–13 (2017).

35. Thorn, C. F. *et al.* Doxorubicin pathways: pharmacodynamics and adverse effects. *Pharmacogenet. Genomics* **21**, 440–446 (2011).

36. Tiago, M. *et al.* Fibroblasts protect melanoma cells from the cytotoxic effects of doxorubicin. *Tissue Eng. - Part A* **20**, 2412–2421 (2014).

37. Flach, E. H., Rebecca, V. W., Herlyn, M., Smalley, K. S. M. & Anderson, A. R. A. Fibroblasts contribute to melanoma tumor growth and drug resistance. *Mol. Pharm.* **8**, 2039–2049 (2011).

38. Li, G. *et al.* Function and regulation of melanoma-stromal fibroblast interactions: When seeds meet soil. *Oncogene* **22**, 3162–3171 (2003).

39. Repesh, L. A. *et al.* Adriamycin-induced inhibition of melanoma cell invasion is correlated with decreases in tumor cell motility and increases in focal contact formation. *Clin. Exp. Metastasis* **11**, 91–102 (1993).

40. Harisi, R. *et al.* Antiproliferative and antimigratory effects of doxorubicin in human osteosarcoma cells exposed to extracellular matrix. *Anticancer Res.* **25**, 805–813 (2005).

41. Langenbach, F. & Handschel, J. Effects of dexamethasone, ascorbic acid and β-glycerophosphate on the osteogenic differentiation of stem cells in vitro. *Stem Cell Res. Ther.* **4**, 1 (2013).

42. Siegal, T., Siegal, T., Shohami, E. & Shapira, Y. Comparison of soluble dexamethasone sodium phosphate with free dexamethasone and indomethacin in treatment of experimental neoplastic spinal cord compression. *Spine* **13**,

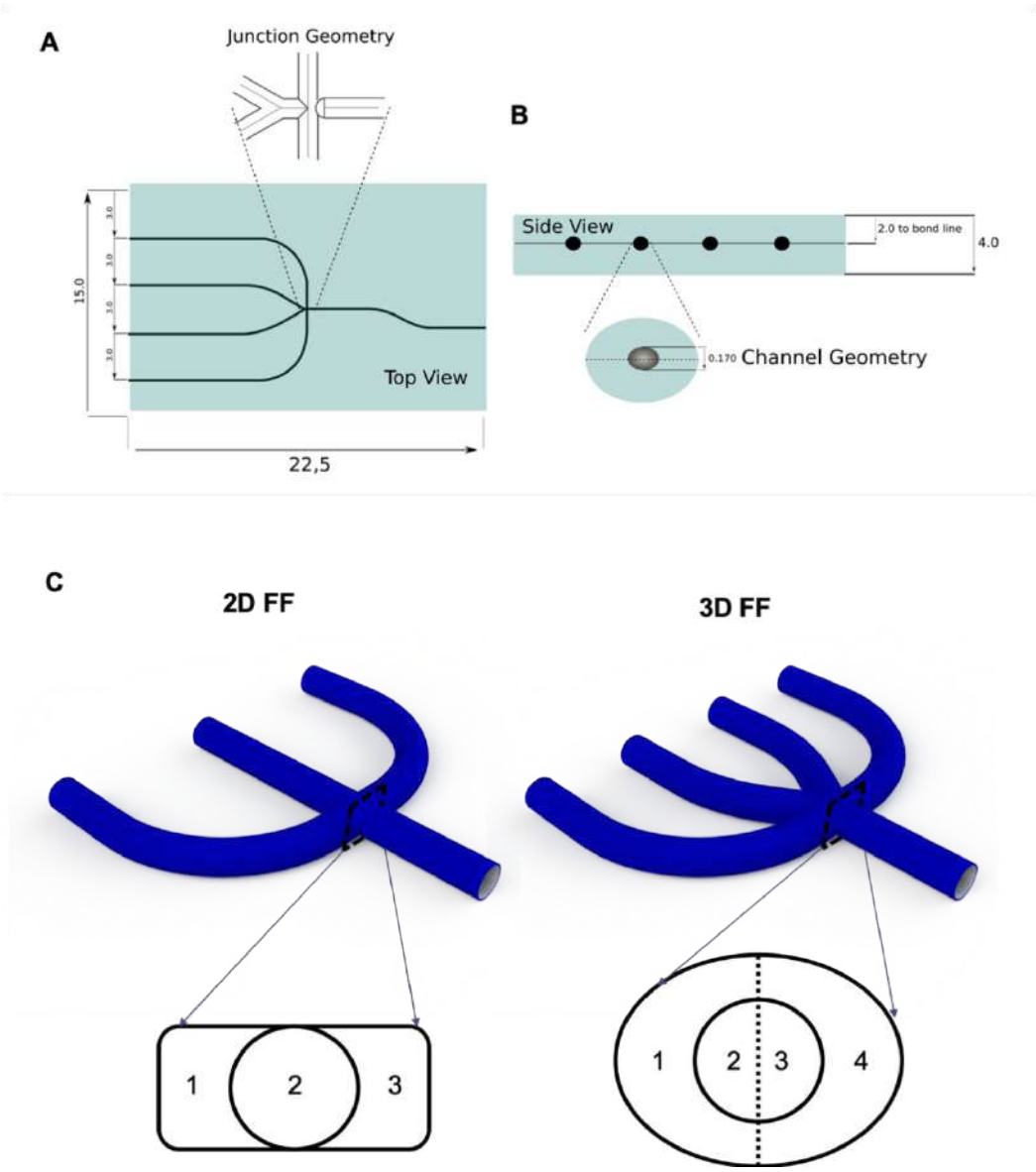
1171–1176 (1988).

43. Schimmer, B. P. & Funder, J. W. Chapter 42. ACTH, Adrenal Steroids, and Pharmacology of the Adrenal Cortex. *Goodman Gilman's Pharmacol. Basis Ther. 12e* (2011).

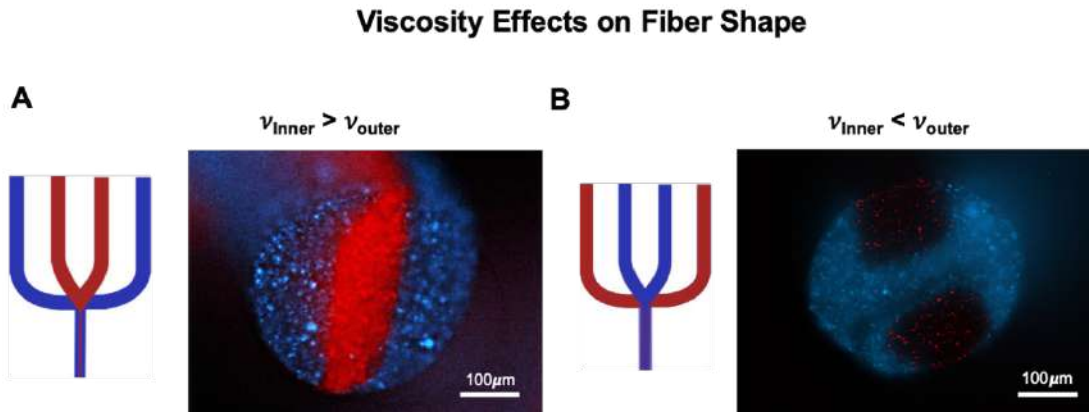
44. Liu, Z. *et al.* Cross-linked vegetable oil with covalently loaded dexamethasone: Linear drug release for osteogenic induction of hBMSCs in vitro. *Soft Matter* **9**, 5609–5615 (2013).

45. Monteiro, N. *et al.* On the use of dexamethasone-loaded liposomes to induce the osteogenic differentiation of human mesenchymal stem cells. *J. Tissue Eng. Regen. Med.* (2015). doi:10.1002/term.1817

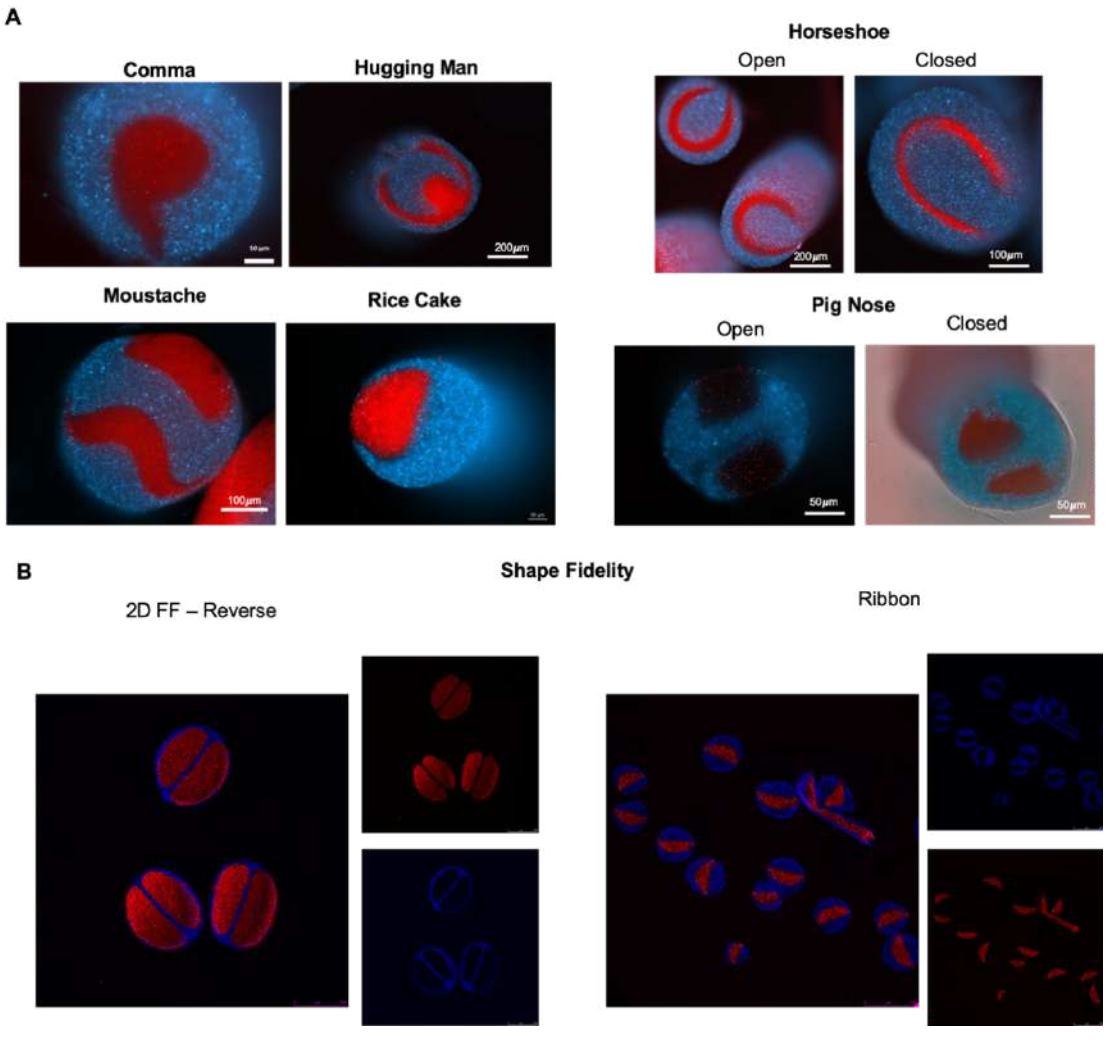
VIII.6. SUPPLEMENTARY MATERIAL:



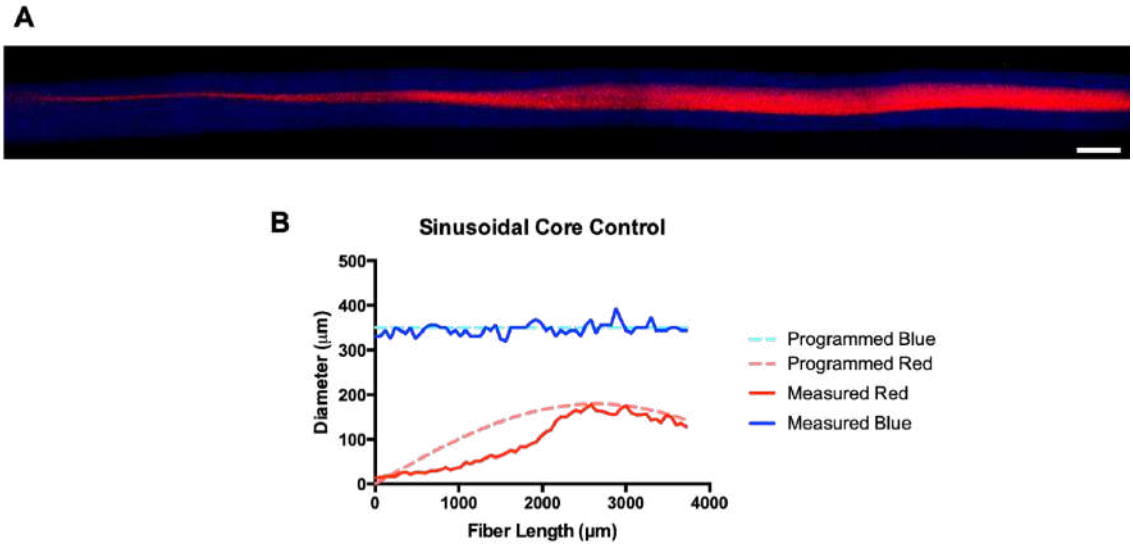
Supplementary Figure VIII-1: Detailed dimensions of the 3D Flow Focusing Chip used in this work in the top (A) and side (B) view. All represented dimensions are in mm. C - Schematics on the differences between the 2D and 3D FF chips, namely junction architecture (in black).



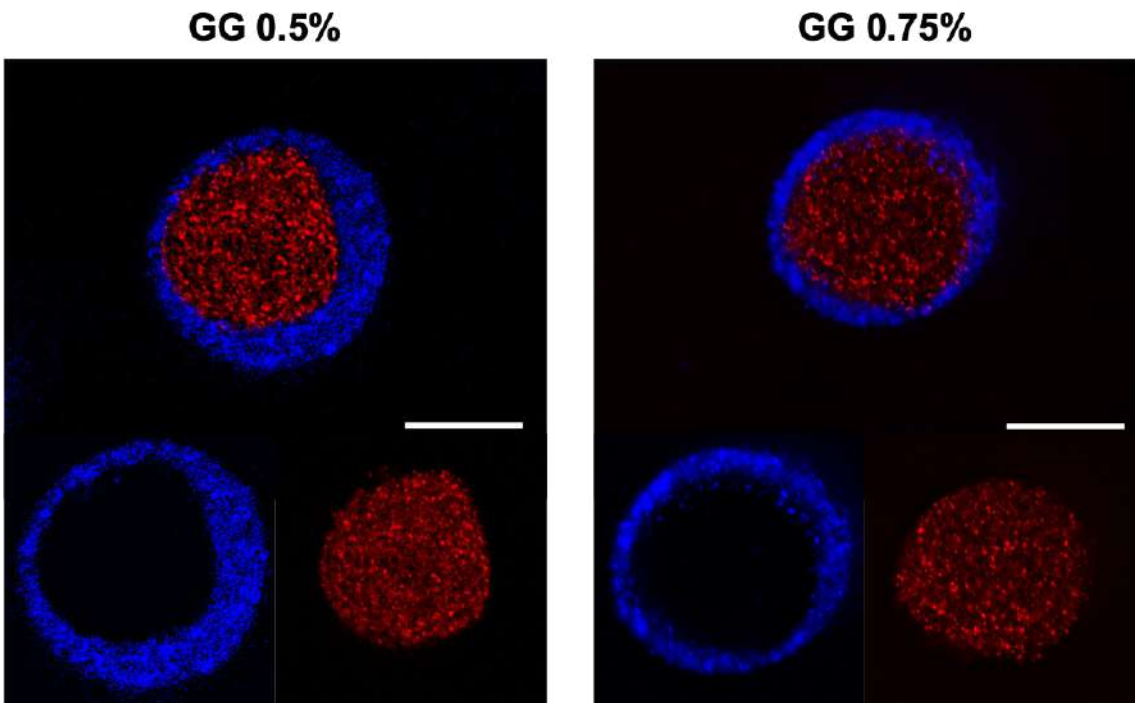
Supplementary Figure VIII-2: Outcomes of solution's viscosity differences in the fiber architecture. When the more viscous red-GG flows in the inner channels, the ribbon can be obtained as the less viscous blue-GG aligns on the side of the inner material (A). Reversing the materials and therefore also the viscosities leads to the loss of the ribbon shape, as the inner less viscous material tends to squeeze around the outer, more viscous counterpart (B). Blue – GG with blue particles (bGG), Red – GG with red particles (rGG).



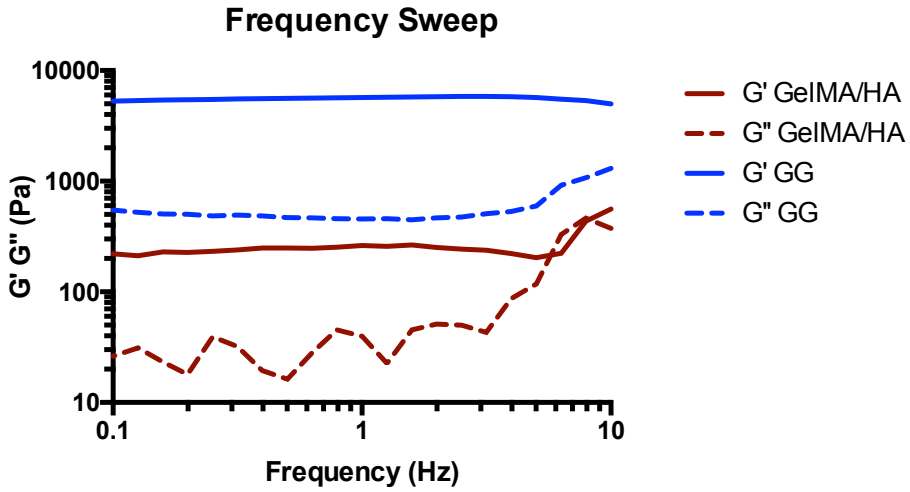
Supplementary Figure VIII-3: Shape variety and fidelity. Fibers with further compartment shapes can be obtained by manipulating the hydrogels at extreme flows which leads to bending of compartments as well as leaking inner-to-outer materials (A). Regardless of the targeted shape, several fibers can be continuously spun and retain their shape throughout the full length, as observed on the multiple axial cuts in distinct locations along the fiber (B). 2D FF – Reverse refers to the fibers fabricated with the 2D Flow Focusing chip (S1 C) with reverse viscosities in comparison to the shape present in the main text (yet still maintaining the same architecture).



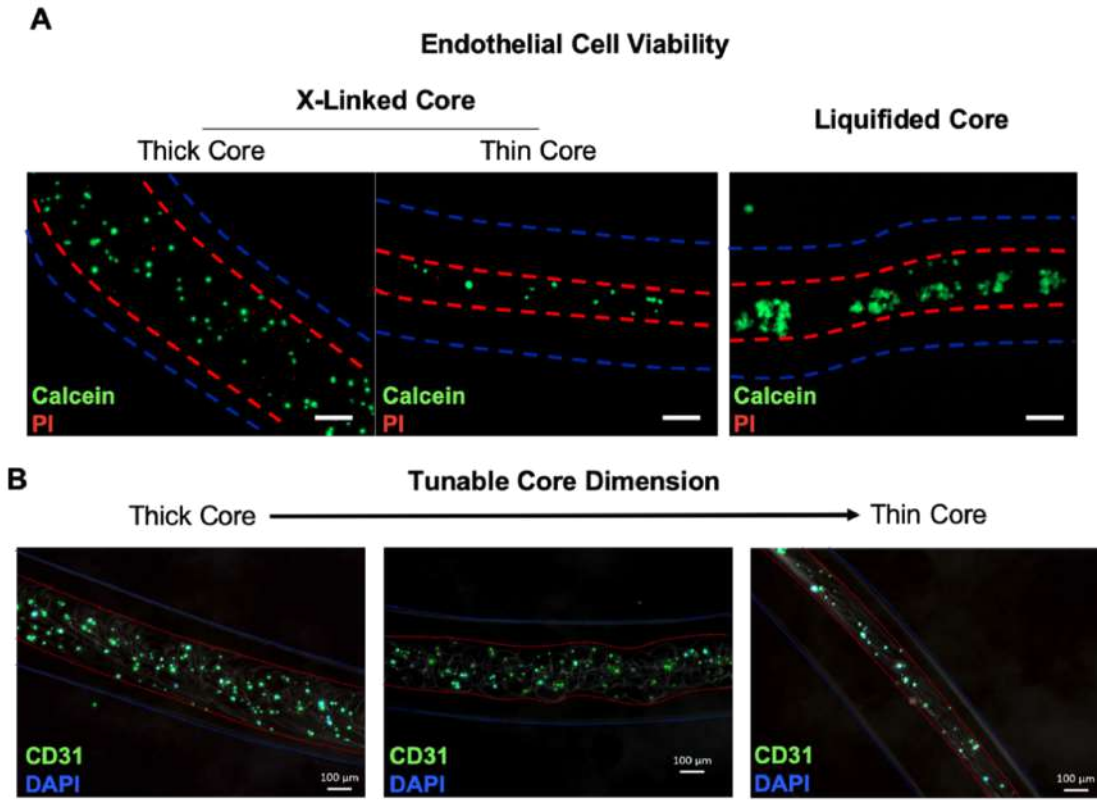
Supplementary Figure VIII-4: By applying pressure according to a time-changing function (e.g. sinusoidal), it is possible to change the dimension of the compartments along the fiber (A). In this example, a constant shell diameter (from center) was maintained, and the pressure applied to the core flow in a sinusoidal fashion led to gradually increasing core diameters (from center) along the fiber (B). Experimentally measured diameters were compared to programmed (estimated) ones showing that it is possible to translate input functions to the final structure. Scale bar: 200µm.



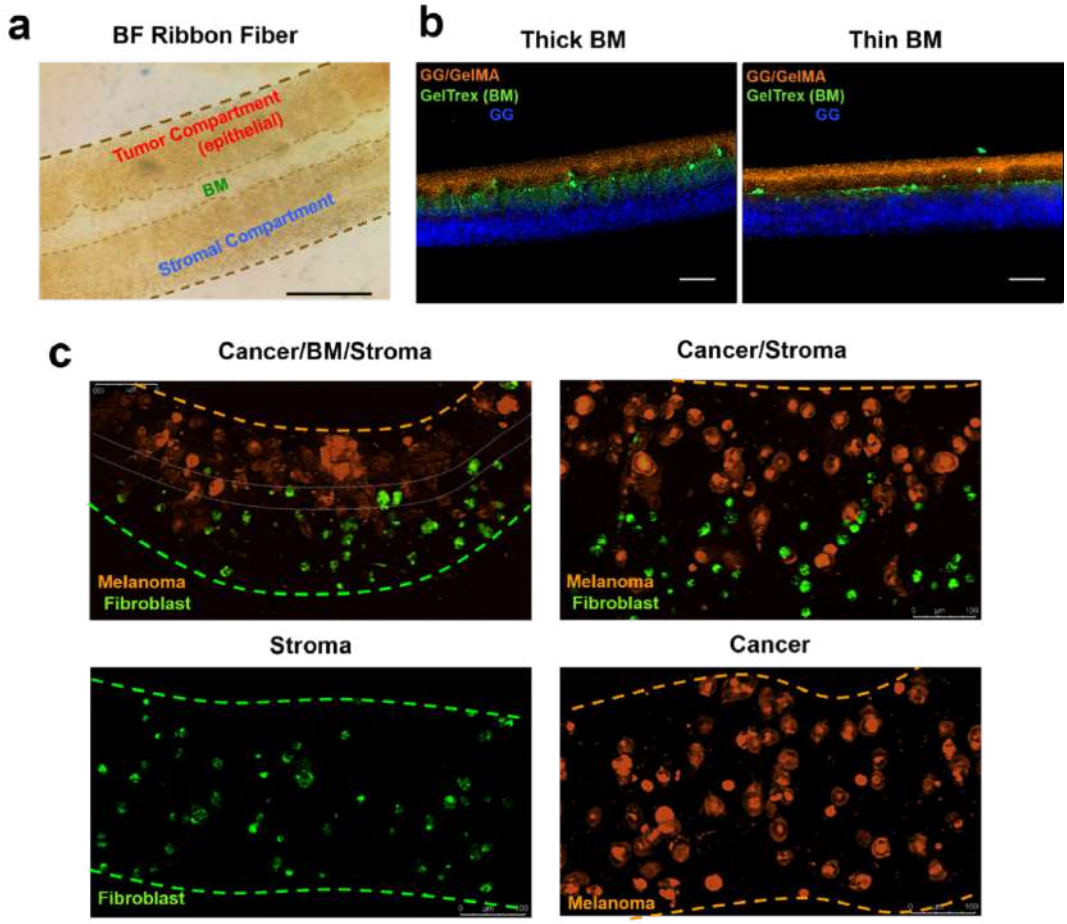
Supplementary Figure VIII-5: Comparison between fibers formed using GG solutions at different concentrations (consequently affecting viscosity and mechanics) showing that the same shape can be obtained, as long as the inner/outer viscosity ratio is maintained, adapting the pressure to the viscosity of the distinct solutions (150-200mbar range for 0.5% GG *versus* 600-800 mbar range for 0.75% GG). Scale bar: 100µm.



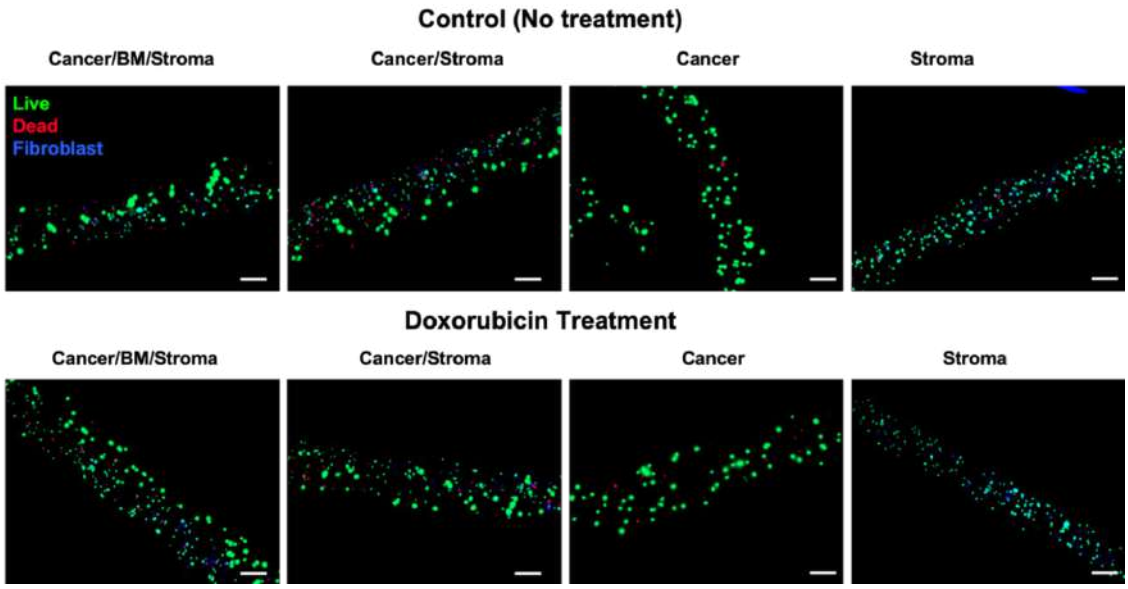
Supplementary Figure VIII-6: Rheological Characterization of core/shell fiber materials. Oscillation characterization of both core and shell hydrogel materials, showing that the core hydrogel (G' 200Pa) is much softer than the GG shell material (G' 5 kPa). Applied strain of 0.1% within the linear viscoelastic region.



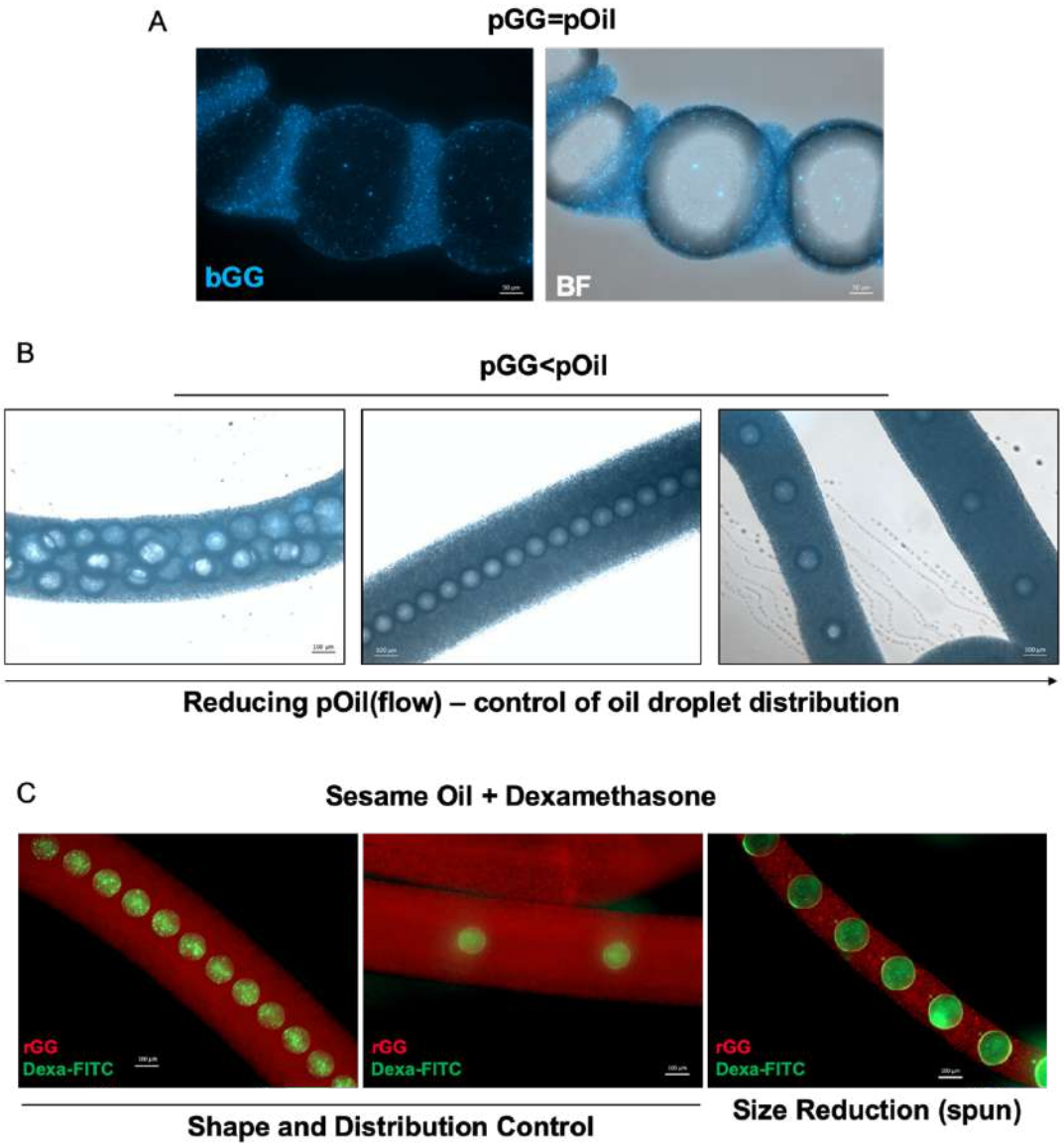
Supplementary Figure VIII-7: Core-Shell Endothelial cell-laden Fibers. A - Staining of viable (Calcein AM, green) and dead (PI, red) endothelial cells encapsulated in the fiber GelMA/HA core showing that the fabrication of this structure does not cause harm. Cells are viable 1 day post fabrication either when the core is crosslinked with UV light (X-linked core) or left liquified. When the core is liquified, endothelial cells quickly begin to form aggregates. Scale bars: 100µm. B – Core thickness can still be manipulated which might lead to the formation of distinct lumen sizes.



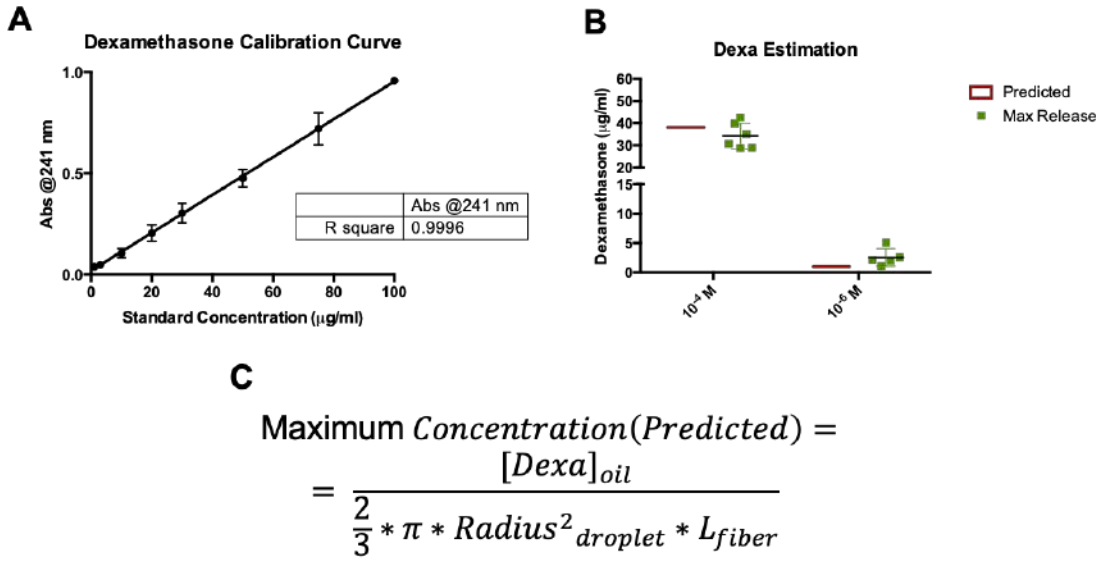
Supplementary Figure VIII-8: Brightfield (a) and Fluorescent (b) images of cancer/BM/stroma fibers, evidencing the possibility to change BM thickness by altering central channer flows. d| Representative details of the behavior of melanoma cells within the modular cancer/BM/stroma fibers upon 7 days of culture. The invasive aspect of cancer cells is more evident in the full model (gray lines highlight an approximate location of the BM which was at this stage overrun by cancer cells). This behavior seems reduced in the absence of basement membrane (cancer/stroma) and not observable in the cancer-only fibers), showing a clear impact of model complexity in cancer cell behavior.



Supplementary Figure VIII-9: Representative Live/Dead fluorescent images of melanoma/stroma cells as used for the quantification presented in the main text. Fibroblasts are tagged with blue tracker together with the Calcein/PI. All the fibers are represented in both control (no treatment) conditions and when treated with the anti-cancer drug doxorubicin dissolved in the culture medium at 10^{-6} M. Scale bars: 100µm. Green: Calcein AM, Red: Propidium Iodide, Blue: Blue Cell Tracker (Fibroblasts).



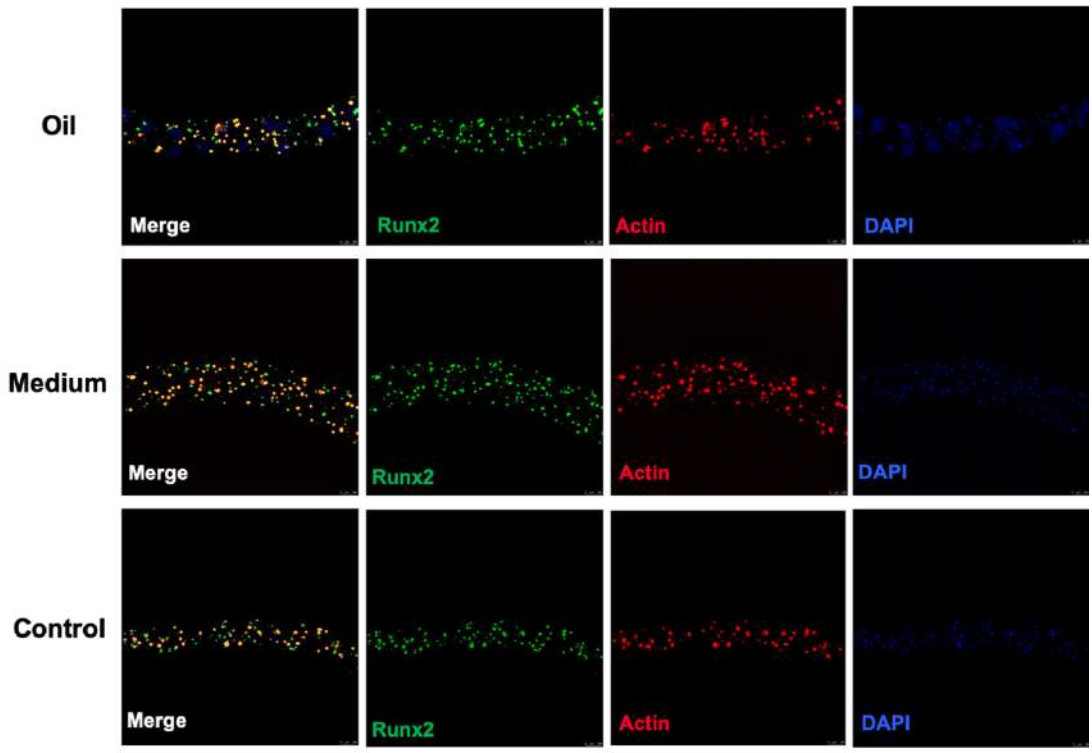
Supplementary Figure VIII-10: Size and distribution manipulation of oil-core hydrogel-shell fibers. A – By flowing oil at a similar pressure to that of GG, large oil droplets can be formed encapsulated by a thin layer of hydrogel. B – Gradually reducing the pressure of oil flow leads to a decrease in oil droplet diameter and distribution along the fiber. C – Similar results can be obtained using the Dexamethasone-FITC dispersion in sesame oil, where a continuous or discrete distribution can be approached (left and middle). Also, in these fibers, the possibility of further spinning upon crosslinking leads to a significant decrease in diameter where the whole fiber structure acquires the diameter of the oil droplets (right).



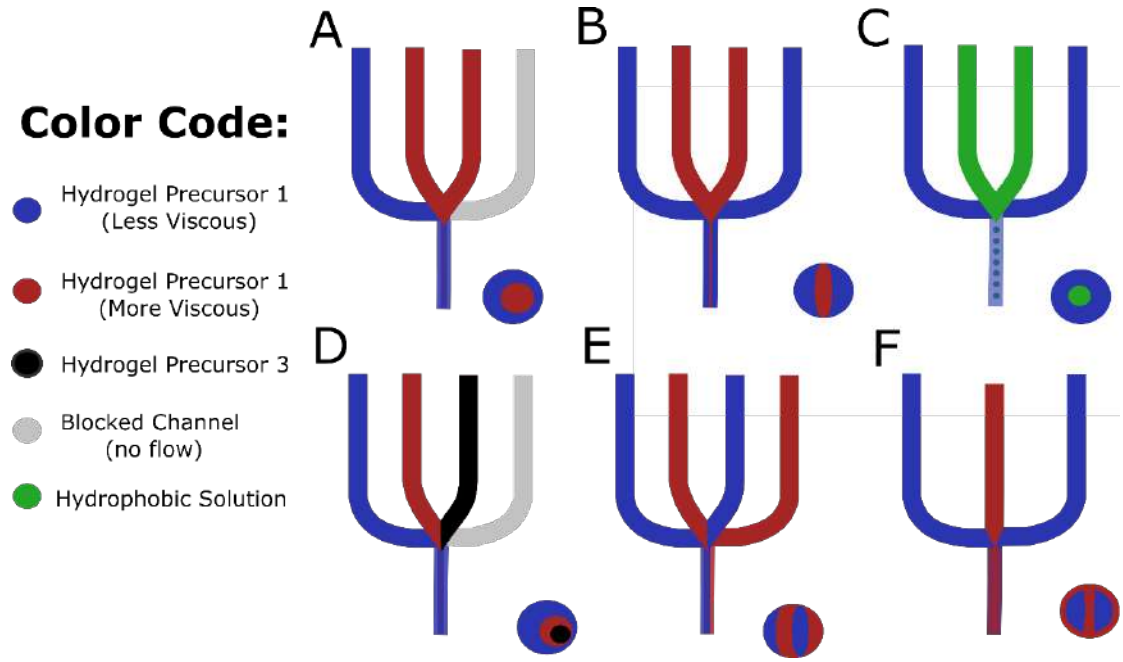
C

$$\text{Maximum } Concentration(Predicted) = = \frac{[Dexa]_{oil}}{\frac{2}{3} * \pi * Radius^2{}_{droplet} * L_{fiber}}$$

Supplementary Figure VIII-11: Dexamethasone Quantification Data. A – Establishment of a calibration curve of standard Dexamethasone solutions by means of reading absorbance at 241 nm. B – Comparison of the maximum concentration of dexamethasone released from fibers in PBS after 12h of incubation *versus* the mathematical estimation considering full release and the different fiber parameters (C). It is possible to observe that the estimation approaches the experimentally obtained concentration at distinct magnitudes (10^{-4}M as the concentration used to obtain the release profile and 10^{-6}M as used for the differentiation of BMSCs).



Supplementary Figure VIII-12: Representative fluorescent images of BMSCs within the GG/GelMA fibers after 72h of culture in standard medium without (Control) and with soluble Dexamethasone (Medium) or in the fibers with oil droplets containing Dexamethasone (Oil).



Supplementary Figure VIII-13: General Diagram of Chip Configurations, Precursor Characteristics and Consequent Fiber Architectures. A) Core-Shell Shape, B) Ribbon Shape, C) Oil-core-Hydrogel-Shell Shape, D) Tri-Coaxial Shape, E) Double Janus, F) Double Core-Shell (2D Flow-Focusing). On the left, a color code identifies

the different solutions studied. At the right of each flow configuration, a schematic of the axial fiber structure is represented.

Supplementary Table VIII-1: Pressure Working Ranges for the fabrication of reported shapes.

Shape	Chip Configuration	Inner Pressure (mbar)	Outer Pressure (mbar)	Pressure (Flow) Limits	Viscosity Limits (relative)
Core-Shell	3D FF, 1 outer channel blocked	**100-150**	**150**	Outer>=Inner, 180 outer 150 inner - upper limit at which core-shell still forms.	Inner > Outer
Ribbon	3D FF	**300-600**	**600**	Outer>=Inner, Varying Changes relative diameters	None. More Stable flows if Inner > Outer.
Oil-Core	3D FF	**100-300**	**300**	Outer >= Inner, Varying changes the size and concentration of oil droplets.	None.
Tri-axial	3D FF, 1 outer channel blocked	**100-150**	**150**	Same as Core-Shell but distinct materials on the inner 2 channels	Inner > Outer Core > 2nd Layer
Double Janus	3D FF	**300-600**	**600**	Same as Ribbon but alternating the materials on the channels	None.
Double Core-Shell	FF (2D)	**400-800 (red inside)** **400-500 (blue inside)**	**400-800 (red inside)** **400-500 (blue inside)**	Overall the shape is maintained across different flows. Changing ratios will affect the thicknesses.	None.

Chapter IX

ENGINEERING POLYSACCHARIDE-BASED HYDROGEL PHOTONIC CONSTRUCTS: FROM MULTI-SCALE DETECTION TO THE BIOFABRICATION OF LIVING OPTICAL FIBERS

ENGINEERING POLYSACCHARIDE-BASED HYDROGEL PHOTONIC CONSTRCUTS: FROM MULTI-SCALE DETECTION TO THE BIOFABRICATION OF LIVING OPTICAL FIBERS

Abstract

Solid-state optics has been the pillar of modern digital age. Integrating soft hydrogel materials with micro/nanooptics could expand the horizons of photonics for bioengineering. Here, wet-spun multilayer hydrogel fibers are engineered through ionic-crosslinked natural polysaccharides that serve as multifunctional platforms. The resulting flexible hydrogel structure and reversible crosslinking provide tunable design properties such as adjustable refractive index and fusion splicing. Modulation of the optical readout via physical stimuli, including shape, compression, and multiple optical inputs/outputs is demonstrated. The unique permeability of the hydrogels is also combined with plasmonic nanoparticles for molecular detection of SARSCoV-2 in fiber-coupled biomedical swabs. A tricoaxial 3D printing nozzle is then employed for the continuous fabrication of living optical fibers. Light interaction with living cells enables the quantification and digitalization of complex biological phenomena such as 3D cancer progression and drug susceptibility. These fibers pave the way for advances in biomaterial-based photonics and biosensing platforms.

This chapter is based on the following publications:

Guimarães, C. F., Ahmed, R., Mataji-Kojouri, A., Soto, F., Wang, J., Liu, S., ..., Reis, R. L. & Demirci, U. (2021). Engineering Polysaccharide-Based Hydrogel Photonic Constructs: From Multiscale Detection to the Biofabrication of Living Optical Fibers. *Advanced Materials*, 2105361.

Guimarães, C. F., Ahmed, R., Reis, R.L., & Demirci, U., Hydrogel Optical Fibers and Their Application and Use, *Patent Filled* .

IX.1. INTRODUCTION

Since the first known uses of glass for optical aesthetics in ancient Rome, decorating the windows of Hagia Sophia and other world treasures, significant progress has been made in the field of photonics that culminated in uncovering microorganisms, exploring faraway stars and igniting the digital revolution with the 60s-70s advent of optical fibers [1–3]. A classical optical fiber is a cylindrical structure that can guide light waves through a 3D space due to refractive index variation between fiber core (inner) and cladding (outer shell). Light propagates in a zigzag fashion due to total internal reflection (TIR) between the core-shell interface. The study of fiber optics and the discovery of split-fusion and doping methods has grown to enable excellent data transmission up to intercontinental ranges [4,5].

Solid-state optical fibers excel in light-guiding and are present in healthcare applications such as imaging and biosensing [6–9]. However, silica fibers present limited biocompatibility [10], are not biodegradable, and their life cycle involves high energy consumption and non-recyclable waste production. The dense silica also hinders the diffusion of biological molecules [11], and presents optical mismatches when interfacing biological tissues [12]. Hydrogels have been explored as more sustainable, degradable photonic alternatives with physiological-level mechanics [13] and better light coupling [12]. Hydrogel optical fibers have been fabricated with synthetic, UV-crosslinking materials such as poly(ethylene glycol) (PEG) [14–19] and acrylamide [20]. These fibers were shown capable of integrating tissues [14,18], stimulating cells [14,19], and sensing varied phenomena [15–17,19,20]. Despite favorably high refractive indices (RI), covalently bound UV-crosslinked core materials lack crosslinking reversibility and dynamicity, thus preventing post-fabrication processes such as split fusion that enables the connection between separate fibers, for either repair or assembly. Furthermore, the need to obtain lower RI for cladding frequently requires using outer layers of materials that crosslink differently, requiring multi-step fabrication. Although existing materials employed so far excel in hydrogel light-guiding, the characteristic of hydrogels, namely the high mesh density and cytotoxic, UV-based crosslinking, also prevent the integration of living entities in the light-guiding core compartment [12].

Herein, we address these limitations by presenting multi-layered hydrogel optical fibers based solely on ionic-crosslinking, cytocompatible, natural polysaccharides, taking advantage of high-throughput wet-spinning fabrication [21,22]. First, we describe how the widely used polysaccharides alginate and gellan gum [23,24] can be manipulated to slightly tune their refractive indices in order to guide light through moderate distances in step-index optical fibers. Second, we demonstrate how the unique

versatility and reversibility of the ionic crosslinking can be explored for post-fabrication fusion, establishing a hydrogel parallel to classic silica fusion splicing in optical fibers. This method allows not only for repairing cut fibers and recovering light guidance, but also for the assembly of varied photonic architectures capable of splitting light and reporting on mechanical deformation and 3D shape, simultaneously capable of guiding different wavelengths of light. Third, we leverage the high permeability of these materials *versus* denser hydrogel meshes or even silica [25,26] to create a plasmonic platform, where resonance-induced shifts in spectra can inform on the presence of a molecular target, proving this concept by the detection of SARS-CoV-2 antigens and viruses. Lastly, we take advantage of the alginate core material's cytocompatibility and common crosslinking across all the optical fiber layers to continuously spin living optical fibers in a single-step fashion. Due to the unique core environment these fibers present, living entities can be directly integrated in the light-guiding core. Cells are then able to interact with light as an active optical material within the fibers, leading to fast, non-invasive optical readouts which can uniquely digitalize complex biological phenomena such as cancer proliferation and drug susceptibility into directly quantifiable data. Overall, these structures are highly tunable and of facile fabrication, thus adaptable by other researchers for a plethora of biomedically relevant applications.

IX.2. MATERIALS AND METHODS

IX.2.1. Ionic Optical Fiber Fabrication

IX.2.1.1. Ionic Optical Fiber Core Fabrication

Alginate and Gellan Gum (Gelzan) were both purchased from Sigma-Aldrich.

Alginate solutions were prepared by dissolving the powder in aqueous solution with stirring overnight at room temperature, in a magnetic stirrer. Gellan gum solutions were prepared by dissolving the powder in an aqueous solution at 90°C magnetically stirring for approximately 15-20 minutes until a clear solution was observable (i.e. without any suspended powder). The different formulations of alginate, gellan gum and blends were characterized optically using a portable refractometer (Milwaukee).

To fabricate the hydrogel fibers, a common microfluidic wet-spinning setup was used for obtaining the fiber core, followed by dip-coating and crosslinking of additional cladding layers. To fabricate the core fiber material, alginate solutions were aspirated into a syringe (BD Plastic) which was then assembled in a syringe pump (Fusion 200, Chemyx). A 21G needle was then inserted into a microfluidic PTFE tube (different needle diameters for different tube diameters). The open end of the tube was then placed into a beaker containing the crosslinking bath solution (0.1M $CaCl_2$). The syringe pump was then turned on with a flow of 0.4ml/min, causing the core hydrogel precursor to flow into the crosslinking bath continuously spinning hydrogel fibers. These were then collected and processed for cladding.

IX.2.1.2. Fiber Cladding

After fabricating the fiber core, the different cladding layers were added by a standard dip-coating protocol. Briefly, the core fiber was dipped in different gellan gum or alginate solutions depending on the testing conditions, and then re-imersed in calcium chloride. Fiber dipping was done by immersing the fiber and immediately removing it, as the diffusion of calcium ions from the core will cause bulky gel formation surrounding the fiber if remaining there for long.

Step-index fibers were fabricated by coating the core with a hydrogel of lower concentration and refractive index (e.g. Alginate 7% and GG 0.25%), while gradient index fibers were fabricated by adding up to 4 total layers of gradually decreasing refractive index. The range of preliminary conditions tested can be seen in Supplementary Tables IX-1 and IX-2.

IX.2.2. Optical Fiber Characterization

The characterization of light-guiding properties of the optical fibers was performed using a light-source and a power meter setup (Supplementary Fig. IX-3).

Hydrogel fibers were maintained in solution before analysis, point at which these were picked up from solution, and placed in a custom-built PMMA support platform (Supplementary Fig. IX-3). The support and fiber were then aligned and coupled to a 100x objective connected to a broadband light source (OSL2 Fiber Illuminator, Thorlabs) as the light input, and a light power meter (Thorlabs) was aligned at the output extremity, for power measurements. For spectrometer measurements, the power

meter was replaced by a collecting lense, connected through a silica optical fiber to a Spectrometer (HR2000+, Ocean Optics).

All readings and analysis were performed in a similar setup, with wet fibers on air, ensuring that all analysis is conducted before drying. All the fiber treatments such as virus incubation, drug exposure, among others, were done in liquid environment. Then, we conducted all the optical measurements in short time frames of within minutes, the longest being the collection of over-time cell data (Figure IX-4), which we limited to 10 continuous minutes. Further prolonged analysis can be possible with fiber re-hydration, but that process was not explored in this work.

In the particular case of fibers with living cells, these were kept in cell culture conditions (37 Celsius, 5% CO2) until any analysis. For analysis, the fibers were washed with calcium-containing PBS solution, in order to remove medium remnants from the hydrogels since certain components (*e.g.,* phenol red) present particular color and optical absorption that could confound other experimental results. After washing with PBS, fibers were stabilized in a 0.01M $CaCl_2$ solution, and then collected and placed in the support platform, connected to the optical setup as previously described.

To obtain the distance-power profile, fibers of 20 cm were placed within the system, and 2 cm were gradually cut from the fiber, with new power readings collected at each step. Attenuation was calculated as $dB=\log_{10}(PI/P0)$, with PI representing the power at each distance point and P0 the maximum power at the smallest fiber dimension (1 cm). To test the ability of light-guiding through 3D biological meshes, core-clad fibers were inserted into a 5% porcine skin gelatin type A hydrogel (Sigma Aldrich). Fiber-bending tests were measured similarly to distance profiles. In brief, fibers were placed in a surface with angle degree grids, aligned with the different angles, and the light power was measured at the end. Cyclic tests were performed by bending fibers to 90° and back to 0°, with power measured at the output at each half-cycle. Representative macroscopic pictures of the fibers were obtained by directly connecting them to an optical fiber end (Thorlabs) and photographed at high-contrast with a standard dual-camera.

IX.2.3. Ionic Core Split Fusion

IX.2.3.1. Ionic Core Split Fusion and Fiber Assembly

Optical fiber core split-fusion was performed by a de-crosslinking and re-crosslinking protocol, as follows:

Fibers with split ends were brought together, and the extremities were locally de-crosslinked by applying a drop of Sodium Citrate 55mM (Sigma Aldrich) for 1-2 mins. Afterwards, the fibers were removed from the de-crosslinking solution to avoid total fiber decrosslinking, and the treated extremities of the fibers were placed together, in close contact (naturally these will be attracted due to water interactions). The de-crosslinked extremities were then re-crosslinked by adding a drop of 0.1M Calcium Chloride solution, and after a minute immersing the full fiber in the crosslinking bath for complete re-crosslinking and fiber fusion.

For assembling multiple input/output architectures, the same procedure was followed but with a larger number of extremities. When aligning multiple de-crosslinking extremities for 1X2, 1X3 or successive arrangements, a microliter-sized alginate droplet of the same concentration as the core material can also be added to the fusion region immediately before re-crosslinking to ease the process. The precursor will help binding all de-crosslinking ends and form a stable and uniform junction ensuring minimum optical loss. After re-crosslinking, multi-armed structures were also immersed in the 0.1M $CaCl_2$ bath for complete stabilization.

IX.2.3.2. Tensile Characterization of Fiber Fusion Mechanical Recovery

For characterizing the mechanical stability of the fused fiber junctions, fused alginate fibers and control alginate fibers (as-spun, not modified) were fabricated as previously described. In order to clamp the fibers to the testing device, the fiber extremities were glued to a common paper support with approximate size to the clamp, with a spacing of 30mm of fiber between both ends, to be then tested. Immediately after gluing and to avoid unnecessary drying, fibers were then clamped into a universal mechanical testing machine (INSTRON 5540), using a 50N load cell. Clamping was done in the paper-glued region, as shown in Supplementary Fig. IX-5, a. A pre-stress of 0.01N was then applied to all samples, point at which a tensile displacement of 5mm/min was applied. Fibers were stretched until breaking, and force/displacement curves were then recorded for multiple replicates. The force at break

values were then extracted at the curve peak right before fiber breakage, and these values were used to compare the mechanical stability and recover of the split-fused fiber joint *versus* as-spun controls.

IX.2.4. Ionic Core Doping

The optical fiber core doping procedure was done with minor modifications to the wet-spinning protocol. In brief, the Calcium Chloride 0.1M solution was replaced by Neodymium Chloride (Sigma Aldrich) 0.1M aqueous solution. The ionic precursor was then wet spun with a similar setup into the rare-earth metal solution. A blue dye (Procion MX, Turquoise) was added to the alginate solution to differentiate the doped core color for visualization only. To confirm the lasing capabilities of the doped fibers, the neodymium alginate core was cladded with 0.25% GG and shielded with 2wt% alginate and aligned in the optical characterization setup. As input light, an 808 nm laser (Thorlabs) was used, and the Power Meter was set to measure light power at both 808nm and 1080nm. The 1080/808nm ratio was then calculated to observe for a shift towards 1080 due to the doping and characteristic light amplification of neodymium.

IX.2.5. Multi-Output and Multi-Input System's Characterization

Multi-output systems were characterized in a manner like the linear optical fibers. Briefly, the light source was coupled at the input fiber side, and the power meter was then aligned with the different outputs to characterize the light power coming out of each of them. Fiber arms were moved to distinct positions and the different outputs were characterized similarly to plot the relationship between output power and optical fiber angles. For compression tests, the dual-output fibers were compressed by cylindrical weights with 5 mm diameter, which were gradually stacked to increase the total mass (m). Compression force (F) was then calculated using the $F=m\times g$ formula, with g being the gravitational acceleration (9.8 ms^{2}).

Multi-input systems were characterized using two different light sources: a broadband light source (OSL2 Fiber Illuminator, Thorlabs), connected to a 100x objective as previously described for the first input and a narrowband red class II laser for the second input. To read the characteristics of guided light, the fiber output was aligned towards a collecting lens (Thorlabs) connected through a silica optical fiber to a spectrometer (HR2000+, Ocean Optics). The different light sources were turned on and off

alternatively and the output spectrum was collected to validate the ability to observe distinct light inputs in a single measurement.

IX.2.6. Engineering Plasmonic-Core Optical Fibers for sensing

Plasmonic-core optical fibers were obtained by encapsulating gold nanoparticles within the fiber core. Bare gold nanoparticles (NanoComposiX) were dispersed in the alginate core solutions (an intermediate 4wt% solution was used) at varying concentrations by vortexing thoroughly to ensure proper mixing. The fibers where then fabricated as previously described towards a core-clad architecture, and the guided light spectrum was obtained as described by aligning the fibers between a light source and lens collector, connected to the spectrometer. Increasing concentrations of gold nanoparticles were tested to observe their contribution to the light spectra. Fibers with AuNPs were also cut axially and freeze-dried for observation under scanning electron microscopy (SEM). For transposing the platform towards the detection of target entities, protein-G coupled gold nanoparticles (100nm) were purchased from Cytodiagnostics. These were used as a versatile platform for binding antibodies.

In order to obtain anti-SARS-CoV-2 Spike protein-conjugated gold particles, the anti-Spike (S1) mouse antibody (Sino Biologicals) was added to the protein-G gold solution at 1:10 dilution and left to bind for 1 hour at room temperature. After binding, the anti-spike gold nanoparticles were encapsulated within the optical fiber core to a final concentration of 20μg/mL (optimized shift) and characterized as fabricated to observe the antibody-induced shift in light. Similar fibers were also incubated in parallel with SARS-CoV-2 Spike protein (S1) (Ray Biotech) for 30 minutes at RT. The antigen was diluted 1:40 in PBS buffer solution (previously optimized detection range 1:40 to 1:4) where the fibers were immersed. After washing with calcium, fibers were aligned in the optical characterization setup to observe the shift in light caused by antigen binding. In all cases, a minimum of 4 individual fibers were tested.

IX.2.7. Swab-Coupled Optical Fibers and SARS-CoV-2 Detection

Sterile 15 cm swabs were purchased from Puritan and modified by cutting the top part of the shaft and creating an indentation for coupling the optical fibers. The swab-coupled fibers were then used to characterize their ability to bind and detect SARS-CoV-2. Anti-Spike gold nanoparticle core fibers were fabricated as previously described and inserted within the swab indentations. The swab tip was separated from the shaft by cutting and the full shaft was split in smaller sections of around 3 cm.

Several of these individual swab-fiber structures were then used as the model of swab-coupled sensing system. To recreate their interaction with bodily fluid and lavage, swab-coupled fibers were soaked with a PBSA solution containing gamma-inactivated SARS-CoV-2 Viruses (Catalog # NR-52287, Isolate USA-WA1/2020, BEI Resources, 1:1000 Dilution), as well as similar incubation without the viral component and with Influenza H3N2 Virus at a similar dilution (Bioworld, Recombinant), for 1 hour at RT. Both fibers were then washed to remove unbound entities and aligned in the light-spectrometer system to derive an optical readout. For all cases, 4 individual swab-coupled fibers were tested.

To validate the presence of SARS-CoV-2 in the hydrogel fibers, a similar protocol was followed up to the virus incubation and washing, point at which a reverse immunofluorescence protocol was pursued. The fibers were first blocked with 3% BSA (Sigma Aldrich) for 30 mins RT. These were then incubated with rabbit anti-nucleocapsid antibody (Sino Biologicals), 1:200 dilution, for 1 hour at RT. After washing thoroughly, the fibers were incubated with an Alexa 488 Anti-Rabbit antibody (Abcam) at 1:200 dilution for 1 hour at RT. The immunofluorescent setup and magnification rationales are further schematized in Supplementary Fig. IX-14. Fibers were then washed thoroughly and taken for fluorescent microscope observation under different magnifications (Observer Z1, Zeiss).

IX.2.8. RNA extraction and LAMP-based detection

To further validate the presence of SARS-CoV-2 viruses after incubation in the functionalized AuNP fibers, RNA was extracted using miRNeasy Kit (Qiagen). After incubation with virus and control solutions, fibers were thoroughly washed and placed on ice. These were incubated for 10 minutes in Sodium Citrate 55mM (Sigma Aldrich) to chelate the calcium ions and facilitate the dissolution of the fibers. These were then processed according to the extraction kit manufacturers instruction. Extracted RNA was then analyzed using the COVID-19 Rapid Isothermal PCR Kit (RT-LAMP) (Raybiotech) according to the manufacturer's instruction. Briefly, extracted RNA and controls were placed in individual PCR tubes and mixed with the primer master mix. Tubes were then placed in a Thermocycler for 30 mins at 60°C for the amplification reaction to take place, and then left at room temperature for stabilization of the reaction during 1hour. At the end, the color changes were captured in a photograph, and the absorbance of the solutions was measured to obtain the 570/650nm ratio, which is above 1 for SARS-CoV-2 positive samples.

IX.2.9. Dot-Blot Validation Tests

To confirm the capability and specificity of anti-spike antibodies to bind to the Spike antigen as well as SARS-CoV-2 viruses, a standard dot blot approach was followed. Briefly, different dilutions of protein/antigen/virus solutions were blotted in a nitrocellulose membrane (BioRad), by pipetting 2µL drops of each solution/replicate to different membrane locations (usually 3-4mm diameter).

After drying, membranes were blocked by soaking in 5% BSA (Sigma Aldrich) solution in TBS-T - 0.05% Tween20 in TBS - (Sigma Aldrich) for 30 minutes, RT. Following blocking, membranes were incubated with primary antibody (Mouse Anti-Spike, 1:500 dilution) overnight at 4°C. Afterwards, membranes were washed three times with TBS-T and were then incubated with the secondary antibody (Goat Anti-Mouse, Alkaline Phosphatase Conjugate, Invitrogen, 1:1000 Dilution), for 1hour at RT. Membranes were then washed three times with TBS-T, and posteriorly revealed with the AP-Conjugate Kit (Biorad). The revealing was stopped once the dots were visible and the membranes were then digitalized and converted to 8-bit.

Using ImageJ blot tools, semi-quantitative analysis was performed to compare the different dot's values between dilutions and sample types.

IX.2.10. Computational Modeling of Plasmonic Gold Transmission

A finite element method is used to model how gold nanoparticles affect transmission of the light through the fiber. The simulation space consists of a gold nanosphere with the diameter of 100 nm, a spherical dielectric shell with refractive index of n=1.33 which surrounds the nanosphere, and a PML layer. An incident plane wave shines the particle and scattered fields are calculated and employed to find the particle's extinction cross-section.

Fiber transmission is calculated using the calculated extinction cross-section, the length of the fiber in experiments, and the concentration of gold nanoparticles in the fiber. Finally, the refractive index of the surrounding media is increased in steps of $\Delta n = 0.01$ and the transmission spectra is calculated for each step. These calculations show that any increase in the refractive index around the nanospheres will redshift the resonance wavelength and decrease the transmission amplitude at long wavelengths.

IX.2.11. Biofabrication of Living Optical Fibers

For continuously printing triple-layered optical hydrogel fibers, a tri-coaxial 3D printing nozzle configuration (Ramé-Hart Instruments) was connected to syringes containing different core, clad layer hydrogel precursors. Fully detailed nozzle and channels dimensions can be found in Supplementary Fig. IX-17.

For initial tests with living cells, 3T3 fibroblasts were cultured with DMEM Complete Medium (Gibco) and upon confluence trypsinized and resuspended in the core Alginate (Sigma) 2wt% solution, in PBS. In order to ensure proper cell distribution, the suspension was thoroughly mixed without vigorous agitation that could induce air bubbles and compromise the fiber optical properties. A cladding layer of 0.5% gellan gum was used on the middle channel and a shielding layer of 1% gellan gum on the outer channel.

All solutions were aspirated into 10 mL syringes (BD Plastic) and connected to individual syringe pumps at a common flow of 0.4ml/min. The tri-coaxial nozzle was then placed in a beaker containing the crosslinking bath of 0.1M $CaCl_2$, as previously described. Several fibers were then continuously spun and collected into a petri dish containing cell culture media to prevent further stress from the calcium chloride solution.

To validate the cytocompatibility of the hydrogel fibers and the wet-spinning protocol, viability tests were performed by Calcein AM/Ethidium Homodimer staining (Live/Dead) (Invitrogen) at 1:1000 dilution. Post-fabricated fibers and fibers cultured for 1 week were incubated in the live/dead solution for 30 minutes followed by imaging under confocal microscope (Zeiss). 3 images per replicate were taken at random, and Cell Profiler [27] software was then used to count the number of live and dead cells. Viability was then calculated as the percentage of live cells. Quantification of light output power as function of cell density was performed by fabricating fibers with varying 3T3 cell density in the core, and output characterization was done using an optical powermeter (Thorlabs) as described in the optical fiber characterization section.

IX.2.12. Fluorescent Fingerprinting Tests

To validate the possibility of light carrying information upon interaction with fluorescent molecules, 3T3 fibroblasts were stained with two model fluorescent markers of different wavelengths, namely Orange Cell Tracker CMRA and Calcein AM (Invitrogen) according to manufacturer's instructions.

Briefly, 3T3 cells in suspension were incubated with each marker for 30 minutes under 37°C, washed with PBS, and introduced in the optical fiber core as described above. Fibers were then fabricated and aligned in the input-output setup as previously described the light source and spectrometer.

Output spectra were collected, and spectral ratios were obtained by dividing the spectra of fluorescent-tagged cell-laden fibers to those without fluorescent molecules, in order to confirm the presence of transmission dips in agreement with the marker's excitation curves. For performing calcein AM overtime metabolic tracking, 4cm-long fibers with unstained cells were aligned in the optical readout setup, and 10µL of a 1:100 Calcein AM solution in CaPBS was added dropwise along the optical fiber's length. The spectral output was then collected every minute for a total of 10 minutes after the beginning of the calcein AM metabolization. The 495nm normalized transmission values were obtained by normalizing all spectral curves to their maximum and extracting the normalized intensity values as an average of the 493-495nm window. These were then plotted overtime.

IX.2.13. Cancer Cell Lines and Spectral Fingerprinting Experiments

LNCaP, 22Rv1, and DU145 cells were purchased from the American Type Culture Collection (ATCC; Manassas, VA). All cell lines were authenticated through Stanford Functional Genomics Facility. FUCRW plasmid was a kind gift from Dr. Owen Witte's laboratory at University of California Los Angeles. 22Rv1 and DU145 cells were infected with FUCRW virus expressing red fluorescent protein (RFP). RFP signal was confirmed 72 hours post infection. LNCaP-RFP-Trop2-OV cells expressing RFP and Trop2 oncogene were generated as previously described [28]. All cells were cultured in RPMI medium supplemented with 10% FBS, 4 mM L-glutamine, and 1% penicillin/streptomycin. Spectral fingerprinting tests with the different cell lines were performed by integrating them within optical hydrogel fibers as described in the previous section. Briefly, cancer cells were resuspended in the core material at a density of 10M/mL and cultured in different conditions, namely control medium, 1.5µM Cisplatin (Biovision) or 1µM Staurosporine (Biovision).

After 48h of culture, the living optical fibers were washed twice with PBS to remove media remains that could interfere with optical readouts (e.g., Phenol Red). Before measurement, fibers were placed in a 1mM $CaCl_2$ solution to facilitate their manipulation and were then aligned in the optical characterization setup with spectrometer connection. RFP-level transmission readouts were immediately obtained from the first output collected, and calcein activity overtime was then tracked by the addition of calcein and spectral recording every minute for 10 minutes, as described in the previous section.

Calcein-level transmissions were then plotted overtime, and Pearson correlation statistical analysis was performed in order to verify the presence of a positive correlation between time and decrease in calcein-level transmission.

To validate fiber-optics data, fibers were also imaged in confocal microscope after incubation with calcein AM. Both RFP and calcein signals were analyzed in several pictures per replicate via Cell Profiler, in order to compare the relative post-incubation signal intensities to the relative decreases in fiber optics transmission at each specific wavelength instantly (RFP) and overtime (calcein).

IX.2.14. Digitalization and Quantification of 3D Cancer Development

In order to evaluate the invasive proliferation of encapsulated cancer cells over time and quantify this response through optics upon exposure to different levels of the anti-proliferative drug cisplatin, the core material was modified by blending alginate with GelTrex (Growth-Factor Reduced Basement Membrane, Thermofisher) at a 50:50 ratio. Fibers with Cells were fabricated as described before with a 10million/mL density and were cultured for 1 week to observe the cancer tissue development and the formation of fiberoid (fiber-shaped organoids) structures.

To do so, fibers were incubated with Calcein AM 1:500 (Invitrogen) and Hoechst 33342 1:1000 (Thermo Scientific), washed with PBS and imaged under confocal microscope (Zeiss). As model cell line, we used the RFP-expressing LNCaP-RFP-Trop2-OV due to its aggressiveness and relevance in metastatic events. To then quantify the effect of cisplatin in the impedance of 3D tumor growth, fibers were cultured over a 5-days period under control conditions and increasing concentrations of cisplatin (1.5, 15 and 150µM). After each time point, fibers were washed twice with CaPBS, briefly dipped in 1mM $CaCl_2$ and aligned in the optical characterization setup.

Two types of immediate readouts were acquired: output power *via* powermeter reading and spectral response through spectrometer connection. Output power was directly used as an indicator of light attenuation induced by tumor growth and spectral data was processed to extract RFP-level transmission values, as plotted in the maintext. In parallel, fibers were also axially sectioned and imaged in confocal microscope for observing the distribution of cancer cells and aggregates within the fiber structure overtime and validate the fiber optics readouts.

IX.2.15. Statistical Analysis

Globally, samples and replicates were firstly tested for the probability of normal distribution *via* Shappiro-Wilk normality test. In the case of a positive normality test, differences between conditions were then analyzed *via* parametric ANOVA or T-test. In the case of a negative normality test, difference between conditions were analyzed *via* non-parametric Kruskal-Wallis or Mann-Whitney tests. The detailed statistical tests are reported in the different data figures and captions. In all cases, differences between conditions were considered statistically significant when $p<0.05$.

IX.3. RESULTS AND DISCUSSION

IX.3.1. Fabrication of Ionic Polysaccharide Hydrogel Optical Fibers

We investigated the continuous fabrication of tunable ionic sugar-based hydrogel optical fibers based on the highly dynamic crosslinking properties of natural polysaccharides (Supplementary Fig. IX-1). Fibers were fabricated by wet-spinning the polysaccharide hydrogel precursor into a crosslinking bath, followed by coating and crosslinking of different hydrogel layers to obtain varying core-clad refractive indices (either step-index or gradient-index hydrogel fibers) (**Figure IX-1, a**, **b,** Supplementary Table IX-1). These hydrogel fibers can be easily collected from solution and coupled with a light source when supported in air, guiding light towards an output collector for analysis in a setup as shown in **Figure IX-1, c**. Naturally, the highly hydrated hydrogel meshes dry when exposed to air for long periods of time (Supplementary Fig. IX-2) and, as such, fibers were kept in solution when not undergoing optical analysis.

To optimize light-guiding capabilities, we studied how the refractive index (RI) of gellan gum (GG) and alginate changed with varying concentrations. We observed a linear relationship between polymer concentration and RI for both materials (Supplementary Fig. IX-1), evidencing similar RI at same concentrations, despite known different molecular weights and consequent viscoelastic properties [29,30]. To maximize total internal reflection, we investigated the lowest GG (0.25%) and highest Alginate (7%) concentrations, at which solutions could still be manipulated and yield stable hydrogels while enabling a considerable RI difference. By increasing core alginate concentration up to 7%, the refractive index increases above 1.34, while maintaining a very low concentration (0.25%) of GG cladding allows for a water-like refractive index of 1.33, hence generating a ~0.01 difference between core and cladding

(**Fig. IX-1, d**, Supplementary Fig. IX-1). To protect the low-concentration GG cladding, 2% alginate was added as a shielding layer, a common silica fiber optics approach. This distinct type of hydrogel core-clad-shield architecture was possible and resulted in well-structured fibers (**Fig. IX-1, d**).

We characterized the optical power of guided broadband light over distance (Supplementary Fig. IX-3). The ability of cladding layers to contain light within the core (**Fig. IX-1, e**) improved light-guiding even within higher RI environments, as with fibers inserted in 3D denatured collagen (gelatin) matrix (**Fig. IX-1, f**). Cladding layers significantly reduced light attenuation and led to efficient light guiding to lengths over 20 cm (**Fig. IX-1, g-i**). Similar distances have been reported for synthetic hydrogel fibers [17], but in this case with lower RI differences. Even though both step-index and gradient-index cladding strategies improved light guiding, step-index fibers performed significantly better than gradient-index ones (**Fig. IX-1, i,** Supplementary Table IX-1 and IX-2). The lower optical performance of gradient-like structures is likely due to the employed approach of using multiple layers with gradually decreasing refractive indices to approximate a gradient-like organization, which may still cause some step effect at each transition. While the step-index architectures present a RI difference of ~0.01 between core and cladding, the gradient-index layering comprises smaller steps to approach a gradient-like transition. Thus, the higher RI difference present in these step-index architectures improves internal reflection more extensively than the gradient-like structures. Further, the gradient-like layering also requires multiple coating steps that may lead to an accumulation of cladding imperfections, increasing optical loss. Since step-index fiber fabrication is more straightforward (fewer cladding steps), and yielded better optical results, these fiber architectures were selected for further testing.

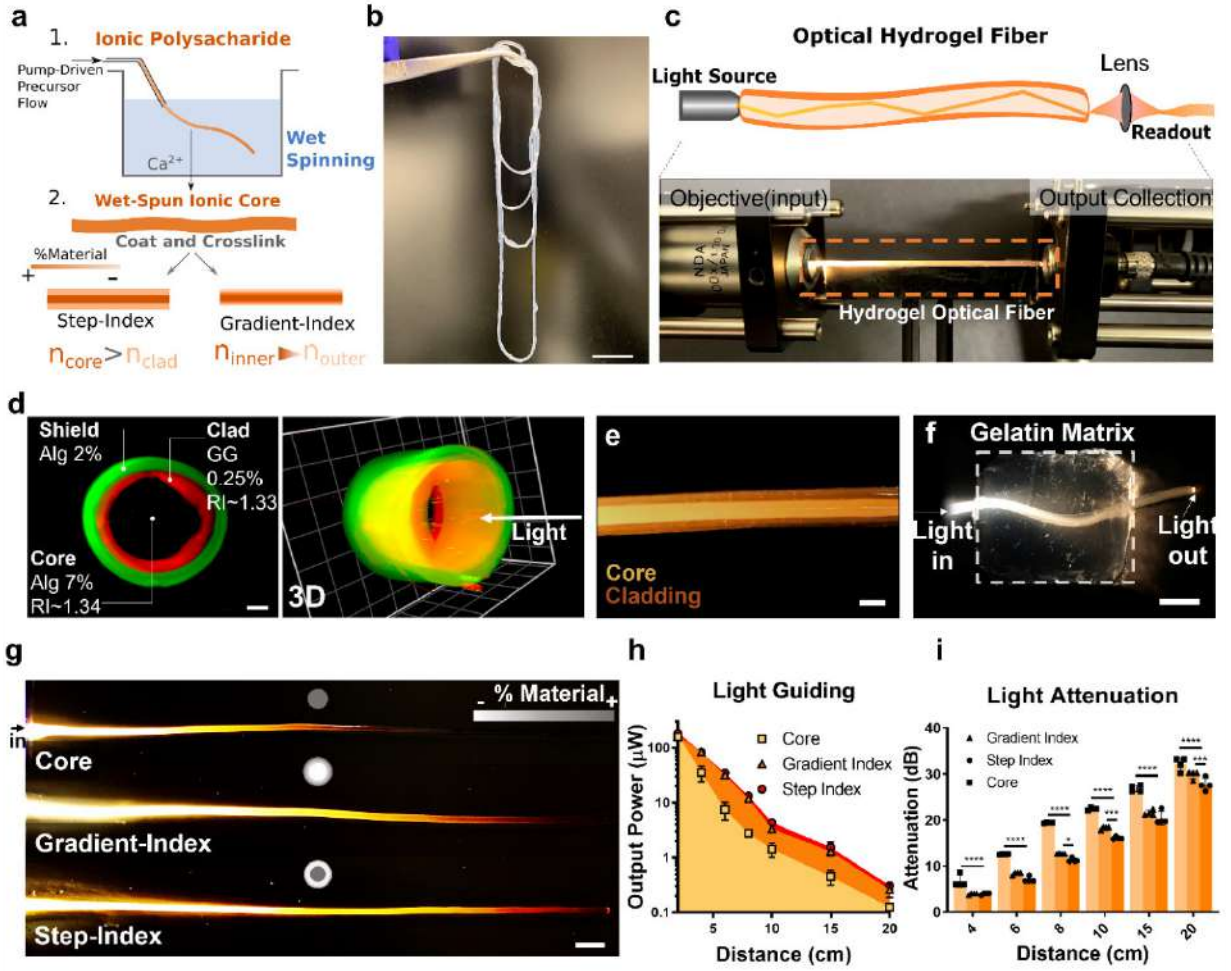


Figure IX-1: Fabrication of Purely Ionic Hydrogel Optical Fibers and their Light-Guiding Characterization. a| Schematic representation of wet-spinning approach to continuously fabricate the optical fiber core (1), which can then be coated with different refractive index (n) hydrogel layers to obtain step- or gradient-index core-cladding architectures (2). b| Photograph of an as-fabricated optical core-clad hydrogel fiber. Scale bar: 1cm. c| Schematic representation of the optical fiber input-output setup for light guiding and collection (top) and actual experimental setup (bottom) for acquiring optical data in semi-dry conditions (wet fiber, out of liquid environment) d | Microscopic 2D and 3D images of transversal core-clad-shield fiber sections. Core: Alginate 7%, Clad: GG 0.25 + nile red fluorescent solution, Shield: Alginate-FITC 2%. Scale bar: 200µm. e | Detail of light-guiding through the core-clad fiber. Scale bar: 1mm. f | Light-guiding by a core-clad-shield fiber inserted within a 3D Gelatin Matrix. Scale bar: 1 cm. g | High-contrast photographs of fibers coupled to a broadband light source. In each picture's center, a representation of the distinct layers and polymer concentration is visible in tones of gray. The black arrow shows the light input direction (in). Scale bar: 1 cm. h | Output Power measurements of light guided through different fiber configurations (core-only, gradient index, step index) with increasing length. i | Calculated attenuation values of light guided as a function of fiber length (distance). Statistical analysis through Turkey's Multiple Comparison, * $p<0.05$, *** $p<0.001$, **** $p<0.0001$.

IX.3.2. Exploring the versatility of soft, ionic crosslinked hydrogel optical fibers

After linear light-guiding, we investigated the modulation of the optical readout under physical stimuli on these easily deformable structures. We tested the fibers' light guidance upon bending (**Fig. IX-2, a**), observing linearly decreasing output power with increasing bending angles (**Fig. IX-2, b**), similar to previous reports on synthetic hydrogel fibers [17]. Cyclic bending demonstrated complete light-guiding recovery with output powers maintained over ten full cycles (**Fig. IX-2, c**). These results demonstrate that light-guiding is maintained in curved configurations and isn't lost when fibers are repeatedly deformed, evidencing the elastic recovery capability of the structure.

We then explored the versatility and reversibility of a fully ionic-crosslinked structure to approach essential fiber optics advances – doping and fusion splicing. We observed that the ionic crosslinking can be easily adapted to the introduction of rare-earth metals for doping fibers in a very facile manner (Supplementary Fig. IX-4, Supplementary Video IX-1 and IX-2), as opposed to the more complex silica rare-earth doping [5,31].

We also hypothesized that ionic crosslinking's reversibility could be explored towards fusion splicing, *i.e.*, the connection of previously separate fibers. We developed a materials method in which fibers separated by a full incision were fused in facile steps. First, a local de-crosslinking of the fiber tips was performed by chelating calcium ions using a sodium citrate solution. This process releases calcium ions binding the alginate chains priming them to establish new ionic bonds. Second, with the treated fiber ends in contact, these were re-crosslinked by adding calcium chloride, causing the once-separated extremities to bind, fusing the fibers into one (**Fig. IX-2, d**). The fused fibers were mechanically stable, being able to withstand 60-70% of the same tensile force of unmodified fibers before break (**Fig. IX-2, e,** Supplementary Fig. IX-5). More importantly, fused fibers recovered their light-guiding capacities, validating this fusion splicing technique as a hydrogel equivalent to traditional silicon approaches (**Fig. IX-2, f-h**).

We then leveraged fusion for assembling complex multi-input divider, multi-output combiner, and multi-input/multi-output (MIMO) optical architectures (**Fig. IX-2, i**). We observed that these integrated systems could split a single input into multiple outputs with low incremental loss: normalized light intensity per output channel number (n) was only partly below 1/n (**Fig. IX-2, j**). This means that as light is divided into the different arms, it splits into almost equal parts, with slight additional loss due to possible imperfections at the junction.

These integrated systems can act as macro-level reporters of force and shape. First, we observed that the fibers' compression led to changes in output light intensity (**Fig. IX-2, k**). A homogeneous force was generated by placing weight on top of the fibers, used to quantify compressive force (F) deformation-induced light-scattering, *S(F),* based on an optical output, *I*, as approximated by equations IX-1 and IX-2.

$$I \sim I_0[1 - S(F)] \quad \text{(Equation IX-1)}$$

Experimentally (**Fig. IX-2, k**) being:

$$I(\mu W) \sim 4.5[1 - 8.2F(N)] \quad \text{(Equation IX-2)}$$

Naturally, the initial or zero-compression output, I_0, will depend on the fiber length (**Fig. IX-1, h**), and the compressive loss factor (here ~8.2μW/N) will depend on the degree of hydrogel fiber deformation due to external forces or weights, which may vary based on the mechanical properties of different hydrogels.

We then leveraged 1x2 coupler systems to inform on the relative angle of the whole structure, considering each output segment as an individual arm. We observed that output light intensity decreased proportionally (-0.0038/degree) to the angle between the output arm and the common input branch. While a fixed arm maintains constant output light intensity (Supplementary Fig. IX-6), changes in shape leading to angular increase can be detected by looking for proportional decreases in light power (**Fig. IX-2, l**). Just as shown for single-fiber bending, as the different arms bend at distinct angles, the amount of light that is detected at the output will vary. As such, by quantifying the optical power of the arms, it is possible to understand the current shape and deformation of the whole structure. This property can be potentially interesting for tracking, e.g., the forces and deformation in biological surfaces, such as skin contraction or wound healing.

Furthermore, the 2x1 splitter can easily be reversed into a 1x2 coupler architecture (**Fig. IX-2, i**), which can combine light from different sources into a single output for readout. By coupling light from a broadband light source (400-800 nm) into one arm and another narrowband light source with 654 nm wavelength into the other arm, light from both sources could be detected at the output, in a single spectrometer readout (**Fig. IX-2, m**). This type of multi-input architecture may be employed to analyze different responses in the different photonic construct arms, by differentiating the type of light being coupled to each arm and then separating both profiles from a common spectrometer readout (*e.g.,* knowing what arm suffering mechanical deformation or bending by analyzing the correspondent wavelength).

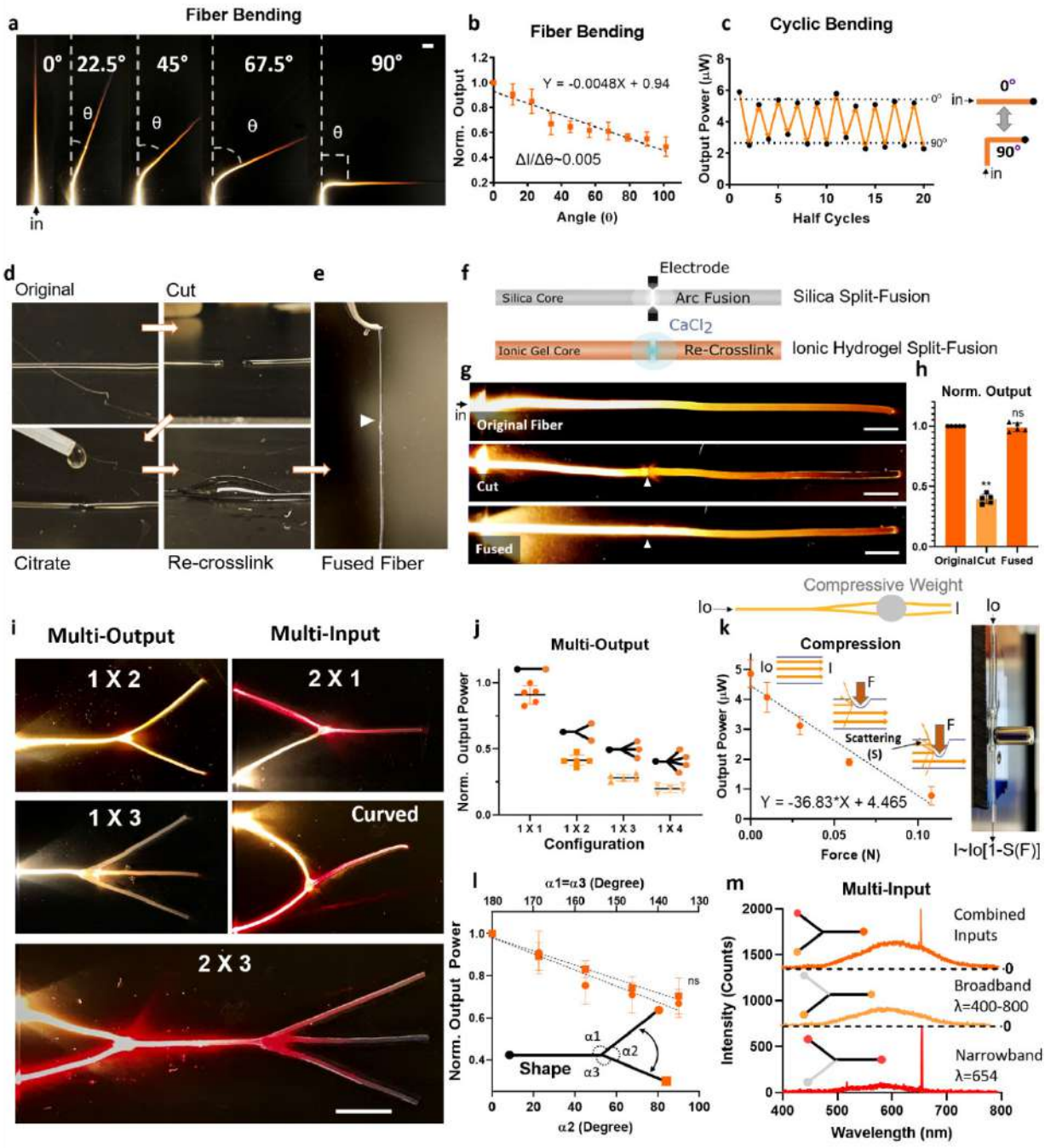


Figure IX-2: Exploring ionic soft hydrogel versatility and fusion splicing for responsiveness to macro-scale force and shape. a | Photographs of light guidance in fibers at increasing angles of bending. The black arrow shows light input direction (in). Scale bar: 1 cm. b | Normalized intensity profile of output light power at increasing bending angles and tis regression line. The line equation is also denoted. c | Output power as measured upon sequential bending/unbending of core/clad fibers. d | Photograph of the main steps for hydrogel fiber split fusion. e | Lifting of a fused fiber. The white arrow indicates the point where fiber was cut and fused. f | Parallel behind silica fiber fusion splicing and re-crosslinked hydrogel fiber fusion. g | High-contrast photographs of light guided through intact, split, and fused hydrogel fibers. White arrows indicate the point of cut/fusion. Scale bar: 1cm. h | Normalized output intensity of as-fabricated, cut, and fused fibers. Statistical comparison between cut/fused fibers and the original

structure performed through Kruskall-Wallis multiple comparison test. i | High-contrast photographs of fusion splicing-assembled multi-output, multi-input, and multi-input/multi-output (MIMO) photonic architectures. j | Characterization of output light intensity with incremental input splicing. k | Evaluation of changes in output light power as a function of fiber compression, including an equation that represents the output intensity (I) as proportional to the input (I_0) minus the amount of light that is blocked/scattered as a function of the compressive force, S(f). l | Quantification of the double-output system intensities with both arms moving at the same angle to the common input branch. m | Multi-input photonic system arrangements and the detection of broadband and narrowband light sources in the same spectrum readout.

IX.3.3. Engineering a nanoplasmonic hydrogel core towards molecular-level detection

After macro-level detection of forces and shapes, we explored nano/micro-scale light-matter interactions to detect biological targets at the molecular level. It is well described that nanostructures such as plasmonic metals respond to surrounding environmental changes due to refractive index-sensitive plasmonic resonance shifting[32,33]. We hypothesized that the integration of plasmonic nanoparticles (NPs) in the core of the hydrogel fibers, could lead to resonance-induced variations in output spectra (**Fig. IX-3, a**). We verified that the encapsulation of gold NPs (AuNPs) within the hydrogel fiber core (Supplementary Fig. IX-7) directly affected the spectral output with gradually increasing AuNPs concentrations leading to higher resonant absorption (**Fig. IX-3, b**).

For a blank fiber, the output intensity spectra $I_B(\lambda)$ can be approximated as a function of the input light, $I_{bulb}(\lambda)$, multiplied by the fiber transmission function, $H_{Fiber}(\lambda)$ (equation IX-3). When AuNPs are introduced into core, the output spectra will further be affected by the gold transmission, T_{AuNP} (equation IX-4**)**.

$$I_B(\lambda) = I_{bulb}(\lambda) \times H_{Fiber}(\lambda) \text{ (Equation IX-3)}$$

$$I_{AuNP}(\lambda) = I_{bulb}(\lambda) \times H_{Fiber}(\lambda) \times T_{AuNP}(\lambda) \quad \text{(Equation IX-4)}$$

By dividing the output spectra of the AuNP-core fiber, I_{AuNP}, by that of the empty fiber, $I_B(\lambda)$, it is possible to isolate the effect of gold transmission T_{AuNP}, or absorption (1-transmission, as amount of back-reflection is negligible) in the final spectra (Supplementary Equations IX-1-5). While low gold concentrations (2.5 μg/mL) show very slight plasmonic resonance-induced variation, at 20μg/mL, a significant resonance effect in light transmission happens (**Fig. IX-3, c**), comparable to computational simulations of 100nm AuNP spectra (Supplementary Fig. IX-8).

Using glycerol solutions, we observed that increasing refractive index shifted plasmonic transmission causing the most prominent decreases in output intensity after the resonance peak wavelength, namely at 700nm-level transmissions (Supplementary Fig. IX-8), which linearly decreased with increasing RI, representing a meaningful detection parameter (Supplementary Fig. IX-9). Therefore, 700nm-level transmission was analyzed to look for varying RI effects due to the presence of biotargets.

Previously, Protein G-based[34] functionalization was used to detect antibody/antigen interactions via changes in local refractive index [35]. We thus encapsulated protein-G-coupled AuNPs within the fiber core, and compared the output light spectra with the same plus antibodies against SARS-CoV-2 Spike (S1) protein [36] (Supplementary Fig. IX-10). As observed in glycerol tests, the antibody binding to the protein-G-AuNPs caused a reduction at higher-wavelength transmission (**Fig. IX-3, d, e**). A further decrease was observed by incubating the functionalized-AuNP fibers with SARS-CoV-2 Spike antigen, lowering the 700 nm intensity at each step, from ~0.65 to ~0.55 (normalized intensity) (**Fig. IX-3, e**). A parallel experiment where protein solution was added to the fibers over time confirmed similar agreement with computational simulations (Supplementary Figs. IX-11, IX-12). This validates the optical fiber detection mechanism based on the resonance shifts caused by binding biotargets (**Fig. IX-3, f**).

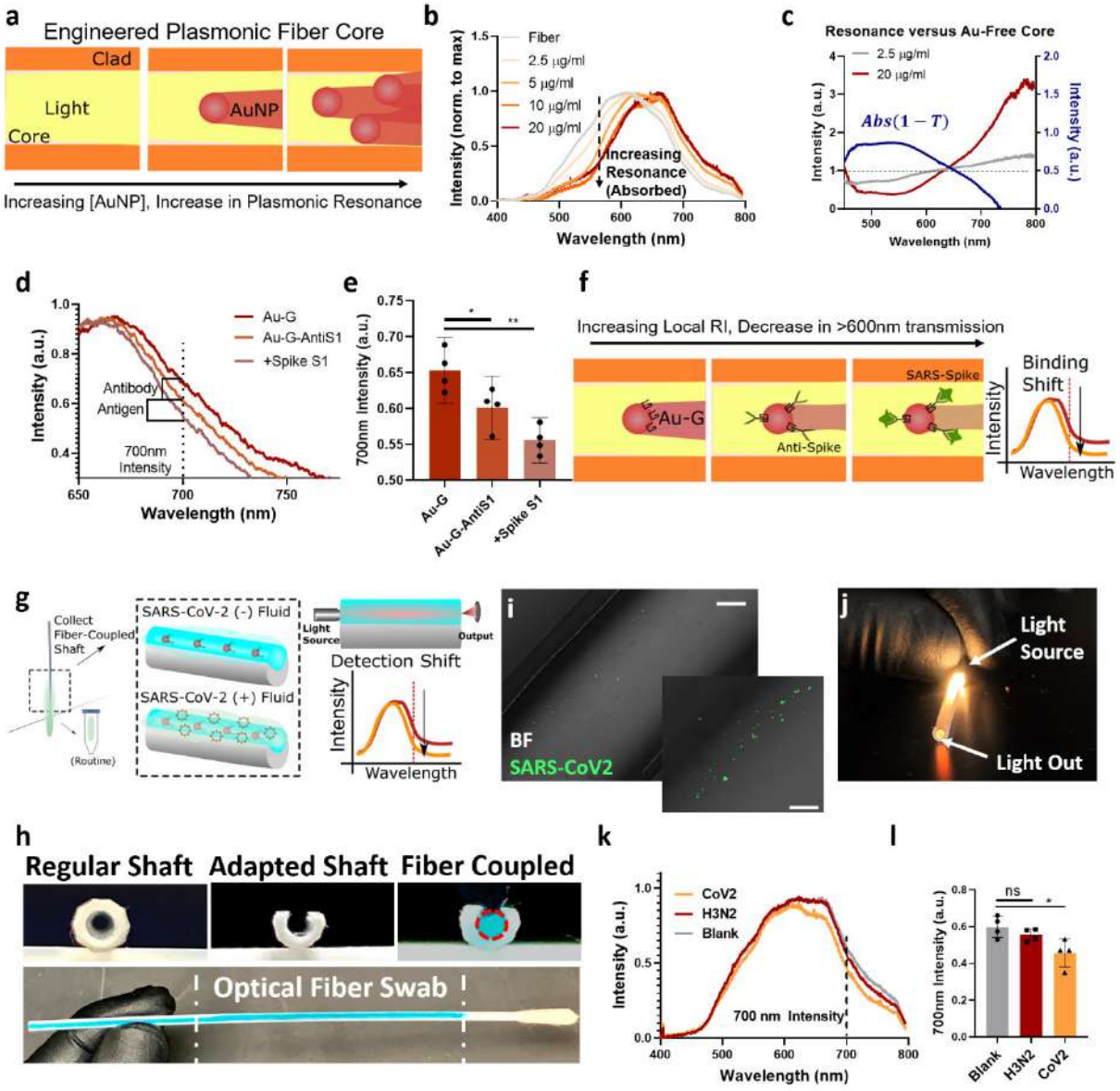


Figure IX-3: Engineering a plasmonic core modified hydrogel fiber for molecular-level SARS-CoV-2 detection. a | Schematic of the rationale behind the integration of gold nanoparticles in the hydrogel fiber and for the integration of sensitive plasmonic resonance. b | Output light spectrum of the hydrogel fibers with increasing AuNPs concentration. Each curve represents the average behavior of 4 individual fibers. c | Resonance curves obtained by normalizing the spectra of Au-NP encapsulating fibers of minimum and maximum tested AuNP concentrations against the empty fiber (no gold). In blue, the calculated absorption (1-transmission) curve for the highest concentration (20μg/mL) is denoted. d | Output light spectra of Protein-G-coupled AuNP-laden fibers before and after addition of Anti-Spike antibodies and incubation with SARS-Spike antigen. Each curve represents the average behavior of 4 individual fibers. e | Normalized intensity (700 nm) values of the different curves upon antibody and antigen binding. Statistical comparisons performed by Mann-Whitney test, * $p < 0.05$, ** $p < 0.01$. f | Schematic representation of the mechanism behind antibody and antigen-induced shifts resulting in decreased 700nm intensity values. g | Rationale behind optical-fiber-coupled swabs, which can be exposed to viral structures present in bodily fluids. Upon flushing the

collected material through the optical fiber, the Q-tip can be collected for routine analysis and the split fiber shaft washed and analyzed in an optical setup to look for the shift taking place in the presence of the virus. h | Steps behind the swab shaft adaptation and insertion of the optical fiber towards an optical-fiber-coupled medical swab. i | Immunofluorescence analysis of the hydrogel fibers upon incubation and reverse staining against SARS-CoV-2 (Further detailed in Supplementary Fig. IX-14). j | Exemplification of how a portion of the exposed fiber-coupled swab can be connected to a light source and derive an in-swab output for analysis. k | Output light spectra of blank (no virus) fibers as well as fibers exposed to a SARS-CoV-2 solution and an Influenza solution (H3N2). All curves represent the average from measurements of 4 individual fibers. l | Normalized light intensity (700 nm) values of the blank (no virus) fibers as well as fibers exposed to a SARS-CoV-2 solution and an Influenza solution (H3N2). Statistical analysis was performed by ordinary one-way ANOVA, * $p < 0.05$, ns – not significant.

We then interrogated the detection of full viral structures using the antibody/virus affinity (Supplementary Fig. IX-13). We interfaced optical hydrogel fibers with medical swabs employed in standard sample collection, adding a layer of positive/negative *in situ* screening (**Fig. IX-3, g, h**). SARS-CoV-2 has sizes ranging from 60 to 140 nm [37], and previous studies showed that these hydrogels have mesh sizes below 200 nm [38] that enable diffusion of viral structures of around 100 nm [25,26], compatible with SARS-CoV-2 structures. Viral capture by the hydrogel fiber was confirmed after incubating plasmonic fibers with gamma-inactivated SARS-CoV-2 for 1 hour (**Fig. IX-3, i,** Supplementary Figs. IX-14, IX-15). Further validation was done by RNA extraction and specific Loop-mediated Isothermal Amplification (LAMP), positively detecting the presence of SARS-CoV-2 RNA in the hydrogel fibers (Supplementary Fix. IX-16).

Afterwards, we exposed swab-coupled hydrogel fibers to SARS-CoV-2 positive, negative (blank), and influenza control (H3N2) solutions. Upon analysis of guided light (**Fig. IX-3, j**), we observed a similar shift to that reported for antibody-antigen events: a decrease in 700nm light intensity from ~0.6 to ~0.5 (**Fig. IX-3, k, l**). Even though a slight decrease was also seen with influenza, it was smaller in magnitude and not statistically significant. The slight variation likely derives from H3N2 viruses that might not thoroughly wash from the hydrogel, remaining there albeit in much smaller number - as these do not bind to the anti-SARS-CoV-2 Spike antibody in the surface of AuNPs.

IX.3.4. The Biofabrication of Living Optical Fibers

To take advantage of the common crosslinking and cytocompatibility of all layer materials, we investigated the continuous printing of hydrogel optical fibers (**Fig. IX-4, a**). Using a tri-coaxial 3D printing nozzle (**Fig. IX-4, b,** Supplementary Fig. IX-17), we were able to continuously spin core-clad-

shield optical fibers in a single step (**Fig. IX-4, c**). Cells were also suspended in the core precursor solution, thus being encapsulated within the light-guiding hydrogel core upon crosslinking. To confirm the cytocompatibility of the hydrogel fibers and fabrication process, a viability assay was performed, showing that 3T3 cells maintain over 80% viability within the hydrogel fiber, both immediately post-fabrication as well as after cell culture (**Fig. IX-4, d,** Supplementary Fig. IX-17). These structures represent the first living optical fibers where cells interact directly with guided light as an active optical component within the core (**Fig. IX-4, e**). Because of this interaction, optical output power decreased with increasing cell density, tested up to 10 million cells/mL (**Fig. IX-4, f, g**).

We then studied the capacity of light to transport wavelength-specific fluorophore information. Using two fluorescent markers (Orange Cell Tracker and Calcein AM), we were able to confirm their effect on the optical transmission, with dips coinciding with the marker's excitation curves (**Fig. IX-4, h, i,** Supplementary Fig. IX-18). As cells contain and express molecules that can interact with specific wavelengths of light, they create a detectable fingerprint in the optical spectra, mostly by decreasing the output intensity at the specific wavelength. These optical fingerprints represent a direct quantification of fluorescent responses happening throughout the cell-laden core, as light travels through the fiber and loses part of its energy each time it comes across with a cell. Moreover, it is possible to observe the metabolic conversion of these molecules by intracellular enzymes in real time. We demonstrated this by adding calcein-AM to the cell-laden optical fiber and tracking the gradual decrease in the calcein-specific wavelength transmission. As this compound enters living cells, it is quickly metabolized into a green-fluorescent molecule, which interacts with light creating a decrease in 495nm-level transmission as the metabolic conversion takes place (**Fig. IX-4, j**). This analysis was performed over a period of 10 minutes, to avoid fiber drying and any significant readout changes due to fluctuations in hydrogel water content.

The optical spectrum fingerprinting was then used to detect, instantly and in a single readout, the expression of proteins of interest, here modeled by transfected RFP expression, combined with the previously described real-time tracking of metabolic calcein conversion (**Fig. IX-4, k**). We performed a proof-of-concept study with distinct cancer cell lines and two model drugs (cisplatin and staurosporine) (**Fig. IX-4, l**). Fiber-optics readouts showed staurosporine's significant reduction in RFP expression (increased RFP-level transmission), as well as a drastic inhibition in the capacity of DU145 cells to metabolize calcein. On the other hand, cisplatin had little impact on both protein expression and calcein metabolism (**Fig. IX-4, m, n**). Other cell lines reported slight variations in readouts, all of which were validated through microscopy (Supplementary Figs. IX-19-21). While staurosporine is a potent inducer of

apoptosis *via* multiple pathways and protein kinase inhibition [39], cisplatin's effect is dependent on its interaction with DNA and as such more significant upon cell division [40]. Here, cells were encapsulated in a mostly inert matrix and analyzed after 48h of culture, hence the limited effect of a low-concentration anti-proliferative drug (cisplatin) *versus* a direct inducer of apoptosis (staurosporine). The fact that these responses can be recapitulated and quantified with detail in the optical fibers shows their potential for fast, accessible, and widely adaptable testing.

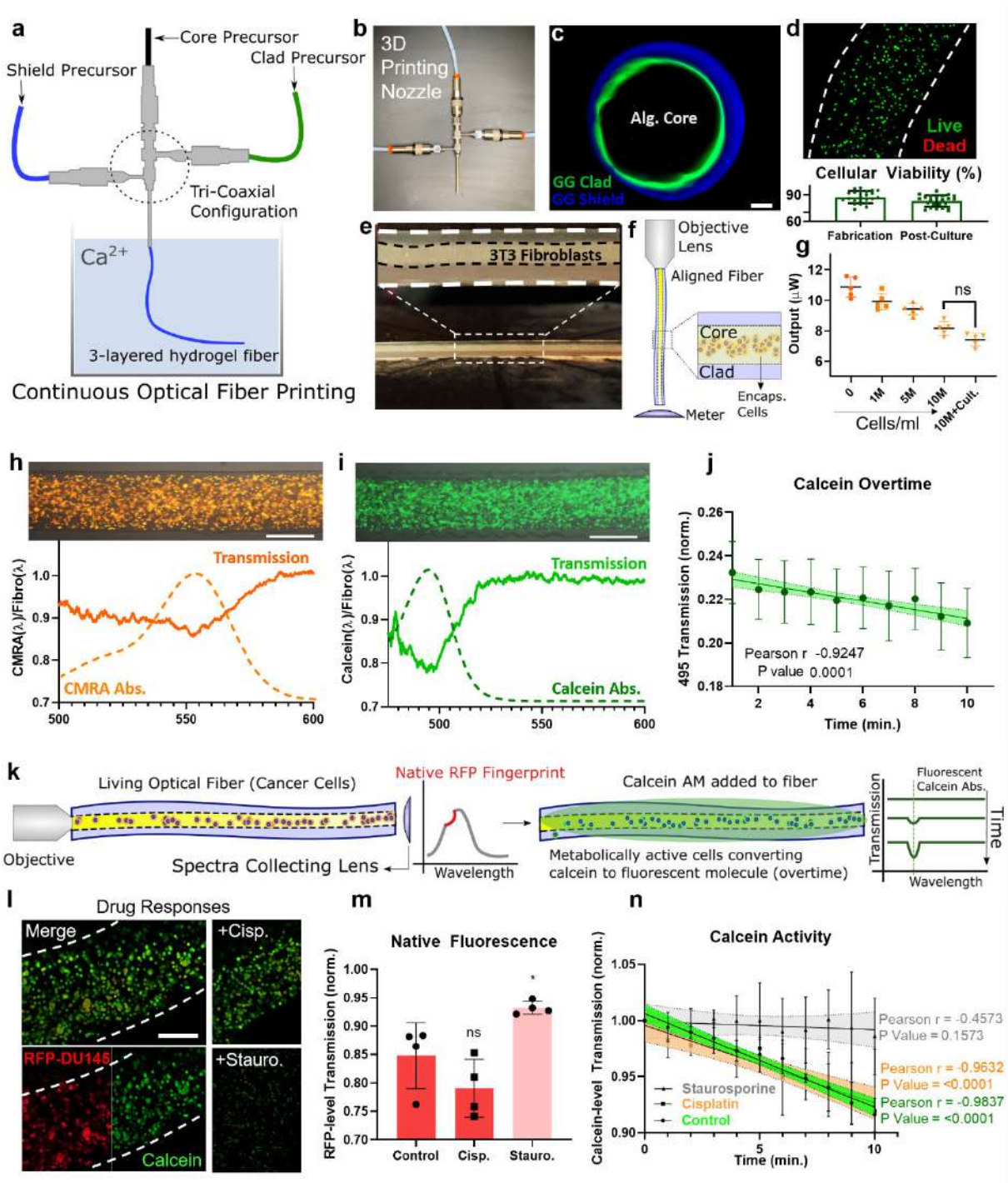


Figure IX-4: Continuous single-step printing of living hydrogel optical fibers. a | Schematic representation of the tri-coaxial 3D printing nozzle used to for continuous optical fiber printing under sterile conditions. b | Photograph of the employed 3D printing nozzle, further detailed in Supplementary Fig. IX-17. c | Microscope imaging of the fabricated fiber axial plane evidencing the successful core-clad-shield structure (hydrogels blended with different color particles). d | Live/Dead (Calcein AM/Ethidium Homodimer) assessment of 3T3 fibroblasts' viability after encapsulation in the fiber core (top) and quantification of the percentage of viable cells post-fabrication and after 5 days of culture (bottom). e | Photograph detail of a light-guiding living optical fiber with 3T3 fibroblasts encapsulated in

the core. f | Schematic representation of living optical fiber platform for the guiding and collection of optical readouts, outside of the liquid environment. g | Effect of cellular density (million cells/mL) in the output optical power, including after culture (+cult.). ns – not significant. h | Optical spectra fingerprinting of encapsulated 3T3 cells stained with orange cell tracker (CMRA), with a decrease in transmission matching the theoretical absorbance (excitation) curve of the cell tracker. CMRA(λ) represents the stained fibroblasts spectrum and Fibro (λ) the unstained fibroblast spectrum. Scale bar 500μm. i | Optical spectra fingerprinting analysis of encapsulated 3T3 cells stained with Calcein AM, evidencing a decrease in transmission matching the theoretical absorbance (excitation) curve of metabolized calcein AM. Calcein (λ) represents the stained fibroblasts spectrum and Fibro (λ) the unstained fibroblast spectrum, Scale bar 500μm. j | Real-time tracking of live-cell metabolic conversion of calcein AM to a fluorescent compound. k | Rationale behind the use of living optical fiber spectral fingerprinting to detect two simultaneous responses: immediate effect on the expression fluorescent-tagged proteins (herein modeled by RFP), combined with the addition of calcein AM solution real-time tracking of metabolic profile. l | Microscopy images of proof-of-concept tests with optical fibers encapsulating prostate cancer cell line DU145 after 48h of culture with model anti-cancer drugs (1.5μM cisplatin, 1μM Staurosporine and control media). Scale bar 200μm. m | Immediate spectral fingerprinting of RFP-level transmission *versus* culture conditions. Statistical analysis through Brown-Forsythe Anova, * $p<0.05$, ns - not significant. n | Metabolic Calcein AM profiles of cells after culture under different conditions, together with Pearson correlation statistical analysis values for each profile.

IX.3.5. Quantitative Assessment of 3D Cancer Invasive Proliferation and Drug Susceptibility

To elicit more prominent biological events in the hydrogel optical fibers, we blended a basement membrane extract with the core material encapsulating LnCAP-RFP-Trop2-OV cancer cells expressing RFP as model fluorescent protein. Upon 1 week of culture, the single cell-laden structure gradually evolved, with cancer cells proliferating and invading the surrounding matrix, leading to a fully occluded cancer core (**Fig. IX-5, a**). When cancer cells are left unchecked, they proliferate and invade their surrounding matrix and eventually take over the core forming a mature cancer fiberoid (fiber-shaped organoid) over the course of a week (**Fig. IX-5, b**). We explored this response together with light guiding and optical readouts to obtain a platform capable of directly converting 3D cancer growth into quantifiable data - the digitalization of a complex biological phenomenon by fast, non-destructive analysis (**Fig. IX-5, c**). These fibers simultaneously serve as a 3D engineered construct where cancer cells can undergo proliferative invasion (almost similarly to what happens within living tissues), and an optical platform where the amount of guided light decreases proportionally to cancer cell-driven optical core occlusion. Since one-week maturation led to fully occluded fibers, we studied the evolution of the

cancerous structure from fabrication to 5 days, both in control conditions and with increasing concentration of cisplatin (**Fig. IX-5, d**). We observed that control fibers presented gradually decreasing output light power, consequence of the cancer growth and optical core occlusion (**Fig. IX-5, e**). The lowest concentration of cisplatin (1.5μM) had no significant impact in this response, but a magnitude higher (15μM) already prevented considerable growth after 3 days, and 150μM of the drug efficiently inhibited the invasive proliferation of the cancer cells within the fiber, with optical output remaining mostly unchanged. Simultaneously with this analysis, spectral fingerprinting of RFP-level responses offered additional insight on the impact of the drugs in the model protein's expression. After 1 day of culture, a significant decrease in expression (increased RFP-level transmission) was observable in the highest cisplatin concentration (150μM), whereas the intermediate 15μM only had noticeable effect after day 3. The lowest concentration of 1.5μM, which does not seem to prevent proliferation, presented some effect in the protein expression by day 5 (**Fig. IX-5, f**).

Overall, by taking advantage of two simple metrics (optical output power and rfp-level transmission), the fiber platform can inform on the 3D growth of cancerous tissue over time, as well as on the expression of proteins of interest, herein modelled by RFP. By shining light in one end of the fiber and immediately collecting this data from the output, it is possible to observe the different biological responses within seconds and without sample destruction typically required for, *e.g.*, immunostaining and imaging. The non-destructive feature further allows to follow-up on the same samples dynamically and over time, which potentiates the study of different drugs and the discovery of inhibitory thresholds for proliferation and protein expression. This technology presents clinical potential, as patient-derived cancer biopsies can be grown and exposed to multiple drugs within these fibers. Therein, the dynamic optical quantification of responses can then inform on precision, data-driven medicine and personalized therapeutics - with higher degree of confidence *versus* current 2D platforms that are dependent on time-consuming, manual steps and analysis.

Overall, this platform enabled us to directly quantify 3D cell invasive growth and its susceptibility to different drug concentrations, pinpointing inhibitory thresholds throughout culture time. The combination of multiple fingerprinting possibilities with variations in output power potentiates tracking multiple responses from cell proliferation to protein expression. Diverse proteins can be tagged with different fluorophores and analyzed together *via* multiplexing. While several methods have been developed for assessing cancer cell invasion and proliferation, most of these rely in 2D cultures or overly time-consuming methods. Examples are scratch assays, Matrigel insert invasion, or other 3D cultures requiring extensive downstream processing [41]. Distinctly, living optical fibers technology allows

for an almost instant and directly quantifiable analysis of true 3D cancer development by optical interactions. The method is non-invasive, and fibers can be analyzed and re-cultured if sterility is maintained, allowing for the follow-up of samples and investigation of time-dependent dynamics. The simplicity and adaptability of this strategy may further be used to inform on distinct responses as specific matrix degradation, the effect of mechanical properties, other type of inhibitory molecules, or important cancer microenvironment components [42,43].

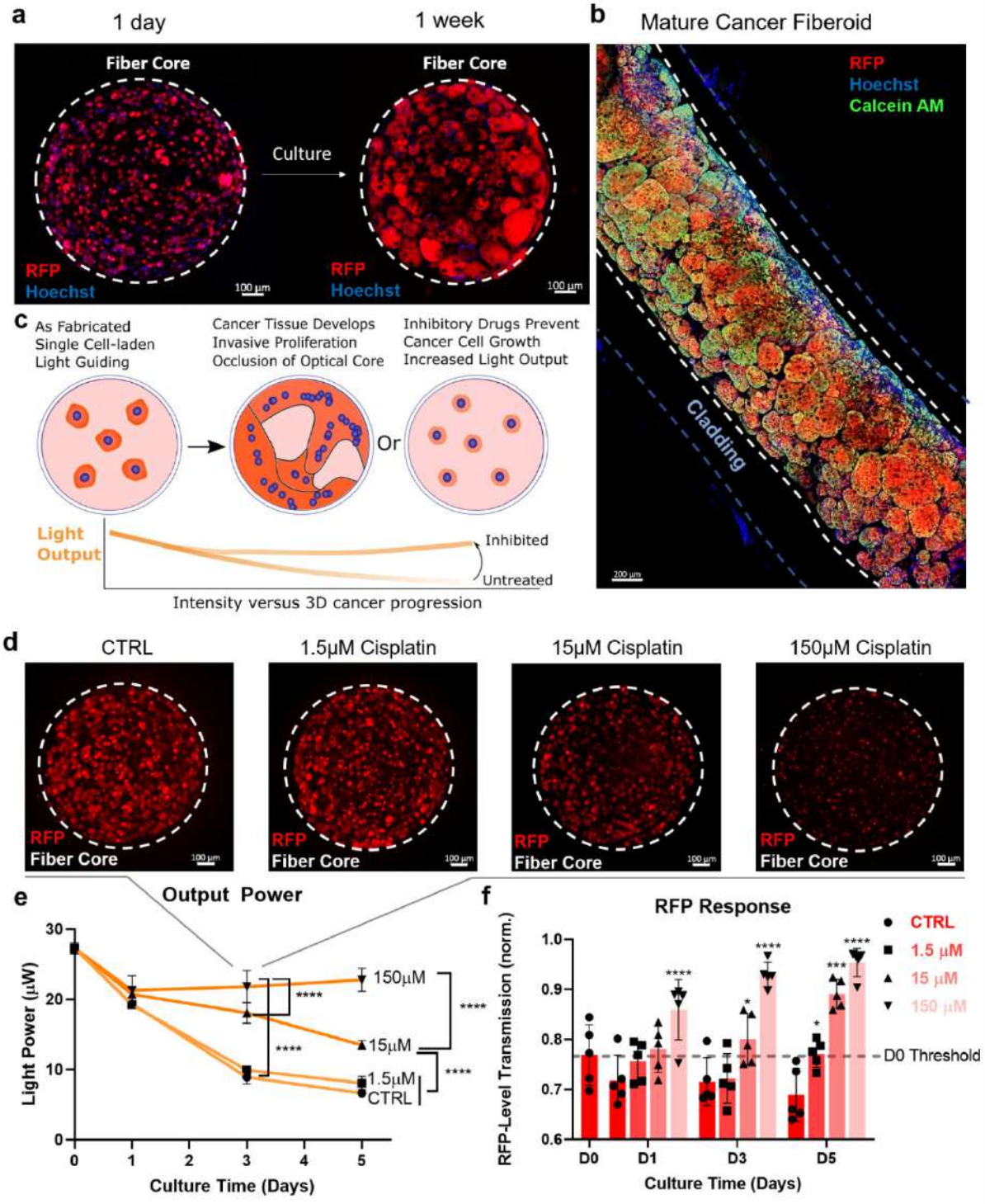


Figure IX-5: Living cancer optical fibers for the digitalization and quantification of 3D cancer growth and drug susceptibility. a | Axial view of a biolabile optical fiber core after 1 day and 1 week of culture, encapsulating LnCaP-RFP-Trop2-OV prostate cancer cells. b | Longitudinal microscope image of a fully overtaken fiber core, as unchecked cancer growth leads to the formation of a mature fiberoid (fiber-shaped organoid). c | Rationale behind the use of optical fiber output to digitalize and quantify the 3D progression of cancer within the engineered core. d | Representative snapshot of axial fiber cores at 3 days of incubation in control and varying drug

concentrations. e | Optical fiber output power as function of culture time, tracking the progress of cancer growth in fibers exposed to different drug levels evidencing a threshold of efficacy above 15μM. Statistical analysis performed through 2-way ANOVA followed by Turkey's multiple comparison test. **p<0.01, ***p<0.0001. f | RFP-level transmission in the optical fibers, reporting the expression level of model molecule RFP along time and upon different culture conditions. The RFP threshold of as-fabricated cell-laden fibers is highlighted in dashed lines. Both output power and RFP readouts are acquired instantly and simultaneously. Statistical analysis performed through multiple t-tests. *p<0.05, ***p<0.001, ****p<0.0001.

IX.4. CONCLUSIONS

The development of optical fibers has been predominately reliant on solid-state materials and static architectures. A tunable soft optical platform that can modulate light-guiding based on biocompatible materials provides a framework for a new class of optical devices, sensors, and actuators where material structure informs the optical output. We have demonstrated that ionic polysaccharides can produce flexible hydrogel fibers in continuous multi-layered architectures. Although hydrogel optical fibers have been previously reported [14–20], specific applications would benefit from more dynamic characteristics.

By a simple wet-spinning, ionic crosslinking protocol, we can provide innovative properties not reported before for optical hydrogel fibers, including (i) the first hydrogel optical fibers based solely on ionic-crosslinking, (ii) the splicing, repairing and fusion of fibers which enable (iv) the hierarchical multi-input/output optical hydrogel fiber photonic architectures, (v) high permeability that facilitates biotarget analyte detection and (vi) the continuous biofabrication of living optical fibers. These hydrogel photonic advances can be attributed to the unique manipulation of natural, cytocompatible polysaccharides and highly dynamic ionic crosslinking.

Due to the simplicity of our platform and easy adaptability to a broad range of applications, researchers may study these fibers as implantable structures on 3D constructs, organoids, or even *in vivo* tissue for multiplex detection or light delivery. Self-healing polymers may also be explored for even more dynamic structures for fiber repair without human intervention. Living optical fibers open exciting research avenues for quantifying complex 3D cellular events, where advances in protein fluorescent tagging can be combined with output power data for tracking the development of healthy and diseased tissues, drug research and functional threshold discovery, and, e.g., the optogenetic stimulation of engineered cells as molecular factories. To adapt this platform to other types of biological models and

responses, characteristics of cell/material interactions can be varied by designing new physical and biochemical hydrogel properties. This may require material changes or modifications to address different biological events than those herein studied.

On a similar note, future work may explore these hydrogel fibers for integration within living tissues. The low refractive index of the studied materials presents a good optical match for releasing light into tissues (high-water content environments) as opposed to the optical mismatch presented by higher RI materials. While advantageous for light delivery, guided distance will naturally decrease, and further strategies may be investigated if the goal is to maximize light guidance within living tissues. For that purpose, further manipulation of the hydrogel core composition will be required, *e.g.*, by combining the ionic-crosslinking polysaccharides with other molecules or interpenetrating hydrogel networks. These strategies may further increase refractive index values while maintaining the biological compatibility of the fibers. This type of approach will also open possibilities for multi-responsive structures, where the new components added to the fiber may enable different functionalities such as electroconductivity or magnetic susceptibility, *i.e.*, important properties to stimulate tissues and organs.

Overall, ionic polysaccharide hydrogel fibers may lead to disruptive opportunities for flexible, soft, cost-effective, and straightforward photonic constructs that efficiently complement their solid-state counterparts with unprecedented possibilities in applications. Overall, ionic polysaccharide hydrogel fibers may lead to disruptive opportunities for flexible, soft, cost-effective, and straightforward photonic constructs that efficiently complement their solid-state counterparts with unprecedented application possibilities.

IX.5. REFERENCES

1. Lin, C. In memory of Charles Kao. *Nat. Photonics* **12**, 715–717 (2018).
2. DeCusatis, C. *Handbook of Fiber Optic Data Communication*. *Handbook of Fiber Optic Data Communication* (2008). doi:10.1016/B978-0-12-374216-2.X5001-7
3. Palais, J. C. Optical communication: Long distance fiber optic communications. in *Broadcasting and Optical Communication Technology* (2017). doi:10.1201/9781420003116
4. Yablon, A. D. *Optical Fiber Fusion Splicing*. *Optical Fiber Fusion Splicing* (Springer, 2005). doi:10.1007/b137759
5. Šulc, J. & Jelínková, H. *Solid-state lasers for medical applications*. *Lasers for Medical Applications: Diagnostics, Therapy and Surgery* (Woodhead Publishing Limited, 2013). doi:10.1533/9780857097545.2.127
6. Taffoni, F., Formica, D., Saccomandi, P., Di Pino, G. & Schena, E. Optical fiber-based MR-compatible sensors for medical applications: An overview. *Sensors (Switzerland)* **13**, 14105–14120 (2013).
7. Fermann, M. E. & Hartl, I. Ultrafast fiber lasers. *Nat. Photonics* **7**, 868–874 (2013).
8. Xu, C. & Wise, F. W. Recent advances in fiber lasers for nonlinear microscopy. *Nat. Photonics* **7**, 875–882 (2013).

9. Gallego, D. & Lamela, H. High-sensitivity ultrasound interferometric single-mode polymer optical fiber sensors for biomedical applications. *Opt. Lett.* **34**, 1807 (2009).

10. Nizamoglu, S., Gather, M. C. & Yun, S. H. All-biomaterial laser using vitamin and biopolymers. *Adv. Mater.* **25**, 5943–5947 (2013).

11. Haufová, P., Knejzlík, Z., Hanuš, J., Zadražil, A. & Štěpánek, F. Reversible buckling and diffusion properties of silica-coated hydrogel particles. *J. Colloid Interface Sci.* **357**, 109–115 (2011).

12. Guimarães, C. F., Ahmed, R., Marques, A. P., Reis, R. L. & Demirci, U. Engineering Hydrogel-Based Biomedical Photonics: Design, Fabrication and Applications. *Adv. Mater.* (2021). doi:10.1002/adma.202006582.

13. Guimarães, C. F., Gasperini, L., Marques, A. P. & Reis, R. L. The stiffness of living tissues and its implications for tissue engineering. *Nat. Rev. Mater.* **5**, 351–370 (2020).

14. Feng, J. *et al.* Printed Degradable Optical Waveguides for Guiding Light into Tissue. *Adv. Funct. Mater.* **2004327**, 1–14 (2020).

15. Elsherif, M., Hassan, M. U., Yetisen, A. K. & Butt, H. Hydrogel optical fibers for continuous glucose monitoring. *Biosens. Bioelectron.* **137**, 25–32 (2019).

16. Zhou, M., Guo, J. & Yang, C. Ratiometric fluorescence sensor for Fe3+ ions detection based on quantum dot-doped hydrogel optical fiber. *Sensors Actuators, B Chem.* **264**, 52–58 (2018).

17. Yetisen, A. K. *et al.* Glucose-Sensitive Hydrogel Optical Fibers Functionalized with Phenylboronic Acid. *Adv. Mater.* **29**, (2017).

18. Choi, M., Humar, M., Kim, S. & Yun, S. H. Step-Index Optical Fiber Made of Biocompatible Hydrogels. *Adv. Mater.* **27**, 4081–4086 (2015).

19. Choi, M. *et al.* Light-guiding hydrogels for cell-based sensing and optogenetic synthesis in vivo. *Nat. Photonics* **7**, 987–994 (2013).

20. Guo, J. *et al.* Highly Stretchable, Strain Sensing Hydrogel Optical Fibers. *Adv. Mater.* **28**, 10244–10249 (2016).

21. Onoe, H. *et al.* Metre-long cell-laden microfibers exhibit tissue morphologies and functions. *Nat. Mater.* **12**, 584–590 (2013).

22. Guimarães, C. F. *et al.* High-throughput fabrication of cell-laden 3D biomaterial gradients. *Mater. Horiz.* **7**, 2414–2421 (2020).

23. Lee, K. Y. & Mooney, D. J. Alginate: Properties and biomedical applications. *Prog. Polym. Sci.* **37**, 106–126 (2012).

24. Oliveira, J. T. *et al.* Gellan gum: A new biomaterial for cartilage tissue engineering applications. *J. Biomed. Mater. Res. - Part A* **93**, 852–863 (2010).

25. Tran, N. M. *et al.* An appropriate selection of a 3d alginate culture model for hepatic Huh-7 cell line encapsulation intended for viral studies. *Tissue Eng. - Part A* **19**, 103–113 (2013).

26. Madrigal, J. L., Shams, S., Stilhano, R. S. & Silva, E. A. Characterizing the encapsulation and release of lentivectors and adeno-associated vectors from degradable alginate hydrogels. *Biomater. Sci.* **7**, 645–656 (2019).

27. Carpenter, A. E. *et al.* CellProfiler: Image analysis software for identifying and quantifying cell phenotypes. *Genome Biol.* **7**, (2006).

28. Hsu, E. C. *et al.* Trop2 is a driver of metastatic prostate cancer with neuroendocrine phenotype via PARP1. *Proc. Natl. Acad. Sci. U. S. A.* **117**, 2032–2042 (2020).

29. Lee, H. P., Gu, L., Mooney, D. J., Levenston, M. E. & Chaudhuri, O. Mechanical confinement regulates cartilage matrix formation by chondrocytes. *Nat. Mater.* **16**, 1243–1251 (2017).

30. Shin, H., Olsen, B. D. & Khademhosseini, A. The mechanical properties and cytotoxicity of cell-laden double-network hydrogels based on photocrosslinkable gelatin and gellan gum biomacromolecules. *Biomaterials* **33**, 3143–3152 (2012).

31. Poole, S. B. P., Payne, D. N. & Fermann, M. E. Fabrication Of Low-Loss Optical Fibers Containing Rare-Earth Ions. *Electron. Lett.* **21**, 737–738 (1985).

32. Bao, Y. *et al.* The redshift of surface plasmon resonance of colloidal gold nanoparticles induced by pressure with diamond anvil cell. *J. Appl. Phys.* **115**, (2014).

33. Tokarev, I., Tokareva, I. & Minko, S. Gold-nanoparticle-enhanced plasmonic effects in a responsive polymer gel. *Adv. Mater.* **20**, 2730–2734 (2008).

34. Björck, L. & Kronvall, G. Purification and some properties of streptococcal protein G, a novel IgG-binding reagent. *J. Immunol.* **133**, 969–74 (1984).

35. Ahmed, R. *et al.* Tunable Fano-Resonant Metasurfaces on a Disposable Plastic-Template for Multimodal and Multiplex Biosensing. *Adv. Mater.* **1907160**, 1–11 (2020).

36. Chi, X. *et al.* A neutralizing human antibody binds to the N-terminal domain of the Spike protein of SARS-CoV-2. *Science (80-.).* **369**, 650–655 (2020).

37. Zhu, N. *et al.* A novel coronavirus from patients with pneumonia in China, 2019. *N. Engl. J. Med.* **382**, 727–733 (2020).

38. Gasperini, L., Mano, J. F. & Reis, R. L. Natural polymers for the microencapsulation of cells. *J. R. Soc. Interface* **11**, 20140817–20140817 (2014).

39. Belmokhtar, C. A., Hillion, J. & Ségal-Bendirdjian, E. Staurosporine induces apoptosis through both caspase-dependent and caspase-independent mechanisms. *Oncogene* **20**, 3354–3362 (2001).

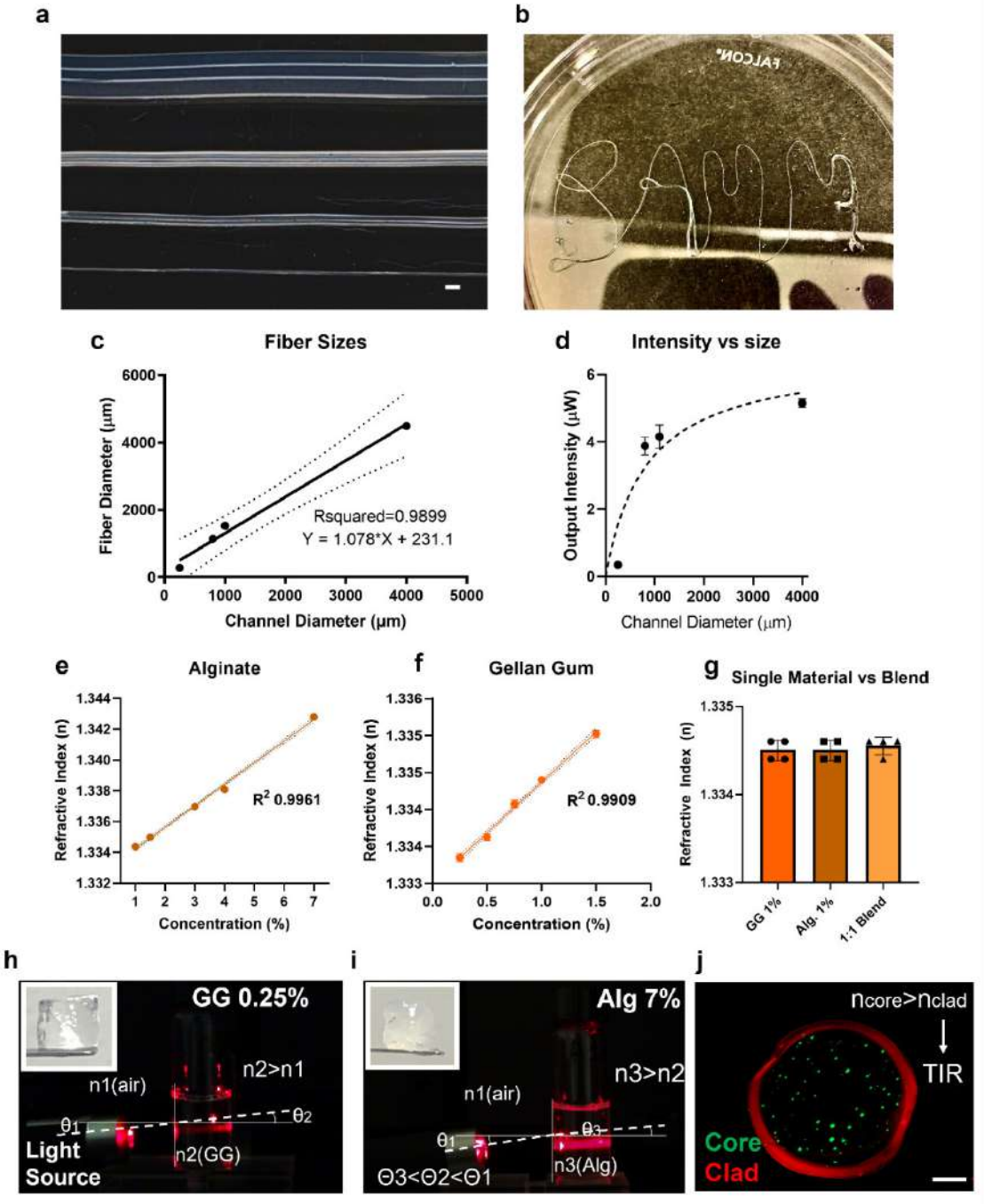
40. Alderden, R. A., Hall, M. D. & Hambley, T. W. The discovery and development of cisplatin. *J. Chem. Educ.* **83**, 728–734 (2006).

41. Moutasim, K. A., Nystrom, M. L. & Thomas, G. J. Cell Migration and Invasion Assays. in *Cancer Cell Culture: Methods and Protocols* (ed. Cree, I. A.) 333–343 (Humana Press, 2011). doi:10.1007/978-1-61779-080-5_27

42. Carvalho, P. D. *et al.* KRAS oncogenic signaling extends beyond cancer cells to orchestrate the microenvironment. *Cancer Res.* **78**, 7–14 (2018).

43. Hanahan, D. & Weinberg, R. A. Hallmarks of cancer: The next generation. *Cell* **144**, 646–674 (2011).

IX.6. SUPPLEMENTARY MATERIAL



Supplementary Figure IX-1: Tunable Core Size Diameter (a) and fiber flexibility at low dimensions (b). Fiber size as a function of flowing channel diameter (c). Output Fiber intensity of full cladded fibers at 10 cm with different core diameters (d), where the collected light at decreased dimensions leads to weaker output. Alginate refractive index as a function of concentration (wt%) (e). Gellan Gum refractive index as a function of concentration (wt%) (f). Comparison of the refractive indexes of Alginate 1wt%, Gellan Gum 1wt%, and a 1:1 blend of both solutions (g). Representation of the interaction of the 0.25% Gellan Gum (h) and 7% Alginate (i) solutions with light, where a change in light angle is

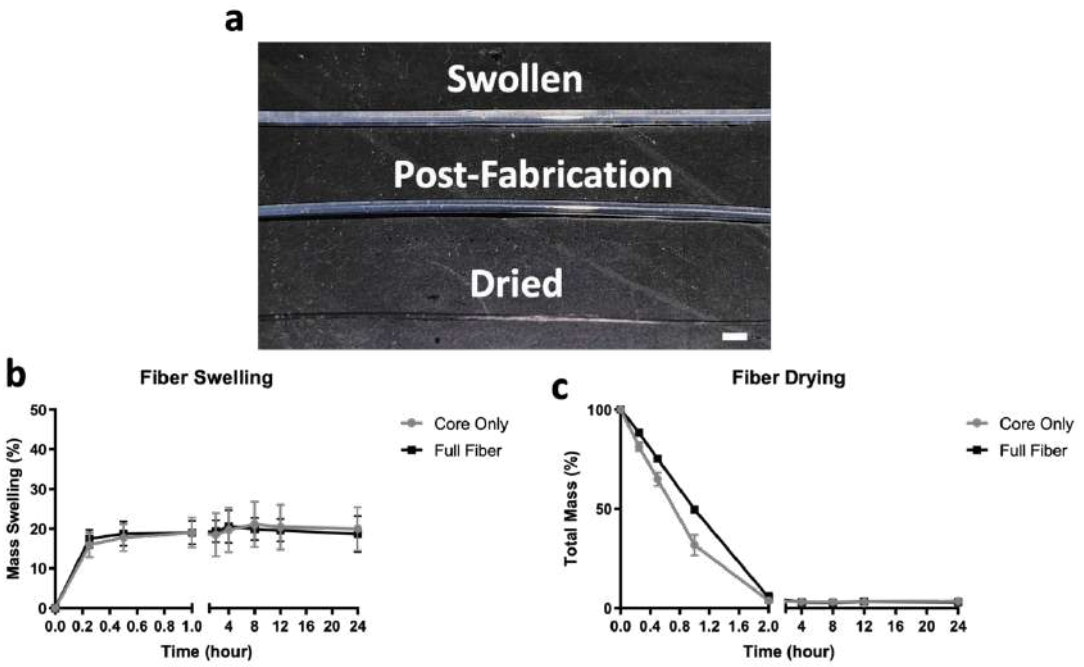
evidence of increasing refractive index. Photographs of each type of hydrogel in a standard cylindrical shape can be observed in the upper left corners. Microscopic image of a transversal fiber cut (j), demonstrating the two hydrogels' layering structure (core stained with green micrometer-sized beads, clad with nile red-fluorescent particles). Scale bar: 200 µm.

Supplementary Table IX-1: Preliminary core-clad and core-clad-shield tests with varying polymer concentrations and visually detectable light guiding distances.

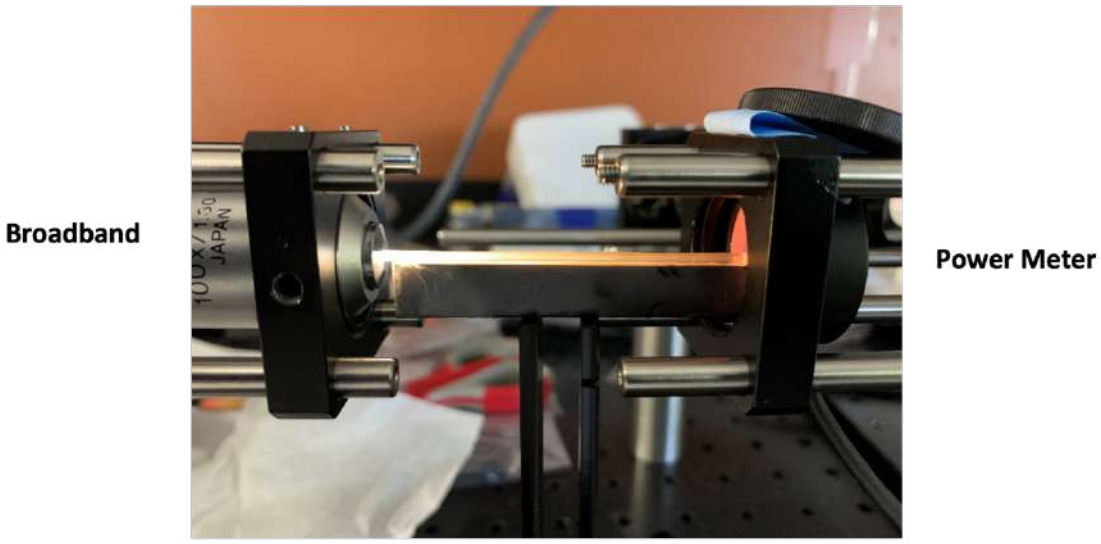
Core	Clad	Shield	Visible Light Output (cm)
GG 1%	NA	NA	4
Alg 2%	NA	NA	4.5
Alg 2%	GG 1%	NA	7
GG 1%	Alg 2%	NA	6
GG 1.5%	Alg 1%	NA	10
GG 1.5%	Alg 1.5%	Alg 1%	9
Alg 2%	Alg 1%	NA	10
Alg 2%	Alg 1.5%	Alg 1%	9
Alg 2%	GG 0.5%	NA	12
Alg 4%	GG 0.25%	Alg 2%	14
Alg 7%	GG 0.25%	Alg 2%	19

Supplementary Table IX-2: Preliminary gradient-index tests with varying polymer concentrations and visually detectable light guiding distances.

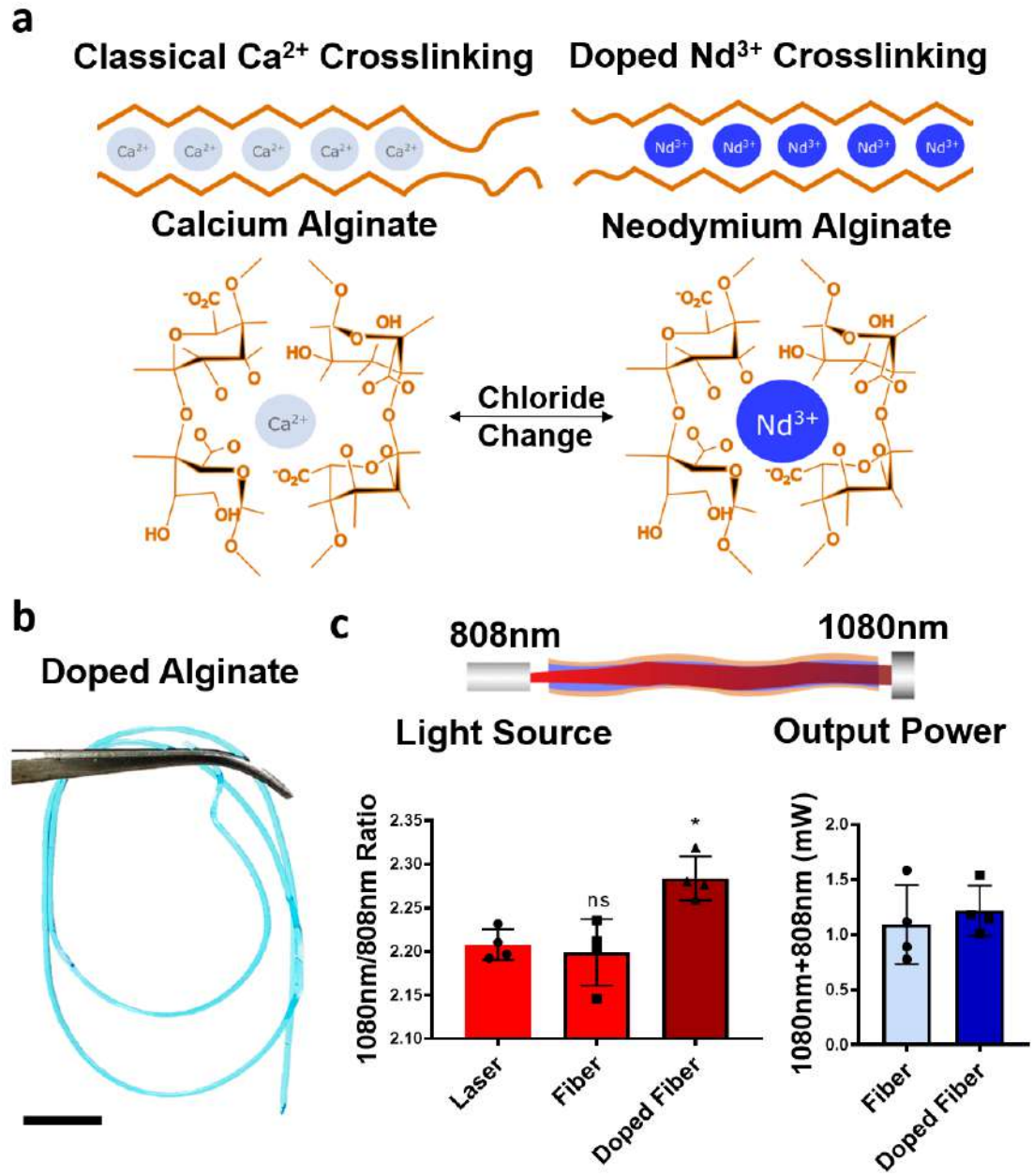
Core	Clad1	Clad2	Clad3	Visible Light Output (cm)
Alg 2%	Alg 1.5%	Alg 1%	NA	11 cm
Alg 3%	Alg 2%	Alg 1%	NA	10cm
Alg 3%	Alg 2%	Alg 1.5%	NA	11 cm
Alg 4%	Alg 2%	Alg 1.5%	Alg 1%	12 cm
Alg 3%	Alg 2%	Alg 1.5%	Alg 1%	16 cm



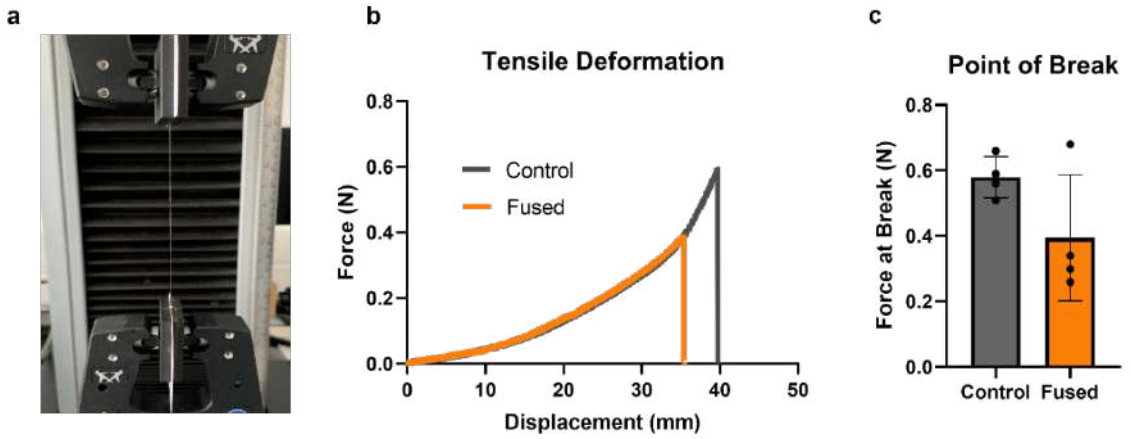
Supplementary Figure IX-2: Comparison of fibers as fabricated, swollen and dried (a), together with the swelling (b) and drying (c) quantitative data over a period of 24h for both core only and full core-clad-shield fibers. Scale bar: 1mm.



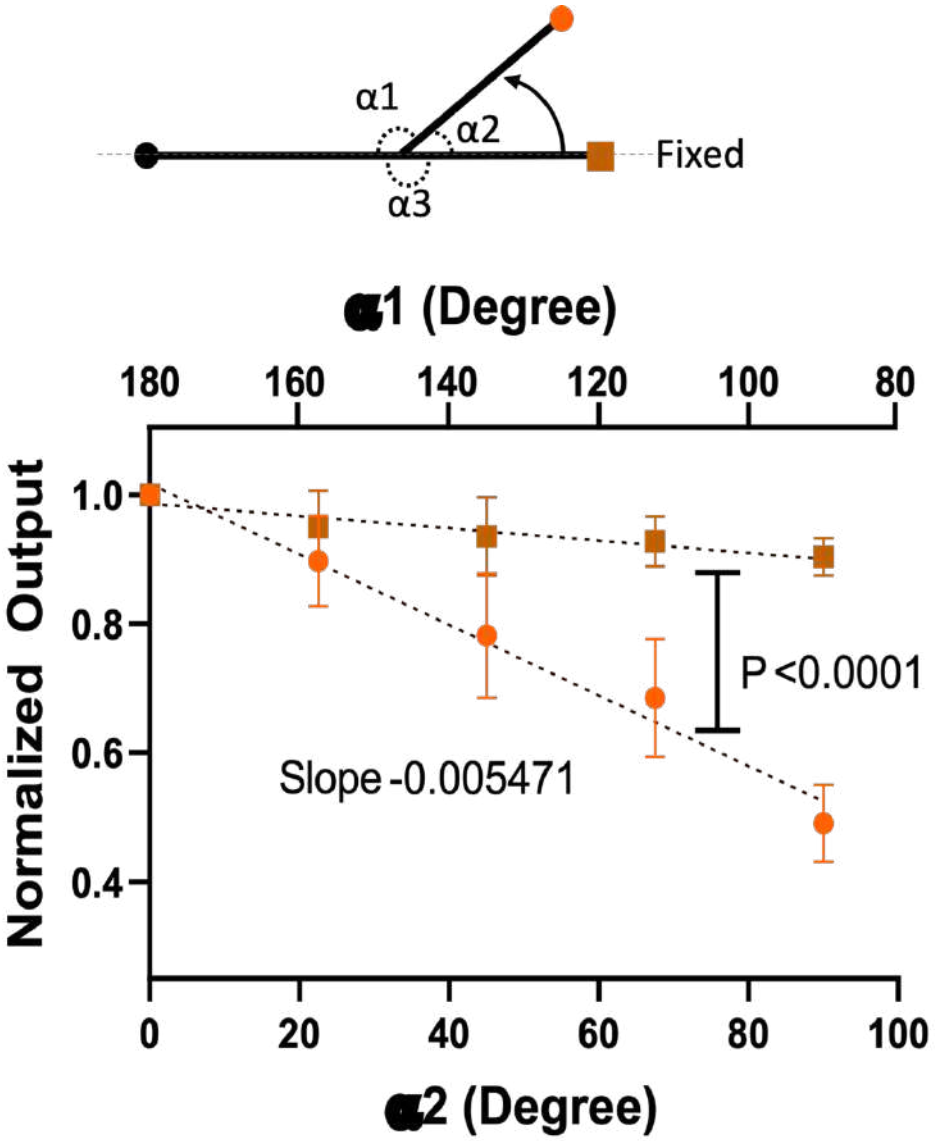
Supplementary Figure IX-3: Photograph of the setup used for Power Meter quantification of light output power.



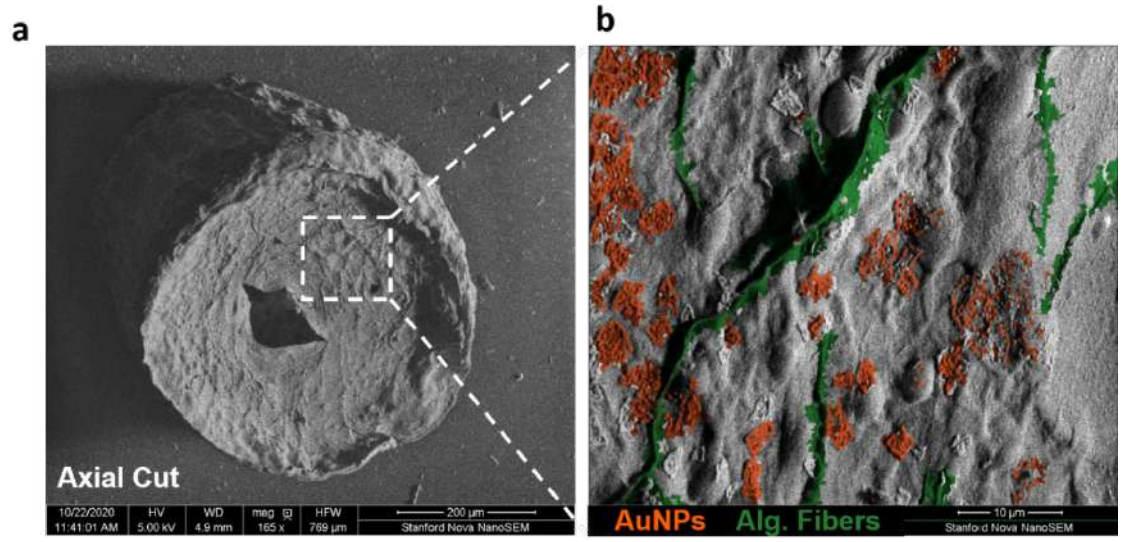
Supplementary Figure IX-4: a | Rationale behind the ion changes for fabricating neodymium-doped alginate hydrogel fibers b | Photograph of a Neodymium: Alginate fiber stained with blue soluble dye. Scale bar: 1cm. c | Doping behavior evaluation setup (top) as used to obtain output ratio (bottom left, 1080nm/808nm) and total output power (bottom right, 1080nm+808nm) [5]. Statistical comparison was performed through Kruskall-Walis multiple comparison test. * $p < 0.05$, ns - not significant.



Supplementary Figure IX-5: a| Photograph of a fused hydrogel fiber undergoing tensile deformation. b | Force/Displacement curves for control fibers (as spun) and fused fibers (following the split fusion protocol). c | Force at break values for different replicates of control fibers and fused fibers, evidencing around 60-70% of mechanical joint recovery, on average values.



Supplementary Figure IX-6: Quantification of the double-output system intensities with one fixed arm and a second one gradually moving away with increasing angle in relation to the common input branch (as schematized on the top).



Supplementary Figure IX-7: a | SEM image of an axial cut of the hydrogel fiber and b | Higher magnification of the cut surface evidencing the presence of 100nm AuNPs throughout the fiber surface with varying proximity and random distribution. Particles and visible fibrous alginate structures were artificially colored orange and green, respectively.

Supplementary Equations for deriving the effect and relationship between gold resonance transmission and absorption.

For the Blank Fiber:

$$I_B(\lambda) = I_{bulb}(\lambda) \times H_{Fiber}(\lambda) \text{ (1)}$$

For the AuNP Embedded Fiber:

$$I_{AuNP}(\lambda) = I_{bulb}(\lambda) \times H_{Fiber}(\lambda) \times T_{AuNP}(\lambda) \text{ (2)}$$

$$T_{AuNP} = 1 - A_{AuNP}(\lambda) \text{ (3)}$$

$$\Rightarrow I_{\mathrm{B}}(\lambda) - \mathrm{I_{AuNP}}(\lambda) = I_{bulb}(\lambda) \times H_{Fiber}(\lambda) \times A_{AuNP}(\lambda) \text{ (4)}$$

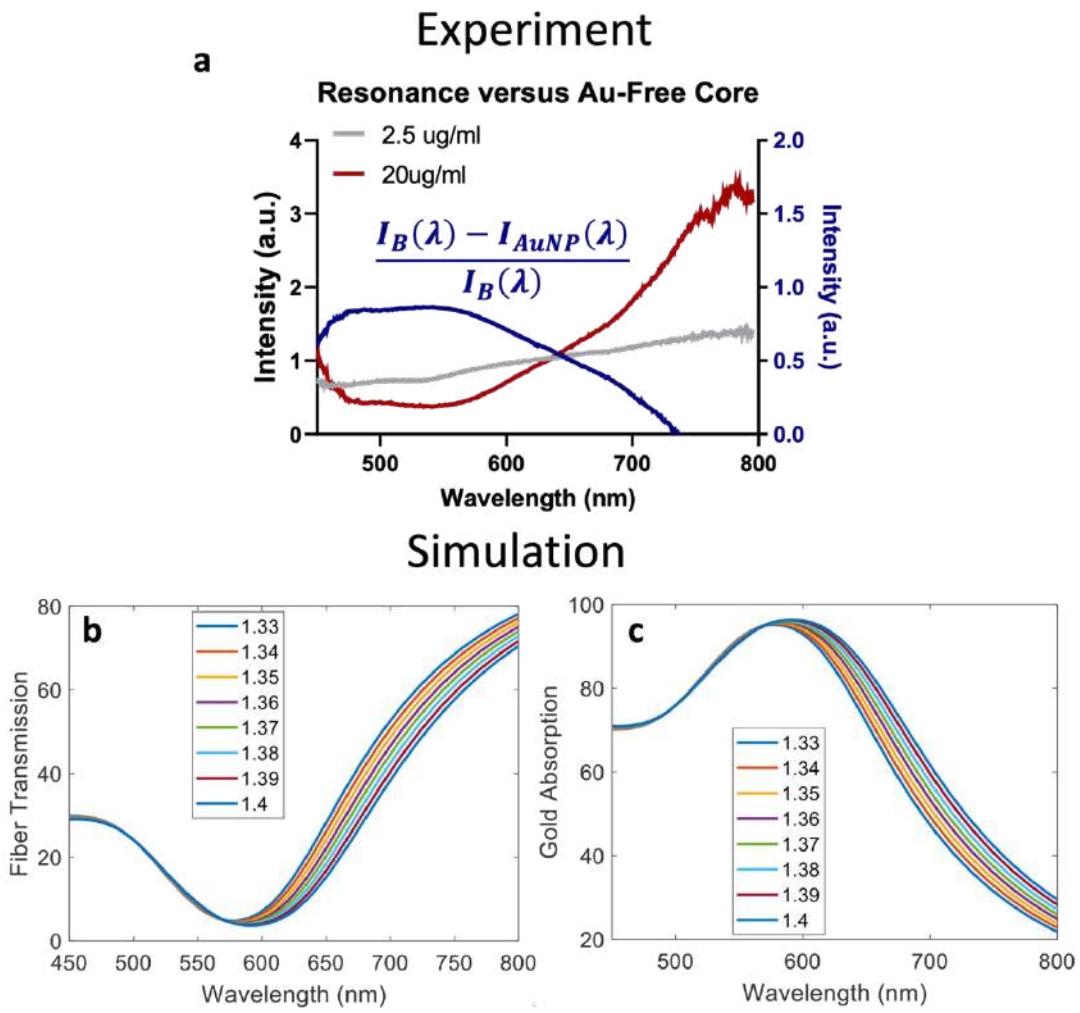
$$A_{AuNP}(\lambda) = \frac{\mathrm{I_B}(\lambda) - I_{AuNP}(\lambda)}{I_B(\lambda)} \text{ (5)}$$

$I_B(\lambda)$: Transmission Spectra of the Blank Fiber

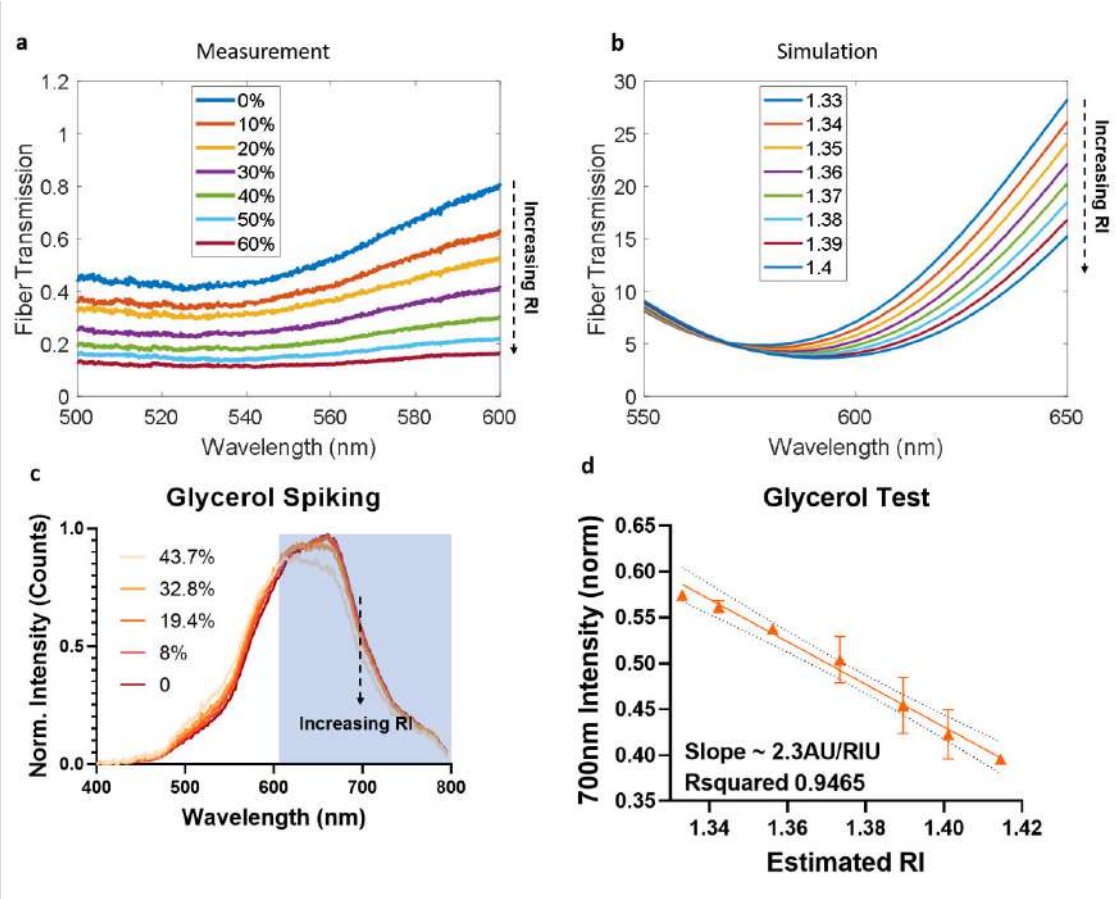
$I_{AuNP}(\lambda)$:Transmission Spectra of the Gold Embedded Fiber

$T_{AuNP}(\lambda)$: Transmission Spectra of Gold Nanoparticles

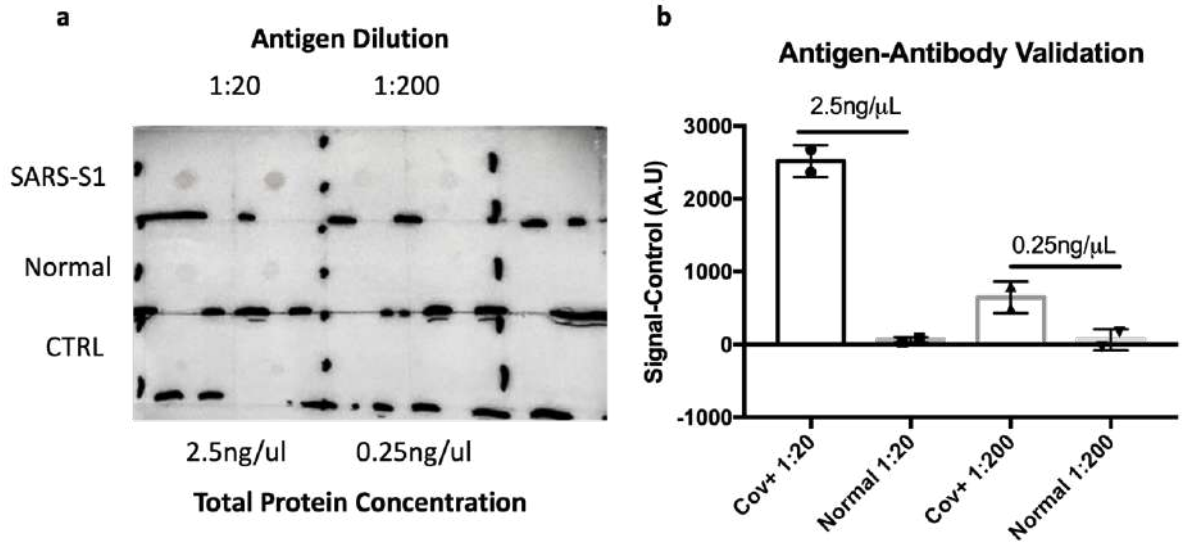
$A_{AuNP}(\lambda)$: Absorption Spectra of Gold Nanoparticles



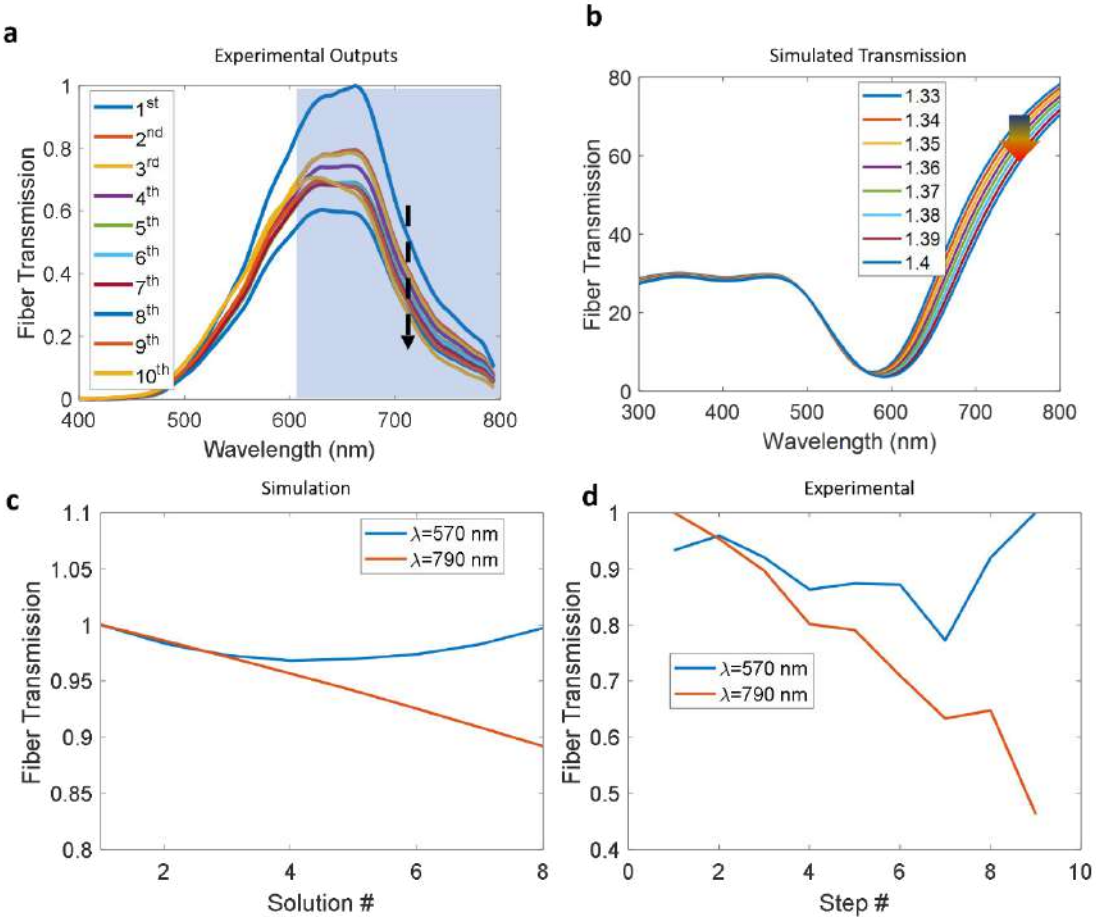
Supplementary Figure IX-8: a | Experimental curves obtained by normalizing AuNP-fiber spectra to empty fiber spectra, representing the gold transmission or, reversely, absorbance (blue). b | Spectra obtained by computational simulation of 100nm gold plasmonic resonance transmission. c | Spectra obtained by computational simulation of 100nm gold plasmonic resonance absorption.



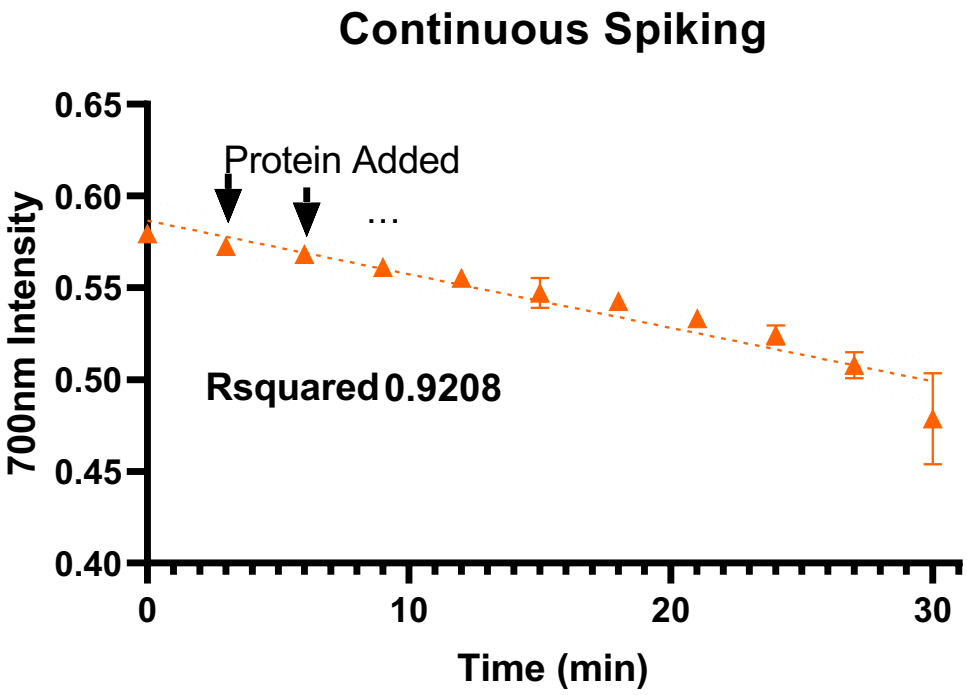
Supplementary Figure IX-9: a | Transmission curves obtained with gradual adition of glycerol solutions of increasing concentration. Curves represent the normalization between AuNP fibers and empty fibers (to derive the resonance-induced effect in transmission. b | Zoomed-in detail of the simulated 100nm gold transmission changes with similar refractive index variation. Of note, in the case of the optical fiber (a), the wavelength change is accompanied by a significant reduction in amplitude by the effect on the environmental refractive index and loss of guided light, which does not happen in the gold-only simulation. c | Resulting output spectra of a range of some glycerol concentrations, where the normalized curves as directly obtained from the spectrometer reflect the consequence of resonance changes leading to a decrease in over-600nm intensities. d | Light intensity (700nm) values of output spectra with gradual spiking of glycerol to higher concentrations and consequent refractive index variations.



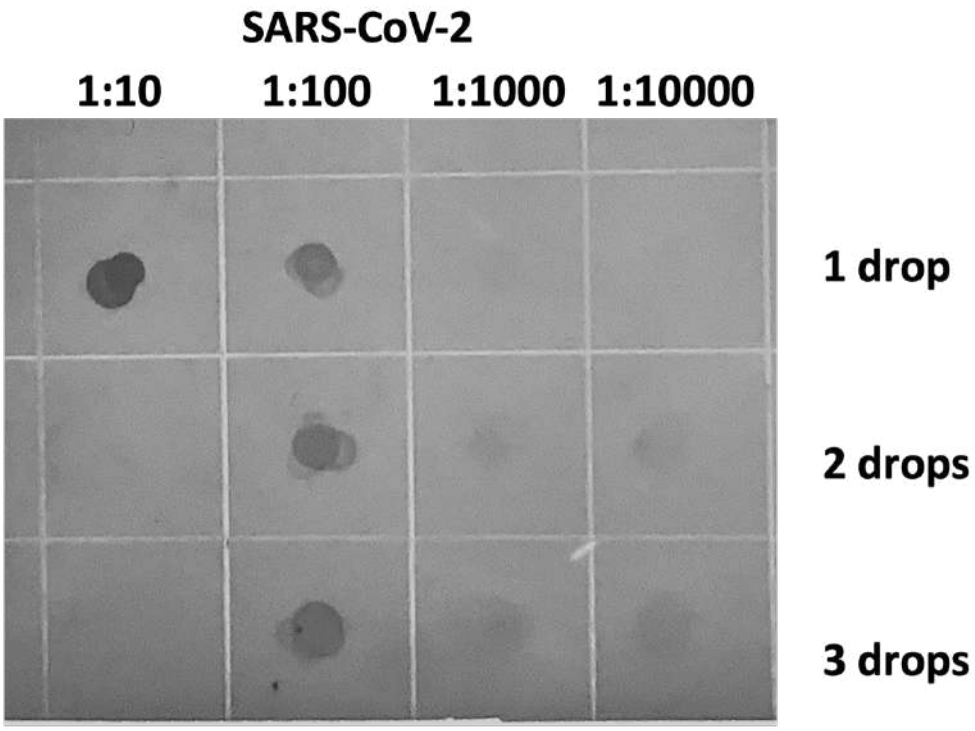
Supplementary Figure IX-10: Dot-blot validation of the Antigen/Antibody affinity (a) and relative quantification data (b). SARS-S1: Supernatant with SARS-Spike antigen, Normal: Normal Supernatant, Control: Normal without first antibody incubation. An intermediate dilution of 1:40 was then used for detection in the optical fibers.



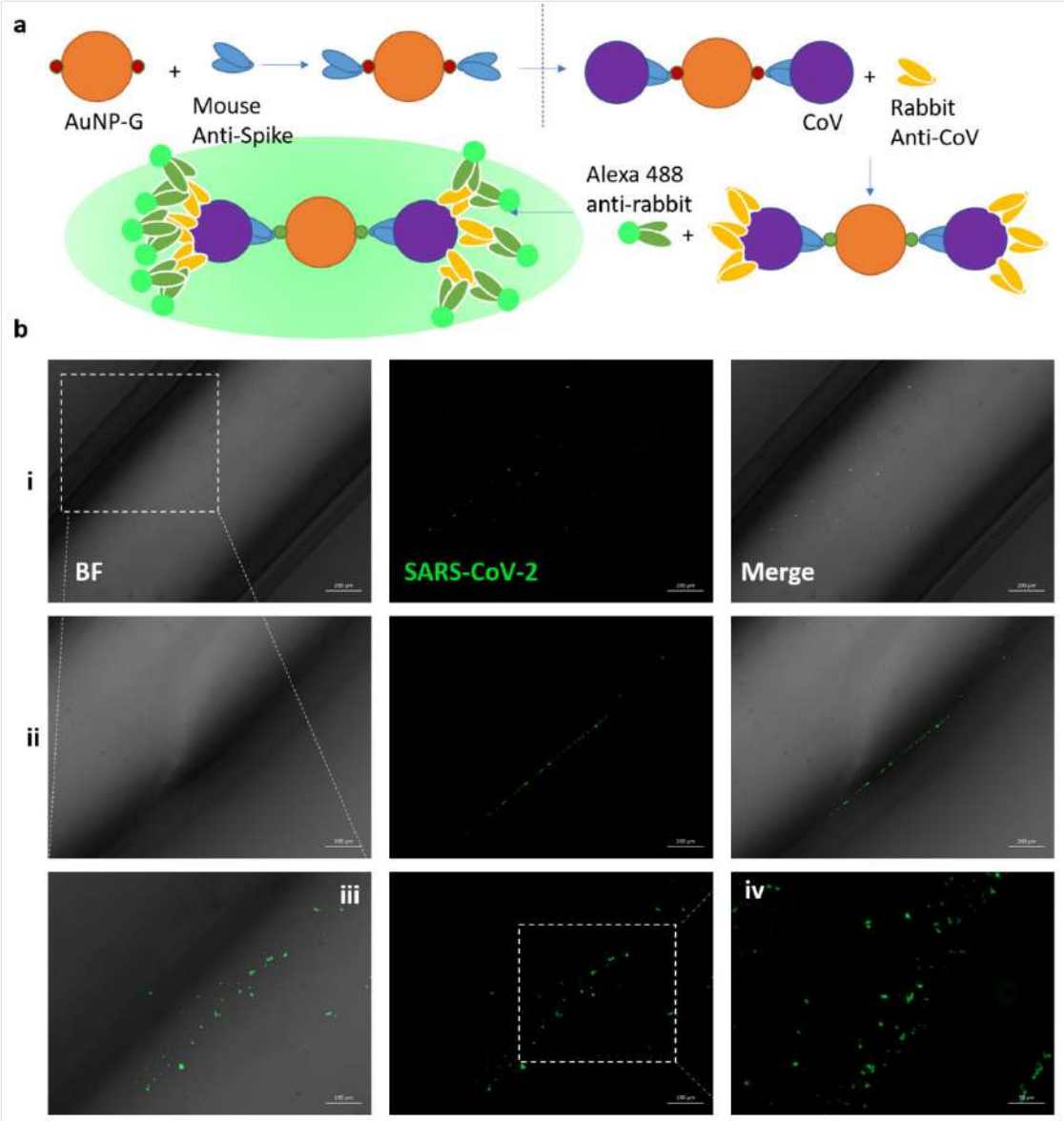
Supplementary Figure IX-11: a | Optical fiber output curves with stepwise addition of SARS-CoV-2 antigen solutions with a total of 10ng protein. b | Simulated spectra of 100nm AuNP plasmonic resonance transmission with changes in refractive index, evidencing that the most significant variations happen after 600nm, c | Simulation of the intensity variation with increasing added protein below 600nm (570 example) and above 600nm (790 example). d | Experimental Intensity values for the same wavelengths, evidencing a similar response to that simulated for 100nm gold AuNPs.



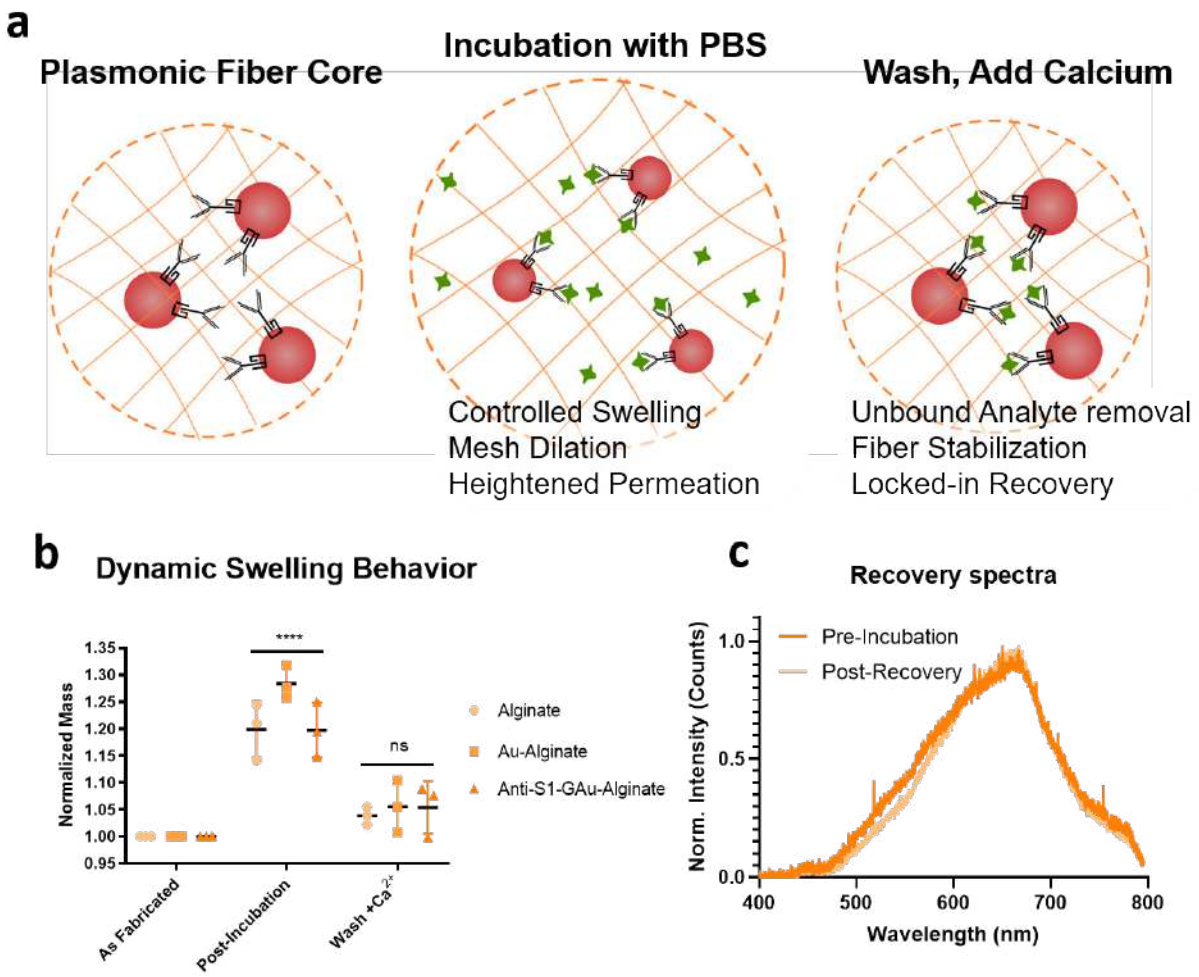
Supplementary Figure IX-12: 700nm intensity variation over time (each measurement represents the addition of ~10ng of protein solution). A linear decrease in 700nm intensity is observed, the parameter used in the main text to detect the binding of targets.



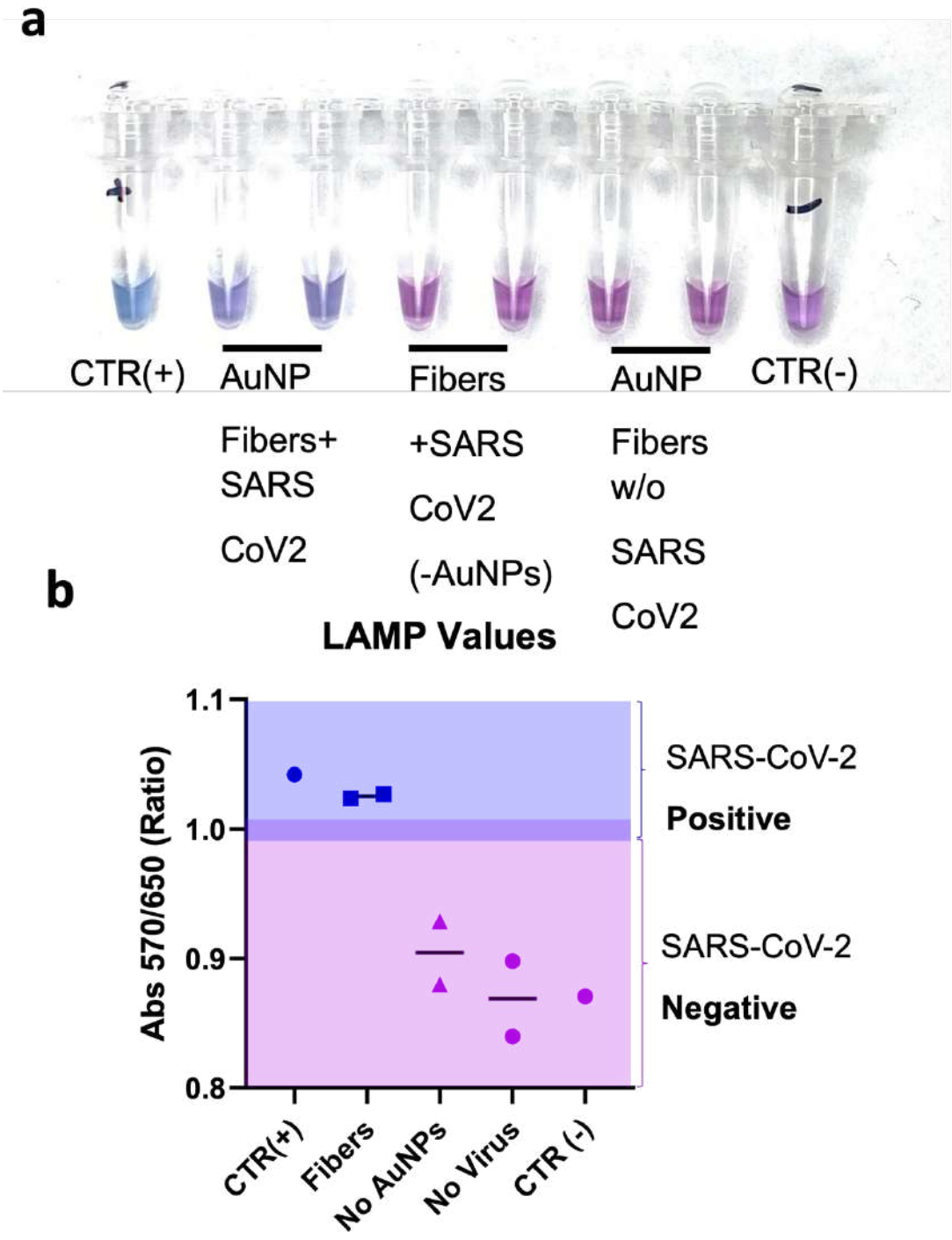
Supplementary Figure IX-13: Dot-blot validation of the antigen-virus interaction. Different Dilutions of the SARS-CoV-2 virus were tested. 1:1000 was used as working dilution as it was the minimum detectable concentration with 1 single drop dot.



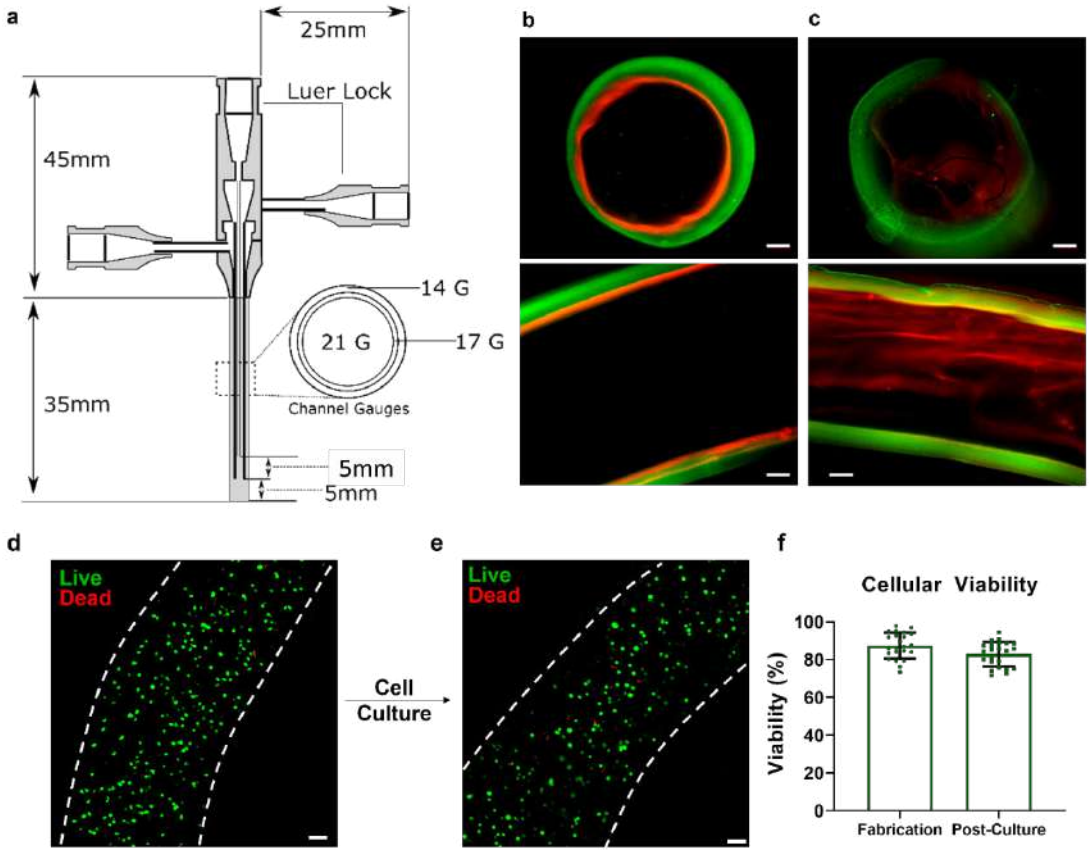
Supplementary Figure IX-14: Schematic representation of the reverse-immuno protocol used to stain and amplify the signal derived from SARS-CoV-2 bound to gold NPs within the fiber (a). Supplementary immunofluorescence figures of the virus within hydrogel fiber both at central (i) and edge (ii) core positions, as well as higher magnification details (iii, iv).



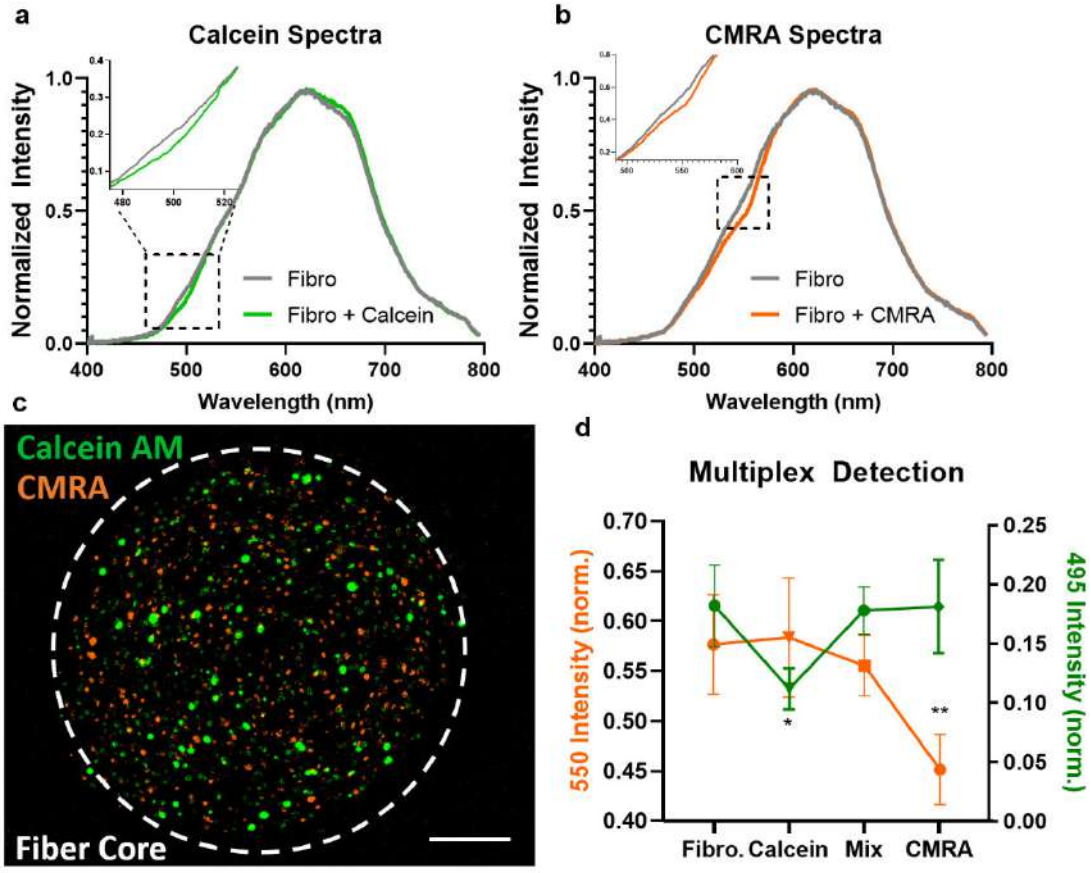
Supplementary Figure IX-15: a | Rationale behind the dynamic swelling behavior of fibers, where a controlled swelling takes place during PBS incubation facilitating molecule permeation, and recovery after washing in the presence of calcium. b | Fiber mass variation after incubation and upon washing with calcium, evidencing the recovery of the hydrogel mesh. c | Output spectra of AuNP-fibers after incubation and post-recovery, showing a similar profile validating that the gold-antibody-antigen complexes are maintained within the fiber structure and not loss during incubation.



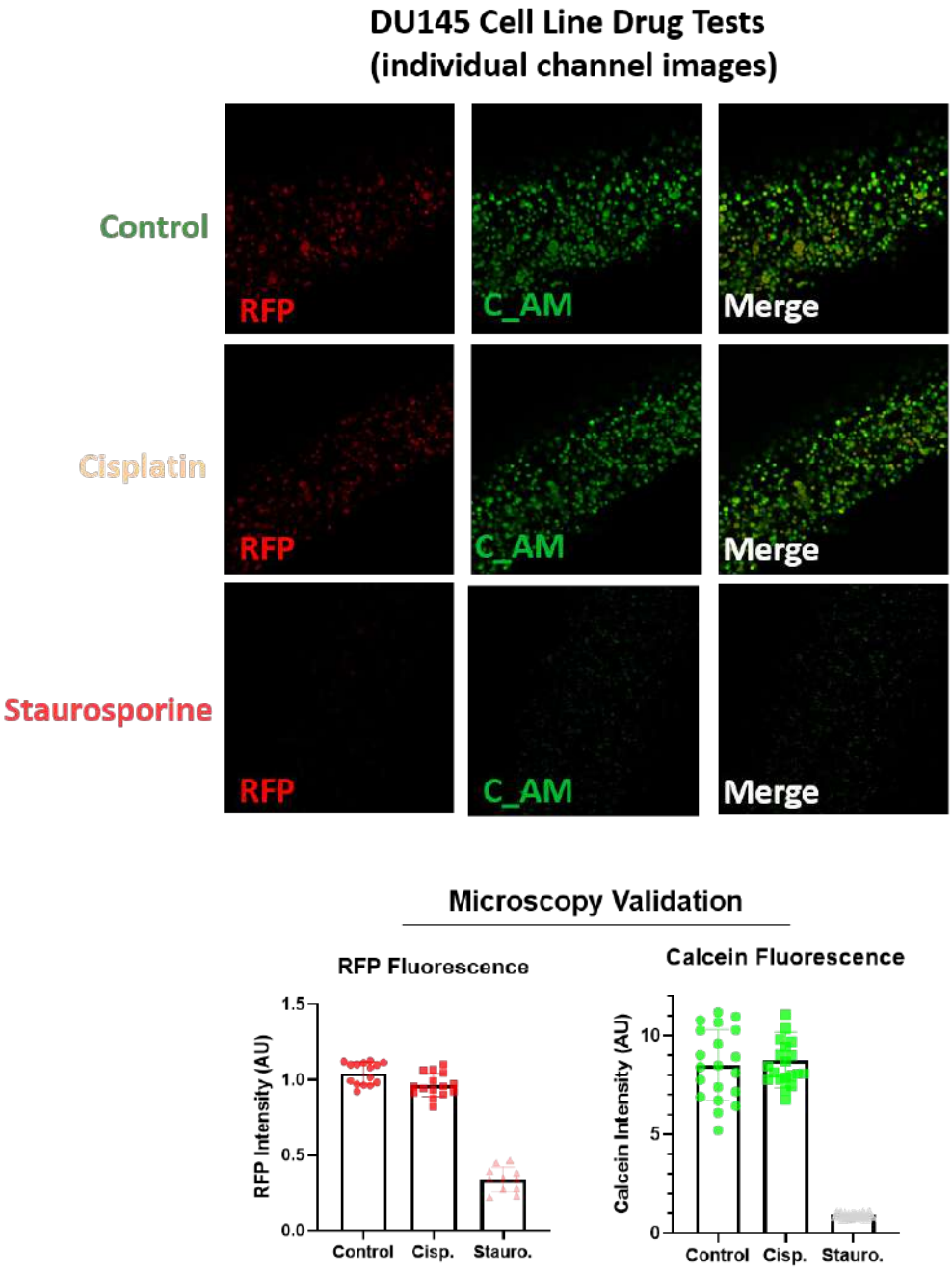
Supplementary Figure IX-16: a | Photograph of PCR tubes after LAMP RNA detection, evidencing the positive change in color in the fibers containing anti-SARS-CoV antibody after SARS-CoV-2 incubation. Positive and negative controls are pictured at the extremes. Fibers incubated with the virus without functionalized gold nanoparticles as well as fibers with gold nanoparticles incubated with blank solution are also present as controls. c | 570/650 absorbance quantification of the different solutions, showing the positive presence of SARS-CoV-2 RNA in fibers with anti-SARS AuNPs which have been incubated with the virus, validating viral capture within the hydrogel fibers.



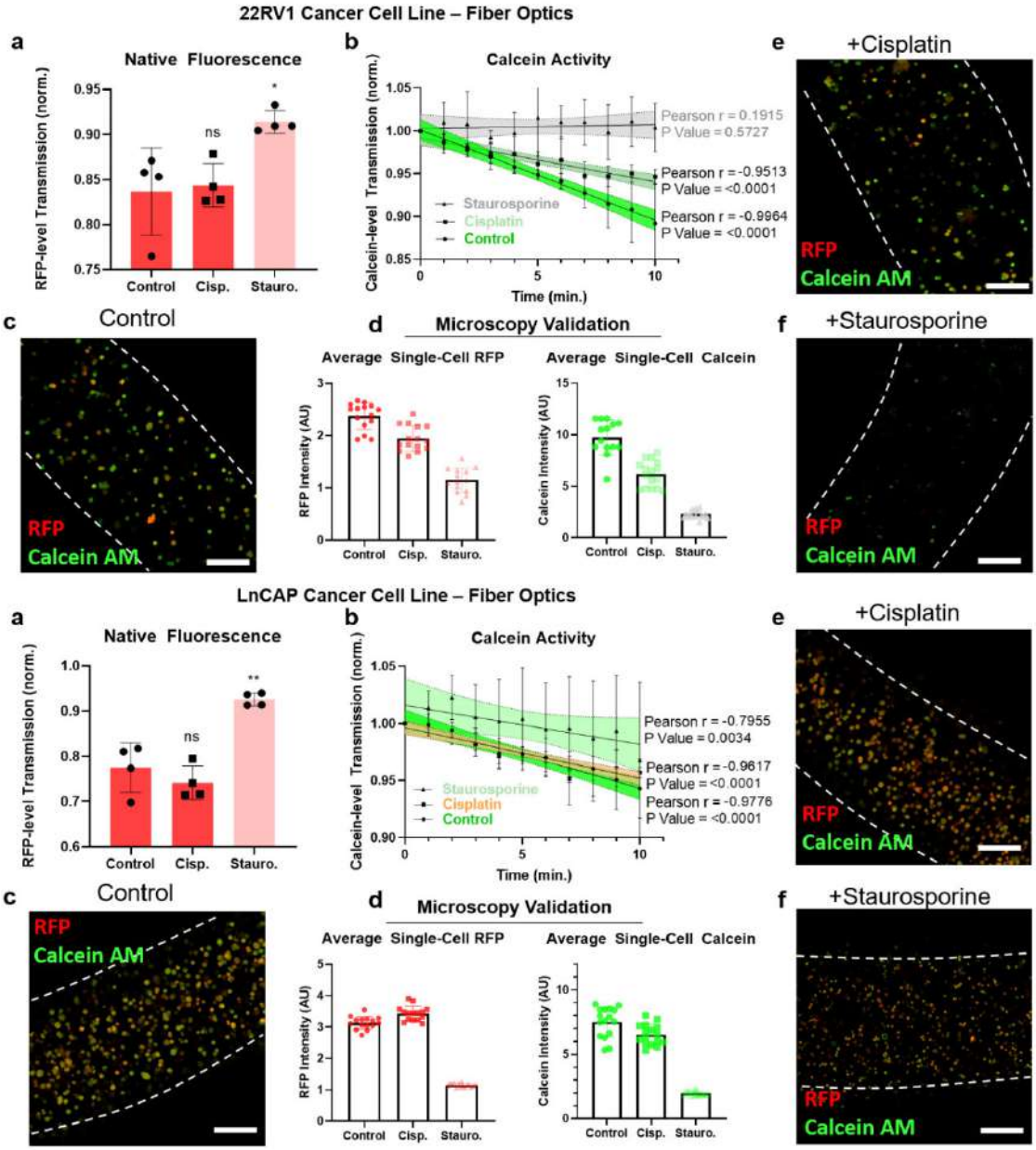
Supplementary Figure IX-17: a| Tri-coaxial nozzle configuration and detailed dimensions. b | Optical hydrogel fiber structures with cladding of 0.5% GG. c | Optical hydrogel fiber structure with cladding layer of 0.25% GG, where the low viscosity hinders the formation of a well arranged architecture, hence the use of a slightly higher concentration for fabrication of living optical fibers. d| Live/Dead Image of encapsulated 3T3 cells in the hydrogel fiber post-fabrication. e | Live/Dead Image of encapsulated 3T3 cells in the hydrogel fiber after cell culture. f | Quantification of the percentage of viable cells within the fiber both post-fabrication and after cell culture. Scale bars: 100 μm.



Supplementary Figure IX-18: a | Comparison between the optical fiber spectrum of cells stained with calcein versus unstained, with zoomed in region around the specific 495nm wavelength of metabolized Calcein AM. b | Comparison between the optical fiber spectrum of cells stained with orange cell tracker CMRA versus unstained, with zoomed in region around the specific 495nm wavelength of metabolized CMRA. c | Axial fiber cut of an optical core with a mixed population of calcein- and CMRA-stained cells. d | Multiplex analysis of fibers with different cell populations and their 495nm (green) and 550nm (orange) transmission intensity values. Fibro: Fibroblasts, unstained. Calcein: Fibroblasts stained with Calcein AM. Mix: 50:50 mixed population of calcein- and CMRA- stained fibroblasts. CMRA: Fibroblasts stained with orange cell tracker only.

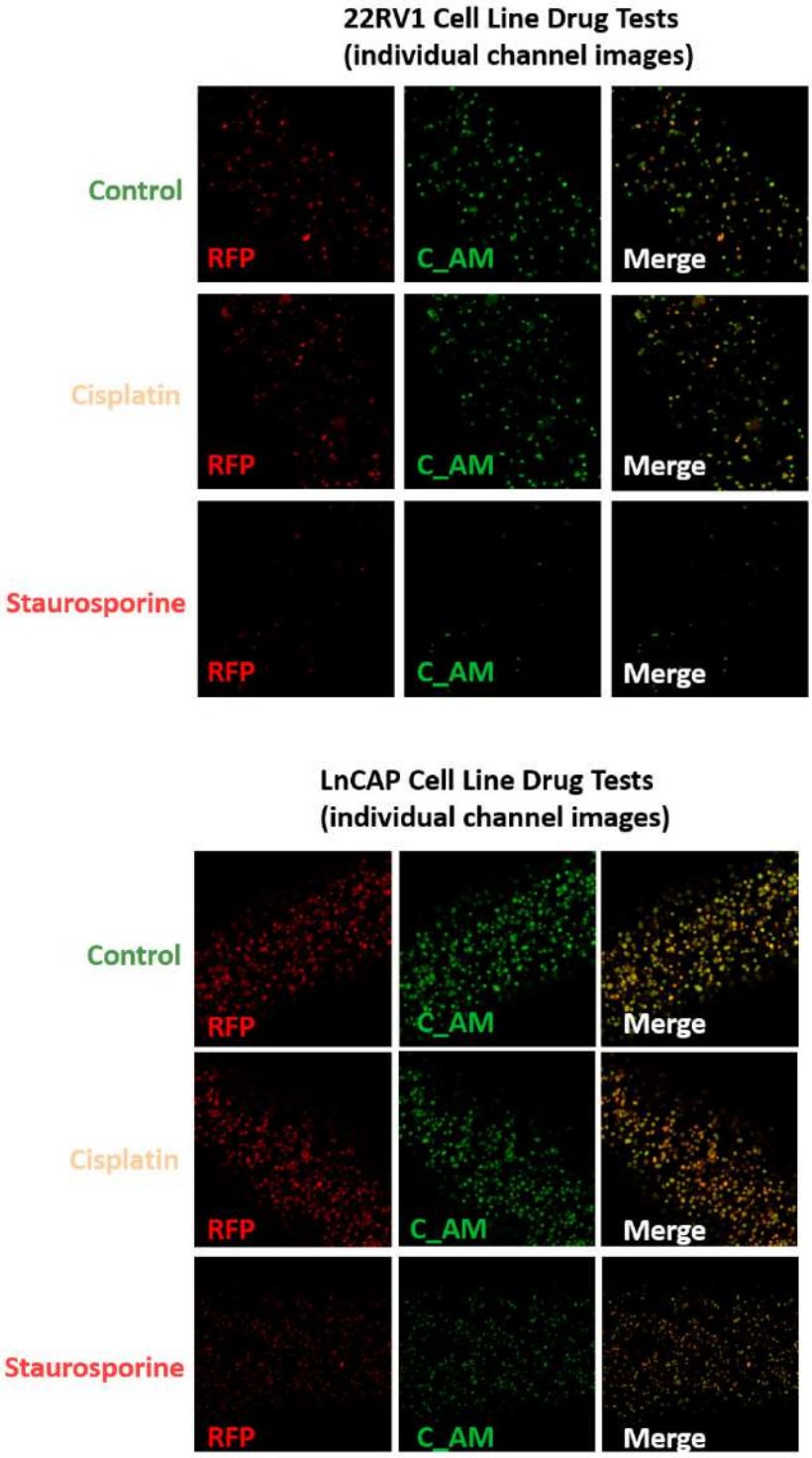


Supplementary Figure IX-19: DU145 individual channel fluorescent tests (representative images) on the top, followed by microscopic image analysis and quantification of RFP and Calcein intensities on different culture conditions (bottom).



Supplementary Figure IX-20: Additional Cell lines tested in optical fiber fingerprinting analysis. a| 22RV1 RFP fingerprinting data upon incubation with cisplatin, staurosporine and control conditions. b| Calcein AM metabolic activity tracked in real-time for the 22RV1 cell line in different culture conditions. c | Fluorescent image of the cells after staining with calcein together with natively expressed RFP. d | Image quantification results of multiple images across replicates for RFP and calcein intensity validation of optical fiber readouts. e, f | Microscopy images of 22RV1 cells after staining with calcein post-culture in the presence of 1.5 μM cisplatin and 1 μM staurosporine, respectively. Bottom: a | LNCaP-RFP-Trop2-OV fingerprinting data upon incubation with cisplatin, staurosporine and control conditions. b| Calcein AM metabolic activity tracked in real-time for the LNCaP-RFP-Trop2-OV cell line in different culture conditions. c | Fluorescent image of the cells after staining with calcein together with natively expressed RFP. d | Image quantification results of multiple images across replicates for RFP and calcein intensity

validation of optical fiber readouts. e, f | Microscopy images of LNCaP-RFP-Trop2-OV cells after staining with calcein post-culture in the presence of 1.5 μM cisplatin and 1 μM staurosporine, respectively.



Supplementary Figure IX-21: Individual channel fluorescent images of representative 22RV1 (top) and LNCaP-RFP-Trop2-OV (bottom) optical fibers after culture in the presence of drugs and control conditions.

SECTION 4

CONCLUDING REMARKS

Chapter X

CONCLUSIONS AND OUTLOOK

CONCLUSIONS AND OUTLOOK

The studies conducted under the scope of this thesis represent necessary steps forward for the fields of biofabrication, tissue engineering, and 3D living models by leveraging microfluidic techniques to create innovative constructs and platforms that integrate critical advances so far unreported, namely:

- **Chapter VII -** High-throughput fabrication of independent cell-laden microfibers with 3D gradient variations in composition, capable of integrating full ranges of i) Polymer concentration and mechanical properties, ii) Types of materials, and iii) Types of crosslinking within a single sample.
- **Chapter VII -** The high-throughput platform combines for the first time i) quick and effortless production, reducing post-processing, ii) continuous, not discrete, analysis of single-cell responses along the gradient, iii) correlation between cellular response, gradient position, and corresponding material composition, through microscopic image analysis, and iv) proven recapitulation of the responses taking places in larger hydrogels, such as the ones eventually applied for tissue engineering and regenerative medicine.
- **Chapter VIII -** Microfluidic 3D flow-focusing hydrogel manipulation, beyond composition, can single-handedly generate a wide variety of 3D microfiber compartment architectures, all of it using a single chip to control precursor flows before crosslinking.
- **Chapter VIII -** The flow-focusing wet-spinning method employed enables a significant reduction of total hydrogel fiber diameter to below 50µm, enabling compartment shape maintenance.
- **Chapter VIII -** The varied shapes can sustain different materials and cell types, which can approach biological environments, such as i) vascular networks, ii) model diseases such as 3D cancer/basement membrane/stroma models, iii) as well as create multi-chemistry constructs capable of transporting stem cells and gradually releasing the factors necessary to stimulate their differentiation.
- **Chapter IX -** Multi-compartment hydrogel fibers were uniquely tuned to guide light, uncovering a yet-untapped interface between natural polysaccharide hydrogels and photonics. The hydrogel fibers can guide light and report on 3D physical cues such as curvature and compression.
- **Chapter IX -** The integration of optically active structures such as plasmonic nanoparticles enables a plasmonic resonance sensing mechanism, which can sense antibody-antigen

interactions for detecting biotargets such as SARS-CoV-2 antigens and whole viruses. These fibers can be easily adapted and manipulated to, e.g., integrate standard medical swabs.

- **Chapter IX -** The unique capacity of the polysaccharides to encapsulate cells enables the creation of living optical fibers where light guidance can be directly combined with the encapsulation of living cells. The cell-light interactions allow for converting varied biological events into a directly quantifiable optical output. This process is then used to digitalize 3D cancer growth and protein expression, enabling the fast identification of functional anti-cancer drug thresholds without sample destruction or any downstream processing.

Even though these results lay essential foundations for the fields of cell/biomaterial screening, 3D tissue modeling, and the capacity to convert biological events into quantifiable biomedical data, there are still important steps to be taken toward expanding their capabilities, namely focusing on:

1. The existing gap between 3D cell/material constructs and high-throughput platforms with truly 3D image screening and analysis. Even if the employed 2D image processing methods enable faster and computationally less demanding analysis of cell responses, the types of parameters that can be screened are still limited (e.g., lack of accurate volume information).
2. The optimization of the material composing the 3D microfibers to obtain improved cellular responses, such as the complete and uniform tubular development of endothelial cell-laden fibers to recapitulate actual vascular lumen structures.
3. The exploration of polysaccharide-based optical fibers to take advantage of the inherent biological compatibility of the hydrogel materials within environments with different compositions, such as directly integrating living tissues for biosensing or monitoring 3D physical deformations.
4. In that scope, the low refractive index of the presented structures may be advantageous for releasing light into tissues (*e.g.*, phototherapy) but present a challenge if the goal is to guide light through the tissues and obtain a readout elsewhere. To overcome that challenge, different approaches should be explored, such as combining the ionic-crosslinking polysaccharides with other molecules or even interpenetrating hydrogel networks, which may increase refractive index values while maintaining the transparency and biological compatibility of the fiber core.
5. Tuning of living optical fibers to analyze different complex 3D responses other than the demonstrated cancer proliferation. Within cancer modeling, the cladding hydrogel layers

may be leveraged to reflect light back into the core and integrate, e.g., different cellular components of the cancer microenvironment, leading to a more complex model where cell-cell crosstalk and dynamic migration events may be quantified using light alone. Naturally, to address different types of responses and integrate varied cell types, specific optimizations in the material composition may have to be performed. These modifications can never ignore the need for a certain degree of transparency that enables light guidance and light-cell interactions to take place.

Together, these avenues of study present exciting future opportunities in hydrogel biofabrication towards engineering ever more relevant 3D models of healthy or disease tissues in dynamic and physiologically relevant environments. Combined with the possibilities that light-driven analysis presents for the fast and accurate quantification of cell responses, the technologies explored in this thesis may be important players in the generation of biological data and their integration with ongoing advances in data science. Together, the combination of next-generation 3D models and reliable quantification of biological events may help realize the promises of truly personalized medicine and data-driven healthcare.